Timing, Kinematics, and Spatial Distribution of Miocene Extension
in the Central Arabian Margin of the Red Sea Rift System

by

Eugene Szymanski

B.S., Bloomsburg University of Pennsylvania, 2000
M.S., Boston College, 2005

Submitted to the graduate degree program in Geology and the Graduate Faculty of the University of Kansas in partial fulfillment of the requirements for the degree of Doctor of Philosophy.

_____

Co-Chair: Daniel F. Stockli

_____

Co-Chair: J. Douglas Walker

_____

Stephen Egbert

_____

Diane Kamola

_____

Anthony Walton

Date Defended: 02/01/2013

The Dissertation Committee for Eugene Szymanski

certifies that this is the approved version of the following dissertation:

Timing, Kinematics, and Spatial Distribution of Miocene Extension
in the Central Arabian Margin of the Red Sea Rift System

_____

Co-Chair: Daniel F. Stockli

_____

Co-Chair: J. Douglas Walker

Date approved: 02/01/2013

1. Abstract

Timing, Kinematics, and Spatial Distribution of Miocene Extension
in the Central Arabian Margin of the Red Sea Rift System

by

Eugene Szymanski

Department of Geology, February 2013

University of Kansas

The Arabian-Nubian Shield (ANS) existed as relatively stable craton on the southern Neo-Tethyan passive margin until rifting of the continental lithosphere borne the Arabian Plate with the advent of the Red Sea-Gulf of Suez rift system. Examination of the thermotectonic record via apatite and zircon (U-Th)/He thermochronometry (AHe and ZHe) on Proterozoic basement rock within the exhumed SW Arabian Plate, detrital AHe thermochronometry on syn-rift sedimentary packages, whole-rock $^{40}Ar/^{39}Ar$ dating and X-Ray fluorescence analyses of syn-and post-rift flood basalts, and numerical time-temperature modeling of AHe and ZHe systems reveal a three-stage thermotectonic history for the central Arabian rift flank (CARF). First, the pre-rift ANS experienced a Paleo-Mesozoic cooling event that brought the proto-CARF to a mid-to-upper crustal structural level where it remained thermally stable through the Mesozoic. Then, a major rift pulse ca. 23 Ma exhumed a 200 km-wide area of the CARF, marking the onset of diffuse lithospheric extension that endured for 8 million years until a middle Miocene regional stress realignment transferred major faulting towards the modern RSR and Gulf of Aqaba. The 23 Ma rift onset age is mirrored in thermochronometric and sequence stratigraphic analyses elsewhere along the full Red Sea Nubian margin and the southern Arabian rift flank in Saudi Arabia and Yemen, confirming that RSR initiation occurred concomitantly along the full Red Sea-Gulf of Suez rift system in opposition to proposed south-to-north rift propagation models. A passive rift model is favored due to the absence of an elevated pre-rift thermal signal within the ANS and the fact that CARF harrat volcanism trailed rift onset by 6 million years. Arabian rift flank architecture differs greatly along RSR-strike; relatively rigid continental lithosphere comprises the southern Arabian margin while a broad zone of deformation begins north of the Makkah-Madinah-Nafud volcanic line and expands through the NW Arabian Plate where it encompasses syn-rift extensional structures such as the Azlam and Tabuk graben and Hamd-Jizl Basin.

2. Acknowledgements

Thank you to my co-advisors Daniel F. Stockli and J. Douglas Walker for the opportunity to learn alongside you. Your mentorship both in the field and the lab holds incalculable value and has made me a far better geologist. Thank you to PhD committee members Diane Kamola, Anthony Walton, and Stephen Egbert for their supervision and thorough revisions. Thank you to Peter R. Johnson for robust revisions to two chapters and for conveying your vast knowledge of Arabian-Nubain Shield geologic history. Your willingness to mentor me and guide my thinking about the Red Sea Rift and Arabian-Nubian Shield greatly improved my research and I share with you any credit for the conclusions. Thank you to Abdullah Al Shammari, my field and cultural liaison. You often managed to make the long working days a bit easier and I often think of sharing tea in the shade of the single living tree you managed to find for miles around in the desert. I'll always remember the feeling of great adventure we shared in the field. .لي جزرا كش

Thank you to Dr. Zohair A. Nawab, president of the Saudi Geological Survey, for allowing tremendous field accommodations and logistical support at the Madinah Earthquake and Volcano Observatory Field Station. From the simplest local bread and *foul* for breakfast to the incredible helicopter support complete with expert pilot (Peter) and fuel, nothing could have been accomplished without your generosity during three lengthy field excursions (2006, 2007, 2009) in the Kingdom. Thank you specifically to SGS associates Fayek H. Kattan, Khaled A. Kadi, Ian C.F. Stewart, and M. John Roobol (especially for the Harrat Rahat field excursion). Thank you to George Vranas. The hospitality you and Peter gave me while in the Kingdom was particularly generous and your observations on life as an expat in Arabia were always entertaining.

Thank you to Shota Adamia for consult on Quaternary volcanism in the Lesser Caucasus and for lively discussion in the field near Akhalkalakhi. Working with you is always enjoyable and enlightening culturally and I'm honored to have the first MGHe-dated Eurasian magnetite come from Sakartvelo.

Thank you to Christian Hager and Roman Kislitsyn for their development of t-T history modeling (*HeMP*) and (U-Th)/He age reduction (*Helios*) software. Without your innovative coding, many of us may still be mired in a sea of uninterpreted data. Thank you to IGL labmates Jeffrey Schroeder, John P. Lee, Markella Hoffman, Melissa R. Wolfe, and T.J. Blackburn. It was a pleasure sharing my time at KU with you. Thank you to Jordan-Leigh Taylor and Steve Reidel for providing CRBG sample WR-1 and helpful discussion regarding the true geologic age. Thank you to Heather Shinogle and David Moore the University of Kansas' Microscopy and Analytical Imaging (MAI) Lab for time-saving instruction on lab instrumentation. Finally, thank you to the following donors for financial contributions to research: The University of Kansas for Summer Research Grants in 2007, 2008, and 2009; the National Science Foundation's MARGINS Program (Grant OCE-0305731 to Stockli); the American Association of Petroleum Geologists (Grant in Aid); The Geological Society of America (Grant No. 8663-07), and NASA Land Processes Distributed Active Archive Center.

3. Dedication

This effort is dedicated to my two loving parents, Gene and Dianne. Your unwavering support in each aspect of life is motivating, worthy of recognition, and appreciated beyond mere words. Thank you for everything.

4. Preamble

This dissertation comprises two main research topics within three separate chapters with the intent to submit each independently as manuscripts for publication. Chapters 1 and 2 present the results of low-T apatite and zircon (U-Th)/He thermochronologic research (AHe and ZHe) in the central Arabian rift flank (CARF) of the Red Sea rift (RSR) system. Our research addresses the thermotectonic development of the SW Arabian Plate from Paleo-Mesozoic deformation in the Arabian-Nubian Shield through the Cenozoic development of extensional structures and rift-related basaltic volcanism within the early Miocene Red Sea Rift margin in Saudi Arabia. Chapter 3 addresses advancements in the magnetite (U-Th)/He geochronometric technique (MGHe) including a refinement of the current analytical method for mafic and intermediate rock-magnetite, an expansion of the dating technique into more felsic-rich host rock types, and an exploration of MGHe age standard development within rhyodacitic rock that bears well-established apatite and zircon (U-Th)/He age standards.

Investigation of the central and northern Arabian rift flanks began under the auspices of the National Science Foundation's MARGINS Rupturing of Continental Lithosphere (RCL) initiative, which set forth to explore the geodynamics of continental lithosphere rifting and subsequent rupture, and quantify the driving forces that shape these margins, at several classic sites of divergent margin development. Our research objectives are well-aligned with three of the five overarching MARGINS RCL initiative themes proposed in the original 2004 MARGINS Science Plan: (1) How is strain partitioned during lithospheric rupturing?, (2) What is the role of magmatism (and volatiles) during extension and what is the relationship between magma petrogenesis and the deformation magnitude and history?, and (3) What is the stratigraphic response to lithospheric rupturing? Chapter 1 focuses specifically on rift flank architecture at

RSR onset and resolves the structural, sedimentological, and volcanological evolution of the Hamd-Jizl Basin (HJB). Fieldwork consisted of geological mapping, and bedrock and basalt sample collection, in the HJB over three field seasons (2006, 2007, and 2009) with full logistical support of the Saudi Geological Survey headquartered in Jeddah. Employed analytical techniques include apatite and zircon (U-Th)/He thermochronometry of footwall exhumation in the Hamd and Jizl half-graben, detrital apatite (U-Th)/He thermochronometry of the syn-rift, siliciclastic Qattar Formation, and whole-rock $^{40}Ar/^{39}Ar$ dating and XRF analysis of harrat basalts that interact with HJB volcano-sedimentary strata and border faults. Chapter 2 addresses the greater Paleo-Mesozoic and younger thermotectonic history of the SW Arabian Plate with a primary concentration on CARF-wide structural evolution from RSR onset through progressive rifting. We present a comparative analysis of strain timing and dissemination between the HJB and the strain markers that frame the modern rift margin, the Hijaz Mountains Fault Complex, via a combined approach of bedrock AHe and ZHe thermochronometry and numerical time-temperature modeling within the MATLAB-based *Helium Modeling Program* (HeMP©) written by Christian Hager.

Chapter 3 introduces a refined magnetite (U-Th)/He age dating method for mafic and intermediate rock types and includes an initial assessment of two potential MGHe age standards, Durango rhyodacite and Fish Canyon dacitic tuff. As part of a high-level correlation of overall dissertation objectives, our initial motivation for refining the MGHe dating method stemmed from the need to date basaltic magnetite for age determination of several Cenozoic basalt flows that lie within the HJB. Arabian basalt analyzed for this research originate from two spatially overlapping basalt provinces, Harrat Kura and Harrat Ishara, that interact with several key basin structural elements and the syn-rift Qattar Formation within the HJB. Accurate MGHe dating of

the SAB suite would provide temporal tie points for basin evolution themes such as the timing, rate, and magnitude of syn-rift sedimentation and the inboard extent of Red Sea Rift-related deformation on the central Arabian rift flank. Refinement of the MGHe technique and application to silica-rich rock types was only possible due to the pioneering effort of Terrence Blackburn and Dr. Daniel Stockli who developed the fundamental MGHe technique at the University of Kansas Isotope Geochemistry Laboratory.

5. Table of Contents

6. Figures List

CHAPTER 1 **PAGE**

CHAPTER 2

7. Tables List

CHAPTER 1 **PAGE**

CHAPTER 2

CHAPTER 3

8. Appendices

CHAPTER 1 **PAGE**

CHAPTER 2

CHAPTER 3

1. Chapter 1: A Sustained Phase of Diffuse Lithospheric Extension in the Central Arabian Flank during Red Sea Rift Initiation: Syn-rift Faulting, Terrigenous Sedimentation, and Basalt Volcanism in the Hamd-Jizl Basin, Saudi Arabia

1.1. Abstract

The Red Sea is a continental rift that has not ruptured in the central and northern sections. Broad dissemination of rift-related lithospheric strain, evidenced by the development of extensional structures within the Arabian rift flank, has prevented full rupture of the continental lithosphere. Multiple lines of evidence prove a genetic tectonic relationship between the modern Red Sea Basin and the Hamd-Jizl Basin, a composite syn-rift structure that comprises two half-graben within the central Arabian rift flank ~200 km inboard of the modern rift margin, thus revealing an initial episode of diffuse lithospheric extension during the first 8 million years of Red Sea rift development.

Hamd-Jizl Basin (HJB) developmental stages are recognized by temporally distinct deformational, depositional, and volcanological events whose timing often coincides with those of the Red Sea Basin. Bedrock and detrital apatite (U-Th)/He thermochronometrics show an initial phase of rapid footwall exhumation in the Hamd and Jizl half-graben ca. 22 Ma, which caused an accumulation of a derivative syn-rift, siliciclastic sedimentary package, the Qattar Formation, proximal to the active border fault in both half-graben. Deposition of the Qattar Formation occurred primarily from ~22-17 Ma, revealing that syn-rift sedimentary product developed across a broad margin of diffuse continental rifting during the early tectonic development of the nascent Red Sea rift system. A second extensional pulse ca. 17 Ma produced disproportionate movement along the border fault in the southern Hamd half-graben and tilted

the syn-rift package ~30° to the NNW prior to strain (and major sedimentary depocenters) migrating basinward to the modern RSR margin in the middle Miocene. Trailing the initial continental lithosphere rift pulse by ~6 million years, voluminous basalt volcanism initiated in the HJB hanging wall contemporaneous to a second stage of footwall exhumaiton. Harrat Ishara produced two geochemically distinct generations of basalt volcanism between 17-12 Ma (Ishara A and B) that covered an area >300 km^2 when they sealed-in the Qattar Formation in the southern and central Hamd half-graben at 17 Ma and 15 Ma, respectively. Ishara basalt units decrease in alkalinity and REE abundances with time; the geochemical shift between Ishara A and B signals either ongoing melt fractionation processes or output from separate magma chambers with time. Diffuse rift flank deformation and basalt volcanism continued through the middle Miocene with footwall exhumation in the Jizl half-graben at Jabal Nahar, minor post-depositional deepening of the Hamd half-graben where intra-basinal faults juxtapose 14.5 Ma Ishara basalt flows against the Qattar Formation, and continued eruption of the uppermost Ishara basalt until 12 Ma. Strain development ceased in the HJB ca. 12 Ma and progressed basinward toward the modern rift margin, contemporaneous with regional tectonic plate margin reorganization.

The identification of syn-rift extensional faulting, terrigenous sedimentation, and basalt volcanism in the HJB certifies the diffuse character of the initial Red Sea rift stage and reveals that at least this portion of the nascent Red Sea rift margin operated as a ~200 km-wide zone of diffuse continental rifting (distance from the modern Red Sea axial trough to the HJB). By proving the syn-rift nature of the HJB, the results of this study expand the area of Arabian rift flank that is recognized to have deformed extensionally during the initiation of Red Sea rifting

and warrant the inclusion of the HJB into the category of "relict basin", alongside other intra-marginal basins that have been abandoned since their origination at the onset of RSR development in the late Oligocene-earlyMiocene.

1.2. Introduction

The Red Sea rift system (RSR) is the classic field setting in which to study the modes and mechanisms of orthogonal rifting in continental lithosphere due to the excellent three-dimensional exposure of both the African and Arabian plate margins. Numerous geologic research expeditions have contributed significantly to the general understanding of Red Sea rift timing and structural style. RSR onset began in the late Oligocene according to evidence provided by marine and terrigenous sedimentary packages in the initial broad rift zone and modern Red Sea basin (Schmidt et al., 1983; Dercourt et al., 1986; Montenat et al., 1988; Crossley et al., 1992; Bosworth et al. 1998; Abou Ouf and Gheith, 1998; Hughes and Johnson, 2005 *and references therein*) and pre-rift volcanic rock suites in Saudi Arabia and Yemen (Coleman et al., 1983; Davison, 1994; Chazot et al., 1998). Tholeiitic dikes trend subparallel to the modern orientation of the RSR axial trough, modify the crust, and create crustal-scale half-graben that contain volcanic and sedimentary rock suites of various Cenozoic ages (Suayah et al., 1991; Suayah, 1992; Coleman, 1993; Johnson and Stewart, 1995). The prominence of these syn-rift elements, found along both Red Sea margins with varying style and degree (Smith, 1979; Abou Ouf and Gheith, 1997, 1998; Hughes and Johnson, 2005), attest to the ubiquitous crustal thinning and brittle straining of rocks from SW-NE oriented extension.

Thermochronological investigations within the Gulf of Suez-Red Sea rift system have identified the timing and nature of some geodynamic processes responsible for continental

lithosphere modification in the northern and southern termini of the RSR (e.g., thermal pulses; Omar and Steckler, 1995) and scarp development along the Sudanese rift flank (Balestrieri et al., 2009), but these results remain relevant to those particular study regions as the RSR conjugate margins show asymmetrical structural deformation which often changes along rift strike (e.g., Lister et al., 1986). Moreover, some studies have insufficient 2-dimensional sample array coverage along the full Arabian rift flank (e.g., Bohannon et al., 1989; Menzies et al., 1992) and/or too broad a sample spacing to capture intra-marginal deformation. Proper characterization of rift style within a rifted margin requires a kilometer-scale level of structural and thermochronological study to accurately capture intra-marginal deformation and chronicle rift flank modification over time. Sample-spacing frequency on the structural component scale (e.g., individual fault blocks) is needed to address the thermal evolution of rift flank basement in order to resolve inherent rift flank structural kinematics and examine the changing relationship between rift elements with progressive deformation, such as the variable rate and style of syn-rift sediment deposition with increased footwall exhumation. Thermochronological study of rift-related crustal deformation within the Arabian margin northwest of the city of Jeddah is essentially non-existent.

We quantify deformation within the central Arabian rift flank by exploring the structural nature and tectonic affinity of the Hamd-Jizl Basin, a fault-bound, syn-rift extensional basin northwest of Jeddah that parallels the trend of the main Red Sea rift ~140 km inboard from the coastal plain fault complex that frames the modern RSR basin (Fig. 1). Abundant extensional structures, exposed sedimentary rock outcrop, and volcanic features within the Hamd-Jizl Basin (HJB) provide opportunity to quantify the timing and magnitude of crustal strain development,

thus revealing the evolution of rift architecture within the central Arabian rift flank (CARF) of the burgeoning Red Sea rift system. Reconnaissance mapping by the Saudi Geologic Survey, and their predecessors, have produced original reports (e.g., Brown, 1970; Kemp, 1981, 1982) that identify the relative age of most geologic elements within the HJB yet, prior to this study, the close genetic association between the Red Sea rift and the HJB had not been proven. We combine multidisciplinary techniques to resolve the spatial and temporal evolution of HJB structural deformation and explore CARF structure not studied in detail previously. We draw evidence for rift-related strain development, and a genetic tie between the HJB and RSR, from the following sources: 1) apatite and zircon (U-Th)/He age data from crystalline basement within the Arabian Shield, 2) detrital apatite (U-Th)/He age data from syn-rift sedimentary rock within the Hamd-Jizl Basin, and both 3) whole-rock $^{40}Ar/^{39}Ar$ age data and 4) major and trace element geochemical data of syn- and post-kinematic basalt flows that erupted from local volcanic centers.

Bedrock apatite and zircon (U-Th)/He thermochronometrics of extensional structures founded on crystalline basement provide a record of rift timing and strain dissemination within the CARF. Sedimentological analyses and detrital apatite (U-Th)/He thermochronological data prove the tectonic provenance and depositional timing of the Qattar Formation, a terrigenous syn-rift sedimentation product of early Miocene age present within the Hamd-Jizl Basin. Our approach treats sediment accumulation in the Hamd-Jizl Basin as a record of Red Sea rift system evolution and we constrain the dynamics of rift flank deformation through the depositional timing and spatial distribution of the Qattar Formation. In addition to bedrock and detrital (U-Th)/He thermochronometry, we employ whole-rock $^{40}Ar/^{39}Ar$ dating and a full geochemical

characterization of basalt flows that enter the HJB from local volcanic centers and overlap syn- and post-kinematic basin structures. Prior to our study, K/Ar age determinations comprised nearly the entire amount of published age data for basalt from Harrat Khaybar and Ishara, the two major basalt provinces in the HJB region (e.g., Brown, 1970; Brown et al., 1989; Camp et al., 1991). Though the age range of these legacy data correctly categorize Harrat Ishara as part of the first volcanic phase (late Oligocene and younger), this collective dataset requires refinement for our study since the K/Ar age dating technique is notoriously inaccurate and existing age data points are either too sparsely located or unreliably cited to extrapolate accurate conclusions regarding the relative timing of Ishara basalt/HJB structure interaction. Our $^{40}Ar/^{39}Ar$ age suite allows a greater resolution of HJB basalt flow ages than has previously been published and, as a primary focus, we provide the first accurate age range and volcanostratigraphic division of Harrat Ishara by documenting the crystallization ages of Ishara basalt in the HJB. Additionally, we detail the major, trace, and rare earth element content of Harrat Ishara to document its geochemical evolution with time.

Our study of HJB rift elements is the first to quantitatively define RSR-related deformational timing and spacing by coupling structural and thermochronological analyses at a scale appropriate to constrain the spatial and temporal strain history of the CARF (and resolve pre-existing data deficiencies). Most importantly, our identification of the tectonic provenance and kinematic framework of the HJB allows us to extrapolate our results onto larger-scale models of continental rift processes specific to the RSR.

1.3. Research Objectives

The continental lithosphere in the central and northern portions of the RSR has not yet ruptured while the southern RSR contains magnetic anomalies that attest to the generation of oceanic crust ca. 6 Ma and ongoing seafloor spreading (Lowell and Genik, 1972; Cochran, 1983; Mooney et al., 1985; Prodehl, 1985; Coleman and McGuire, 1988; Voggenreiter et al., 1988; Coleman, 1993; Cochran and Karner, 2007 *and references therein*). This changeover in rift development occurs across ~23 ºN latitude and is coincident with apparent, along-strike changes in flanking geologic features such as the presence of intra-margin extensional basins in the central and northern, but not the southern, Arabian rift flank (Cochran and Martinez, 1988; Martinez and Cochran, 1988). This variability implies that lithospheric character, inherent to the Arabian margin, exerts control on rift style. Thus, structural, sedimentological, and volcanological analyses of rift elements in the central portion of the RSR, which specifically define CARF rift character, can reveal possible cause for the dissimilarity of northern versus southern rift styles. Our research efforts concentrate on extensional deformation, sedimentation, and basalt volcanism in the Hamd-Jizl Basin, the most prominent RSR-related strain marker within the CARF.

Ultimately, our characterization of HJB spatiotemporal evolution allows an exploration of broader questions concerning continental rift evolution, especially those regarding the influence and interaction of pre-existing lithospheric structural grain, pre- and syn-rift sedimentation, and magmatism. The following questions are the focus of this research: When and why did the HJB develop within the Arabian rift flank? What fundamentally controls the spatial distribution of extensional structures and how does their strain accommodation role evolve with progressive

rifting? How is shallow lithospheric strain disseminated across the rift margin throughout the lifetime of a continental rift system from initial lithospheric stretching to the onset of seafloor spreading? What is the true depositional age of syn-rift sedimentary packages in the HJB? How laterally extensive was the development of marginal syn-rift sedimentary packages derived from Red Sea rifting and what does their generation reveal about the stratigraphic response to crustal extension? Finally, how does harrat volcanism in the vicinity of the HJB vary geochemically and volumetrically with time? What insight does this provide regarding the role of magmatism during initial lithospheric extension and how does flood basalt petrogenesis then evolve with progressive basin deformation?

1.4. Geologic Setting

1.4.1. Precambrian to Mesozoic Geology of the CARF in the HJB region

The central Arabian rift flank (CARF) includes a large portion of exposed Precambrian basement within the Arabian Plate, known as the "Arabian Shield", that is an assemblage of temporally separate but spatially inter-related structural domains of various age imprinted upon geologic terranes of Proterozoic age. Prior to the origination of the Arabian Plate in the Cenozoic, the proto-CARF formed part of the Arabian-Nubian Shield (ANS) as an agglomeration of multiple geologic terranes that sutured to Africa and east Gondwana during the East African Orogen (Johnson, 1998 *and references therein*). This shield-building event marks the beginning of the Proterozoic Hijaz Orogenic Cycle, a long-lived series of orogenic events that includes periods of island arc and ophiolite accretion (780-680 Ma), granitoid plutonism, mafic dike injection, and large scale strike-slip faulting (580-530 Ma) known as Najd faulting (Brown and Jackson, 1960 in Moore, 1979; Brown and Coleman, 1972; Fleck et al., 1976;

Johnson, 2006). The late Proterozoic Najd Fault System (NFS; Moore, 1979) is a 1200-km long, 300-km wide zone of en echelon strike-slip faults oriented NW-SE that completely cut across pre-existing tectonic terrane boundaries and imprinted a deep-seated structural fabric, during more than one episode (Agar, 1987), that pervades a good portion of the exposed Arabian and Nubian Shields (Stern, 1985; Sultan et al., 1988; Ghebreab and Talbot, 2000). Within the CARF, this structural grain exists as an organized set of inactive WNW-ESE-trending transcurrent faults that, to varying degrees, exerted control on the orientation of subsequent normal faults, erosional valleys, and, consequently, the channels that direct Cenozoic basalt flows peripheral to the main basalt fields.

Situated mostly within the Hijaz Terrane, one of the accreted Proterozoic terranes that form the ANS (Johnson, 2006), the modern CARF has a structural architecture that encompasses portions of regional Phanerozoic geologic elements such as the Ha'il–Rutbah Arch, the Makkah-Madinah-Nafud (MMN) volcanic line, mafic dike swarms parallel to the Red Sea axial trend, and a few pre- and syn-rift extensional basins bound by pervasive Cenozoic faults found within the Arabian rift margin (Al Laboun, 1986; Pallister, 1987; Camp et al., 1989; Bosworth et al., 2005 *and references therein*; Roobol and Kadi, 2008). Bedrock in the HJB region is comprised primarily of three Proterozoic age units: silicic volcanic rock of the Farri Group, shallow to deep marine volcano-sedimentary sequences of the Al Ays Group, and marine realm basaltic to andesitic volcanic rock of the Hadiyah Group, each of which has collectively undergone at least three greenschist-grade and one amphibolite-grade phases of metamorphism (Kemp, 1981). Scattered within these units are subordinate volumes of granitic, monzonitic, and dioritic

intrusive rock suites of the Proterozoic age Rithmah and Abu Safiyah Complexes and a large, unnamed granodiorite of indeterminate Protero-Paleozoic age (Pellaton, 1979; Kemp, 1981).

During the greater part of the Paleozoic and Mesozoic eras, the ANS operated as a portion of the southern passive margin of the Tethyan oceanic realm. In places, thick marine sedimentary sequences developed along the passive margin on either side of a NNW-SSE paleo-topographic high (Powers et al., 1966) in the area that was to become the northeastern Arabian Plate, including the Arabian Gulf. Today, a significant portion of these marine strata is preserved as a large subaerial expanse of rock known as the "sedimentary cover sequence" that emerged after the deposition of shallow marine carbonate shelf in the early Cenozoic (Sharland et al., 2001 *and references therein*), likely due to the complete subduction of the Neo-Tethyan oceanic crust beneath Eurasia. Contrarily, the proto-CARF region remained at a relatively high position within the crust during the period that the ANS served as a passive margin with no evidence of significant burial beneath sedimentary rock according to local stratigraphic sequences (Guiraud et al., 2005; Szymanski et al., *in prep.*). Nearly flat erosional surfaces of Oligocene age in Saudi Arabia and Yemen (Coleman, 1993) verify that the ANS region had remained devoid of significant topographic relief from the late Cenozoic to the inception of the Arabian Plate and none of the Paleo-Mesozoic sedimentary rock strata that exists elsewhere on the Arabian Plate is present in the CARF.

1.4.2. Cenozoic Geology and Structure of the CARF

Syn-rift extensional structures, their derivative sedimentary rock packages, and expansive flood basalt fields constitute the majority of Cenozoic age geologic elements on the CARF. Most pre-rift structures lay buried beneath subsequent volcano-sedimentary strata in the modern

Red Sea basin while many syn-rift elements survive on the uplifted rift flank. Roobol and Kadi (2008) define the Cenozoic faults along the Arabian rift flank as the Red Sea Fault System and subdivide this system into two groups: the Foothills Fault System and the Red Sea Coastal Plain Faults with the "Master Listric Coastal Fault", a large normal fault (or set of faults) delineating the border between the two structural domains. "Pre-rift" features in the Foothills Fault System include extensional structures that host steeply inclined dikes that injected into the NW Arabian Plate during a period of crustal attenuation prior to the first phase of Red Sea rift extension (Buck, 2004; Roobol and Stewart, 2009). Located in NW Saudi Arabia at the border with Jordan, the Tabuk graben, is founded upon the Great Ja'adah Dike and serves as a fine example of a "pre-rift" structure (Phoenix Corporation, 1985; Roobol and Stewart, 2009).

The Red Sea Coastal Plain Faults are the down-dropped, younger set of Cenozoic faults that originated during the first extensional phase of RS rifting (Roobol and Kadi, 2008), demonstrate normal rotational fault kinematics, and provide a pathway of least resistance for syn-rift basalt intrusion and voluminous flood basalt development. This structural domain hosts several extensional structures such as the Midyan, Esh el Mellaha, Aznam, and Yanbu Basins (Smith, 1979; Kemp, 1981; Suayah, 1991, 1992; Moustafa, 2002; Hughes and Johnson, 2005; d'Almeida, 2010). Bosworth et al. (2005) postulate that these extensional structures are "relict basins" that formed during initial RSR development but were subsequently abandoned during RSR strain localization ca. 15 Ma. Accordingly, Roobol and Kadi (2008) propose that the Red Sea Coastal Plain Faults developed within the area of continental crust that extended to form the main Red Sea Basin during rift onset while the neighboring Arabian Shield remained relatively undeformed. The primary focus of this investigation, the Hamd-Jizl Basin (HJB), lies inboard of

the "Master Listric Coastal Fault" within the relatively lesser-deformed Arabian Shield yet it shares a tectonic lineage with basins located proximal to the modern RSR basin. The HJB is positioned between 24.5° and 26° N latitude within the Hijaz Terrane of the Arabian Shield, ~140 km inboard from the Red Sea Coastal Plain Faults and ~80 km northwest of Al Madinah al Munawwarah (Fig. 1). Previously referred to as the "Jizl trough" and "Hamd graben" (Kemp, 1981; USGS, 1993; Johnson, 1998), the HJB is a NW-trending, composite extensional structure that composes two linked half-graben that jointly measure ~140 km along strike and up to 20 km in width (Fig. 2). Each half-graben is named for the primary wadi system within the basin; Jizl ("bounteous/abundant") and Hamd (*"praise"*).

Geologists working in the region have long recognized that structural fabrics developed during the Hijaz Orogenic Cycle effectively predetermine the course of many RSR structures (e.g., Brown, 1970; Davies, 1984; Dixon et al., 1987, 1989; Sultan et al., 1988; Ghebreab and Talbot, 2000). Three major terrane sutures within the CARF, the Yanbu, Bi'r Umq-Nakasib, and Ad Damm sutures, display NNE-SSW orientations that intersect the ~330° strike of the RSR at a high angle (Johnson, 1998). These sutures act as weak points in the lithosphere that rupture preferentially and control both the geometry of the Red Sea axial trough and the position of offshore deltas (Crane and Bonatti, 1987; Mitchell et al., 1992). Relatedly, three primary rift accommodation zones, the Shagara, Zabargad, and The Brothers Fracture Zones (Crane and Bonatti, 1987; Fig. 1), offset the central and northern Red Sea axial trough, transfer strain laterally, and prevent the development of high rift flank topography, a phenomenon observed in extended terranes including the Gulf of Suez (Faulds and Varga, 1998; Bosworth et al., 1998; Moustafa, 1997; 2002).

1.4.2.1. Red Sea rift structural models

Simple shear continental breakup models (Wernicke, 1985) best explain the juxtaposition of volcanic and structural elements at many points along the RSR conjugate rift margins. However, no singular temporal model applies to the complete rift from the Afar to the Gulf of Suez (Szymanski et al., *in prep.*; Cochran and Martinez, 1988; Martinez and Cochran, 1988; Cochran and Karner, 2007) and local geologic evidence must be invoked to explain the relative timing of syn-rift flank extension, sedimentation, and volcanism. In the southern RSR, a low-angle, mylonitic detachment zone with associated exposed basement core complexes on the Eritrean margin, east-dipping brittle detachment faults with monoclinal flexure, and timing of volcanism in the southern Arabian Shield indicate an Arabian upper plate margin (Bohannon, 1986, 1989; Voggenreiter et al., 1988a, 1988b; Voggenreiter and Hotzl, 1989; Talbot and Ghebreab, 1997). Further northwest along the Arabian margin, intra-basinal fracture zones (Crane and Bonatti, 1987) may indicate the position of polarity reversals in the primary RSR detachment fault orientation similar to models developed by Lister and others (1986) as the rift setting of the Arabian rift flank changes from upper to lower to upper plate, south to north, along strike of the RSR. Located along axial strike of the Shagara Fracture Zone, the CARF is thought to constitute the lower plate margin due to the southwest-dipping normal fault orientation in the HJB (*this study*) and the widespread presence of gneissic and amphibolitic rocks on the conjugate rift margin in Egypt, specifically peridotites and other ultramafic facies on Zabargad Island (Bonatti et al., 1983; Bonatti and Seyler, 1987 *and references therein*). RSR detachment fault polarity again reverses across the Zabargad Fracture Zone north of Al Wajh and forms an upper plate margin in the northern Arabian rift flank (Favre and Stampfli, 1992 *and references therein*).

Competing models exist to explain initial continental rift architecture in the central and northern RSR. Cochran (1981, 1983) proposes the possibility of diffuse continental rifting in the northern RSR during rift onset and estimates that lithospheric breakup proceeded across a 100 km-wide zone prior to strain localization along the modern RSR axis with the advent of the Gulf of Aqaba transform ca. 15 Ma (Richardson and Arthur, 1988; Coleman, 1993; Bosworth and McClay, 2001). In close agreement with Cochran (1981, 1983), Bosworth (1993) uses structural evidence from the aborted Gulf of Suez rift to cite 90 km for the width of the proto-Red Sea continental rift. These estimates are two to three times greater than opposing models that assume the northern RSR is underlain fully by oceanic crust, lithospheric breakup occurred within a ~25 km-wide rift valley, and the African and Arabian plates separated as rigid bodies with little to no intraplate deformation (e.g., Sultan et al., 1992, 1993; Girdler and Southren, 1997). This end-member model is in agreement with initial rift basin width estimates of 20-30 km for the southern RSR (Bohannon and Eittreim, 1991). The position of the HJB within the Arabian rift flank allows us to provide answers regarding the outstanding issues of width, style, and longevity of continental breakup in the centraland northern RSR.

1.4.2.2. Cenozoic sedimentary rock on the CARF

The greater volume of Cenozoic age sedimentary rock in Saudi Arabia is present as syn-rift product along both the modern coastal plain and within the Red Sea Basin proper. The sedimentary strata that overlie extended continental crust of the near and off-shore Arabian Red Sea margin were first explored extensively for hydrocarbon potential several decades ago and continue to interest exploration in the northern Red Sea (Scott et al., 2011 *AAPG abstract*). Due to the economic potential of these regions, many determinative studies exist to prove the age and

depositional setting of syn-rift strata along the modern RSR margin (e.g., Dullo et al., 1983; Hughes et al., 1999; Bosworth et al., 2005 *and references within*) but very few explore the relatively hydrocarbon-poor strata exposed subaerially on the CARF.

Sparse occurrences of Cenozoic age sedimentary rock are present within the vast dissected terrain of the Arabian Shield. These strata are mapped mainly as undifferentiated units with few paleoenvironmental details because their source is either unstudied or indeterminate (e.g., Smith, 1979; Kemp, 1981, 1982). Moreover, investigation of their nuanced tectonic provenance either goes unexplored or is attributed directly, in bulk, to general Red Sea rift-related processes (e.g., the Raghama Formation northwest of Yanbu al Bahr; Pellaton, 1979). Reconnaissance geologic mapping efforts were often successful at identifying syn-rift products, as in the HJB, where Kemp (1981) first accurately recognized the extent and character of the Qattar Formation in broad terms. In a Saudi Geological Survey report on the Wadi al ‘Ays geologic quadrangle, Kemp (1981) maps two occurrences of “Tertiary age” sedimentary rock as unnamed, isolated geologic map units in a structure called the Jizl trough (now known as the HJB). Kemp (1981) regards the strata as an erosional product of highlands proximal to the Jizl trough, and, by stating the similarity between the Jizl trough and the Aznam basin to the northwest (Smith, 1979), infers that the strata are of Oligocene age and thus are syn-rift. Those same strata defined by Kemp (1981, 1982) are the focus of this research.

1.4.2.3. Provincial flood basalt fields (harrat) in the CARF

An extensive system of mafic dikes, volcanic centers, and regional flood basalts (*harrat*), covering an area of ~180,000 km^2, have erupted within the Arabian rift flank since the early Oligocene (Fig. 3; Coleman et al., 1983; Camp et al., 1987; Coleman, 1993; Chazot et al., 1998).

Their age and distribution serves as a record of change in Red Sea rift style and their geochemistry reveals magma provenance. Cenozoic basalt is classified temporally into three major groups: >26 Ma, 25-15 Ma, and 15 Ma-present. These magmatic phases are sometimes classified into "pre-, syn-, and post-rift" groups (e.g., Chazot et al., 1998) but the validity and timing of these classifications is contingent upon location within the rift margin. Considerable temporal overlap of magmatic phases exists as RSR progression and style is not continuous along the full rift strike, harrat are often active for millions of years (e.g., Harrat Hadn, 28-15 Ma; Stern and Johnson, 2010), and the Afar Plume has created a vastly different tectono-magmatic environment in the southern RSR. In the CARF, early Miocene-and-younger magmatic phases have a distinct temporal and structural trend and the HJB exists at their general intersection.

The oldest magmatic phase, composed of Oligocene through middle Miocene-aged rock, is concentrated within the Ethiopian and Yemen Traps and Harrat As Sirat in the southern RSR though it is also preserved further NNW in the Afro-Nubian Shield at Harrat Hadn and Harairah (du Bray et al., 1991; Menzies et al., 1992, 1997; Bosworth et al., 2005). The general linear trend of the oldest harrat parallels the ~N30°W trend of the modern Red Sea rift axis (Coleman, 1993; Stern and Johnson, 2010; Szymanski et al., *this study*) and laterite deposits preserved beneath the basal flows of several volcanic fields (e.g., Harrat Hadn; Coleman et al., 1983) show that these harrat erupted onto a basin-and-range type topography of moderate relief within the Afro-Nubian Shield. This initial period of volcanism preceded the onset of Red Sea rift-related lithospheric extension in the CARF by ~7 million years (Szymanski et al., *in prep.*). The second volcanic phase (25-15 Ma) began with a period of significant crustal modification via

widespread dike injection and harrat emplacement ca. 25-20 Ma that affected the region of the ANS that was to become the Red Sea-Gulf of Suez rift (Brown, 1972; Eyal et al., 1981; Sebai et al., 1991; Pallister, 1987; Camp and Roobol, 1989, 1992; Baldridge et al., 1991; Ukstins et al., 2002; Bosworth et al., 2005 *and references therein*). This volcanic phase accompanied the onset of RSR lithospheric extension in the CARF as evidenced by the intercalation of Harrat Ishara basalt flows with syn-rift fluvatile siliciclastics of Aquitanian age (Szymanski et al., *this study*). The most recent volcanic phase began in the middle Miocene and has continued into recorded history with a "post-Neolithic" eruption at Harrat Rahat in 1256 A.D. (Brown, 1970; Camp et al., 1987; Camp and Roobol, 1989). Harrat within the Makkah-Madinah-Nafud (MMN; Fig. 3) volcanic line comprise the largest basalt province within this group and serve as a good example of the modern volcanic style of the Arabian rift flank. These harrat follow a ~N20°W-N10°E structural trend of half-graben structures that act as conduits for magma systems (Camp and Roobol, 1989) and contain basalt geochemically distinct from previous volcanic phases (Coleman and McGuire, 1988; Camp et al., 1991; Camp and Roobol, 1992). Topographic inversion processes have preserved the course of NE-SW-trending paleochannels that drained basalt from Harrat Rahat (10-2.5 Ma) towards the RSR (Johnson and Vranas, 1994).

1.5. Analytical Methodology and Geologic Sampling Strategy

This study systematically combines traditional structural and sedimentological analyses with geo- and thermochronometric analytical techniques to explore the modes and mechanisms of rift margin development within the central Arabian rift flank, north of Jeddah. Apatite and zircon (U-Th)/He thermochronometric data from both crystalline basement and syn-rift sedimentary section, and whole-rock $^{40}Ar/^{39}Ar$ dating of basalt, define the spatiotemporal relationship

between rift flank extensional structures and regional basalt volcanism. This approach permits the reconstruction of the tectonic margin from early rift architecture to strain distribution during progressive rifting and through subsequent whole-scale modifications of the rift flank due to thermal and isostatic factors, including consideration of the role of pre-existing crustal fabrics.

1.5.1. (U-Th)/He Thermochronologic Method

Apatite and zircon (U-Th)/He thermochronometry (AHe and ZHe) is an investigative tool well-suited for geologic study of the HJB. These thermochronometers, present as accessory minerals in many rock types that comprise the CARF, have the ability to resolve the timing and magnitude of crustal-scale thermal disturbances caused by rift-related geologic processes.

As a dating system, the AHe and ZHe techniques are relatively newer than the well-known apatite and zircon fission-track methods (AFT and ZFT), and have been implemented steadily in geological study of extended terrain for several decades (Reiners et al., 2005), but have yet to be applied as widely to study of the Arabian rift flank as AFT and ZFT (e.g., Bohannon et al., 1989). AHe and ZHe techniques have the ability to resolve changing thermal conditions within cooler temperature ranges than the AFT and ZFT systems and have gained favorability as the preferred low-temperature thermochronologic technique. The successful application of AHe and ZHe techniques to deduce structural evolution in extended terranes has been well documented (Stockli, 2005 *and references therein*). Employing AHe and ZHe techniques in extensional terranes is practical since normal faulting processes commonly draw rock from mid-crustal structural levels to the near surface quickly, rapidly lowering the temperature of a rock body via footwall exhumation. The onset and rate of extensional faulting can be resolved if the throw

magnitude along the fault is great enough to exhume thermally reset thermochronometers to the near surface (Stockli et al., 2000).

(U-Th)/He thermochronological techniques are founded on the fact that radioactive isotopes ^{235}U, ^{238}U, ^{232}Th, and ^{149}Sm, commonly found in a range of common minerals, generate ^{4}He nuclei (α particles) as a product of their decay series. The apparent cooling age of a thermochronometer is calculated by measuring the parent/daughter isotope ratios that exist within the mineral after accounting for variables within the thermochronometric system known to affect age determination. Measureable ^{4}He volumes may accrue within thermochronometeric minerals over geologic time with temperature, individual mineral crystal dimension, and radioactive isotope dissemination within the mineral acting as major controls on ^{4}He retention.

^{4}He retention within (U-Th)/He thermochronometers is largely temperature dependent and the retention magnitude for a particular thermochronometer varies within a specific temperature range known as the helium partial retention zone (PRZ). At temperatures above the upper PRZ boundary, all internally generated ^{4}He is lost from the mineral via thermally activated diffusion while the lower thermal boundary is the temperature at which quantitative retention of ^{4}He begins. Important assumptions include rapid (>10 °C/m.y.) and monotonic cooling of the host rock from a supra-PRZ thermal domain through the closure temperature (T_c) of the thermochronometric system. Isochemical (U-Th)/He thermochronometers that exist within their relevant PRZ for extended periods of geologic time often yield apparent cooling ages inconsistent with one another, which are a tell-tale indicator of their thermal history. The PRZs that define the apatite and zircon thermochronometric systems coincide with typical geothermal temperature ranges of the continental crust; ~80-40 °C for apatite (Wolf et al., 1996) and ~200-

120 °C for zircon (Reiners et al., 2002; Wolfe and Stockli, 2010). Assuming a mean annual surface temperature of 20 ± 10 °C and geothermal gradient of 25 ºC/km for the CARF during RSR onset, the AHe system detects thermal perturbations in the shallow crust (~1.5-3 km) that may record rift-related deformation (e.g., rotation of crustal blocks along developing normal faults) while the ZHe system resolves deformation at shallow to mid-crustal levels (~5-7.5 km depth).

High kinetic energy generated during α particle emission causes both recoil of the parent isotope (resulting in structural damage to the host mineral) and significant travel of the daughter product with possible ejection of the α particle from the host mineral itself. This phenomenon changes both mineral crystallographic properties and isotope distribution enough to necessitate several corrections to attain an accurate AHe or ZHe cooling age.

All analyzed apatite and zircon grain dimensions surpass recognized minimum grain size standards to avoid problems associated with small grains (Reiners and Farley, 2001) and the standard α-ejection correction (F_T; Farley, 2002), based on a calculation of grain morphology, was applied to all analyzed grains. Radiation damage to apatite crystal structure from α recoil controls helium diffusion kinetics and, consequently, creates deviation from the established typical closure temperature of the apatite thermochronometer by systematically increasing T_c overtime (Shuster et al., 2006; Shuster and Farley, 2009). Greater damage from α recoil consequently results in older, incorrect apparent AHe cooling ages. Zircon experiences structural damage that may affect diffusion kinetics at radiation levels where metamictization develops (Reiners, 2005). Thus a pre-screening process that eliminated metamict grains also prevented analyzing unfavorable zircon. For apatite samples, plotting individual derived AHe

ages versus effective uranium concentration (eU = U + 0.2302 Th + 0.005 Sm) is a useful way to assess the extent of radiation damage and the validity of the age determination. No correlation exists in our data to illustrate greater AHe age with greater [eU] concentration for CARF bedrock apatite, which verifies no underlying control of AHe age by radiation damage to the apatite crystal (Fig. 4).

All apatite and zircon (U-Th)/He thermochronology results were determined in the Isotope Geochemistry Laboratory (IGL) at the University of Kansas using standard industry techniques (e.g., Stockli et al., 2000; House et al., 2001). Similar to other geochronometric dating methods, the (U-Th)/He method analyzes and dates multiple sub-samples (aliquots) then pools their collective ages to determine the cooling age of a sample. Individual AHe or ZHe sample ages are reported as the average of two or more sub-sample (aliquot) ages and the associated age uncertainties, 6% (2σ) for AHe and 8% (2σ) for ZHe, reflects the analytical error inherent to the technique (Farley, 2002). Tables 1 and 2 lists all AHe and ZHe age data.

1.5.1.1. Bedrock apatite and zircon (U-Th)/He thermochronology

Bedrock samples obtained for apatite and zircon (U-Th)/He thermochronological analysis are from both the hanging wall and footwall of the Hamd and Jizl half-graben (Fig. 1). Samples within unfaulted portions of the CARF test for significant amounts of rift flank erosion and provide cooling ages that document the background thermal evolution of the Arabian Shield. Footwall samples collected several kilometers behind the Hamd and Jizl half-graben border faults establish the lateral reach of rift flank deformation. Within the footwall of the Hamd and Jizl half-graben immediately adjacent to basin-bounding normal faults, footwall elevation transects were collected in the form of a linear array of samples spaced ~50 meters vertically and

angled perpendicular to basin strike. Footwall elevation transects traverse the complete, exposed footwall to determine the timing, rate, and magnitude of footwall exhumation as well as address HJB evolution issues such as structural control on syn-rift deposition.

Scant quality apatite and zircon thermochronologic information is available for the HJB region because most exposed Proterozoic age basement rock units in the CARF (e.g., the Farri, Al Ays, and Hadiyah Groups) rarely contain analytical-grade apatite and zircon, making them unfavorable for thermochronologic study. Within these units are subordinate volumes of granitic, monzonitic, and dioritic intrusive rock suites of the Proterozoic age Rithmah and Abu Safiyah Complexes and a large, unnamed granodiorite of indeterminate Protero-Paleozoic age (Pellaton, 1979; Clark, 1981; Kemp, 1981; Johnson, 2006). These felsic intrusive suites generally comprise excellent apatite and zircon-bearing rock types and were sampled wherever possible.

1.5.1.2. Detrital apatite (U-Th)/He thermochronology

Detrital apatite (U-Th)/He thermochronology permits an examination of the sedimentary record in search of pre-, syn-, and post-depositional cooling signals that may reveal thermo-tectonic processes such as protolith exhumation, detrital grain provenance, sedimentation rate, and/or structural deformation of the sedimentary column. Due to the possibility that any single sedimentary rock sample may contain detrital apatite from a range of sources, the detrital AHe method does not use age pooling techniques. Rather, each aliquot is analyzed and considered singularly to search for unique AHe cooling ages from different cooling events. Once each AHe cooling age present within a sample is plotted according to relative frequency, a signal may appear that is often characteristic of a particular geologic process. For example, rapid and steady

footwall exhumation, coupled with penecontemporaneous deposition in a proximal basin, commonly produces an inverted unroofing sequence with the oldest AHe cooling ages at the base of the sedimentary record and a demonstrable younging upsection. The position of the greatest relative-frequency peak most often represents the onset of source rock exhumation, a proxy for the commencement of normal faulting in an extensional structural regime. The application of this technique has proven successful in diverse geologic terranes including rift settings. In this study, the detrital AHe method serves a dual purpose: 1) to determine the depositional age of the Qattar Formation by identifying the onset of cooling in the proximal source area induced by footwall exhumation and 2) to resolve thermo-tectonic events within the southwest Arabian Shield that pre-date RSR-related strain development.

Samples for detrital AHe age analysis were collected from select sandstone intervals within three Qattar Formation measured sections in the Hamd half-graben: the type section at Wadi al Qattar and two measured sections beneath Jabal Antar. Whenever possible, ten aliquots were analyzed per sample in order to resolve all thermo-tectonic events represented by the range of detrital AHe cooling ages. Some exceptions exist due to unpredictable analytical difficulties such as analyzing grains with very low ^{4}He concentration or complex mineralogy. Moreover, few apatite-rich sandstone layers exist within the Qattar Formation, limiting analyzed horizons to those that provided quality apatite. No detrital zircon were analyzed.

1.5.2. Whole-rock basalt $^{40}Ar/^{39}Ar$ geochronology and major, trace, and REE geochemistry

The HJB lies within the central Arabian rift flank at the general intersection of two primary volcanic trends (Fig. 3) and basalt flows from Harrat Khaybar and Harrat Ishara enter the HJB at several points along basin strike, contacting both HJB border faults and the Qattar Formation.

These contacts are excellent temporal tie-points to resolve the relative timing of HJB syn-rift structural, volcanic, and sedimentological elements. To elucidate HJB structural and morphological evolution, this study employs whole-rock $^{40}Ar/^{39}Ar$ age dating methods to obtain basalt crystallization ages at strategic locations of basalt/basin element interaction. Twenty-one basalt samples were collected for age and geochemical constituent determination: 2 in the Jizl half-graben at Wadi al Jizl, 5 at Jabal Antar, 9 at Wadi al Qattar, and 5 from other key locations within the Hamd half-graben. Basalt samples consist of fresh, unweathered basalt collected from the middle of entablature layers whenever possible to avoid introducing contamination from entrained clasts and/or sample deterioration via chemical weathering.

1.5.2.1. Whole-rock basalt $^{40}Ar/^{39}Ar$ geochronology

Whole-rock $^{40}Ar/^{39}Ar$ analyses were conducted on laser-heated basalt chips at both the University of Lausanne Institute of Mineralogy and Geochemistry in Lausanne, Switzerland and at the USGS $^{40}Ar/^{39}Ar$ geochronology laboratory in Denver, Colorado. Basalt samples and standards analyzed at the University of Lausanne were irradiated in the Oregon State TRIGA Reactor (OSTR) at Oregon State University Radiation Center (OSURC) and those analyzed at the USGS were irradiated in the USGS TRIGA reactor located at the Denver Federal Center.

1.5.2.2. Major, trace, and REE geochemistry of basalt from X-ray Fluorescence (XRF) and Inductively Coupled Plasma Mass Spectroscopy (ICP-MS)

To construct basalt stratigraphy and determine magma provenance, X-ray Fluorescence (XRF) and Inductively Coupled Plasma Mass Spectroscopy (ICP-MS) analytical techniques were used to determine the major, trace, and rare earth element (REE) composition of basalt from volcanic sources surrounding the HJB. All basalt geochemical analyses were conducted on

crushed sample product derived from whole-rock basalt at the Washington State University (WSU) GeoAnalytical Lab. Major element concentrations were determined using the single bead low-dilution fusion technique for XRF analysis (Johnson et al., 1999) while 14 REE and 13 trace element concentrations were determined using a WSU proprietary combination fusion-dissolution method for ICP-MS analysis. Basalt nomenclature is derived from the total alkali-silica classification fields defined by the International Union of Geological Sciences (Le Bas et al., 1986) and the alkali olivine basalt (AOB)/olivine transitional basalt (OTB) field boundary by Irvine and Baragar (1971). REE abundances are normalized to chondrite via Nakamura (1974). Prior to final drafting, all discrimination diagrams were originally plotted using the *Geochemical Data Toolkit (GCDkit)* freeware by Janousek et al. (2006).

1.6. Results

1.6.1. Bedrock (U-Th)/He Thermochronology and HJB Structural Framework

The relative frequency of bedrock AHe and ZHe ages from the HJB region (Fig. 5**)** reveals the majority of AHe ages concentrate within a Cenozoic to late Cretaceous age range while the ZHe ages split into either Carboniferous or Devonian age groups. These age distributions, and their correlative sample locations, represent a distinct spatiotemporal cooling history within this portion of the CARF that is tied directly to HJB structural elements. Footwall samples adjacent to the border fault tend to show an Oligocene-Miocene age affinity while hanging wall samples are mostly of Paleocene and older ages (Table 3).

The distribution of AHe and ZHe ages in Figure 5 is multi-modal and each group necessitates separate treatment. The majority of AHe age data are Cretaceous and younger but three samples from the Jizl half-graben hanging wall yield Jurassic AHe ages and collectively represent the

oldest AHe age group. All twelve ZHe age results present Permian and older ages with a notable grouping at ~300 Ma; no bedrock sample collected within either the hanging wall or footwall of the Hamd or Jizl half-graben yields a Cenozoic ZHe age. Pre-Cenozoic AHe and ZHe age results within this dataset are assumed indirectly related to Red Sea rift development. The tectonic implications of these data are addressed later as they relate to RSR-related structural deformation in the HJB region but a detailed exploration of their provenance lies outside the immediate scope of this research.

1.6.1.1. Hamd-Jizl Basin Structural Framework

The Hamd-Jizl Basin (HJB) is a composite structure comprising an en-echelon set of two half-graben: the Hamd half-graben in the southeast and Jizl half-graben in the northwest (Fig. 2). Each half-graben is bound to the north by a SSW-dipping primary normal fault that locally splays into smaller sub-parallel synthetic faults. Near the middle of the HJB, the two half-graben are linked by a diffuse zone of small normal faults with relatively minimal displacement (~10-100 m) that coincides with an extensive zone of sheared Proterozoic bedrock emplaced in the Arabian Shield basement rock by the late Proterozoic Najd Fault System (NFS; Moore, 1979). NFS structural fabrics are present in northwest HJB where they control the strike orientation of the Jizl half-graben border fault. The Hamd half-graben is considered the dominant structure of the two major half-graben since it retains a greater record of CARF structural deformation, syn-rift sedimentary rock section, and RSR coeval flood basalt emplacement. As such, the structural character of the Hamd half-graben is addressed first.

1.6.1.1.1. Hamd half-graben

At the northern end of the Hamd half-graben, the primary border normal fault forms the SW flank of Jabal Abu An Na'am and a minor sub-parallel normal fault splay underlies a portion of the active Wadi al Hamd (Fig. 2). Along the entire central section of the Hamd half-graben, the primary border fault is obscured by prominent alluvial fans and ancient basin fill except in a small brecciated outcrop near Jabal an Nu'ayyimah where the fault juxtaposes Proterozoic Al Ays Group silicic volcanics against the Cenozoic syn-rift Qattar Formation (Fig. 6). At this location, the Hamd half-graben is 6.7 km wide and at its widest point. No recent displacement (e.g., offset alluvial terraces) is recognized anywhere along the full trace of the basin-bounding border fault.

AHe and ZHe ages exist for two footwall and three hanging wall samples in the northern Hamd half-graben (Fig. 2; Table 3). Al Ays Group metavolcaniclastics in the footwall behind the primary border fault at Jabal an Nu'ayyimah yield an AHe age of 40.3 ± 2.4 Ma and a Rithmah Complex dacite yields a ZHe age of 320.4 ± 25.6 Ma from the footwall behind the minor normal fault splay. In the hanging wall, samples 06SA077 and 06SA079 yield AHe cooling ages of 51.5 ± 3.1 Ma and 67.9 ± 4.1 Ma, respectively, from small Protero-Paleozoic granodioritic plutons west of Harrat Ishara. A leucotuff NNW of Jabal Antar, possibly part of the Harrat Ishara volcanic sequence, yields the lone Cenozoic ZHe cooling age (13.6 ± 1.1 Ma) obtained within the HJB region (Fig. 7).

At the southern terminus of the Hamd half-graben in Wadi al Qattar, the border fault bifurcates into two discrete normal fault segments; the primary fault continues the local trend of the border fault (149°) until it terminates in Wadi Rashad while a second fault splays to the south (198°) and bounds the type section of the Qattar Formation (Fig. 2). Near the point of fault

bifurcation, a granodiorite in the footwall at Jabal al Anqa yields two (U-Th)/He cooling ages: an AHe cooling age of 21.1 ± 1.3 Ma and a ZHe cooling age of 465.0 ± 37.2 Ma. Two samples from Upper Proterozoic felsic intrusive suites ~50 km ENE of Wadi al Qattar provide AHe and ZHe ages for the Arabian Shield behind the footwall of the southern Hamd half-graben. Rhyolite at Jabal Shihabah yields an AHe cooling age of 73.9 ± 4.4 Ma and the granodiorite near Ad Dulu village yields both an AHe cooling age of 54.8 ± 3.3 Ma and ZHe cooling age of 533.9 ± 42.7 Ma (Table 3; Fig. 6).

In the hanging wall, the base of the Qattar formation in Wadi al Qattar lies nonconformably on Proterozoic Al Ays Group metavolcanic and metasedimentary rock. Post-depositional folding and faulting of the Qattar Formation is apparent. Along the primary border fault, the entire type section is tilted ~30° to the north to constitute the limb of a monocline (Fig. 6). Also at this location is a set of post-folding, en-echelon normal faults that trend ~260° and intersect the primary border fault at an oblique angle. Some individual normal faults within this set show dip-slip displacement >10 m and cut several generations of overlying Ishara basalt flows.

AHe and ZHe ages within the southern Hamd half-graben hanging wall come from four sample locations. Just 600 m west of the primary border fault in Wadi Rashad, sample 06SA009 yields a ZHe cooling age of 554.4 ± 44.4 Ma. Near the head of Wadi al Qattar where the Proterozoic basement is in contact with the Qattar Formation, sample 06SA089 yields a ZHe cooling age of 390.7 ± 31.3 Ma and, 10 kilometers further southwest, sample 06SA090 yields an AHe cooling age of 32.7 ± 2.0 Ma. Finally, approximately 12 km southeast of the Hamd half-graben, sample 07SA029 at Jabal Admar yields AHe and ZHe cooling ages of 38.7 ± 2.3 Ma and 302.7 ± 24.2 Ma, respectively. The four aforementioned samples were obtained from an

unnamed Protero-Paleozoic granodiorite pluton, and its associated dikes, within a larger felsic intrusive suite (Pellaton, 1979) that comprises the CARF south and west of the Hamd half-graben.

1.6.1.1.2. Central Hamd-Jizl Basin

Providing the structural linkage between the Hamd and Jizl half-graben is an intermediate structural zone defined by a diffuse set of normal faults with minimal individual slip. Faults in this intermediate zone show no prevailing orientation and the regional boundaries are indefinite due to the lack of an identifiable deformational style. Extensive outcrop of Proterozoic Hadiyah Group and Al Ays Group basement rock in this region, and a lack of Qattar Formation, indicates a shallower basin floor relative to the the neighboring Hamd and Jizl half-graben. A portion of the regional WNW-ESE structural grain produced by the NFS overlaps this region and some fault planes align in this orientation but with contrasting displacement markers. For example, at Jabal Jurfayn, a NE-dipping fault plane exposed in the Proterozoic Hadiyah Group displays both strike-slip and dip-slip slickenline orientations but near-zero offset of both basement rock geologic contacts and Cenozoic basalt horizons show that this structure has minimal Cenozoic age dip slip displacement (Fig. 2).

The approximate southern boundary of the intermediate structural zone lies near Jabal Abu an Na'am where the Hamd half-graben border fault becomes distinct (Fig. 2). No pervasive NFS structural grain exists either at this location or south of the intermediate structural zone in the Hamd half-graben. A wide range of AHe and ZHe ages come from this region. Near the point where the Jizl half-graben hanging wall trends into the central HJB, a dacite in the Proterozoic Siqam Formation yields a ZHe age of 417.8 ± 33.4 Ma. Four samples lie within a 125 km^2 area

located NE of the collective set of normal faults that comprise the intermediate soft-linkage zone. The Proterozoic Abu Safiyah Complex contains a diorite that yields both an AHe age of 0.6 ± 0.0 Ma, the youngest obtained in this study, and a ZHe cooling age of 348.7 ± 27.9 Ma. A rhyolite from the same complex yields a ZHe age of 544.9 ± 43.6 Ma and an andesite from the host Al Ays Group yields a ZHe age of 552.2 ± 44.2 Ma. Lastly, furthest northeast of the central HJB, granite from an unnamed Proterozoic formation at Jabal Gharrah yields an AHe cooling age of 54.2 ± 3.3 Ma.

1.6.1.1.3. Jizl half-graben

Extensional accommodation in the Jizl half-graben is distributed across two primary SSW-dipping, border faults at Jabal al Qihaba and Jabal Nahar, respectively (Fig. 8). At Jabal al Qihaba, the border fault lies within a zone of sheared Proterozoic gneiss (Kemp, 1981) and a strong correlation exists between the orientation of the fault and the trend of NFS shear fabric (Table 4). The southeasterly trend of the normal fault at Jabal Jamlah shows that the border fault continues to parallel NFS shear fabric trends between Jabal al Qihaba and the structural linkage zone in the central HJB. A correlation between NFS and Cenozoic fault strike is also observed along the southwest margin of the Aznam Trough near Dhuba (Smith, 1979). In contrast, at Jabal Nahar, the Jizl half-graben lies outside the major NFS shear fabric zone and the border fault strike lies 40° counter-clockwise to the fault at Jabal al Qihaba.

AHe ages from Proterozoic basement rock in the Jizl half-graben footwall were obtained behind both primary border faults. At Jabal al Qihaba an Al Ays Group orthogneiss yields an AHe cooling age of 45.8 ± 2.7 Ma and, at Jabal Nahar, alkali granite from the Abu Safiyah Complex yields an AHe cooling age of 14.7 ± 0.9 Ma. AHe and ZHe ages were obtained from

hanging wall samples both proximal to the Jizl half-graben and from exposed basement rock in CARF regions further to the southwest (Fig. 8). Closest to the border fault, two samples from a vertical elevation transect on the south flank of a 400 m-high, basalt-capped promontory in Wadi al Batha yield reproducible late Triassic AHe cooling ages of 203.2 ± 12.2 Ma and 218.4 ± 13.1 Ma within a Protero-Paleozoic granitoid pluton. A monzogranite near Jabal Hammat sixty kilometers to the WSW yields a late Permian AHe cooling age of 252.4 ± 15.1 Ma. ZHe cooling ages of 278.6 ± 22.3 Ma and 425.3 ± 34.0 Ma were obtained from granite in the Fara' trondhjemite (Kemp, 1981) at Jabal Batra and an area NE of Harrat Lunayyir, respectively.

1.6.2. HJB Sedimentary Record and Detrital Apatite (U-Th)/He Thermochronology

1.6.2.1. Qattar Formation

The Qattar Formation is a terrigenous siliciclastic sequence contained within the Hamd-Jizl Basin that comprises numerous successions of conglomerate, sandstone, and siltstone. Outcrop along the hinge of the Hamd half-graben show the Qattar Formation lies nonconformably on saprolitized Proterozoic metavolcanic and granitic basement rock and thickens to the NE where it juxtaposes against the SE-striking, Hamd half-graben border fault. The entire Qattar Formation section is overlain by voluminous syn- to post-extensional basalt flows (17 Ma and younger) from the adjacent Harrat Khaybar and Harrat Ishara volcanic fields (Fig. 9).

Exposure of the Qattar Formation is sparse, yet appreciable accumulations exist at three distinct locations along basin strike: 1) 20 km northwest of the town of Umm Dharb in the Jizl half-graben; 2) 15 km northwest of the town of Al Buwayr beneath the flood basalts of Jabal Antar in the Hamd half-graben, and 3) immediately southeast of the village of Taytad in Wadi al Qattar in the Hamd half-graben (Figs. 6, 7, and 8). Wadi al Qattar contains the most continuous

and best-preserved exposure of syn-rift section in the HJB and thus serves as the namesake and type section for the Qattar Formation.

Detailed genetics-based facies interpretation of measured section within the Hamd-Jizl Basin and sampling for detrital apatite (U-Th)/He thermochronology lead here to the first accurate determination of depositional age, environment, and tectonic provenance of this geologically distinct, syn-rift unit of Aquitanian age on the CARF. The name "Qattar Formation" is designated here for the first time. Four measured sections were obtained along the HJB. Each measured section is described lithologically and subdivided into individual units according to interpreted depositional environment, which is based on grain size, roundness, sorting, clast composition, and primary and secondary sedimentary structures (when observed). Clast size classification is based on the Wentworth scale (1922).

1.6.2.1.1. Hamd half-graben

1.6.2.1.1.1. Wadi al Qattar (Section T)

The type section of the Qattar Formation (Fig. 10) forms the limb of a monocline that tilts ~30° to the NNW along the southernmost portion of the Hamd half-graben border normal fault, exposing ~480 m of continuous section at the current wadi elevation. The base of section rests at the hinge of the monocline and is obscured below modern wadi deposits but outcrop in Wadi Rashad shows the unconformable contact with underlying Proterozoic Al Ays Group (Fig. 6). Quartz arenite is the dominant rock type though significant siltstone and conglomerate components are present. Centimeter-scale planar and trough cross-bedding are common through the sandstone component and multiple bedding contacts exhibit scoured bases up to 0.5 meter in scale. Some sandstones exhibit planar cross-bedding on the 0.5-1 meter scale, commonly within

a massive layer of sandstone with indistinguishable sedimentary structures. These bedforms rarely occur as more than a single layer thick though one interval with pervasive planar cross-bedding exists at the 205 m mark.

Siltstones are found throughout the section and commonly contain root and other organic traces. Siltstone with varying clay content commonly occurs in the lowermost 175 m of section where it provides a source for rip-up clasts found at the base of scour structures within interbedded quartz arenite. Several well developed but heavily weathered rhizolith horizons are present within silt-rich strata near the base of section.

Polymict pebble to cobble conglomerate is found throughout the Wadi al Qattar section most commonly as poorly sorted, 5-20 cm thick interbeds within quartz arenite layers though some conglomerate is present as either lenses or lag deposits within scoured bases. Predominant clast composition is angular to sub-rounded quartz with varying amounts of metavolcanic, metasedimentary, and granitic rock from nearby Proterozoic Al Ays Group and Paleozoic pluton basement rock. No discernable bedforms exist within the conglomerate.

1.6.2.1.1.1.1. Late-stage conglomerate deposition

An angular unconformity exists near the top of the Qattar Formation type section in Wadi al Qattar. Overlying this unconformity in the Hamd half-graben is Unit A2, a coarse conglomerate that caps ~480 meters of Qattar Formation section in Wadi al Qattar and also directly overlies Proterozoic Al Ays Group metasedimentary rock in the adjacent Wadi Rashad (Fig. 6). Unit A2 is light gray in color and characterized lithologically by sub-angular to rounded, medium to coarse sand and pebble to small boulder conglomerate with various plutonic, volcanic, and metamorphic rock clasts from the surrounding Precambrian bedrock. The distinct absence of

basalt clasts within Unit A2 indicates that it predates the development of Harrat Ishara in the Wadi al Qattar region. Contacts between Unit A2 and overlying basalt show that it was eroded into extensive paleochannels that acted as preferred pathways for basalt emplacement. A 17.2 ± 0.3 Ma $^{40}Ar/^{39}Ar$ age from a paleochannel-fill basalt flow in Wadi Rashad constrains the minimum depositional age of Unit A2 to the early Miocene.

Unit A2 is distinct from a second coarse gravel deposit in Wadi al Qattar, Unit A1, which contains both Proterozoic basement rock and Cenozoic basalt clasts. Unit A1 formed after the development of local harrat volcanism making it geologically recent relative to the Qattar Formation. Unit A1 forms terraces >5 meters high that flank the active Wadi al Qattar channel and represents a former active wadi surface (Fig. 6).

The only other mappable sedimentary unit younger than Proterozoic age in the HJB, besides the Qattar Formation, is a ~2 meter-thick laterite horizon that lies unconformably overtop Proterozoic Al Ays Group volcanics and beneath Harrat Ishara basalt. Observed in some parts of Wadi Rashad and nowhere else in the HJB, this iron-rich laterite with multiple layers of plant impressions and bioturbation appears similar to Paleocene age laterite horizons located on the Arabian rift flank beneath other harrat with first volcanic phase affinity, specifically Harrats Hadan and As Sirat, as described by Coleman and others (1983). Therefore, we assign this laterite to that unnamed unit.

1.6.2.1.1.2. Central Hamd half-graben (Sections JA_1 and JA_2)

The Qattar Formation in the central Hamd half-graben (Fig. 7) is laterally extensive, as indicated by the presence of numerous small outcrops in modern drainage channels at the current wadi elevation. Two well-exposed sections beneath Jabal Antar, JA_1 and JA_2 (Figs. 11 and 12),

measure 50 and 74 meters thick, respectively. Separated by 2.8 km, each measured section is capped by basalt from Harrat Ishara and the base of each section is obscured by Quaternary alluvium though both JA_1 and JA_2 are located close (0.7-1.0 km) to outcrop that shows the Qattar Formation directly overlying Proterozoic silicic volcanic rock (Kemp, 1981).

Compared to the Qattar Formation type section in Wadi al Qattar, the measured sections at Jabal Antar shows a significant increase in the silt content of sandstones, a greater presence of meter-scale siltstone deposits, and a marked decrease in the abundance of conglomeratic sandstone. Gypsiferous nodules 1-4 cm in diameter are unique to many sandstone units in the Jabal Antar region. These nodules are found often in great abundance within planar crossbed sets where their cement creates a distinctive knobby outcrop-scale weathering pattern. Section JA_1 contains fine-grained sandstone almost exclusively though both sections include sandstone units that have no discernable sedimentary structures and exhibit an exfoliation-style weathering pattern due to their high silt content. 5-10 cm thick red brown siltstone layers typically bracket the fine sandstone units. The siltstone rarely contains root traces and black organic clay coatings but one instance at the 20 m mark of JA_2 shows a well-established root system preserved as calcified root casts 1-10 cm in diameter.

Medium to coarse-grained quartz arenite dominates section JA_2. Similar to the type section in Wadi al Qattar, these sandstone units contain 5-10 cm thick planar and trough crossbeds with abundant red-brown silt rip-up clasts and pebble conglomerate in channel lag deposits. Clast composition remains similar as well with an abundance of quartz, porphyritic andesite, granite, and various Proterozoic rocks sourced from local basement terranes.

1.6.2.1.2. Jizl half-graben

1.6.2.1.2.1. Wadi al Jizl (Section J)

Wadi al Jizl contains the only measureable section of the Qattar Formation in the Jizl half-graben. Several large hills of uneroded sediment are located 1-2 km south of Jabal al Qihaba (Fig. 8) and each is heavily concealed by basalt scree, an erosional product of basalt flows that once blanketed the area. Estimate of the volume of basalt that once existed in Wadi al Jizl is difficult since no significant thickness of in-situ basalt cover remains and no major volcanic fields are situated nearby at this structural level; most basalt cover was likely emplaced by local dikes.

Sixty-seven meters of continuous measured section at Wadi al Jizl shows predominantly siltstone interbedded with fine to medium-grained sandstone and pebble to cobble conglomerate (Fig. 13). The siltstone contains abundant root casts and white gypsum mineralization pervades some layers, appearing as both an in-situ spotted pattern and in crystal form as secondary deposits in modern cracks. Gypsiferous nodules 0.5-1 cm in diameter were observed in a sandstone layer at the 34 m mark. Compared to the sections at Wadi al Qattar and Jabal Antar, the Qattar Formation at Wadi al Jizl contains less fine-grained sandstone and more polymict cobble conglomerate. Clast composition remains Proterozoic metavolcanic, metasedimentary, and plutonic rock, diagnostic of the Qattar Formation in other areas.

The base of measured section at Wadi al Jizl is obscured by Quaternary alluvium but the lowermost portion of the Qattar Formation is exposed along the border fault at Jabal al Qihaba ~4 km to the northwest (Fig. 8). Almost exclusively present is a medium pebble to large cobble, angular to sub-angular, poorly sorted orthoconglomerate composed of Proterozoic Al Ays Group gneiss and quartzite. This exposure is both heavily faulted and eroded, making accurate

measurement impractical. Individual beds are absent of sedimentary structures, range from 1-5 m thick, and contain rare interbeds of well-sorted fine sand.

1.6.2.2. Detrital Apatite (U-Th)/He Thermochronology

Detrital AHe sample ages were determined for ten Qattar Formation sandstone intervals from two measured sections (Figs. 10 and 12). Collectively, these intervals span the full stratigraphic column of the Qattar Formation from the basal unconformity on Proterozoic basement to the top of the existing section. Table 5 summarizes the detrital AHe data and Figure 14 displays the relative frequency of detrital AHe sample ages.

Figure 14 presents a subdivision of the complete detrital AHe dataset into four AHe age spectra that show the evolution of the detrital AHe age signal from the base to the top of the Qattar Formation. Figure 14(a) presents the AHe age data of sample $A_{2\text{-}1}$ collected from the 10 m mark of Section JA_2 at Jabal Antar and is representative of the lowermost component of the Qattar Formation in the Hamd half-graben. This AHe age spectrum contains a wide range of ages with concentrations at ~40-100 Ma, ~180 Ma, and ~300-325 Ma. Moving up in the section between 60-255 m, the AHe age plot in Figure 14(b) contains the first early Miocene signal with the greatest AHe age peak at ~22 Ma. The AHe age plots in Figures 14(c) and 14(d) collectively represent the top half of the Qattar Formation type section from the 255-500 m mark and are very similar to one another. Both AHe age spectra exhibit their greatest AHe age peak at ~20 Ma, a spread of Cenozoic and Cretaceous ages, and early Jurassic and Carboniferous signals similar to those observed in the lowermost portion of the section. All detrital AHe age spectra throughout the section show a systematic decrease in the frequency of older ages to the right of the greatest signal but this pattern is most well-developed in Figure 14(d).

1.6.3. Whole-rock basalt geochemistry and $^{40}Ar/^{39}Ar$ geochronology

Twenty-three basalt samples were collected and analyzed exclusively for this study; twenty were dated using the whole–rock $^{40}Ar/^{39}Ar$ age dating method and twenty-one were analyzed for whole-rock major, trace, and REE geochemistry (Table 6; *APPENDIX A*). Figure 15 lists the volcanic source assignment of all 23 HJB basalt samples. $^{40}Ar/^{39}Ar$ age and geochemical data allow a clear classification of HJB basalt samples and show that two primary volcanic centers, Harrat Khaybar and Harrat Ishara, extruded basalt into the HJB region throughout the Miocene. Basalt erupted from vent systems at the center of Harrats Khaybar and Ishara as well as from local fissures whose vent structures have been virtually destroyed by erosion in most cases. Major, trace, and REE characteristics of HJB basalt samples identify genetic relationships between basalt flows which assists in assigning samples to their volcanic source and allows a basic volcanostratigraphic column to be built for the HJB, including the first volcanostratigraphic segregation of Harrat Ishara. Figure 16 displays the full range of whole-rock basalt $^{40}Ar/^{39}Ar$ ages from this study and Figures 6 thru 8 show their location in the HJB. This dataset is a significant improvement over the existing K-Ar age database for basalt in the HJB and is the most robust and accurate age suite yet produced for Harrat Ishara.

The basalt lithology discrimination plot in Figure 17 shows the analyzed basalt suite consists of 7 olivine transitional basalt (OTB) and 14 alkali olivine basalt (AOB), including two of borderline AOB composition: 1 AOB/basanite and 1 AOB/hawaiite. It is evident from the TAS diagram that no absolute lithological boundaries delineate Harrat Kura from Harrat Ishara basalt. Since basalt from either source cannot be discriminated lithologically, classification of basalt provenance relies on REE associations and field relationships. The following sections address,

by structural region, the dissemination and geochemical variation of Harrat Ishara and Harrat Khaybar basalt flows within the HJB.

1.6.3.1. Hamd half-graben

1.6.3.1.1. Ishara basalt (Harrat Ishara)

Harrat Ishara is the primary contributor of basalt to the central and southern Hamd half-graben. Harrat Ishara lies to the SW of the Hamd half-graben, covers an area of 570 km^2 (Camp et al., 1991), and is one of several basalt fields in the region associated with the first phase of volcanism in the Red Sea region (Coleman et al., 1983; Camp and Roobol, 1992; Coleman, 1993). Harrat Ishara began erupting in the early Miocene, lagging behind deposition of the Qattar Formation by a minimum of 3 million years. $^{40}Ar/^{39}Ar$ ages show that the youngest Harrat Ishara product is ~ 2 m.y. older than the oldest Kura basalt from Harrat Khaybar (Camp et al., 1991) though their eruption longevity is similar; both volcanic centers contributed basalt to the HJB for approximately 5 million years. No contact between the two basalt fields is observed.

1.6.3.1.1.1. <u>Harrat Ishara volcanostratigraphy</u>

Ishara basalt is the sole identified volcanic stratum of Harrat Ishara and no known literature has proposed a volcanostratigraphic subdivision of this primary unit. We propose a subdivision of Ishara basalt into two volcanostratigraphic units, Ishara A and B, based on major, trace, and REE basalt geochemistry and $^{40}Ar/^{39}Ar$ ages that show the contemporaneous extrusion of two geochemically distinct units during the middle Miocene. Ishara A is predominantly AOB, generally contains 47-49% SiO_2 and has an age range of 17.2-14.5 Ma (Figs. 16 and 17). Ishara B is mostly OTB with an age range of 16.0-12.3 Ma, which shows that its generation outlasted the lower unit by ~2 million years (Fig. 16). Though the two Ishara B basalts with the greatest

deviant total alkali-element concentration are both located at Wadi al Jizl, their trace element profiles closely match the rest of the Ishara B suite.

Geochemical dissimilarity between the Ishara A and B basalt units provides the greatest support for Ishara basalt subdivision. Apparent discrimination between well-grouped data points occurs in SiO_2, TiO_2, FeO [total], CaO, and P_2O_5 in the major elements and La, Ce, Y, and Zr in the trace elements (Figs. 18, 19, and 20). On average, Ishara A contains greater REE abundances relative to Ishara B, especially in the LREE range, while relative abundances in the major elements are observable in the TiO_2, FeO [total], and P_2O_5 groups.

Though separated by 33 km, the basal basalt flows at Jabal Antar and Wadi al Qattar are both Ishara A basalt from the same source according to their similar $^{40}Ar/^{39}Ar$ ages (e.g., 06SA004 and 06SA050) and inherent major, trace, and REE geochemistry. Their relative locations, coupled with the location of other Ishara A samples, demonstrates that the outpouring of Ishara A basalt from Harrat Ishara was >300 km^2. Ishara A capped the Qattar Formation in the southern and central Hamd half-graben at 17.2 ± 0.3 Ma and 15.16 ± 0.11 Ma, respectively.

The basal flow at Jabal Antar is Ishara A basalt but Ishara B basalt constitutes the remainder of the basalt column at Jabal Antar and Jabal Jurfayn (18 km to the NW) as well as the greater volume of basalt in the central Hamd half-graben. An OTB from the topmost remaining in-situ basalt flow at Jabal Antar (06SA047) yields a $^{40}Ar/^{39}Ar$ age of 12.7 ± 0.3 Ma. When matched against the 15.16 ± 0.11 Ma age of the Jabal Antar basal flow (06SA050) at this location, the 12.7 ± 0.3 Ma age and elevation of 06SA047 reveals that basalt emplacement at Jabal Antar endured for >2 million years while building a >310 m thick volcanostratigraphic column of more than 30 superimposed basalt flows (Dalfour and Dhellemmes, 1980).

Both Ishara basalt units were generated during the early to middle Miocene. However, $^{40}Ar/^{39}Ar$ ages within Harrat Ishara are unevenly distributed (Fig. 16) and sub-unit age groups suggest at least two periods of punctuated basalt generation within each unit. In Ishara A, four of nine samples closely group ~17 Ma and the remainder ~15 Ma. Three of six Ishara B samples clearly group ~13 Ma while the other half have $^{40}Ar/^{39}Ar$ ages that overlap the lower unit. We are confident that this age distribution is not the result of sampling bias as we collected basalt samples at regularly spaced intervals within the Harrat Ishara volcanostratigraphic column, using the 300 m-thick outcrop thickness at Jabal Antar as control.

1.6.3.1.2. Kura basalt (Harrat Khaybar)

Kura basalt, the basal volcanostratigraphic unit within the Harrat Khaybar volcanic province, is found throughout the Hamd half-graben. Kura basalt enters the HJB at two locations according to geologic maps by Pellaton (1979, 1981), Delfour and Dhellemmes (1980), and Kemp (1981); from the Harrat Khaybar highlands near the central structural linkage zone of the HJB and at the southern terminus of the Hamd half-graben (Fig. 2). Kura basalt is dominantly AOB with some differentiated basanite and hawaiite components (Baubron and Maury, 1979; Delfour and Dhellemmes, 1980; Camp et al., 1991).

Four AOB basalt samples from the central portion of the HJB closely match the geochemical data for the lone Kura AOB sample reported by Camp et al. (1991: GSA Repository data). In this region, all Kura basalt samples have similar HREE values while differentiation is apparent in the LREE levels (Fig. 18). Relative to Ishara basalt, the Kura basalt identified in this study has no distinctive geochemistry and its major and trace element concentrations commonly overlap

Ishara basalt values. In general, younger Kura basalt contains higher LREE values, which may be a result of magma fractionation if these originated from the same source.

Kura basalt is demonstrably younger than all other basalt in the HJB (Fig. 16). The 10.6-5.7 Ma $^{40}Ar/^{39}Ar$ age range for all dated Kura basalt samples falls within the accepted Harrat Kura age range of ~5.5 Ma-11.5 Ma designated by Camp et al. (1991) based on compiled K/Ar age data collected by both themselves and other authors. No temporal overlap is observed in the eruption ages of Harrats Ishara and Khaybar; the oldest Kura basalt in the HJB is ~2 million years younger than the youngest Ishara basalt.

1.6.3.2. Jizl half-graben

1.6.3.2.1. Ishara basalt (Harrat Ishara)

A minor volume of basalt exists in the Jizl half-graben, relative to the Hamd half-graben, and only Ishara B is present. At Wadi al Jizl, most basalt has weathered to a thin colluvium cover with nearly no retention of original flood basalt horizons. In-place basalt remains at only one location as a dike/cap set intruded into (and overlying) the Qattar Formation (Fig. 8). The basalt cap is the stratigraphically lowest basalt flow at this location. $^{40}Ar/^{39}Ar$ age determinations show that both features are middle Miocene in age with the dike slightly older than the cap (13.0 ± 0.3 Ma versus 12.3 ± 0.2 Ma). No crosscutting field relationship was observed to corroborate this result due to poor outcrop exposure.

Differing geochemistry and $^{40}Ar/^{39}Ar$ ages indicate that the dike/cap pair are not directly correlatable though they both classify as Ishara B basalt. The samples show an increase in both total alkalinity and LREE concentration from dike (subalkaline/OTB) to cap (AOB). Though both basalts classify as Ishara B, their major and trace element concentrations occasionally plot

in the intermediate range between the two Ishara basalt units (e.g., Ca, La, and Rb). Their age and geochemical signature closely correlates with the youngest Ishara B basalt (06SA047) from the apex of Jabal Antar ~100 km to the southeast. Discussed later are Ishara B magma source implications as they relate to the wide-ranging occurrence of Ishara B basalt at each terminus of the HJB [*see section* 1.7.5.].

1.7. Discussion

1.7.1. Developmental timing, structural kinematics, and tectonic affinity of the HJB

1.7.1.1. RSR signals observed in the HJB via (U-Th)/He thermochronology

Strong evidence for significant RSR-related footwall exhumation is found in the AHe age of footwall samples at both the northern and southern termini of the HJB. Jabal Nahar within the Jizl half-graben and Jabal al Anqa within the Hamd half-graben feature Miocene AHe cooling ages of 14.7 ± 0.9 Ma and 21.1 ± 1.3 Ma, respectively. These two sample ages verify that the HJB is a syn-rift structure that originated within the RSR system during RSR onset in the Miocene (Coleman, 1993; Hughes and Johnson, 2005 *and references therein*; Szymanski et al., *in prep.*) and continued to evolve through a period of regional plate reorganization in the middle Miocene (Bosworth et al., 2005 *and references therein*). However, the AHe sample ages alone do not provide the absolute timing of HJB footwall development because they are an incomplete part of separate multi-sample footwall transects. None of the accompanying samples in their respective transects generated reproducible AHe ages and, without the context provided by accurate AHe ages from adjacent samples, the possibility exists that these two samples yield partially reset AHe ages. However, correlation of each AHe age with other rift timing evidence reveals a dual-stage HJB deformational history.

First, the 21.1 ± 1.3 Ma AHe age from Jabal al Anqa provides sound corroborating evidence for an initial rift pulse when combined with detrital AHe results that identify depositional onset of the Qattar Formation at 22 Ma. Second, normal faults internal to the Hamd half-graben cut multiple ~16 million-year-old Ishara A basalt flows that had sealed the basin at Wadi al Qattar (Fig. 6). These intra-basinal faults corroborate the 14.7 ± 0.9 Ma AHe age at Jabal Nahar and confirm a second RSR extensional pulse in the HJB in the middle Miocene. Related extensional structures exist as sets of small conjugate normal faults, with sub-meter displacement, within the Qattar Formation in the central Hamd half-graben (Table 4; Fig. 7). These intra-basinal faults, as well as the monocline within the Qattar Formation at Wadi al Qattar, show differential displacement along the border fault and provide strong evidence for deepening of the central Hamd half-graben after deposition of the Qattar Formation. This post-depositional basin deepening is a direct result of extension in the HJB ca. 15 Ma. Together these bedrock and detrital AHe thermochronological datasets place initial HJB footwall exhumation ~21 Ma with further basin deepening ~15 Ma, confirming that the HJB is an expression of extension within the larger RSR system.

1.7.1.2. The limited spatial dissemination of RSR strain markers in the HJB

AHe and ZHe age data provide minimum constraints on exhumation and erosion of the Hamd and Jizl half-graben footwalls and hanging walls that reveal dissemination of RSR strain in the HJB is limited spatially. The greatest footwall exhumation exists at both termini of the HJB. Footwall exhumation magnitude varies along strike, and quickly diminishes behind, the HJB-bounding fault. Additionally, the lack of Oligocene-Miocene AHe and ZHe ages in the hanging wall regions indicates minimal RSR-related erosion.

1.7.1.2.1. AHe dataset

Four of four samples from the Hamd half-graben hanging wall yield AHe ages that range from late Cretaceous to early Oligocene (06SA077, 06SA079, 06SA090, and 07SA029; Table 3). No major Cenozoic fault structures (relative to the scale of the HJB) separate these samples so it is acceptable to conclude they are part of the same, undivided structural domain. Assuming that the Hamd half-graben hanging wall deformed as a single, rigid structure, hanging wall AHe ages that fall in the range of ~30-70 million-years-old likely represent rock that resided in the AHe PRZ prior to Red Sea rifting. The rate and magnitude of Red Sea rift-related hanging wall erosion was too insufficient to expose thermally reset apatite.

A Proterozoic monzogranite near Jabal Hammat yields a late Permian AHe age result (252.4 ± 15.1 Ma) in a Jizl half-graben hanging wall exposure of unfaulted basement sixty kilometers WSW of Wadi al Jizl. When coupled with two nearby late Triassic AHe ages in the hanging wall at Wadi al Batha, this three-sample suite accounts for the oldest age group observed in the AHe age dataset. Collectively, these data may contain cooling ages related to older tectonic events such as the Hercynian rifting event that created extensive block faulting observed magnetically beneath the Arabian Platform (Johnson and Stewart, 1995) and postulated to have effected regions further westward within the proto-Arabian Shield (Johnson, *pers. comm.*).

In the Hamd and Jizl half-graben footwalls, samples with Eocene AHe ages indicate both along-strike and inboard limits on the magnitude of RSR-related footwall exhumation in the HJB. Located proximal to HJB-bounding faults, footwall samples from Jabal an Nu'ayyimah in the Hamd half-graben footwall and Jabal al Qihaba in the Jizl half-graben footwall yield AHe ages of 40.3 ± 2.4 Ma and 45.8 ± 2.7 Ma, respectively (06SA073 and 06SA093; Table 3). These

two Eocene AHe ages contrast the RSR-related Oligocene-Miocene exhumation signal observed at other footwall locations in each half-graben. The total dip-slip displacement at these two locations is estimated at less than ~1.8 km since border fault displacement was too insignificant to exhume thermally reset apatite during HJB development.

Four footwall samples located several tens of kilometers behind the HJB-bounding faults yield late Cretaceous and Paleocene AHe and ZHe ages similar to many hanging wall samples (07SA020, 07SA022, 07SA037; Table 3). Exceptionally, an alkali granite of the Proterozoic Abu Safiyah Complex (07SA045) yields the youngest AHe age obtained in this study: 0.55 ± 0.0 Ma. This Pleistocene age is not a result of RSR-related exhumation but rather indicates a likely thermal resetting of the apatite thermochronometer by an overlying Kura basalt flow. Because of their comparable AHe age range, HJB footwall and hanging wall samples of Eocene age were a likely a collective part of the same structurally undivided Arabian Shield prior to the existence of the HJB and, therefore, experienced a similar thermal history that involved residence within the AHe PRZ prior to HJB formation. Summarily, footwall samples with Eocene and older AHe ages show that no considerable RSR-related deformation affected far-inboard portions of the footwall and the most significant RSR-related deformation is limited to the northern and southern termini of the HJB proximal to the Hamd and Jizl half-graben border faults.

1.7.1.2.2. ZHe dataset

All twelve ZHe analyses of bedrock samples from the HJB region yield Permian and older age results (Fig. 5; Table 3). These ZHe age data represent remnant cooling events that occurred within the proto-CARF and predate Cenozoic RSR development. Importantly, they show that no thermally reset zircon were exposed in the HJB region either by major hanging wall erosion or

rapid footwall exhumation during Red Sea rifting. This limits hanging wall erosion and footwall exhumation magnitudes to less than ~ 6.0 km, assuming a mean annual surface temperature of 20 ± 10 °C and geothermal gradient of 25 ºC/km for the CARF.

The lone Cenozoic ZHe age obtained from the HJB region is from a fluvially reworked leucotuff (13.6 ± 1.1 Ma) in the Hamd half-graben hanging wall near Jabal Antar. This ZHe age is unrelated to HJB structural development as it was likely imparted by heat from an overlying Ishara basalt flow. It remains unclear whether this age dates the Ishara basalt flow unit since it may represent only a partial resetting of the zircon thermochronometer. No whole-rock $^{40}Ar/^{39}Ar$ age is yet available for the basalt.

1.7.2. HJB Structure

The Hamd and Jizl half-graben that comprise the HJB are a set of related extensional structures generated during the continental lithosphere rifting mode of the Red Sea rift system, though various sedimentological, structural, and thermochronological indicators show a difference in the structural character of the two half-graben. The primary difference in Jizl and Hamd half-graben kinematics is differential control on half-graben structural development by pre-existing Proterozoic Najd Fault System structural fabric (NFS; Moore, 1979) within the rift flank; the Jizl half-graben resulted from normal fault development along NFS foliation planes as illustrated by the correlation in strike direction between the border fault and local NFS foliation (108° ± 9° and 116° ± 13°, respectively; Table 4) while Hamd half-graben is footed in a portion of the Arabian Shield unaffected by NFS structural grain. The overwhelming structural control of the NFS on the orientation of early Red Sea rift basins was first recognized on other structures

in both the Arabian and Eritrean rift flanks (Brown, 1970; Davies, 1984; Sultan et al., 1988; Ghebreab and Talbot, 2000).

In the absence of borehole or geophysical data, no definite basin depth or subsurface structural architecture is known for either the Jizl or Hamd half-graben and depth-to-crystalline basement estimates nearest the border fault are difficult to determine. In the Jizl half-graben, basin depth is especially poorly constrained and complicated by the fact that the location of greatest footwall exhumation at Jabal Nahar lies 18 km northwest of the area of greatest syn-rift sediment retention at Jabal al Qihaba (Fig. 8). Basin depth estimates at Jabal al Qihaba range between 280 and ≤ 1800 meters based on the elevation difference between the peak of the footwall and the base of Qattar Formation measured section as well as the absence of a Miocene AHe age in the footwall. In contrast, the 15.1 ± 0.9 Ma AHe age in the Jabal Nahar footwall indicates >1.8 km exhumation during the middle Miocene but the absence of remnant Qattar Formation at the same location indicates that it was not a syn-rift depocenter.

Compared to the Jizl half-graben, the Hamd half-graben has a well-defined border fault trace and retains a more detailed record of syn-rift sedimentation. The northern portion of the Hamd half-graben at Jabal an Nu'ayyimah has an estimated basin depth range of ~0.35-1.8 km. The minimum basin depth estimation is based on a trigonometric determination that incorporates the thickness of the Qattar Formation in measured sections JA_1 and JA_2, their distance from the Proterozoic Al Ays Gp./Qattar Formation contact to the southwest, and the 6.7 km width of the Hamd half-graben at Jabal an Nu'ayyimah (Fig. 7). Maximum basin depth estimation is ≤1.8 km due to the presence of a partially reset AHe age (40.3 ± 2.4 Ma) in the footwall at Jabal an Nu'ayyimah, though Hamd basin depth increases along strike from north to south. An AHe age

(21.1 ± 1.3 Ma) within the footwall at Jabal al Anqa (Fig. 6) indicates exhumation ≥1.8 km in the early Miocene and demonstrates that the Hamd half-graben at Wadi al Qattar is deeper than the basin near Jabal an Nu'ayyimah.

1.7.3. Age, provenance, and depositional setting of the Qattar Formation

1.7.3.1. Depositional age

The Qattar Formation classification is applied to all siliciclastic rock linked to either syn-rift deformational stage in the HJB. Based on intraformational detrital AHe ages, piecewise deposition of the greater volume of Qattar Formation sedimentary rock occurred between 23-17 million years ago. The intercalation of the topmost strata with Ishara A basalt shows that the southern Hamd half-graben contained an active, though less productive, syn-rift depocenter that waned and ended in the middle Miocene.

Figure 14 presents a subdivision of the complete detrital AHe dataset into 4 AHe age spectra that show the evolution of the footwall exhumation signal from the base of section to the top. The bottommost spectrum presents the AHe age data of a sample (A2-1) collected from the 10m mark of Section JA_2 at Jabal Antar and is representative of the first sediment introduced to the Hamd half-graben. This AHe age spectrum contains a wide range of ages with concentrations at ~40-100 Ma, ~180 Ma, and ~300-325 Ma. The Cretaceous/Paleogene age group originates from samples in the AHe PRZ that were the first to shed from the exhumed footwall during HJB development while the early Jurassic and Carboniferous age groups represent AHe signals inherited from older tectonic events. Most regional geologic terranes that could possibly serve as a sediment source are either early Paleozoic or Proterozoic in age (Johnson, 1998) so the Carboniferous and younger age groups within our AHe dataset represents apatite cooling ages

younger than the original emplacement age of the source terrane. The variance in source terranes is detectable by tracking the Th/U ratios of individual aliquots within the sampled stratigraphic horizons (Table 5).

The AHe age plot in Figure 14(b) contains the first conclusive evidence of early Miocene footwall exhumation. These data, obtained from two samples from Wadi al Qattar (T6 and T19), show the greatest AHe age peak at ~22 Ma. Total footwall exhumation is estimated to be greater than ~1.8 km at this time in the sedimentary record since that is the minimum displacement needed to exhume fully reset apatite based on our assumption of surface and shallow crust thermal conditions at RSR onset. The early Jurassic and Carboniferous age groups are not observed here but that does not preclude their existence in this portion of the section.

The AHe age plots in Figures 14(c) and 14(d) are very similar. They both exhibit the highest AHe age peak at ~20 Ma, a spread of Cenozoic and Cretaceous ages, and the early Jurassic and Carboniferous signals. In both plots, the decrease in frequency of older ages to the right of the greatest signal is indicative of an exhumed footwall that contains both thermally reset apatite and the AHe PRZ. This age "coda", more well-developed in plot 14(d) than plot 14(c), confirms that the Hamd half-graben is fully developed at this point in the sedimentary record, which correlates to an age of ~20 Ma.

1.7.3.1.1. Late stage syn-rift sedimentation in the HJB

Minimum depositional age constraints come mostly from the few remaining in-situ geologic contacts between Cenozoic basalt and syn-rift section. Yet these locations effectively show that deposition of the Qattar Formation in the HJB lasted into the second stage of extensional deformation ~15 Ma. At Wadi al Jizl, middle Miocene $^{40}Ar/^{39}Ar$ age determinations of the basalt

dike and cap features (13.0 ± 0.3 Ma and 12.3 ± 0.2 Ma) set the minimum depositional age of the Qattar Formation in the Jizl half-graben at ~13 Ma. In the southern Hamd half-graben, Ishara A directly overlies both the Qattar Formation and Al Ays Gp. basement rocks in Wadi Rashad and yields whole-rock $^{40}Ar/^{39}Ar$ ages of 17.2 ± 0.3 Ma and 16.8 ± 1.2 Ma (Fig. 21). These flows partially seal the basin at this location so they provide both a minimum depositional age for the Qattar Formation as well as a maximum deformational age for the monoclinal warping of the syn-rift section along the border fault at Wadi al Qattar. Since the earliest depositional age of the Qattar Formation is ~20 Ma at Wadi al Qattar based on detrital AHe age data, monocline development is likely of Burdigalian age.

The Qattar Formation shows no measurable regional dip in the Jabal Antar area and the overlying Harrat Ishara basalt flows also exhibit a regional horizontality. This relationship indicates a relatively flat paleotopographic surface at the time of Ishara basalt extrusion yet, in the central and southern Hamd half-graben, sediment/basalt contacts within the lowermost Harrat Ishara volcanostratigraphic units are consistent with basalt extrusion into an active wadi. Flow channelization, evidenced from lateral thinning and pinching-out of basalt flows, occurred as the initial basalt incursion filled paleotopographic lows and intercalated with wadi deposits.

The most prominent example of basal Ishara basalt flow/wadi deposit intercalation is an extensive sediment horizon observed between the first and second Ishara basalt flow units at Wadi al Qattar and Jabal Antar (where the sediment horizon is preserved on the SE side). Two mappable sediment horizons of meter-scale thickness exist in the southern portion of Wadi al Qattar above the Unit A2/Ishara basalt unconformity (Figs. 6 and 9). Lithologically similar to Unit A2 but with much greater sand and silt content, these are two of numerous sediment

horizons intercalated with Ishara A basalt flows that show sediment transport through the Hamd half-graben did not cease immediately with the onset of volcanism. Generally, these sediment horizons are unobserved higher in section than two flow units of the overlying Ishara basalt stratigraphy. The top of each sediment horizon exhibits a zone of red discoloration that formed from in-situ heating by an overlying basalt flow.

1.7.3.2. Depositional setting and sediment provenance

No complete section of the Qattar Formation is preserved within the HJB. The absence of a complete section is due, in part, to basin evacuation processes that removed a great volume of sediment from the HJB after the development of stream piracy at the confluence of Wadi al Jizl and Wadi al Hamd (Brown, 1970; Brown et al., 1989; USGS, 1993). Minor volumes remain within low hills scattered throughout the HJB, such as the small exposure of several tens of meters of Qattar Formation trapped beneath basal Kura basalt flows at sample location 06SA061 (Fig. 2). Mostly obscured by basalt colluvium, its presence at this locale shows that the Hamd half-graben was not yet evacuated of sediment below this elevation in the late Miocene. Moreover, the fact that the ~480 m thick type section in Wadi al Qattar contains a near complete record of syn-rift sedimentation shows that, while the Qattar Formation is laterally extensive, it never surpassed thicknesses much greater than ~500 m so any sediment evacuation estimate that assumes a full basin of sediment may be exaggerated.

The Qattar Formation at Wadi al Qattar constitutes a fluvial system with minor alluvial fan influence. Sedimentary facies changes within the measured section (Fig. 10) indicate a general progression over time from a mixed braided and meandering river system in the lower half of the section to a dominant braided river system in the top half of the section. In general, clast size

decreases away from the border fault of each half-graben. No synchronicity is observed between the (U-Th)/He age record of footwall exhumation and syn-rift sediment deposition at a resolution below one that proves causality (i.e., footwall exhumation and erosion led to sedimentation). This lack of resolution is due partly to an overall lack of analytical-grade apatite in footwall rock.

The lower ~175 m of measured section contains meandering river indicators such as numerous siltstone layers with varying clay content, commonly interbedded with quartz arenite, that provide a source for rip-up clasts found in channel lag deposits. Well-developed rhizolith horizons exist in silt-rich strata near the base of section. Siltstones throughout the section commonly contain root and other organic traces outlined with green reduction halos and are interpreted as overbank deposits proximal to stream channels. Sets of braided river indicators are also present in the form of multiple planar crossbed sets within sand bodies and the presence of pebble to cobble conglomerate lenses and lag deposits within scoured bases. Gypsiferous nodules 1-4 cm in diameter are found often in great abundance within planar crossbed sets where their cement creates a distinctive knobby outcrop-scale weathering pattern. Their presence within these planar crossbed sets may indicate a fluvial system with highly variable and seasonally dependent water flow rates and fluctuating groundwater levels. These features are present throughout the Qattar Formation in the Hamd half-graben though they most commonly occur in many mid-section sandstone units in the Jabal Antar region and become more rare upsection. Additionally, some arenites contain unique, “leopard print” liesegang bands that appear to form by differential water flow through permeability gradients around planar crossbeds.

Higher than the 210 m mark, where the braided river system tends to assume control, thicker sand bodies with irregular grain size trends dominate the sedimentary section and less fine overbank material is present, including just one siltstone unit. Polymict pebble to cobble conglomerate is found throughout the Wadi al Qattar section but more commonly upsection often as poorly sorted, 5-20 cm thick interbeds within quartz arenite, though many are present as lenses and lag deposits within scoured bases. Clast composition is dominantly angular to sub-rounded quartz with varying amounts of metavolcanic, metasedimentary, and plutonic clasts drawn from the surrounding Proterozoic basement rock. No discernable bedforms exist within the conglomerate layers, which were likely deposited near the boundary between a fluvial sand flat environment and the toe of alluvial fan.

This general trend from a meandering to a braided river system may have resulted from greater sediment volume input to the system by a changing source terrain such as an increased rate or greater magnitude of footwall exhumation with time. This phenomenon is verified by the evolution of the characteristic "coda" shape in the detrital AHe relative frequency diagrams (Fig. 14) that illustrates the waning frequency of older AHe ages upsection. Evidence for meandering river systems still exist in this portion of the Qattar Formation. At the 300 m mark, a meter-scale, sloping bedform partially overlies and truncates a layer with extensive trough cross-bedding. This 5 m thick, silt-rich feature is unique to the section and likely embodies a slumped river channel wall and levee.

Of the four Qattar Formation measured sections, the type section at Wadi al Qattar contains the greatest overall proportion of coarse clastic rock as well as the coarsest conglomerate in the Qattar Formation, Unit A2, because it was deposited proximal to the sediment source region. In

the southern terminus of the Hamd half-graben, Unit A2 is a laterally continuous, polymict fluvial and alluvial fan-influenced deposit that grades into finer clasts up section toward the southwest, suggesting a NE or SE clast source. The lack of coarse alluvial material at the Wadi al Jizl and Jabal Antar measured sections (Figs. 11-13) is likely due to the fact that the measured sections are located ~3 km and ~7 km, respectively, from the HJB border fault and footwall, the assumed source for the derivative syn-rift sediment.

Paleocurrent analysis of planar crossbeds in Qattar Formation fluvial sandstones proves difficult due to the scarcity of reliable cross-bedding planes and severity of outcrop weathering though measurements were obtained at two locations (Table 4; Figs. 6 and 7). In the central Hamd half-graben near Jabal Antar, crossbed measurements show a general paleocurrent direction of 87° ± 44° (*n=6)* while those in Wadi Rashad and Wadi al Qattar show a dissimilar trend of 338° ± 13° (*n=6)*. High variability in crossbed orientation is expected given the multitude of active wadis that brought sediment into the HJB and the general orientation of these structures suggests that river systems drained into the HJB from the WSW hanging wall and ran sub-parallel along the base of the exhumed Hamd half-graben footwall. This supports the existence of a highland to the NE of the HJB during Qattar Formation deposition, especially considering the presence of intercalated sediment/Ishara basalt horizons that signal no hiatus in sedimentation between the first outpouring of Ishara A and B basalt at Jabal Antar (Fig. 9).

As in the Hamd half-graben, erosion has removed great volumes of the Qattar Formation from the Jizl half-graben. Few exposures of syn-rift sediment remain along the border fault at Jabal al Qihaba, which once provided a backstop for the deposition of Qattar Formation in this

area, and scattered outcrop is all that remains of what once was an extensive syn-rift sedimentary record within this portion of the HJB.

The sandstone and conglomerate units at Wadi al Jizl contain relatively very few sedimentary structures though scoured bases, cm-scale fluvial channels with polymict conglomerate lag deposits, and silt overbank deposits suggest deposition of the Qattar Formation by an active fluvial system at this locale. The Qattar Formation basal section along the front of Jabal Qihaba (Fig. 8) is almost exclusively a medium pebble to large cobble, angular to sub-angular, poorly sorted orthoconglomerate composed of Proterozoic Al Ays Group gneiss and quartzite. The oligomict nature and lack of alteration by transport processes in the basal section at Wadi al Jizl signals an immaturity of the conglomerate here, especially relative to other locales where the basal syn-rift section is often an intercalation of quartz arenite and polymict pebble-to-cobble conglomerate. The apparent textural and compositional immaturity of the Qattar Formation in the Jizl half-graben substantiates the idea that these outcrops are located close to the proposed sediment source, a highland at Jabal al Qihaba, and likely represent interfingering middle-to-outer alluvial fan and fluvial plain environments.

The uppermost strata of the Qattar Formation is exposed in Wadi al Qattar ~3.5 km SSW of the type section as a lithic-rich, medium pebble to large cobble conglomerate with sub-angular to angular, poorly sorted clasts of local Al Ays Group gneiss, quartzite, and actinolite schist. Bed thickness ranges between 1-5 meters with common sub-meter interbeds of tan well-sorted fine sandstone. No bedforms or clast imbrication is observable and the topmost contact is unconformable with basalt from Harrat Ishara. Owing to the fact the Qattar Formation formed within an active half-graben, this uppermost section lies unconformably on Proterozoic Al Ays

Gp. where it was deposited far from the source and breached the hanging wall hinge of the Hamd half-graben to the SSW. This relationship between the Qattar Formation and underlying Proterozoic basement is also observed in the central HJB near Jabal Antar where the syn-rift section filled the Hamd half-graben and spilled to the southwest.

1.7.3.3. Lithostratigraphic equivalents to the Qattar Formation within the Arabian Margin

The Qattar Formation is lithostratigraphically equivalent to all basal members of terrigenous syn-rift strata within the Arabian rift flank. Though speculative correlation has been noted between "continental rift valley" siliciclastics and sub-basalt sediment within the HJB (Kemp, 1982; Brown et al., 1989), no published correlations have yet been drawn to the Qattar Formation due to the previously undetermined tectonic provenance of the HJB and the fact that most syn-rift sedimentary sections within the rift flank have some significant marine component (Hughes and Johnson, 2005 *and references therein*). Based on depositional age, lithology, and structural position overtop the Precambrian basement unconformity, we propose stratigraphic equivalency between the Qattar Formation in the HJB, the lower Shumaysi Formation in the Suqah trough east of Jeddah (Karpoff, 1957; Al-Shanti, 1966; Spencer, 1987; Abou Ouf and Gheith, 1998), and the Wadi al Hamd Mbr. of the Tayran Formation (Raghama Gp.) in the Midyan Basin at the northwest end of the Arabian rift flank (Dullo et al., 1983; Bayer et al., 1988). Both the lower Shumaysi (late Oligocene-early Miocene; 180 m-thick) and Tayran Formations (Aquitanian; 114 m-thick) consist of fluvatile, commonly cross-bedded, sandstone and pebble-to-cobble conglomerate strata that directly overlie the Precambrian basement unconformity (Schmidt et al., 1982; Dullo et al., 1983; Abou Ouf and Gheith, 1998 *and references therein*; Hughes et al., 1999). Correlation of these strata with the Qattar Formation

ends after the first 100-200 m as both formations begin to incorporate lacustrine then marine sedimentary facies upsection; the Qattar Formation indicates no marine incursion into the HJB (assuming that overlying transgressive facies have not eroded over time). Notably, Abou Ouf and Gheith (1998) cite a resemblance of the Shumaysi Formation to quartz sandstone and pebble conglomerate of the informal Ayyanah formation (Jizan Group; 20-40 m-thick) that lie near Al Qunfudhah in the southern Red Sea coastal plain (Hadley, 1975; Schmidt et al., 1982). Oolitic ironstone has also been described in the middle Shumaysi Formation (Al-Shanti, 1966; Mesaed et al., 2011). These strata appear similar to bioturbated ironstone that overlies Proterozoic Al Ays Gp. metavolcanic rock in Wadi Rashad (Fig. 6) that has not yet been proven to correlate with the Qattar Formation

Hughes and Johnson (2005) made considerable revisions to Red Sea lithostratigraphic nomenclature after comparing regional borehole data with surface outcrop. Consequently, the Shumaysi Formation (Karpoff, 1957; Al-Shanti, 1966), labeled as obsolete, is now part of the Usfan Formation (Suqah Gp.) and the Wadi al Hamd Mbr. of the Tayran Formation (Raghama Gp.; Dullo et al., 1983; Bayer et al., 1988) is now classified as Al Wajh Formation (Tayran Gp.). Because interpretation of the depositional environment and syn-rift classification of both sedimentary packages has not changed significantly, we cite the lithostratigraphic names assigned in the original descriptions. Still outstanding is the likelihood of correlation between the Qattar Formation and basal sedimentary strata within the Aznam (Suayah et al., 1991) and Tabuk graben as well as the recently exposed, via road building, fluvio-lacustrine Bathan Formation in Al-Rehaili, North Jeddah (Ghandour and Al-Washimi, 2011).

1.7.4. Volcanic and geomorphologic evolution of the HJB

1.7.4.1. Age of the Wadi al Hamd

The modern Wadi al Hamd has existed close to its present course in the HJB since the late Miocene, when stream capture processes redirected its course towards the Red Sea Basin near Wadi al Jizl (Brown, 1970; Brown et al., 1989; USGS, 1993). The positions of three key Kura basalt entry points into the HJB provide temporal tie points to determine the age and extent of the active wadi channel in the Hamd half-graben (Fig. 2). One entry point of the Kura basalt into the HJB (#1; Fig. 2) is located in the northern portion of the Hamd half-graben, SE of Jabal Abu an Na'am, where an active wadi was operating to direct the basalt flow trend at the time of basalt deposition in the late Miocene. The 7.9 ± 0.2 Ma age of sample 06SA055, taken from the basal flow in this area, provides a minimum age for the Wadi al Hamd channel and shows that the general orientation of the modern channel has existed since at least the Tortonian. Corroborating evidence for the ancient orientation of the Wadi al Hamd channel is found 5 km further along trend to the NW where the outcrop pattern shows that basalt was channeled down a paleolow to the SW prior to spilling into the middle of the HJB just west of Jabal Abu An Na'am (at 25°15'N, 38°50'E).

Another entry point is located at the structural accommodation zone in the middle of the HJB (#2; Fig. 2) where Kura basalt flowed SW down a paleotopographic low incised in the Precambrian basement before diverting to the northwest and southeast along a paleo-Wadi al Hamd channel. Basalt sample 06SA061, collected from the SE flow, yields a $^{40}Ar/^{39}Ar$ age of 10.7 ± 0.4 Ma and shows that the present course of the Wadi al Hamd at this location existed as early as the middle Miocene. Geologic contacts between post-Qattar Formation wadi sediments and Kura basalt support this estimation and reveal a long-lived interaction between the Wadi al

Hamd and Kura basalt. A Hijaz Railway railroad cut SE of Hadiyah village exposes a single, 3 meter-thick layer of cross-bedded silt-rich conglomeratic sandstone intercalated with a 6.55 ± 0.11 million-year-old Kura basalt flow within the HJB structural linkage zone (06SA058; Table 6; Fig. 2). This sediment/basalt relationship shows an active wadi present at this location during basalt emplacement. Coleman and others (1983) state that no sediment is observed to interlayer with the basal flows of Harrat Khaybar proper yet this outcrop in the HJB proves that intercalation of wadi sediment and Kura basalt basal flows occurred at least along the perimeter of Harrat Khaybar during the late Miocene. Notably, the relative age of this sediment precludes it from inclusion in the Qattar Formation and this uncommon sediment package is currently unassigned to any recognized geologic unit.

The third key Kura basalt entry point lies near the southern terminus of the HJB and confirms the Messinian age of this water gap north of the Hamd half graben border fault (#3; Fig. 2). A 5.67 ± 0.07 million-year-old basalt flow (07SA052; Table 6) directly overlies Proterozoic Al Ays Group proving that the Qattar Formation, if formerly present, was evacuated from this position before the Messinian. Moreover, the presence and age of this water gap shows that the Wadi al Hamd had actively flowed down this course instead of the structurally controlled low in Wadi al Qattar, which it possibly did at some point in the geologic past during Qattar Formation deposition.

1.7.5. Syn- to post-rift basalt volcanism in the HJB

1.7.5.1. Perched basalt occurrences in the Hamd and Jizl half-graben

Basalt in the central Hamd half-graben erupted and flowed from both the eruptive center of Harrat Ishara as well as local dikes. Kemp (1981) observed depositional patterns of basalt flows

in the HJB and postulated that basin-filling processes may account for the presence of perched basalt plateaus atop local topographic highs. Noting the thickness of the basalt flows at Jabal Antar and no cross-cutting relationship between the basalt and dikes at Jabal Abu an Na'am, Kemp (1981) states that basalt likely reached the highest elevations only after filling the "Jizl trough" (now known as the HJB).

06SA075 was collected from a perched basalt unit at the top of Jabal Uwayjir (Fig. 21) to explore the possibility of basalt pooling and basin-filling processes postulated by Kemp (1981). 06SA075 is an AOB that plots just below trachybasalt field (Fig. 17) and yields a $^{40}Ar/^{39}Ar$ age of 9.34 ± 0.18 Ma. Both the age and LREE geochemical signature of 06SA075 establish it as Kura basalt from Harrat Khaybar. In the nearby Wadi al Hamd, another Kura basalt flow (06SA055) lies at a ~600 m lower elevation. Its similar $^{40}Ar/^{39}Ar$ age of 7.9 ± 0.2 Ma confirms it was emplaced relatively soon after 06SA075 but at a much lower elevation. This relationship shows that, while basalt pooling may have occurred locally to a significant degree in the Hamd-half-graben where vents sat near the base of paleotopographic highs, local dikes emplaced 06SA075 atop Jabal Uwayjir and are mostly responsible for perched basalt units in the HJB.

In the Jizl half-graben, geologic contacts and REE geochemical analyses show that local dikes emplaced Ishara B at Wadi al Jizl but a geologic reconnaissance map by Kemp (1981) shows this unit grouped as part of the "Ishara basalt", a unit of perched basalt plateaus that incorporates both Harrat Ishara and Jabal Khirsat (now known as Harrat Harairah). Though Harrat Harairah is the closest major volcanic field to the Jizl half-graben basalt occurrences, the volcanic features developed independently. First, Harrat Harairah developed during the early Miocene (Brown et al., 1989; Coleman, 1993 *and references therein*), making it older than the

middle Miocene Ishara B basalt at Wadi al Jizl. Second, the near-horizontal basalt flows of Harrat Harairah lie ~12 km to the SW on a topographic promontory and 340 m higher than the basal flow in Wadi al Jizl. The current elevation difference cannot be explained structurally. A Protero-Paleozoic granitoid pluton on the south flank of the basalt-capped promontory yields reproducible late Triassic AHe cooling ages of 203.2 ± 12.2 Ma and 218.4 ± 13.1 Ma, indicating that the promontory was formed via erosional processes that produced inverted topography. The age disparity and lack of proof that rift-related faulting is responsible for the prominent south-to-north topographic change demonstrates that Ishara B at Wadi al Jizl and the basalt of Harrat Harairah developed at separate times at different structural levels. However, these conclusions do not preclude the two basalt occurrences from sharing a similar melt provenance that may have contributed magma at different times. Future courses of HJB basalt study should incorporate a comparative geochemical analysis between the two basalt occurrences.

1.7.5.2. Harrat Ishara magma sources

Ishara A and B units likely originated from different magma sources or evolved via magma chamber melt fractionation processes given the fact that their overlapping Miocene age ranges establish a penecontemporaneous eruption period (Fig. 16). Both of these possibilities have been proposed to explain the geochemical variation observed in regional harrat systems across the Arabian rift flank (e.g., Suayah et al., 1991; Suayah, 1992; Coleman, 1993).

In certain parts of the Hamd half-graben, either Ishara A or B exists as the basal stratigraphic basalt flow that unconformably overlies Proterozoic basement. A 14.9 ± 0.4 million-year-old Ishara B OTB at Jabal al Mahdirah (06SA067; Fig. 2), ~17 km to the NW of Jabal Antar, unconformably overlies the Proterozoic Hadiyah Group and has a similar age, and the same

geologic relationship to basement, as several Ishara A AOB flows at in the southern Hamd half-graben (e.g., 06SA084). The contemporaneous eruption of Ishara A and B into the Hamd half-graben during the middle Miocene indicates that multiple magma sources operated simultaneously during Harrat Ishara development and illustrates the spatiotemporal complexity of volcanic products in the HJB.

The documentation of simultaneous eruptions of multiple basalt types from the same vent system is new for Harrat Ishara but this result is not unprecedented. Camp et al. (1987) reported a similar phenomenon in their examination of basalt from the Madinah eruption at Harrat Rahat. These observations build on the original ideas of Coleman (1975) who hypothesized that all Arabian rift flank basalt may be sourced form the same homogenous mantle before differentiating due to dissimilar degrees of partial melting and fractionation.

Host rock lithology may play a key role in final basalt geochemistry. Ishara B is erupted within the Jizl half-graben at Wadi al Jizl and throughout the Hamd half-graben based on age and REE geochemical correlations (Figs. 16 and 18). Ishara B basalt contains low LREE concentrations, relative to Ishara A and Kura basalts (Camp et al., 1991), and comparable trace, MREE, and HREE abundances but some geochemical variance is observable. The increased alkali content and LREE abundances within Ishara B at Wadi al Jizl likely results from a greater degree of crustal contamination of melt relative to units in the Hamd half-graben. Ishara B basalt extruded through a different lithologic subunit of the Proterozoic Al Ays Group, which may be the contributing factor in final basalt geochemistry. The bedrock underlying Wadi al Jizl is a paragneiss derived from an undetermined silicic member of the Al Ays Group while the Jabal

Antar region is underlain by the silicic volcanic rock sequence (mostly rhyolitic ash flow tuffs) of the Kura and Jizl Formations (Kemp, 1981).

1.7.5.3. On age discrepancies and inaccuracies in legacy Harrat Ishara volcanostratigraphy

Prior study of basalt age and geochemistry in the HJB region is limited (e.g., Brown et al., 1970; Kemp, 1981, 1982; Brown et al., 1989; Coleman, 1993 *and references therein*). In some cases, published ages are either contradictory in separate reports, nonspecific regarding sample location, or misattributed to different Harrat Ishara basalt generations by mistakenly assigning basalt flows to different regional volcanostratigraphic levels based on outcrop weathering pattern, K/Ar ages, and geochemical data. Some mapping efforts mistakenly confuse the Ishara basalt (from Harrat Ishara) with the late Miocene Kura basalt from Harrat Kura (e.g., Pellaton, 1979, 1981; Delfour and Dhellemmes, 1980). Mistakes arise due to inaccurate results from the K/Ar age dating technique as well as the fact that the age range of Harrat Ishara activity partially overlaps the oldest volcanic activity from Harrat Khaybar. The close proximity of the two fields, whose proposed volcanic centers lie <50 km apart, provided additional complexity since the products of Harrats Ishara and Kura nearly overlap at the southern end of the HJB. Kemp (1981) has since shown that it is possible to distinguish between Kura and Ishara basalts geochemically, temporally and structurally via comparison of their full temporal range of volcanic activity and differences in harrat/sub-basalt Precambrian basement contacts.

The incorrect citation of a single sample may lead to improper age assignments for certain basalt generations. For instance, Brown (1972) provides the first attempt at dating Harrat Ishara basalt by reporting 28.3 ± 2.9 Ma and 21.2 ± 2.1 Ma K/Ar ages for samples 910 and 911, respectively, from Harra Al Jarf on the northwest side of the Ishara field. Coleman (1975) later

lists an age of 20.4 Ma for sample "910" from Jabal Antar using an uncited source. Though these samples share the common name of "910", they do not correlate in either age or location. It is possible Coleman (1975) lists this sample name according to its collected elevation and is thus an unrelated sample that coincides with the name used by Brown (1972). However, this sample nomenclature is inconsistent with most other samples from the study of Coleman (1975), which indicates that it was drawn from an outside source and is likely an incorrect citation of Brown (1972). In a later paper, Coleman and others (1983) specifically and accurately cites Brown (1972) for a sample "910" from Harra Al Jarf with a K/Ar age of 28.3 ± 2.9 Ma, an age approximately 8 m.y. older and in a different location than reported in Coleman (1975). This citation in Coleman and others (1983) suggests that the reported 20.4 Ma age and location of "Jabal Antar" basalt in Coleman (1975) is incorrect and is not a fair contribution to the historical suite of K-Ar ages available for Harrat Ishara.

Additional reports of Ishara basalt ages prove inaccurate as well. Delfour and Dhellemmes (1980) report a 9.62 Ma K/Ar age (sample JCB 464) for basalt at Jabal Antar proper yet their listed sample location (25°05'40"N, 38°38'09"E) is actually 22 km west of Jabal Antar just north of Jabal Buwayrid. This distance discrepancy is great enough to have sufficient implications in terms of delineating the timing of HJB structural development. Most recently, Camp and Roobol (1991) provide an unpublished K-Ar age of 11.03 ± 1.51 Ma for a sample from an unspecified location within Harrat Ishara, which likely correlates to Ishara B but cannot be verified due to the lack of a listed sample location and sample geochemistry.

According to our $^{40}Ar/^{39}Ar$ age results, basalt volcanism in the HJB area began ~6 million years after initial HJB structural development then persisted for 4.5 million years. In the early

Miocene, the first basalt flows were extruded into active wadi channels and most individual basal flow units are not laterally extensive; subsequent basalt flows stacked vertically and laterally beside older flows. At Jabal Antar, one 5 m-thick sediment horizon separates Ishara A and B (Fig. 12) while no evidence exists further upsection for an interruption of basalt emplacement in the Hamd half-graben. The oldest ages obtained for the basal flows of Ishara basalt at Wadi al Qattar and Jabal Antar are 17.2 Ma and 15.2 Ma, respectively. Notably, our oldest age determinations are ~4-11 m.y. younger than those reported by Brown (1972) for samples 910 & 911 from Harra al Jarf and our youngest age determination, from the stratigraphically topmost basalt flow at Jabal Antar proper, is ~4 m.y. older than the age reported by Delfour and Dhellemmes (1980).

1.7.5.4. Future volcanostratigraphic study of Harrat Ishara

Trends in the eruption ages of Ishara A and B basalt indicate that further subdivision of our proposed two Harrat Ishara volcanostratigraphic units may be possible. For example, two groups of four samples align with a cluster of $^{40}Ar/^{39}Ar$ ages at either ~15 Ma or ~17 Ma (samples 06SA001, -004, -050, and 084 versus samples 06SA002, -010, -007, and -082; Fig. 16). This possibility is unsurprising given the limited available accurate age data for Harrat Ishara (outside of this study) relative to the geochronometric age suites that exist for neighboring harrat. We cannot discriminate a greater subdivision based on our existing age and geochemical database. Additional age analyses and geochemical research is necessary to fully resolve the apparent complexity of Harrat Ishara eruption timing, extent of basalt flow emplacement, and their varied geochemistry.

1.7.6. Implications for the timing and style of the RSR

Thermochronological, structural, sedimentological, and volcanological evidence shows that the Hamd-Jizl Basin is a primary component of the Red Sea Rift system. The association of the HJB with the initial continental lithosphere rupture phase ~23 Ma has two important implications for the breadth, kinematic style, and driving force behind continental lithosphere rupturing dynamics in the CARF. First, the initial RSR rupture phase in the CARF was long-lived (23-15 Ma) and operated a wide zone of extension. Second, intrusive basalt volcanism was not a primary driver of continental lithosphere rupture in the CARF.

Bedrock apatite (U-Th)/He age evidence proves the syn-rift character of the HJB and shows extensional deformation lasting from 23-15 Ma, which requires an adjustment to the estimates of diffuse rupture width and timing in the CARF. Cochran (1981, 1983) first recognized the diffusness of initial Red Sea rifting and estimated that diffuse extension began in the RSR over a 100 km-wide zone, with 65% extension, prior to strain localization along the modern RSR axis. In close agreement, Bosworth (1993) cites 90 km for the width of the proto-Red Sea continental rift based on the width of the aborted Gulf of Suez rift. 260 km is the present distance between the Hamd half-graben border fault and the RSR axial trough trace, projected along rift strike from the northernmost point of seafloor spreading at 23.3° N, 37.1° E. Including the 65% extension estimate of Cochran (1981, 1983), and assuming orthogonal rifting, we propose an extension-adjusted, diffuse rupture zone ~170 km-wide on the CARF alone. This result is 140% greater than the initial diffuse rupture width provided by Cochran (1983) who assumes a pure shear rift model that symmetrically distributes strain to both margins of the incipient rift. This result expands the area of CARF continental lithosphere that is recognized to have extended during the Red Sea rift initiation as defined by Roobol and Kadi (2008), greatly differs from

initial rift basin width estimates of 20-30 km for the southern RSR (Bohannon and Eittreim, 1991) and may lessen total extension estimates that assume thinned continental lithosphere is limited to the Red Sea basin margins (e.g., Girdler and Southren, 1997).

Strain dissemination within the Arabian rift flank, via the development of extensional structures like the HJB, has effectively accommodates strain and prevented full-scale rifting of the continental lithosphere. The absence of Serravallian and younger AHe ages in exhumed Hamd and Jizl half-graben footwalls indicates RSR-related strain abandonment of the HJB ~15 Ma. This timing of RSR strain localization is coincident with the advent of the Dead Sea transform fault and regional stress reorganization (Richardson and Arthur, 1988; Coleman, 1993; Bosworth and McClay, 2001) and permits the classification of the HJB as a "relict basin" (Bosworth et al., 2005 *and references therein*). Extension in the HJB lasted for ~8 million years prior to abandonment, a full one-third of the existence of the RSR, which shows that a prolonged stage of diffuse rupture has a lasting impact on subsequent rift architecture. The absence of seafloor spreading indicators in the RSR north of 21° N latitude shows that the central and northern sections of the RSR system remain in a continental rift mode (Cochran and Martinez, 1988; Martinez and Cochran, 1988; Cochran and Karner, 2007).

Aeromagnetic data shows the northwestern Arabian rift flank rife with magnetic lineaments whose pattern corresponds to regional tectonic elements such as the Najd Fault System, iron-rich rock suites within accreted Proterozoic terranes, and a major ~25-20 million-year-old dike swarm that parallels the Red Sea Basin along the entire length of the Arabian margin from the Asir Mountains to Sinai (Eyal et al., 1981; Camp and Roobol, 1992; Zahran et al., 2002; Nehlig et al., 2002 *and references therein*; Johnson, 1996; Bosworth et al., 2005 *and references therein*;

Roobol and Stewart, 2009). In the northern Arabian rift flank, the Tabuk, Fayha, Tayma, Qur Mulayh, and Tufayhah graben overlie and align with long magnetic lineaments, which are interpreted as subsurface dikes, the largest being the Great Ja'adah Dike beneath the Tabuk graben (Phoenix Corporation, 1985; Johnson, 1998 *and references therein*; Roobol and Stewart, 2009). Roobol and Kadi (2008) classify these graben as "pre-rift" features because they lie inboard of the structural domain that eventually down-dropped to form the modern coastal plain overtop the area of greatest crustal extension. This coincidence of graben development overtop dike-modified continental lithosphere is an expected consequence of thermal modification of the lithosphere according to Buck (2004) who postulates that pervasive dike injection is an integral part of the continental rupturing process. The idea of foundering syn-rift basins overtop major dike swarms appears accurate in the Aznam and Tabuk graben in the northern Arabian rift flank but little aeromagnetic or volcanological evidence exists to suggest that intrusive basalt volcanism was a driving force in the development of the Hamd and Jizl half-graben. Geochronological analysis of Harrat Ishara and Khaybar shows no evidence of extensive basalt volcanism older than ~17 Ma (i.e., as old or older than the HJB) and the absence of large, linear magnetic anomalies parallel to HJB structure is corroborates the belief that the HJB developed independently of large-scale dike injection (Johnson and Stewart, 1995; Roobol and Stewart, 2009). Extensive basalt volcanism in the HJB is temporally coincident with the eruption and emplacement of the second stage of basaltic volcanism that began in the middle Miocene, approximately 6 million years later than the onset of extension in the Hamd and Jizl half-graben. In summary, while the thermal modification of lithosphere may facilitate rupture development, a pre-treatment of continental lithosphere is not necessary for the development of large-scale

extensional features, especially those like the HJB that may exploit pre-existing lithologic weaknesses in the Arabian Shield basement.

1.8. Conclusions

The HJB is a major component of the Red Sea rift system that accommodated extension for the first ~8 million years of the RSR, genetically linked to the Red Sea Basin by a common tectonic history that began during the late Oligocene. Widespread rift flank dissection by normal faulting and exhumation of continental lithosphere fault blocks within the CARF signals the onset of the first phase of Red Sea rift development in the Oligocene-Miocene. In response to this tension ca. 22 Ma, the Hamd and Jizl half-graben developed ~140 km inboard from the coastal fault complex that frames the modern Red Sea Basin. Collectively, RSR-related strain markers in the HJB define an area of concentrated syn-rift extension, which certifies the diffuse character of the initial rift stage and classifies the CARF as a ~200 km wide diffuse rift margin (from the modern Red Sea axial trough to the HJB). Furthermore, the position of the northern HJB underscores the importance of pre-existing fault exploitation during progressive rifting since the Jizl half-graben is structurally delineated by normal faults originally formed as part of the transpressional Neoproterozoic Najd shear zone fabric.

The HJB developed during four distinct stages (Figs. 21 and 22). First, broad RSR-normal tension across the region in the early Miocene caused widespread dissection of CARF terranes, delineating the HJB border faults and demarcating the furthest extent of inboard deformation (Stage 1). Then, rapid footwall exhumation and erosion caused an accumulation of the syn-rift, siliciclastic sedimentary Qattar Formation proximal to the active border fault in both the Hamd and Jizl half-graben ca. 22 Ma (Stage 2). Qattar Formation outcrop patterns and paleocurrent

directions, subparallel to the modern basin strike, agree with other analyses that conclude that the Qattar Formation formed in a basin with highlands to the NNE, which is very similar to the NW-SE orientation of the mostly evacuated basin present today. The sedimentary record at Wadi al Qattar shows that the greater volume of syn-rift sedimentation occurred from ~22-17 Ma before asymmetrical throw along the border fault, due to deepening of the Hamd half-graben nearer to Jabal An Nu'ayyimah, caused the Qattar Formation to tilt ~30° to the NNW and form a monocline that comprises the type section in Wadi al Qattar. The most frequent detrital AHe cooling signal ~20 Ma pegs the initial age of rapid footwall exhumation in the early Miocene and proves that the Qattar Formation is a syn-rift sedimentary deposit and, by proxy, the Hamd half-graben formed as a syn-rift corollary of the modern Red Sea Basin.

Trailing the initial continental lithosphere rift pulse by ~6 million years, active basalt volcanism accompanied inboard deformation in the Hamd half-graben ca. 17 Ma (Stage 3). Two generations of Ishara basalt, decreasing in alkalinity and REE abundances with time, outpoured from Harrat Ishara in the early to middle Miocene and sealed-in the Qattar Formation in the southern and central Hamd half-graben at 17 Ma and 15 Ma, respectively, covering an area >300 km^2. Either melt fractionation processes or separate magma sources are responsible for the geochemical shift with time of the Ishara basalt. Both possibilities are cited by other researchers for the geochemical evolution of regional harrats on the Arabian rift flank.

Diffuse rift flank deformation continued through the middle Miocene with footwall exhumation in the Jizl half-graben at Jabal Nahar (AHe age: 15.1 ± 0.9 Ma) and minor post-depositional deepening of the Hamd half-graben where intra-basinal faults near Wadi al Qattar

juxtapose 14.5 Ma Ishara basalt flows against syn-rift sediments (Stage 4). No recent displacement is recognized anywhere along the full trace of the Hamd-Jizl border faults.

1.9. References

Abou Ouf, M. A., and Gheith, A. M., 1997, Paleo-environmental interpretation of synrift and prerift sediments of the eastern flank of the central Red Sea, Jeddah Region-Saudi Arabia: Arab Gulf Journal of Scientific Research, v. 15, no. 2, p. 32.

-, 1998, Sedimentary evolution of early rift troughs on the central Red Sea margin, Jeddah, Saudi Arabia: Sedimentary and tectonic evolution of rift basins: the Red Sea–Gulf of Aden: London, Chapman and Hall, p. 10.

Al-Hajri, S., and Owens, B., 2000, Stratigraphic palynology of the Palaeozoic of Saudi Arabia, Arabian Printing and Publishing House.

Al-Laboun, A. A., 1986, Stratigraphy and hydrocarbon potential of the Paleozoic succession in both Tabuk and Widyan basins, Arabia: Future Petroleum provinces of the world. American Association of Petroleum Geologist Memoir, v. 40, p. 399-425.

Al-Shanti, A. M., 1966, Oolitic Iron Ore Deposits in Wadi Fatima: Between Jeddah and Mecca, Saudi Arabia, Ministry of Petroleum and Mineral Resources.

Balestrieri, M. L., Abbate, E., Bigazzi, G., and El Bedri Ali, O., 2009, Thermochronological data from Sudan in the frame of the denudational history of the Nubian Red Sea margin: Earth Surface Processes and Landforms, v. 34, no. 9, p. 1279-1290.

Baubron, J. C., and Maury, R. C., 1979, Age and petrology of the Jabal al Abyad volcanic chain (Khaybar plateau, Saudi Arabia): Geodynamic évolution of the Afro-Arabie Rift System (int. Cong. Rome), p. 645-655.

Bayer, H. J., Hötzl, H., Jado, A. R., Röscher, B., and Voggenreiter, W., 1988, Sedimentary and structural evolution of the northwest Arabian Red Sea margin: Tectonophysics, v. 153, no. 1, p. 137-151.

Best, J. A., Barazangi, M., Al-Saad, D., Sawaf, T., and Gebran, A., 1993, Continental margin evolution of the northern Arabian platform in Syria: AAPG Bulletin (American Association of Petroleum Geologists);(United States), v. 77, no. 2.

Bohannon, R. G., 1986, Tectonic configuration of the western Arabian continental margin, southern Red Sea: Tectonics, v. 5, no. 4, p. 477-499.

-, 1989, Style of extensional tectonism during rifting, Red Sea and Gulf of Aden: Journal of African Earth Sciences (and the Middle East), v. 8, no. 2-4, p. 589-602.

Bohannon, R. G., and Eittreim, S. L., 1991, Tectonic development of passive continental margins of the southern and central Red Sea with a comparison to Wilkes Land, Antarctica: Tectonophysics, v. 198, no. 2-4, p. 129-154.

Bohannon, R. G., Naeser, C. W., Schmidt, D. L., and Zimmermann, R. A., 1989, The timing of uplift, volcanism, and rifting peripheral to the Red Sea: A case for passive rifting?: Journal of Geophysical Research, v. 94, no. B2, p. 1683-1701.

Bosworth, W., Huchon, P., and McClay, K., 2005, The Red Sea and Gulf of Aden Basins: Journal of African Earth Sciences, v. 43, no. 1-3, p. 334-378.

Bosworth, W., and McClay, K., 2001, Structural and stratigraphic evolution of the Gulf of Suez rift, Egypt: a synthesis: Mémoires du Muséum national d'histoire naturelle, v. 186, p. 567-606.

Brown, G. F., 1970, Eastern margin of the Red Sea and the coastal structures in Saudi Arabia: Philosophical Transactions for the Royal Society of London. Series A, Mathematical and Physical Sciences, p. 75-87.

-, 1972, Tectonic Map of the Arabian Peninsula: US Geological Survey, scale 1: 4,000,000.

Brown, G. F., and Coleman, R. G., The tectonic framework of the Arabian Peninsula1972, International Geological Congress.

Brown, G. F., and Jackson, R. O., The Arabian Shield1960, Volume 9, p. 69-77.

Buck, W. R., 2004, Consequences of asthenospheric variability on continental rifting: Rheology and deformation of the lithosphere at continental margins, p. 1-30.

Camp, V. E., Hooper, P. R., Roobol, M. J., and White, D. L., 1987, The Madinah eruption, Saudi Arabia: magma mixing and simultaneous extrusion of three basaltic chemical types: Bulletin of volcanology, v. 49, no. 2, p. 489-508.

Camp, V. E., and Roobol, M. J., 1989, The Arabian continental alkali basalt province: Part I. Evolution of Harrat Rahat, Kingdom of Saudi Arabia: Geological Society of America Bulletin, v. 101, no. 1, p. 71-95.

-, 1991, Comment on “Topographic and volcanic asymmetry around the Red Sea: Constraints on rift models” by TH Dixon, ER Ivins, and JF Brenda: Tectonics, v. 10, no. 3, p. 649-652.

-, 1992, Upwelling asthenosphere beneath western Arabia and its regional implications: Journal of Geophysical Research, v. 97, no. 15, p. 255-271.

Camp, V. E., Roobol, M. J., and Hooper, P. R., 1989, Intraplate alkalic volcanism and magmatic processes along the 600 km-long Makkah–Madinah–Nafud volcanic line, western Saudi Arabia: Continental Magmatism, 39 IAVCEI General Assembly, Santa Fe, NM, New Mexico Bureau of Mines Geological Bulletin, p. 131.

-, 1991, The Arabian continental alkali basalt province: Part II. Evolution of Harrats Khaybar, Ithnayn, and Kura, Kingdom of Saudi Arabia: Geological Society of America Bulletin, v. 103, no. 3, p. 363-391.

Chazot, G., Menzies, M. A., and Baker, J., 1998, Pre-, syn-and post-rift volcanism on the south-western margin of the Arabian plate, v. Sedimentation and tectonics in rift basins: Red Sea–Gulf of Aden case, p. 5.

Cherniak, D. J., Watson, E. B., and Thomas, J. B., 2009, Diffusion of helium in zircon and apatite: Chemical Geology, v. 268, no. 1, p. 155-166.

Clark, M. D., 1981, Geologic Map of the Al Hamra Quadrangle, Sheet 23C, Kingdom of Saudi Arabia, scale 1: 250 000.

Cochran, J. R., 1981, The Gulf of Aden: structure and evolution of a young ocean basin and continental margin: Journal of Geophysical Research, v. 86, no. B1, p. 263-287.

-, 1983, A model for the development of the Red Sea: Am. Assoc. Petrol. Geol, v. 67, p. 41-69.

Coleman, R. G., 1993, Geologic evolution of the Red Sea, Oxford University Press.

Coleman, R. G., Fleck, R. J., Hedge, C. E., Ghent, E. D., and Project, G. S. S. A., 1975, The volcanic rocks of southwest Saudi Arabia and the opening of the Red Sea, US Geological Survey.

Coleman, R. G., Gregory, R., Brown, G. F., Arabia, S., and Survey, G., 1983, Cenozoic volcanic rocks of Saudi Arabia, US Department of the Interior, Geological Survey.

Coleman, R. G., and McGuire, A. V., 1988, Magma systems related to the Red Sea opening: Tectonophysics, v. 150, no. 1-2, p. 77-100.

Corp., P., 1985, The interpretation of an airborne geophysical survey of the Cover Rocks region, Kingdom of Saudi Arabia.

Crane, K., and Bonatti, E., 1987, The role of fracture zones during early Red Sea rifting: structural analysis using Space Shuttle radar and LANDSAT imagery: Journal of the Geological Society, v. 144, no. 3, p. 407-420.

Crossley, R., Watkins, C., Raven, M., Cripps, D., Carnell, A., and Williams, D., 1992, The sedimentary evolution of the Red Sea and Gulf of Aden: Journal of Petroleum Geology, v. 15, p. 157-172.

Davies, F. B., 1984, Strain analysis of wrench faults and collision tectonics of the Arabian-Nubian Shield: The Journal of Geology, p. 37-53.

Davies, F. B., and McEwen, G., 1985, Geographic Map of the Al Wajh Quadrangle, Sheet 26B, Kingdom of Saudi Arabia, Ministry of Petroleum and Mineral Resources, Deputy Ministry for Mineral Resources.

Davison, I., Al-Kadasi, M., Al-Khirbash, S., Al-Subbary, A. K., Baker, J., Blakey, S., Bosence, D., Dart, C., Heaton, R., and McClay, K., 1994, Geological evolution of the southeastern Red Sea Rift margin, Republic of Yemen: Geological Society of America Bulletin, v. 106, no. 11, p. 1474-1493.

Delfour, J., and Dhellemmes, R., 1980, Geologic Map of the Khaybar quadrangle, sheet 25D, Kingdom of Saudi Arabia, scale 1:250,000.

Dercourt, J., Zonenshain, L. P., Ricou, L. E., Kazmin, V. G., Le Pichon, X., Knipper, A. L., Grandjacquet, C., Sbortshikov, I. M., Geyssant, J., and Lepvrier, C., 1986, Geological evolution of the Tethys belt from the Atlantic to the Pamirs since the Lias: Tectonophysics, v. 123, no. 1, p. 241-315.

Dixon, T. H., Ivins, E. R., and Franklin, B. J., 1989, Topographic and volcanic asymmetry around the Red Sea: Constraints on rift models: Tectonics, v. 8, no. 6, p. 1193-1216.

Dixon, T. H., Stern, R. J., and Hussein, I. M., 1987, Control of Red Sea rift geometry by Precambrian structures: Tectonics, v. 6, no. 5, p. 551-571.

du Bray, E. A., Stoeser, D. B., and McKee, E. H., 1991, Age and petrology of the Tertiary As Sarat volcanic field, southwestern Saudi Arabia: Tectonophysics, v. 198, no. 2-4, p. 155-180.

Dullo, W. C., Hötzl, H., and Jado, A. R., 1983, New stratigraphical results from the Tertiary sequence of the Midyan area, NW Saudi Arabia. Contributions to the geology of the eastern margin of the Red Sea No. 1 A joint DFG-UPM-Project; Publication No. 5 of SFB 108: Newsletters on Stratigraphy, v. 12, no. 2, p. 75-83.

Ehlers, T. A., and Farley, K. A., 2003, Apatite (U–Th)/He thermochronometry: methods and applications to problems in tectonic and surface processes: Earth and Planetary Science Letters, v. 206, no. 1, p. 1-14.

Eyal, M., Eyal, Y., Bartov, Y., and Steinitz, G., 1981, The tectonic development of the western margin of the Gulf of Elat (Aqaba) rift: Tectonophysics, v. 80, no. 1, p. 39-66.

Farley, K. A., 2002, (U-Th)/He dating: Techniques, calibrations, and applications: Reviews in mineralogy and geochemistry, v. 47, no. 1, p. 819-844.

Faulds, J. E., and Varga, R. J., 1998, The role of accommodation zones and transfer zones in the regional segmentation of extended terranes: Geological Society of America Special Papers, v. 323, p. 1-45.

Favre, P., and Stampfli, G. M., 1992, From rifting to passive margin: the examples of the Red Sea, Central Atlantic and Alpine Tethys: Tectonophysics, v. 215, no. 1-2, p. 69-97.

Fleck, R. J., Coleman, R., Cornwall, H., Greenwood, W., Hadley, D., Schmidt, D., Prinz, W., and Ratte, J., 1976, Geochronology of the Arabian shield, western Saudi Arabia: K-Ar results: Geological Society of America Bulletin, v. 87, no. 1, p. 9-21.

Ghandour, I. M., and Al-Washmi, H. A., 2011, Stratigraphic architecture of the fluvio-lacustrine deposits, Bathan Formation, Al-Rehaili area, North Jeddah, Saudi Arabia: Arabian Journal of Geosciences, p. 1-16.

Girdler, R. W., 1991, The Afro-Arabian rift system--an overview: Tectonophysics, v. 197, no. 2-4, p. 139-153.

Girdler, R. W., and Southren, T. C., 1987, Structure and evolution of the northern Red Sea.

Guiraud, R., Bosworth, W., Thierry, J., and Delplanque, A., 2005, Phanerozoic geological evolution of Northern and Central Africa: an overview: Journal of African Earth Sciences, v. 43, no. 1-3, p. 83-143.

Hadley, D. G., 1975, Geology of the Al Qunfudhah quadrangle, sheet 19/41C, Kingdom of Saudi Arabia, scale 1:100,000.

Hofmann, C., Courtillot, V., Feraud, G., Rochette, P., Yirgu, G., Ketefo, E., and Pik, R., 1997, Timing of the Ethiopian flood basalt event and implications for plume birth and global change: Nature, v. 389, no. 6653, p. 838-841.

House, M. A., Wernicke, B. P., and Farley, K. A., 2001, Paleo-geomorphology of the Sierra Nevada, California, from (U-Th)/He ages in apatite: American Journal of Science, v. 301, no. 2, p. 77-102.

Hughes, G. W., and Johnson, R. S., 2005, Lithostratigraphy of the Red Sea Region: GeoArabia, v. 10, no. 3, p. 49-126.

Hughes, G. W., Perincek, D., Grainger, D. J., Abu-Bshait, A., and Jarad, A., 1999, Lithostratigraphy and depositional history of part of the Midyan region, northwestern Saudi Arabia: GeoArabia, v. 4, no. 4, p. 500-542.

Irvine, T. N., and Baragar, W. R. A., 1971, A guide to the chemical classification of the common volcanic rocks: Canadian Journal of Earth Sciences, v. 8, no. 5, p. 523-548.

Janousek, V., Farrow, C. M., and Erban, V., 2003, GCDkit: new PC software for interpretation of whole-rock geochemical data from igneous rocks: Geochimica et Cosmochimica Acta Supplement, v. 67, p. 186.

-, 2006, Interpretation of whole-rock geochemical data in igneous geochemistry: introducing Geochemical Data Toolkit (GCDkit): Journal of Petrology, v. 47, no. 6, p. 1255-1259.

Johnson, D. M., Hooper, P. R., and Conrey, R. M., 1999, XRF analysis of rocks and minerals for major and trace elements on a single low dilution Li-tetraborate fused bead: Advances in X-ray Analysis, v. 41, p. 843-867.

Johnson, P. R., 1998, Tectonic map of Saudi Arabia and adjacent areas: Deputy Ministry for Mineral Resources.

-, 2006, Proterozoic geology of western Saudi Arabia with Explanatory Notes.

Johnson, P. R., and Stewart, I. C. F., 1995, Magnetically inferred basement structure in central Saudi Arabia: Tectonophysics, v. 245, no. 1-2, p. 37-52.

Johnson, P. R., and Vranas, G. J., 1994, Paleovalley constraints on the uplift history of the central Arabian Red Sea margin, American Geophysical Union Fall Meeting, Volume H52D-02.

Jonsson, S., Lu, Z., El-Hadidy, S., and Zahran, H., The 2009 Magmatic Intrusion and Faulting in Harrat Al-Shaqah (Lunayyir), western Saudi Arabia, Observed by Satellite Radar Interferometry (InSAR)2009, Volume 1, p. 07.

Karpoff, R., 1957, Sur l'existance de Maastrichtian au nord Djiddah (Arabie Saoudite): Compte-rendu Sommaire des Séances de la Société Géologique de France, v. 255, p. 2.

Kemp, J., 1981, Geologic map of the Wadi al Ays quadrangle, sheet 25C, Kingdom of Saudi Arabia, scale 1:250,000.

-, 1982, Reconnaissance geology of the Harrat Lunayyir Quadrangle, 25/37 D.

Le Bas, M. J., Le Maitre, R. W., Streckeisen, A., and Zanettin, B., 1986, A chemical classification of volcanic rocks based on the total alkali-silica diagram: Journal of Petrology, v. 27, no. 3, p. 745-750.

Lowell, J. D., and Genik, G. J., 1972, Sea-floor spreading and structural evolution of southern Red Sea: AAPG Bull, v. 56, no. 2, p. 247-259.

Menzies, M., Gallagher, K., Yelland, A., and Hurford, A. J., 1997, Volcanic and nonvolcanic rifted margins of the Red Sea and Gulf of Aden: Crustal cooling and margin evolution in Yemen: Geochimica et Cosmochimica Acta, v. 61, no. 12, p. 2511-2527.

Mesaed, A. A., Taj, R., and Harbi, H., 2011, Stratigraphic setting, facies types, depositional environments and mechanism of formation of Ash Shumaysi ironstones, Wadi Ash Shumaysi, Jeddah district, West Central Saudi Arabia: Arabian Journal of Geosciences, p. 1-21.

Mitchell, D. J. W., Allen, R. B., Salama, W., and Abouzakm, A., 1992, Tectonostratigraphic framework and hydrocarbon potential of the Red Sea: Journal of Petroleum Geology, v. 15, p. 187-210.

Montenat, C., Ott D'Estevou, P., Purser, B., Burollet, P. F., Jarrige, J. J., Orszag-Sperber, F., Philobbos, E., Plaziat, J. C., Prat, P., and Richert, J. P., 1988, Tectonic and sedimentary evolution of the Gulf of Suez and the northwestern Red Sea: Tectonophysics, v. 153, no. 1-4, p. 161-177.

Mooney, W. D., Gettings, M. E., Blank, H. R., and Healy, J. H., 1985, Saudi Arabian seismic-refraction profile: a traveltime interpretation of crustal and upper mantle structure: Tectonophysics, v. 111, no. 3-4, p. 173-197, 201-202, 205-206, 209-210, 213-215, 223-224, 227-246.

Moore, J. M. M., 1979, Tectonics of the Najd transcurrent fault system, Saudi Arabia: Journal of the Geological Society, v. 136, no. 4, p. 441-452.

Moustafa, A. R., 1997, Controls on the development and evolution of transfer zones: the influence of basement structure and sedimentary thickness in the Suez rift and Red Sea: Journal of Structural Geology, v. 19, no. 6, p. 755-768.

-, 2002, Controls on the geometry of transfer zones in the Suez rift and northwest Red Sea: Implications for the structural geometry of rift systems: AAPG bulletin, v. 86, no. 6, p. 979-1002.

Mukhopadhyay, B., Mogren, S., Mukhopadhyay, M., and Dasgupta, S., 2012, Incipient status of dyke intrusion in top crust–evidences from the Al-Ays 2009 earthquake swarm, Harrat Lunayyir, SW Saudi Arabia.

Nakamura, N., 1974, Determination of REE, Ba, Fe, Mg, Na and K in carbonaceous and ordinary chondrites: Geochimica et Cosmochimica Acta, v. 38, no. 5, p. 757-775.

Omar, G. I., Kohn, B. P., Lutz, T. M., and Faul, H., 1987, The cooling history of Silurian to Cretaceous alkaline ring complexes, south Eastern Desert, Egypt, as revealed by fission-track analysis: Earth and Planetary Science Letters, v. 83, no. 1-4, p. 94-108.

Omar, G. I., and Steckler, M. S., 1995, Fission track evidence on the initial rifting of the Red Sea: two pulses, no propagation: Science, v. 270, no. 5240, p. 1341.

Omar, G. I., Steckler, M. S., Buck, W. R., and Kohn, B. P., 1989, Fission-track analysis of basement apatites at the western margin of the Gulf of Suez rift, Egypt: evidence for synchroneity of uplift and subsidence: Earth and Planetary Science Letters, v. 94, no. 3, p. 316-328.

Pallister, J. S., 1987, Magmatic history of Red Sea rifting: Perspective from the central Saudi Arabian coastal plain: Geological Society of America Bulletin, v. 98, no. 4, p. 400-417.

Pallister, J. S., McCausland, W. A., Jónsson, S., Lu, Z., Zahran, H. M., El Hadidy, S., Aburukbah, A., Stewart, I. C. F., Lundgren, P. R., and White, R. A., 2010, Broad accommodation of rift-related extension recorded by dyke intrusion in Saudi Arabia: Nature Geoscience, v. 3, no. 10, p. 705-712.

Park, Y., Nyblade, A. A., Rodgers, A. J., and Al-Amri, A., 2007, Upper mantle structure beneath the Arabian Peninsula and northern Red Sea from teleseismic body wave tomography: implications for the origin of Cenozoic uplift and volcanism in the Arabian Shield: Geochemistry, Geophysics, Geosystems, v. 8, p. Q06021.

-, 2008, S wave velocity structure of the Arabian Shield upper mantle from Rayleigh wave tomography: Geochem. Geophys. Geosyst, v. 9, p. Q07020.

Pellaton, C., 1979, Geologic map of the Yanbu al Bahr quadrangle, sheet 24C, Kingdom of Saudi Arabia, scale 1: 250,000.

-, 1981, Geologic Map of the Al Madinah Quadrangle, Sheet 24D, Kingdom of Saudi Arabia, scale 1: 250 000.

Pellaton, C., and Dhellemmes, R., 1978, Geology and mineral exploration of the Jabal Dhulay'ah quadrangle 25/38A: French BRGM Technical Record 78 JED, v. 3, p. 16.

Powers, R. W., Ramirez, L. F., Redmond, C. D., and Elberg, E. L., 1966, Geology of the Arabian Peninsula: Geological survey professional paper, v. 560, p. 1-147.

Prodehl, C., 1985, Interpretation of a seismic-refraction survey across the Arabian Shield in western Saudi Arabia: Tectonophysics, v. 111, no. 3-4, p. 247-282.

Reiners, P. W., 2005, Zircon (U-Th)/He thermochronometry: Reviews in mineralogy and geochemistry, v. 58, no. 1, p. 151-179.

Reiners, P. W., Ehlers, T. A., and Zeitler, P. K., 2005, Past, present, and future of thermochronology: Reviews in mineralogy and geochemistry, v. 58, no. 1, p. 1-18.

Reiners, P. W., and Farley, K. A., 2001, Influence of crystal size on apatite (U–Th)/He thermochronology: an example from the Bighorn Mountains, Wyoming: Earth and Planetary Science Letters, v. 188, no. 3, p. 413-420.

Reiners, P. W., Farley, K. A., and Hickes, H. J., 2002, He diffusion and (U-Th)/He thermochronometry of zircon: initial results from Fish Canyon Tuff and Gold Butte: Tectonophysics, v. 349, no. 1-4, p. 297-308.

Richardson, M., and Arthur, M. A., 1988, The Gulf of Suez--northern Red Sea neogene rift: a quantitive basin analysis: Marine and Petroleum Geology, v. 5, no. 3, p. 247-270.

Roobol, M. J., and Kadi, K. A., 2008, Cenozoic Faulting in the Rabigh Area, Central West Saudi Arabia (includingthe sites of King Abdullah Economic City and King Abdullah University for Science and Technology).

Roobol, M. J., and Stewart, I. C. F., 2009, Cenozoic Faults and Recent Seismicity in Northwest Saudi Arabia and the Gulf of Aqaba Region.

Schmidt, D. L., Hadley, D. G., and Brown, G. F., 1983, Middle Tertiary continental rift and evolution of the Red Sea in southwestern Saudi Arabia: US Department of the Interior, Geological Survey.

Sharland, P. R., Archer, R., Casey, D. M., Davies, R. B., Hall, S. H., Heyward, A. P., Horbury, A. D., and Simmons, M. D., 2001, Arabian Plate Sequence Stratigraphy, Gulf PetroLink, GeoArabia Special Publication 2, 371 p.:

Shuster, D. L., and Farley, K. A., 2009, The influence of artificial radiation damage and thermal annealing on helium diffusion kinetics in apatite: Geochimica et Cosmochimica Acta, v. 73, no. 1, p. 183-196.

Shuster, D. L., Flowers, R. M., and Farley, K. A., 2006, The influence of natural radiation damage on helium diffusion kinetics in apatite: Earth and Planetary Science Letters, v. 249, no. 3, p. 148-161.

Smith, J. W., 1979, Geology of the Wadi Azlam Quadrangle, Sheet 27/36 C Kingdom of Saudi Arabia: Saudi Arabia Directorate General of Mineral Resources Geologic Map GM, p. 30.

Spencer, C. H., 1987, Provisional Stratigraphy and Correlation of the Tertiary Rocks in the Jiddah Region: Ministry of the Petroleum and Mineral Resources. Deputy Ministry for Mineral Resources. Open File Report of, p. 06-17.

Stern, R. J., 1985, The Najd Fault System, Saudi Arabia and Egypt: A Late Precambrian rift-related transform system?: Tectonics, v. 4, no. 5, p. 497-511.

Stern, R. J., and Johnson, P., 2010, Continental lithosphere of the Arabian Plate: a geologic, petrologic, and geophysical synthesis: Earth-Science Reviews, v. 101, no. 1-2, p. 29-67.

Stockli, D. F., 2005, Application of low-temperature thermochronometry to extensional tectonic settings: Reviews in mineralogy and geochemistry, v. 58, no. 1, p. 411-448.

Stockli, D. F., Farley, K. A., and Dumitru, T. A., 2000, Calibration of the apatite (U-Th)/He thermochronometer on an exhumed fault block, White Mountains, California: Geology, v. 28, no. 11, p. 983-986.

Suayah, I. B., Rogers, J. J. W., and Dabbagh, M. E., 1991, High-Ti continental tholeiites from the Aznam trough, northwestern Saudi Arabia: evidence of ``abortive'' rifting in the ``embryonic'' stage of Red Sea opening: Tectonophysics, v. 191, no. 1-2, p. 75-87.

Sultan, M., Arvidson, R. E., Duncan, I. J., Stern, R. J., and El Kaliouby, B., 1988, Extension of the Najd Shear System from Saudi Arabia to the Central Eastern Desert of Egypt based on integrated field and Landsat observations: Tectonics, v. 7, no. 6, p. 1291-1306.

Sultan, M., Becker, R., Arvidson, R. E., Shore, P., Stern, R. J., El Alfy, Z., and Attia, R., 1993, New constraints on Red Sea rifting from correlations of Arabian and Nubian Neoproterozoic outcrops: Tectonics, v. 12, no. 6, p. 1303-1319.

Sultan, M., Becker, R., Arvidson, R. E., Shore, P., Stern, R. J., El Alfy, Z., and Guinness, E. A., 1992, Nature of the Red Sea crust: A controversy revisited: Geology, v. 20, no. 7, p. 593-596.

Survey, U. S. G., 1993, Quarterly progress report of the USGS Mission, Kingdom of Saudi Arabia, for the second quarter of the fiscal year 1993.

Talbot, C. J., and Ghebreab, W., 1997, Red Sea detachment and basement core complexes in Eritrea: Geology, v. 25, no. 7, p. 655-658.

Voggenreiter, W., and Hötzl, H., 1989, Kinematic evolution of the southwestern Arabian continental margin: implications for the origin of the Red Sea: Journal of African Earth Sciences (and the Middle East), v. 8, no. 2, p. 541-564.

Voggenreiter, W., Hötzl, H., and Jado, A. R., 1988, Red Sea related history of extension and magmatism in the Jizan area (Southwest Saudi Arabia): indication for simple-shear during early Red Sea rifting: Geologische Rundschau, v. 77, no. 1, p. 257-274.

Voggenreiter, W., Hötzl, H., and Mechie, J., 1988, Low-angle detachment origin for the Red Sea Rift system?: Tectonophysics, v. 150, no. 1-2, p. 51-56, 58-75.

Wentworth, C. K., 1922, A scale of grade and class terms for clastic sediments: The Journal of Geology, v. 30, no. 5, p. 377-392.

Wernicke, B., 1985, Uniform-sense normal simple shear of the continental lithosphere: Canadian Journal of Earth Sciences, v. 22, no. 1, p. 108-125.

Wolfe, M. R., and Stockli, D. F., 2010, Zircon (U–Th)/He thermochronometry in the KTB drill hole, Germany, and its implications for bulk He diffusion kinetics in zircon: Earth and Planetary Science Letters, v. 295, no. 1, p. 69-82.

Zahran, H. M., McCausland, W. A., Pallister, J. S., Lu, Z., El-Hadidy, S., Aburukba, A., Schawali, J., Kadi, K., Youssef, A., and Ewert, J. W., Stalled eruption or dike intrusion at Harrat Lunayyir, Saudi Arabia?2009, Volume 1, p. 2072.

Zahran, H. M., Stewart, I. C. F., Johnson, P. R., and Basahel, M. H., 2002, Aeromagnetic-anomaly maps of central and western Saudi Arabia, scale 1:2,000,000.

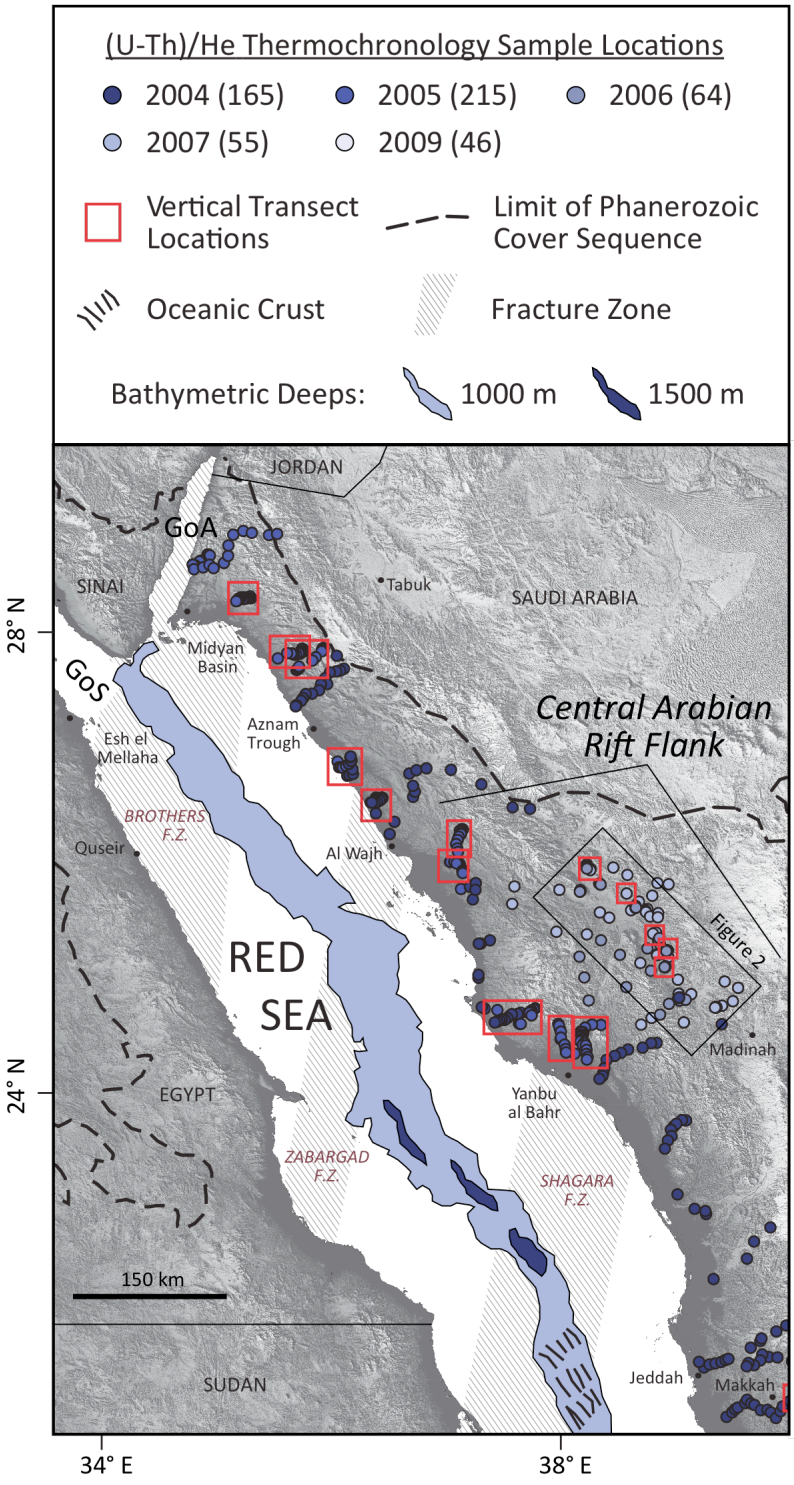
(U-Th)/He Thermochronology Sample Locations
2004 (165)
2005 (215)
2006 (64)
2007 (55)
2009 (46)
Vertical Transect Locations
Limit of Phanerozoic Cover Sequence
Oceanic Crust
Fracture Zone
Bathymetric Deeps:
1000 m
1500 m
JORDAN
GoA
SINAI
Tabuk
SAUDI ARABIA
Midyan Basin
GoS
Central Arabian Rift Flank
Esh el Mellaha
Aznam Trough
BROTHERS F.Z.
Quseir
Al Wajh
RED SEA
Figure 2
Madinah
EGYPT
Yanbu al Bahr
ZABARGAD F.Z.
SHAGARA F.Z.
150 km
SUDAN
Jeddah
Makkah
28° N
24° N
34° E
38° E

Figure 1 - Position of the Central Arabian Rift Flank in the Red Sea Rift System

Sub-regional terrain from SRTM data. Position of oceanic crust magnetic lineaments and fracture zones with bathymetric depths from Cochran (1983) and Crane and Bonatti (1987), respectively. Sample locations include apatite and zircon (U-Th)/He thermochronology samples listed by year with annual sample totals noted parenthetically. GoS = Gulf of Suez; GoA = Gulf of Aqaba; location of international borders approximate and unofficial

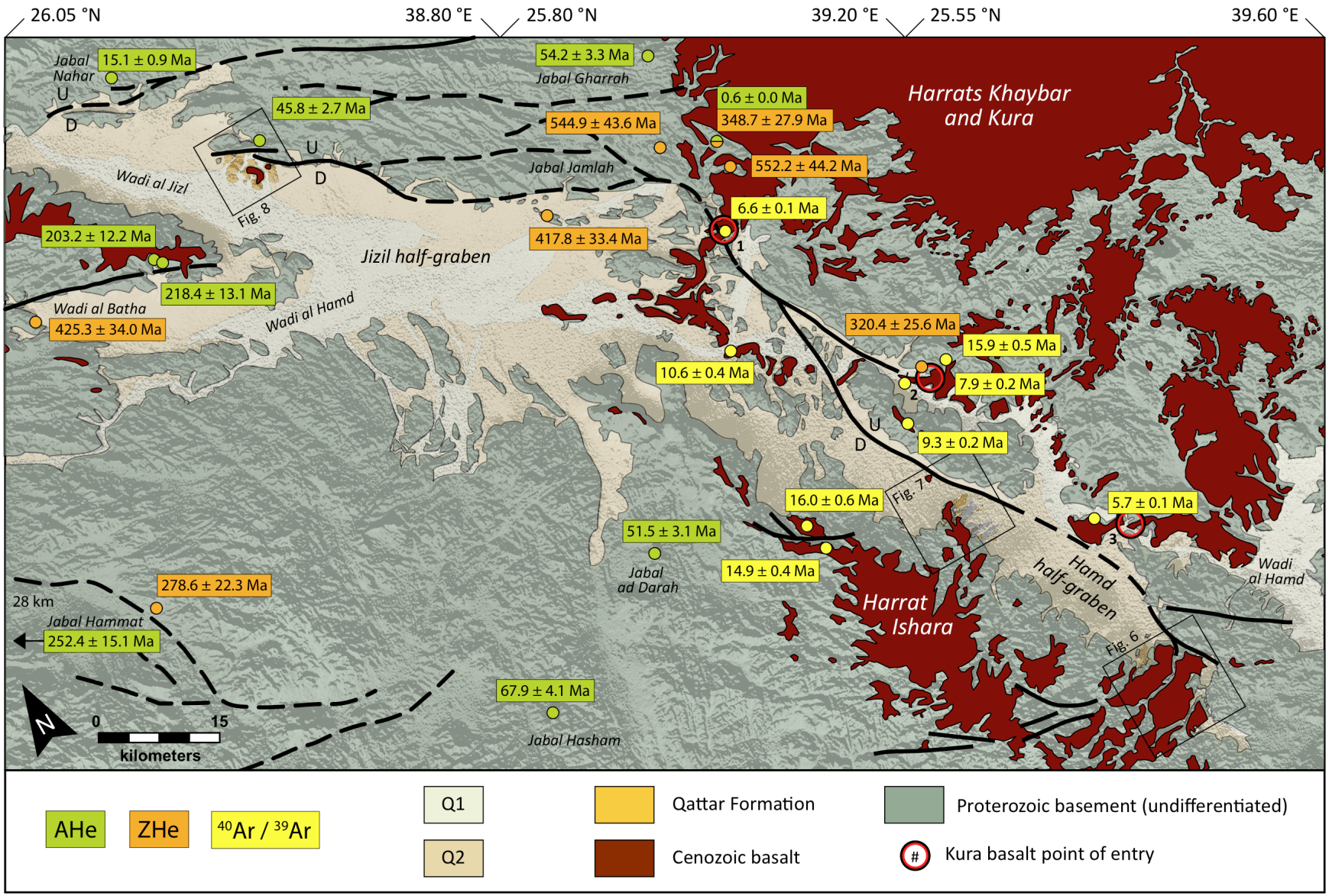
26.05 °N
38.80 °E
25.80 °N
39.20 °E
25.55 °N
39.60 °E
Jabal Nahar
15.1 ± 0.9 Ma
U
D
45.8 ± 2.7 Ma
Wadi al Jizl
Fig. 8
U
D
54.2 ± 3.3 Ma
Jabal Gharrah
544.9 ± 43.6 Ma
Jabal Jamlah
0.6 ± 0.0 Ma
348.7 ± 27.9 Ma
552.2 ± 44.2 Ma
Harrats Khaybar and Kura
6.6 ± 0.1 Ma
1
417.8 ± 33.4 Ma
203.2 ± 12.2 Ma
Jizil half-graben
218.4 ± 13.1 Ma
Wadi al Batha
425.3 ± 34.0 Ma
Wadi al Hamd
320.4 ± 25.6 Ma
15.9 ± 0.5 Ma
10.6 ± 0.4 Ma
7.9 ± 0.2 Ma
2
U
D
9.3 ± 0.2 Ma
Fig. 7
16.0 ± 0.6 Ma
5.7 ± 0.1 Ma
3
51.5 ± 3.1 Ma
Jabal ad Darah
14.9 ± 0.4 Ma
Hamd half-graben
Wadi al Hamd
Harrat Ishara
Fig. 6
278.6 ± 22.3 Ma
28 km
Jabal Hammat
252.4 ± 15.1 Ma
67.9 ± 4.1 Ma
Jabal Hasham
N
0
15
kilometers
AHe
ZHe
40Ar / 39Ar
Q1
Q2
Qattar Formation
Cenozoic basalt
Proterozoic basement (undifferentiated)
Kura basalt point of entry

Figure 2 - Hamd-Jizl Basin Geologic Map

Circles indicate the location of bedrock AHe (green) and ZHe (orange) ages. Yellow circles show the location of whole-rock basalt $^{40}Ar/^{39}Ar$ ages. Kura basalt entry points into the HJB shown with black/red circles. Thin black boxes identify the location of the Wadi al Jizl, Jabal Antar, and Wadi al Qattar study areas. Base shaded relief map from 10m SRTM.

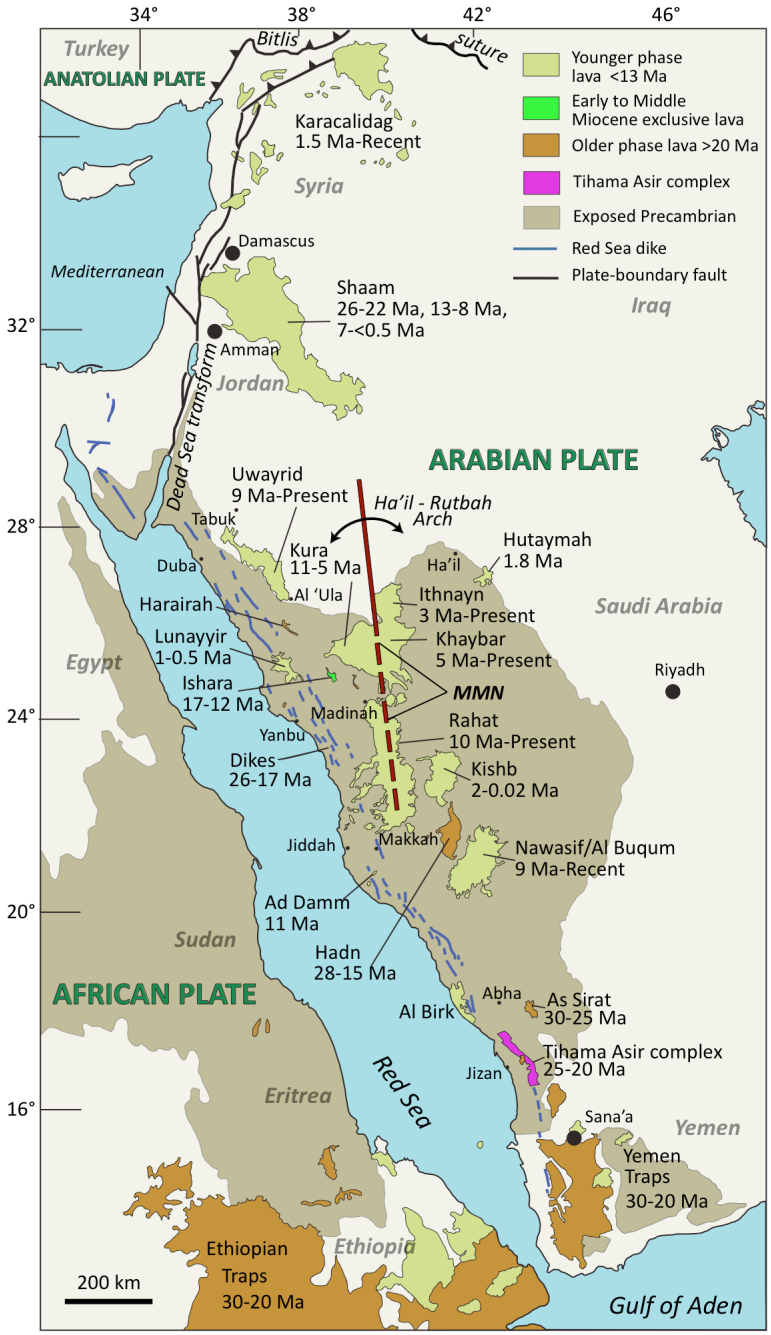
34°
38°
42°
46°
32°
28°
24°
20°
16°
Turkey
ANATOLIAN PLATE
Bitlis
suture
Karacalidag
1.5 Ma-Recent
Syria
Damascus
Mediterranean
Shaam
26-22 Ma, 13-8 Ma,
7-<0.5 Ma
Amman
Jordan
Iraq
Dead Sea transform
ARABIAN PLATE
Uwayrid
9 Ma-Present
Tabuk
Ha'il - Rutbah
Arch
Kura
11-5 Ma
Hutaymah
1.8 Ma
Duba
Ha'il
Al 'Ula
Ithnayn
3 Ma-Present
Saudi Arabia
Harairah
Lunayyir
1-0.5 Ma
Khaybar
5 Ma-Present
Egypt
Riyadh
Ishara
17-12 Ma
MMN
Madinah
Rahat
10 Ma-Present
Yanbu
Dikes
26-17 Ma
Kishb
2-0.02 Ma
Jiddah
Makkah
Nawasif/Al Buqum
9 Ma-Recent
Ad Damm
11 Ma
Sudan
Hadn
28-15 Ma
AFRICAN PLATE
Abha
As Sirat
30-25 Ma
Al Birk
Tihama Asir complex
25-20 Ma
Jizan
Red Sea
Eritrea
Sana'a
Yemen
Yemen
Traps
30-20 Ma
Ethiopian
Traps
30-20 Ma
Ethiopia
200 km
Gulf of Aden
Younger phase
lava <13 Ma
Early to Middle
Miocene exclusive lava
Older phase lava >20 Ma
Tihama Asir complex
Exposed Precambrian
Red Sea dike
Plate-boundary fault

Figure 3 - Cenozoic Basalt in Arabia and NE Africa

Position and age of regional harrat in the Red Sea Rift System. Modified from Stern and Johnson (2010) with permission.

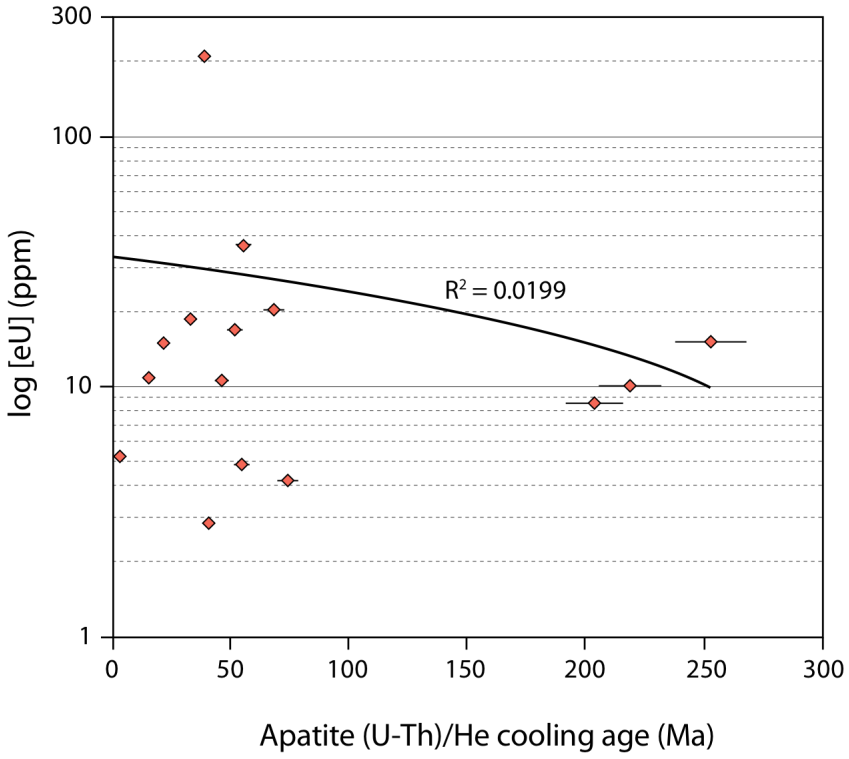
300
100
10
1
log [eU] (ppm)
R² = 0.0199
0
50
100
150
200
250
300
Apatite (U-Th)/He cooling age (Ma)

Figure 4 - [eU] Characterization of all Hamd-Jizl Basin Bedrock Apatite

See Tables 1 and 2 for age data.

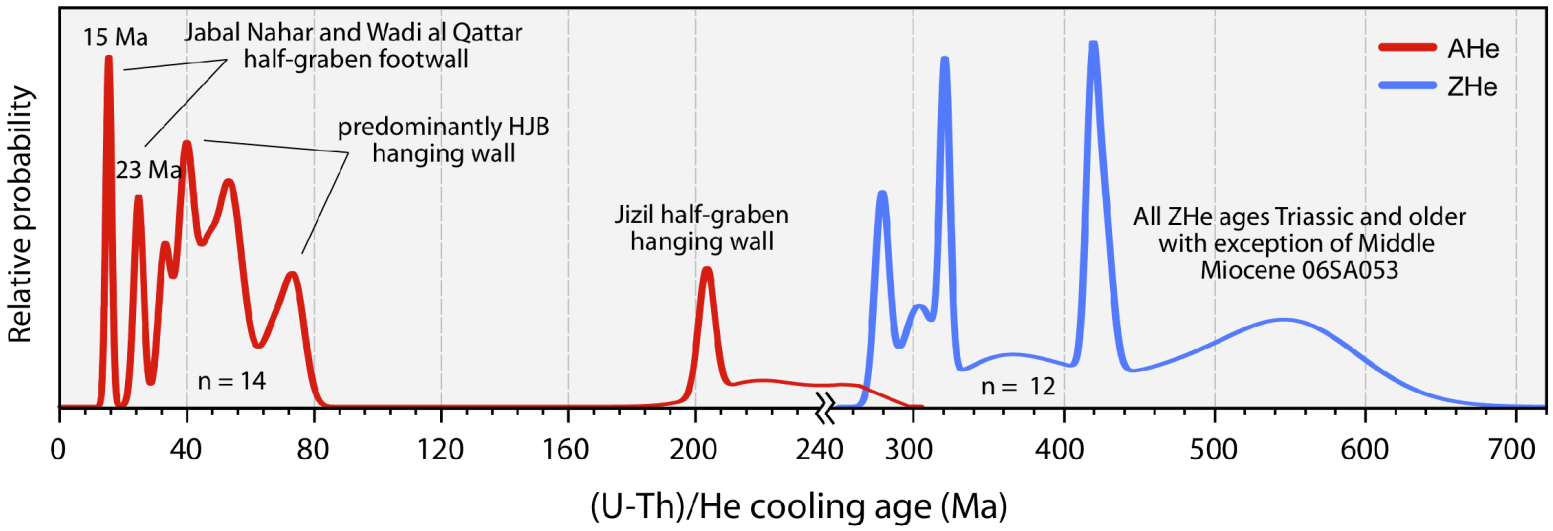
15 Ma
Jabal Nahar and Wadi al Qattar
half-graben footwall
23 Ma
predominantly HJB
hanging wall
n = 14
Jizil half-graben
hanging wall
n = 12
All ZHe ages Triassic and older
with exception of Middle
Miocene 06SA053
AHe
ZHe
Relative probability
0
40
80
120
160
200
240
300
400
500
600
700
(U-Th)/He cooling age (Ma)

Figure 5 - Bedrock Apatite and Zircon (U-Th)/He Cooling Ages: Hamd-Jizl Basin

"n" = number of samples included in determination. Note the difference in the (U-Th)/He cooling age scale (x-axis) on either side of the 240 Ma mark. See Tables 1 and 2 for age data.

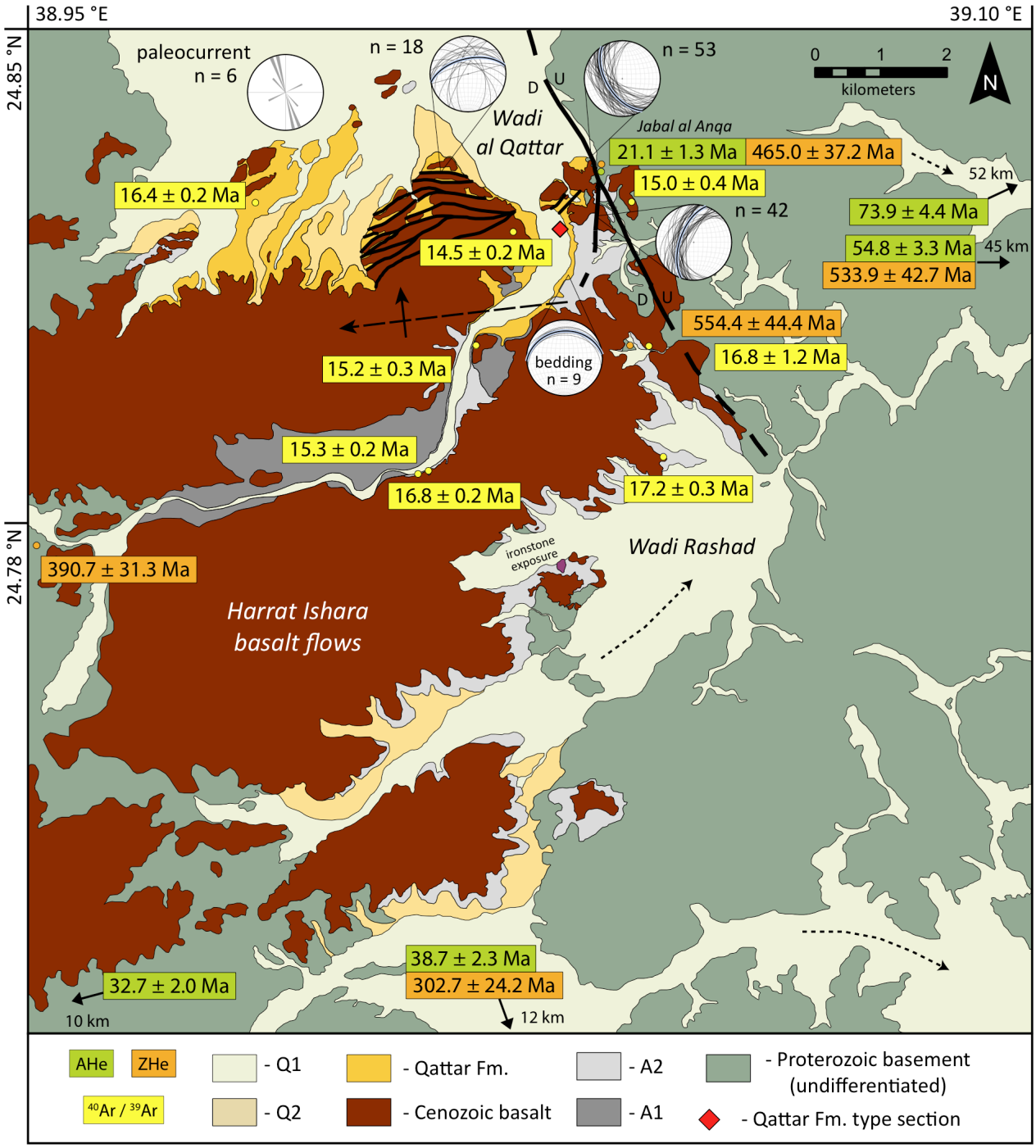
38.95 °E
39.10 °E
24.85 °N
24.78 °N
paleocurrent
n = 6
n = 18
n = 53
n = 42
bedding
n = 9
D
U
Wadi
al Qattar
Jabal al Anqa
0
1
2
kilometers
N
21.1 ± 1.3 Ma
465.0 ± 37.2 Ma
15.0 ± 0.4 Ma
52 km
73.9 ± 4.4 Ma
54.8 ± 3.3 Ma
45 km
533.9 ± 42.7 Ma
554.4 ± 44.4 Ma
16.8 ± 1.2 Ma
16.4 ± 0.2 Ma
14.5 ± 0.2 Ma
15.2 ± 0.3 Ma
15.3 ± 0.2 Ma
16.8 ± 0.2 Ma
17.2 ± 0.3 Ma
Wadi Rashad
ironstone
exposure
390.7 ± 31.3 Ma
Harrat Ishara
basalt flows
38.7 ± 2.3 Ma
302.7 ± 24.2 Ma
12 km
32.7 ± 2.0 Ma
10 km
AHe
ZHe
40Ar / 39Ar
- Q1
- Q2
- Qattar Fm.
- Cenozoic basalt
- A2
- A1
- Proterozoic basement
(undifferentiated)
- Qattar Fm. type section

Figure 6 - Wadi al Qattar Geologic Map

Stereonets show dip of border fault at Jabal an Anqa (n=53), border fault splay in Wadi al Qattar (n=42), Qattar Formation bedding orientation at type section (n=9), and intra-basinal faulting of Ishara basalt (n=18). Rose diagram shows paleocurrent measurements (n=6) from Qattar Formation. Boxes and corresponding dots show AHe (green), ZHe (orange), whole-rock $^{40}Ar/^{39}Ar$ (yellow) ages at sample location. Dashed arrows show modern drainage direction. Paleocene age ironstone exposure labeled in Wadi Rashad. A1 = basalt clast-dominant alluvim (Recent); A2 = basalt-free alluvium (early Miocene); Q1 = active alluvial channel; Q2 = older alluvial surface; Cb = Harrat Ishara Cenozoic basalt

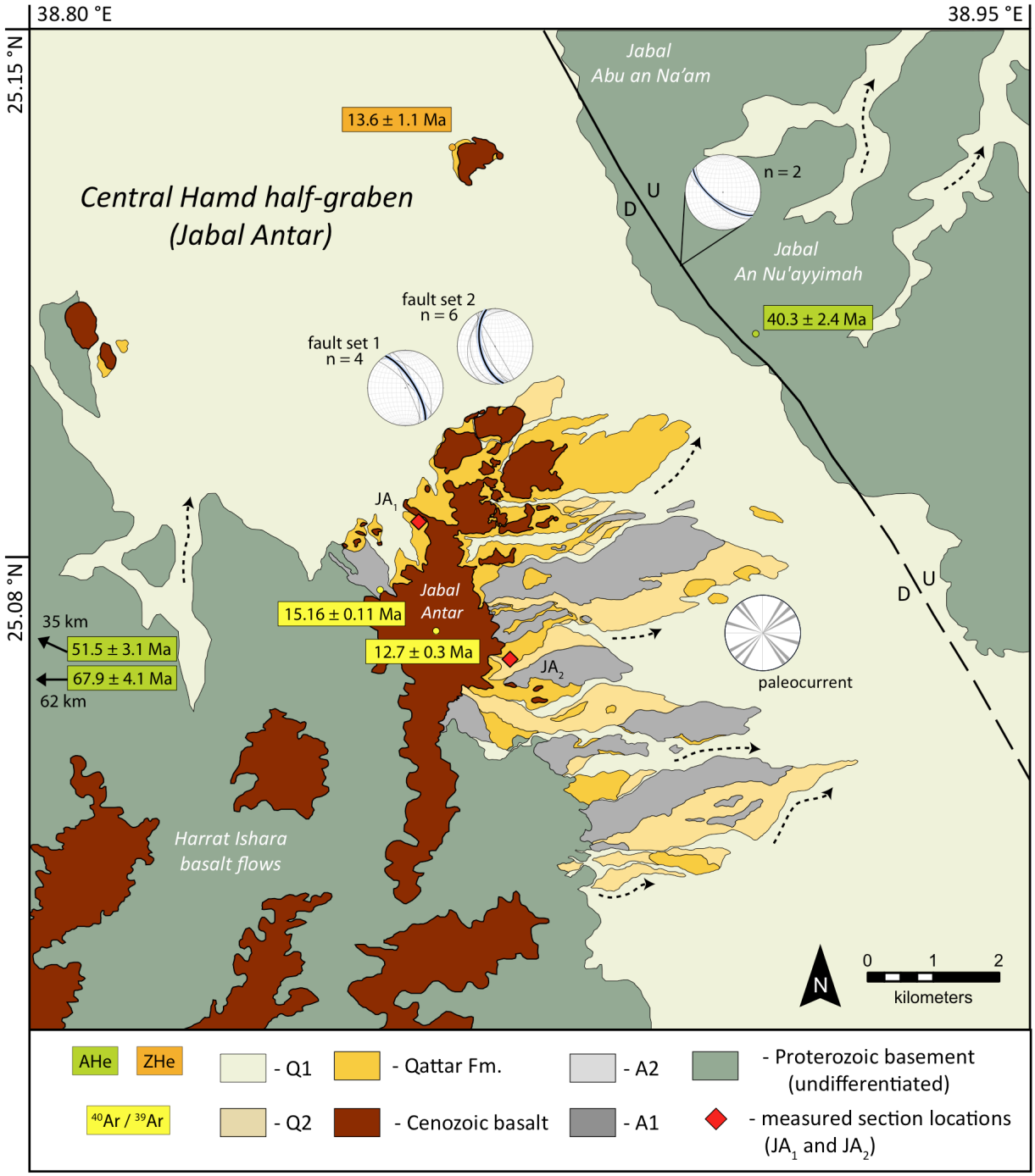
38.80 °E
38.95 °E
25.15 °N
25.08 °N
Jabal
Abu an Na'am
13.6 ± 1.1 Ma
Central Hamd half-graben
(Jabal Antar)
n = 2
U
D
Jabal
An Nu'ayyimah
40.3 ± 2.4 Ma
fault set 2
n = 6
fault set 1
n = 4
JA1
Jabal
Antar
15.16 ± 0.11 Ma
12.7 ± 0.3 Ma
JA2
paleocurrent
35 km
51.5 ± 3.1 Ma
67.9 ± 4.1 Ma
62 km
Harrat Ishara
basalt flows
N
0
1
2
kilometers
AHe
ZHe
40Ar / 39Ar
- Q1
- Q2
- Qattar Fm.
- Cenozoic basalt
- A2
- A1
- Proterozoic basement
(undifferentiated)
- measured section locations
(JA1 and JA2)

Figure 7 - Central Hamd Basin Geologic Map

Stereonets show dip of border fault at Jabal an Nu'ayyimah (n=2) and two sets of intra-basinal faulting (n=4 and 6) of Qattar Formation at foot of Jabal Antar. Qattar Formation bedding nearly horizontal at measured section locations (red diamonds). Rose diagram shows paleocurrent measurements from Qattar Formation. Boxes and corresponding dots show AHe (green), ZHe (orange), whole-rock $^{40}Ar/^{39}Ar$ (yellow) ages at sample location. Dashed arrows show modern drainage direction. A1 = basalt clast-dominant alluvim (Recent); A2 = basalt-free alluvium (early Miocene); Q1 = active alluvial channel; Q2 = older alluvial surface; Cb = Harrat Ishara Cenozoic basalt

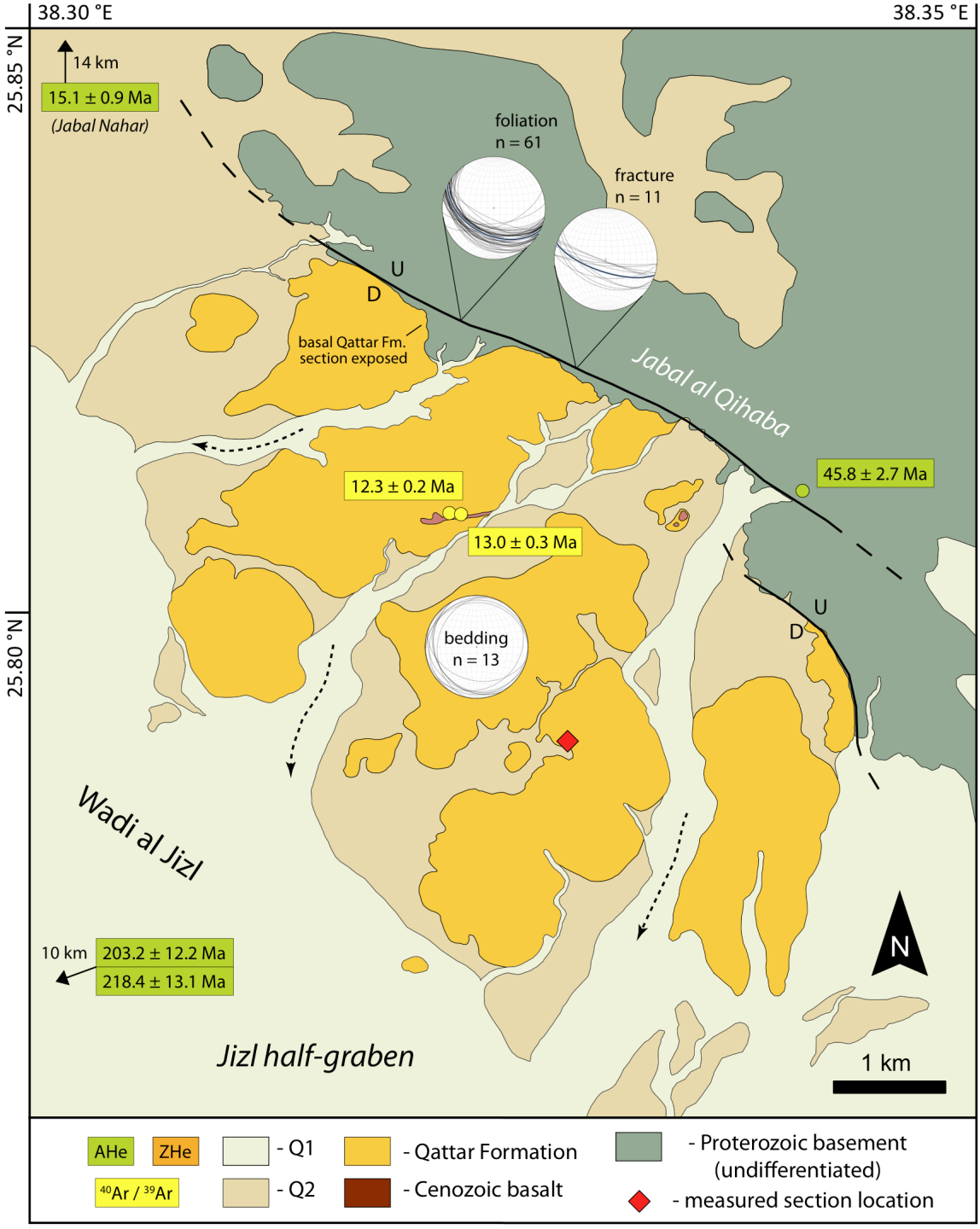
38.30 °E
38.35 °E
25.85 °N
25.80 °N
14 km
15.1 ± 0.9 Ma
(Jabal Nahar)
foliation
n = 61
fracture
n = 11
U
D
basal Qattar Fm.
section exposed
Jabal al Qihaba
45.8 ± 2.7 Ma
12.3 ± 0.2 Ma
13.0 ± 0.3 Ma
bedding
n = 13
U
D
Wadi al Jizl
10 km
203.2 ± 12.2 Ma
218.4 ± 13.1 Ma
N
Jizl half-graben
1 km
AHe
ZHe
40Ar / 39Ar
- Q1
- Q2
- Qattar Formation
- Cenozoic basalt
- Proterozoic basement
(undifferentiated)
- measured section location

Figure 8 - Wadi al Jizl Geologic Map

Stereonets show dip of border fault (n=11) and orientation of Proterozoic Najd Fault System foliation (n=61) at Jabal al Qihaba and Qattar Formation bedding orientation at measured section (red diamond; n=13). Boxes and corresponding dots show AHe (green) and whole-rock $^{40}Ar/^{39}Ar$ (yellow) ages at sample location. Dashed arrows show modern drainage direction. Q1 = active alluvial channel; Q2 = older alluvial surface; Cb = Harrat Ishara Cenozoic basalt

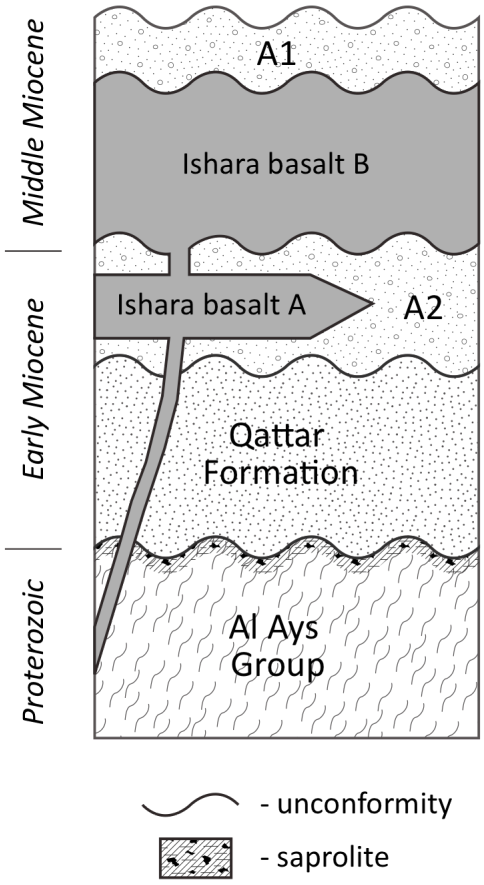
Middle Miocene
Early Miocene
Proterozoic
A1
Ishara basalt B
Ishara basalt A
A2
Qattar
Formation
Al Ays
Group
- unconformity
- saprolite

Figure 9 - Hamd-Jizl Basin: Composite Stratigraphic Section

Composite stratigraphic section built from observations atWadi al Qattar, Jabal Antar, and Wadi al Jizl measured sections. See Figure 16 for Ishara basalt $^{40}Ar/^{39}Ar$ ages. A1 = basalt clast-dominant alluvim (Recent); A2 = basalt-free alluvium (early Miocene)

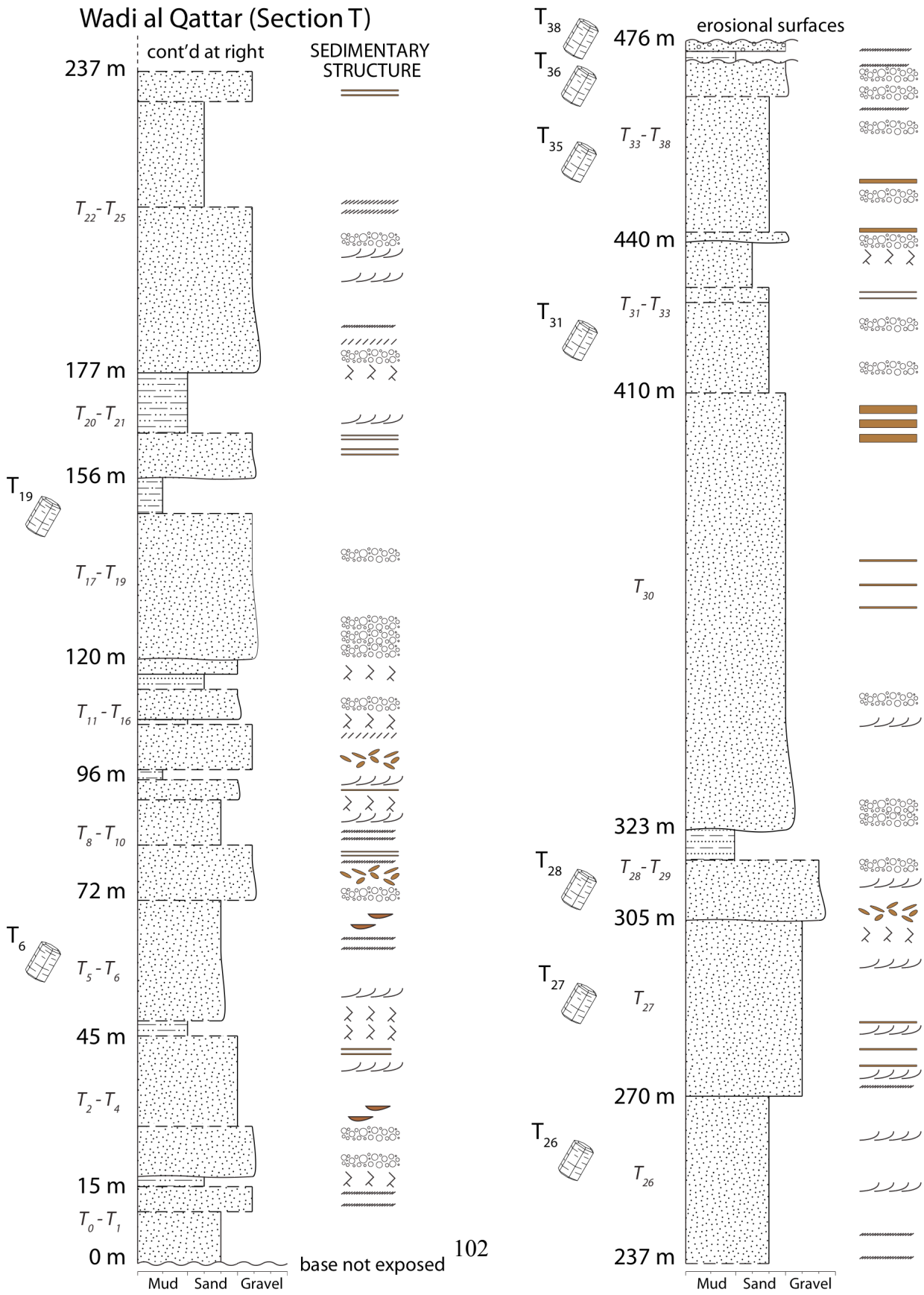
Wadi al Qattar (Section T)
cont'd at right
SEDIMENTARY STRUCTURE
237 m
T22 - T25
177 m
T20 - T21
156 m
T19
T17 - T19
120 m
T11 - T16
96 m
T8 - T10
72 m
T6
T5 - T6
45 m
T2 - T4
15 m
T0 - T1
0 m
base not exposed
Mud
Sand
Gravel
T38
T36
T35
erosional surfaces
476 m
T33 - T38
440 m
T31 - T33
T31
410 m
T30
323 m
T28
T28 - T29
305 m
T27
T27
270 m
T26
T26
237 m
Mud
Sand
Gravel

Figure 10 - Qattar Formation Measured Section: Wadi al Qattar (Section T; Type Section)

Horizons sampled for detrital apatite (U-Th)/He thermochronology study marked with apatite symbol and unit designation. Sedimentary structures labeled beside their position in the measured section. Basal Qattar Formation conglomerate unobserved at the measured section locale due to modern alluvial cover. See Figure 11 for symbol legend.

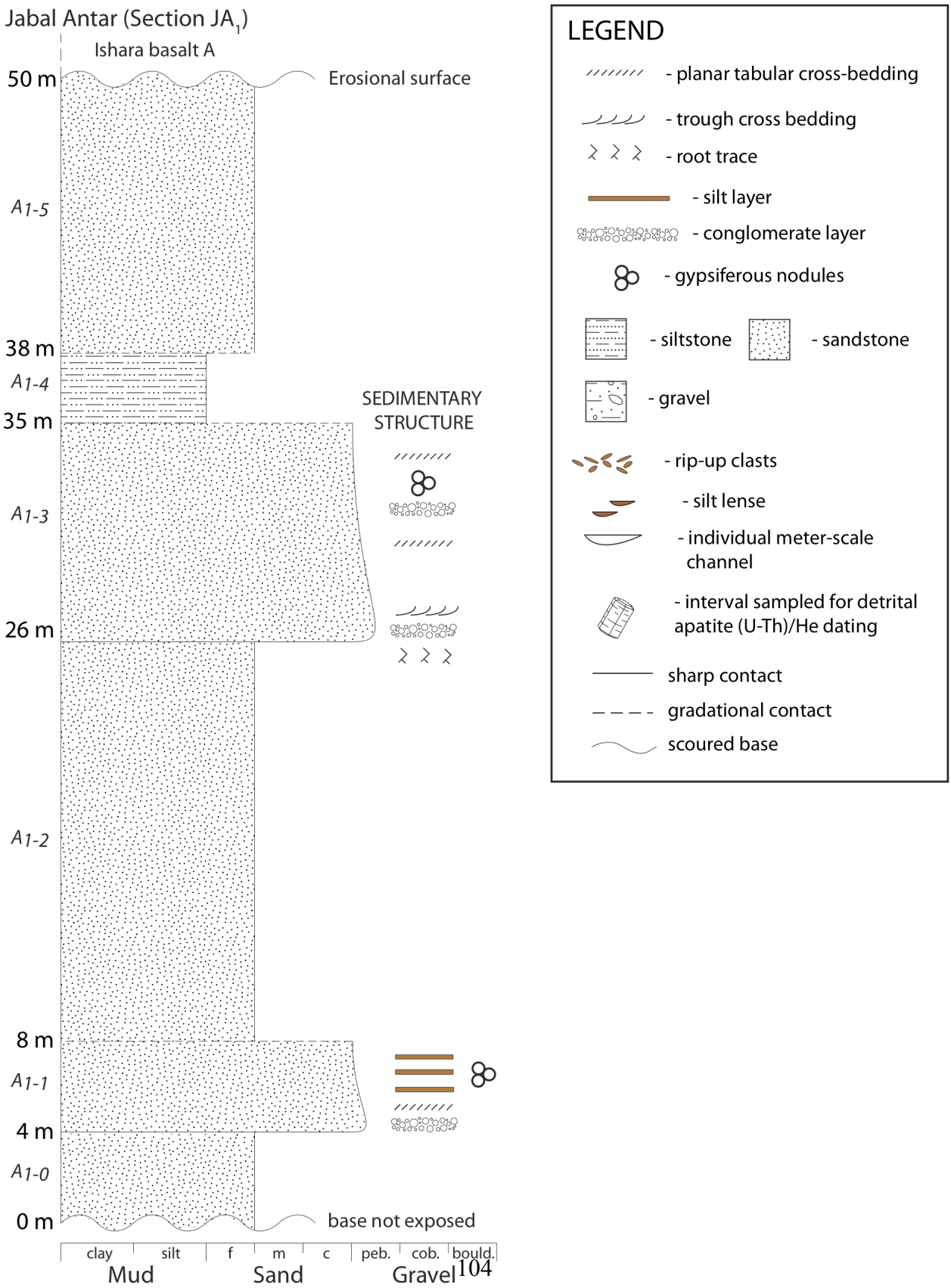
Jabal Antar (Section JA1)
Ishara basalt A
50 m
Erosional surface
A1-5
38 m
A1-4
SEDIMENTARY STRUCTURE
35 m
A1-3
26 m
A1-2
8 m
A1-1
4 m
A1-0
0 m
base not exposed
clay
silt
f
m
c
peb.
cob.
bould.
Mud
Sand
Gravel
LEGEND
- planar tabular cross-bedding
- trough cross bedding
- root trace
- silt layer
- conglomerate layer
- gypsiferous nodules
- siltstone
- sandstone
- gravel
- rip-up clasts
- silt lense
- individual meter-scale channel
- interval sampled for detrital apatite (U-Th)/He dating
sharp contact
gradational contact
scoured base

Figure 11 - Qattar Formation Measured Section: Jabal Antar (Section JA_1)

Sedimentary structures labeled beside their position in the measured section. Basal Qattar Formation conglomerate unobserved at the measured section locale due to modern alluvial cover.

Jabal Antar (Section JA_2)

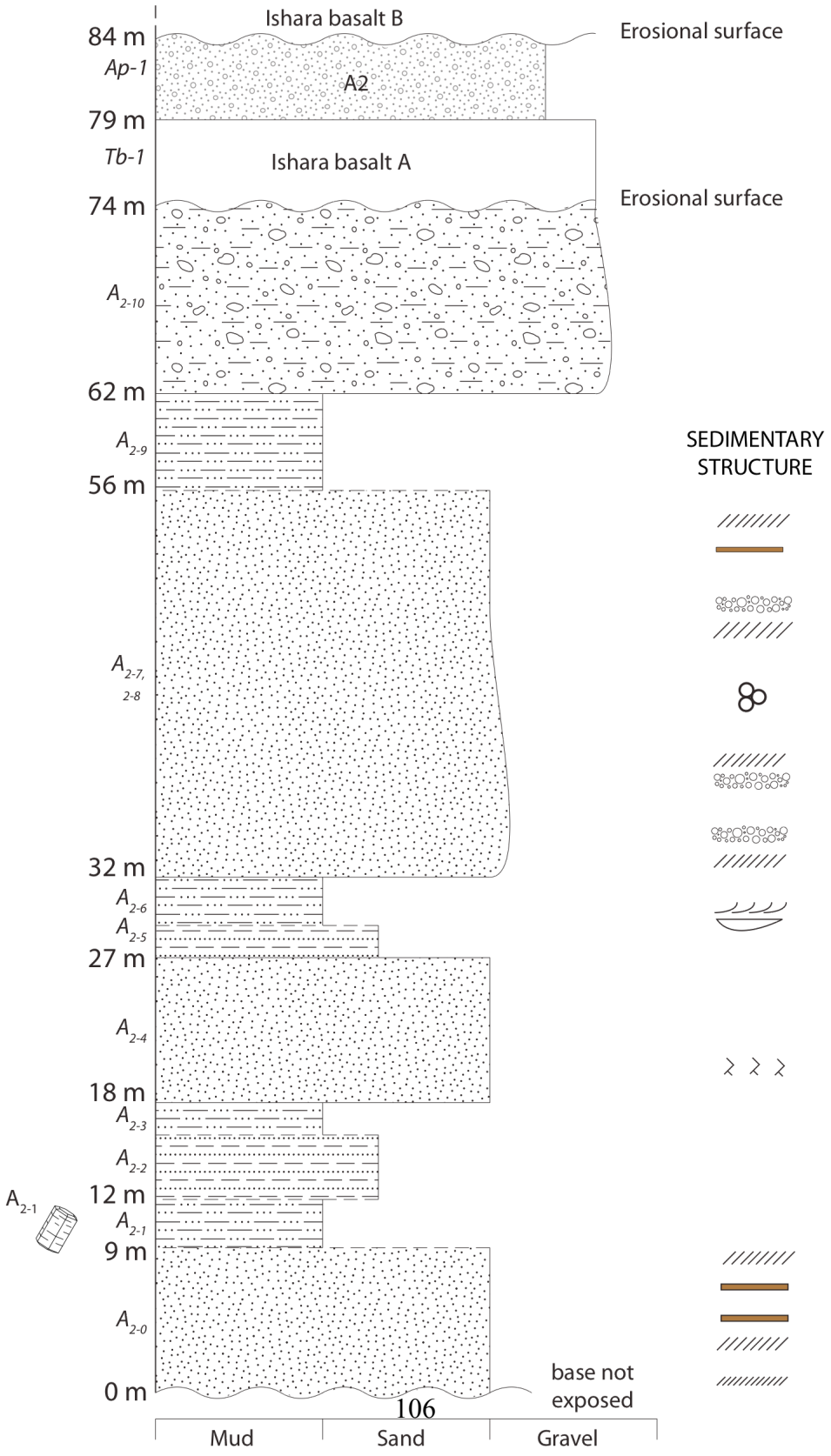

Figure 12 - Qattar Formation Measured Section: Jabal Antar (Section JA_2)

Horizon sampled for detrital apatite (U-Th)/He thermochronology study marked with apatite symbol and unit designation. Sedimentary structures labeled beside their position in the measured section. Basal Qattar Formation conglomerate unobserved at the measured section locale due to modern alluvial cover. See Figure 11 for symbol legend.

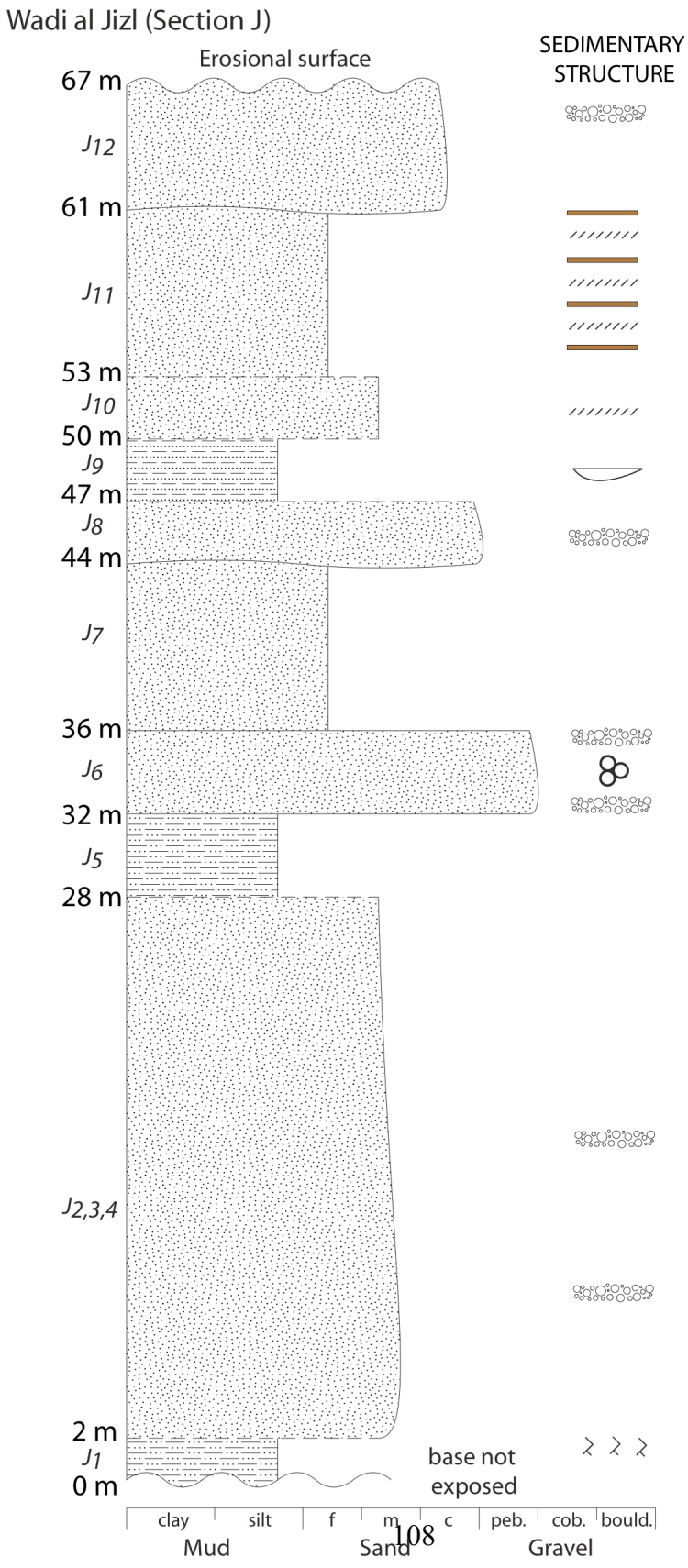
Wadi al Jizl (Section J)
Erosional surface
SEDIMENTARY STRUCTURE
67 m
J12
61 m
J11
53 m
J10
50 m
J9
47 m
J8
44 m
J7
36 m
J6
32 m
J5
28 m
J2,3,4
2 m
J1
0 m
base not exposed
clay
silt
f
m
c
peb.
cob.
bould.
Mud
Sand
Gravel

Figure 13 - Qattar Formation Measured Section: Wadi al Jizl (Section J)

Sedimentary structures labeled beside their position in the measured section. Basal Qattar Formation conglomerate unobserved at the measured section locale due to modern alluvial cover. See Figure 11 for symbol legend.

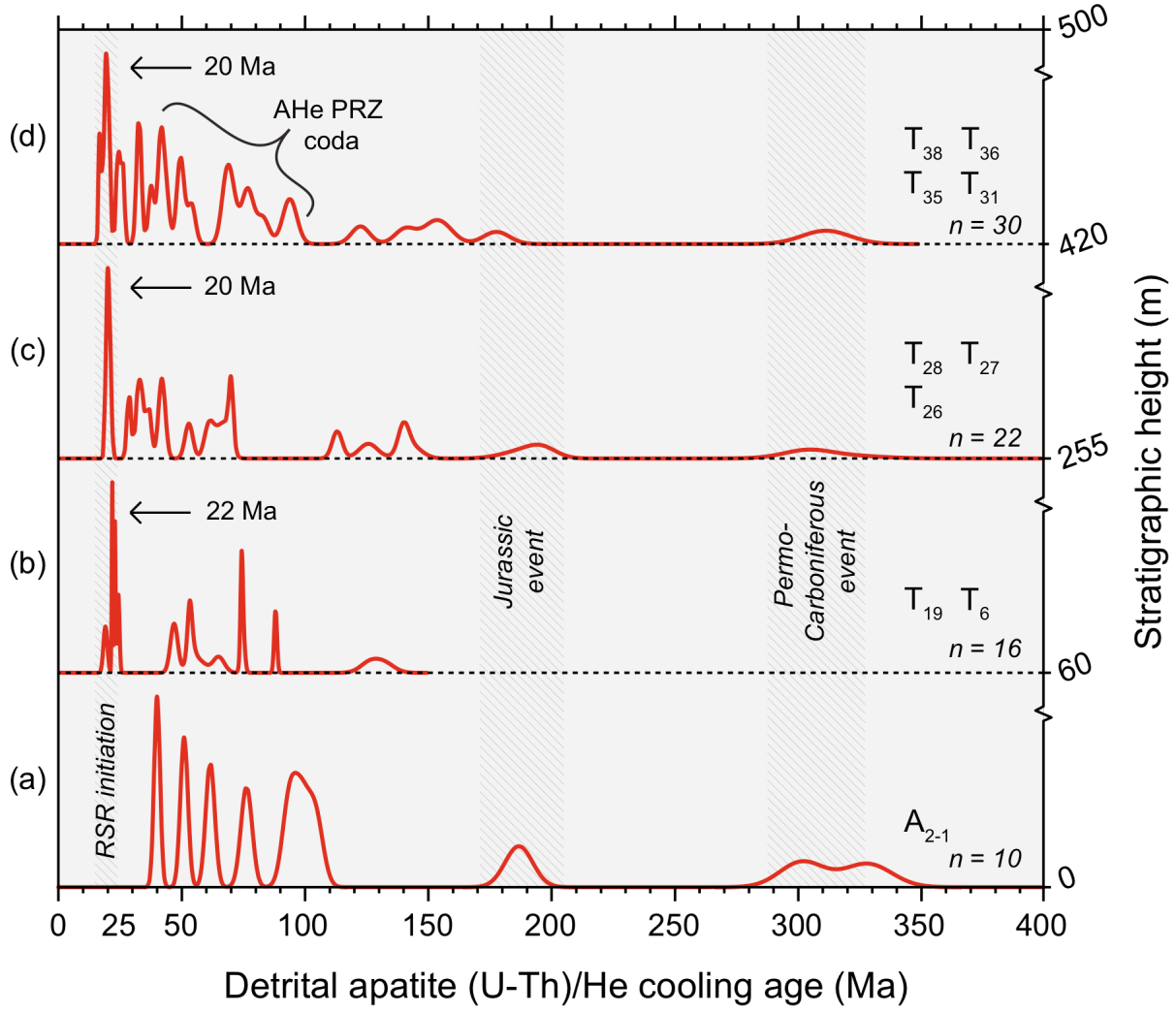
(d)
20 Ma
AHe PRZ
coda
T38 T36
T35 T31
n = 30
(c)
20 Ma
T28 T27
T26
n = 22
(b)
22 Ma
Jurassic
event
Permo-
Carboniferous
event
T19 T6
n = 16
(a)
RSR initiation
A2-1
n = 10
500
420
255
60
0
Stratigraphic height (m)
0 25 50 100 150 200 250 300 350 400
Detrital apatite (U-Th)/He cooling age (Ma)

Figure 14 - Detrital Apatite (U-Th)/He Age Data: Qattar Formation

Subplot (a) contains data from Section JA_2 at Jabal Antar (Fig. 12). Subplots (b) thru (d) contain data from Section T at Wadi al Qattar (Fig. 10). Unit designations of sampled intervals from measured sections (e.g., T_{19}) included at right. "n" = number of samples included in determination. Overlain in hatch pattern are three thermo-tectonic events recognized in the CARF, including the onset of the Red Sea rift. See Table 5 for age data.

Harrat Khaybar *Kura basalt*		***Harrat Ishara*** *Ishara A*		*Ishara B*	
06SA055	06SA075	06SA001	06SA050	06SA025	06SA053#
06SA058*	06SA094#	06SA002	06SA082	06SA026	06SA066
06SA061	07SA052*	06SA004	06SA083	06SA041	06SA067
		06SA007	06SA084	06SA047	
		06SA010	06SA102#		

Figure 15 - HJB Basalt: Volcanic Source Assignment

Assignment according to whole-rock geochemistry and $^{40}Ar/^{39}Ar$ geochronology. Asterisk (*) denotes samples with only $^{40}Ar/^{39}Ar$ age data and octothorpe (#) denotes samples with only whole-rock major, trace, and REE geochemical data.

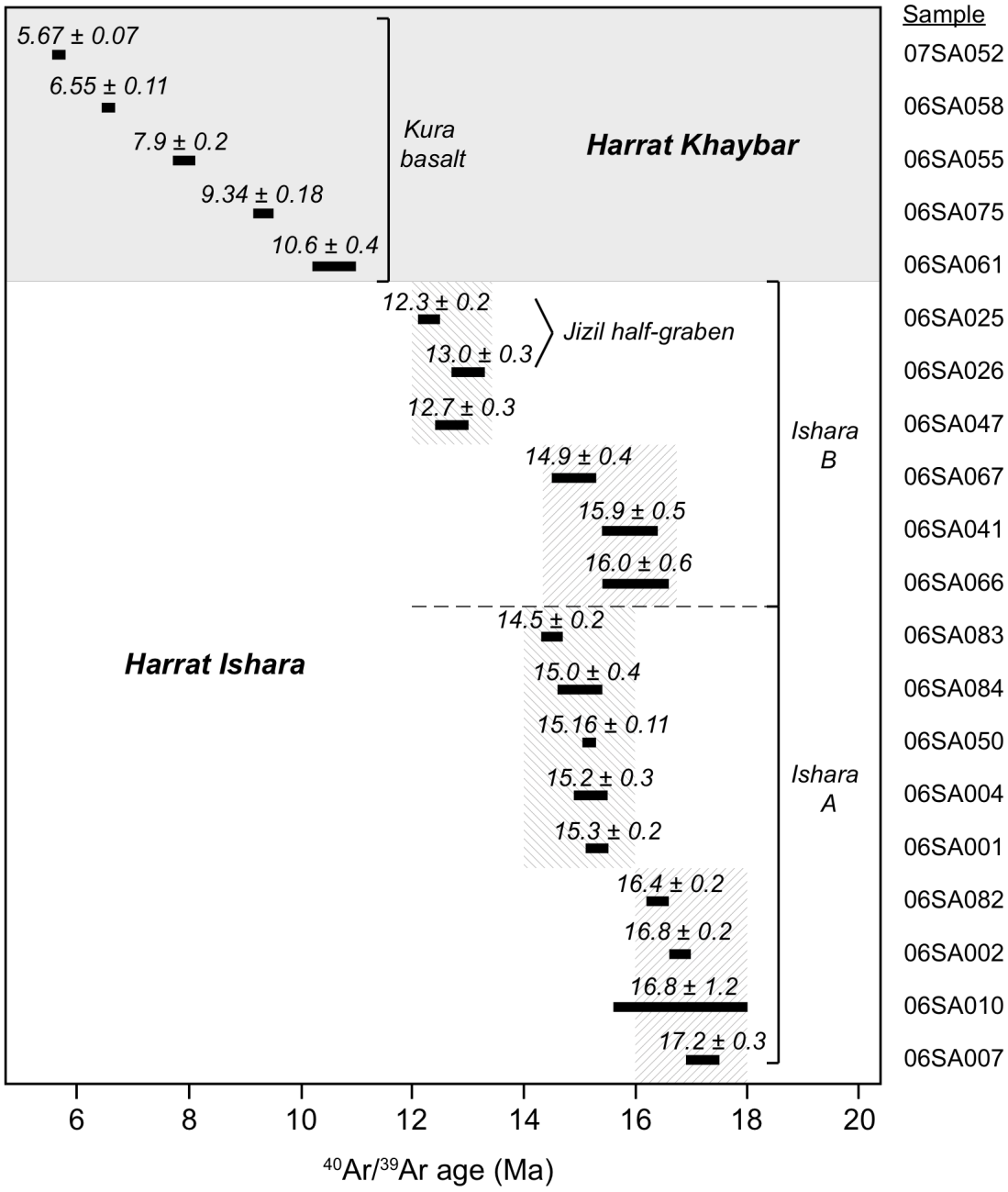
Sample
07SA052
06SA058
06SA055
06SA075
06SA061
06SA025
06SA026
06SA047
06SA067
06SA041
06SA066
06SA083
06SA084
06SA050
06SA004
06SA001
06SA082
06SA002
06SA010
06SA007
5.67 ± 0.07
6.55 ± 0.11
7.9 ± 0.2
9.34 ± 0.18
10.6 ± 0.4
Kura basalt
Harrat Khaybar
12.3 ± 0.2
13.0 ± 0.3
Jizil half-graben
12.7 ± 0.3
14.9 ± 0.4
15.9 ± 0.5
16.0 ± 0.6
Ishara B
14.5 ± 0.2
Harrat Ishara
15.0 ± 0.4
15.16 ± 0.11
15.2 ± 0.3
15.3 ± 0.2
Ishara A
16.4 ± 0.2
16.8 ± 0.2
16.8 ± 1.2
17.2 ± 0.3
6
8
10
12
14
16
18
20
40Ar/39Ar age (Ma)

Figure 16 - HJB Basalt: Whole-rock $^{40}Ar/^{39}Ar$ Age Data

Data bars encompass age ± error. Shaded boxes delineate sub-unit classification. See Figure 15 for volcanic source assignment.

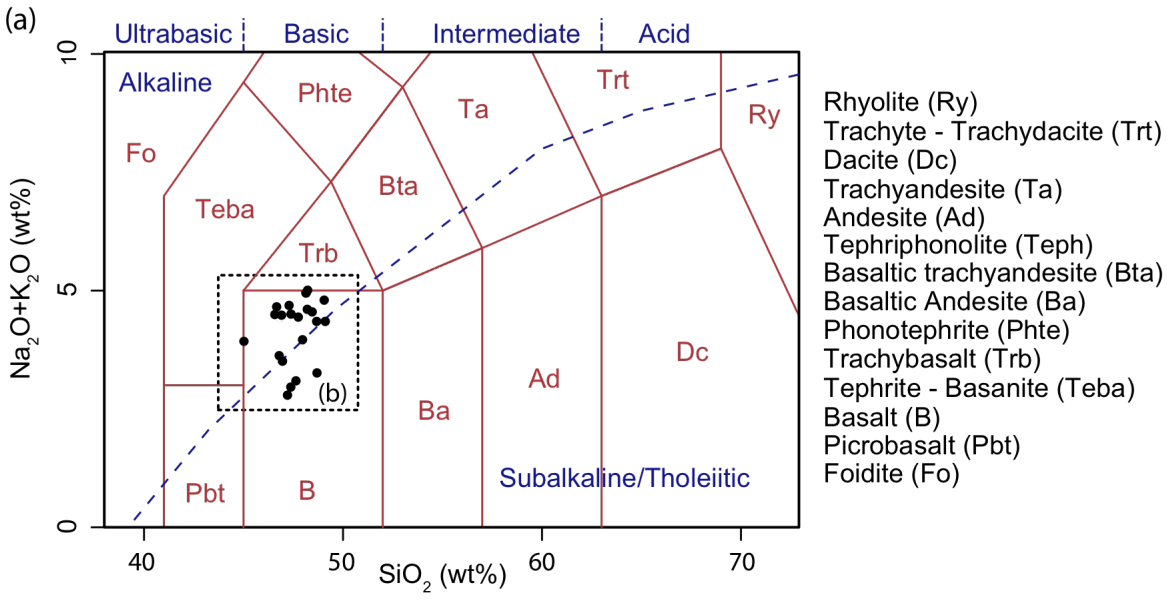
(a)
Ultrabasic
Basic
Intermediate
Acid
Alkaline
Phte
Ta
Trt
Ry
Fo
Teba
Bta
Trb
(b)
Ba
Ad
Dc
Pbt
B
Subalkaline/Tholeiitic
Na2O+K2O (wt%)
SiO2 (wt%)
Rhyolite (Ry)
Trachyte - Trachydacite (Trt)
Dacite (Dc)
Trachyandesite (Ta)
Andesite (Ad)
Tephriphonolite (Teph)
Basaltic trachyandesite (Bta)
Basaltic Andesite (Ba)
Phonotephrite (Phte)
Trachybasalt (Trb)
Tephrite - Basanite (Teba)
Basalt (B)
Picrobasalt (Pbt)
Foidite (Fo)

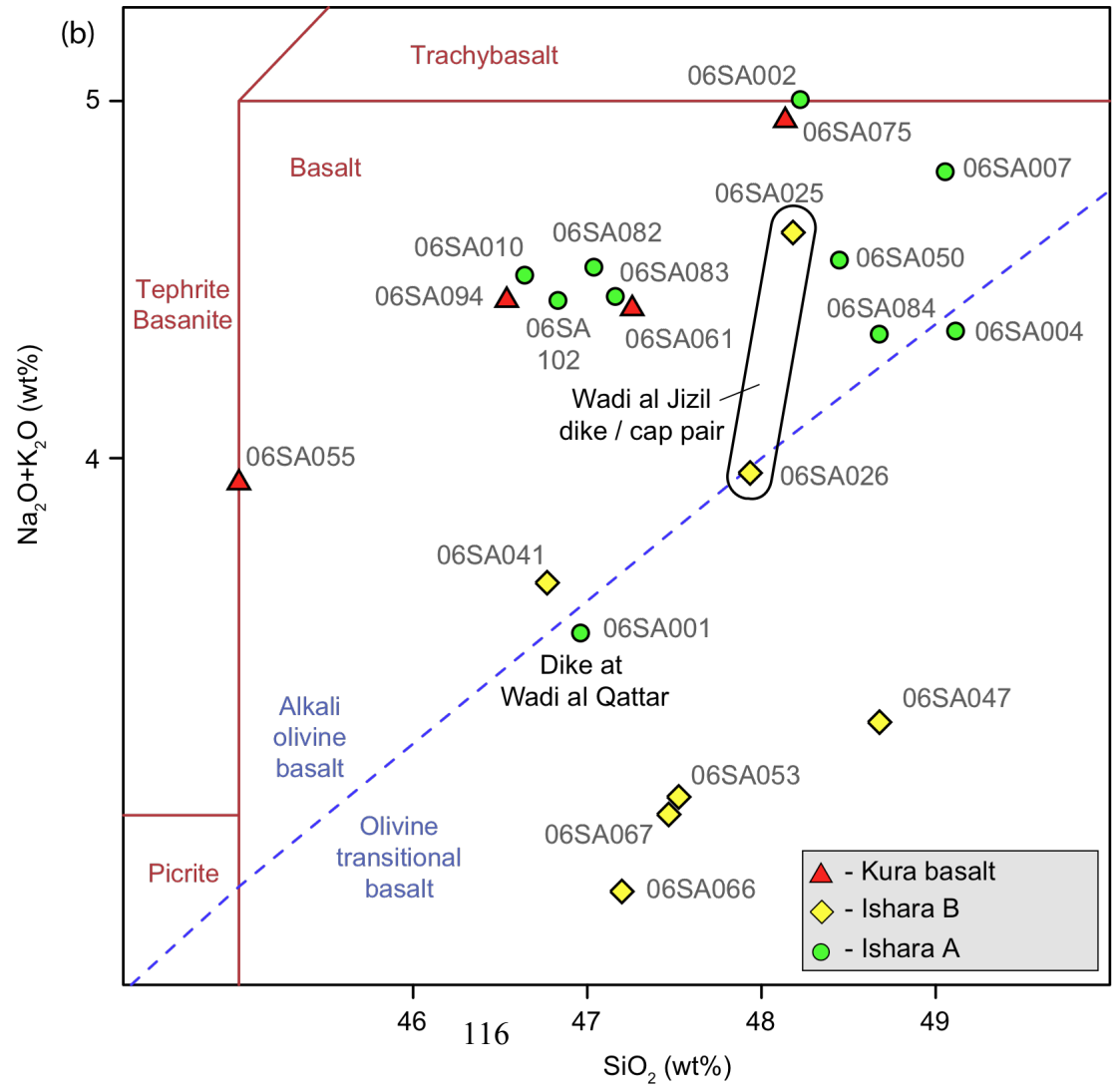
(b)
Trachybasalt
Basalt
Tephrite
Basanite
Alkali
olivine
basalt
Olivine
transitional
basalt
Picrite
06SA002
06SA075
06SA007
06SA025
06SA010
06SA082
06SA083
06SA050
06SA094
06SA084
06SA004
06SA102
06SA061
Wadi al Jizil
dike / cap pair
06SA055
06SA026
06SA041
06SA001
Dike at
Wadi al Qattar
06SA047
06SA053
06SA067
06SA066
- Kura basalt
- Ishara B
- Ishara A
Na2O+K2O (wt%)
SiO2 (wt%)

Figure 17 - HJB Basalt: Lithologic Classification

Part (a) shows basalt sample classification according to total alkali-silica (TAS) diagram of Le Bas et al. (1986) and alkali olivine basalt (AOB)/olivine transitional basalt (OTB) field boundary by Irvine and Baragar (1971). Part (b) shows detail of (a) inset. See legend for abbreviation detail. Red triangles = Kura basalt; yellow diamonds = Ishara B; green circles = Ishara A.

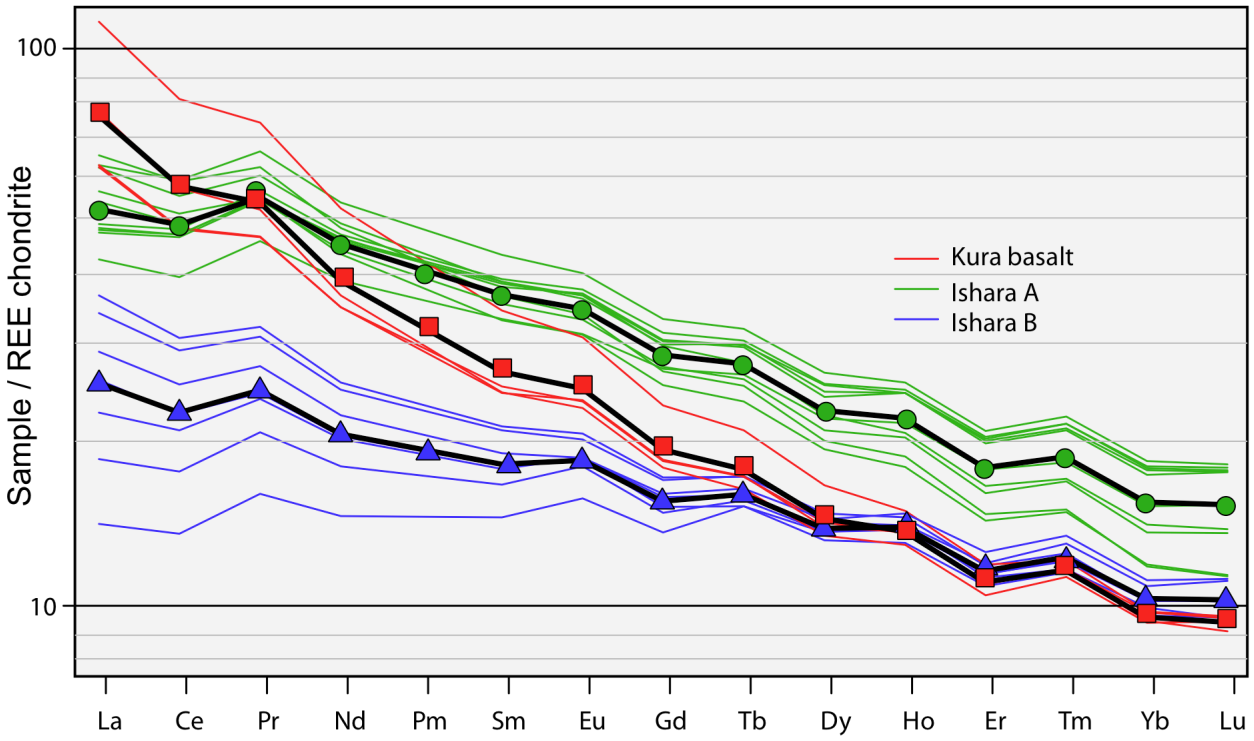
100
10
Sample / REE chondrite
Kura basalt
Ishara A
Ishara B
La
Ce
Pr
Nd
Pm
Sm
Eu
Gd
Tb
Dy
Ho
Er
Tm
Yb
Lu

Figure 18 - HJB Basalt: REE Concentration

Summary of all basalt geochemical data normalized to chondrite and grouped by volcanic source: Average data in decorated bold black line. 21 total basalt samples.

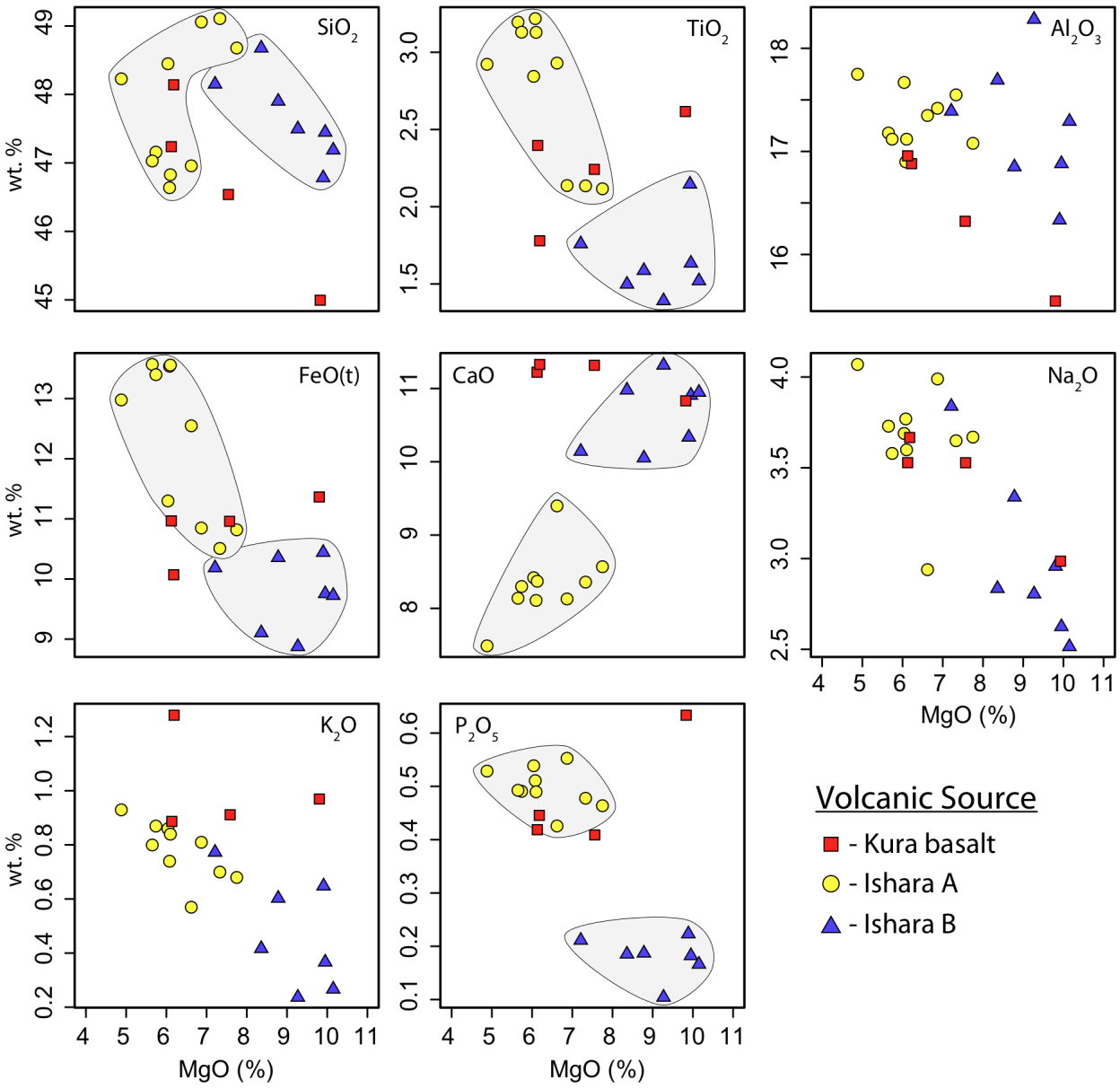
SiO2
TiO2
Al2O3
FeO(t)
CaO
Na2O
K2O
P2O5
wt. %
MgO (%)
Volcanic Source
- Kura basalt
- Ishara A
- Ishara B

Figure 19 - HJB Basalt: MgO vs. Major Elements

The greatest discrimination between well-grouped data points, denoted by the gray regions, occurs in SiO_2, TiO_2, FeO, CaO, and P_2O_5. Weight percent value scales (y-axis) vary between each plot. See Appendix C for geochemical metadata and Figure 15 for volcanic source assignment.

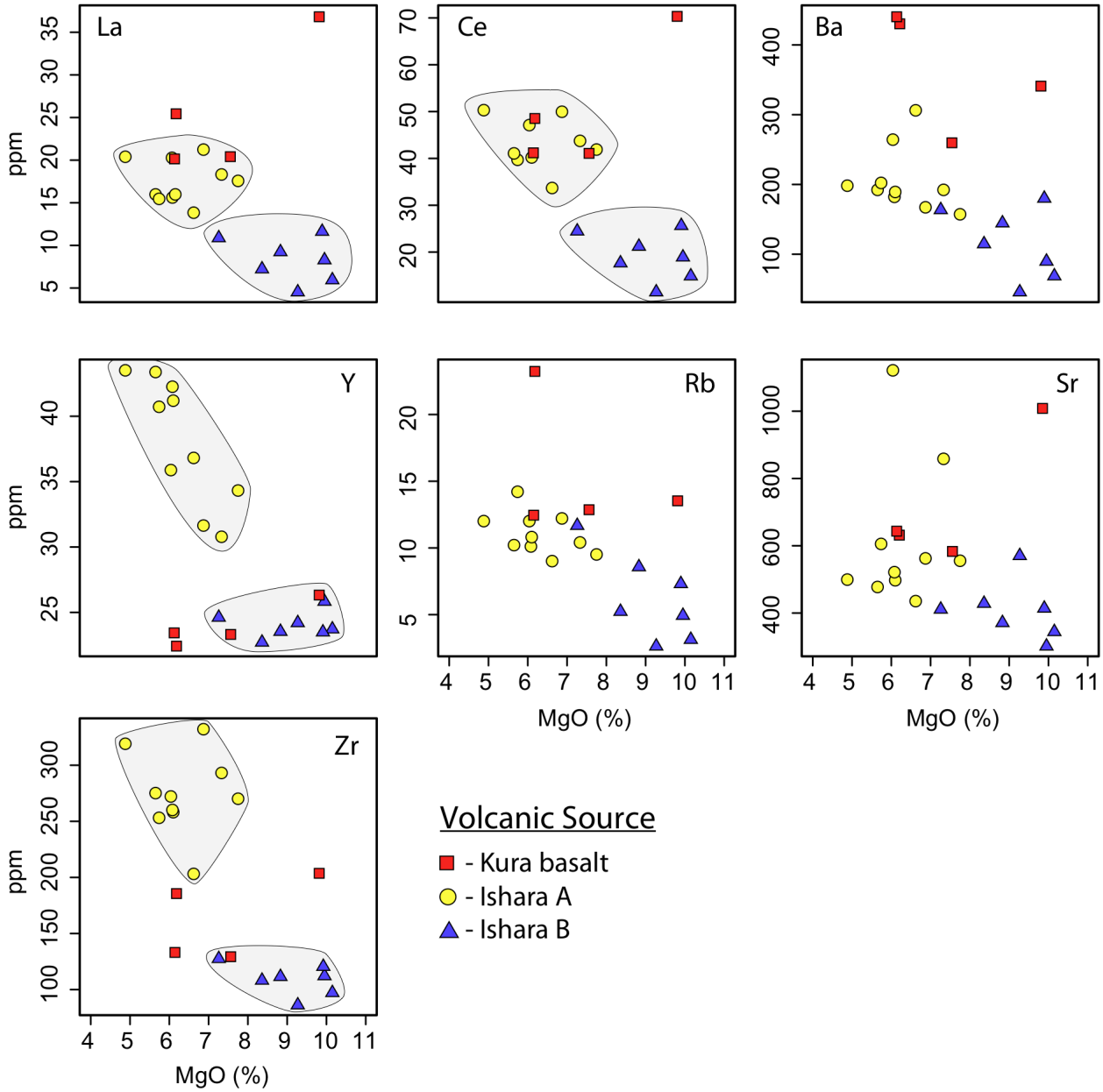
La
Ce
Ba
Y
Rb
Sr
Zr
ppm
MgO (%)
Volcanic Source
- Kura basalt
- Ishara A
- Ishara B

Figure 20 - HJB Basalt: MgO vs. Trace Elements

The greatest discrimination between well-grouped data points, denoted by the gray regions, occurs in La, Ce, Y, and Zr. Concentration scales (y-axis) vary between each plot. See Appendix C for geochemical metadata and Figure 15 for volcanic source assignment.

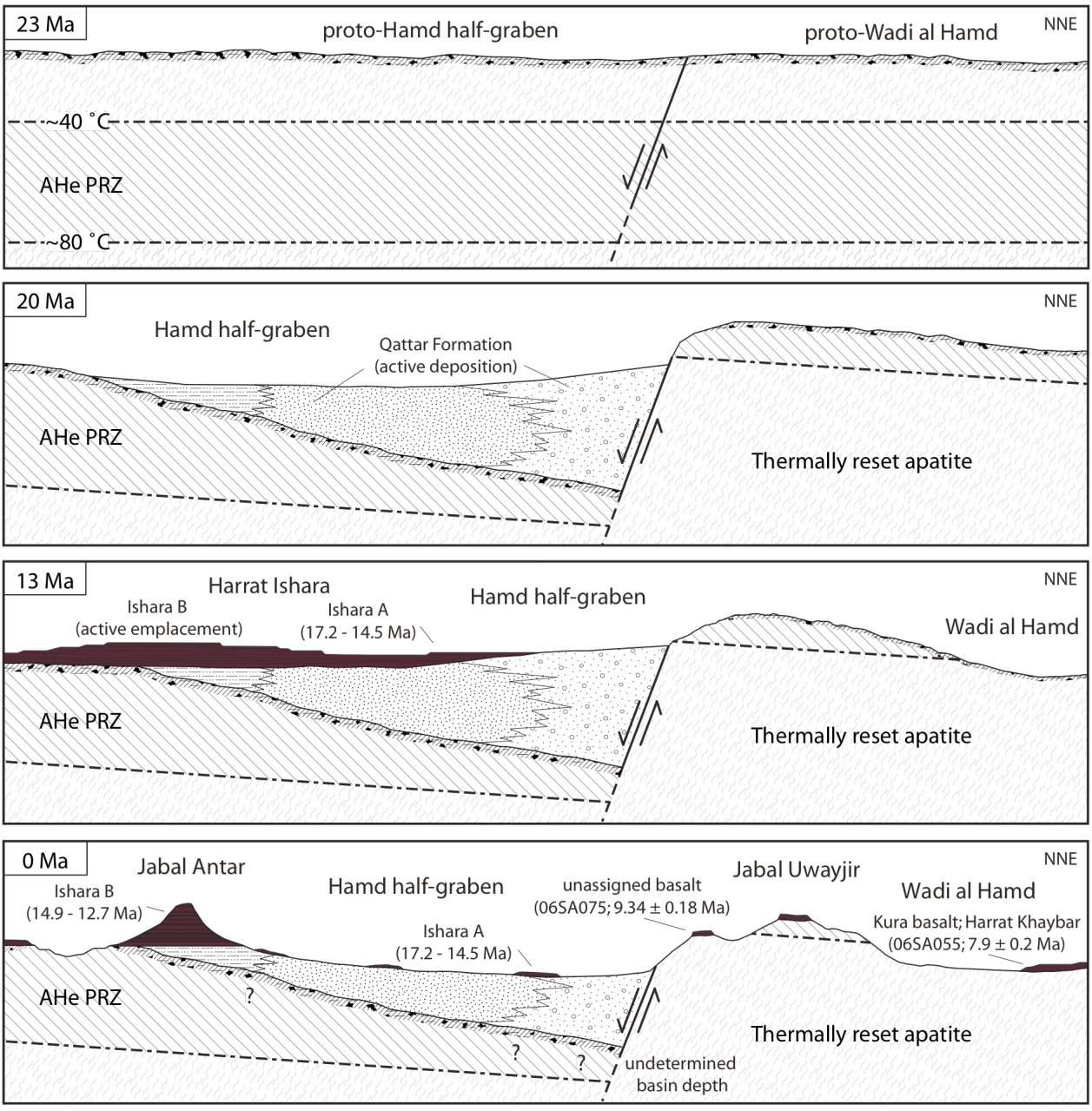
23 Ma
proto-Hamd half-graben
proto-Wadi al Hamd
NNE
~40 ˚C
AHe PRZ
~80 ˚C
20 Ma
NNE
Hamd half-graben
Qattar Formation
(active deposition)
AHe PRZ
Thermally reset apatite
13 Ma
Harrat Ishara
Ishara B
(active emplacement)
Ishara A
(17.2 - 14.5 Ma)
Hamd half-graben
NNE
Wadi al Hamd
AHe PRZ
Thermally reset apatite
0 Ma
Jabal Antar
Ishara B
(14.9 - 12.7 Ma)
Hamd half-graben
unassigned basalt
(06SA075; 9.34 ± 0.18 Ma)
Jabal Uwayjir
Wadi al Hamd
NNE
Kura basalt; Harrat Khaybar
(06SA055; 7.9 ± 0.2 Ma)
Ishara A
(17.2 - 14.5 Ma)
AHe PRZ
?
?
?
Thermally reset apatite
undetermined
basin depth
Basalt
Saprolitized
Basement
AHe PRZ
Undifferentiated
Proterozoic Basement
Conglomerate
Sandstone
Silty Sandstone
Syn-rift Sedimentary Basin Fill
(Qattar Formation)

Figure 21 - Hamd-Jizl Basin Cross-Section

Composite SW-NE cross-section of Hamd-half-graben from Jabal Antar to Wadi al Hamd. Composition of Qattar Formation basin fill is schematic. "AHe PRZ" = apatite (U-Th)/He thermochronometer partial retention zone. "Thermally reset apatite" identifies rock bodies that theoretically contain apatite thermochronometers that show a Red Sea rift signal.

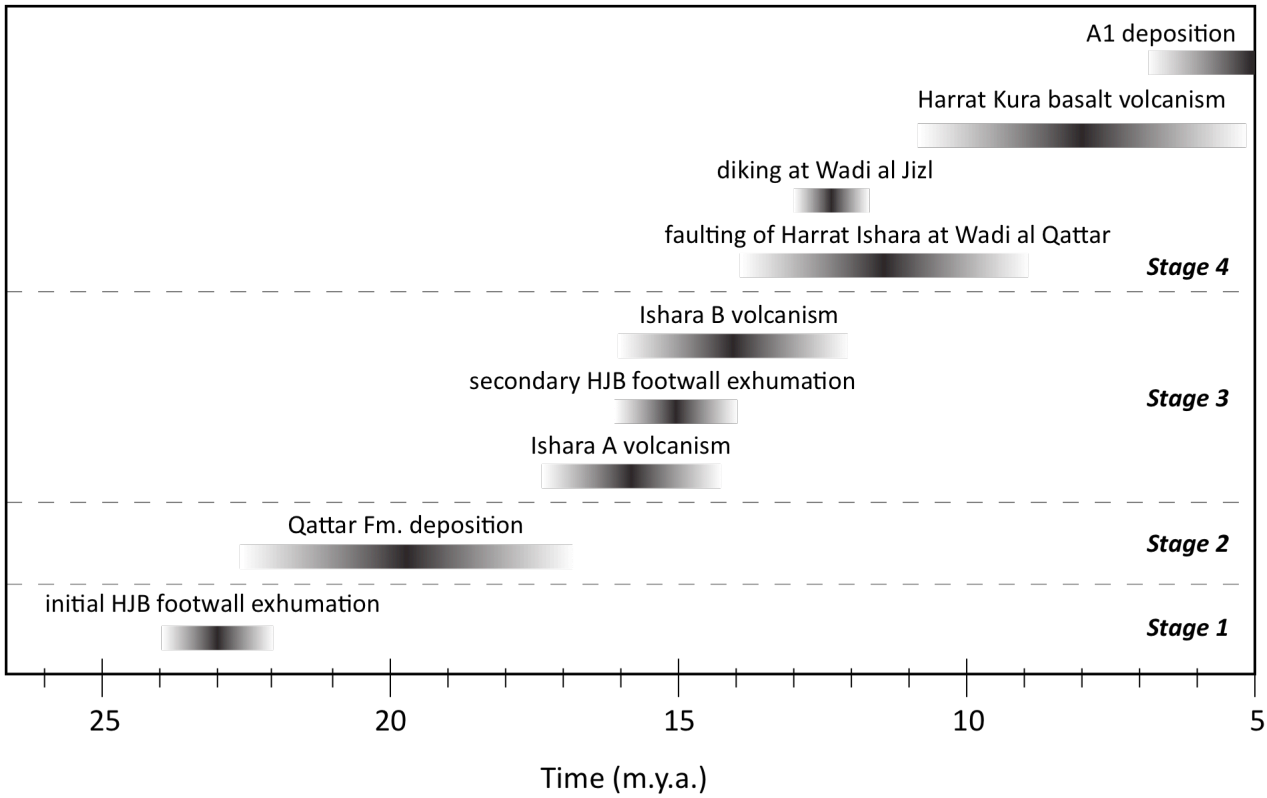
A1 deposition
Harrat Kura basalt volcanism
diking at Wadi al Jizl
faulting of Harrat Ishara at Wadi al Qattar
Stage 4
Ishara B volcanism
secondary HJB footwall exhumation
Stage 3
Ishara A volcanism
Qattar Fm. deposition
Stage 2
initial HJB footwall exhumation
Stage 1
25
20
15
10
5
Time (m.y.a.)

Figure 22 - Hamd-Jizl Basin: Rift Element Timing

Significant geologic events in HJB history plotted chronologically. Stage 1: broad RSR-normal tension across the region in the early Miocene caused widespread dissection of CARF terranes, delineating the HJB border faults and demarcating the furthest extent of inboard deformation. Stage 2: rapid footwall exhumation and erosion caused an accumulation of the syn-rift, siliciclastic sedimentary Qattar Formation proximal to the active border fault in both the Hamd and Jizl half-graben ca. 22 Ma. Stage 3: active basalt volcanism accompanied inboard deformation in the Hamd half-graben ca. 17 Ma. Stage 4: diffuse rift flank deformation with footwall exhumation in the Jizl half-graben at Jabal Nahar and minor post-depositional deepening of the Hamd half-graben where intra-basinal faults near Wadi al Qattar juxtapose 14.5 Ma Ishara basalt flows against syn-rift sediments.

Apatite Aliquot	Age (Ma)	± 6% (Ma)	U (ppm)	Th (ppm)	Sm (ppm)	Th/U	[eU]	mass (µg)	^{4}He yield (ncc / µg)	F_T	SDOM (Ma)
2006 Collection Campaign											
06SA016-1*	13.9	0.8	7.2	5.3	54.9	0.7	8.7	5.0	0.0102	0.68	
06SA016-2	15.2	0.9	11.7	7.4	63.8	0.6	13.7	5.2	0.0177	0.68	
06SA016-3	15.0	0.9	6.9	4.5	48.6	0.6	8.2	4.7	0.0101	0.67	0.7
AVG	**15.1**	**0.9**	**9.3**	**5.9**	**56.2**	**0.6**	**10.9**	**5.0**	**0.0139**	**0.68**	**0.2**
06SA022-1*	222.7	13.4	8.1	11.0	308.9	1.4	12.2	4.5	0.2375	0.66	
06SA022-2	205.0	12.3	5.4	9.3	212.2	1.7	8.6	3.2	0.1455	0.62	
06SA022-3	201.5	12.1	5.8	7.9	209.7	1.4	8.6	3.2	0.1445	0.63	11.3
AVG	**203.2**	**12.2**	**5.6**	**8.6**	**211.0**	**1.6**	**8.6**	**3.2**	**0.1450**	**0.63**	**2.5**
06SA023-1	223.5	13.4	6.2	11.8	206.4	1.9	10.0	2.2	0.1678	0.57	
06SA023-2	213.3	12.8	6.5	11.2	236.6	1.7	10.3	1.6	0.1785	0.55	----
AVG	**218.4**	**13.1**	**6.4**	**11.5**	**221.5**	**1.8**	**10.1**	**1.9**	**0.1732**	**0.56**	**7.2**
06SA073-1	44.5	2.7	1.6	3.6	51.9	2.3	2.7	2.4	0.0005	0.66	
06SA073-2*	343.5	20.6	-0.4	7.9	27.4	-20.3	1.6	1.6	0.0019	0.60	
06SA073-3	41.8	2.5	1.7	8.7	49.2	5.0	4.0	2.0	0.0006	0.65	
06SA073-4	34.5	2.1	0.6	4.3	55.9	6.9	1.9	0.9	0.0002	0.54	151.7
AVG	**40.3**	**2.4**	**1.3**	**5.6**	**52.3**	**4.8**	**2.9**	**1.7**	**0.0004**	**0.62**	**5.2**
06SA077-1	55.8	3.3	10.5	37.8	180.3	3.6	20.1	4.9	0.0042	0.67	
06SA077-2	47.2	2.8	7.2	26.1	137.6	3.6	13.9	3.9	0.0024	0.64	
06SA077-3*	198.5	11.9	12.3	37.9	211.8	3.1	22.0	2.9	0.0151	0.61	85.0
AVG	**51.5**	**3.1**	**8.9**	**32.0**	**159.0**	**3.6**	**17.0**	**4.4**	**0.0033**	**0.65**	**6.1**
06SA079-1*	41.7	2.5	7.5	33.9	226.7	4.5	16.4	2.9	0.0024	0.61	
06SA079-2	67.3	4.0	10.3	38.6	226.1	3.8	20.3	3.2	0.0048	0.62	
06SA079-3*	57.8	3.5	6.8	35.2	249.9	5.2	16.2	3.2	0.0033	0.62	
06SA079-4	68.6	4.1	10.9	36.7	183.1	3.4	20.3	2.9	0.0048	0.61	12.4
AVG	**67.9**	**4.1**	**10.6**	**37.7**	**204.6**	**3.6**	**20.3**	**3.1**	**0.0048**	**0.61**	**0.9**
06SA090b-1	33.5	2.0	18.5	17.8	128.9	1.0	23.3	8.8	0.0027	0.63	
06SA090b-2*	28.0	1.7	11.2	12.9	136.4	1.1	14.9	8.6	0.0014	0.62	
06SA090b-3	31.8	1.9	10.9	11.6	126.7	1.1	14.2	14.5	0.0017	0.68	2.8
AVG	**32.7**	**2.0**	**14.7**	**14.7**	**127.8**	**1.0**	**18.7**	**11.7**	**0.0022**	**0.65**	**1.2**
06SA093b-1*	25.1	1.5	10.1	2.3	22.9	0.2	10.7	15.5	0.0010	0.69	
06SA093b-2	47.2	2.8	10.3	2.4	23.0	0.2	11.0	15.8	0.0020	0.70	
06SA093b-3	44.5	2.7	9.6	2.0	20.2	0.2	10.2	14.5	0.0017	0.69	12.0
AVG	**45.8**	**2.7**	**10.0**	**2.2**	**21.6**	**0.2**	**10.6**	**15.2**	**0.0018**	**0.69**	**1.9**

Apatite Aliquot	Age (Ma)	± 6% (Ma)	U (ppm)	Th (ppm)	Sm (ppm)	Th/U	[eU]	mass (µg)	^{4}He yield (ncc / µg)	F_T	SDOM (Ma)
06SA104-1	24.8	1.5	11.2	13.8	87.9	1.2	14.8	3.4	0.0013	0.64	
06SA104-2*	27.5	1.7	13.4	14.7	92.3	1.1	17.3	2.8	0.0016	0.62	
06SA104-3	21.2	1.3	11.2	12.5	80.7	1.1	14.4	3.2	0.0011	0.63	
06SA104-4	17.5	1.0	12.3	12.4	90.8	1.0	15.6	3.1	0.0009	0.63	
06SA104-5*	12.7	0.8	11.0	13.3	92.5	1.2	14.5	5.9	0.0007	0.69	5.9
AVG	**21.1**	**1.3**	**11.5**	**12.9**	**86.5**	**1.1**	**14.9**	**3.2**	**0.0011**	**0.63**	**3.7**
2007 Collection Campaign											
07SA014b-1	241.0	14.5	9.3	8.8	101.8	0.9	11.8	8.1	0.0098	0.61	
07SA014b-2	282.1	16.9	12.2	12.3	136.0	1.0	15.7	10.2	0.0158	0.63	
07SA014b-3	234.0	14.0	13.9	14.7	91.0	1.1	17.7	8.1	0.0142	0.62	----
AVG	**252.4**	**15.1**	**11.8**	**11.9**	**109.6**	**1.0**	**15.1**	**8.8**	**0.0133**	**0.62**	**26.0**
07SA020-1	82.9	5.0	3.4	3.1	28.3	0.9	4.3	11.1	0.0015	0.76	
07SA020-2	67.2	4.0	2.6	3.3	16.8	1.3	3.5	10.8	0.0010	0.75	
07SA020-3*	109.9	6.6	3.3	5.6	20.6	1.7	4.7	24.0	0.0023	0.80	
07SA020-4	71.6	4.3	4.2	2.6	12.8	0.6	4.8	22.3	0.0015	0.81	19.2
AVG	**73.9**	**4.4**	**3.4**	**3.0**	**19.3**	**0.9**	**4.2**	**14.7**	**0.0013**	**0.77**	**8.1**
07SA022-1	55.4	3.3	21.2	73.7	53.6	3.5	38.5	6.2	0.0081	0.69	
07SA022-2	54.0	3.2	26.1	42.5	26.2	1.6	36.1	8.3	0.0077	0.72	
07SA022-3	54.9	3.3	23.1	60.2	47.3	2.6	37.2	4.7	0.0075	0.67	----
AVG	**54.8**	**3.3**	**23.5**	**58.8**	**42.4**	**2.6**	**37.3**	**6.4**	**0.0077**	**0.69**	**0.7**
07SA029-1*	67.9	4.1	41.9	184.4	637.4	4.4	87.5	3.62	0.1221	0.68	
07SA029-2	38.5	2.3	48.8	158.3	621.0	3.2	88.4	3.98	0.0762	0.70	
07SA029-3	39.1	2.3	199.8	327.0	340.3	1.6	276.8	4.04	0.2412	0.72	
07SA029-4	38.5	2.3	179.5	355.9	493.3	2.0	263.9	3.01	0.1684	0.68	14.6
AVG	**38.7**	**2.3**	**142.7**	**280.4**	**484.8**	**2.3**	**209.7**	**3.7**	**0.1619**	**0.70**	**0.3**
07SA037-1	58.3	3.5	2.0	7.0	57.3	3.5	3.9	14.0	0.0010	0.76	
07SA037-2	54.9	3.3	2.0	6.4	63.8	3.2	3.8	12.4	0.0009	0.75	
07SA037-3	49.4	3.0	3.9	11.3	79.6	2.9	7.0	10.0	0.0014	0.74	----
AVG	**54.2**	**3.3**	**2.7**	**8.2**	**66.9**	**3.2**	**4.9**	**12.1**	**0.0011**	**0.75**	**4.5**
07SA045-1	0.5	0.0	2.8	4.3	14.0	1.5	3.9	22.6	8.47E-06	0.80	
07SA045-2	0.5	0.0	4.7	7.8	20.5	1.7	6.6	13.5	1.35E-05	0.77	
07SA045-3	0.6	0.0	3.5	5.1	16.9	1.5	4.7	30.9	1.18E-05	0.82	
07SA045-4	0.7	0.0	3.4	6.5	18.4	1.9	5.0	15.9	1.46E-05	0.78	----
AVG	**0.6**	**0.0**	**3.6**	**5.9**	**17.5**	**1.6**	**5.0**	**20.7**	**1.21E-05**	**0.79**	**0.1**

Table 1 - Bedrock Apatite (U-Th)/He Age Data

Zircon Aliquot	Age (Ma)	± 8% (Ma)	U (ppm)	Th (ppm)	Sm (ppm)	Th/U	[eU]	mass (µg)	^{4}He yield (ncc / µg)	F_T	SDOM (Ma)
2006 Collection Campaign											
z06SA009-4	567.8	45.4	107.1	39.6	22.4	0.4	116.3	3.6	0.2701	0.73	
z06SA009-5	596.3	47.7	87.7	28.2	3.5	0.3	94.2	3.3	0.2292	0.72	
z06SA009-7	541.0	43.3	89.1	32.9	3.4	0.4	96.7	3.5	0.2127	0.72	----
AVG	**568.4**	**45.5**	**94.6**	**33.6**	**9.8**	**0.4**	**102.4**	**3.5**	**0.2374**	**0.73**	**27.7**
z06SA044-1	320.2	25.6	97.9	34.4	3.6	0.4	105.8	4.1	0.1408	0.75	
z06SA044-2*	357.2	28.6	216.4	74.9	8.6	0.3	233.6	6.7	0.3617	0.78	
z06SA044-3	320.5	25.6	118.0	41.6	4.7	0.4	127.6	7.2	0.1757	0.78	21.3
AVG	**320.4**	**25.6**	**107.9**	**38.0**	**4.1**	**0.4**	**116.7**	**5.6**	**0.1583**	**0.77**	**0.2**
z06SA052-1	13.6	1.1	300.8	141.5	----	0.5	----	4.2	0.0179	0.73	
z06SA052-2*	9.9	0.8	251.8	98.4	----	0.4	----	4.8	0.0110	0.75	
z06SA052-3	13.7	1.1	94.0	45.6	----	0.5	----	3.7	0.0056	0.73	2.1
AVG	**13.6**	**1.1**	**197.4**	**93.5**	----	**0.5**	----	**3.9**	**0.0118**	**0.73**	**0.0**
z06SA089-1	392.0	31.4	232.1	76.6	5.0	0.3	249.8	2.3	0.3808	0.70	
z06SA089-2*	411.8	32.9	187.3	55.5	4.3	0.3	200.1	5.1	0.3489	0.76	
z06SA089-3	389.5	31.2	239.0	77.0	7.2	0.3	256.8	6.7	0.4358	0.78	12.2
AVG	**390.7**	**31.3**	**235.6**	**76.8**	**6.1**	**0.3**	**253.3**	**4.5**	**0.4083**	**0.74**	**1.8**
z06SA104-1*	516.3	41.3	81.3	24.4	0.7	0.3	86.9	5.3	0.1925	0.76	
z06SA104-2	459.7	36.8	117.5	30.9	0.8	0.3	124.6	9.4	0.2572	0.80	
z06SA104-3*	513.5	41.1	80.6	26.2	0.8	0.3	86.6	4.8	0.1899	0.76	
z06SA104-4	470.3	37.6	122.9	39.4	0.9	0.3	132.0	6.1	0.2666	0.77	29.2
AVG	**465.0**	**37.2**	**120.2**	**35.2**	**0.8**	**0.3**	**128.3**	**7.8**	**0.2619**	**0.79**	**7.5**
2007 Collection Campaign											
z07SA013-1*	237.5	19.0	258.4	87.5	7.7	0.3	278.6	7.0	0.2648	0.73	
z07SA013-2	277.6	22.2	241.5	92.0	26.9	0.4	262.8	9.3	0.3034	0.76	
z07SA013-3	279.6	22.4	147.9	40.9	6.5	0.3	157.4	8.9	0.1831	0.76	23.7
AVG	**278.6**	**22.3**	**194.7**	**66.4**	**16.7**	**0.3**	**210.1**	**9.1**	**0.2433**	**0.76**	**1.5**
z07SA016-1	410.7	32.9	173.9	53.5	6.4	0.3	186.3	2.5	0.3021	0.71	
z07SA016-2*	213.6	17.1	338.0	99.8	14.8	0.3	361.1	2.9	0.3061	0.73	
z07SA016-3	439.9	35.2	123.7	33.1	5.9	0.3	131.4	5.0	0.2480	0.77	123.1
AVG	**425.3**	**34.0**	**148.8**	**43.3**	**6.2**	**0.3**	**158.8**	**3.8**	**0.2750**	**0.74**	**20.6**
z07SA022-1	542.8	43.4	196.3	133.1	1.4	0.7	227.0	4.5	0.5212	0.75	
z07SA022-2*	434.9	34.8	242.9	125.4	1.3	0.5	271.8	5.1	0.5019	0.76	
z07SA022-3	525.1	42.0	229.6	140.3	2.4	0.6	261.9	4.8	0.5804	0.75	57.9
AVG	**533.9**	**42.7**	**212.9**	**136.7**	**1.9**	**0.6**	**244.4**	**4.7**	**0.5508**	**0.75**	**12.5**

Zircon Aliquot	Age (Ma)	± 8% (Ma)	U (ppm)	Th (ppm)	Sm (ppm)	Th/U	[eU]	mass (µg)	^{4}He yield (ncc / µg)	F_T	SDOM (Ma)
z07SA029-1	298.9	23.9	397.4	220.7	27.5	0.6	448.3	4.9	0.5585	0.76	
z07SA029-2	306.6	24.5	462.8	201.2	39.1	0.4	509.3	5.8	0.6651	0.77	
z07SA029-3*	376.7	30.1	256.4	138.1	8.6	0.5	288.2	6.7	0.4693	0.78	42.9
AVG	**302.7**	**24.2**	**430.1**	**211.0**	**33.3**	**0.5**	**478.8**	**5.4**	**0.6118**	**0.76**	**5.4**
z07SA040-1	415.1	33.2	58.3	42.9	2.3	0.7	68.2	4.6	0.1181	0.75	
z07SA040-2*	348.6	27.9	104.8	35.2	1.0	0.3	112.9	7.8	0.1730	0.79	
z07SA040-3	420.5	33.6	58.4	16.6	0.7	0.3	62.3	7.6	0.1154	0.79	40.0
AVG	**417.8**	**33.4**	**58.4**	**29.7**	**1.5**	**0.5**	**65.2**	**6.1**	**0.1167**	**0.77**	**3.8**
z07SA042-1	498.4	39.9	81.4	32.9	6.4	0.4	89.0	2.3	0.1714	0.69	
z07SA042-2	589.3	47.1	59.0	15.2	5.6	0.3	62.5	2.1	0.1432	0.69	
z07SA042-3	546.9	43.8	72.7	29.1	10.8	0.4	79.5	2.7	0.1714	0.70	----
AVG	**544.9**	**43.6**	**71.1**	**25.7**	**7.6**	**0.4**	**77.0**	**2.3**	**0.1620**	**0.70**	**45.5**
z07SA045-1*	470.3	37.6	342.4	222.8	6.9	0.7	393.7	12.5	0.8294	0.80	
z07SA045-2	321.8	25.7	431.2	368.7	8.0	0.9	516.1	13.9	0.7297	0.79	
z07SA045-3	375.6	30.0	433.8	342.2	8.9	0.8	512.6	11.7	0.8474	0.79	75.2
AVG	**348.7**	**27.9**	**432.5**	**355.4**	**8.5**	**0.8**	**514.4**	**12.8**	**0.7886**	**0.79**	**38.0**
z07SA046-1*	611.0	48.9	196.0	76.3	3.9	0.4	213.6	4.0	0.5444	0.74	
z07SA046-2	538.2	43.1	94.1	46.9	7.8	0.5	104.9	2.8	0.2279	0.72	
z07SA046-3	566.2	45.3	126.5	47.9	7.1	0.4	137.6	2.2	0.3057	0.70	36.7
AVG	**552.2**	**44.2**	**110.3**	**47.4**	**7.5**	**0.4**	**121.3**	**2.5**	**0.2668**	**0.71**	**19.8**

Table 2 - Bedrock Zircon (U-Th)/He Age Data

Sample No.	AHe	ZHe	LAT	LONG	Elev. (m)	Location	Structure	Formation*	Age*	Lithology
Hamd half-graben										
06SA009	----	554.4 ± 44.4	24.803	39.034	735	Wadi Rashad	hanging wall	*unnamed*	Upper Proterozoic	Granodiorite
06SA052	----	13.6 ± 1.1	25.116	38.860	542	Hamd half-graben	hanging wall	*unnamed*	Cenozoic	Leucotuff
06SA077	51.5 ± 3.1	----	25.201	38.516	563	Jabal ad Darah	hanging wall (far-field)	*unnamed*	Paleozoic	Monzodiorite
06SA079	67.9 ± 4.1	----	25.002	38.205	1305	Jabal Hasham	hanging wall (far-field)	*unnamed*	Proterozoic	Granite
06SA089	----	390.7 ± 31.3	24.774	38.942	911	SW Wadi al Qattar	hanging wall (far-field)	*unnamed*	Proterozoic	Granodiorite
06SA090b	32.7 ± 2.0	----	24.679	38.865	1339	Jabal al Qiladah	hanging wall (far-field)	*unnamed*	Proterozoic	Granodiorite
07SA029	38.7 ± 2.3	302.7 ± 24.2	24.610	39.073	1181	Jabal Admar	hanging wall (far-field)	*unnamed*	Upper Proterozoic	Granodiorite
06SA044	----	320.4 ± 25.6	25.232	38.922	597	Wadi al Hamd	footwall (proximal)	Rithmah Complex	Proterozoic	Dacite
06SA073	40.3 ± 2.4	----	25.092	38.905	583	Jabal an Nu'ayyimah	footwall (proximal)	Al Ays Group	Proterozoic	Metavolcaniclastic
06SA104	21.1 ± 1.3	465.0 ± 37.2	24.826	39.030	653	Wadi al Qattar	footwall (proximal)	*unnamed*	Upper Proterozoic	Granodiorite
07SA020	73.9 ± 4.4	----	24.912	39.543	1215	Jabal Shihabah	footwall (far-field)	*unnamed*	Upper Proterozoic	Rhyolite
07SA022	54.8 ± 3.3	533.9 ± 42.7	24.795	39.501	970	Ad Dulu	footwall (far-field)	*unnamed*	Upper Proterozoic	Granodiorite

Sample No.	AHe	ZHe	LAT	LONG	Elev. (m)	Location	Structure	Formation*	Age*	Lithology
Linkage Zone										
07SA040	----	417.8 ± 33.4	25.590	38.614	376	SW of Jabal Jamlah	hanging wall	Siqam Formation	Proterozoic	Dacite
07SA037	54.2 ± 3.3	----	25.715	38.797	905	Jabal Gharrah	footwall	*unnamed*	Proterozoic	Granite
07SA042	----	544.9 ± 43.6	25.586	38.740	491	Hadiyah	footwall	Abu Safiyah Complex	Proterozoic	Rhyolite
07SA045	0.6 ± 0.0	348.7 ± 27.9	25.562	38.850	556	Jabal al Masakk	footwall	Abu Safiyah Complex	Proterozoic	Diorite
07SA046	----	552.2 ± 44.2	25.526	38.847	583	Masakk al Mutawassimah	footwall	Al Ays Group	Proterozoic	Andesite
Jizil half-graben										
06SA022	203.2 ± 12.2	----	25.757	38.171	658	Wadi al Batha	hanging wall (far-field)	*unnamed*	Proterozoic	Granite
06SA023	218.4 ± 13.1	----	25.749	38.170	601	Wadi al Batha	hanging wall (far-field)	*unnamed*	Proterozoic	Granite
07SA013	----	278.6 ± 22.3	25.401	37.961	535	NE of Harrat Lunayyir	hanging wall (far-field)	*unnamed*	Proterozoic	Granite
07SA014b	252.4 ± 15.1	----	25.643	37.576	387	Jabal Hammat	hanging wall (far-field)	*unnamed*	Proterozoic	Monzogranite
07SA016	----	425.3 ± 34.0	25.767	37.987	512	Jabal Batra	hanging wall	*unnamed*	Proterozoic	Granite
06SA016	15.1 ± 0.9	----	25.971	38.224	700	Jabal Nahar	footwall	Abu Safiyah Complex	Proterozoic	Granite
06SA093b	45.8 ± 2.7	----	25.811	38.349	421	Jabal al Qihaba	footwall	Al Ays Group	Proterozoic	Orthogneiss

Table 3 - Hamd-Jizl Basin Structural Elements: (U-Th)/He Age and Location

See geologic maps for map location of AHe and ZHe ages (Figs. 2, 6, 7, and 8).

locale	LAT	LONG	structure type	#	strike mean (STDEVP)	dip mean (STDEVP)	trend (STDEVP)	plunge (STDEVP)	structural relevance	comment
Jizil half-graben										
Jabal Nahar	25° 56'	38° 15'	joint / fracture plane	14	67 (13)	54 (11)	----	----	border fault	RSR orientation
	"	"	slickenline	3	----	----	127 (20)	51 (12)	border fault	RSR orientation
Jabal al Qihaba	25° 49'	38° 20'	fracture plane	11	108 (9)	70 (14)	----	----	border fault	----
	"	"	slickenline	2	----	----	292 (11)	9 (4)	border fault	NFS orientation
	"	"	foliation plane	58	116 (13)	46 (11)	----	----	border fault	NFS orientation
	25° 47'	38° 20'	bedding plane	13	variable	15 (9)	----	----	Qattar fm.	near horizontality
Jabal Jamlah	25° 36'	38° 39'	fracture plane	19	127 (10)	46 (7)	----	----	border fault	RSR orientation
	"	"	slickenline	5	----	----	259 (11)	37 (2)	border fault	RSR orientation
Linkage Zone										
Jabal Abu Ruwaydah	25° 12'	38° 50'	fracture plane	12	199 (30)	59 (15)	----	----	transfer fault	----
	"	"	slickenline	7	----	----	295 (22)	59 (20)	transfer fault	----
Jabal Mijbiyah	25° 17'	38° 51'	joint plane	5	117 (12)	57 (8)	----	----	----	no observed slickenlines
Jabal Murdi	25° 14'	38° 54'	joint plane	8	155 (16)	52 (12)	----	----	----	no observed slickenlines
	"	"	foliation plane	9	139 (17)	46 (7)	----	----		NFS orientation
Hamd half-graben										
Jabal Jurfayn	25° 07'	38° 41'	fracture plane	6	310 (9)	65 (3)	----	----	fault	limited displacement
	"	"	slickenline (set 1)	5	----	----	44 (1)	64 (2)	fault	RSR orientation
	"	"	slickenline (set 2)	5	----	----	321 (2)	13 (0)	fault	NFS orientation
Jabal An Nu'ayyimah	25° 06'	38° 53'	fracture plane	2	128 (8)	66 (4)	----	----	border fault	----
Jabal Antar	25° 02'	38° 52'	fracture plane (set 1)	6	167 (17)	58 (21)	----	----	basin-internal faulting	Qattar formation
	"	"	fracture plane (set 2)	4	328 (10)	71 (13)	----	----	basin-internal faulting	Qattar formation; conjugate to set 1
	25° 03'	38° 51'	PTXB	6	----	----	87 (44)	----	paleocurrent	----

locale	LAT	LONG	structure type	#	strike mean (STDEVP)	dip mean (STDEVP)	trend (STDEVP)	plunge (STDEVP)	structural relevance	comment
Wadi al Qattar										
Strand 1	24° 49'	39° 01'	fracture plane (set 1)	42	199 (20)	60 (12)	----	----	border fault: west strand	----
	"	"	fracture plane (set 2)	8	63 (17)	44 (5)	----	----	border fault: west strand	conjugate to set 1
	"	"	slickenline (set 1)	5	----	----	223 (18)	31 (7)	border fault: west strand	----
	"	"	slickenline (set 2)	7	----	----	326 (23)	53 (22)	border fault: west strand	----
Strand 2	24° 48'	39° 02'	fracture plane (set 1)	53	148 (22)	56 (14)	----	----	border fault: east strand	----
	"	"	fracture plane (set 2)	21	327 (18)	53 (14)	----	----	border fault: east strand	conjugate to set 1
	"	"	slickenline	5	----	----	257 (42)	36 (15)	border fault: east strand	----
Al Qattar	24° 48'	39° 01'	bedding plane	9	265 (9)	30 (6)			Qattar fm.	----
formation	24° 46'	39° 01'	PTXB	6	----	----	338 (13)	----	paleocurrent	4 in Wadi Rashad; 2 restored from type section
Taytad	24° 49'	39° 00'	fracture plane	18	257 (41)	57 (16)	----	----	basin-internal faulting	----

Table 4 - Hamd-Jizl Basin Structural Measurements

See geologic maps for map location of structural elements (Figs. 6, 7, and 8).

Stratigraphic Position (m)	Apatite Aliquot	Age [Ma]	± 6% [Ma]	U [ppm]	Th [ppm]	Sm [ppm]	Th/U	He [ncc/mg]	mass [mg]	F_T	comment
Wadi al Qattar (Section T)											
480	T38-1	18.8	1.1	0.3	12.8	16.0	38.8	0.28	12.2	0.80	
	T38-2	140.9	8.5	1.7	9.8	21.9	5.9	2.6	18.0	0.82	
	T38-3	94.6	5.7	4.8	33.4	18.8	7.0	5.29	13.0	0.81	
	T38-4	54.0	3.2	0.4	12.5	14.4	31.6	0.83	18.3	0.82	
	T38-5	156.8	9.4	1.4	21.9	17.2	15.5	4.40	7.9	0.77	
	T38-6*	----	----	----	----	----	----	----	----	----	bad data
	T38-7	49.8	3.0	0.7	11.9	20.0	17.0	0.80	14.8	0.81	
	T38-8	37.7	2.3	0.6	10.1	17.5	17.1	0.53	20.5	0.83	
	T38-9	77.5	4.6	0.7	2.3	21.4	3.4	0.49	15.3	0.82	
	T38-10	41.4	2.5	0.8	4.9	22.9	6.2	0.40	20.0	0.83	
470	T36-1	20.6	1.2	1.2	7.8	24.0	6.5	0.28	7.4	0.77	
	T36-2	19.6	1.2	2.0	7.3	23.7	3.7	0.3	6.8	0.76	
	T36-3	83.0	5.0	0.3	0.7	26.2	2.8	0.23	10.1	0.79	
	T36-4	151.5	9.1	12.4	14.1	23.0	1.1	11.07	23.2	0.84	
	T36-5	16.9	1.0	1.3	11.7	9.2	8.8	0.31	13.1	0.80	
	T36-6	24.1	1.4	0.8	7.9	17.2	9.6	0.31	23.8	0.83	
	T36-7	49.4	3.0	1.3	7.8	19.9	6.0	0.69	8.8	0.78	
	T36-8	314.4	18.9	1.4	14.6	24.6	10.7	6.77	9.4	0.78	
	T36-9	41.7	2.5	0.9	10.4	17.6	11.1	0.68	28.9	0.85	
	T36-10	33.0	2.0	0.8	9.3	16.8	11.9	0.47	25.0	0.84	
455	T35-1	76.2	4.6	1.0	5.5	25.5	5.5	0.87	28.8	0.85	
	T35-2	70.9	4.3	1.1	3.8	20.7	3.6	0.7	22.6	0.84	
	T35-3	309.0	18.5	0.8	2.3	21.9	2.9	2.22	47.0	0.87	
	T35-4	93.4	5.6	7.1	13.2	9.9	1.9	4.13	9.6	0.79	
	T35-5	32.5	1.9	0.6	4.0	22.7	6.8	0.24	10.1	0.79	
	T35-6	26.0	1.6	1.5	5.7	14.1	3.9	0.32	8.2	0.78	
	T35-7	68.9	4.1	0.6	3.2	18.2	5.5	0.42	7.6	0.77	
	T35-8	177.9	10.7	0.8	4.6	7.0	5.5	1.54	12.0	0.80	
	T35-9	67.8	4.1	0.7	3.1	26.5	4.6	0.47	11.3	0.80	
	T35-10	43.8	2.6	0.7	3.8	25.6	5.5	0.33	7.0	0.76	
420	T31-1*	----	----	----	----	----	----	----	----	----	zircon
	T31-2*	----	----	----	----	----	----	----	----	----	bad data
	T31-3	122.7	7.4	0.6	2.5	16.9	4.4	0.69	13.5	0.81	

Stratigraphic Position (m)	Apatite Aliquot	Age [Ma]	± 6% [Ma]	U [ppm]	Th [ppm]	Sm [ppm]	Th/U	He [ncc/mg]	mass [mg]	F_T	comment
***Wadi al Qattar (Section T)* - continued**											
310	T28-1	21.0	1.3	2.2	13.3	22.1	6.1	0.53	28.7	0.85	
	T28-2	42.6	2.6	2.3	10.0	25.9	4.4	0.9	25.9	0.84	
	T28-3	33.9	2.0	1.8	11.7	25.1	6.4	0.75	30.3	0.85	
	T28-4	28.7	1.7	1.5	6.5	19.6	4.4	0.39	11.0	0.80	
	T28-5	53.0	3.2	2.2	12.4	31.0	5.5	1.12	3.9	0.72	
	T28-6	41.5	2.5	2.2	14.2	25.8	6.3	1.01	8.2	0.77	
	T28-7	20.1	1.2	2.5	16.9	30.1	6.6	0.58	10.0	0.79	
	T28-8	36.7	2.2	1.2	5.3	20.3	4.4	0.39	5.9	0.75	
	T28-9	32.2	1.9	3.3	24.6	36.4	7.5	1.15	3.3	0.70	
	T28-10	19.6	1.2	2.2	13.8	24.4	6.4	0.44	4.8	0.73	
285	T27-1	143.0	8.6	2.8	5.0	8.8	1.8	2.24	3.3	0.71	
	T27-2	68.4	4.1	2.5	1.5	19.4	0.6	0.9	5.3	0.76	
	T27-3	303.8	18.2	6.9	9.7	23.9	1.4	12.58	10.8	0.80	
255	T26-1	125.9	7.6	4.0	4.5	12.5	1.1	2.92	15.1	0.82	
	T26-2	61.0	3.7	0.8	4.1	20.5	5.3	0.5	21.1	0.83	
	T26-3	196.3	11.8	1.4	5.4	6.3	3.9	2.44	24.8	0.84	
	T26-4	70.2	1.8	4.5	15.4	23.1	3.5	2.37	5.9	0.75	
	T26-5	187.7	16.1	1.3	7.9	30.7	6.2	2.45	3.4	0.70	
	T26-6	113.2	4.1	2.1	7.5	13.5	3.6	1.84	5.4	0.75	
	T26-7*	----	----	----	----	----	----	----	----	----	no grain
	T26-8	64.8	4.6	1.1	7.6	26.5	6.7	0.91	17.5	0.82	
	T26-9	314.8	31.8	1.1	5.3	30.5	5.0	3.71	26.5	0.85	
	T26-10	140.2	4.3	3.1	7.8	17.4	2.5	3.18	17.7	0.82	
150	T19-1	65.1	4.7	1.0	5.4	20.5	5.5	0.70	16.4	0.82	
	T19-2	74.4	0.9	4.0	13.0	8.0	3.3	2.41	23.7	0.84	
	T19-3	23.0	0.5	0.9	16.3	11.6	17.9	0.49	15.4	0.81	
	T19-4	21.9	0.4	1.5	18.2	11.7	12.1	0.57	17.1	0.82	
	T19-5	88.2	1.2	8.6	18.5	10.7	2.1	4.47	3.5	0.71	
	T19-6	53.4	1.7	3.5	14.9	22.8	4.2	1.49	3.8	0.72	
	T19-7	74.8	1.6	5.1	20.4	22.8	4.0	3.04	5.1	0.74	
	T19-8	24.4	0.9	2.4	20.6	23.7	8.4	0.65	2.2	0.66	
	T19-9	47.0	3.1	1.2	8.1	25.0	6.7	0.66	8.3	0.77	
	T19-10*	----	----	----	----	----	----	----	----	----	contamination

Stratigraphic Position (m)	Apatite Aliquot	Age [Ma]	± 6% [Ma]	U [ppm]	Th [ppm]	Sm [ppm]	Th/U	He [ncc/mg]	mass [mg]	F_T	comment
***Wadi al Qattar (Section T)* - continued**											
60	T6-1	53.7	3.2	1.0	2.8	3.8	2.8	0.31	1.9	0.65	
	T6-2*	----	----	----	----	----	----	----	----	----	zircon
	T6-3	126.3	7.6	26.2	6.2	54.7	0.2	14.16	3.8	0.73	
	T6-4	132.4	7.9	10.1	6.4	15.9	0.6	6.26	5.0	0.74	
	T6-5	19.1	1.6	1.6	2.0	13.9	1.3	0.16	3.4	0.72	
	T6-6*	----	----	----	----	----	----	----	----	----	zircon
	T6-7	56.8	5.9	0.9	3.3	15.1	3.7	0.39	3.5	0.71	
	T6-8*	----	----	----	----	----	----	----	----	----	zircon
	T6-9*	436.9	21.3	14.5	3.8	12.3	0.3	30.79	12.5	0.82	zircon inclusion
	T6-10	47.0	3.0	1.1	1.3	9.9	1.2	0.30	11.2	0.80	
Jabal Antar (J2)											
10	A2-1-1	328.6	19.7	0.6	2.3	18.8	3.6	1.85	8.8	0.78	
	A2-1-2	61.7	3.7	1.9	7.1	19.9	3.7	0.99	10.1	0.79	
	A2-1-3	40.1	2.4	1.8	6.4	20.5	3.5	0.59	9.0	0.78	
	A2-1-4	51.1	3.1	1.2	5.8	14.7	4.7	0.60	11.4	0.80	
	A2-1-5	93.7	5.6	0.8	2.4	26.3	3.1	0.61	7.7	0.77	
	A2-1-6	104.2	6.3	1.2	5.2	12.6	4.3	1.09	6.2	0.75	
	A2-1-7	98.5	5.9	0.9	2.5	27.5	2.7	0.72	8.2	0.77	
	A2-1-8	76.4	4.6	0.9	3.0	25.9	3.4	0.56	6.3	0.76	
	A2-1-9	187.0	11.2	0.8	2.4	26.8	3.0	1.24	8.6	0.78	
	A2-1-10	302.0	18.1	0.6	2.4	24.0	4.0	1.64	4.4	0.73	

Table 5 - Qattar Formation: Detrital Apatite (U-Th)/He Age Data

Asterisk (*) indicates data not included in relative frequency determination. See Figures 10 and 12 for location of sampled intervals in measured sections.

Sample	Basalt geochemistry	$^{40}Ar/^{39}Ar$ age	Age Type	Geochemical Provenance	Location	LAT (WGS84)	LONG (WGS84)	Elev. (m)	Comment
06SA001	OTB	15.3 ± 0.2	plateau	*indeterminate*	Wadi al Qattar	24.785	39.003	722	Dike in Wadi al Qattar
06SA002	AOB/hawaiite	16.8 ± 0.2	plateau	Harrat Ishara	Wadi al Qattar	24.785	39.003	757	Flow intruded by 06SA001
06SA004	OTB	15.2 ± 0.3	plateau	Harrat Ishara	Wadi al Qattar	24.802	39.011	715	Flow in Wadi al Qattar over A2
06SA007	AOB	17.2 ± 0.3	integrated	Harrat Ishara	Wadi Rashad	24.787	39.040	708	Channel fill in west wadi Rashad
06SA010	AOB	16.8 ± 1.2	integrated	Harrat Ishara	Wadi Rashad	24.802	39.038	726	Basal flow over Pt. basement
06SA025	AOB	12.3 ± 0.2	plateau	local fissure	Wadi al Jizl	25.809	38.317	482	Cap in Wadi al Jizl
06SA026	OTB	13.0 ± 0.3	plateau	local fissure	Wadi al Jizl	25.809	38.321	366	Dike intruding Al Qattar fm. in Wadi al Jizl
06SA041	AOB	15.9 ± 0.5	plateau	*indeterminate*	Hamd half-graben	25.240	38.932	994	Overtop vertical transect (VT-5)
06SA047	OTB	12.7 ± 0.3	plateau	Harrat Ishara	Jabal Antar	25.051	38.857	1045	Jabal Antar Section (nearly highest flow)
06SA050	AOB	15.16 ± 0.11	plateau	Harrat Ishara	Jabal Antar	25.057	38.848	736	Jabal Antar Section (basal flow)
07SA052	*undetermined*	5.67 ± 0.07	plateau	*indeterminate*	Hamd half-graben	24.983	39.019	460	Check age of Wadi al Hamd
06SA055	AOB/basanite	7.9 ± 0.2	plateau	Harrat Ishara	Hamd half-graben	25.234	38.893	405	Wadi al Hamd basalt flow provenance check
06SA058	*undetermined*	6.55 ± 0.11	plateau	*indeterminate*	soft-linkage zone	25.469	38.799	454	Check age of Wadi al Hamd
06SA061	AOB	10.6 ± 0.4	plateau	Harrat Ishara	soft-linkage zone	25.349	38.722	459	Overtop alluvial channel
06SA066	OTB	16.0 ± 0.6	plateau	Harrat Ishara	Jabal Jurfayn	25.139	38.704	815	SW of Jabal Jurfayn
06SA067	OTB	14.9 ± 0.4	plateau	Harrat Ishara	Jabal Jurfayn	25.116	38.705	906	SW of Jabal Jurfayn
06SA075	AOB	9.34 ± 0.18	plateau	Harrat Ishara	Hamd half-graben	25.175	38.875	1009	Jabal Uwayjir
06SA082	AOB	16.4 ± 0.2	plateau	Harrat Ishara	Wadi al Qattar	24.822	38.978	763	Cap at Taytad village
06SA083	AOB	14.5 ± 0.2	plateau	Harrat Ishara	Wadi al Qattar	24.818	39.017	727	Basal flow west of Wadi al Qattar mouth
06SA084	AOB	15.0 ± 0.4	plateau	Harrat Ishara	Wadi al Qattar	24.822	39.035	782	Overlying Al Ays Gp. east of Wadi al Qattar mouth

Table 6 - HJB Basalt: Whole-rock $^{40}Ar/^{39}Ar$ Age Data

See geologic maps for map location of $^{40}Ar/^{39}Ar$ age data (Figs. 2, 6, 7, and 8).

APPENDICES

Appendix A1 - Whole-rock Basalt Major, Trace, and Rare Earth Element Geochemical Data: Wadi al Jizl and Central Hamd-Jizl Basin

TRACE elements reported as cation concentration in [ppm]; recalculated from original normalized XRF analytical report data. REE reported as original [ppm] concentration values from ICP-MS data.

Sample no.	06SA025	06SA026	06SA041	06SA055	06SA061	06SA075	06SA094
Location	Wadi al Jizil		central Hamd-Jizil Basin				
Field / Flow	Ishara B			Kura basalt			
Rock Type	Basalt	OTB	Basalt	Basanite	Basalt	AOB	Basalt
OXIDES (wt %)							
SiO2	48.18	47.93	46.78	45.00	47.24	48.14	46.54
TiO2	1.773	1.600	2.147	2.617	2.401	1.781	2.248
Al2O3	17.41	16.87	16.33	15.56	16.96	16.88	16.33
FeO*	10.22	10.39	10.45	11.38	10.97	10.08	10.97
MnO	0.172	0.172	0.171	0.193	0.180	0.176	0.177
MgO	7.23	8.80	9.93	9.84	6.16	6.21	7.58
CaO	10.17	10.08	10.33	10.84	11.24	11.33	11.32
Na2O	3.85	3.35	2.98	2.97	3.53	3.67	3.53
K2O	0.78	0.61	0.65	0.97	0.89	1.28	0.91
P2O5	0.215	0.191	0.223	0.634	0.419	0.446	0.410
Total	***100.00***	***100.00***	***100.00***	***100.00***	***100.00***	***100.00***	***100.00***
TRACE (cation ppm) [XRF determined]							
Ni	99.6	166.5	210.2	165.2	88.7	148.2	135.0
Cr	151.2	239.6	313.5	237.2	138.2	224.0	195.0
Sc	29.5	31.9	31.3	27.0	31.4	23.7	29.8
V	204.3	203.4	219.8	196.0	210.0	163.1	195.6
Ba	164.4	151.9	180.7	343.7	451.5	426.5	261.2
Rb	11.9	8.7	7.6	13.2	12.9	22.7	13.1
Sr	404.1	367.4	415.5	970.7	619.9	600.2	569.9
Zr	129.3	113.9	125.7	201.7	130.3	181.0	133.3
Y	24.6	22.9	23.3	25.4	23.2	20.3	22.6
Nb	13.0	10.7	19.5	56.3	32.5	35.0	33.6
Ga	17.5	18.2	16.1	17.8	17.8	16.8	18.0
Cu	78.6	79.1	80.2	59.7	56.5	60.7	66.2
Zn	86.3	83.4	80.0	88.9	80.6	80.3	81.9
Pb	0.7	0.8	0.7	1.6	0.0	0.0	0.5
La	13.1	9.4	11.5	34.4	18.2	25.7	17.9
Ce	24.5	19.8	30.6	68.2	42.2	47.6	43.3
Th	1.7	1.5	1.3	4.3	2.8	3.8	3.2
Nd	15.7	13.8	17.7	30.9	23.0	25.7	20.9
U	0.4	0.5	1.3	1.8	1.9	1.9	1.9
Bi	0.0	0.0	0.0	0.0	0.0	0.0	0.0
Cs	0.0	0.0	0.0	0.0	0.0	0.0	0.0
As	0.0	3.6	3.7	0.0	0.5	0.0	8.0
W	0.0	0.0	0.0	0.0	0.0	0.0	0.0

	Sample no.	06SA025	06SA026	06SA041	06SA055	06SA061	06SA075	06SA094
	Location	Wadi al Jizil		central Hamd-Jizil Basin				
	Field / Flow	Ishara B			Kura basalt			
	Rock Type	Basalt	OTB	Basalt	Basanite	Basalt	AOB	Basalt
REE (ppm) [ICP-MS determined]	La	11.07	9.43	11.91	36.87	20.21	25.48	20.40
	Ce	24.82	21.56	26.18	70.34	41.05	48.59	41.22
	Pr	3.41	3.01	3.55	8.26	5.14	5.75	5.16
	Nd	15.39	13.83	15.83	32.60	21.67	22.70	21.62
	Sm	4.19	3.82	4.26	6.88	5.03	4.90	4.89
	Eu	1.53	1.42	1.57	2.33	1.79	1.74	1.80
	Gd	4.63	4.32	4.69	6.32	5.02	4.88	5.05
	Tb	0.80	0.74	0.80	0.97	0.80	0.76	0.80
	Dy	5.02	4.72	4.84	5.65	4.83	4.58	4.75
	Ho	1.01	0.97	0.98	1.04	0.94	0.90	0.95
	Er	2.65	2.56	2.53	2.66	2.48	2.35	2.46
	Tm	0.37	0.36	0.35	0.36	0.35	0.34	0.35
	Yb	2.25	2.27	2.18	2.15	2.06	2.05	2.14
	Lu	0.35	0.35	0.32	0.33	0.31	0.32	0.32
	Ba	166	147	184	344	441	429	260
	Th	1.10	0.95	1.18	3.74	1.82	3.29	1.82
	Nb	13.86	11.00	19.74	59.32	34.67	37.56	34.43
	Y	24.74	23.66	23.69	26.33	23.44	22.48	23.33
	Hf	3.11	2.80	3.12	4.64	3.22	4.15	3.21
	Ta	0.94	0.74	1.33	3.82	2.16	2.44	2.14
	U	0.35	0.29	0.34	1.02	0.55	0.95	0.53
	Pb	1.19	1.05	0.91	2.10	1.28	2.06	1.31
	Rb	11.8	8.7	7.5	13.6	12.5	23.3	12.9
	Cs	0.12	0.12	0.11	0.16	0.15	0.19	0.14
	Sr	416	376	421	1007	643	632	584
	Sc	27.8	28.8	28.0	26.0	31.2	23.7	28.2
	Zr	129	113	123	204	133	186	130
CIPW norms	Q	0	0	0	0	0	0	0
	Or	4.61	3.605	3.841	5.732	5.26	7.564	5.378
	Ab	32.578	28.347	25.216	25.131	29.87	28.871	27.798
	An	27.919	29.192	29.261	26.26	27.803	25.804	26.025
	Ne	0	0	0	0	0	1.183	1.122
	Di	12.166	11.419	10.681	11.689	13.673	17.108	15.817
	Hy	0	3.778	3.349	0	0	0	0
	Ol	8.667	9.003	11.516	13.378	6.31	5.282	8.092
	Il	0.368	0.368	0.366	0.413	0.385	0.377	0.379
	Tn	0.943	3.452	4.798	1.533	3.295	0	0
	Pf	2.035	0	0	3.023	1.457	2.695	3.488
	Ru	0	0	0	0	0	0	0
	Ap	0.509	0.452	0.528	1.502	0.992	1.056	0.971
	Sum	***89.795***	***89.616***	***89.556***	***88.661***	***89.046***	***89.94***	***89.07***

Appendix A2 - Whole-rock Basalt Major, Trace, and Rare Earth Element Geochemical Data: Jabal Antar Region

TRACE elements reported as cation concentration in [ppm]; recalculated from original normalized XRF analytical report data. REE reported as original [ppm] concentration values from ICP-MS data.

Sample no.	06SA047	06SA053	06SA066	06SA067	06SA050
Location	Jabal Antar Region				
Field / Flow	Ishara B				Ishara A
Rock Type	OTB	OTB	OTB	OTB	Basalt
OXIDES (wt %)					
SiO2	48.69	47.51	47.20	47.46	48.45
TiO2	1.504	1.397	1.526	1.640	2.845
Al2O3	17.70	18.29	17.30	16.89	17.67
FeO*	9.12	8.89	9.74	9.77	11.30
MnO	0.203	0.158	0.166	0.173	0.180
MgO	8.36	9.27	10.15	9.95	6.04
CaO	10.99	11.33	10.96	10.92	8.42
Na2O	2.84	2.81	2.52	2.63	3.69
K2O	0.42	0.24	0.27	0.37	0.86
P2O5	0.187	0.106	0.168	0.184	0.539
Total	***100.00***	***100.00***	***100.00***	***100.00***	***100.00***
TRACE (cation ppm) [XRF determined]					
Ni	97.6	173.1	209.7	177.3	43.6
Cr	188.2	165.9	332.1	360.7	47.2
Sc	30.9	35.1	34.6	37.8	21.6
V	181.3	184.1	191.9	205.0	158.3
Ba	115.8	44.8	70.5	91.4	264.3
Rb	5.2	2.7	2.5	4.4	13.6
Sr	417.2	557.9	335.3	292.8	1079.9
Zr	107.5	86.7	97.7	110.8	265.1
Y	22.7	24.9	22.9	25.7	33.6
Nb	9.0	6.3	8.2	14.0	28.6
Ga	15.3	14.2	15.8	16.0	21.4
Cu	70.4	121.4	93.2	77.0	41.5
Zn	70.1	61.9	74.2	71.3	87.6
Pb	0.3	0.0	0.0	0.5	0.6
La	9.0	6.1	6.9	6.7	15.1
Ce	17.1	13.0	14.0	17.8	44.7
Th	1.6	0.7	2.0	2.5	1.7
Nd	12.4	9.9	12.2	10.9	28.1
U	0.5	0.0	0.0	0.5	1.1
Bi	0.0	0.0	0.0	0.0	0.0
Cs	0.0	0.0	0.0	0.0	0.0
As	5.7	2.6	2.7	5.1	0.0
W	0.0	0.0	0.0	0.0	0.0

Sample no.	06SA047	06SA053	06SA066	06SA067	06SA050
Location	Jabal Antar Region				
Field / Flow	Ishara B				Ishara A
Rock Type	OTB	OTB	OTB	OTB	Basalt
REE (ppm) [ICP-MS determined]					
La	7.33	4.63	6.05	8.39	20.17
Ce	17.84	11.65	15.06	19.10	47.08
Pr	2.63	1.78	2.29	2.70	6.63
Nd	12.54	9.13	11.20	12.71	30.60
Sm	3.57	2.93	3.35	3.62	7.74
Eu	1.42	1.20	1.37	1.42	2.77
Gd	4.15	3.74	4.06	4.38	8.08
Tb	0.71	0.71	0.73	0.76	1.28
Dy	4.49	4.64	4.66	4.89	7.54
Ho	0.91	0.98	0.96	1.03	1.43
Er	2.44	2.68	2.57	2.81	3.69
Tm	0.34	0.39	0.36	0.40	0.51
Yb	2.11	2.39	2.24	2.45	3.08
Lu	0.32	0.38	0.35	0.38	0.47
Ba	116	47	70	91	264
Th	0.53	0.52	0.48	0.85	1.79
Nb	9.09	6.60	7.95	14.99	29.33
Y	22.78	24.27	23.79	25.90	35.87
Hf	2.62	2.15	2.35	2.66	5.98
Ta	0.56	0.43	0.52	0.92	1.86
U	0.11	0.15	0.14	0.24	0.36
Pb	0.78	0.63	0.79	0.69	1.87
Rb	5.3	2.7	3.2	5.0	12.0
Cs	0.07	0.05	0.05	0.05	0.12
Sr	431	573	347	304	1121
Sc	30.0	33.6	32.9	37.8	22.2
Zr	109	87	98	113	272
CIPW norms					
Q	0	0	0	0	0.143
Or	2.482	1.418	1.596	2.187	5.082
Ab	24.031	23.777	21.324	22.254	31.224
An	34.307	36.584	35.095	33.188	29.11
Ne	0	0	0	0	0
Di	11.326	11.432	10.521	11.483	0
Hy	12.831	6.215	11.354	10.454	15.044
Ol	1.921	8.111	6.342	6.311	0
Il	0.434	0.338	0.355	0.37	0.385
Tn	3.131	2.993	3.287	3.548	6.442
Pf	0	0	0	0	0
Ru	0	0	0	0	0.018
Ap	0.443	0.251	0.398	0.436	1.277
Sum	***90.907***	***91.12***	***90.272***	***90.23***	***88.726***

Appendix A3 - Whole-rock Basalt Major, Trace, and Rare Earth Element Geochemical Data: Wadi al Qattar Region

TRACE elements reported as cation concentration in [ppm]; recalculated from original normalized XRF analytical report data. REE reported as original [ppm] concentration values from ICP-MS data.

Sample no.	06SA001	06SA002	06SA004	06SA007	06SA010	06SA082	06SA083	06SA084	06SA102
Location	Wadi al Qattar								
Field / Flow	Ishara A								
Rock Type	OTB	Hawaiite	OTB	Basalt	Basalt	Basalt	Basalt	Basalt	Basalt
OXIDES (wt %)									
SiO2	46.96	48.23	49.11	49.06	46.64	47.03	47.16	48.68	46.83
TiO2	2.931	2.923	2.136	2.138	3.219	3.196	3.131	2.117	3.130
Al2O3	17.35	17.75	17.55	17.42	16.90	17.18	17.12	17.08	17.12
FeO*	12.55	12.98	10.51	10.85	13.54	13.57	13.40	10.82	13.56
MnO	0.256	0.194	0.170	0.177	0.217	0.213	0.209	0.179	0.218
MgO	6.62	4.88	7.33	6.87	6.08	5.65	5.74	7.75	6.10
CaO	9.40	7.49	8.36	8.13	8.38	8.14	8.30	8.57	8.11
Na2O	2.94	4.07	3.65	3.99	3.77	3.73	3.58	3.67	3.60
K2O	0.57	0.93	0.70	0.81	0.74	0.80	0.87	0.68	0.84
P2O5	0.426	0.529	0.478	0.553	0.511	0.493	0.491	0.464	0.490
Total	***100.00***	***100.00***	***100.00***	***100.00***	***100.00***	***100.00***	***100.00***	***100.00***	***100.00***
TRACE (cation ppm) [XRF determined]									
Ni	77.8	18.8	106.0	97.1	32.4	22.5	28.2	114.8	28.6
Cr	157.7	10.0	184.8	165.1	10.9	3.0	4.8	237.2	6.4
Sc	28.1	18.1	22.9	19.6	23.5	23.4	22.2	22.7	23.7
V	199.2	122.1	131.5	119.0	183.5	172.6	174.6	135.8	178.5
Ba	307.9	198.9	190.4	168.3	189.9	195.2	198.7	157.4	190.3
Rb	9.5	11.6	9.8	11.8	10.2	10.1	13.9	10.3	11.4
Sr	428.2	475.5	831.8	550.1	501.6	452.2	578.6	538.3	475.7
Zr	204.7	307.4	285.6	326.2	256.6	266.4	249.7	269.4	254.4
Y	36.7	41.5	29.9	30.6	41.5	40.5	39.7	33.0	38.9
Nb	15.7	24.6	23.6	28.4	19.8	19.8	19.3	22.1	18.4
Ga	18.9	17.9	17.0	17.6	18.6	20.1	17.0	17.0	18.6
Cu	47.8	32.2	48.3	45.1	36.1	34.7	35.3	51.2	34.9
Zn	95.2	90.8	83.4	85.8	103.3	105.8	99.9	79.0	99.4
Pb	0.0	1.0	1.7	2.2	2.5	1.2	0.4	1.5	1.0
La	14.1	19.4	15.4	22.5	13.6	14.5	16.8	20.4	9.3
Ce	33.9	46.6	35.6	53.9	32.8	40.7	33.1	41.7	39.6
Th	3.3	2.9	2.3	2.9	2.6	3.2	2.2	2.1	2.8
Nd	21.9	32.1	25.1	30.7	24.9	29.2	24.5	27.5	28.7
U	0.6	0.6	0.2	1.1	0.8	0.0	1.1	1.4	1.5
Bi	0.0	0.0	0.0	0.0	0.0	0.0	0.0	0.0	0.0
Cs	0.0	0.0	0.0	0.0	0.0	0.0	0.0	0.0	0.0
As	2.0	0.0	2.3	3.7	2.9	0.0	0.0	3.0	0.0
W	0.0	0.0	0.0	0.0	0.0	0.0	0.0	0.0	0.0

	Sample no.	06SA001	06SA002	06SA004	06SA007	06SA010	06SA082	06SA083	06SA084
	Location	Wadi al Qattar							
	Field / Flow	Ishara A							
	Rock Type	OTB	Hawaiite	OTB	Basalt	Basalt	Basalt	Basalt	Basalt
REE (ppm) [ICP-MS determined]	La	13.82	20.38	18.30	21.22	15.60	15.96	15.44	17.55
	Ce	33.65	50.27	43.71	49.93	40.15	41.04	39.67	41.86
	Pr	5.06	7.33	6.05	6.86	6.03	6.22	5.99	6.00
	Nd	24.20	33.35	26.91	30.02	28.82	29.25	28.47	27.42
	Sm	6.63	8.65	6.61	7.30	7.59	7.83	7.69	7.07
	Eu	2.36	3.04	2.36	2.56	2.80	2.85	2.78	2.51
	Gd	7.34	9.03	6.87	7.27	8.27	8.52	8.24	7.41
	Tb	1.22	1.48	1.09	1.17	1.38	1.41	1.37	1.20
	Dy	7.44	8.99	6.54	6.78	8.53	8.59	8.14	7.08
	Ho	1.49	1.76	1.24	1.30	1.69	1.71	1.69	1.40
	Er	3.94	4.63	3.20	3.28	4.49	4.52	4.40	3.58
	Tm	0.54	0.65	0.44	0.45	0.64	0.64	0.62	0.50
	Yb	3.32	4.00	2.61	2.59	3.92	3.88	3.77	2.98
	Lu	0.51	0.61	0.39	0.38	0.60	0.60	0.59	0.46
	Ba	306	198	192	167	182	192	202	157
	Th	1.13	1.80	1.81	2.12	1.11	1.24	1.16	1.74
	Nb	16.49	25.45	24.48	28.95	19.20	20.49	19.54	22.28
	Y	36.80	43.50	30.77	31.63	42.25	43.37	40.71	34.31
	Hf	4.75	6.97	6.27	6.97	5.77	6.14	5.76	6.01
	Ta	1.09	1.68	1.63	1.96	1.27	1.37	1.33	1.43
	U	0.35	0.30	0.37	0.68	0.34	0.35	0.32	0.47
	Pb	1.26	2.13	1.86	2.10	1.72	1.87	1.78	1.73
	Rb	9.0	12.0	10.4	12.2	10.1	10.2	14.2	9.5
	Cs	0.34	0.12	0.13	0.12	0.10	0.08	0.10	0.10
	Sr	435	499	858	562	521	477	605	555
	Sc	26.7	16.6	20.2	18.2	22.4	24.0	21.3	22.0
	Zr	203	319	293	332	260	275	253	270
CIPW norms	Q	1.328	0.522	0	0	0	0	0.186	0
	Or	3.369	5.496	4.137	4.787	4.373	4.728	5.141	4.019
	Ab	24.877	34.439	30.885	33.762	31.901	31.562	30.293	31.055
	An	32.46	27.416	29.435	27.229	27.005	27.771	28.074	28.122
	Ne	0	0	0	0	0	0	0	0
	Di	1.701	0	1.668	2.132	0.677	0	0	3.652
	Hy	15.7	12.155	16.257	11.775	10.57	13.49	14.297	12.851
	Ol	0	0	0.86	3.048	2.985	0.409	0	3.335
	Il	0.548	0.415	0.364	0.379	0.464	0.456	0.447	0.383
	Tn	6.488	4.43	4.774	4.759	7.302	6.619	6.974	4.702
	Pf	0	0	0	0	0	0	0	0
	Ru	0	0.9	0	0	0	0.26	0.055	0
	Ap	1.009	1.253	1.132	1.31	1.21	1.168	1.163	1.099
	Sum	***87.48***	***87.027***	***89.512***	***89.18***	***86.488***	***86.462***	***86.631***	***89.218***

2. Chapter 2: Thermochronological Evidence for Long-Lived Diffuse Rifting of Continental Lithosphere and Two Extensional Rift Phases within the Central Arabian Margin of the Red Sea Rift

2.1. Abstract

The northern and southern portions of the Red Sea Rift system (RSR) exhibit wholly different patterns of continental lithosphere deformation. While sea-floor spreading initiated in the southern RSR ca. 5 Ma, the northern RSR has evolved from a relatively stable continental lithosphere to an extended, and presently unruptured, margin. Using a combined approach of apatite and zircon (U-Th)/He thermochronologic analyses (AHe and ZHe) and numerical time-temperature models in the *Helium Modeling Program* (HeMP©), we investigate the along-strike variance in rift state by deducing the evolution of structural deformation within the central Arabian rift flank (CARF) of the NW Arabian Plate. In contrast to the well-studied northern and southern termini of the RSR, the CARF contains the entire rift record and permits a spatial and temporal exploration of RSR development from early rift architecture, to strain dissemination during progressive rifting, through subsequent whole-scale modifications of the Arabian rift flank due to thermal and isostatic factors. Prior to this study, the CARF was unexplored in terms of (U-Th)/He thermochronologic research and no (U-Th)/He ages were published for regions anywhere along the full length of the Arabian margin. With this contribution, we are now able to address outstanding issues regarding the inboard extent of continental lithosphere extension in the central and northern Arabian margin, the perceived along-strike variance in rift phase timing between the southern and northern RSR, and the viability of comprehensive RSR evolution models.

Ninety-three total CARF samples yield dissimilar AHe and ZHe cooling age modes when plotted according to geographic location, which indicates inherent differences in Cenozoic fault spacing, footwall exhumation magnitude, and the degree of post-exhumation erosion between inboard and basin-proximal regions and leads to our identification of two primary structural domains: the Hijaz Mountains Fault Complex (HFC), and the inboard Hamd-Jizl Basin region (HJB). Thermal models of AHe and ZHe systems confirm the existence of Oligocene-Miocene and middle Miocene rift extension pulses and reveal a common three-stage thermotectonic t-T evolution for the HFC and HJB. First, the pre-rift Arabian-Nubian Shield experienced a Paleo-Mesozoic cooling event that brought the proto-CARF to a mid-to-upper crustal structural level where it remained relatively thermally stable through the Mesozoic. Then, a pulse of major extension ca. 23 Ma exhumed a widespread area of the CARF and marked the beginning of a phase of diffuse lithospheric rifting. Highly segmented rift flank dissection and episodic dike injection in the HFC accompanied footwall exhumation and terrigenous sedimentation in the HJB contemporaneously to delineate a ~200 km-wide zone of CARF extension. AHe and ZHe sample transects inboard of the coastal promontory define the HFC itself as a 35 km-wide zone (upper bound) of onshore extended continental lithosphere. Distributed block faulting, as opposed to regional flank uplift, was the dominant structural style during early Miocene RSR development and fault blocks within both the HFC and Hamd half-graben were exhumed along numerous rift-parallel faults from pre-rift flank depths of 0.5-3.9 km with some isolated HFC fault blocks exhumed by as much as 4.5-5.2 km. A second, and relatively minor, extensional RSR phase occurred ca. 14 Ma, coincident with regional plate reorganization and establishment of the Dead Sea-Gulf of Aqaba transform. The exhumation of Jabal Nahar in the Jizl half-graben

ca. 15 Ma and final deepening of the Hamd half-graben ca. 12 Ma signals the end of inboard HJB deformation while the absence of AHe cooling ages in the HFC younger than ~13 Ma confirms the basinward migration of major extensional faulting with progressive rifting during this phase. The Jizl half-graben is structurally bound by faults within the Neoproterozoic Najd shear zone fabric and middle Miocene footwall exhumation at Jabal Nahar underscores the role of pre-existing crustal weaknesses in RSR development, in accordance with observations elsewhere in the northern Arabian and Nubian RSR margins.

CARF thermal models indicate 28-40 °C/km as the most likely operational paleo-geothermal gradient range during RSR onset, which overlaps both apatite fission track-derived estimates and existing detailed geologic data for the Red Sea Basin. CARF thermal models also indicate no burial by significant accumulations of pre-rift volcanic or Paleo-Mesozoic sedimentary overburden and/or increased heat flow in mid-to-upper-crustal levels from active rifting processes. The absence of an elevated pre-rift thermal signal decreases the likelihood of regional uplift prior to rift onset and, coupled with the fact that HJB harrat volcanism trailed rift onset by 6 million years, we favor a passive rift model. Furthermore, the 23 Ma rift onset age is mirrored in thermochronometric and sequence stratigraphic analyses elsewhere along the full Red Sea Nubian margin and the southern Arabian rift flank in Saudi Arabia and Yemen, confirming that RSR initiation, and associated basin development, occurred concomitantly along the full Red Sea-Gulf of Suez rift system in the late Oligocene-early Miocene in opposition to proposed south-to-north rift propagation models. The subsequent pattern of post-23 Ma lithospheric modification differs greatly between the northern and southern Arabian rift margins. A structural zone (wedge) of diffuse extension operated in the central and northern Arabian margin during

both RSR extensional phases. This deformed wedge begins at the coincident intersection of the Makkah-Madinah-Nafud volcanic line with the Red Sea axial trough and expands through the NW Arabian Plate where it encompasses pre- and syn-rift graben (e.g., Hamd-Jizl Basin, Azlam, Tabuk) and incorporates a style of diffuse continental lithosphere extension altogether different from the relatively rigid lithosphere that forms the southern Arabian RSR margin.

2.2. Introduction

The central and northern RSR is an excellent present day analogue for rifted continental margins with adjacent sedimentary basins ("Atlantic-type") due to the outstanding exposure of largely non-volcanic conjugate rift margins and a nearly pure extensional rift geometry set within a formerly stable continental lithosphere (Fig. 1). Detailed geologic data used to reconstruct RSR evolution come mainly from either terminus of the system where rift development is constrained with dating methods that identify key rift phases from rift initiation through subsequent exhumational, sedimentary, and volcanic episodes. Yet the far northern and southern RSR regions fail to provide a full and impartial rift history and leave unresolved questions about RSR style and rift phase timing.

The Gulf of Suez illustrates early rift architecture and interplay of syn-rift sedimentation and faulting but continental breakup was arrested in the middle Miocene by the initiation of the Gulf of Aqaba Transform and further extension north of the fault zone ceased (Steckler and ten Brink, 1986; Richardson and Arthur, 1988; Coleman, 1993; Bosworth and McClay, 2001; Bosworth et al., 2005). The southern Nubian and Arabian rift flanks in Ethiopia, Eritrea, and Yemen record the full Cenozoic rift history but their middle Oligocene and younger record is greatly influenced by substantial volcanism and heat from the Afar Plume (Zeyen et al., 1997) and complex

boundary effects from Gulf of Aden rifting. Furthermore, the central and northern RSR has evolved from relatively stable continental lithospheric craton to an unruptured extended margin while the southern RSR experienced full-scale continental breakup and the onset of sea-floor spreading in the late Miocene. This dissimilar south vs. north rift history indicates major along-strike variation in RSR system dynamics and, as such, no singular RSR evolution model is yet agreed upon due to along-strike incompatibilities on the initiation of major rift phases. Non-consensus occurs partially from poor constraint on rift evolution along the full Arabian margin, especially in NW Arabia where rift phase timing is based mainly on stratigraphy from compartmentalized, primitive rift basins, dike injection ages, and the projection of isotopic age data from regions elsewhere that experienced a clearly different rift history (e.g., GoS).

We examine RSR evolution in an area we call the central Arabian rift flank (CARF), a region of the NW Arabian Plate that lies between the coastal cities of Al Wajh and Yanbu al Bahr and stretches inboard to the Arabian Shield/Phanerozoic sedimentary cover sequence boundary (Fig. 2). Unlike the southern Arabian rift flank, the majority of the CARF lacks vast expanses of Cenozoic basalt, appears influenced minimally by neighboring plate boundary effects and high heat flow from the Afar mantle plume (Zeyen et al., 1997), and contains a long-lived continuous record of RSR development from rift inception, through progressive rifting, to the modern rift margin structural setting. This unrestricted rift record occupies a critical position within the RSR system, presenting the opportunity to develop a RSR evolution model that addresses topics such as the nature of along-strike change in Arabian rift flank architecture and resolves the long-standing issue of whether GoS-RSR-GoA rifting proceeded either concomitantly along the full

length of the system or propagated from south-to-north (Girdler, 1984, 1991; Makris and Rihm, 1991).

2.2.1. Arabian rift flank architecture

The northern and southern portions of the RSR exhibit continental lithosphere deformation with wholly different strain patterns. Seismic surveys in the northern Red Sea Basin offshore Egypt and in the Midyan Basin on the Arabian rift flank show an extended continental lithosphere with concentrated bathymetric deeps (Miller and Barakat, 1988; Mougenot and Al-Shakis, 1999; Cochran, 2005 *and references therein*). In the southern Red Sea Basin, focused sea-floor spreading processes began ~5 m.y.a. and formed a well-defined axial trough adjacent to rigid continental lithosphere, a rift architecture altogether different from the extended continental lithosphere that underlies the northern basin (Cochran, 1983; Mooney et al., 1985; Prodehl, 1985; Cochran and Karner, 2007 *and references therein*).

Diminishing Arabian rift flank topography and a change in the distribution and orientation of Cenozoic volcanic provinces mirror along strike changes in Red Sea Basin architecture from south to north. At about 21° N latitude, the prominent coastal escarpment that forms the Asir Mountains in southern Arabia quickly loses elevation and topography becomes more diffuse (Coleman, 1993) at a point coincident with the northernmost extent of sea-floor spreading. This location is also the southernmost point of the Makkah-Madinah-Nafud volcanic line that delineates the greatest concentration of N-S-trending volcanic vents associated with a wholesale changeover in volcanic style during the middle Miocene (Camp et al., 1989). The intersection of these two prominent geologic features in the CARF suggests this region is the locus of a changing rift style between the southern and northern portions of the RSR system.

The timing, rate, and magnitude of structural deformation during each RSR stage imparted a distinct thermal signature on the CARF. We examine the spatial distribution of AHe and ZHe cooling ages from individual samples and multi-sample array transects that span normally rotated fault blocks to delineate independent CARF structural domains and employ numerical modeling techniques to reveal the t-T history of major rift aspects such as the pre-rift depth of exhumed fault blocks and post-rift Arabian margin erosional magnitude. We first determine the thermal state of the pre-rift ANS and assess the implications of pre-Eocene ZHe cooling signals on proto-CARF thermo-tectonic development. We then identify the initiation age, duration, and style of continental rift processes in the CARF from rift onset through major phases of lithospheric extension. Early rift architecture is reconstructed according to the spatial and temporal distribution of associated strain markers present as inboard half-graben and rift-adjacent fault complexes that bound rotated fault blocks. We reveal the life span of these strain markers, their structural role during different CARF extension phases, and their current significance in the modern structural architecture of the central and northern Arabian rift flank. We propose a subregional structural model that validates the unruptured state of the central and northern RSR and discuss when (or whether) and how this portion of the RSR will changeover from >20 million years of diffuse extension of continental lithosphere to production of oceanic lithosphere in the axial trough, similar to the changeover in rift style that occurred in the southern RSR ca. 5 Ma.

2.2.2. Developing a unified Red Sea Rift evolution model

RSR evolution models based upon investigative analyses of geologic rift features remain a contested debate topic as disagreement exists regarding the sequencing of volcanism, uplift, and

rifting in the RSR. Most models focus on sedimentological, volcanological, structural, and thermochronological data from the southern Arabian and Nubian rift flanks due to the presence of a large basalt province, prominent coastal escarpment, and active sea-floor spreading in the southern Red Sea axial trough. Studies in the southern Red Sea region yield results that fit conventional rift sequence paradigms such as those outlined by Sengor and Burke (1978) but contrasting results sometimes often come from the same rift flank region. Evidence within the southern RSR on the Arabian and Eritrean rift flank aligns with the traditional "passive" rift development sequence of magmatism-rifting-uplift (Bohannon et al., 1989; Drury et al., 1994) while contrasting evidence from $^{40}Ar/^{39}Ar$ basalt geochronology and AFT study in Yemen supports an "active" sequence of uplift-magmatism-rifting (Menzies et al., 1997).

Few rift evolution models are based in the central and northern RSR. Along the Arabian margin, hybrid passive-to-active rift models have been proposed to explain the perceived out-of-order sequencing of magmatism, rifting, and uplift as well as the high rift Arabian flank topography (e.g., Camp and Roobol, 1992; Davison et al., 1994; Hansen et al., 2007). Even an unconventional rift evolution model proposes simultaneous rifting, uplift and erosion, and volcanism along the full length of the RSR (Omar and Steckler, 1995). Altogether, these cited studies reinforce the notion that, as of yet, no observed rift pattern is clear enough to prompt an agreement on a singular best fit RSR evolution model. Most empirically derived models are inherently biased in their assessment of how the RSR evolved from a relatively stable continental lithosphere to a rifted margin and neglect to explain the present unruptured state of the central and northern RSR system.

2.3. Geologic History and Modern Tectonic Setting of the CARF

2.3.1. Pre-rift history of the Arabian-Nubian Shield

The CARF includes a large portion of exposed Precambrian basement (the "Arabian Shield") that is an assemblage of independent structural domains of various age imprinted upon geologic terranes of Proterozoic age. Prior to the origination of the Arabian Plate in the Cenozoic, the Arabian Shield formed part of the Arabian-Nubian Shield (ANS) as an agglomeration of multiple geologic terranes that sutured to Africa and east Gondwana during the East African Orogen (Stern, 1994; Johnson, 1998; Johnson et al., 2011 *and references therein*). This shield-building event marks the beginning of the Proterozoic Hijaz Orogenic Cycle (Brown and Coleman, 1972), a long-lived series of orogenic events that includes periods of island arc and ophiolite accretion (780-680 Ma; Johnson, 2004), grantoid plutonism, mafic dike injection, and large scale strike-slip faulting (580-530 Ma; Fleck et al., 1976) known as Najd faulting (Brown and Jackson, 1960 *in Moore, 1979*).

The ANS developed several orientations of structural fabric during the Proterozoic Hijaz Orogenic Cycle that would effectively predetermine the course of many early RSR structures (e.g., Brown, 1970; Dixon et al., 1987, 1989; Talbot and Ghebreab, 1997). The Yanbu and Bi'r Umq-Nakasib sutures within the CARF (Johnson, 1998) display orientations that are essentially orthogonal to the ~330° strike of the modern RSR yet these sutures acted as weak points in the lithosphere during early rifting that broke preferentially to control offset in the Red Sea axial trough (Crane and Bonatti, 1987) and the position of offshore deltas (Mitchell et al., 1992). In contrast, the ESE-WNW-trending Najd Fault System (NFS) is a 1200-km long, 300-km wide, zone of en echelon strike-slip faults and shear zones (Moore, 1979) that cut across pre-existing

Proterozoic terrane boundaries and imprint a deep-seated structural fabric on the CARF that controlled the orientation of Cenozoic extensional structures (Szymanski et al., *in prep.*; Fig. 1).

During the greater part of the Paleozoic and Mesozoic eras, the ANS formed a portion of the southern passive margin of the Tethyan oceanic realm (Johnson, 1998) and thick marine sedimentary sequences developed on either side of a NNW-SSE paleo-topographic high (Powers et al., 1966) in the area of the ANS that was to become the northeastern Arabian Plate. Significant portions of Paleo-Mesozoic marine and volcanic strata remain preserved in a large expanse of rock (Phanerozoic Cover Sequence; Fig. 1) that emerged subaerially in the early Cenozoic (Sharland et al., 2001 *and references therein*), following the complete subduction of Neo-Tethyan oceanic crust beneath Eurasia. In contrast, the proto-CARF region remained at a relatively high position within the crust during this period with no evidence of significant burial according to local stratigraphic sequences (Guiraud et al., 2005). Nearly flat erosional surfaces of Oligocene age in Saudi Arabia and Yemen (Coleman, 1993) verify that the proto-CARF region remained devoid of significant topographic relief through most of the Cenozoic prior to the development of the RSR.

2.3.2. Origin of the Arabian Plate and modern geologic features

Late Oligocene-early Miocene RSR onset is recorded in the Gulf of Suez/Sinai region (Kohn and Eyal, 1981), the southern Arabian rift margin in Saudi Arabia and Yemen (Bohannon, 1986; Bohannon et al., 1989; Menzies et al., 1992, 1997), and along the Nubian margin in Egypt, Sudan, and Eritrea (Omar et al. 1987, 1989; Kenea et al., 2001; Abbate et al. 2002; Ghebreab et al., 2002). Few studies imply extensional onset either in the early Oligocene (Steckler and Omar, 1994; Omar and Steckler, 1995) or in the late to middle Miocene (Davison et al., 1994).

Due to the prior lack of thermochronological investigations in the NW Arabian Plate, only sedimentological studies performed for hydrocarbon exploration provide constraints on RSR initiation (e.g., Barnard et al., 1992 *and references therein*). Coastal plain and offshore boreholes place the initiation of RSR-related sedimentary product in the late Oligocene to early Miocene in the Yanbu and Midyan Basins (Mitchell et al., 1992; Hughes et al., 1999). The timing of sedimentary deposition may indicate the generation of rift flank relief but this only approximates rift onset by proxy, assuming a near zero lag time between uplift, erosion, and deposition.

A widespread episode of Oligocene-Miocene mafic dike injection ca. 25-20 Ma affected the region of the ANS that was to become the Red Sea-Gulf of Suez rift (Eyal et al., 1981; Sebai et al., 1991; Pallister, 1987; Camp and Roobol, 1989, 1992; Ukstins et al., 2002; Bosworth et al., 2005 *and references therein*). Steeply inclined dikes span the length of the Red Sea-Gulf of Suez rift system sub-parallel to the modern RSR axial trace, which indicates modification of ANS continental lithosphere during a period of crustal attenuation that also exerted some control on the location of rift-related faults that accommodated parting of the Arabian and African plates (Camp and Roobol, 1989; Buck, 2004; Roobol and Stewart, 2009).

Harrat volcanism within the Arabian Plate developed through the Cenozoic with eruptions continuing into recorded history (Brown, 1970; Camp et al., 1997; Chazot et al., 1998). The largest basalt province within the western Arabian Plate is the Makkah-Madinah-Nafud (MMN; Fig. 1) volcanic line that has extruded basalt for the past 10 m.y. that is geochemically distinct from the first major volcanic pulse (Camp et al., 1991; Camp and Roobol, 1992). The MMN line comprises a 600 km-long linear vent system that interrupts the northward trend of elevated rift

flank topography from the Asir Mountains and overlies a north-south structural trend of half-graben structures which act as conduits for magma systems (Camp and Roobol, 1989).

2.3.3. CARF structural domains

The Hamd-Jizl Basin and Hijaz Mountains Fault Complex are the two primary CARF structural domains and each has a unique structural style. The Hamd-Jizl Basin (HJB) is primarily a major syn-rift structure composed of the asymmetric Hamd and Jizl half-graben ~140 km inboard of the modern rift margin (Fig. 3; Szymanski et al., *in prep.*). Significant overlap exists in the orientation of local Proterozoic NFS shear fabric and the border fault of the Miocene Jizl half-graben, indicating the exploitation of NFS structural grain during RSR development within the HJB. Congruous results from bedrock AHe and detrital AHe thermochronologic studies show that initial HJB development ca. 22 Ma caused penecontemporaneous accumulation of the terrigenous siliciclastic Qattar Formation proximal to the footwall of each half-graben. HJB deformation continued for 8 million years through the middle Miocene with footwall exhumation in the Jizl half-graben ca. 15 Ma and minor post-depositional deepening of the Hamd half-graben where intra-basinal faults juxtapose 14.5 Ma basalt flows from Harrat Ishara against the Qattar Formation.

The Hijaz Mountains in the central and northern Arabian rift flank are the continuation of a long trend of dynamic topography that begins at the Yemen Arch basalt plateau (Coleman, 1974) and includes the Great Escarpment in the Asir Mountains (Figs. 1 and 3). The CARF Hijaz Mountains Fault Complex (HFC) is the structural domain that composes two subdivisions of CARF Cenozoic faults: the “pre-rift” Foothills Fault System and the “syn-rift” Red Sea Coastal Plain Faults (Roobol and Kadi, 2008). Structures within the Foothills Fault System host steeply

inclined dikes that injected into the NW Arabian Plate during a period of crustal attenuation prior to the onset of major RSR extension. The prime example of a "pre-rift" structure is the Tabuk graben which is founded upon the Great Ja'adah Dike in NW Saudi Arabia at the border with Jordan (Phoenix Corporation, 1985; Roobol and Stewart, 2009). The "syn-rift" Red Sea Coastal Plain Faults originated during the first major RSR extensional phase ca. 23 Ma, demonstrate normal rotational fault kinematics, and provide a pathway for voluminous basalt extrusion. The subsurface of the Arabian rift flank coastal plain is likely highly dissected by Red Sea Coastal Plain Faults between Rabigh, a city ~150 km south of Yanbu al Bahr, and northwestern Saudi Arabia (Roobol and Kadi, 2008; Roobol and Stewart, 2009). Faults in Precambrian Arabian Shield in the Hijaz Mountains are a principal target of our sampling (Fig. 3) in order to determine whether they represent a subaerial equivalent of the Red Sea Coastal Plain Faults.

2.4. Analytical and Numerical Modeling Methodology and Geologic Sampling Strategy

2.4.1. Apatite and zircon (U-Th)/He thermochronology

Apatite and zircon (U-Th)/He thermochronometric systems (AHe and ZHe) are investigative tools well-suited for geologic study in the CARF since these thermochronometers are sensitive to thermal changes caused by footwall exhumation in extensional settings (Stockli, 2005 *and references therein*) and they are nearly ubiquitously present as accessory minerals in many CARF Proterozoic igneous and metamorphic rock suites (Pellaton, 1979; Clark, 1981; Kemp, 1981; Johnson, 2006). Rift phases involving extensional block-faulting commonly draw rock from mid-crustal structural levels to the near surface quickly, rapidly lowering the temperature of a rock body via footwall exhumation. The onset and rate of extensional faulting and post-rift erosional processes can be resolved if the fault throw magnitude is great enough to exhume

thermally reset thermochronometers to the near surface (Stockli et al., 2000 *and references therein*). AHe and ZHe operate within a temperature range lower than that of the well-known apatite and zircon fission-track systems (AFT and ZFT) that have been implemented steadily in rock body thermal evolution study for several decades (Reiners and Ehlers, 2005 *and references therein*) and are sensitive to thermal changes at shallower crustal levels.

Radioactive isotopes ^{235}U, ^{238}U, ^{232}Th, and ^{149}Sm generate ^{4}He nuclei (α particles) as a product of their decay series and measureable ^{4}He volumes may accrue within thermochronometeric minerals over geologic time. (U-Th)/He thermochronological techniques calculate the apparent cooling age of a thermochronometer by measuring the existing parent/daughter isotope ratios within the mineral host after accounting for variables known to affect age determination such as temperature, individual mineral crystal dimension, and radioactive isotope dissemination. ^{4}He retention is largely temperature dependent and the retention magnitude for a particular thermochronometer varies within a specific temperature range known as the helium partial retention zone (PRZ). At temperatures higher than the upper PRZ boundary, all internally generated ^{4}He is lost from the mineral via thermally activated diffusion while the lower thermal boundary is the temperature at which quantitative retention of ^{4}He begins. Important assumptions include rapid (>10 °C/m.y.) and monotonic cooling of the host rock from a supra-PRZ thermal domain through the closure temperature (T_c) of the thermochronometric system. Isochemical (U-Th)/He thermochronometers that exist within their relevant PRZ for extended periods of geologic time commonly yield apparent cooling ages inconsistent with one another, which are an indicator of their thermal history. Assuming a mean annual surface temperature of 20 ± 10 °C and geothermal gradient of 25 ºC/km for the CARF,

the ~40-80 °C AHe PRZ (Wolf et al., 1996) and ~140-200 °C ZHe PRZ (Reiners et al., 2002; Wolfe and Stockli, 2010) coincide with typical temperature ranges found within shallow (1.5-3 km) and middle (5-7.5 km) continental crustal depths.

High kinetic energy generated during α particle emission causes recoil of the parent isotope, resulting in structural damage to the host mineral, and significant travel of the daughter product with possible ejection from the host mineral domain. Radiation damage to apatite crystal structure from α recoil controls helium diffusion kinetics and systematically increases T_c overtime (Shuster et al., 2006; Shuster and Farley, 2009). Thus, greater damage from α recoil consequently results in older, incorrect apparent AHe cooling ages. The effective uranium concentration ([eU] = U + 0.2302 Th + 0.005 Sm) assesses the extent of radiation damage and the validity of the age determination. No correlation exists to illustrate greater AHe age with greater [eU] concentration for CARF apatite, which verifies no underlying control on AHe ages by radiation damage to the apatite crystal (Fig. 4). Zircon suffers structural damage that may affect diffusion kinetics at radiation levels where metamictization develops (Reiners, 2005). All candidate apatite and zircon crystals were pre-screened to meet minimum grain size standards (Reiners and Farley, 2001) and eliminate metamict zircon prior to applying standard α-ejection corrections (F_T; Farley, 2002).

All AHe and ZHe age results were determined in the Isotope Geochemistry Laboratory (IGL) at the University of Kansas using standard dating techniques (e.g., Stockli et al., 2000; House et al., 2001). Similar to other geochronometric dating methods, the (U-Th)/He method analyzes and dates multiple sub-samples (aliquots) then pools their collective ages to determine the cooling age of a sample. AHe and ZHe sample ages are reported as the average of two or more

aliquot ages and the associated age uncertainties, 6% (2σ) for AHe and 8% (2σ) for ZHe, reflects the analytical error inherent to the technique (Farley et al., 2001).

2.4.2. Geologic sampling strategy for (U-Th)/He thermochronologic study

Geologic samples collected at twenty-nine separate point locations and along seven short- and long-baseline multi-sample transects yielded 172 AHe and 184 ZHe age aliquots (Figs. 2 and 3; Tables 1 and 2). This multi-scale sampling technique allowed resolution of structural deformation at the individual fault block and rift flank scale, permitting a systematic reconstruction of early rift architecture, strain distribution during progressive rifting, and subsequent whole-sale modifications of the CARF such as significant rift margin denudation. Point sample collection allows full 2D rift margin coverage by targeting apatite and zircon-bearing silicic intrusive complexes (e.g., Cryogenian Jar Salajah Complex) scattered throughout the CARF composed dominantly of apatite and zircon-poor metasedimentary and metavolcanic rock (e.g., Neoproterozoic Farri Group paragneisses). Point samples may yield the cooling history of a particular fault block if collected along a known fault. If collected within largely unfaulted areas, point samples may yield a record of the ambient thermal history of the CARF.

Short-baseline multi-sample transects map footwalls of individual extensional structures within the HFC and HJB structural domains to constrain the timing, rate, and magnitude of rift-related crustal block rotation along strike of the CARF. Long-baseline transects resolve the spatial and temporal distribution of extensional strain within the CARF generated during the continental lithosphere rifting process. Our study includes a 450 km long, rift-normal Central Arabian Shield Transect that traverses the entire width of the exposed Arabian Shield between Madinah and the Phanerozoic Cover Sequence boundary near Buraydah. This transect reveals

the thermotectonic history of the exposed Arabian Shield inboard of the HJB structural domain to constrain the extent of RSR-related strain and complements CARF-wide sample coverage to form a complete 2D investigation that characterizes the distribution of extensional strain throughout the CARF.

2.4.3. Numerical modeling: Helium Modeling Program (HeMP)

Numerical modeling of CARF (U-Th)/He thermochronological age data was conducted via the computational *Helium Modeling Program* (HeMP) developed by Hager (2011, *in prep.*). Time-temperature (t-T) modeling modules within HeMP permit both forward and inverse modeling of point samples and multi-sample arrays (Hager and Stockli, 2009, 2010). The multi-sample array modeling capability, necessary to our modeling goals, supplements the single-sample processing capabilities of other modeling programs such as DECOMP (Meesters and Dunai (2002a, 2002b)) and HeFTy (Ketcham, 2005). The forward modeling module builds theoretical t-T paths based on inherent REE concentrations and other apatite and zircon grain parameters to direct the generation of t-T model constraints. The inverse modeling algorithm uses a Monte Carlo simulation to generate random monotonic t-T paths (each a proxy for a single t-T history) for single and multi-sample arrays based on user-defined t-T constraints. HeMP then compares the model-generated apatite and zircon (U-Th)/He ages (AHe and ZHe) with analytically derived AHe and ZHe sample ages and assigns the particular t-T path a quality rating according to the congruence between modeled and analytical sample ages ($\pm 2\sigma$). Using contributing factors such as parent nuclide concentrations, mineral grain dimension, and kinetic parameters defined and tailored for each dataset, HeMP computes AHe and ZHe ages using

standard helium production and finite difference diffusion equations (e.g., Crank-Nicolson method) as summarized by Ketcham (2005 *and references therein*).

AHe cooling ages that exhibit even a weak nonlinear positive correlation with effective uranium content ([eU]) may indicate underlying control on helium diffusion kinetics by radiation damage from α-production via U and Th decay over geologic time, which systematically skews the AHe closure temperature (Shuster et al., 2006). To accurately model helium diffusion with age, radiation damage estimates and age corrections for the CARF apatite suite were made using the radiation damage accumulation and annealing model (RDAAM) of Flowers et al., (2009). No CARF transect displays a strong positive correlation between AHe and [eU] (Fig. 4) yet we account for radiation damage effects since the RDAAM is best suited for apatite suites, such as those in the CARF, that may have experienced a long residence period within the AHe PRZ, reheating after an initial cooling phase, and/or slow monotonic cooling rates (1-0.1 °C/m.y.). Several point samples from our research were used in the Beta testing phase of HeMP development (Hager, *in prep.*) to explore the congruency of the HeMP RDAAM programming code with HeFTy (Ketcham, 2005).

Zircon requires no special treatment since helium diffusion kinetics are essentially the same for zircon with either low or high uranium concentrations, except for very high concentrations (>1000 ppm; Reiners et al., 2004). These high radiation dosages are apparent at the macroscopic scale as metamictization and zircon with this character are rejected for analysis at the mineral selection stage. Zircon aliquots that contain uranium concentrations greater than 1000 ppm often yield irreproducible ZHe ages and were excluded from further analysis.

2.4.3.1. HeMP time-temperature model organization

We model AHe and ZHe ages in one of three ways: as point samples, composite samples, or multi-sample arrays (Table 3). Point samples are age data from one sample location within the CARF and often have no neighboring sample age data. This model type is commonly used to model the exhumation history of an individual structure, such as a footwall. Composite samples represent neighboring point samples with overlapping AHe and ZHe ages; these samples commonly lie at similar elevations within the same transect. For example, just 77 vertical meters separate samples 05SA212, 05SA213, and 05SA214 within the Jabal Mushayt transect and each sample yields similar cooling ages and radionuclide values for both thermochronometers. We combine these three samples to form a composite AHe and ZHe age for Jabal Mushayt-Block B and model it as if it were from a single sample location. Finally, short and long-baseline elevation transects are modeled as multi-sample arrays. These models incorporate multiple point samples, each with unique AHe and ZHe cooling ages, separated over a significant vertical distance. Multi-sample arrays determine the exhumation rate and magnitude of a particular fault block over geologic time. Prior to multi-sample array modeling, samples are assigned to a fault block as dictated by the commonality of their AHe and ZHe cooling ages. For example, the variability in the ZHe cooling age data across Jabal Mushayt shows that this transect traverses three fault blocks (Blocks B through D; Fig. 3). Each fault block is modeled independently since each has a unique thermal history.

2.4.3.2. Time-temperature model boundary conditions, age constraints, and error assignment

The average thermal (time-temperature; t-T) model consists of a starting t-T point, an AHe and ZHe t-T window through which each candidate t-T path must pass from the initial to final thermal state, an end t-T point representing modern conditions, three random t-T nodes between

each t-T constraint, and a 3.5 °C temperature increment per 4 to 5 million years. Model boundary conditions are set by both analytically derived AHe and ZHe ages as well as assumptions regarding the state of the following three geologic conditions during CARF tectonic development: geothermal gradient, average annual surface temperature, and the initial t-T point of rock bodies from which rock samples were collected.

Each t-T model incorporates a geothermal gradient range from 20-50 °C/km and a mean annual surface temperature of 25 °C. This wide range accounts for modern geothermal gradients along the Red Sea Basin (Girdler, 1970; Bohannon, 1989; Barnard et al., 1992) as well as possibly greater paleo-geothermal gradients likely introduced by rift-related heating mechanisms such as far-field heating effects by the Afar plume and localized increases in the geothermal gradient from widespread dike emplacement within the Red Sea-Gulf of Suez rift system during the Oligocene (Bosworth et al., 2005 *and references therein*; Ravat et al., 2011). The starting point for each model is a paired t-T constraint composed of the rock unit age of the sample (Tables 1 and 2) and 300 °C. The model starting age is often many millions of years older than the raw AHe and ZHe cooling ages to permit the possibility that older cooling events may have affected the (U-Th)/He system. The initial temperature value ensures a near-zero ^{4}He concentration in the sample since it is higher than the thermal reset points of the apatite and zircon (U-Th)/He thermochronometers.

AHe and ZHe cooling ages, and their associated errors, determine the minimum period of each t-T window and the maximum temperature boundary is set according to the (U-Th)/He cooling temperature (T_C) of either the AHe or ZHe thermochronometer. A "good" or "acceptable" fit is defined as a t-T path that satisfies both the AHe and ZHe age within either 1σ

or 2σ error. Point and composite sample models are limited to 100 good fit t-T history iterations. Each multi-sample array model contains 100,000 t-T history iterations and a successful model is defined as any t-T path that incorporates each sample in the array (minus the outliers) for any given geothermal gradient between 20-50 °C/km. Some t-T paths require erratic and/or unusually rapid changes (>10 °C/m.y.) in the temperature of a sample to gain either a good or acceptable fit for one or more geothermal gradients. Geologic processes common to the CARF, such as dike injection, could produce rapid heating at these rates, thus t-T paths that necessitate either erratic or unusual rapid heating rates are considered on a case-by-case basis as dictated by geologic context.

Age errors are assigned to samples individually according to age reproducibility with the minimum 2σ AHe and ZHe age error set at 6% and 8%, respectively, based upon the inter-aliquot reproducibility of an apatite or zircon sample of optimal quality (Farley et al., 2001). Model constraints and age errors (Table 3) are adjusted upon consideration of influential factors such as age reproduciblity and/or the presence of known atypical thermal conditions (e.g., heat input from dike injection). See Appendices A and B for detail on the statistical treatment of CARF AHe and ZHe age data and selection criteria for modeled samples.

2.5. Apatite and Zircon (U-Th)/He Thermochronology and HeMP time-Temperature Modeling Results

2.5.1. Apatite and zircon (U-Th)/He cooling ages throughout the CARF

CARF bedrock samples yield sixty-seven AHe and sixty-six ZHe ages with forty-four samples yielding both an AHe and ZHe age (Fig. 2; Tables 1 and 2). Unsuitable rock lithology and/or poor mineral quality are common limiting factors in obtaining a reproducible AHe and

ZHe age from each sample. Analytical results are presented as cumulative probability density plots (Figs. 5 and 6) where peaks represent a collective of overlapping mean AHe or ZHe cooling ages and analytical errors (6% and 8%) from one or more CARF samples. Higher peaks indicate the most common AHe and ZHe cooling ages and peak clusters identify sample groups that relate to a common regional cooling event.

Plots of the entire CARF AHe and ZHe age catalog illustrate a marked difference in the distribution of ages obtained from the two thermochronometers (Fig. 5). While dominant age modes lie at 21.5 Ma and 20 Ma, the AHe age spectrum consists mostly of Eocene-and-younger ages while the ZHe record identifies older cooling events through the Paleozoic. AHe and ZHe ages cluster at several pre-Cenozoic age intervals: 120-160 Ma; 200-260 Ma; ~300 Ma; and ~500 Ma. AHe and ZHe age distributions are distinctive for each CARF structural domain (Fig. 6). In the HFC, AHe ages cluster within the Miocene with prominent age peaks at 21.5 Ma, 15.5 Ma and 13.5 Ma; few samples yield Paleogene-and-older ages. The HFC ZHe age population contains a range of ages from Miocene to Paleozoic. In contrast, HJB AHe cooling ages show a greater distribution with three distinct clusters; a Cenozoic age cluster, similar to the HFC, and two significant Mesozoic age clusters between 120-160 Ma and 200-260 Ma (Fig. 6(a)). The two primary Miocene age modes represent footwall cooling ages from each half-graben: 21.1 ± 1.3 Ma in the Hamd half-graben and 15.1 ± 0.9 Ma in the Jizl half-graben. Multiple AHe age peaks in the ~30-80 Ma age range represent samples from the Hamd and Jizl half-graben hanging walls. Three of four samples within the Central Arabian Shield Transect (CAST) group at ~130 Ma while the fourth is Permian in age. All HJB and CAST samples are of Carboniferous ZHe age or older and show no strong age clustering.

2.5.2. Time-temperature modeling of CARF AHe and ZHe ages by structural domain

Due to the unique variation of mean AHe and ZHe cooling ages across the CARF, the following sections present t-T modeling results by structural domain. Seven point samples, two composite samples, and five multi-sample arrays were modeled in total (Tables 3 and 4). All modeled samples but one lie within the HFC (Fig. 3) since most HJB and CAST samples fail to meet basic model qualification criteria (see *APPENDIX B***)**. Some modeled samples lie within the same HFC fault block (e.g., Wadi Nabat multi-sample array and point sample 05SA228). Comparison of intra-block samples provides a secondary quality control on t-T modeling if agreement is observed in model results.

2.5.2.1. Hamd-Jizl Basin (HJB) and Central Arabian Shield Transect

The Hamd and Jizl half-graben that compose the HJB are the only multi-kilometer-scale, extensional structures that exist inboard of the Hijaz Mountains (Szymanski et al., *in prep.*) and sample 06SA104 provides the single t-T constraint on footwall exhumation in the HJB region. The majority of t-T paths show that 06SA104 originally cooled in the Cambrian to a relatively shallow structural level where is existed at or below AHe PRZ temperatures prior to rapid exhumation from a depth of 4.5-1.8 km at 21.1 ± 1.1 Ma (Fig. 7). No samples were modeled further inboard than the HJB as the large spacing between CAST sample locations do not permit the creation of t-T models.

2.5.2.2. Hijaz Mountains Fault Complex (HFC)

Four structural sub-domains, Blocks A through D, compose the HFC and thermal models built from 5 point samples and 6 multi-sample arrays are used to constrain their deformational timing (Fig. 3; Table 3). Block A is defined as crystalline basement underlying the coastal plain

with the Master Listric Fault (Roobol and Kadi, 2008) as the easternmost boundary. Block A is undivided further since no existing thermochronologic age data are available for this domain. Blocks B, C, and D encompass groups of subaerially exposed fault blocks of Precambrian Arabian Shield inboard of the Master Listric Fault. Fault block boundaries are based on the interpretation of geomorphic features such as drainage patterns, 1:250,000-scale geologic maps (e.g., Pellaton, 1979), and deviations in AHe and ZHe age trends within multi-sample array transects. Faults are recognized in transects either when samples of similar AHe age span an abrupt topographic change or a rapid change in cooling age trend occurs with a steady increase in elevation.

2.5.2.2.1. Wadi af Far'ah

In the Wadi af Far'ah transect east of the coastal plain at Yanbu al Bahr, the Proterozoic Admar Suite yields three samples with Oligocene-Miocene AHe ages (Block B) while, further inboard, AHe ages increase with northeastward progress across a prominent Cenozoic fault (Block C; Fig. 8). Block B was modeled as a composite point sample by weight-averaging the three AHe ages and using the single available ZHe age (Table 1). The weighted average approach is justified by a large 2σ error on the 04SA097 AHe age. Thermal modeling of Block B reveals a range of suitable t-T paths with two possible end members (Fig. 9), each beginning with cooling in the late Paleozoic. One end member possibility shows the fault block cooling through the upper range of the ZHe PRZ and remaining thermally stable for ~250 m.y. prior to exhumation in the Miocene while the other exhibits fault block cooling through the AHe PRZ with slow reheating prior to a cycle of rapid heating and cooling in the Cenozoic. The greater number of good fits prefer an intermediate t-T history though they each require fault blocks

temperatures near 150 °C prior to rapid cooling. Total Cenozoic exhumation estimates range from 5.8-2.3 km with an average pre-rift temperature of 140 °C for Block B (Table 4).

2.5.2.2.2. Jabal Radwa

The Jabal Radwa transect crosses the peaks of Jabal Jar and Jabal Radwa before dropping down to the coastal plain northeast of Yanbu al Bahr (Fig. 3). Jabal Radwa is both the highest peak (2200 m) and the area of greatest topographic relief within the CARF. AHe ages within the transect gradually increase with elevation starting near the coastal plain with three samples that yield Miocene AHe ages adjacent to a major Cenozoic fault (Pellaton, 1979) and ending at 2200 meters elevation with a sample that yields overlapping Paleozoic AHe and ZHe cooling ages (Fig. 10). Reproducible AHe cooling ages were limited within the top half of the transect due to either poor apatite crystal quality or the altogether absence of apatite in the peralkaline Radwa granite batholith (Moufti et al., 2002). Most samples from the Jabal Radwa transect exhibit ZHe ages within the 250-400 Ma age range and only a single sample yields a ZHe age younger than Jurassic age (Table 1).

The range and shape of acceptable t-T paths for the Jabal Radwa fault block are dependent upon the paleo-geothermal gradient (Fig. 11). The greatest number of acceptable t-T paths are found in the 30-40 °C/km range and include model fits that account for the overlapping AHe and ZHe ages of 05SA178 at 2200 m elevation (Figs. 11(b) and 11(c)). These results show that this portion of the HFC cooled rapidly to shallow crustal levels during the Carboniferous where it remained at or above the AHe PRZ prior to a second exhumational stage in the Miocene. Total Cenozoic exhumation estimates for Jabal Radwa range from 4.8-0.1 km across a paleo-geothermal gradient range of 20-50 °C/km, respectively (Table 4).

2.5.2.2.3. Jabal Mushayt

55 kilometers inboard from the modern coastal plain, the Jabal Mushayt transect traverses three fault blocks and 1000 m of vertical relief within the Jar Salajah Batholith (Johnson, 2006; Fig. 3). Eight of nine samples from this transect yield Oligocene-Miocene AHe ages while ZHe ages range from the Ordovician to Oligocene (Table 1). Numerous faults exist in this region (Pellaton (1979) and fault block boundaries coincide with the location of offset in the AHe and ZHe age trends. Block B contains three samples with a mean AHe age of 22.3 ± 1.3 Ma and Triassic ZHe ages; Block C contains two samples: one with a middle Miocene AHe age and an Oligocene ZHe age and a second with an Eocene AHe age (no available ZHe age); and Block D contains three samples with an average AHe age of 16.6 ± 1.0 and Ordovician ZHe cooling ages (Fig. 12; Table 1).

Thermal modeling of the Jabal Mushayt transect was conducted according to individual fault block (Fig. 13; Table 3). Fault blocks B and D experienced a similar t-T history as both cooled through the ZHe PRZ to lower and middle crustal levels in the Paleozoic, experienced slow reheating through the Mesozoic, and were exhumed in the Miocene from depths between 6.8-2.7 km and 4.6-3.1 km, respectively. Drastically different from the t-T history of adjacent fault blocks, Block C shows a long period of slow heating through the Mesozoic at temperatures greater than 180 °C prior to rapid exhumation in the Miocene from crustal depths between 7.8-3.1 km (Table 4).

2.5.2.2.4. Wadi Nabat, Jabal Salajah Foothills, and Jabal al Qishr

These sample transects examine the evolution of the HFC within the coastal promontory between Yanbu al Bahr and Umm Lajj. The Wadi Nabat and Jabal Salajah Foothills sample

transects examine the first subaerial exposure of Precambrian Arabian Shield adjacent to the coastal plain (Block B) and both yield comparable Miocene AHe ages and Cretaceous ZHe ages at similar elevations (Fig. 14; Table 1). Miocene AHe and ZHe cooling ages overlap at the base of Wadi Nabat then increase further inboard with greater elevation; ZHe ages increase rapidly to Cretaceous age while AHe ages increase at a significantly lesser rate. Positioned ~10 km southeast and at an elevation higher than Wadi Nabat, the Jabal Salajah Foothills yield three samples between 330-760 m elevation with Oligocene-Miocene AHe ages and Cretaceous ZHe ages. Thermal models show that the t-T history of samples within these two transects began with a Paleozoic cooling event that brought them to a mid-crustal level (Fig. 15). Wadi Nabat remained at a fairly constant depth through the Mesozoic prior to exhumation in the Oligocene-Miocene from depths between 6.2-2.4 km while the Jabal Salajah Foothills show moderate and slow cooling through most of the Mesozoic, with increased cooling in the late Cretaceous, prior to rapid cooling in the Miocene from depths between 4.5-3.1 km (Table 4).

Further inboard, and at higher elevations, the Jabal al Qishr transect explores the Precambrian Jar Salajah Complex within the Hijaz Mountains. The majority of samples yield Miocene AHe ages and Cambrian to Devonian ZHe ages and t-T modeling shows that the Jabal al Qishr fault block cooled through the ZHe PRZ to relatively shallow crustal levels in the Paleozoic (Figs. 14 and 15). The fault block then slowly heated to temperatures ~110 °C through the Mesozoic, rapidly heated to ~140 °C in the late Cretaceous, and then finally cooled during exhumation in the Miocene from a depth range of 5.7-3.6 km (Table 4). Notably, no "good" model fits (1σ) were attained for Jabal al Qishr but numerous acceptable fits (2σ) show that these t-T paths prefer the middle-to-low end geothermal gradient range. A high reproducibility of

aliquot ages led to small SDOMs, thus relaxed error constraints were required to allow model fits and subsequent models used AHe errors of +/- 5 m.y. of mean age (13.6-31.8% of mean) while ZHe errors were assigned the standard analytical reproducibility of 8%. ZHe ages were generated for samples with no age data (05SA221 and 05SA223) by averaging the ZHe ages of the five other samples (Table 1).

2.5.2.2.5. HFC Point Samples

Five point samples from the HFC yield reproducible AHe and ZHe ages ranging from the Cambrian to the Miocene (Fig. 3; Table 1) and each has a respective t-T model. 04SA109 and 04SA110 are the northernmost control points on structural deformation within the HFC. Separated by just 3 km along the Umm Lajj coast, their respective t-T models reflect two unique cooling histories (Fig. 16). 04SA109 was exhumed to a shallow crustal depth in the late Paleozoic where it remained (with minimal temperature variation) prior to rapid Cenozoic exhumation from a depth of 3.8 km. 04SA110 yields a Miocene AHe age of 19.7 ± 1.2 Ma and an Oligocene ZHe age of 31.1 ± 2.5 Ma. The t-T model indicates this sample experienced rapid exhumation from depths greater than 7 km in the late Paleogene (Table 4). At Jabal aq Qaid, 05SA228 yields an early Cretaceous ZHe age and Miocene AHe age, similar to those recorded at the same elevation 10 km to the SE in the Wadi Nabat transect. Thermal modeling shows that the 05SA228 fault block rested at middle to shallow crustal levels between temperatures of ~100-140 °C before rapid exhumation in the Miocene brought 05SA228 from depths ranging between 3.8-1.5 km (Fig. 17; Table 4). Basinward of the fault that forms the base of Jabal al Qishr, 05SA224 yields similar Paleozoic ZHe ages but a middle Miocene AHe age. Thermal model results (Fig. 17) confirm that the host fault block of 05SA224 was exhumed after Jabal al

Qishr yet from a similar pre-rift depth (3.3 km vs. 3.6 km; Table 4). Lastly, 05SA205 yields AHe and ZHe cooling ages similar to those from the adjacent Jabal Radwa, Jabal Mushayt, and Wadi af Far'ah transects (Table 1). Thermal modeling shows 05SA205 had existed at a shallow crustal depth since the Paleozoic prior to exhumation on the order of ~3.8 km ca. 27.1 ± 1.6 Ma (Fig. 17; Table 4).

2.6. Discussion

2.6.1. Tectonic evolution, thermal state, and structural position of the pre-rift Arabian-Nubian Shield in the proto-CARF

2.6.1.1. Paleo-Mesozoic evolution of the ANS from AHe and ZHe cooling signals

The commonality of Paleo-Mesozoic AHe and ZHe cooling ages across the CARF suggests that these trends may represent regional tectonic events and the proto-CARF region may have acted as an undivided structural domain prior to RSR development. Relatively weak AHe and ZHe cooling age peaks cluster at both ~100-150 Ma and ~200-250 Ma (Figs. 5 and 6). Permo-Triassic ages parallel the rift timing of the Tethyan margin that penetrated into the northern proto-Arabian Plate and produced the early Mesozoic Rutbah uplift south of the Palmyride aulacogen (Best et al., 1993; Guiraud and Bosworth, 1999). Carboniferous age peaks in the ZHe cooling age spectrum mirror the greater "Hercynian Orogeny" tectonic signal that is recognized throughout northeast Africa and Arabia and manifests itself beneath the Arabian Platform as widespread block-faulted Precambrian basement with vertical displacements up to 1000 m (Stewart et al., 1996), in Yemen and Oman as an unconformity below the ~342-315 Ma Berwath Formation, and in the proto-Sinai/Egypt rift margin region as the "pre-Unayzah" unconformity (Al-Hajri and Owens, 2000; Sharlan et al., 2001). Moreover, this cooling signal is documented

via zircon fission-track thermochronometry in the nearby Sinai Peninsula and within the Egyptian rift margin (Kohn et al., 1992; Bojar et al., 2002).

Late Jurassic to early Cretaceous ages coincide with a time of continued fragmentation of Pangaea, rift basin development in Yemen, and the development of the proto-Indian Ocean. The inboard portion of the Central Arabian Shield Transect yields a Cretaceous mean AHe age that correlates to a mode of ZHe cooling ages observed in samples widespread across the CARF (Fig. 5). These Cretaceous AHe and ZHe cooling ages record a regional cooling signal that may have developed in response to far-field forces affecting the proto-Arabian Plate. Sedimentary deposition along the passive southwest Neo-Tethyan margin at this time could have induced hinterland flexural doming within the proto-CARF portion of the ANS. The timing of this cooling event is mirrored by an erosive period in the early Cretaceous when clastic material shed from the interior ANS (Sharland et al., 2001 *and references therein*), encountered the Cretaceous southern Tethyan shoreline (Ziab and Ramsay, 1986), and sourced the massive influx of clastic sediment to the east-southeastern ANS margin, in the region now known as Yemen and Oman (Ellis et al., 1996; Al-Fares et al., 1998).

2.6.1.2. Thermal state and geothermal gradient modification via dike injection

During the late Oligocene-early Miocene, a widespread episode of dike injection affected the region of the ANS that was to become the Red Sea-Gulf of Suez rift (Eyal et al., 1981; Sebai et al., 1991; Pallister, 1987; Camp and Roobol, 1989, 1992; Ukstins et al., 2002; Bosworth et al., 2005 *and references therein*). The subparallel orientation of this collective dike swarm and the initial Red Sea-Gulf of Suez rift axial trend (Camp and Roobol, 1989) indicates the dikes exerted some control on the location of rift-related faults (Buck, 2004). AHe and ZHe

thermochronometers in the ANS host rock may have been reset by heat from either localized dike injection along faults in the dike-weakened crust or a regional increase in crustal temperature (Ravat et al., 2011).

t-T paths within the Jabal Mushayt Blocks B and D, Jabal al Qishr, and 04SA110 thermal models tolerate this possibility (Figs. 12, 14, and 16). Figures 12(a), 12(b), and 14 show relatively steady Paleo-Mesozoic t-T paths heating to temperatures ~120-160 °C in the Cenozoic with some paths tolerating either a full or partial resetting of the ZHe thermochronometer (Jabal Mushayt Block B and Jabal al Qishr, respectively). Thermal modeling of 04SA110 reveals a ZHe cooling event ca. 30 Ma that fails to align with any other observed CARF cooling trends, including the adjacent 04SA109, thus this may be a partially reset ZHe age that resulted from localized heating via dike injection. Notably, reheating events in t-T models may also exist to accommodate the (less-preferred) greater magnitude Paleo-Mesozoic ZHe cooling events (e.g., Wadi af Far'ah Block B). In those cases, reheating paths are not considered to represent actual geologic events.

2.6.1.3. Paleo-geothermal gradient of the proto-CARF

We estimate the pre-rift paleo-geothermal gradient of the ANS proto-CARF to have been between 28-40 °C/km since the greatest total number of "good" and "acceptable" t-T path fits to our multi-sample array models fall within this range. Though individual models prefer slightly different geothermal gradient ranges, Jabal Radwa yields the most accurate approximation within the model group since this transect reveals a fully exhumed AHe PRZ, bracketed by overlapping Paleozoic AHe and ZHe ages at the top of the transect and a Miocene AHe age at the base (Fig. 10). The exhumed shallow crustal cross section at Jabal Radwa grants a unique opportunity for

thermal modeling to identify the most viable geothermal gradients that produced these AHe trends since we consider valid any thermal history whose t-T path can incorporate the topmost and bottommost sample from this transect. Figure 11 shows the variance of acceptable t-T paths over four different geothermal gradients (20, 30, 40, and 50 °C/km). Plots 11(a) and 11(d) contain numerous invalid t-T paths since they yield no fits for the topmost sample while plots 11(b) and 11(c) contain the greatest number of overall t-T path fits that include the topmost sample to varying degrees. Given that the exposed AHe PRZ at Jabal Radwa is the most complete record of Cenozoic exhumation, the 28-40 °C/km range preferred by this model frames the most likely operational paleo-geothermal gradient range for the proto-CARF. Our estimation assumes the existence of well-developed AHe and ZHe PRZs within the proto-CARF prior to exhumation. This assumption is reasonable given that no evidence exists of complex or significant pre-rift temperature changes in the Cenozoic thermal record of the Jabal Radwa transect. Notably, the high end of our Paleo-Mesozoic geothermal gradient is cooler than the estimated Neoproterozoic (~600 Ma) gradient of ~30-50 °C/km derived from petrologic temperature indicators (Stern and Johnson, 2010 *and references therein*).

Our 28-40 °C/km paleo-geothermal gradient estimation overlaps both AFT-derived estimates and publicly available modern data for the Red Sea Basin. Omar et al. (1987) report an estimated paleo-geothermal gradient of ~40-50 °C/km from AFT work in the southern Eastern Desert of Egypt on the conjugate Nubian margin directly opposite the CARF while AFT study on the southern Arabian coastal plain yields a paleo-geothermal gradient of 22 °C/km for granitic shield rock (Bohannon et al., 1989). 36.5-45.6 °C/km is the modern geothermal gradient range for the shallow marine coastal shelf south of Yanbu al Bahr in the central and northern Red Sea

Basin and the average for the Egyptian margin (Barnard et al., 1992). Modern gradients on the southern Arabian coastal plain, derived from borehole measurements and subject to high error, range widely from 28 °C/km and 42 °C/km for rock salt and sandstone, respectively (Girdler, 1970) to 45.6-54.7 °C/km and greater for highly variable sedimentary rock (Barnard et al., 1992).

2.6.1.4. Overburden thickness on the proto-CARF

Most HFC fault blocks experienced a long residence period in the mid-to-upper crust between their ZHe and AHe cooling events with little to no reheating (Wadi Nabat, Jabal al Qishr, and Jabal Mushayt-Block D; Figs. 13 and 15). Thermal modeling of these blocks shows that any Paleozoic and younger overburden that may have developed overtop the proto-CARF was too thin to produce a significant reheating signal in either thermochronometer, in contrast to a significant thickness of Paleo-Mesozoic strata that overlies the northeastern Arabian Plate. Common t-T paths indicate slow denudation, in concert with a flattening of topography, at the proto-CARF surface through the Mesozoic and accord with observations from regional stratigraphic study of the Paleozoic-and-younger sedimentary sequences within the Arabian Plate (e.g., Coleman, 1993; Sharland et al., 2001; Guiraud et al., 2005).

Most of ANS was exposed sub-aerially through the Paleo-Mesozoic except for minor marine incursions from the Tethyan and Indian Oceans (Mitchell et al., 1992) including, most notably, a Tethyan transgressive sequence during the Cretaceous that formed an embayment whose southern limit is well-documented along the Egyptian margin as far south as 20°N (Brown, 1970). Accordingly, the sedimentary record is concentrated along ANS margins proximal to Paleo-Mesozoic marine basins; the central Red Sea Basin contains fewer occurrences of Paleo-

Mesozoic strata (Bosworth et al., 2005 *and references therein*) while thicker Cretaceous pre-rift strata is found in the Midyan Basin (Hughes et al., 1991) and Gulf of Suez region.

Oligocene pre-rift strata intermittently occur throughout the Nubian and Arabian rift margins. Crossley et al. (1992) cite the presence of late Oligocene quartz arenite on crystalline basement in two wells off the Sudanese coast near 21° N (across from Jeddah) but none along the offshore CARF. Hughes et al. (1991, 1999) report no Oligocene strata in the Midyan Basin. The pattern of Oligocene pre-rift strata locations reflects the geometric pattern of localized basin development prior to the formation of a unified RSR basin when some smaller basins were abandoned during strain focusing (e.g., Al Wajh and Yanbu "relict basins"; Bosworth et al., 2005). This architectural possibility was suggested by Coleman et al. (1983) and supported by sedimentological research in the northern Red Sea-Gulf of Suez region (e.g., Jarrige, 1986; Bosworth, 1994) and southern Arabian margin (e.g., Schmidt et al, 1983). Sustained footwall exhumation in the HJB from the early to middle Miocene prevents its inclusion into this relict basin category and warrants further research into the lifespan of similar structures.

Uplifted erosional plateaus and laterite horizons of Oligocene age in Saudi Arabia and Yemen (Coleman, 1993) verify that the proto-CARF region remained devoid of significant topographic relief through most of the Cenozoic prior to the development of the RSR. Southwest of Harrat Uwayrid and ~80 km along strike to the NW of the Jizl half-graben, Brown (1970) reports that a boulder bed at 1000 m elevation proves "widespread subaerial erosion" in the Oligocene. Laterite horizons are reported at several locations within the central and southern Arabian rift flank, such as beneath the Oligocene-Miocene Jizan Complex (Schmidt et al., 1983; Brown et al., 1989) and several Arabian basalt fields of Oligocene age including Harrats As

Sarat and Hadan (Overstreet et al., 1977; Coleman et al., 1983) in the south and Harrat Ishara in the CARF (Szymanski et al., *in prep.*). Elsewhere in the HJB, the Miocene Qattar Formation overlies saprolitized Precambrian Al Ays Gp. basement rock (Kemp, 1981) beneath Jabal Antar, and laterite contacts Precambrian Al Ays Gp. rocks unconformably in Wadi Rashad, indicating an elevation near sea level prior to Hamd half-graben development.

2.6.1.5. Pre-rift depth estimates for the proto-CARF

Pre-rift crustal depth estimates for CARF fault blocks (Table 4) vary with their structural domain association, the in-situ paleo-geothermal gradient, and the position of the analyzed sample in the exhumed fault block (whether representing the base of an exposed footwall or a transect tracking exhumation across the full fault block). For a 28-40 °C/km geothermal gradient range, CARF point and composite sample locations yield corresponding pre-rift depths estimates from 1.9-5.2 km while individual multi-sample array transects yield a shallower range of 0.5-4.0 km.

Maximum exhumation estimates are constrained by ZHe age data. Just 04SA110 and Jabal Mushayt Block C contain Cenozoic ZHe ages, indicating that most CARF exhumation was too insufficient to rapidly exhume and expose footwalls from mid-crustal depths that exceed the bottom of the ZHe PRZ (~4.4 km). Relative to the HJB structural domain, the HFC contains a greater number of Cenozoic faults and exhibits a wider distribution of high-magnitude fault block exhumation (Fig. 3). This exhumation disparity with inboard distance from the modern RSR basin is comparable in scale to deformation on the conjugate Nubian rift flank in the south Eastern Desert of Egypt where more pronounced uplift occurs within 100 km of the modern coast (Omar et al., 1987).

Our CARF exhumation estimates generally match those along the central and northern Arabian and Nubian RSR flanks (Omar et al., 1978, 1989) and are on average greater than AFT-derived uplift estimates attributed to the southern Arabian and Nubian RSR flanks once normalized to 28-40 °C/km (e.g., Bohannon et al., 1989). This along-strike disparity is unsurprising given that both stratigraphic evidence and thermal modeling results indicate no significant pre-rift overburden thickness of volcanic or sedimentary cover existed on the proto-CARF region, a condition dissimilar to those in the pre-rift Afar (Davison et al., 1994; Ukstins et al., 2002 *and references therein*) and Gulf of Suez.

On the Nubian rift flank opposite the CARF, Omar et al. (1987) report average and maximum uplift estimates of 2.0-2.5 km and 3.5-4 km using paleo-geothermal gradients of ~40-50 °C/km and 22 °C/km, respectively, while Balestrieri et al. (2009) cite 5 km as their high-end exhumation estimate. In the Egyptian Gulf of Suez, Omar et al. (1989) use the modern geothermal gradient of ~21 °C/km to calculate 4.6-5.5 km of "vertical motion" (fault throw plus regional isostatic uplift) for samples at the modern day surface elevation. Omar et al. (1989) recognize this as an absolute maximum estimate since the paleo-geothermal gradient was likely greater. Derived primarily from AFT analysis, pre-rift flank depths for the southern Arabian escarpment (Bohannon, 1986; Bohannon et al., 1989; van der Beek et al., 1994) and Eritrean rift flank (Abbate et al., 2002; Balestrieri et al., 2009) consistently fall in the 3.3-4 km range. Notably, Bohannon (1986) and Abbate (2002) base their estimates on paleo-geothermal gradients of 22 °C/km and 25-30 °C/km, respectively.

2.6.2. Timing and extent of two RSR extensional phases in the CARF

Extended rift margins commonly comprise rotated crustal blocks separated by normal faults of varying scale and spacing. In regions with closely spaced faults, such as the HFC, several exhumed footwalls yield similar AHe cooling ages that produce dominant modes within the AHe and ZHe age population and reveal the timing and extent of major exhumation events. CARF AHe and ZHe cooling ages reveal a primary RSR extensional pulse in the early Miocene ca. 20.9 ± 0.7 Ma and a secondary extensional pulse in the middle Miocene ca. 15.0 ± 1.2 Ma (Figs. 5(a) and 5(b)). These cooling ages correspond to rift timing determinations from other parts of the Gulf of Suez-Red Sea rift system, which supports concomitant rift onset along the full length of the system and opposes proposed south-to-north rift propagation models (e.g., Girdler, 1984; Voggenreiter et al., 1988).

2.6.2.1. Phase One (early Miocene)

RSR-related exhumation in the CARF began in the early Miocene as indicated by dominant cooling age modes within HJB and HFC AHe and ZHe age data and numerical modeling results from six CARF point samples and four HFC fault blocks (Figs. 6(b) and 6(c); Table 4). Early Miocene exhumation in the CARF agrees with observations of uplift and exhumation throughout the Gulf of Suez/Sinai region, the southern Arabian rift margin in Saudi Arabia and Yemen, and the Nubian margin in Egypt, Sudan and Eritrea. Uplift in the Sinai region at 26.6 ± 3 Ma (Kohn and Eyal, 1981) predates the ~22-20 Ma intrusion age of basaltic dikes on the western Gulf of Aqaba (*Gulf of Elat*; Eyal et al., 1981) that are part of the ~25-20 Ma dike swarm present throughout ANS that is thought to signal RSR onset (Pallister, 1987; Camp and Roobol, 1992). RSR uplift in the Eastern Desert of Egypt and on the western Gulf of Suez margin began ~23-21 Ma along pre-existing structural fabrics that maintained strong control on rift orientation (Omar

et al., 1987 and 1989). The results of Omar et al. (1989) are revised by Steckler and Omar (1994) and then incorporated by Omar and Steckler (1995) who report a spatially limited earlier rift phase ca. 34 Ma but still acknowledge RSR extension ~25-20 Ma along the Egyptian margin.

In the Jizan region of the southern Arabian rift flank, initial extension and resultant faulting occurred ~25-23 Ma in Saudi Arabia based on undeformed 23-20 Ma Ad Darb volcanics and AFT data (Bohannon, 1986; Bohannon et al., 1989). AFT data from Yemen provide a minimum age for volcanism-driven exhumation ~20-16 Ma prior to extension ~18-10 Ma (Davison et al., 1994). Maintaining the results of Davison et al. (1994), Menzies et al. (1997) report AFT results that show "widespread and rapid cooling" on the southern Arabian rift margin in Yemen since 25 Ma. Menzies et al. (1997) base this estimate on the lack of extensional structures in the ~31-26 Ma Yemen Large Igneous Province (Baker et al., 1994, 1996) and set their best estimate of initial uplift and extension along the volcanic Arabian margin at 26-20 Ma.

On the Nubian flank in Sudan, pre-existing sutures in the Precambrian basement helped to localize RSR-related normal faults after a period of felsic volcanism ~29 Ma (Kenea et al., 2001). Further basinward than Kenea et al. (2001), Ghebreab et al. (2002) identify a late Oligocene-early Miocene cooling event along the Eritrean margin that produced as much as 500 m of normal throw. This fault timing is temporally coincident with the estimated onset of extension along the conjugate rift margin in Yemen by Menzies et al. (1992, 1997). Also on the Eritrean margin, an AFT cooling signal shows a "post-rifting accelerated phase of denudation" ca. 20 Ma in response to significant topographic relief produced by Red Sea rifting (Abbate et al., 2002).

Not all RSR initiation estimates along the southern Nubian margin align with ours. In Ethiopia, Wolfenden et al. (2004) report an onset of faulting 29-26 Ma, followed by a multi-stage rift evolution with progressive strain localization, and the first linkage between the Ethiopian and Red Sea rifts ca. 11 Ma. This portion of the southern Nubian RSR margin is exceedingly complex due to the influence of the Afar Plume on lithospheric thermal conditions that, in turn, control fault kinematics and rift sequencing.

2.6.2.2. Phase Two (middle Miocene)

Middle Miocene modes in CARF AHe age spectra indicate a second extensional rift pulse. The timing of this pulse matches numerous observations along the length of the RSR as this was a time of regional plate reorganization that peaked with the establishment of the Dead Sea-Gulf of Aqaba transform and the consequent abandonment of a strong kinematic linkage between the Red Sea-Gulf of Suez rift. This middle Miocene extensional pulse may also mark the timing of subaerial exhumation of carbonate reef platforms that currently rest several tens of meters above sea level along the Arabian coast near Yanbu al Bahr and Al Wajh (Purser and Hotzl, 1988; Brown et al., 1989). Similar structures are present on the African margin (Bosworth et al., 1998).

Evidence for middle Miocene exhumation is found within the Jizl half-graben footwall at Jabal Nahar (15.1 ± 0.9 Ma), the only middle Miocene AHe age from the HJB, and as a composite signal at 14.5 ± 0.7 Ma in HFC AHe age data (Fig. 6(c)). Three different HFC fault block transects are footed by ~14 Ma AHe ages (Jabal Radwa and Jabal Mushayt-Blocks C and D). The t-T history of two modeled fault blocks from the HFC have a strong affinity towards middle Miocene exhumation (05SA224 and Jabal Mushayt Block D; Table 4**;** Figs. 13 and 17).

This supports the reliability of the ~16-14 Ma AHe age modes as accurate determinants for a second RSR extensional phase. Supplementary evidence for this phase is limited within other studies of RSR flank deformation. Bohannon et al. (1989) determine "at least 2.5 km of uplift and denudation since 13.8 Ma", as part of the only thermochronological research study to observe middle Miocene flank deformation on the southern Arabian margin.

2.6.2.3. On the possibility of late Eocene-early Oligocene RSR initiation

Not all results from other regional thermochronological research align so well with our late Oligocene-early Miocene age for onset of rift-related CARF exhumation. Steckler and Omar (1994), Omar and Steckler (1995), and Balestrieri et al. (2009) published results that claim AFT age data support initial rift-related uplift and exhumation during the late Eocene-early Oligocene ca. 34 Ma prior to a secondary rift interval ~25-20 Ma. Steckler and Omar (1994) and Omar and Steckler (1995) contend that uplift, created by extension, commenced ~34 Ma along the Egyptian margin of the Red Sea and Gulf of Suez as well as the southern Arabian rift flank in Saudi Arabia with Balestrieri et al. (2009) supporting this claim along the Nubian margin solely. The evidence provided by each research team is unconvincing.

AFT data from both the northern RSR-Gulf of Suez (Kohn and Eyal, 1981; Omar et al., 1987) and the southern RSR (Bohannon et al. 1989) show a consistency in rift timing ca. 25 Ma and flank uplift magnitude. In contrast, Omar and Steckler (1995) reassessed 12 samples from Bohannon et al. (1989) and concluded that these samples demonstrate a "one-to-one correspondence" with their late Eocene-early Oligocene AFT trends observed in Egypt. The accuracy of this reassessment is doubtful as no structural or stratigraphic data from the northern Red Sea-Gulf of Suez (Bosworth and McClay, 2001 *and references therein*) or AFT and

structural data from the Eritrean and southern Arabian margin (Bohannon, 1986; Davison et al., 1994; Menzies et al., 1992, 1997; Abbate et al., 2002) substantiate an late Eocene-early Oligocene rift phase. Omar and Steckler (1995) cite Bayer et al. (1988 *and references therein*) who assign a Rupelian age to the Sharik Formation and report it as the oldest syn-rift in the Midyan Basin. Jado et al. (1990) assign a Chattian age to the next highest strata in the Midyan Basin sequence, the Musayr Formation, and contend that rifting began in the late Eocene or early Oligocene. However, the basal syn-rift section in the Midyan Basin was reassigned an Aquitanian age by Hughes et al. (1999) based on a reinterpretation of the microfauna and correlation with regional stratigraphy. This updated Aquitanian age invalidates the correlation by Omar and Steckler (1995) of late Eocene-early Oligocene rifting and sedimentation in the Midyan Basin. It also better suits the original RSR onset interpretation by Bayer et al. (1988) who note "increased tectonic activity, rapid extension and subsidence of the graben, uplift of the graben shoulders and intense blockfaulting and tilting" ca. 23 Ma.

Balestrieri et al. (2009) also argue that an early Oligocene cooling event affected the Egyptian, and possibly Eritrean, margin ca. 34 Ma prior to major extension along the entire Nubian margin in the early Miocene (20-25 Ma). Evidence for the early Oligocene event in Eritrea is drawn partially from a single AFT cooling age (G8; 32 ± 3 Ma) reported by Ghebreab et al. (2002) that the authors themselves do not present as evidence for rifting. Furthermore, AFT thermal models from Sudan by Balestrieri et al. (2002) neither confirms nor excludes an early Oligocene cooling phase that would correlate with their observations from Egypt. Finally, Balestrieri et al. (2002) contend that this "spottily recorded" Oligocene cooling phase is unrecorded in Yemen and Eritrea due to the insufficiency of Oligocene denudation to exhume

the reset AFT system. While this last argument is valid based on their observations of rift flank geomorphology, it cannot be used to argue for the presence of an unobserved cooling signal.

Though several Paleogene age modes appear in the CARF AHe age spectra (Fig. 5), we do not recognize their presence as late Eocene-early Oligocene extension in the CARF. Footwall samples that yield CARF Paleogene AHe ages represent an exhumed AHe PRZ since they lie either updip of younger AHe ages that signal the true exhumation age (e.g., Jabal al Qishr, Jabal Radwa) or within fault blocks that underwent exhumation too insufficient to expose thermally reset thermochronometers (e.g., Wadi af Far'ah-Block C). No thermal models indicate a concentrated cooling event ca. 34 Ma.

2.6.3. Thermal history and structural evolution of the CARF

2.6.3.1. A standard CARF thermal history model

Nine CARF fault blocks models yield a common thermal history, indicating a concurrent recording of widespread Paleozoic-to-recent CARF deformation (Jabal Radwa, Jabal al Qishr, Wadi af Far'ah-Block B, Jabal Mushayt-Blocks B and D, 04SA109, 05SA205, 05SA224, and 06SA104; Figs. 7, 9, 11, 13, 15, 16, and 17). Though these t-T model results (Table 4) indicate some variation in rift exhumation style and magnitude across the CARF, a standard CARF deformation model emerges that comprises a two-stage thermal evolution. First, either a Paleozoic or Mesozoic tectonic event rapidly exhumed CARF fault blocks to mid-to-upper crustal levels (~3-5 km) that correspond to thermal horizons above or within the topmost level of the ZHe PRZ with some brought to even shallower levels (e.g., Jabal Radwa). The frequent overlap of ZHe ages from widely separated structural domains (Fig. 4(b)) indicates that the initial event had significant regional extent since a Paleo-Mesozoic ZHe cooling signal appears

widespread throughout the proto-CARF. Numerical modeling alone does not reveal the geologic processes responsible for Paleo-Mesozoic cooling though footwall exhumation via normal faulting and regional lithospheric flexure are two common cooling mechanisms. Following Paleo-Mesozoic cooling, CARF fault blocks maintained their relative crustal depths and experienced negligible temperature changes through the Mesozoic prior to onset of major RSR extension in the Oligocene-Miocene which rapidly exhumed the same fault blocks to near-surface structural levels where erosion has exposed them subsequently. The long residence period in the shallow crust between cooling events suggests slow denudation in concert with a flattening of topography at the surface.

2.6.3.2. Variability in the standard CARF thermal history model

Of those thermal models that collectively form the general CARF thermal history model, few include acceptable t-T paths that tolerate the possibility of Paleozoic exhumation to shallow crustal levels with slow to abrupt reheating through the Mesozoic prior to Oligocene-Miocene exhumation (Jabal Mushayt Blocks B and D, Wadi af Far'ah Block B, and Jabal al Qishr; Figs. 9, 13, and 15). These exceptional t-T paths often occur in models with relaxed error constraints (e.g., Jabal al Qishr AHe age ± 13.6-23.5%; Table 3), indicating they do not represent accurately the true CARF cooling history. However, individual model evaluation is necessary due to two crustal reheating mechanisms common to rifts: burial by pre-rift volcanic or sedimentary overburden and increased temperature from an asthenospheric or volcanic heat source.

First, while it is possible that a pre-rift sedimentary cover developed overtop the proto-CARF during this long stretch of time, the majority of well-constrained t-T models indicate that overburden was too thin to produce a significant reheating signal in either thermochronometer

(e.g., Jabal Radwa; Fig. 11(b)). This result is concordant with evidence for limited pre-rift burial from regional Paleo-Mesozoic stratigraphic studies (e.g., Sharland et al., 2001 *and references therein*), eliminating consideration of this reheating mechanism. Second, a relatively shallow asthenosphere will produce regional increases in crustal temperature, alongside other significant effects such as increased volcanic activity and elevated topography along rift margins, similar to modern conditions in the southern RSR near the Afar Plume. Such a large thermal feature would imprint a significant Cenozoic thermal signature across the CARF and, since the best-constrained models do not tolerate this possibility, it is unlikely to have occurred. However, widespread dike injection, which may precondition stable continental lithosphere for rifting (Buck, 2004), is recognized as a late Oligocene-early Miocene event ca. 25-20 Ma that affected the ANS in the Red Sea and Gulf of Suez region (Bosworth et al., 2005 *and references therein*) and likely elevated the regional proto-CARF geothermal gradient with individual dikes capable of producing even greater temperature increases (Ravat et al., 2011). Cenozoic faults that bound rotated CARF crustal blocks may act as preferred pathways for mafic dike intrusion and four HFC samples from these areas yield partially-to-fully reset AHe and ZHe ages that tolerate the possibility of reheating. Point sample 04SA110, 05SA196 within Jabal Radwa, 05SA206 within Jabal Mushayt-Block C, and 05SA222 within Jabal al Qishr yield atypically low AHe and ZHe ages relative to local age trends (Table 1; Figs. 10, 12, 14).

In general, the reheating of CARF AHe and ZHe samples via heat from dike injection appears rare and does not skew our RSR initiation estimate since the footwall exhumation signal is obtained prevalently from areas where no major dikes are mapped (e.g., the Hamd half-graben footwall). Additionally, the synchronous temporal development of NW-trending dikes and

CARF footwall exhumation suggests that any minor AHe age resetting is inconsequential to the overall goal of identifying the onset of RSR extension in the CARF.

2.6.3.3. Fault style and evolution in the HFC

Thermal modeling of adjacent and intra-block sample arrays indicates that the prevalent deformational style in the CARF during both RSR extensional phases was one of localized block faulting and not wholesale rift flank uplift. Block faulting in the HFC is highly selective, operating on individual fault blocks during either RSR extensional phase as evidenced by disparity in the t-T history between neighboring fault blocks and along-strike variation in total throw on Cenozoic faults. Jabal Mushayt Blocks B, C, and D exhibit distinct exhumation histories though they lie adjacent to one another within one of the greatest areal concentrations of major mapped Cenozoic faults within the HFC (Pellaton, 1979; Fig. 3). Blocks B and D yield a t-T history that fits the general CARF thermal history model. Both were first cooled to a middle-to-shallow crustal level during a Paleozoic cooling event where they remained between ~110-160 °C before exhuming from depths of 4.5-3.1 km during the first RSR extensional phase (Fig. 13; Table 4). In contrast, Block C yields cooling ages coincident with both RSR extensional phases and was exhumed from 5.2-3.9 kilometers, the greatest crustal depths of any sampled fault block. The Paleo-Mesozoic thermal history of Block C is relatively ambiguous due to the spread of good model fits, yet the majority of t-T path fits lie below the ZHe PRZ prior to Cenozoic exhumation. 04SA109 and 04SA110 reveal an analogous relationship between Blocks A and B near Umm Lajj (Figs. 3 and 16) in terms of t-T history disparity.

Several major HFC Cenozoic faults exhibit disproportionate throw along strike, such as the Master Listric Fault (Roobol and Kadi, 2008) that separates Jabal Mushayt, 05SA205, and Jabal

Radwa (Block B, collectively) from the Yanbu coastal plain fault domain (Block A; Fig. 3). Portions of Block B exhumed to different crustal levels during one of two Paleozoic cooling events before the whole Block B domain was exhumed to comparable shallow crustal levels in the early Miocene. A progressive increase in total Cenozoic exhumation from east to west is observed with Jabal Radwa and Jabal Mushayt-Block B undergoing the least (1.5-0.5 km) and greatest (4.5-3.4 km) exhumation, respectively (Figs. 11 and 13; Table 4).

Disproportionate exhumation along strike of the RSR is observed on a larger scale as well. Further north along the CARF, Block B (05SA228, Wadi Nabat, and Jabal Salajah Foothills) exhibits ~0.9 km greater average exhumation than the southern Block B complement. At this location, Block B exhibits proportional intra-block exhumation as 05SA228, Wadi Nabat, and Jabal Salajah Foothills share similar early Cretaceous ZHe and Miocene AHe ages and a comparable t-T history, which indicates they experienced synchronous along-strike deformation during CARF evolution (Figs. 15 and 17; Table 4). In addition, Wadi Nabat contains the base of an exhumed ZHe PRZ defined by a lowermost sample, 04SA106, with overlapping Miocene AHe and ZHe ages (19.4 ± 1.2 Ma and 19.9 ± 1.6 Ma, respectively) and an increase in ZHe ages with elevation. 04SA106 is nearest to the Block A/Block B bounding fault while the oldest ZHe age is located furthest inboard (Fig. 3). The relative position of these samples implies that the greatest exhumation occurred nearest to the fault, which conforms to the general structural model of the extended Arabian margin as rotated crustal blocks separated by listric normal faults (Mougenot and Al-Shakis, 1999).

2.6.4. The distribution and progression of RSR strain in the CARF

RSR strain is distributed diffusely across the CARF due to the contemporaneous early-to-middle Miocene development of the Hijaz Mountains Fault Complex (HFC) and Hamd-Jizl Basin (HJB) structural domains. Each structural domain yields unique AHe and ZHe thermal records due to inherent differences in the timing and spatial dissemination of RSR faults, magnitude of exhumation, and degree of post-rift initiation erosion. Relative to the HJB, the HFC exhibits closer RSR fault spacing with multiple crustal fault blocks and a greater degree of footwall exhumation, each of which has contributed to the reduction of the Paleo-Mesozoic AHe thermal record within this structural domain.

The boundary that separates the HFC and HJB is the along-strike trace of the exhumed fossil pre-rift AHe PRZ is exposed within the rift flank (Figs. 3 and 18). Notably, the HJB ZHe age population (Fig. 6(b)) contains no Triassic or younger ages. CARF extension is evenly distributed within a wide zone along numerous faults with small individual throw magnitude and the absence of a Cenozoic ZHe signal results from the inability of rift-related exhumation to expose thermally reset ZHe thermochronometers from mid-crustal depths (≥ 5 km) too far inboard from the rift margin. Small throw on CARF faults due to distributed strain may also explain our slightly lesser CARF pre-rift burial estimates relative to those published for the southern Arabian margin.

2.6.4.1. On the width and inboard extent of diffuse CARF extension

In the HJB, 06SA104 yields a t-T history (Fig. 7) that shows the Wadi al Qattar footwall originally cooled in the Cambrian during an event that may have brought it to depths of 3.3-2.3 km where it remained at (or slowly reheated to) temperatures ~115° prior to rapid exhumation ca. 21.1 ± 1.3 Ma. This t-T history aligns with the standard CARF thermal history model found

within many HFC fault blocks, demonstrating their genetic relationship and proving that the HJB and HFC deformed concomitantly as part of a diffuse extensional system in the CARF. Further inboard, the absence of Cenozoic AHe and ZHe cooling ages within the Central Arabian Shield Transect shows that no resolvable RSR-related deformation affected the Arabian Shield east of the Hamd and Jizl half-graben border faults, the furthest inboard RSR strain markers. No appreciable amount of rapid exhumation is recorded elsewhere in the HJB region and ambient exhumation estimates from the hanging wall samples are irresolvable.

The minimum width of diffuse extension within the CARF is ~150 km based on the average distance between the HJB border fault and the modern coastal plain (HFC-Block A). Our identification of Cenozoic extension far inboard of the modern coastal plain widens the recognized syn-rift fault zone to a degree greater than previously outlined (e.g., Roobol and Kadi, 2008) and has direct bearing on total divergence estimates between the African and Arabian plates since those estimates traditionally rely on assumed widths of extended lithosphere. Within the CARF at the present latitude of 25°N, Cochran (1981) recognizes a 120 km-wide pre-rift zone that laid the groundwork for diffuse extension up to the present day (Cochran, 1983). Cochran (1981) does not incorporate diffuse rifting as far inboard as the HJB but it does acknowledge the major presence of extended continental lithosphere in the northern Red Sea, later confirmed through seismic surveys (Mougenot and Al-Shakis, 1999). With the aid of satellite imagery, some structural reconstructions of Precambrian Arabian-Nubian Shield suture zones indicate that motion between Africa and Arabia can be modeled using a single Euler pole from an initial rift basin 14 km wide (Sultan et al., 1992, 1993). We disagree with this contrary conclusion based on our thermochronological evidence for diffuse rifting and the

author's assumption that nearly all crustal extension was accommodated by sea-floor spreading, an assumption know to be false (e.g., Cochran and Martinez, 1988).

In the Jizan region of the southern RSR, our estimation of initial rift width is 1.3-7.5 times greater than published estimates of 20-50 km, 60 km, and 80-120 km (Bohannon, 1986; Bohannon et al., 1989; and Davison et al., 1994). Though the estimation of 80-120 km by Davison et al. (1994) for the Yemeni RSR flank is the closest match to our observation, this comparison is unsuitable since we attribute wholly different rift architecture to the northern (diffuse plate) and southern (rigid plate) Arabian RSR flanks and initial rift width estimates would obviously differ between the two inherent plate conditions.

2.6.4.2. Basinward migration of RSR strain with progressive rifting

The change in geographical dispersion of coeval CARF AHe ages with progressive rifting shows that RSR strain in the CARF migrated basinward in the late Miocene. Early to middle Miocene AHe ages in the HJB signal early diffuse lithospheric extension but no direct thermochronological or structural evidence supports basin deepening much after ~12 Ma and, accordingly, the youngest HFC AHe ages indicate no major cooling event after ~13.5 Ma. Moreover, five of the ten samples with middle Miocene AHe cooling ages are located within the Jabal Mushayt transect, which may indicate that this portion of the rift flank was a focal point of extension during a middle Miocene rift pulse. These observations accord with the idea of progressive RSR reorganization wherein a widely diffuse rift zone developed during initial rifting in the early Miocene prior to strain localization via the abandonment of rift basins peripheral to the modern RSR axial trough (e.g., Almond, 1986; Bosworth, 1994). Bosworth et al. (2005 *and references therein*) cite the presence of the Al Wajh and Yanbu "relict basins" on

the CARF as evidence for local basin abandonment. We now categorize the Hamd-Jizl Basin as such a relict basin because extensional strain ceased in the region soon after the eruption of ~12 Ma Ishara basalt (Szymanski et al., *in prep*.).

2.6.5. RSR evolution model

Sengor and Burke (1978) use the temporal sequencing of volcanism, rifting, and uplift to define two end-member rift evolution models: active (uplift/doming/volcanism-rifting) and passive (rifting-flank uplift-volcanism). Active rift evolution could be recognized regionally since heat generated during active rifting would partially or fully reset thermochronometers across the CARF, establish an elevated regional geothermal gradient, and manifest as a singular reheating event. Passive rifting would simply exhume CARF crustal blocks with no prior modification to the established geothermal gradient and AHe and ZHe PRZs.

No strong trends within CARF thermal models support exclusively an active or passive rift evolution model since no singular Cenozoic reheating event is revealed and t-T path fits show no collective affinity towards a particular geothermal gradient range, though the greatest concentration of model fits lie in the 28-40 °C/km range (Fig. 19**)**. The Jabal al Qishr and Jabal Mushayt transects in the HFC and the Hamd half-graben footwall in the HJB exemplify this conclusion. Along-strike parallel fault blocks Jabal al Qishr and Jabal Mushayt-Block D developed separately during the Oligocene-Miocene and middle Miocene extensional phases and exhibit dissimilar exhumation magnitudes of 3.6 km and 3.1 km, respectively (30 °C/km g.g.; Table 4**)**. A similar, smaller scale disparity exists internal to the Jabal Mushayt transect where the t-T history of adjacent Blocks B and C shows they exhumed from different crustal depths during different rift phases: Block B exhumed from 3.4 km depth ca. 23 Ma and Block C later

exhumed from 3.9 km depth (40 °C/km g.g.; Fig. 13). Jabal al Qishr also displays deviations in the AHe and ZHe cooling age trends that are attributed mostly to relatively minor intra-block faulting (Fig. 14). In the HFC, regional block faulting, as opposed to regional doming, explains the apparent selectivity of the rifting process within a relatively stable geothermal gradient.

No apparent rift evolution sequence emerges from the developmental timing of HJB structural and volcanic elements. No collective uplift signal appears in the HJB AHe and ZHe age database and an early Miocene rifting-to-volcanism succession preceded a period when both processes were active. First, the Hamd half-graben developed ca. 21 Ma, initiating footwall erosion and deposition of the syn-rift Qattar Formation (*Szymanski et al., in prep.*). Basalt volcanism then followed initial footwall development 4 million years later when flood basalts erupted from Harrat Ishara (17-12 Ma; *Szymanski et al., in prep.*) and Harrat Kura (11-5 Ma; Camp et al., 1991) and accompanied further deepening of the HJB at Jabal Nahar in the Jizl half-graben (AHe: 15.1 ± 0.9 Ma). Most recently, basalt has extruded into the HJB from Harrats Khaybar, Ithnayn, and Rahat (Camp et al., 1991) while mafic dike injection has been recorded further basinward in the HFC at Harrat Lunayyir (Zahran et al., 2009).

Altogether, our structural and volcanological observations, coupled with the absence of a significant regional pre-rift thermal signal in CARF thermal models, indicate that the prevalent rift style in the CARF during both RSR extensional phases was one of localized block faulting and not wholesale rift flank uplift. We favor a passive rift model during RSR initiation before a changeover in the HJB to contemporaneous development of overlapping volcanic and extensional structures. No flank-wide uplift is observed in the CARF. Unconventional hybrid passive/active rift models have been proposed previously to explain the perceived out-of-order

sequencing of magmatism, rifting, and uplift along the Arabian rift flank (e.g., Camp and Roobol, 1992; Davison et al., 1994).

Elsewhere in the RSR system, no singular rift model is adequate, as no overall consensus exists regarding the relative timing of volcanism, uplift, and extension. Moreover, contrasting results sometimes come from the same study region. Geologic elements on Arabian and Eritrean rift flanks in the southern RSR show a magmatism-rifting-uplift development sequence that aligns with traditional "passive" rift models (Bohannon et al., 1989; Drury et al., 1994). However, Menzies et al. (1997) cite both $^{40}Ar/^{39}Ar$ basalt and AFT age results and report to observe a contrasting "active" sequence in Yemen south of the study area of Bohannon et al. (1989). On the Nubian margin in Sudan, Kenea et al. (2001) observe an unconventional rift development sequence that begins with extensional faulting first prior to, and then contemporaneous with, basalt emplacement ca. 30 Ma. This sequence counters the conventional active rift sequence usually observed to develop above shallow hot asthenosphere regions like the Afar Plume.

Omar and Steckler (1995) postulate a unique RSR evolution model where rifting, uplift and erosion, and volcanism occurred simultaneously along the full length of the RSR at ~34 Ma. The authors acknowledge that their AFT data fit no preconceived rift model, cite the exceptional tectonic environment of the southern RSR, and propose that passive lithospheric extension over an anomalously hot asthenosphere in the Afar produced a rift evolution pattern that displays the temporal synchronicity they observe. We reject this model because the age and trend of cooling that would be produced on the Arabian margin by this model is absent in the CARF AHe and

ZHe cooling age database. Altogether, the studies cited here reinforce the notion that, as of yet, no observed pattern is clear enough to prompt an agreement on a singular RSR model.

2.6.6. Central and northern Arabian rift flank architecture

Clearly the full RSR system is an ill fit for an end member rift evolution model as the Nubian and Arabian rift flanks express out-of-order volcanic, rifting, and uplift phases along strike that do not fit preconceived models of either active or passive rift sequences. Applying a singular rift evolution model to the full RSR system is inappropriate because exceptional along-strike changes in Arabian rift flank geologic elements create fundamental mechanical differences in the continental lithosphere of the Arabian flank, cause rifting to progress uniquely, and define independent southern and northern Arabian rift flank domains.

2.6.6.1. Architecture of extended continental lithosphere in the NW Arabian Plate

The northern Arabian rift flank comprises numerous complex geologic features that make it unique from the rift flank south of Jeddah in terms of rift flank architecture. Significant along-strike changes in geological features include the uneven distribution of Precambrian (Najd) basement fabric, Cenozoic volcanic fields, and pre- and syn-rift basins, and the south-to-north decrease and eventual loss of a both a prominent coastal escarpment and magnetic anomalies in the RSR axial trough. The orientation of these elements demarcates a "wedge" of central and northern Arabian rift flank diffuse deformation that is bound to the east and southeast by the Makkah-Madinah-Nafud (MMN) volcanic line (Camp et al., 1989) and its intersection with both the coastal escarpment and the Shagara Fracture Zone (Crane and Bonatti, 1987; Fig. 1). The deformed wedge expands to the north and northwest along the MMN line and modern RSR axial trough and incorporates the Precambrian Najd Fault System (NFS; Moore, 1979 *and references*

therein), which crosses the interior Arabian Shield and approaches the RSR margin where it controlled the location and frequency of Cenozoic faults in the central and northern Arabian rift flank (Brown, 1970; Omar et al., 1987, 1989; Szymanski et al., *in prep.*). This wedge of diffuse continental lithosphere extension illustrates major structural differences in rift architecture between the southern and northern Arabian rift flank. The southeastern boundary of the deformed wedge marks the changeover from rigid plate deformation, concentrated proximal to the modern rift basin, on the southern Arabian rift flank to distributed strain within the central and northern Arabian rift flank.

The Shagara Fracture Zone (Crane and Bonatti, 1987) offsets the RSR axial trough at 21°N and marks the northernmost extent of magnetic anomalies from sea-floor spreading (Cochran, 1983) coincident with the intersection of the MMN line and the prominent coastal escarpment (Fig. 1). The character of both the Red Sea axial trough and the coastal escarpment changes significantly on either side of this intersection, indicating an abrupt change in Arabian rift flank architecture from south to north controlled by major along-strike differences in the structural integrity of the Arabian rift flank. Bathymetry and seismic reflection profiles show extended continental lithosphere in the northern RSR where organized sea-floor spreading (s.f.s.) is unobserved north of 23°N (Cochran, 1983; Miller and Barakat, 1988; Mougenot and Al Shakis, 1998; and Cochran and Karner, 2007).

The diminishment and eventual loss of the prominent coastal escarpment is the most apparent geomorphological difference between the southern and northern Arabian rift flank. Starting from the southern tip of Yemen, the escarpment forms a continuous ~2-3 km-high feature that comprises the Asir Mountains until it quickly loses relief, becomes diffuse, and effectively ends

at an intersection with the southern trace of the MMN near 21°N (Fig. 1). The absence of a prominent coastal escarpment in the central and northern Arabian rift flank is due to the redistribution of extensional strain from the large-throw coastal faults that bound the southern RSR to more dispersed structures within the deformed wedge. Three major fault zones (Shagara, Zabagad, and The Brothers; Crane and Bonatti, 1987) offset the northern Red Sea axial trough, transfer strain laterally, and prevent the buildup of high rift flank topography in the manner described by Faulds and Varga (1998) for numerous extended terranes and Moustafa (2002) for the Gulf of Suez, specifically. Structural control on relief is evident in the Hijaz Mountains, the geomorphologic equivalent of the Asir, where highlands inboard of the coastal plain maintain elevations that average 300-500 m in height and infrequently achieve heights taller than 1500 m until the Gulf of Aqaba. Importantly, the simultaneous development of the HFC and the HJB in a diffuse zone of extended continental lithosphere during rifting means a prominent coastal escarpment never existed on the Arabian rift flank further north than its present position. In the southern RSR, the differing role and lifespan of transfer zones may explain why no significant axial trough offset is observed south of 21°N. Transfer faults exist on the Jizan coastal plain (Voggenreiter, 1988) but, since they do not penetrate the Red Sea axial trough, they do not appear to be as long-lived as their northern counterparts. These transfer faults likely developed during the earliest rift stage as part of a set of localized graben that failed to advance to form a single, continuous fault zone in a manner similar to the northern RSR. Thus they were abandoned and strain concentrated near the trace of the modern RSR axial trough to form the modern coastal escarpment.

Numerical models of rifting in stable continental lithosphere shows 100-150 km of distributed extension prior to lithospheric necking, continental break-up and concentrated production of oceanic lithosphere (Schmeling, 2009). Using magnetic and gravity profile data and assuming that rifting is confined to the main rift basin, Cochran (1981) calculated 160 km total extension at 25°N and 140 km total extension at 17°N, prior to s.f.s. commencement in the southern Red Sea axial trough ca. 5 Ma (Cochran, 1983). Just 20 m.y. passed between initial RSR extension ca. 25 Ma and the onset of s.f.s. in the southern RSR, yet the central and northern RSR remains unruptured. Since CARF AHe and ZHe data support the idea that extension began concomitantly along the full RSR, inherent differences in rift flank structural kinematics along strike likely explain the dissimilarity in deformation between the southern and northern RSR.

The north-trending vent systems of the MMN line are a manifestation of deeper-seated structural heterogeneities (Camp and Roobol, 1991b) that demarcate a weak zone in the continental lithosphere. The MMN line is the axial trace of the West Arabian Swell (Camp and Roobol, 1992), the northern component of the Afro-Arabian Dome (Almond, 1986), whose N-S-trending axis delineates a channel of upwelling asthenosphere that either emanates from a mantle plume beneath the Arabian Plate or connects to the Afar Plume beneath the Ethiopian Dome. Within the shallow crust, a 50 km-long fault scarp runs north-to-south beneath Harrat Khaybar and serves as a pathway for basalt extrusion (Camp et al., 1991). Camp and Roobol (1992) present a plumbing model that shows a much larger, en echelon chamber system beneath the MMN line that interconnects at depth to create a single, kilometer-scale oblate chamber. We propose that the piping beneath the MMN line may effectively decouple the Arabian Plate

lithosphere west–to-east across its strike and allow for diffuse extension in the central and northern Arabian rift flank.

Support for effective lithosphere decoupling exists at the northern terminus of the MMN line where it trends into the Ha'il-Rutbah Arch (Fig. 1). According to Camp and Roobol (1992), the two features are irrevocably linked and, while the MMN line first extruded flood basalt in the Miocene, the Ha'il-Rutbah Arch may be as long-lived as the Precambrian (al-Laboun, 1986). Powers et al. (1966) contend that the Ha'il Arch was "merely a stable headland" in the Paleozoic around which sedimentary units were evenly deposited on the Neo-Tethyan margin until uplift in the Cretaceous made it a positive topographic feature and created a loss of communication between the Tabuk Basin in the west and the Midyan Basin in the east. Al-Laboun (1986) provides more detailed Paleozoic stratigraphy based on subcrop maps that indicates the Ha'il-Rutbah Arch was a positive topographic feature in the late Devonian-early Carboniferous; all indications show that no sedimentary strata were deposited to the west of the Ha'il-Rutbah Arch during either the Carboniferous or Permian periods. If the MMN line and the Ha'il-Rutbah Arch are definitely linked, then the anomalously high position of the Ha'il-Rutbah Arch may be explained due to buoyancy of relatively shallow asthenosphere which, in turn, is documented as a long-lived sub-crustal feature beneath the ANS. Furthermore, it is possible that the buoyant forces responsible for the Afro-Arabian Dome (Almond, 1986) are similar to those that allowed the pre-rift ANS in the CARF region to maintain a relatively high structural position during the Mesozoic, according to HFC thermal models.

Asthenosphere channelization beneath the Arabian Plate is supported by shear wave-splitting results that illustrate a N-S-oriented mantle anisotropy near the lithosphere-asthenosphere

boundary (LAB; Hansen et al., 2006), which is attributed to mantle flow in the asthenosphere from sources as far away as the core-mantle boundary beneath South Africa (Daradich et al., 2003). Channelization may stem from a backstop of lithospheric mantle where LAB depths rapidly increase from 120 km to 160 km near the Arabian Shield/Paleozoic Cover sequence boundary (Hansen et al., 2007). This step-down in the LAB may be a vestige of lithospheric thicknesses prior to the accretion of island arcs that formed the ANS (Hansen et al., 2007) and, if so, this lends credence to the theory that the Ha'il-Rutbah Arch is a Precambrian feature whose positive position in the crust is dynamically supported by a relatively thick lithosphere.

2.6.6.2. HJB analogs in the northern Arabian rift flank

The HJB is likely not the only syn-rift extensional structure of Aquitanian age that formed within the Arabian rift flank during the initial RSR extensional phase. Several HJB similar features may exist within the Arabian rift flank in the form of Paleogene and Neogene graben distributed along the Arabian coastal plain and further inboard, buried beneath the Paleozoic cover sequence (Johnson, 1998). West of the HJB, along the Red Sea coast near Duba, the boundaries of the Azlam graben (*Aznam graben*; Dabbagh, 1988) exhibit NFS orientation and stratigraphic evidence suggests that this graben is Miocene in age. North of the HJB lie the Tabuk graben, Fayha graben, Tayma graben, Qur Mulayh graben, and Tufayhah graben (Johnson, 1998 *and references therein*). The orientation of these graben is not coincident with NFS orientation. Rather, they lie parallel to the RSR within a wide zone of closely spaced, NW-trending Cenozoic faults (Roobol and Stewart, 2009). Aeromagnetic data shows the northwestern Arabian Plate is rife with magnetic lineaments that correspond to regional tectonic elements such as the NFS and a large system of Cenozoic dikes that parallel the Red Sea Basin

(e.g., Zahran et al., 2002; Nehlig et al., 2002 *and references therein*) and, accordingly, the major ~25-20 Ma dike swarm found along the entire length of the Arabian margin including Sinai (Eyal et al., 1981; Camp and Roobol, 1992). Nearly each of the graben structures in NW Arabia is founded upon one of these long magnetic lineaments, which are interpreted as subsurface dikes, the largest being the Great Ja'adah Dike beneath the Tabuk graben (Phoenix Corporation, 1985; Roobol and Stewart, 2009). A bedrock and detrital AHe and ZHe thermochronologic investigation of the evolution of these graben and their accompanying syn-deformational sedimentary sequence is necessary to constrain the timing of footwall exhumation and explore whether their cooling signal has an affinity to either RSR extensional phase.

2.6.6.3. The implications of recent CARF seismic events

Regional seismic studies show both historical and recent deformation around these embedded graben. Ambraseys and Melville (1989) cite at least 3 large earthquakes during the past 11 centuries in NW Arabia near the Tabuk graben, including a very strong earthquake that killed 20,000 people (Ambraseys et al., 1994). Investigating the 2004 Tabuk earthquake swarm whose strength peaked in the main shock on June 22nd (Mw = 5.1), Aldamegh et al. (2009) report a shallow source of ~4-5 km and a preferred NW-SE-trending focal mechanism that parallels the Tabuk graben border faults. The authors attribute the tectonic origin of this swarm to active rifting beneath the Tabuk area but explore the issue no further. In May 2009, an earthquake swarm beneath Harrat Lunayyir created a spectacular, ~8 km-long ground fissure (Kozdroj Wiesiek Andrzej and Peter Johnson, *pers. comm.*). Models of InSAR-derived surface deformation are best fit by a "narrow (~2 m wide), 8-km-long dike to shallow crustal levels" whose orientation fits the regional dike pattern as revealed by aeromagnetic data (Zahran et al.,

2009). Harrat Lunayyir has produced episodic earthquake swarms since 2007, prior to the May 2009 episode that culminated in a M5.4 event (Zahran et al., 2009).

If the widespread dike swarm identified in aeromagnetic data that created the graben structures in NW Arabia (e.g., Tabuk, Fayha graben) correlates temporally to the syn-rift Arabian rift flank dike swarm ca. 25-20 Ma, they jointly signal a period of diffuse rift flank modification contemporaneous to the onset of major CARF extension. Moreover, the operation of dike injection during both the initial RSR extensional phase and today, evidenced by modeling of the May 2009 Harrat Lunayyir earthquake swarm, signals that a similar rift style is proceeding today as it was in the nascent stages of RSR development. This aligns well with our postulation of a deformed wedge in the central and northern Arabian rift flank.

2.7. Conclusions

Our results comprise the first direct evidence for the extent and timing of RSR development within the CARF. By linking study regions from the southern and northern portions of the RSR, CARF AHe and ZHe age data and thermal models prove definitively a common early rift history for the full RSR system. The Arabian rift flank proceeded to evolve structurally unique northern and southern Arabian rift flank portions on either side of the MMN line that are evident today as margins with dissimilar structural architecture.

(1) The CARF AHe and ZHe system captures RSR initiation as a pulse of major extension ca. 21 Ma. This rift onset age is mirrored elsewhere along the full Red Sea Nubian margin and the southern Arabian rift flank in Saudi Arabia and Yemen, confirming that RSR initiation and associated basin development began with a concomitant opening of the full Red Sea-Gulf of Suez rift system in the late Oligocene-early Miocene. Highly segmented rift flank dissection and

episodic dike injection in the HFC accompanied footwall exhumation and terrigenous sedimentation in the HJB to delineate a ~200 km-wide zone of diffuse CARF extension. Distributed block faulting, as opposed to rigid, regional flank uplift and denudation was the dominant structural style in the CARF during Phase One of RSR development. Harrat volcanism in the HJB trailed rift onset by 6 million years and continues today.

(2) A secondary, relatively minor extensional RSR phase occurs ca. 15 Ma, coincides with regional plate reorganization and the establishment of the Dead Sea-Gulf of Aqaba transform, and represents the beginning of CARF strain localization. The exhumation of Jabal Nahar ca. 15 Ma and final deepening of the Hamd half-graben ca. 12 Ma signals the end of inboard HJB deformation. Within the HFC, the absence of AHe cooling ages younger than ~13 Ma confirms that major extensional faulting migrated basin-ward in the middle Miocene.

(3) Thermal models reveal a common three-stage thermotectonic t-T evolution for most CARF fault blocks. In nearly every instance, thermal models show the ANS experienced a Paleo-Mesozoic cooling event that brought the CARF to a mid-to-upper crustal structural level where it remained relatively thermally stable through the Mesozoic. Then, beginning with the Continental Lithosphere Rift Phase, CARF fault blocks were exhumed along numerous rift-parallel faults from pre-rift flank depths of 0.5-3.9 km. Minimal reheating paths indicate no burial by significant accumulations of pre-rift volcanic or Paleo-Mesozoic sedimentary overburden and/or increased heat flow in mid-to-upper-crustal levels from active rifting processes. Accordingly, we favor a passive rift model since the absence of a significant pre-rift thermal signal rejects the likelihood of regional uplift.

(4) A diffuse structural zone (wedge) operated in the central and northern Arabian margin to accommodate strain during both RSR extensional phases. This deformed wedge begins at the coincident intersection of the MMN line with the Red Sea axial trough and expands to the NW where it encompasses pre- and syn-rift graben (e.g., Hamd-Jizl Basin, Azlam, Tabuk) and defines a region of diffuse continental lithosphere extension, altogether different from the relatively rigid lithosphere on the southern Arabian margin.

2.8. References

Abbate, E., Balestrieri, M. L., and Bigazzi, G., 2002, Morphostructural development of the Eritrean rift flank (southern Red Sea) inferred from apatite fission track analysis: Journal of Geophysical Research, v. 107, no. B11, p. 2319.

Agar, R., 1987, The Najd fault system revisited; a two-way strike-slip orogen in the Saudi Arabian Shield: Journal of Structural Geology, v. 9, no. 1, p. 41-48.

Al-Fares, A. A., Bouman, M., and Jeans, P., 1998, A new look at the Middle to Lower Cretaceous stratigraphy, offshore Kuwait: GeoArabia, v. 3, no. 4, p. 543-560.

Al-Hajri, S., and Owens, B., 2000, Stratigraphic palynology of the Palaeozoic of Saudi Arabia, Arabian Printing and Publishing House.

Al-Laboun, A. A., 1986, Stratigraphy and hydrocarbon potential of the Paleozoic succession in both Tabuk and Widyan basins, Arabia: Future Petroleum provinces of the world. American Association of Petroleum Geologist Memoir, v. 40, p. 399-425.

Aldamegh, K. S., Abou Elenean, K. M., Hussein, H. M., and Rodgers, A. J., 2009, Source mechanisms of the June 2004 Tabuk earthquake sequence, Eastern Red Sea margin, Kingdom of Saudi Arabia: Journal of seismology, v. 13, no. 4, p. 561-576.

Almond, D., 1986, Geological evolution of the Afro-Arabian dome: Tectonophysics, v. 131, no. 3-4, p. 301-332.

Ambraseys, N. N., and Melville, C. P., 1989, Evidence for intraplate earthquakes in northwest Arabia: Bulletin of the Seismological Society of America, v. 79, no. 4, p. 1279-1281.

Ambraseys, N. N., Melville, C. P., and Adams, R. D., 1994, The seismicity of Egypt, Arabia and the Red Sea: a historical review, United States of America, Cambridge University Press, 181 p.

Badri, M., 1991, Crustal structure of central Saudi Arabia determined from seismic refraction profiling: Tectonophysics, v. 185, no. 3, p. 357-374.

Baker, J. A., Menzies, M., Snee, L., and Thirlwall, M., 1994, Stratigraphy, 40Ar/39Ar geochronology and geochemistry of flood volcanism in Yemen: Mineralogical Magazine 58A, p. 42-43.

Baker, J. A., Thirlwall, M. F., and Menzies, M. A., 1996, Sr-Nd-Pb isotopic and trace element evidence for crustal contamination of plume-derived flood basalts: Oligocene flood

volcanism in western Yemen: Geochimica et Cosmochimica Acta, v. 60, no. 14, p. 2559-2581.

Balestrieri, M. L., Abbate, E., Bigazzi, G., and El Bedri Ali, O., 2009, Thermochronological data from Sudan in the frame of the denudational history of the Nubian Red Sea margin: Earth Surface Processes and Landforms, v. 34, no. 9, p. 1279-1290.

Balestrieri, M. L., Stuart, F. M., Persano, C., Abbate, E., and Bigazzi, G., 2005, Geomorphic development of the escarpment of the Eritrean margin, southern Red Sea from combined apatite fission-track and (U–Th)/He thermochronometry: Earth and Planetary Science Letters, v. 231, no. 1, p. 97-110.

Barnard, P. C., Thompson, S., Bastow, M. A., Ducreux, C., and Mathurin, G., 1992, Thermal maturity development and source□rock occurrence in the Red Sea and Gulf of Aden: Journal of Petroleum Geology, v. 15, p. 173-186.

Bayer, H. J., Hötzl, H., Jado, A. R., Röscher, B., and Voggenreiter, W., 1988, Sedimentary and structural evolution of the northwest Arabian Red Sea margin: Tectonophysics, v. 153, no. 1, p. 137-151.

Best, J. A., Barazangi, M., Al-Saad, D., Sawaf, T., and Gebran, A., 1993, Continental margin evolution of the northern Arabian platform in Syria: AAPG Bulletin (American Association of Petroleum Geologists);(United States), v. 77, no. 2.

Bohannon, R. G., 1986, How much divergence has occurred between Africa and Arabia as a result of the opening of the Red Sea?: Geology, v. 14, no. 6, p. 510-513.

-, 1989, Style of extensional tectonism during rifting, Red Sea and Gulf of Aden: Journal of African Earth Sciences (and the Middle East), v. 8, no. 2-4, p. 589-602.

Bohannon, R. G., Naeser, C. W., Schmidt, D. L., and Zimmermann, R. A., 1989, The timing of uplift, volcanism, and rifting peripheral to the Red Sea: A case for passive rifting?: Journal of Geophysical Research, v. 94, no. B2, p. 1683-1701.

Bojar, A. V., Fritz, H., Kargl, S., and Unzog, W., 2002, Phanerozoic tectonothermal history of the Arabian-Nubian shield in the Eastern Desert of Egypt: Evidence from fission track and paleostress data: Journal of African Earth Sciences, v. 34, no. 3-4, p. 191-202.

Bosworth, W., 1994, A model for the three-dimensional evolution of continental rift basins, north-east Africa: Geologische Rundschau, v. 83, no. 4, p. 671-688.

Bosworth, W., Crevello, P., Winn, R., and Steinmetz, J., 1998, Structure, sedimentation, and basin dynamics during rifting of the Gulf of Suez and northwestern Red Sea: Sedimentation and Tectonics of Rift Basins: Red Sea–Gulf of Aden. Chapman and Hall, London, p. 77-96.

Bosworth, W., Huchon, P., and McClay, K., 2005, The Red Sea and Gulf of Aden Basins: Journal of African Earth Sciences, v. 43, no. 1-3, p. 334-378.

Bosworth, W., and McClay, K., 2001, Structural and stratigraphic evolution of the Gulf of Suez rift, Egypt: a synthesis: Mémoires du Muséum national d'histoire naturelle, v. 186, p. 567-606.

Bosworth, W., Sultan, M., Stern, R. J., Arvidson, R. E., Shore, P., and Becker, R., 1993, Nature of the Red Sea crust: A controversy revisited: Comment and Reply: Geology, v. 21, no. 6, p. 574-576.

Brown, G. F., 1970, Eastern margin of the Red Sea and the coastal structures in Saudi Arabia: Philosophical Transactions for the Royal Society of London. Series A, Mathematical and Physical Sciences, p. 75-87.

Brown, G. F., and Coleman, R. G., The tectonic framework of the Arabian Peninsula1972, International Geological Congress.

Brown, G. F., and Jackson, R. O., The Arabian Shield1960, Volume 9, p. 69-77.

Buck, W. R., 2004, Consequences of asthenospheric variability on continental rifting: Rheology and deformation of the lithosphere at continental margins, p. 1-30.

Camp, V. E., and Roobol, M. J., 1989, The Arabian continental alkali basalt province: Part I. Evolution of Harrat Rahat, Kingdom of Saudi Arabia: Geological Society of America Bulletin, v. 101, no. 1, p. 71-95.

-, 1991, Comment on "Topographic and volcanic asymmetry around the Red Sea: Constraints on rift models" by TH Dixon, ER Ivins, and JF Brenda: Tectonics, v. 10, no. 3, p. 649-652.

-, 1992, Upwelling asthenosphere beneath western Arabia and its regional implications: Journal of Geophysical Research, v. 97, no. 15, p. 255-271.

Camp, V. E., Roobol, M. J., and Hooper, P. R., 1989, Intraplate alkalic volcanism and magmatic processes along the 600 km-long Makkah–Madinah–Nafud volcanic line, western Saudi Arabia: Continental Magmatism, 39 IAVCEI General Assembly, Santa Fe, NM, New Mexico Bureau of Mines Geological Bulletin, p. 131.

-, 1991, The Arabian continental alkali basalt province: Part II. Evolution of Harrats Khaybar, Ithnayn, and Kura, Kingdom of Saudi Arabia: Geological Society of America Bulletin, v. 103, no. 3, p. 363-391.

Chazot, G., Menzies, M. A., and Baker, J., 1998, Pre-, syn-and post-rift volcanism on the south-western margin of the Arabian plate, v. Sedimentation and tectonics in rift basins: Red Sea–Gulf of Aden case, p. 5.

Clark, M. D., 1981, Geologic Map of the Al Hamra Quadrangle, Sheet 23C, Kingdom of Saudi Arabia, scale 1: 250 000.

Cochran, J. R., 1981, The Gulf of Aden: structure and evolution of a young ocean basin and continental margin: Journal of Geophysical Research, v. 86, no. B1, p. 263-287.

-, 1983, A model for the development of the Red Sea: Am. Assoc. Petrol. Geol, v. 67, p. 41-69.

-, 2005, Northern Red Sea: Nucleation of an oceanic spreading center within a continental rift: Geochemistry Geophysics Geosystems, v. 6, no. 3, p. Q03006.

Cochran, J. R., and Karner, G. D., 2007, Constraints on the deformation and rupturing of continental lithosphere of the Red Sea: the transition from rifting to drifting: Geological Society, London, Special Publications, v. 282, no. 1, p. 265-289.

Coleman, R. G., 1993, Geologic evolution of the Red Sea, Oxford University Press.

Coleman, R. G., Gregory, R., Brown, G. F., Arabia, S., and Survey, G., 1983, Cenozoic volcanic rocks of Saudi Arabia, US Department of the Interior, Geological Survey.

Corp., P., 1985, The interpretation of an airborne geophysical survey of the Cover Rocks region, Kingdom of Saudi Arabia.

Crane, K., and Bonatti, E., 1987, The role of fracture zones during early Red Sea rifting: structural analysis using Space Shuttle radar and LANDSAT imagery: Journal of the Geological Society, v. 144, no. 3, p. 407-420.

Crossley, R., Watkins, C., Raven, M., Cripps, D., Carnell, A., and Williams, D., 1992, The sedimentary evolution of the Red Sea and Gulf of Aden: Journal of Petroleum Geology, v. 15, p. 157-172.

Daradich, A., Mitrovica, J. X., Pysklywec, R. N., Willett, S. D., and Forte, A. M., 2003, Mantle flow, dynamic topography, and rift-flank uplift of Arabia: Geology, v. 31, no. 10, p. 901-904.

Davison, I., Al-Kadasi, M., Al-Khirbash, S., Al-Subbary, A. K., Baker, J., Blakey, S., Bosence, D., Dart, C., Heaton, R., and McClay, K., 1994, Geological evolution of the southeastern Red Sea Rift margin, Republic of Yemen: Geological Society of America Bulletin, v. 106, no. 11, p. 1474-1493.

Dercourt, J., Zonenshain, L. P., Ricou, L. E., Kazmin, V. G., Le Pichon, X., Knipper, A. L., Grandjacquet, C., Sbortshikov, I. M., Geyssant, J., and Lepvrier, C., 1986, Geological evolution of the Tethys belt from the Atlantic to the Pamirs since the Lias: Tectonophysics, v. 123, no. 1, p. 241-315.

Dixon, T. H., Ivins, E. R., and Franklin, B. J., 1989, Topographic and volcanic asymmetry around the Red Sea: Constraints on rift models: Tectonics, v. 8, no. 6, p. 1193-1216.

Dixon, T. H., Stern, R. J., and Hussein, I. M., 1987, Control of Red Sea rift geometry by Precambrian structures: Tectonics, v. 6, no. 5, p. 551-571.

Drury, S. A., Kelley, S. P., Berhe, S. M., Collier, R. E. L., and Abraha, M., 1994, Structures related to Red Sea evolution in northern Eritrea: Tectonics, v. 13, no. 6, p. 1371-1380.

Ehlers, T. A., and Farley, K. A., 2003, Apatite (U–Th)/He thermochronometry: methods and applications to problems in tectonic and surface processes: Earth and Planetary Science Letters, v. 206, no. 1, p. 1-14.

Ellis, A. C., Kerr, H. M., Cornwell, C. P., and Williams, D. O., 1996, A tectono-stratigraphic framework for Yemen and its implications for hydrocarbon potential: Petroleum Geoscience, v. 2, no. 1, p. 29-42.

Faulds, J. E., and Varga, R. J., 1998, The role of accommodation zones and transfer zones in the regional segmentation of extended terranes: Geological Society of America Special Papers, v. 323, p. 1-45.

Fleck, R. J., Coleman, R., Cornwall, H., Greenwood, W., Hadley, D., Schmidt, D., Prinz, W., and Ratte, J., 1976, Geochronology of the Arabian shield, western Saudi Arabia: K-Ar results: Geological Society of America Bulletin, v. 87, no. 1, p. 9-21.

Flowers, R. M., Ketcham, R. A., Shuster, D. L., and Farley, K. A., 2009, Apatite (U-Th)/He thermochronometry using a radiation damage accumulation and annealing model: Geochimica et Cosmochimica Acta, v. 73, no. 8, p. 2347-2365.

Gettings, M. E., Blank Jr., H. R., Mooney, W. D., and Healey, J. H., 1986, Crustal structure of southwestern Saudi Arabia: Journal of Geophysical Research, v. 91, no. B6, p. 21.

Ghebreab, W., 1998, Tectonics of the Red Sea region reassessed: Earth-Science Reviews, v. 45, no. 1-2, p. 1-44.

Ghebreab, W., Carter, A., Hurford, A. J., and Talbot, C. J., 2002, Constraints for timing of extensional tectonics in the western margin of the Red Sea in Eritrea: Earth and Planetary Science Letters, v. 200, no. 1, p. 107-119.

Ghebreab, W., and Talbot, C. J., 2000, Red Sea extension influenced by Pan-African tectonic grain in eastern Eritrea: Journal of Structural Geology, v. 22, no. 7, p. 931-946.

Girdler, R. W., 1970, A review of Red Sea heat flow: Philosophical Transactions of the Royal Society of London. Series A, Mathematical and Physical Sciences, v. 267, no. 1181, p. 191-203.

-, 1984, The evolution of the Gulf of Aden and Red Sea in space and time: Deep Sea Research Part A. Oceanographic Research Papers, v. 31, no. 6, p. 747-762.

-, 1991, The Afro-Arabian rift system--an overview: Tectonophysics, v. 197, no. 2-4, p. 139-153.

Guiraud, R., and Bosworth, W., 1999, Phanerozoic geodynamic evolution of northeastern Africa and the northwestern Arabian platform: Tectonophysics, v. 315, no. 1-4, p. 73-104.

Guiraud, R., Bosworth, W., Thierry, J., and Delplanque, A., 2005, Phanerozoic geological evolution of Northern and Central Africa: an overview: Journal of African Earth Sciences, v. 43, no. 1-3, p. 83-143.

Hager, C., and Stockli, D. F., 2009, A NEW MATLAB©-BASED HELIUM MODELING PACKAGE ("HeMP") FOR THERMAL HISTORY RECOVERY FROM SINGLE AND MULTI-THERMOCHRONOMETER (U-TH)/HE DATA AND DATA ARRAYS, Geological Society of America Annual Meeting, Volume Paper No. 186-8: Portland, OR.

Hansen, S. E., Rodgers, A. J., Schwartz, S. Y., and Al-Amri, A., 2007, Imaging ruptured lithosphere beneath the Red Sea and Arabian Peninsula: Earth and Planetary Science Letters, v. 259, no. 3, p. 256-265.

Hansen, S. E., Schwartz, S., Al-Amri, A., and Rodgers, A., 2006, Combined plate motion and density-driven flow in the asthenosphere beneath Saudi Arabia: Evidence from shear-wave splitting and seismic anisotropy: Geology, v. 34, no. 10, p. 869-872.

House, M. A., Wernicke, B. P., and Farley, K. A., 2001, Paleo-geomorphology of the Sierra Nevada, California, from (U-Th)/He ages in apatite: American Journal of Science, v. 301, no. 2, p. 77-102.

Hughes, G. W., and Johnson, R. S., 2005, Lithostratigraphy of the Red Sea Region: GeoArabia, v. 10, no. 3, p. 49-126.

Hughes, G. W., Perincek, D., Grainger, D. J., Abu-Bshait, A., and Jarad, A., 1999, Lithostratigraphy and depositional history of part of the Midyan region, northwestern Saudi Arabia: GeoArabia, v. 4, no. 4, p. 500-542.

Hughes, G. W., Varol, O., and Beydoun, Z. R., 1991, Evidence for Middle Oligocene rifting of the Gulf of Aden and for Late Oligocene rifting of the southern Red Sea: Marine and Petroleum Geology, v. 8, no. 3, p. 354-358.

Jado, A. R., Hotzl, H., and Roscher, B., 1989, Development of sedimentation along the Saudi Arabian Red Sea coast: Jour. of King Abdulaziz Univ., Earth Science, v. 3, p. 863-887.

Jarrige, J. J., d'Estevou, P. O., Burollet, P. F., Montenat, C., Prat, P., Richert, J. P., and Thiriet, J. P., 1990, The multistage tectonic evolution of the Gulf of Suez and northern Red Sea continental rift from field observations: Tectonics, v. 9, no. 3, p. 441-465.

Jarrige, J. J., d'Estevou, P. O., Burollet, P. F., Thiriet, J. P., Icart, J. C., Richert, J. P., Sehans, P., Montenat, C., and Prat, P., 1986, Inherited discontinuities and Neogene structure: the Gulf of Suez and the northwestern edge of the Red Sea: Philosophical Transactions of the Royal Society of London. Series A, Mathematical and Physical Sciences, v. 317, no. 1539, p. 129-139.

Johnson, P. R., 1998, Tectonic map of Saudi Arabia and adjacent areas: Deputy Ministry for Mineral Resources.

-, 2006, Proterozoic geology of western Saudi Arabia with Explanatory Notes.

Johnson, P. R., Andresen, A., Collins, A. S., Fowler, A. R., Fritz, H., Ghebreab, W., Kusky, T., and Stern, R. J., 2011, Late Cryogenian-Ediacaran history of the Arabian-Nubian Shield: A review of depositional, plutonic, structural, and tectonic events in the closing stages of the northern East African Orogen: Journal of African Earth Sciences.

Johnson, P. R., Kattan, F. H., and Al-Saleh, A. M., 2004, Neoproterozoic ophiolites in the Arabian Shield: Field relations and structure: Developments in Precambrian Geology, v. 13, p. 129-162.

Kemp, J., 1981, Geologic map of the Wadi al Ays quadrangle, sheet 25C, Kingdom of Saudi Arabia, scale 1:250,000.

Kenea, N. H., Ebinger, C. J., and Rex, D. C., 2001, Late Oligocene volcanism and extension in the southern Red Sea Hills, Sudan: Journal of the Geological Society, v. 158, no. 2, p. 285-294.

Ketcham, R. A., 2005, Forward and inverse modeling of low-temperature thermochronometry data: Reviews in mineralogy and geochemistry, v. 58, no. 1, p. 275-314.

Kohn, B. P., and Eyal, M., 1981, History of uplift of the crystalline basement of Sinai and its relation to opening of the Red Sea as revealed by fission track dating of apatites: Earth and Planetary Science Letters, v. 52, no. 1, p. 129-141.

Kohn, B. P., Eyal, M., and Feinstein, S., 1992, A major Late Devonian-Early Carboniferous (Hercynian) thermotectonic event at the NW margin of the Arabian-Nubian shield: evidence from zircon fission track dating: Tectonics, v. 11, no. 5, p. 1018-1027.

Lowell, J. D., and Genik, G. J., 1972, Sea-floor spreading and structural evolution of southern Red Sea: AAPG Bull, v. 56, no. 2, p. 247-259.

Makris, J., and Rihm, R., 1991, Shear-controlled evolution of the Red Sea: pull apart model: Tectonophysics, v. 198, no. 2, p. 441-466.

Martinez, F., and Cochran, J. R., 1988, Structure and tectonics of the northern Red Sea: Catching a continental margin between rifting and drifting: Tectonophysics, v. 150, no. 1-2, p. 1-31.

Meesters, A. G. C. A., and Dunai, T. J., 2002a, Solving the production-diffusion equation for finite diffusion domains of various shapes: Part I. Implications for low-temperature (U-Th)/He thermochronology: Chemical Geology, v. 186, no. 3-4, p. 333-344.

-, 2002b, Solving the production-diffusion equation for finite diffusion domains of various shapes: Part II. Application to cases with [alpha]-ejection and nonhomogeneous distribution of the source: Chemical Geology, v. 186, no. 3-4, p. 347-363.

Menzies, M., Gallagher, K., Yelland, A., and Hurford, A. J., 1997, Volcanic and nonvolcanic rifted margins of the Red Sea and Gulf of Aden: Crustal cooling and margin evolution in Yemen: Geochimica et Cosmochimica Acta, v. 61, no. 12, p. 2511-2527.

Menzies, M. A., Baker, J., Bosence, D., Dart, C., Davison, I., Hurford, A., Al'Kadasi, M., McClay, K., Nichols, G., and Al'Subbary, A., 1992, The timing of magmatism, uplift and crustal extension: preliminary observations from Yemen: Geological Society, London, Special Publications, v. 68, no. 1, p. 293-304.

Miller, P. M., and Barakat, H., 1988, Geology of the Safaga Concession, northern Red Sea, Egypt: Tectonophysics, v. 153, no. 1-4, p. 123-136.

Mitchell, D. J. W., Allen, R. B., Salama, W., and Abouzakm, A., 1992, Tectonostratigraphic framework and hydrocarbon potential of the Red Sea: Journal of Petroleum Geology, v. 15, p. 187-210.

Montenat, C., Ott D'Estevou, P., Purser, B., Burollet, P. F., Jarrige, J. J., Orszag-Sperber, F., Philobbos, E., Plaziat, J. C., Prat, P., and Richert, J. P., 1988, Tectonic and sedimentary evolution of the Gulf of Suez and the northwestern Red Sea: Tectonophysics, v. 153, no. 1-4, p. 161-177.

Mooney, W. D., Gettings, M. E., Blank, H. R., and Healy, J. H., 1985, Saudi Arabian seismic-refraction profile: a traveltime interpretation of crustal and upper mantle structure:

Tectonophysics, v. 111, no. 3-4, p. 173-197, 201-202, 205-206, 209-210, 213-215, 223-224, 227-246.

Moore, J. M. M., 1979, Tectonics of the Najd transcurrent fault system, Saudi Arabia: Journal of the Geological Society, v. 136, no. 4, p. 441-452.

Moufti, A. M. B., 2010, Field, Mineralogical and Geochemical Characteristics of As-Sarat Laterite Profiles, SW Saudi Arabia: Earth Sciences, v. 21, no. 2, p. 28.

Moufti, M. R., Hassanen, M. A., and Hashad, M. H., 2002, Geochemistry and petrogenesis of peralkaline-calk alkaline granites from the Radwa-Qashara Complex, Arabian Shield: Annals of the Geological Survey of Egypt, v. XXV, p. 24.

Mougenot, D., and Al-Shakhis, A. A., 1999, Depth imaging sub-salt structures: a case study in the Midyan Peninsula (Red Sea): GeoArabia, v. 4, p. 335-463.

Moustafa, A. R., 1997, Controls on the development and evolution of transfer zones: the influence of basement structure and sedimentary thickness in the Suez rift and Red Sea: Journal of Structural Geology, v. 19, no. 6, p. 755-768.

-, 2002, Controls on the geometry of transfer zones in the Suez rift and northwest Red Sea: Implications for the structural geometry of rift systems: AAPG bulletin, v. 86, no. 6, p. 979-1002.

Nehlig, P., Genna, A., and Asfirane, F., 2002, A review of the Pan-African evolution of the Arabian Shield: GEOARABIA-MANAMA-, v. 7, p. 103-124.

Omar, G. I., Kohn, B. P., Lutz, T. M., and Faul, H., 1987, The cooling history of Silurian to Cretaceous alkaline ring complexes, south Eastern Desert, Egypt, as revealed by fission-track analysis: Earth and Planetary Science Letters, v. 83, no. 1-4, p. 94-108.

Omar, G. I., and Steckler, M. S., 1995, Fission track evidence on the initial rifting of the Red Sea: two pulses, no propagation: Science, v. 270, no. 5240, p. 1341.

Omar, G. I., Steckler, M. S., Buck, W. R., and Kohn, B. P., 1989, Fission-track analysis of basement apatites at the western margin of the Gulf of Suez rift, Egypt: evidence for synchroneity of uplift and subsidence: Earth and Planetary Science Letters, v. 94, no. 3, p. 316-328.

Overstreet, W. C., Overstreet, E. F., and Goudarzi, G. H., 1973, Mineralogical and Chemical Investigation of the Laterite in the As-Sarat Mountains: Kingdom of Saudi Arabia, United State Geological SurveySaudi Arabian Project Report, v. 46, p. 66.

Overstreet, W. C., Stoeser, D. B., Overstreet, E. F., and Goudarzi, G. H., 1977, Tertiary laterite of the As Sarat Mountains, Asir Province, Kingdom of Saudi Arabia. Directorate General of Mineral Resources: Mineral Resources Bulletin, v. 21.

Pallister, J. S., 1987, Magmatic history of Red Sea rifting: Perspective from the central Saudi Arabian coastal plain: Geological Society of America Bulletin, v. 98, no. 4, p. 400-417.

Pellaton, C., 1979, Geologic map of the Yanbu al Bahr quadrangle, sheet 24C, Kingdom of Saudi Arabia, scale 1: 250,000.

Pellaton, C., and Dhellemmes, R., 1978, Geology and mineral exploration of the Jabal Dhulay'ah quadrangle 25/38A: French BRGM Technical Record 78 JED, v. 3, p. 16.

Plaziat, J. C., Baltzer, F., Choukri, A., Conchon, O., Freytet, P., Orszag-Sperber, F., Raguideau, A., and Reyss, J. L., 1998, Quaternary marine and continental sedimentation in the northern Red Sea and Gulf of Suez (Egyptian coast): influences of rift tectonics, climatic changes and sea-level fluctuations: Sedimentation and Tectonic in Rift Basins Red Sea-Gulf of Aden, p. 537-573.

Powers, R. W., Ramirez, L. F., Redmond, C. D., and Elberg, E. L., 1966, Geology of the Arabian Peninsula: Geological survey professional paper, v. 560, p. 1-147.

Prodehl, C., 1985, Interpretation of a seismic-refraction survey across the Arabian Shield in western Saudi Arabia: Tectonophysics, v. 111, no. 3-4, p. 247-282.

Purser, B. H., and Hötzl, H., 1988, The sedimentary evolution of the Red Sea rift: a comparison of the northwest (Egyptian) and northeast (Saudi Arabian) margins: Tectonophysics, v. 153, no. 1-4, p. 193-208.

Ravat, D., Salem, A., Abdelaziz, A. M. S., Elawadi, E., and Morgan, P., 2011, Probing magnetic sea bottom and crustal temperature variaitons along the Red Sea margin of Egypt: Tectonophysics, v. 510, p. 7.

Reiners, P. W., 2005, Zircon (U-Th)/He thermochronometry: Reviews in mineralogy and geochemistry, v. 58, no. 1, p. 151-179.

Reiners, P. W., Ehlers, T. A., and Zeitler, P. K., 2005, Past, present, and future of thermochronology: Reviews in mineralogy and geochemistry, v. 58, no. 1, p. 1-18.

Reiners, P. W., and Farley, K. A., 2001, Influence of crystal size on apatite (U–Th)/He thermochronology: an example from the Bighorn Mountains, Wyoming: Earth and Planetary Science Letters, v. 188, no. 3, p. 413-420.

Reiners, P. W., Farley, K. A., and Hickes, H. J., 2002, He diffusion and (U-Th)/He thermochronometry of zircon: initial results from Fish Canyon Tuff and Gold Butte: Tectonophysics, v. 349, no. 1-4, p. 297-308.

Reiners, P. W., Spell, T. L., Nicolescu, S., and Zanetti, K. A., 2004, Zircon (U-Th)/He thermochronometry: He diffusion and comparisons with 40Ar/39Ar dating: Geochimica et Cosmochimica Acta, v. 68, no. 8, p. 1857-1887.

Richardson, M., and Arthur, M. A., 1988, The Gulf of Suez--northern Red Sea neogene rift: a quantitive basin analysis: Marine and Petroleum Geology, v. 5, no. 3, p. 247-270.

Roobol, M. J., and Kadi, K. A., 2008, Cenozoic Faulting in the Rabigh Area, Central West Saudi Arabia (includingthe sites of King Abdullah Economic City and King Abdullah University for Science and Technology).

Roobol, M. J., and Stewart, I. C. F., 2009, Cenozoic Faults and Recent Seismicity in Northwest Saudi Arabia and the Gulf of Aqaba Region.

Ryan, W. B. F., Carbotte, S. M., Coplan, J. O., O'Hara, S., Melkonian, A., Arko, R., Weissel, R. A., Ferrini, V., Goodwillie, A., and Nitsche, F., 2009, Global multi-resolution topography synthesis: Geochemistry Geophysics Geosystems, v. 10, no. Q03014.

Schmeling, H., 2010, Dynamic models of continental rifting with melt generation: Tectonophysics, v. 480, no. 1-4, p. 33-47.

Schmidt, D. L., Hadley, D. G., and Brown, G. F., 1983, Middle Tertiary continental rift and evolution of the Red Sea in southwestern Saudi Arabia: US Department of the Interior, Geological Survey.

Sebai, A., Zumbo, V., Féraud, G., Bertrand, H., Hussain, A., Giannerini, G., and Campredon, R., 1991, 40Ar/39Ar dating of alkaline and tholeiitic magmatism of Saudi Arabia related to the early Red Sea Rifting: Earth and Planetary Science Letters, v. 104, no. 2, p. 473-487.

Sengör, A. M. C., and Burke, K., 1978, Relative timing of rifting and volcanism on Earth and its tectonic implications: Geophysical Research Letters, v. 5, no. 6, p. 419-421.

Sharland, P. R., Archer, R., Casey, D. M., Davies, R. B., Hall, S. H., Heyward, A. P., Horbury, A. D., and Simmons, M. D., 2001, Arabian Plate Sequence Stratigraphy, Gulf PetroLink, GeoArabia Special Publication 2, 371 p.:

Shuster, D. L., and Farley, K. A., 2009, The influence of artificial radiation damage and thermal annealing on helium diffusion kinetics in apatite: Geochimica et Cosmochimica Acta, v. 73, no. 1, p. 183-196.

Shuster, D. L., Flowers, R. M., and Farley, K. A., 2006, The influence of natural radiation damage on helium diffusion kinetics in apatite: Earth and Planetary Science Letters, v. 249, no. 3, p. 148-161.

Steckler, M. S., and Omar, G. I., 1994, Controls on erosional retreat of the uplifted rift flanks at the Gulf of Suez and northern Red Sea: Journal of Geophysical Research, v. 99, no. B6, p. 12159-12112,12173.

Steckler, M. S., and ten Brink, U. S., 1986, Lithospheric strength variations as a control on new plate boundaries: examples from the northern Red Sea region: Earth and Planetary Science Letters, v. 79, no. 1-2, p. 120-132.

Stern, R. J., 1985, The Najd Fault System, Saudi Arabia and Egypt: A Late Precambrian rift-related transform system?: Tectonics, v. 4, no. 5, p. 497-511.

-, 1994, Arc-Assembly and Continental Collision in the Neoproterozoic African Orogen: Implications for the Consolidation of Gondwanaland: Annual Review of Earth and Planetary Sciences, v. 22, p. 319-351.

Stern, R. J., and Johnson, P., 2010, Continental lithosphere of the Arabian Plate: a geologic, petrologic, and geophysical synthesis: Earth-Science Reviews, v. 101, no. 1-2, p. 29-67.

Stern, R. J., Johnson, P. R., Kröner, A., and Yibas, B., 2004, Neoproterozoic Ophiolites of the Arabian-Nubian Shield: Developments in Precambrian Geology, v. 13, p. 95-128.

Stewart, I. C. F., Connally, T. C., and Copley, J. H., 1996, Stratigraphic Interpretation of Magnetotelluric Data in Central Saudi Arabia: GeoArabia, v. 1, no. 1, p. 11.

Stockli, D. F., 2005, Application of low-temperature thermochronometry to extensional tectonic settings: Reviews in mineralogy and geochemistry, v. 58, no. 1, p. 411-448.

Stockli, D. F., Farley, K. A., and Dumitru, T. A., 2000, Calibration of the apatite (U-Th)/He thermochronometer on an exhumed fault block, White Mountains, California: Geology, v. 28, no. 11, p. 983-986.

Sultan, M., Becker, R., Arvidson, R. E., Shore, P., Stern, R. J., El Alfy, Z., and Attia, R., 1993, New constraints on Red Sea rifting from correlations of Arabian and Nubian Neoproterozoic outcrops: Tectonics, v. 12, no. 6, p. 1303-1319.

Sultan, M., Becker, R., Arvidson, R. E., Shore, P., Stern, R. J., El Alfy, Z., and Guinness, E. A., 1992, Nature of the Red Sea crust: A controversy revisited: Geology, v. 20, no. 7, p. 593-596.

Survey, U. S. G., 1993, Quarterly progress report of the USGS Mission, Kingdom of Saudi Arabia, for the second quarter of the fiscal year 1993.

Talbot, C. J., and Ghebreab, W., 1997, Red Sea detachment and basement core complexes in Eritrea: Geology, v. 25, no. 7, p. 655-658.

Ukstins, I. A., Renne, P. R., Wolfenden, E., Baker, J., Ayalew, D., and Menzies, M., 2002, Matching conjugate volcanic rifted margins:< sup> 40</sup> Ar/< sup> 39</sup> Ar chrono-stratigraphy of pre-and syn-rift bimodal flood volcanism in Ethiopia and Yemen: Earth and Planetary Science Letters, v. 198, no. 3, p. 289-306.

van der Beek, P., Cloetingh, S., and Andriessen, P., 1994, Mechanisms of extensional basin formation and vertical motions at rift flanks: Constraints from tectonic modelling and fission-track thermochronology: Earth and Planetary Science Letters, v. 121, no. 3-4, p. 417-433.

Voggenreiter, W., Hötzl, H., and Mechie, J., 1988, Low-angle detachment origin for the Red Sea Rift system?: Tectonophysics, v. 150, no. 1-2, p. 51-56, 58-75.

Wolf, R. A., Farley, K. A., and Silver, L. T., 1996, Helium diffusion and low-temperature thermochronometry of apatite: Geochimica et Cosmochimica Acta, v. 60, no. 21, p. 4231-4240.

Wolfe, M. R., and Stockli, D. F., 2010, Zircon (U–Th)/He thermochronometry in the KTB drill hole, Germany, and its implications for bulk He diffusion kinetics in zircon: Earth and Planetary Science Letters, v. 295, no. 1, p. 69-82.

Wolfenden, E., Ebinger, C., Yirgu, G., Renne, P. R., and Kelley, S. P., 2005, Evolution of a volcanic rifted margin: Southern Red Sea, Ethiopia: Geological Society of America Bulletin, v. 117, no. 7-8, p. 846-864.

Zahran, H. M., McCausland, W. A., Pallister, J. S., Lu, Z., El-Hadidy, S., Aburukba, A., Schawali, J., Kadi, K., Youssef, A., and Ewert, J. W., Stalled eruption or dike intrusion at Harrat Lunayyir, Saudi Arabia?2009, Volume 1, p. 2072.

Zahran, H. M., Stewart, I. C. F., Johnson, P. R., and Basahel, M. H., 2002, Aeromagnetic-anomaly maps of central and western Saudi Arabia, scale 1:2,000,000.

Zeyen, H., Volker, F., Wehrle, V., Fuchs, K., Sobolev, S. V., and Altherr, R., 1997, Styles of continental rifting: crust-mantle detachment and mantle plumes: Tectonophysics, v. 278, no. 1-4, p. 329-352.

Ziab, A. M., and Ramsay, C. R., 1986, Geologic map of the Turbah quadrangle, sheet 21E, Kingdom of Saudi Arabia, scale 1:250,000.

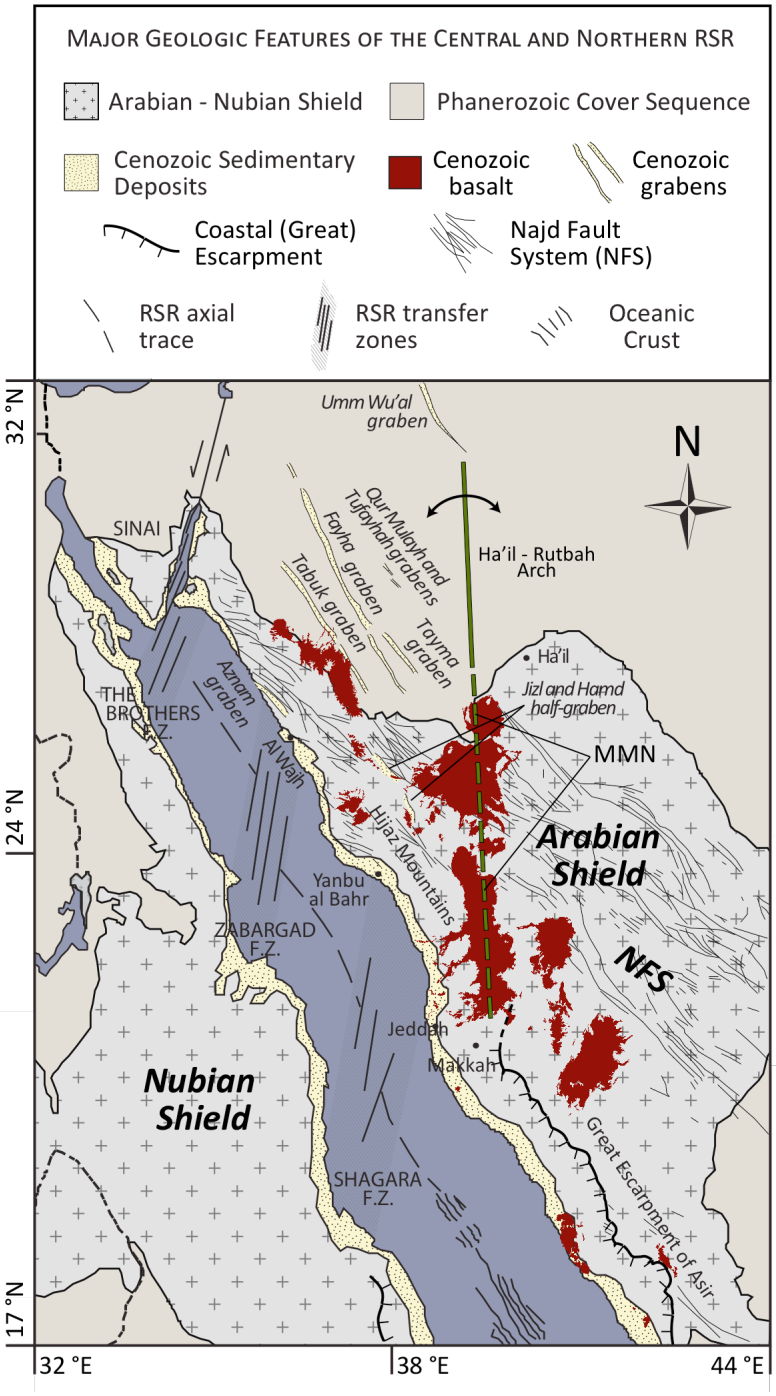
MAJOR GEOLOGIC FEATURES OF THE CENTRAL AND NORTHERN RSR
Arabian - Nubian Shield
Phanerozoic Cover Sequence
Cenozoic Sedimentary Deposits
Cenozoic basalt
Cenozoic grabens
Coastal (Great) Escarpment
Najd Fault System (NFS)
RSR axial trace
RSR transfer zones
Oceanic Crust
32 °N
24 °N
17 °N
32 °E
38 °E
44 °E
N
Umm Wu'al graben
Qur Mulayh and Tufaylah grabens
Fayha graben
Tabuk graben
Tayma graben
Ha'il - Rutbah Arch
Ha'il
Jizl and Hamd half-graben
MMN
SINAI
THE BROTHERS F.Z.
Aznam graben
Al Wajh
Hijaz Mountains
Yanbu al Bahr
ZABARGAD F.Z.
Arabian Shield
NFS
Jeddah
Makkah
Nubian Shield
SHAGARA F.Z.
Great Escarpment of Asir

Figure 1 - Major Geologic Features of the Central and Northern Red Sea Rift

Large-scale geologic features within the central and northern Arabian rift flank include Cenozoic harrat with a highlighted trend of the Makkah-Medina-Nafud volcanic line (MMN, *Camp and Roobol, 1992*), fracture zones that comprise right-lateral transform faults to offset the RSR axial trough (*Coleman, 1987; Dixon et al., 1987, 1989*), graben and half-graben internal to the rift flank (Johnson, 1998), and transform faults of the Precambrian Najd Fault System (NFS; Brown and Jackson, 1960 *in* Moore, 1979).

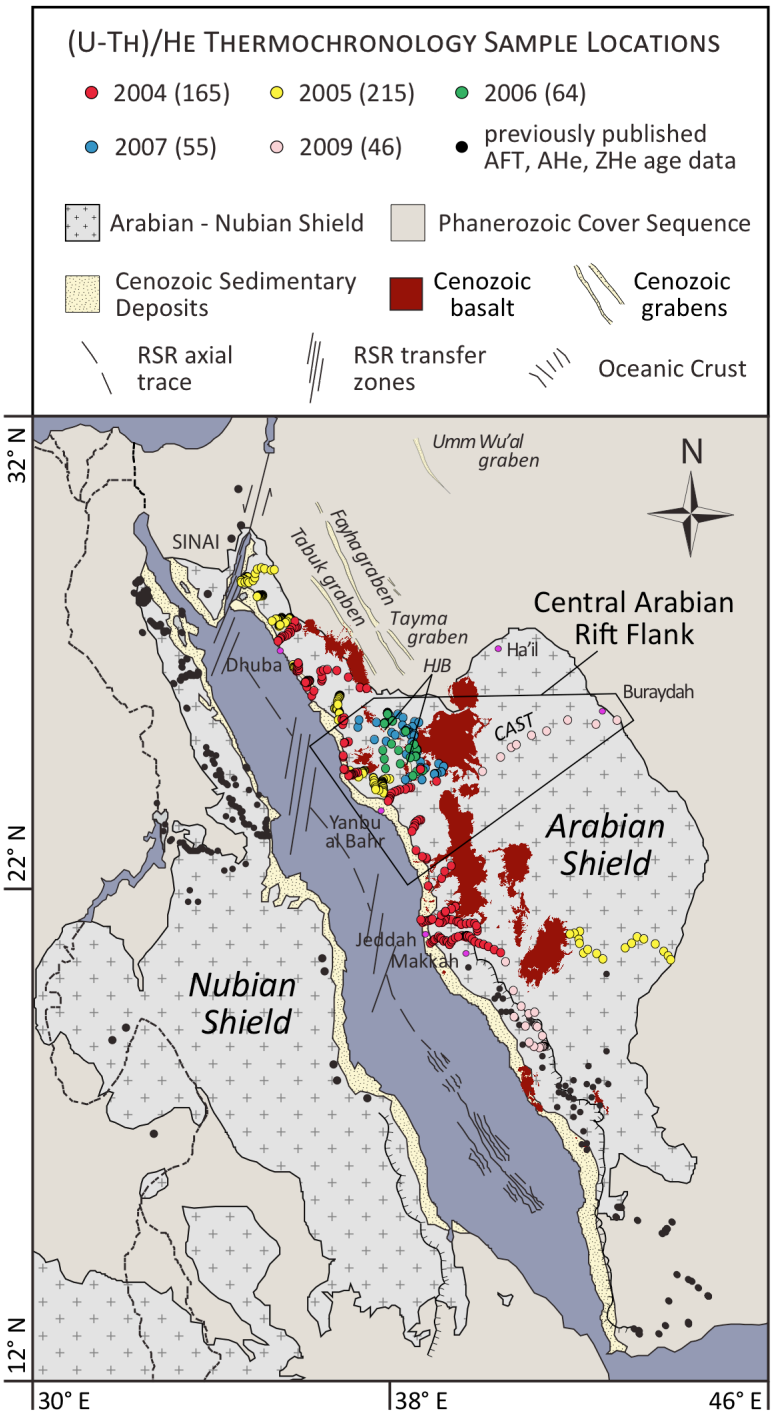
(U-Th)/He Thermochronology Sample Locations
2004 (165)
2005 (215)
2006 (64)
2007 (55)
2009 (46)
previously published AFT, AHe, ZHe age data
Arabian - Nubian Shield
Phanerozoic Cover Sequence
Cenozoic Sedimentary Deposits
Cenozoic basalt
Cenozoic grabens
RSR axial trace
RSR transfer zones
Oceanic Crust
N
Umm Wu'al graben
SINAI
Tabuk graben
Fayha graben
Tayma graben
Central Arabian Rift Flank
Dhuba
HJB
Ha'il
Buraydah
CAST
Yanbu al Bahr
Arabian Shield
Jeddah
Makkah
Nubian Shield
32° N
22° N
12° N
30° E
38° E
46° E

Figure 2 - Red Sea Rift Apatite and Zircon (U-Th)/He Sample Locations

Total rock samples collected along the Arabian rift flank for thermochronological analysis with number of samples collected *per annum* noted parenthetically. Samples analyzed for this study fall within *Central Arabian Rift Flank* bounding box (Tables 1 and 2; Fig. 3). CAST = Central Arabian Shield Transect. Previously published apatite fission-track (AFT) and apatite and zircon (U-Th)/He thermochronology sample locations on Sinai and the southern Arabian and Nubian rift flanks from Kohn and Eyal (1981), Bohannon (1986), Bohannon et al. (1989), Omar et al. (1987, 1989), Davidson et al. (1994), Steckler and Omar (1994), Omar and Steckler (1995), Menzies et al. (1997), Kenea et al. (2001), Abbate et al. (2002), Ghebreab et al. (2002), and Balestrieri et al. (2009).

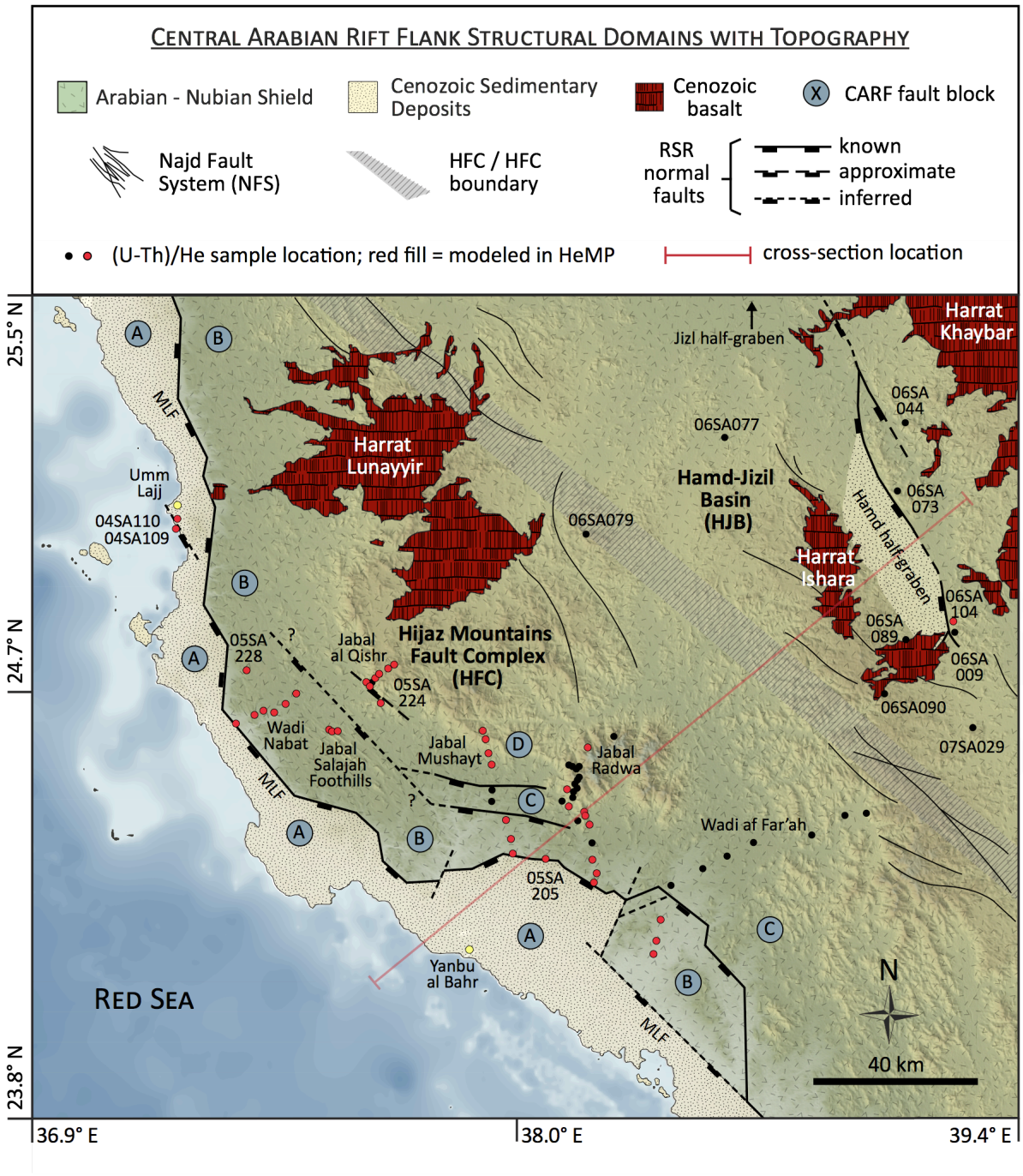
CENTRAL ARABIAN RIFT FLANK STRUCTURAL DOMAINS WITH TOPOGRAPHY
Arabian - Nubian Shield
Cenozoic Sedimentary Deposits
Cenozoic basalt
CARF fault block
Najd Fault System (NFS)
HFC / HFC boundary
RSR normal faults
known
approximate
inferred
(U-Th)/He sample location; red fill = modeled in HeMP
cross-section location
25.5° N
24.7° N
23.8° N
36.9° E
38.0° E
39.4° E
Harrat Khaybar
Jizl half-graben
06SA 044
06SA077
Harrat Lunayyir
Hamd-Jizil Basin (HJB)
06SA 073
Umm Lajj
04SA110
04SA109
06SA079
Hamd half-graben
Harrat Ishara
06SA 104
06SA 089
06SA 009
06SA090
07SA029
05SA 228
Jabal al Qishr
Hijaz Mountains Fault Complex (HFC)
05SA 224
Wadi Nabat
Jabal Salajah Foothills
Jabal Mushayt
Jabal Radwa
Wadi af Far'ah
05SA 205
Yanbu al Bahr
RED SEA
MLF
A
B
C
D
N
40 km

Figure 3 - Central Arabian Rift Flank Structural Domains

Position of the Hijaz Mountains Fault Complex (HFC) and Hamd-Jizil Basin (HJB) structural domains within the central Arabian rift flank (CARF). Mapped faults are either master faults that delineate structural domain boundaries, including crustal-scale fault blocks normally rotated to accommodate extension in the HFC, or smaller-scale, intra-domain fault blocks that accommodate local deformation. Precambrian and Cenozoic fault locations derived from raw AHe and ZHe age trends, *HeMP* thermal models, and the following: Najd Fault System from Moore (1979); HFC from Pellaton (1979), Master Listric Fault from Roobol and Kadi (MLF; 2008); and HJB from Szymanski et al. (*in prep.*). Black circles indicate AHe and ZHe sample locations and highlighted red if incorporated into *HeMP* thermal models. Deeper relative water depth of Red Sea indicated by darker blue color.

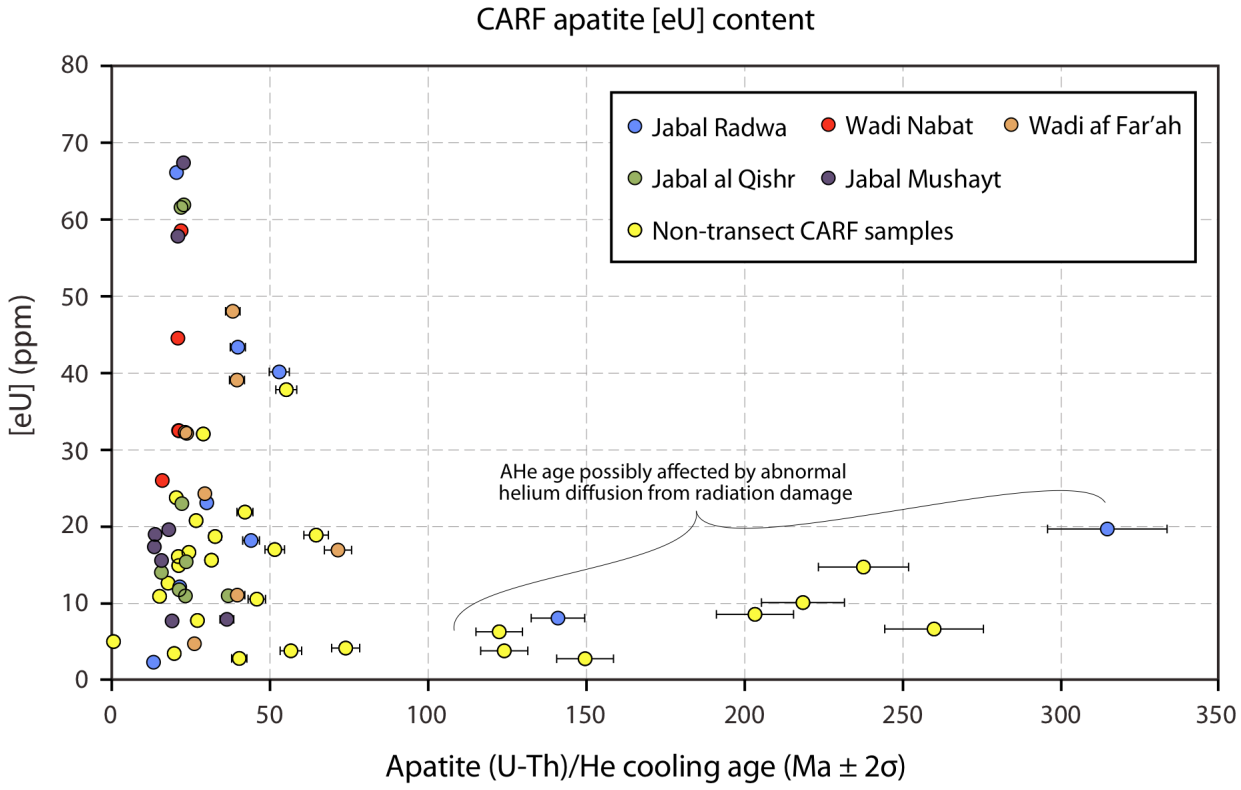
CARF apatite [eU] content
[eU] (ppm)
Apatite (U-Th)/He cooling age (Ma ± 2σ)
Jabal Radwa
Wadi Nabat
Wadi af Far'ah
Jabal al Qishr
Jabal Mushayt
Non-transect CARF samples
AHe age possibly affected by abnormal
helium diffusion from radiation damage
0
10
20
30
40
50
60
70
80
0
50
100
150
200
250
300
350

Figure 4 - Effective Uranium Concentration [eU] of CARF Apatite

Five multi-sample array transects (grouped by color) show no correlation between [eU] and AHe age, indicating no radiation damage control on AHe age. Some remaining CARF apatite (yellow circles) show a weak non-linear positive correlation, indicative of radiation damage-controlled diffusion. Two samples with anomalously high [eU] not illustrated in plot: 05SA214 (23.2 ± 1.4 Ma; 168.9 ppm) and 07SA029 (38.7 ± 2.3 Ma; 209.7 ppm).

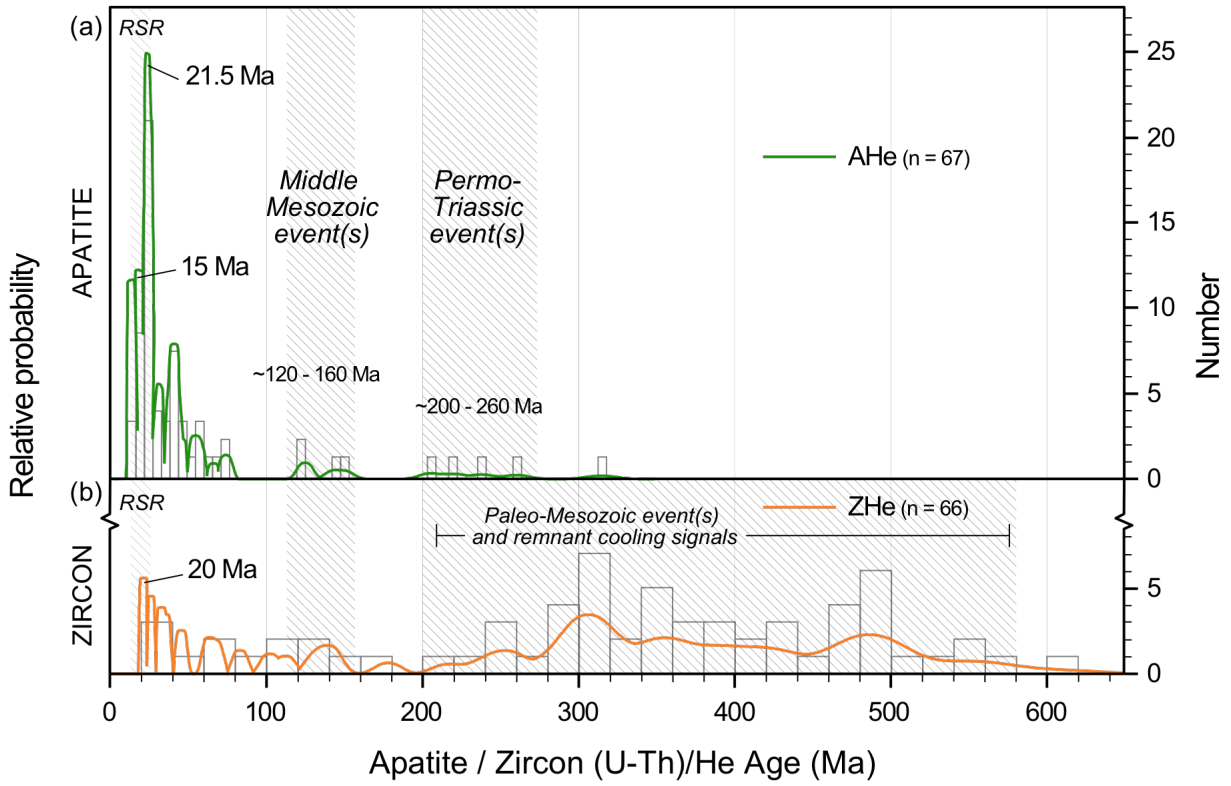
(a)
RSR
21.5 Ma
15 Ma
Middle
Mesozoic
event(s)
Permo-
Triassic
event(s)
~120 - 160 Ma
~200 - 260 Ma
AHe (n = 67)
APATITE
(b)
RSR
20 Ma
Paleo-Mesozoic event(s)
and remnant cooling signals
ZHe (n = 66)
ZIRCON
Relative probability
Number
0
5
10
15
20
25
0
5
0
100
200
300
400
500
600
Apatite / Zircon (U-Th)/He Age (Ma)

Figure 5 - CARF AHe and ZHe Age Relative Probability Plot

AHe (a) and ZHe (b) ages from all analyzed CARF bedrock samples. Vertical scale normalized between (a) and (b). Bin size 5 m.y. for AHe and 20 m.y. for ZHe. 'n' = number of sample ages included in determination (*'y-axis' right*). See Tables 5 and 6 for age data. Shaded areas indicate AHe and ZHe age clusters that may represent older, regional cooling events.

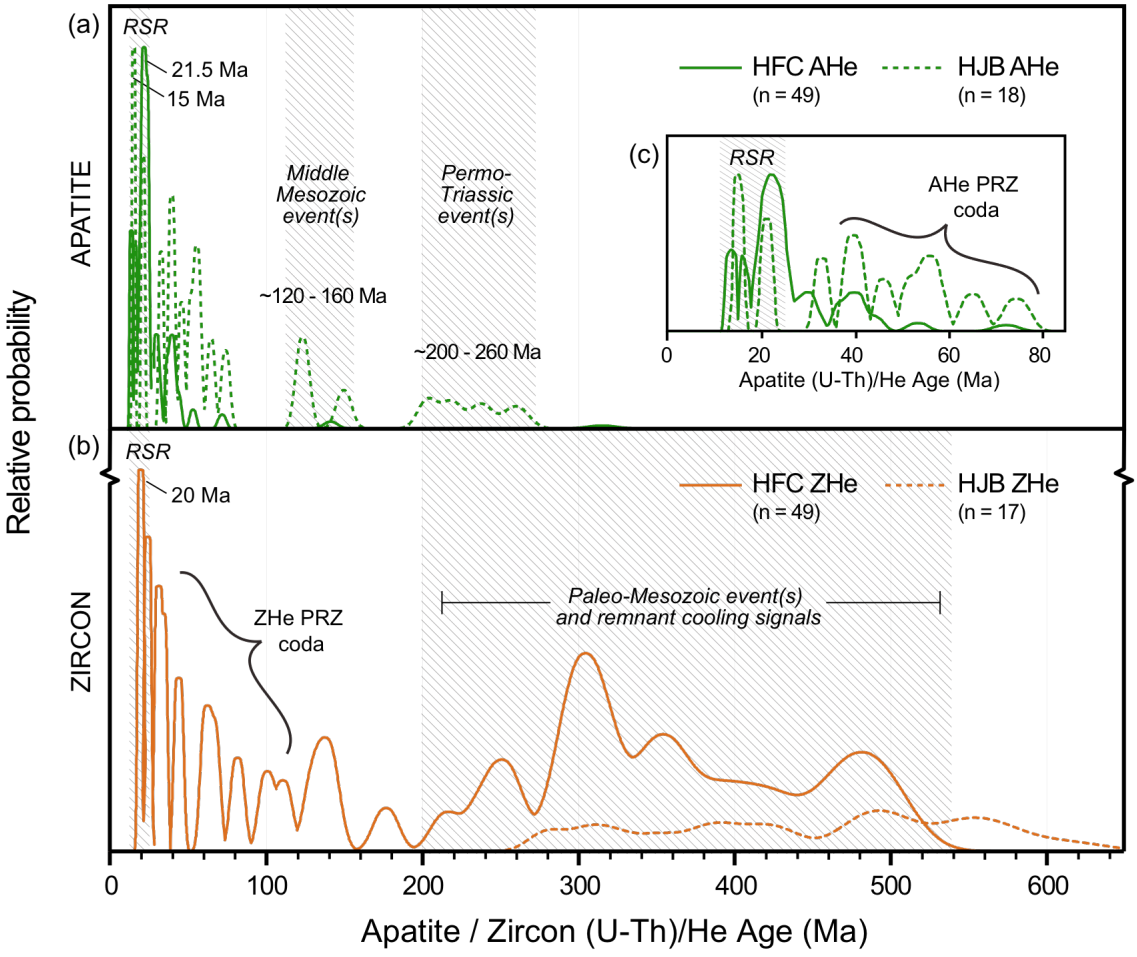
(a)
RSR
21.5 Ma
15 Ma
APATITE
Middle Mesozoic event(s)
Permo-Triassic event(s)
~120 - 160 Ma
~200 - 260 Ma
HFC AHe
(n = 49)
HJB AHe
(n = 18)
(c)
RSR
AHe PRZ coda
0
20
40
60
80
Apatite (U-Th)/He Age (Ma)
(b)
RSR
20 Ma
ZIRCON
ZHe PRZ coda
Paleo-Mesozoic event(s) and remnant cooling signals
HFC ZHe
(n = 49)
HJB ZHe
(n = 17)
Relative probability
0
100
200
300
400
500
600
Apatite / Zircon (U-Th)/He Age (Ma)

Figure 6 - HFC and HJB AHe and ZHe Age Relative Probability Plots

Comparison of bedrock AHe (a) and ZHe (b) ages between the Hijaz Mountains Fault Complex (solid line) and the Hamd-Jizl Basin (dashed line) structural domains, including the Central Arabian Shield Transect (Tables 1 and 2). Late Cretaceous and younger detail of HFC and HJB AHe age distribution in (c). Vertical scale normalized between subplot (a) and (b). Bin size 5 m.y. for AHe and 20 m.y. for ZHe. 'n' = number of sample ages included in each determination. Shaded areas indicate AHe and ZHe age clusters that may represent older, regional cooling events. The rapid decrease in peak height with increasing age through the Eocene is highly indicative of extensional terranes with rapidly cooled samples.

These plots showcase exceptional differences in the AHe and ZHe thermal records of each structural domain. Overlapping ages from multiple samples that span a wide geographic range likely signify a common, CARF-wide exhumation phase (shaded regions). In contrast, single-sample nodes are not particularly useful for drawing conclusions about exhumation timing as they often come from point locations that lack nearby intra-block samples to provide context. Each of the HFC AHe ages represents samples collected from the footwall of crystalline basement fault blocks.

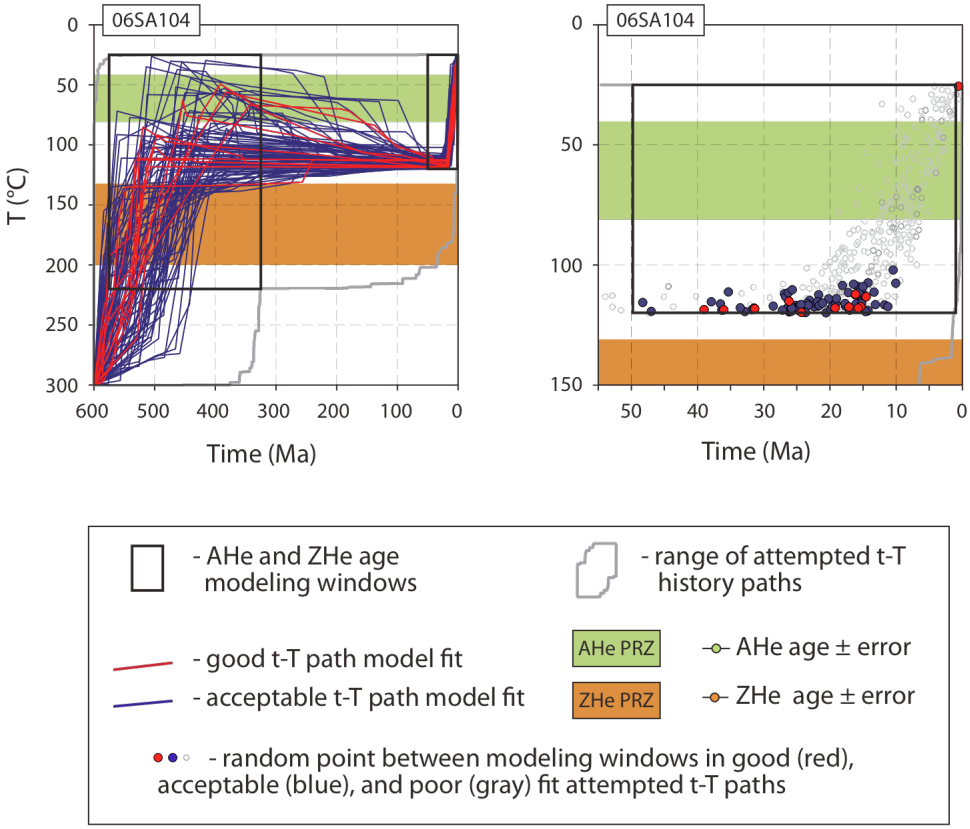
06SA104
T (°C)
Time (Ma)
06SA104
Time (Ma)
- AHe and ZHe age modeling windows
- range of attempted t-T history paths
- good t-T path model fit
- acceptable t-T path model fit
AHe PRZ
ZHe PRZ
AHe age ± error
ZHe age ± error
- random point between modeling windows in good (red), acceptable (blue), and poor (gray) fit attempted t-T paths

Figure 7 - 06SA104: Thermal Models

HeMP time-temperature plots for single sample model 06SA104. Sample age data in Table 2. Left column shows acceptable t-T path fits of sample data for the full-modeled history. Right column shows Cenozoic detail with t-T nodes.

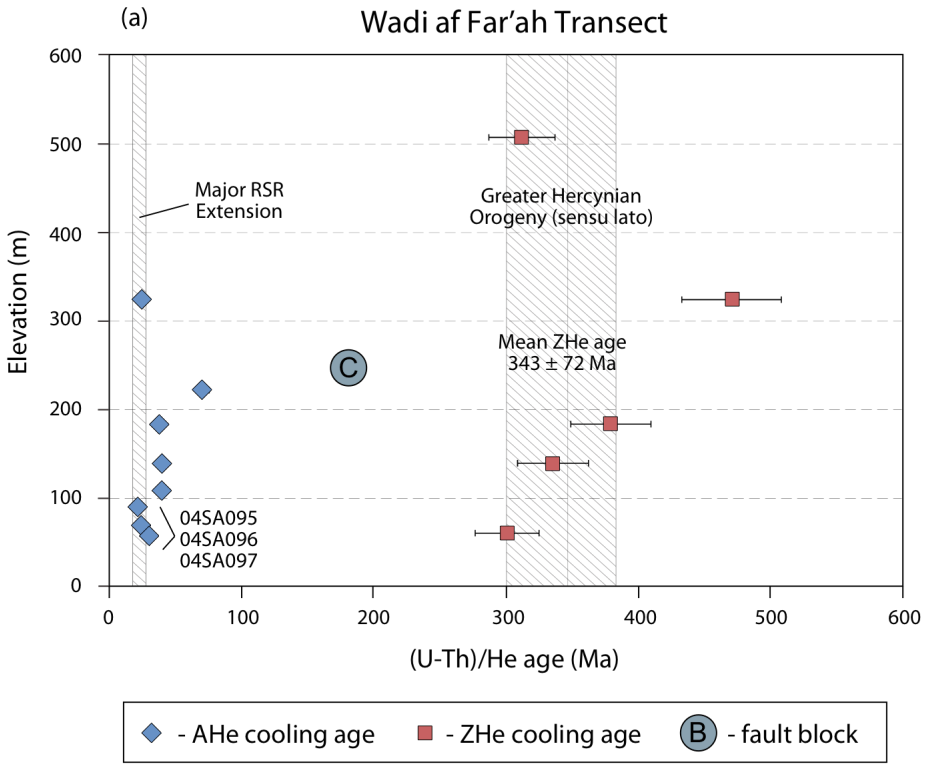
(a)
Wadi af Far'ah Transect
Elevation (m)
(U-Th)/He age (Ma)
Major RSR Extension
Greater Hercynian Orogeny (sensu lato)
Mean ZHe age 343 ± 72 Ma
C
04SA095
04SA096
04SA097
- AHe cooling age
- ZHe cooling age
B - fault block

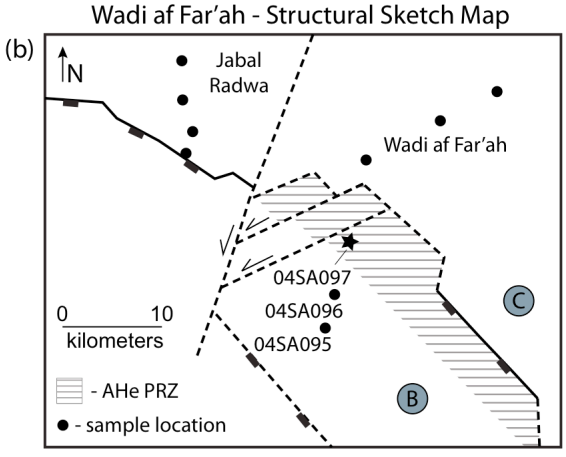
Wadi af Far'ah - Structural Sketch Map
(b)
N
Jabal Radwa
Wadi af Far'ah
04SA097
04SA096
04SA095
0 10
kilometers
- AHe PRZ
- sample location
C
B

Figure 8 - Wadi af Far'ah: (U-Th)/He Age vs. Elevation Plot

(a) Blue diamonds and red squares represent AHe and ZHe cooling ages, respectively. Error bars show 2σ mean age error. Sample age data is listed in Table 1. Blue circle indicates location of sample transect in HFC fault block. See Figure 3 for CARF structural domain map. Shaded areas bracket periods of major regional tectonic events. (b) Structural sketch map indicates sample location relative to idealized fault geometry. Location of block-bounding faults is diagramatic. Star indicates position of 04SA097 in AHe PRZ of Block B.

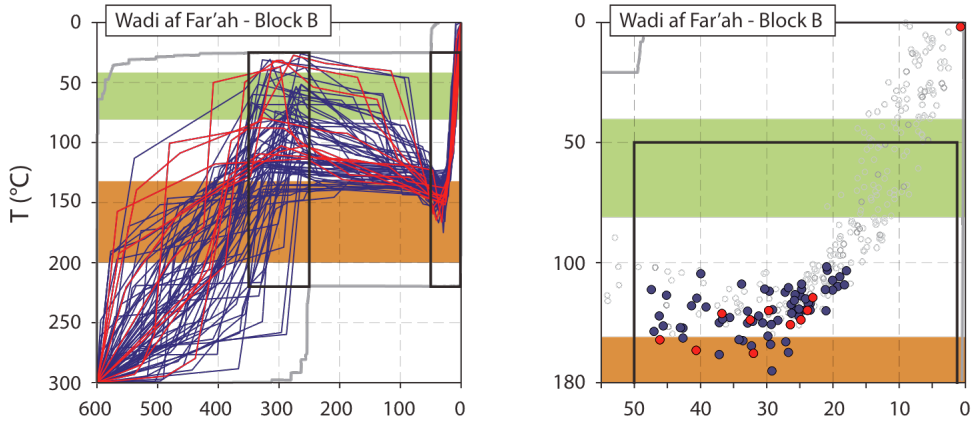
Wadi af Far'ah - Block B
T (°C)
0
50
100
150
200
250
300
600
500
400
300
200
100
0
Wadi af Far'ah - Block B
0
50
100
180
50
40
30
20
10
0

Figure 9 - Wadi af Far'ah-Block B: Thermal Models

HeMP time-temperature plots for single sample model Wadi af Far'ah-Block B. Left column shows acceptable t-T path fits of sample data for the full-modeled history. Right column shows Cenozoic detail with t-T nodes. See Figure 7 for legend.

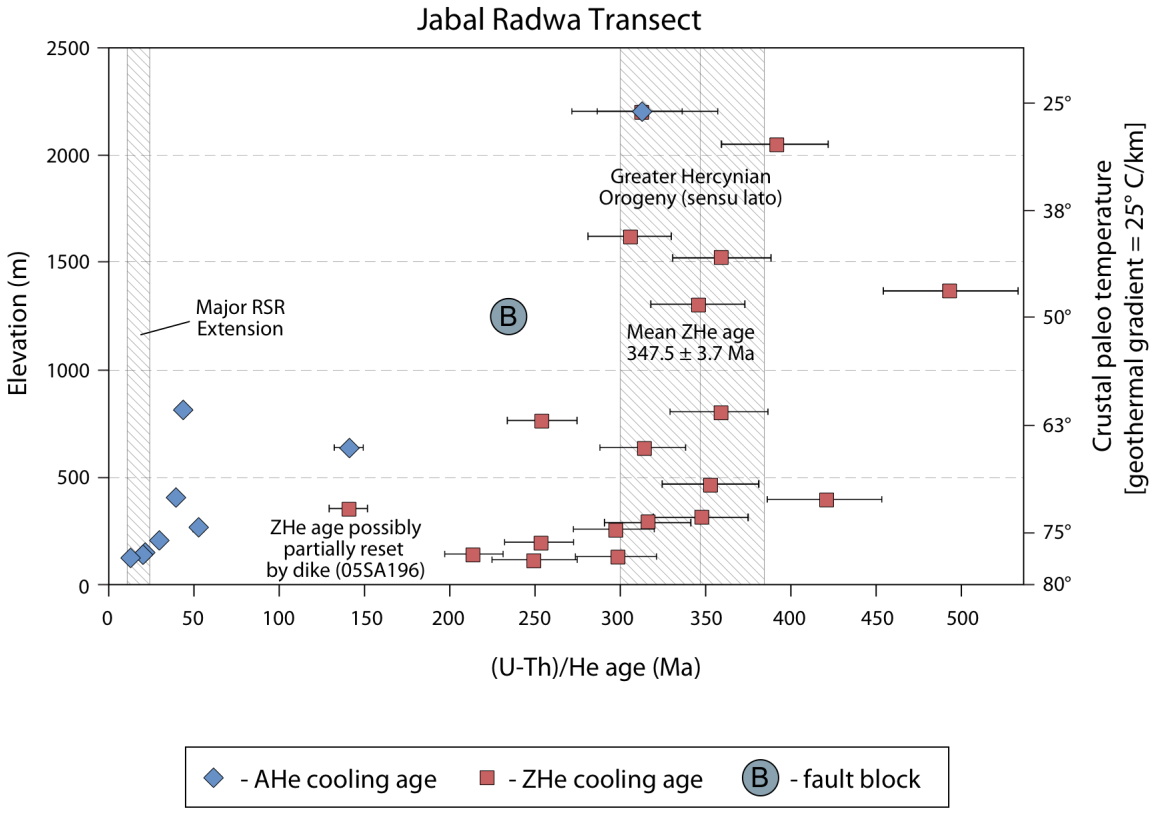
Jabal Radwa Transect
Elevation (m)
2500
2000
1500
1000
500
0
0
50
100
150
200
250
300
350
400
450
500
(U-Th)/He age (Ma)
Crustal paleo temperature
[geothermal gradient = 25° C/km]
25°
38°
50°
63°
75°
80°
Greater Hercynian
Orogeny (sensu lato)
Major RSR
Extension
B
Mean ZHe age
347.5 ± 3.7 Ma
ZHe age possibly
partially reset
by dike (05SA196)
- AHe cooling age
- ZHe cooling age
B - fault block

Figure 10 - Jabal Radwa: (U-Th)/He Age vs. Elevation Plot

Blue diamonds and red squares represent AHe and ZHe cooling ages, respectively. Error bars show 2σ mean age error. Sample age data is listed in Table 1. Blue circle indicates location of sample transect in HFC fault block. See Figure 3 for CARF structural domain map. Shaded areas bracket periods of major regional tectonic events.

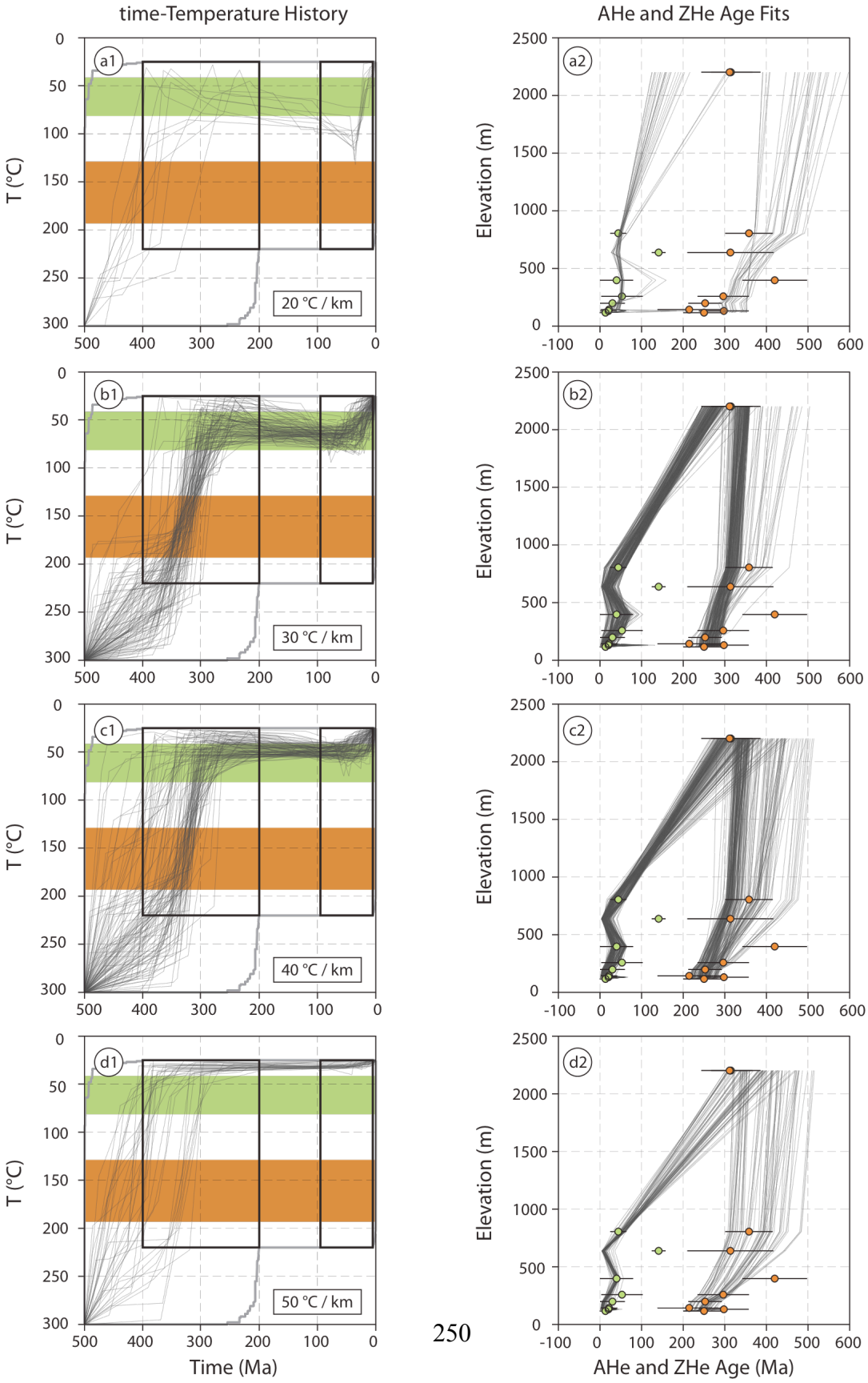
time-Temperature History
AHe and ZHe Age Fits
a1
a2
b1
b2
c1
c2
d1
d2
20 °C / km
30 °C / km
40 °C / km
50 °C / km
T (°C)
Elevation (m)
Time (Ma)
AHe and ZHe Age (Ma)

Figure 11 - Jabal Radwa: Thermal Models

HeMP time-temperature plots for the Jabal Radwa multi-sample array. Left column shows acceptable t-T path fits of sample data for the full-modeled history (a1-d1) for four different paleo-geothermal gradients (20, 30, 40, and 50 °C/km). Right column shows adherence of acceptable t-T paths to raw mean AHe and ZHe ages and errors for each paleo-geothermal gradient (a2-d2). The best t-T path fits are seen in the 30 and 40 50 °C/km models (b2 and c2). See Figure 7 for legend.

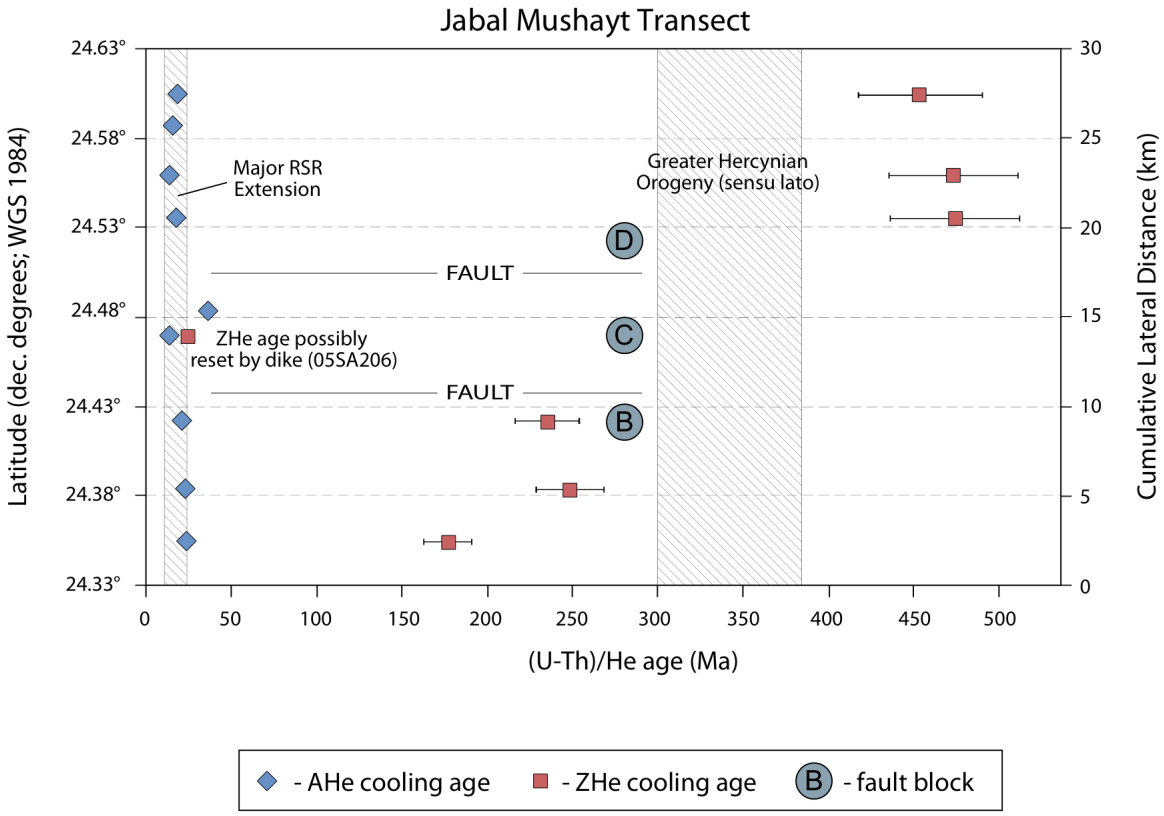
Jabal Mushayt Transect
Latitude (dec. degrees; WGS 1984)
24.63°
24.58°
24.53°
24.48°
24.43°
24.38°
24.33°
Cumulative Lateral Distance (km)
30
25
20
15
10
5
0
0
50
100
150
200
250
300
350
400
450
500
(U-Th)/He age (Ma)
Major RSR
Extension
Greater Hercynian
Orogeny (sensu lato)
D
FAULT
C
ZHe age possibly
reset by dike (05SA206)
FAULT
B
- AHe cooling age
- ZHe cooling age
B
- fault block

Figure 12 - Jabal Mushayt: (U-Th)/He Age vs. Elevation Plot

Blue diamonds and red squares represent AHe and ZHe cooling ages, respectively. Error bars show 2σ mean age error. Sample age data is listed in Table 1. Blue circle indicates location of sample transect in HFC fault block. Location of block-bounding faults is diagramatic. See Figure 3 for CARF structural domain map. Shaded areas bracket periods of major regional tectonic events.

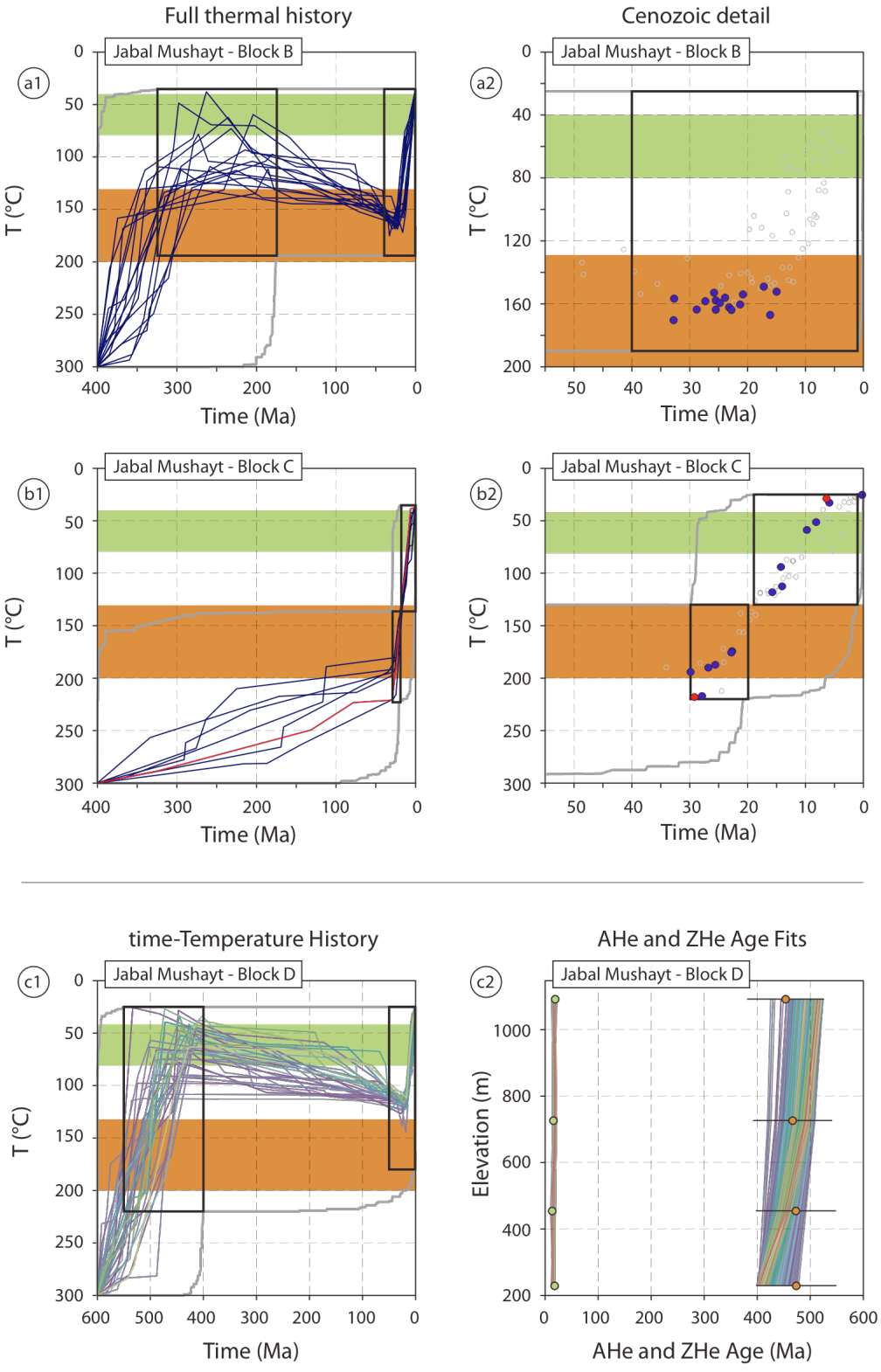
Full thermal history
Cenozoic detail
Jabal Mushayt - Block B
a1
a2
T (°C)
Time (Ma)
Jabal Mushayt - Block C
b1
b2
time-Temperature History
AHe and ZHe Age Fits
Jabal Mushayt - Block D
c1
c2
Elevation (m)
AHe and ZHe Age (Ma)

Figure 13 - Jabal Mushayt: Thermal Models

HeMP time-temperature plots for Jabal Mushayt; Blocks B and C are single sample models and Block D is a multi-sample array. Left column shows acceptable t-T path fits of sample data for the full-modeled history (a1, b1, and c1). Right column shows Cenozoic detail with t-T nodes for single sample models (a2 and b2) and adherence of acceptable t-T paths to raw mean AHe and ZHe ages and errors for the multi-sample array (c2). See Figure 7 for legend.

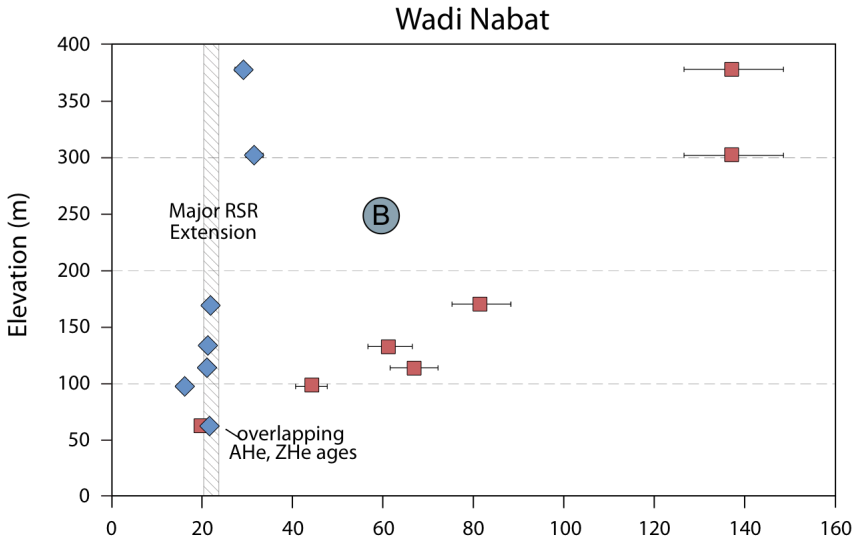
Wadi Nabat
Elevation (m)
Major RSR
Extension
B
overlapping
AHe, ZHe ages
0
50
100
150
200
250
300
350
400
0
20
40
60
80
100
120
140
160

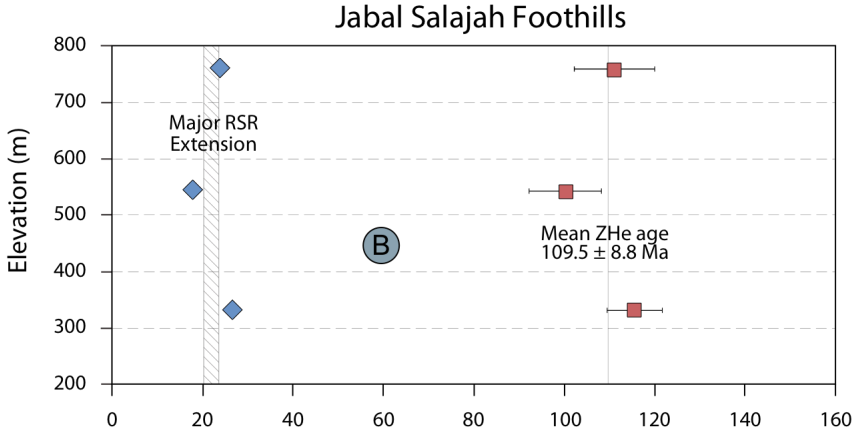
Jabal Salajah Foothills
Elevation (m)
Major RSR
Extension
B
Mean ZHe age
109.5 ± 8.8 Ma
200
300
400
500
600
700
800
0
20
40
60
80
100
120
140
160

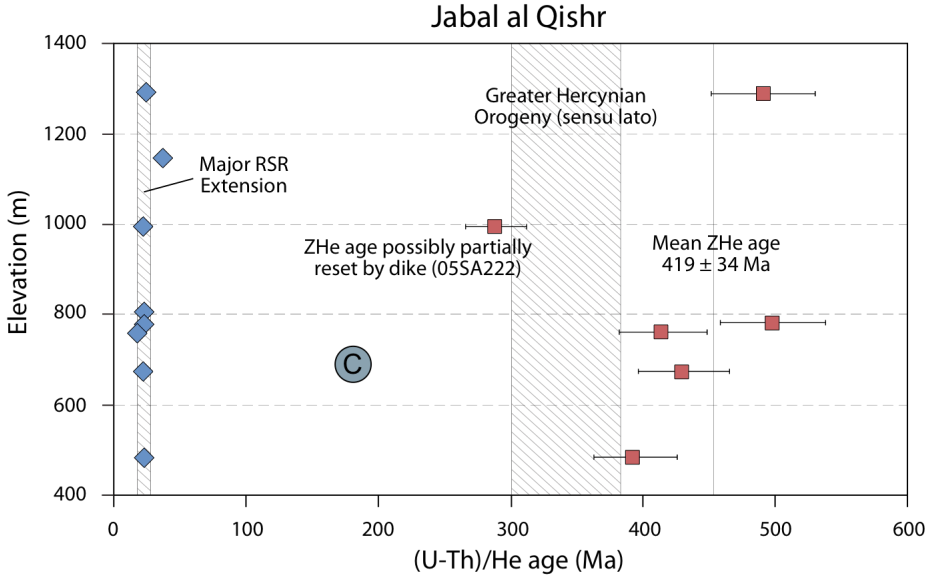
Jabal al Qishr
Elevation (m)
Greater Hercynian
Orogeny (sensu lato)
Major RSR
Extension
ZHe age possibly partially
reset by dike (05SA222)
Mean ZHe age
419 ± 34 Ma
C
400
600
800
1000
1200
1400
0
100
200
300
400
500
600
(U-Th)/He age (Ma)

Figure 14 - Wadi Nabat, Jabal Salajah Foothills, Jabal al Qishr: (U-Th)/He Age vs. Elevation Plot

Blue diamonds and red squares represent AHe and ZHe cooling ages, respectively. Error bars show 2σ mean age error. Sample age data is listed in Table 1. Blue circle indicates location of sample transect in HFC fault block. See Figure 3 for CARF structural domain map. Shaded areas bracket periods of major regional tectonic events.

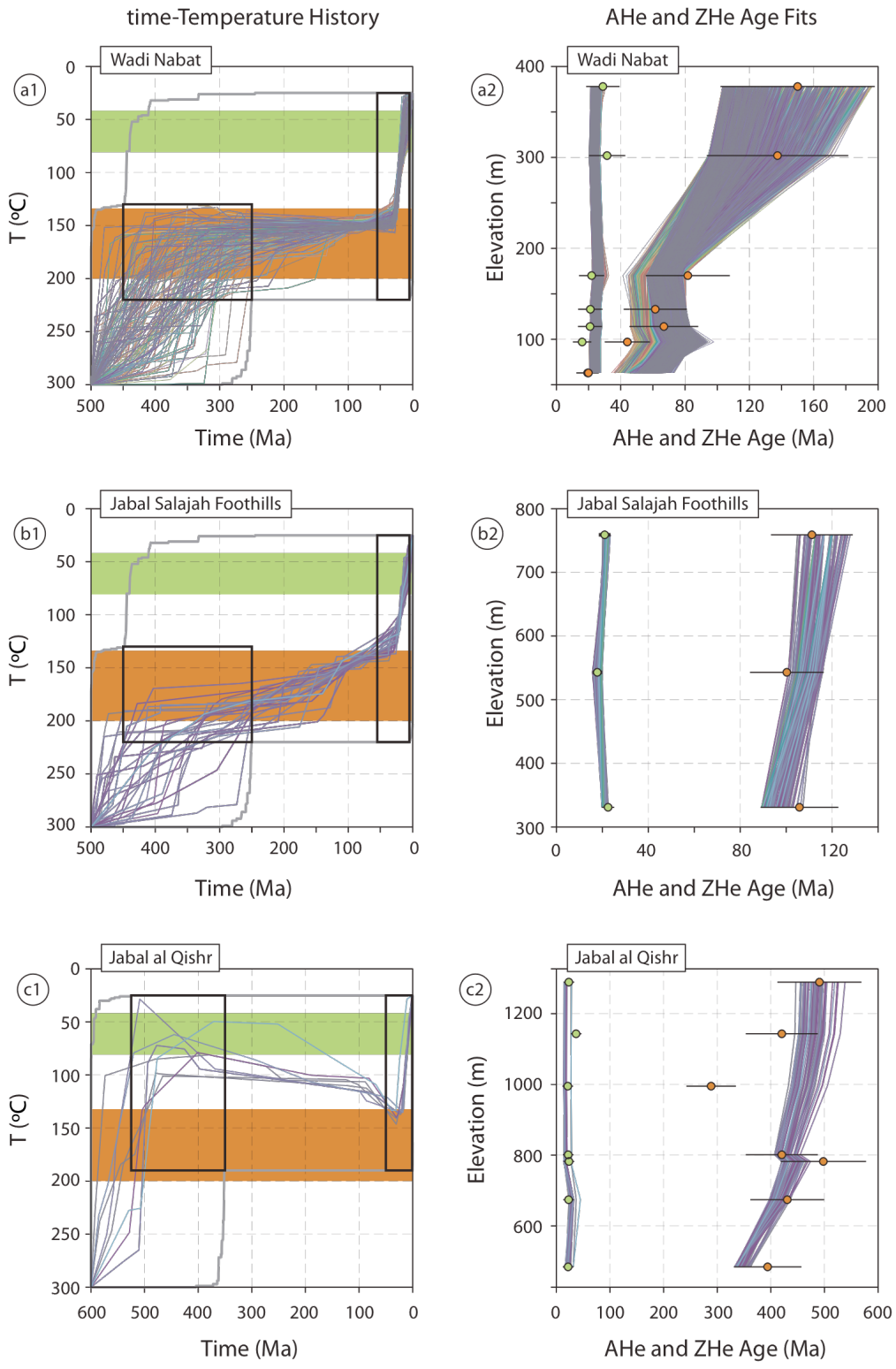
time-Temperature History
AHe and ZHe Age Fits
Wadi Nabat
a1
a2
T (ºC)
Time (Ma)
Elevation (m)
AHe and ZHe Age (Ma)
Jabal Salajah Foothills
b1
b2
Jabal al Qishr
c1
c2

Figure 15 - Wadi Nabat, Jabal Salajah Foothills, and Jabal al Qishr: Thermal Models

HeMP time-temperature plots for the Wadi Nabat, Jabal Salajah Foothills, and Jabal al Qishr multi-sample arrays. Left column shows acceptable t-T path fits of sample data for the full-modeled history (a1, b1, and c1). Right column shows adherence of acceptable t-T paths to raw mean AHe and ZHe ages and errors (a2, b2, and c2). See Figure 7 for legend.

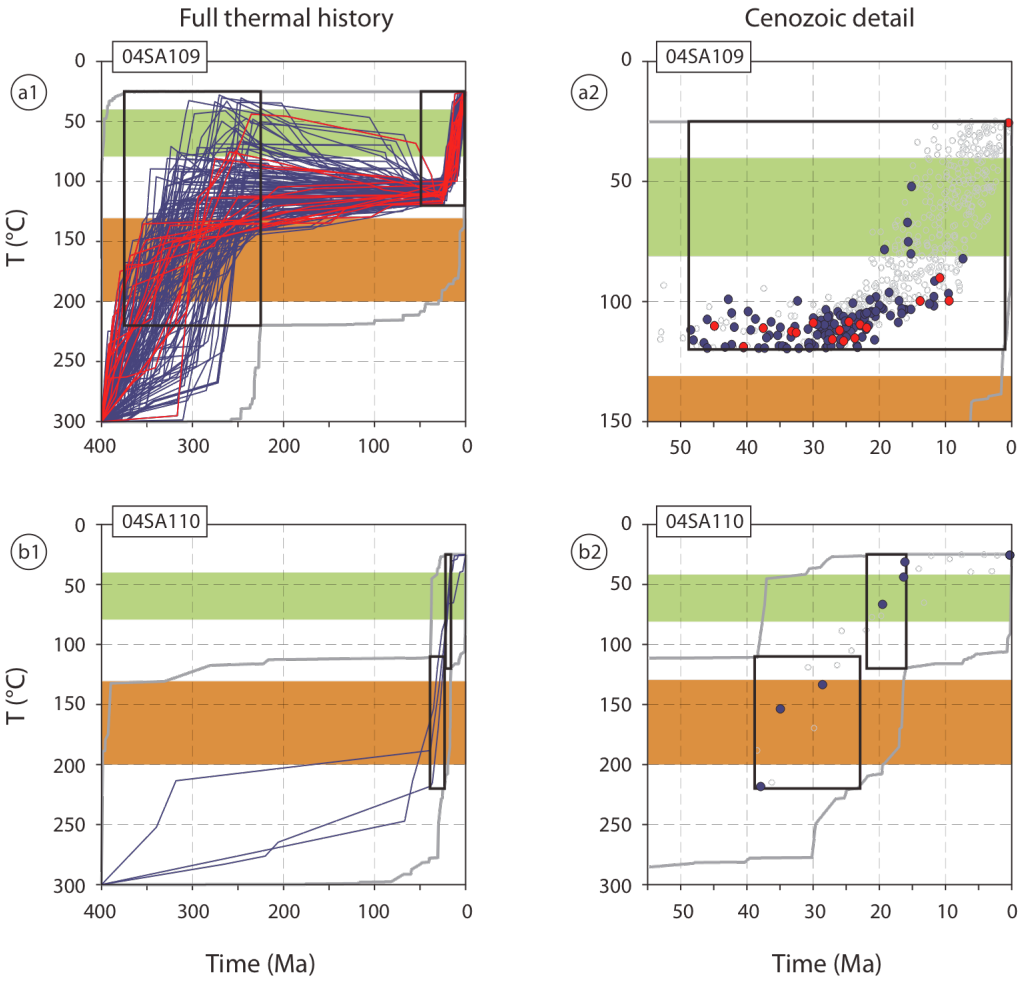
Full thermal history
Cenozoic detail
04SA109
a1
a2
04SA110
b1
b2
T (°C)
Time (Ma)
0
50
100
150
200
250
300
400
300
200
100
0
50
40
30
20
10

Figure 16 - 04SA109 and 04SA110: Thermal Models

HeMP time-temperature plots for single sample models 04SA109 and 04SA110. Sample age data is listed in Table 1. Left column shows acceptable t-T path fits of sample data for the full-modeled history. Right column shows Cenozoic detail with t-T nodes. See Figure 7 for legend.

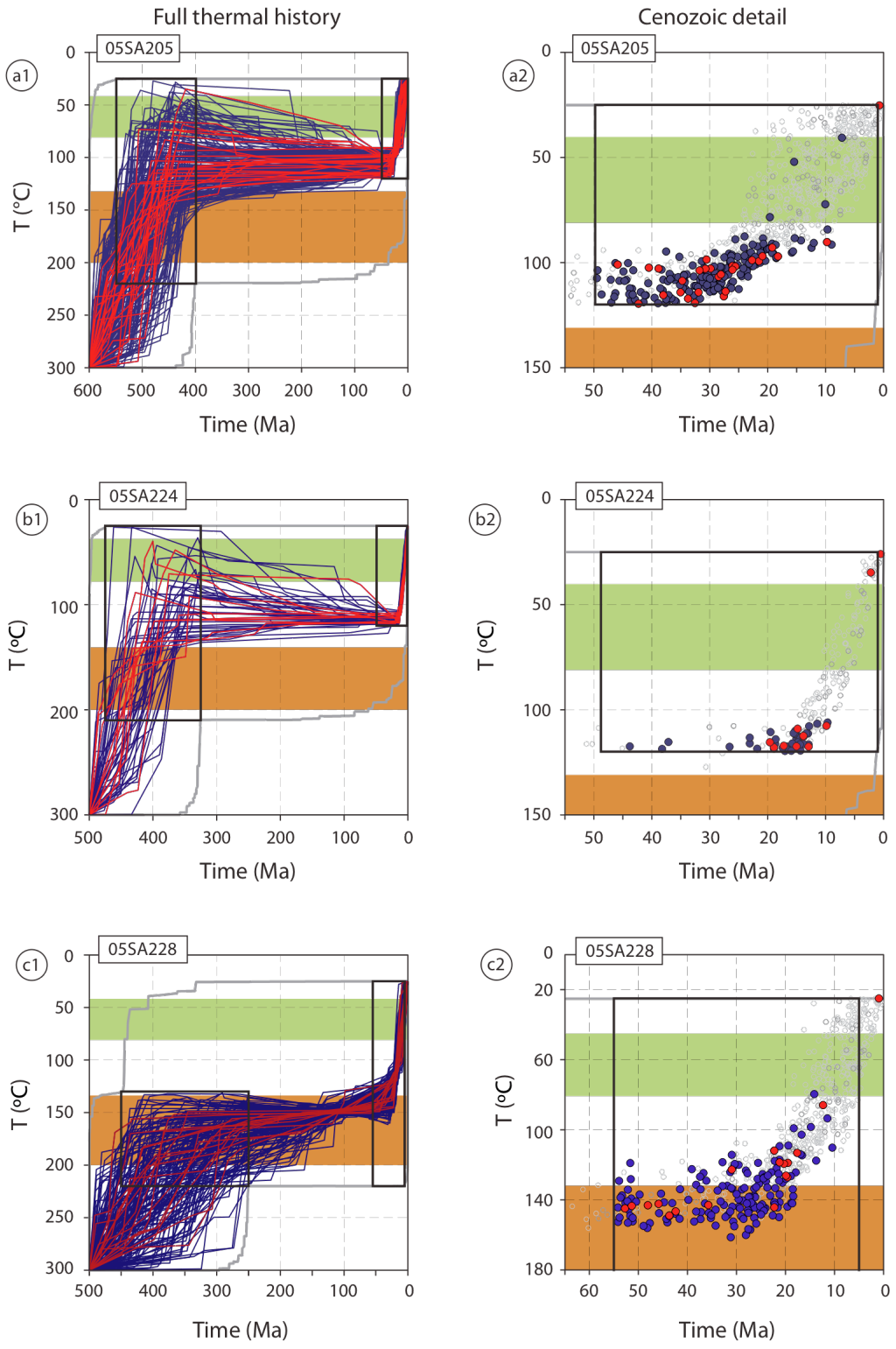
Full thermal history
Cenozoic detail
a1
05SA205
a2
05SA205
b1
05SA224
b2
05SA224
c1
05SA228
c2
05SA228
T (°C)
Time (Ma)

Figure 17 - 05SA205, 05SA224 and 05SA228: Thermal Models

HeMP time-temperature plots for single sample models 05SA205, 05SA224 and 05SA228. Sample age data is listed in Table 1. Left column shows acceptable t-T path fits of sample data for the full-modeled history. Right column shows Cenozoic detail with t-T nodes. See Figure 7 for legend.

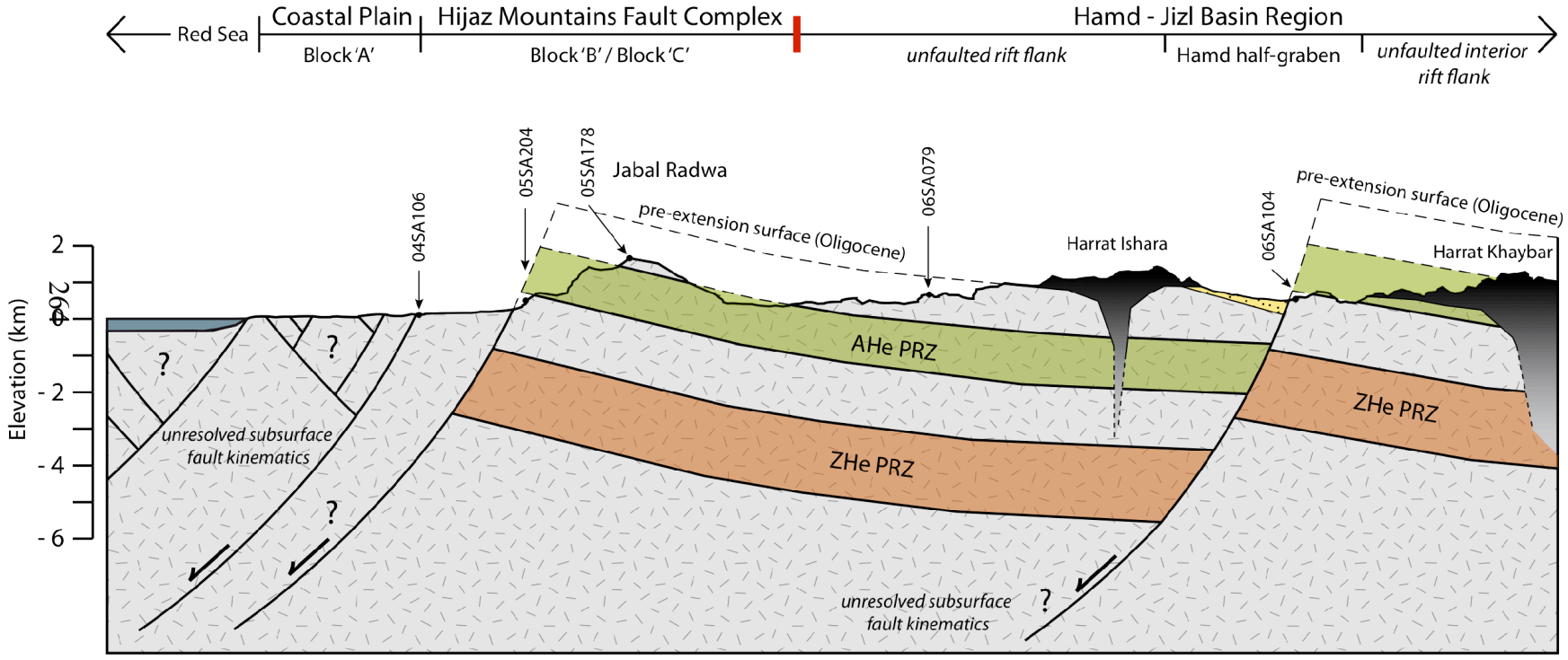
Red Sea
Coastal Plain
Block 'A'
Hijaz Mountains Fault Complex
Block 'B' / Block 'C'
Hamd - Jizl Basin Region
unfaulted rift flank
Hamd half-graben
unfaulted interior rift flank
04SA106
05SA204
05SA178
Jabal Radwa
pre-extension surface (Oligocene)
06SA079
Harrat Ishara
06SA104
pre-extension surface (Oligocene)
Harrat Khaybar
Elevation (km)
2
0
- 2
- 4
- 6
AHe PRZ
ZHe PRZ
ZHe PRZ
unresolved subsurface fault kinematics
unresolved subsurface fault kinematics
?
?
?
?

Figure 18 - CARF Crustal Cross-Section

Line of x-section marked in Figure 3. Red line delineates the boundary between the Hijaz Mountains Fault Complex (HFC) and Hamd-Jizil Basin region (HJB) structural domains. AHe and ZHe PRZ boundaries assume 25 °C/km geothermal gradient and 25 °C annual surface temperature.

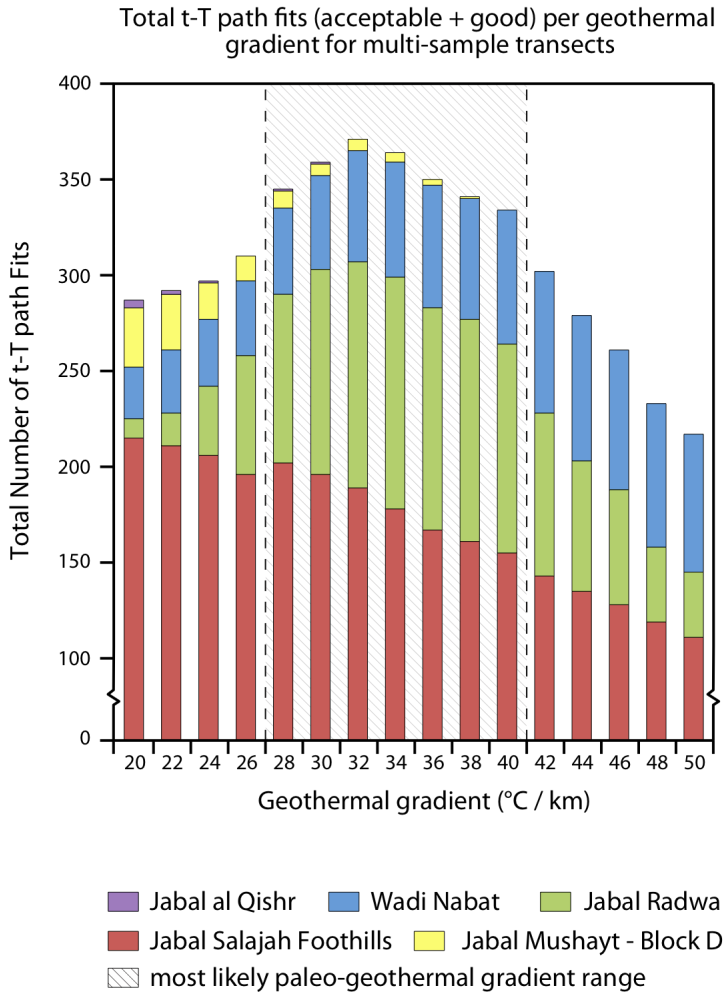
Total t-T path fits (acceptable + good) per geothermal gradient for multi-sample transects
Total Number of t-T path Fits
400
350
300
250
200
150
100
0
20 22 24 26 28 30 32 34 36 38 40 42 44 46 48 50
Geothermal gradient (°C / km)
Jabal al Qishr
Wadi Nabat
Jabal Radwa
Jabal Salajah Foothills
Jabal Mushayt - Block D
most likely paleo-geothermal gradient range

Figure 19 - Paleo-Geothermal Gradient Histogram

Total time-temperature path fits (acceptable + good) per geothermal gradient for five multi-sample transect models in the HFC. Shaded area represents paleo-geothermal gradient range that most likely existed in the CARF during Red Sea rifting.

Hijaz Mountains Fault Complex (HFC) structural domain

Transect Name / Geographic Location		Sample	AHe age (Ma) ± 6% error	n	ZHe age (Ma) ± 8% error	n	LAT (WGS84)	LONG (WGS84)	Elev. (m)	Lithology*	Geologic Unit*	Crystallization Age*
Footwall transects (multi-sample arrays)												
Wadi af Far'ah	Block C	04SA088	----	----	312.1 ± 25.0	2	24.433	38.835	507	Granodiorite	Admar Suite	Cryogenian - Ediacaran
		04SA090	22.0 ± 1.3	2	470.5 ± 37.6	2	24.389	38.714	324	Granite		
		04SA091	71.5 ± 4.3	2	113.1 ± 9.1^{+}	3	24.374	38.586	222	Granodiorite		
		04SA092	38.2 ± 2.3	2	379.3 ± 30.3	3	24.346	38.526	183	Diorite		
		04SA093	39.6 ± 2.4	3	335.6 ± 26.8	2	24.319	38.472	139	Granodiorite		
		04SA094	39.7 ± 2.4	2	----	----	24.285	38.401	106	Granodiorite		
	Block B	04SA095$^{\#}$	23.2 ± 1.4	2	----	----	24.214	38.379	89	Granodiorite		
		04SA096$^{\#}$	23.7 ± 1.4	2	----	----	24.171	38.369	69	Granodiorite		
		04SA097$^{\#}$	29.4 ± 1.8	2	300.9 ± 24.1	2	24.145	38.362	60	Granodiorite		
Wadi Nabat		04SA101$^{\#}$	21.9 ± 1.3	3	81.7 ± 6.5	2	24.650	37.537	170	Diorite / Tonalite	Jar Salajah Complex	Cryogenian
		04SA102$^{\#}$	21.1 ± 1.3	3	61.5 ± 4.9	2	24.633	37.512	133	Diorite / Tonalite		
		04SA103$^{\#}$	20.9 ± 1.3	3	66.8 ± 5.3	2	24.636	37.488	114	Diorite / Tonalite		
		04SA104$^{\#}$	16.0 ± 1.0	2	44.1 ± 3.5	2	24.627	37.468	97	Diorite / Tonalite		
		04SA106$^{\#}$	19.4 ± 1.2	2	19.9 ± 1.6	2	24.610	37.426	63	Diorite / Tonalite		
		05SA215$^{\#}$	31.5 ± 1.9	2	137.5 ± 11.0	3	24.672	37.560	302	Diorite / Tonalite		
		05SA216$^{\#}$	28.9 ± 1.7	2	218.1 ± 17.4^{+}	3	24.695	37.651	378	Diorite / Tonalite		
Jabal Radwa		05SA177	----	----	393.1 ± 31.5	3	24.590	38.272	2051	Peralkalic Granite	Radwa granite	Ediacaran
		05SA178$^{\#}$	314.6 ± 42.8	3	311.6 ± 24.9	3	24.566	38.211	2202	Peralkalic Granite		
		05SA179	----	----	307.7 ± 24.6	2	24.517	38.194	1597	Peralkalic Granite		
		05SA180	----	----	482.5 ± 38.6^{+}	2	24.526	38.192	1771	Peralkalic Granite		
		05SA182	----	----	348.0 ± 27.8	2	24.530	38.172	1321	Peralkalic Granite		
		05SA183	----	----	497.4 ± 39.8	2	24.527	38.178	1375	Peralkalic Granite		
		05SA184	----	----	362.2 ± 29.0	2	24.524	38.187	1509	Peralkalic Granite		
		05SA191$^{\#}$	44.0 ± 2.6	3	358.1 ± 28.7	3	24.476	38.181	805	Peralkalic Granite		
		05SA192	----	----	257.4 ± 20.6	2	24.480	38.169	758	Peralkalic Granite		

Hijaz Mountains Fault Complex (HFC) structural domain - *continued*

Transect Name / Geographic Location		Sample	AHe age (Ma) ± 6% error	n	ZHe age (Ma) ± 8% error	n	LAT (WGS84)	LONG (WGS84)	Elev. (m)	Lithology*	Geologic Unit*	Crystallization Age*
Jabal Radwa (cont'd)		05SA194	----	----	356.2 ± 28.5	2	24.456	38.163	456	Diorite / Tonalite	Jar Salajah Complex	Cryogenian
		05SA195	----	----	350.0 ± 28.0	3	24.456	38.156	290	Granite		
		05SA196	145.7 ± 8.7^{+}	3	141.8 ± 11.3	2	24.446	38.172	353	Diorite / Tonalite		
		05SA197$^{\#}$	52.9 ± 3.2	3	296.4 ± 23.7	3	24.428	38.208	258	Diorite / Tonalite		
		05SA198$^{\#}$	39.8 ± 2.4	2	420.0 ± 33.6	2	24.433	38.205	397	Granite		
		05SA199$^{\#}$	141.0 ± 8.5	2	313.4 ± 25.1	3	24.414	38.193	638	Granite		
		05SA200$^{\#}$	30.0 ± 1.8	3	252.6 ± 20.2	3	24.409	38.218	198	Diorite / Tonalite		
		05SA201	----	----	318.7 ± 25.5	2	24.371	38.225	268	Granite		
		05SA202$^{\#}$	20.5 ± 1.2	3	297.7 ± 23.8	2	24.336	38.226	131	Diorite / Tonalite		
		05SA203$^{\#}$	21.5 ± 1.3	3	214.4 ± 17.1	3	24.310	38.234	143	Diorite / Tonalite		
		05SA204$^{\#}$	13.2 ± 0.8	3	----	----	24.288	38.227	116	Diorite / Tonalite		
Jabal Mushayt	Block D	05SA207$^{\#}$	13.5 ± 0.8	2	472.9 ± 37.8	2	24.554	37.992	455	Granite	Jar Salajah Complex	Cryogenian
		05SA208$^{\#}$	19.1 ± 1.1	3	453.6 ± 36.3	2	24.599	37.978	1092	Diorite / Tonalite		
		05SA209$^{\#}$	15.7 ± 0.9	2	447.1 ± 35.8^{+}	3	24.582	37.985	727	Diorite / Tonalite		
		05SA210$^{\#}$	18.0 ± 1.1	3	473.7 ± 37.9	2	24.530	37.999	229	Diorite / Tonalite		
	Block C	05SA206	13.7 ± 0.8	2	24.3 ± 1.9	2	24.464	37.999	146	Diorite / Tonalite		
		05SA211	36.4 ± 2.2	2	232.7 ± 18.6^{+}	3	24.478	38.000	160	Granite		
	Block B	05SA212$^{\#}$	20.9 ± 1.3	3	234.9 ± 18.8	2	24.417	38.032	150	Diorite / Tonalite		
		05SA213$^{\#}$	22.7 ± 1.4	3	248.4 ± 19.9	2	24.379	38.044	103	Diorite / Tonalite		
		05SA214$^{\#}$	23.2 ± 1.4	3	176.7 ± 14.1^{+}	2	24.349	38.048	82	Diorite / Tonalite		

Hijaz Mountains Fault Complex (HFC) structural domain - *continued*

Transect Name / Geographic Location	Sample	AHe age (Ma) ± 6% error	n	ZHe age (Ma) ± 8% error	n	LAT (WGS84)	LONG (WGS84)	Elev. (m)	Lithology*	Geologic Unit*	Crystallization Age*
Jabal al Qishr	05SA217#	21.9 ± 1.3	2	394.1 ± 31.5	3	24.694	37.720	484	Diorite / Tonalite	Jar Salajah Complex	Cryogenian
	05SA218#	22.8 ± 1.4	2	430.7 ± 34.5	3	24.689	37.726	674	Diorite / Tonalite		
	05SA219#	23.5 ± 1.4	2	498.0 ± 39.8	2	24.733	37.779	782	Diorite / Tonalite		
	05SA220#	23.3 ± 1.4	3	490.6 ± 39.3	3	24.724	37.766	1289	Diorite / Tonalite		
	05SA221#	36.8 ± 2.2	2	320.7 ± 25.7+	2	24.713	37.745	1143	Diorite / Tonalite		
	05SA222#	21.3 ± 1.3	2	288.7 ± 23.1	3	24.704	37.737	995	Diorite / Tonalite		
	05SA223#	22.1 ± 1.3	2	----	----	24.696	37.731	801	Diorite / Tonalite		
Jabal Salajah Foothills	05SA225#	21.0 ± 1.3	3	111.2 ± 8.9	2	24.600	37.635	759	Schist, amphibolite, paragneiss	Al Hinu Formation	Neoproterozoic
	05SA226#	17.8 ± 1.1	3	100.3 ± 8.0	2	24.596	37.641	543			
	05SA227#	22.5 ± 1.3	3	116.9 ± 9.4+	3	24.596	37.653	331			
Point samples											
Umm Lujj	04SA109#	24.4 ± 1.5	3	298.1 ± 23.9	2	25.000	37.284	21	Diorite / Tonalite	Jar Salajah Complex	Cryogenian
	04SA110#	19.7 ± 1.2	3	31.1 ± 2.5	3	25.025	37.282	21	Diorite / Tonalite		
SW of Jabal Radwa	05SA205#	27.1 ± 1.6	2	488.7 ± 39.1	2	24.338	38.120	126	Diorite		
SE of Jabal al Qishr	05SA224#	15.7 ± 0.9	2	415.0 ± 33.2	3	24.671	37.744	761	Diorite		
Jabal al Qaid	05SA228#	20.4 ± 1.2	3	129.5 ± 10.4	2	24.719	37.449	238	Diorite		
Jabal Liban	05SA234	42.1 ± 2.5+	3	34.2 ± 2.7+	3	25.991	37.117	637	Diorite		

Table 1 - Bedrock Apatite and Zircon (U-Th)/He age data: Hijaz Mountains Fault Complex

Bedrock apatite and zircon (U-Th)/He thermochronology age data grouped by collection transect. Dashed entry (----) indicates unanalyzable thermochronometer quality. Plus sign (+) indicates age data not used in relative frequency plots due to irreproducibility. 'n' indicates the number of aliquots used in sample (U-Th)/He age determination. Octothorpe (#) indicates samples whose t-T history was modeled in HeMP. Asterisk (*) indicates information drawn from from Pellaton (1979), Kemp (1981), and Johnson (2006).

Hamd-Jizil Basin (HJB) structural domain

Transect Name / Geographic Location	Sample	AHe age (Ma) ± 6% error	n	ZHe age (Ma) ± 8% error	n	LAT (WGS84)	LONG (WGS84)	Elev. (m)	Lithology*	Geologic Unit*	Crystallization Age*
Point samples											
Wadi Rashad	06SA009	----	----	554.4 ± 44.4	2	24.803	39.034	735	Granite	Admar Suite	Cryo. - Edia.
Jabal Nahar	06SA016	15.1 ± 0.9	2	----	----	25.971	38.224	700	Granodiorite	*unassigned*	*unassigned*
Wadi al Batha	06SA022	203.2 ± 12.2	2	----	----	25.757	38.171	658	Granite	Jar Salajah Complex	Cryogenian
Wadi al Batha	06SA023	218.4 ± 13.1	2	----	----	25.749	38.170	601	Granite	Jar Salajah Complex	Cryogenian
Wadi al Hamd	06SA044	----	----	320.4 ± 25.6	2	25.232	38.922	597	Metased.	Al Ays Group	Ediacaran
Jabal an Nu'ayyimah	06SA073	40.3 ± 2.4	3	----	----	25.092	38.905	583	Metased.	Al Ays Group	Ediacaran
Jabal ad Darah	06SA077	51.5 ± 3.1	2	----	----	25.201	38.516	563	Monzodiorite	Mardabah Complex	Ediacaran
Jabal Hasham	06SA079	64.6 ± 3.9	3	488.0 ± 39.0	2	25.002	38.205	1305	Monzonite	Admar Suite	Cryo. - Edia.
SW Wadi al Qattar	06SA089	----	----	390.7 ± 31.3	2	24.774	38.942	911	Granodiorite	Admar Suite	Cryo. - Edia.
Jabal al Qiladah	06SA090	32.7 ± 2.0	2	----	----	24.679	38.865	1339	Granodiorite	Admar Suite	Cryo. - Edia.
Jabal al Qihaba	06SA093	45.8 ± 2.7	2	----	----	25.811	38.349	421	Gneiss	*unassigned*	*unassigned*
Wadi al Qattar	06SA104#	21.1 ± 1.3	3	500.0 ± 40.0	3	24.826	39.030	653	Granite	Admar Suite	Ediacaran
Wadi Marmiyah	07SA013	----	----	278.6 ± 22.3	2	25.401	37.961	535	Dior. / Ton.	Fara trondhjemite	Cryogenian
Jabal Hammat	07SA014	237.5 ± 14.3	2	104.8 ± 8.4+	3	25.643	37.576	387	Dior. / Ton.	Jar Salajah Complex	Cryogenian
Jabal Batra	07SA016	----	----	425.3 ± 32.9	2	25.767	37.987	512	Granite	Jar Salajah Complex	Cryogenian
Jabal Shihabah	07SA020	73.9 ± 3.1	3	----	----	24.912	39.543	1215	Rhyolite	Shufayyah Complex	Cryogenian
Ad Dulu Pluton	07SA022	54.8 ± 3.3	3	533.9 ± 42.7	2	24.795	39.501	970	Granodiorite	Admar Suite	Cryo. - Edia.
Jabal Admar	07SA029	38.7 ± 2.3	3	302.7 ± 24.2	2	24.610	39.073	1181	Granodiorite	Admar Suite	Cryo. - Edia.
Jabal Gharrah	07SA037	56.6 ± 7.1	2	----	----	25.715	38.797	905	Gneiss	*unassigned*	*unassigned*
SW of Jabal Jamlah	07SA040	----	----	417.8 ± 33.4	2	25.590	38.614	376	Metased.	Hadiyah Group	Cryogenian
N of Hadiyah village	07SA042	----	----	568.1 ± 45.4	2	25.586	38.740	491	Rhyolite	Abu Safiyah Complex	Proterozoic
Jabal am Masakk	07SA045	0.6 ± 0.0+	4	348.7 ± 27.9	2	25.562	38.850	556	Rhyolite	Abu Safiyah Complex	Proterozoic
Massak am Mutawassimah	07SA046	----	----	552.2 ± 44.2	2	25.526	38.847	583	Metased.	Al Ays Group	Ediacaran

Hamd-Jizil Basin (HJB) structural domain - *continued*

Transect Name / Geographic Location	Sample	AHe age (Ma) ± 6% error	n	ZHe age (Ma) ± 8% error	n	LAT (WGS84)	LONG (WGS84)	Elev. (m)	Lithology*	Geologic Unit*	Crystallization Age*
Central Arabian Shield transect											
Hanakiyah	09SA001	259.8 ± 7.5	2	490.2 ± 39.2	2	24.796	40.412	910	Granitoid	Admar Suite	Cryo. - Edia.
Abraq af Fuhud	09SA002	122.4 ± 3.3	2	477.4 ± 38.2	2	25.114	40.808	1043		Syn- to post-Isamah formation intrusives	Cryogenian
Arja	09SA003	----	----	610.7 ± 48.9	2	25.330	41.037	1066			Cryogenian
	09SA004	----	----	478.1 ± 38.2^{+}	3	25.392	41.146	1074			Cryogenian
Nuqrah	09SA005	163.1 ± 9.8^{+}	----	396.6 ± 31.7^{+}	3	25.604	41.480	968			Cryogenian
Jafen	09SA006	149.6 ± 20.9	3	----	----	25.709	41.813	884		Suwaj suite	Cryogenian
Jabal Qutng	09SA007	----	----	714.4 ± 57.2^{+}	1	25.961	42.277	863		Idah suite	Ediacaran
Al Basra	09SA008	----	----	379.5 ± 30.4	2	25.903	42.913	813		Abanat suite	Ediacaran
Al Qurayn	09SA009	124.0 ± 7.4	2	355.5 ± 28.4^{+}	3	26.006	43.383	680		Khishaybi suite	Cryogenian

Table 2 - Bedrock Apatite and Zircon (U-Th)/He age data: Hamd-Jizil Basin

Bedrock apatite and zircon (U-Th)/He thermochronology age data grouped by collection transect. Dashed entry (----) indicates unanalyzable thermochronometer quality. Plus sign (+) indicates age data not used in relative frequency plots due to irreproducibility. 'n' indicates the number of aliquots used in sample (U-Th)/He age determination. Octothorpe (#) indicates samples whose t-T history was modeled in HeMP. Asterisk (*) indicates information drawn from from Pellaton (1979), Kemp (1981), and Johnson (2006).

Model Type - Sample / Transect Name	AHe, ZHe age pairs	Allowed Outliers	AHe age (Ma)	AHe error (2σ) Raw (± m.y.)	AHe error (2σ) % of mean age	ZHe age (Ma)	ZHe error (2σ) Raw (± m.y.)	ZHe error (2σ) % of mean age	Model Run Delimiter	Model Fits* Good	Model Fits* Acc.	Total t-T Paths
Point Samples												
04SA109	1	----	24.4	1.5	6.0 #	298.1	27.0	9.1		100	811	40,263
04SA110	1	----	19.7	1.2	6.0 #	31.1	9.6	30.9		100	396	2,057
05SA205	1	----	27.1	1.6	6.0 #	488.7	39.1	8.0 #		100	769	28,197
05SA224	1	----	15.7	0.9	6.0 #	415.0	33.2	8.0 #	100 good fits	100	775	76,902
05SA228	1	----	20.4	1.9	9.3	129.5	10.4	8.0 #		100	793	75,424
06SA104	1	----	21.1	3.7	17.5	500.0	40.0	8.0 #		100	972	41,726
Jabal Mushayt - Block 'C'	1	----	13.7	0.8	6.0 #	24.3	1.9	8.0 #		100	860	12,564
Composite Samples (+)												
Jabal Mushayt - Block 'B'	2	----	22.5	2.6	11.6	241.7	19.3	8.0 #	100 good fits	100	806	96,061
Wadi af Far'ah - Block 'B'	3	----	23.4	1.4	6.0 #	300.9	37.0	12.3		100	708	64,368
Multi-sample Arrays												
Jabal Radwa	9	3	----	----	6.0 - 53.0 #	----	----	8.0 - 17.8 #		----	----	100,000
Jabal al Qishr	7	2	----	5.0	13.6 - 23.5	----	----	8.0 #		----	----	"
Wadi Nabat	7	2	----	----	18.0	----	----	16.0	100,000 t-T paths	----	----	"
Jabal Mushayt - Block 'D'	4	0	----	3.0	15.7 - 22.3	----	----	8.0 #		----	----	"
Jabal Salajah Foothills	3	0	----	----	6.0 #	----	----	8.0 #		----	----	"

Table 3 - HeMP Thermal Model Constraints

(+) Composite sample modeled ages represent collective AHe and ZHe age data combined from closely spaced samples within same fault block. (#) 2σ modeled as minimum inter-aliquot reproducibility for optimal-quality apatite (6%) and zircon (8%). Otherwise, 2σ modeled as SDOM of AHe and ZHe age. (*) Total fits for all geothermal gradients. See Figure 19 for a histogram of fits per individual geothermal gradient. (----) inapplicable model constraint

Model Type - Sample / Transect Name	ZHe cooling event age *	AHe cooling event age (± 2σ; Ma) *	Pre-rift fault block temp. (˚C)	Cenozoic Exhumation by Geothermal Gradient								RSR Phase Affinity ◊
				Total Exhumation[#] (km)				*Exhumation Rate[†] (mm yr^{-1})*				
				20, 30, 40, and 50 ˚C/km				20, 30, 40, and 50 ˚C/km				
Point Samples												
04SA109	Paleozoic	24.4 ± 1.5	100	3.8	2.5	1.9	1.5	0.16	0.10	0.08	0.06	1st
04SA110	Cenozoic	19.7 ± 1.2	----	----	----	----	----	----	----	----	----	----
05SA205	Paleozoic	27.1 ± 1.6	100	3.8	2.5	1.9	1.5	0.14	0.09	0.07	0.06	1st
05SA224	Paleozoic	15.7 ± 0.9	115	4.5	3.3	2.3	1.8	0.29	0.21	0.15	0.11	2nd
05SA228	Paleozoic	20.4 ± 1.2	140	5.8	3.8	2.9	2.3	0.28	0.19	0.14	0.11	1st
06SA104	Cambrian	21.1 ± 1.3	115	4.5	3.3	2.3	1.8	0.21	0.16	0.11	0.09	1st
Jabal Mushayt - Block 'C'	Cenozoic	13.7 ± 0.8	180	7.8	5.2	3.9	3.1	0.57	0.38	0.28	0.23	----
Composite Samples [(+)]												
Jabal Mushayt - Block 'B'	Mesozoic	22.5 ± 2.6	160	6.8	4.5	3.4	2.7	0.30	0.20	0.15	0.12	1st
Wadi af Far'ah - Block 'B'	Paleozoic	23.4 ± 1.4	140	5.8	3.8	2.9	2.3	0.25	0.16	0.12	0.10	1st
Multi-sample Arrays												
Jabal Radwa	Paleozoic	----	80^	4.8	1.5	0.5	0.1					1st
Jabal al Qishr	Paleozoic	Miocene	140	5.7	3.6	----	----					1st
Wadi Nabat	Paleozoic	Oligocene	140	6.2	4.0	3.0	2.4			*variable*		1st
Jabal Mushayt - Block 'D'	Paleozoic	Miocene	110	4.6	3.1	----	----					2nd
Jabal Salajah Foothills	Paleozoic	Miocene	110	4.5	3.1	----	----					1st

Table 4 - HeMP Thermal Model Results

(+) Composite sample modeled ages represent collective AHe and ZHe age data combined from closely spaced samples within same fault block; (*) analytically derived or modeled age of event that exhumed the sample through either the AHe or ZHe PRZ; 2σ = 6% mean AHe age; (◊) recognized major RSR extensional phases: ca. 21 Ma (1^{st}) and ca. 14 Ma (2^{nd}); (#) values for single and composite sample based upon: AHe T_c70 °C; ZHe T_c = 200 °C; mean annual surface T = 25 ˚C; values for multi-sample arrays from *HeMP*; (†) average rate of final AHe cooling event from onset of RSR-related exhumation; (----) inapplicable model constraint

Apatite Aliquot	Age (Ma)	± 6% (2σ)	U (ppm)	Th (ppm)	Sm (ppm)	Th/U	[eU]	mass (µg)	^{4}He yield (ncc / µg)	F_T	SDOM (Ma)
2004 Collection Campaign											
04SA090-1	27.1	1.6	2.5	5.7	91.0	2.3	4.2	2.5	0.0089	0.60	
04SA090-2*	16.7	1.0	2.8	6.9	103.5	2.5	4.9	1.9	0.0061	0.57	
04SA090-3	25.1	1.5	3.3	6.5	113.1	2.0	5.3	2.5	0.0102	0.58	5.5
AVG	**26.1**	**1.6**	**2.9**	**6.1**	**102.0**	**2.2**	**4.8**	**2.5**	**0.0095**	**0.59**	**1.4**
04SA091b-1*	113.3	6.8	14.9	18.6	59.4	1.3	19.5	10.7	0.1761	0.65	
04SA091b-2	61.4	3.7	12.9	24.0	48.9	1.9	18.7	11.2	0.0915	0.65	
04SA091b-3	81.5	4.9	10.9	17.6	44.3	1.6	15.2	11.6	0.0976	0.64	26.2
AVG	**71.5**	**4.3**	**11.9**	**20.8**	**46.6**	**1.7**	**17.0**	**11.4**	**0.0945**	**0.64**	**14.2**
04SA092-1	40.9	2.5	28.7	54.0	34.8	1.9	41.3	4.4	0.1348	0.65	
04SA092-2	35.6	2.1	38.3	71.2	35.9	1.9	54.8	4.8	0.1610	0.67	
04SA092-3*	48.5	2.9	40.3	75.6	51.8	1.9	57.9	4.7	0.2305	0.67	6.5
AVG	**38.2**	**2.3**	**33.5**	**62.6**	**35.4**	**1.9**	**48.1**	**4.6**	**0.1479**	**0.66**	**3.7**
04SA093-1	38.7	2.3	40.0	79.1	39.3	2.0	58.4	1.3	0.1685	0.61	
04SA093-2*	44.2	2.7	31.6	63.4	54.4	2.0	46.5	1.9	0.1618	0.64	
04SA093-3	38.7	2.3	23.1	42.1	41.4	1.8	33.0	1.2	0.0942	0.60	
04SA093-4	41.3	2.5	21.6	18.6	18.2	0.9	25.9	1.6	0.0816	0.63	2.6
AVG	**39.6**	**2.4**	**28.2**	**46.6**	**33.0**	**1.6**	**39.1**	**1.4**	**0.1147**	**0.61**	**1.5**
04SA094b-1	38.8	2.3	5.9	22.6	133.2	3.8	11.8	13.7	0.0389	0.67	
04SA094b-2	40.5	2.4	5.9	17.1	127.6	2.9	10.4	13.1	0.0350	0.65	
04SA094b-3*	83.9	5.0	15.1	38.9	124.3	2.6	24.7	11.9	0.1676	0.65	25.6
AVG	**39.7**	**2.4**	**5.9**	**19.9**	**130.4**	**3.4**	**11.1**	**13.4**	**0.0370**	**0.66**	**1.2**
04SA095-1*	29.2	1.7	22.0	69.9	21.7	3.2	38.2	4.6	0.0902	0.66	
04SA095-2	23.9	1.4	16.5	53.8	23.7	3.3	29.0	4.1	0.0552	0.65	
04SA095-3	22.5	1.3	21.8	59.1	18.7	2.7	35.5	4.3	0.0639	0.65	3.5
AVG	**23.2**	**1.4**	**19.2**	**56.4**	**21.2**	**3.0**	**32.3**	**4.2**	**0.0595**	**0.65**	**1.0**
04SA096-1	25.0	1.5	17.7	49.3	18.5	2.8	29.1	3.8	0.0569	0.64	
04SA096-2	22.4	1.3	20.7	62.5	14.7	3.0	35.2	3.7	0.0617	0.64	
04SA096-3*	32.0	1.9	24.5	70.0	21.7	2.9	40.7	4.4	0.1052	0.66	5.0
AVG	**23.7**	**1.4**	**19.2**	**55.9**	**16.6**	**2.9**	**32.2**	**3.8**	**0.0593**	**0.64**	**1.8**
04SA097-1	34.1	2.0	15.0	45.2	14.7	3.0	25.5	3.2	0.0671	0.63	
04SA097-2	24.7	1.5	14.2	38.4	15.0	2.7	23.1	3.4	0.0441	0.63	
04SA097-3*	51.7	3.1	14.7	50.0	33.8	3.4	26.4	3.8	0.1059	0.63	13.7
AVG	**29.4**	**1.8**	**14.6**	**41.8**	**14.8**	**2.9**	**24.3**	**3.3**	**0.0556**	**0.63**	**6.7**
04SA101b-1	21.3	1.3	53.8	13.3	39.7	0.2	57.1	20.0	0.1059	0.72	
04SA101b-2	22.0	1.3	47.7	12.0	41.8	0.3	50.6	23.5	0.0981	0.73	
04SA101b-3	22.5	1.3	63.0	20.4	47.0	0.3	67.9	22.9	0.1344	0.73	0.6
AVG	**21.9**	**1.3**	**54.8**	**15.2**	**42.9**	**0.3**	**58.5**	**22.1**	**0.1128**	**0.72**	**0.6**

Apatite Aliquot	Age (Ma)	± 6% (2σ)	U (ppm)	Th (ppm)	Sm (ppm)	Th/U	[eU]	mass (µg)	^{4}He yield (ncc / µg)	F_T	SDOM (Ma)
04SA102-1	20.3	1.2	28.4	12.4	33.2	0.4	31.4	6.3	0.0553	0.71	
04SA102-2	21.2	1.3	22.1	7.6	24.9	0.3	24.0	8.4	0.0452	0.73	
04SA102-3	21.8	1.3	40.3	7.7	28.7	0.2	42.2	6.9	0.0809	0.72	0.8
AVG	**21.1**	**1.3**	**30.3**	**9.2**	**28.9**	**0.3**	**32.5**	**7.2**	**0.0605**	**0.72**	**0.8**
04SA103b-1	21.4	1.3	39.0	27.7	21.2	0.7	45.5	24.5	0.0857	0.72	
04SA103b-2	20.1	1.2	36.3	25.0	18.1	0.7	42.1	25.0	0.0746	0.73	
04SA103b-3	21.2	1.3	39.4	28.4	21.4	0.7	46.1	24.2	0.0855	0.72	0.7
AVG	**20.9**	**1.3**	**38.2**	**27.1**	**20.2**	**0.7**	**44.6**	**24.6**	**0.0819**	**0.72**	**0.7**
04SA104b-1	16.2	1.0	23.5	6.5	29.3	0.3	25.2	17.7	0.0348	0.70	
04SA104b-2	15.7	0.9	24.6	9.1	36.5	0.4	26.9	18.5	0.0362	0.70	
04SA104b-3*	13.8	0.8	23.6	8.1	33.3	0.3	25.7	18.2	0.0304	0.70	1.2
AVG	**16.0**	**1.0**	**24.1**	**7.8**	**32.9**	**0.3**	**26.0**	**18.1**	**0.0355**	**0.70**	**0.3**
04SA106-1*	15.5	0.9	29.2	2.9	26.2	0.1	30.0	4.6	0.0389	0.69	
04SA106-2	19.9	1.2	33.9	4.7	34.7	0.1	35.2	5.2	0.0591	0.70	
04SA106-3	22.5	1.4	29.1	2.6	22.8	0.1	29.8	6.2	0.0584	0.72	3.5
AVG	**21.2**	**1.3**	**31.5**	**3.7**	**28.8**	**0.1**	**32.5**	**5.7**	**0.0588**	**0.71**	**1.9**
04SA109b-1	22.9	1.4	12.9	6.3	33.1	0.5	14.6	15.9	0.0281	0.69	
04SA109b-2	24.5	1.5	15.3	8.4	34.0	0.5	17.4	17.5	0.0362	0.70	
04SA109b-3	25.7	1.5	15.9	8.4	38.1	0.5	18.0	16.4	0.0393	0.70	1.4
AVG	**24.4**	**1.5**	**14.7**	**7.7**	**35.1**	**0.5**	**16.7**	**16.6**	**0.0345**	**0.69**	**1.4**
04SA110-1	19.8	1.2	4.3	2.1	9.0	0.5	4.8	17.0	0.0092	0.79	
04SA110-2	19.5	1.2	3.4	2.2	10.1	0.7	4.0	13.8	0.0074	0.78	
04SA110-3	20.0	1.2	1.5	0.9	3.1	0.6	1.7	20.0	0.0033	0.80	0.2
AVG	**19.7**	**1.2**	**3.1**	**1.8**	**7.4**	**0.6**	**3.5**	**16.9**	**0.0066**	**0.79**	**0.2**
2005 Collection Campaign											
05SA178-1	343.3	34.8	2.9	87.4	320.7	29.8	24.6	2.4	0.7286	0.66	
05SA178-2	325.6	43.8	0.7	49.2	230.8	72.7	13.2	3.4	0.3877	0.69	
05SA178-3	274.7	49.8	2.8	69.3	512.8	24.8	21.3	8.4	0.5940	0.76	
05SA178-4*	534.3	30.1	2.8	218.4	380.8	77.8	55.0	8.3	2.8517	0.76	113.7
AVG	**314.6**	**42.8**	**2.1**	**68.6**	**354.8**	**42.4**	**19.7**	**4.7**	**0.5701**	**0.70**	**35.6**
05SA191-1	34.0	2.0	11.2	30.7	299.0	2.7	19.8	5.2	0.0578	0.67	
05SA191-2	44.6	2.7	13.1	44.5	389.7	3.4	25.3	2.4	0.0838	0.58	
05SA191-3*	109.4	6.6	5.4	18.9	355.0	3.5	11.5	1.6	0.0911	0.54	
05SA191-4	53.5	3.2	4.8	16.1	208.2	3.4	9.5	4.0	0.0426	0.64	33.7
AVG	**44.0**	**2.6**	**9.7**	**30.4**	**299.0**	**3.2**	**18.2**	**3.9**	**0.0614**	**0.63**	**9.8**
05SA196-1*	162.3	9.7	3.0	9.6	100.0	3.2	5.7	2.3	0.0698	0.58	
05SA196-2*	232.3	13.9	6.1	12.0	172.8	2.0	9.7	2.2	0.1699	0.58	
05SA196-3*	42.5	2.5	4.7	8.9	111.1	1.9	7.3	4.4	0.0264	0.66	96.0
AVG	***145.7***	***8.7***	----	----	----	----	----	----	----	----	----

Apatite Aliquot	Age (Ma)	± 6% (2σ)	U (ppm)	Th (ppm)	Sm (ppm)	Th/U	[eU]	mass (µg)	^{4}He yield (ncc / µg)	F_T	SDOM (Ma)
05SA197-1	62.9	3.8	20.3	79.6	170.3	3.9	39.5	2.6	0.1873	0.61	
05SA197-2	55.6	3.3	12.7	54.9	267.8	4.3	26.6	3.3	0.1175	0.63	
05SA197-3	40.2	2.4	29.6	104.4	140.4	3.5	54.3	6.0	0.1867	0.69	11.6
AVG	**52.9**	**3.2**	**20.9**	**79.6**	**192.9**	**3.9**	**40.2**	**4.0**	**0.1638**	**0.64**	**11.6**
05SA198-1	43.4	2.6	16.8	89.7	249.1	5.4	38.7	1.9	0.1172	0.56	
05SA198-2*	31.6	1.9	5.7	33.1	146.7	5.8	14.0	2.2	0.0323	0.57	
05SA198-3	36.3	2.2	21.8	110.9	146.3	5.1	48.1	3.4	0.1362	0.63	
05SA198-4*	46.4	2.8	9.2	49.9	99.6	5.5	21.1	6.1	0.0832	0.68	6.7
AVG	**39.8**	**2.4**	**19.3**	**100.3**	**197.7**	**5.2**	**43.4**	**2.7**	**0.1267**	**0.59**	**5.0**
05SA199-1*	250.5	15.0	4.3	7.5	97.8	1.8	6.5	1.8	0.1183	0.56	
05SA199-2	138.7	8.3	4.4	6.8	99.8	1.5	6.5	2.2	0.0678	0.59	
05SA199-3	143.2	8.6	7.2	7.8	140.7	1.1	9.7	2.6	0.1077	0.60	63.3
AVG	**141.0**	**8.5**	**5.8**	**7.3**	**120.3**	**1.3**	**8.1**	**2.4**	**0.0878**	**0.60**	**3.2**
05SA200-1*	78.0	4.7	22.1	10.1	161.2	0.5	25.2	2.9	0.1532	0.63	
05SA200-2	32.3	1.9	15.9	6.0	142.9	0.4	18.0	4.8	0.0494	0.68	
05SA200-3	26.0	1.6	16.5	6.3	133.8	0.4	18.6	6.4	0.0423	0.71	
05SA200-4	31.7	1.9	27.6	18.1	200.1	0.7	32.7	6.8	0.0911	0.71	24.2
AVG	**30.0**	**1.8**	**20.0**	**10.1**	**158.9**	**0.5**	**23.1**	**6.0**	**0.0609**	**0.70**	**3.5**
05SA202-1	19.3	1.2	55.8	60.4	63.7	1.1	70.0	3.7	0.1067	0.65	
05SA202-2	21.7	1.3	51.3	50.2	66.3	1.0	63.2	3.5	0.1064	0.64	
05SA202-3*	25.8	1.5	45.6	33.9	60.2	0.7	53.7	4.5	0.1129	0.67	
05SA202-4	20.4	1.2	51.1	59.6	75.8	1.2	65.1	2.7	0.0994	0.61	2.8
AVG	**20.5**	**1.2**	**52.7**	**56.7**	**68.6**	**1.1**	**66.1**	**3.3**	**0.1042**	**0.63**	**1.2**
05SA203-1	19.6	1.2	11.6	15.3	179.8	1.3	16.0	1.0	0.0229	0.58	
05SA203-2	22.9	1.4	6.9	10.1	154.2	1.5	10.0	1.4	0.0180	0.61	
05SA203-3	21.8	1.3	7.5	9.6	153.5	1.3	10.5	1.7	0.0184	0.63	1.7
AVG	**21.5**	**1.3**	**8.7**	**11.7**	**162.5**	**1.4**	**12.2**	**1.4**	**0.0198**	**0.61**	**1.7**
05SA204-1	13.2	0.8	1.9	2.6	32.4	1.4	2.7	1.1	0.0026	0.59	
05SA204-2	10.1	0.6	1.6	2.6	33.0	1.6	2.4	0.9	0.0017	0.56	
05SA204-3	16.3	1.0	1.3	2.6	18.8	2.0	2.0	1.2	0.0025	0.60	3.1
AVG	**13.2**	**0.8**	**1.6**	**2.6**	**28.0**	**1.7**	**2.4**	**1.1**	**0.0023**	**0.58**	**3.1**
05SA205-1*	21.2	1.3	7.7	10.9	38.8	1.4	10.4	2.3	0.0161	0.59	
05SA205-2	26.2	1.6	7.7	9.2	44.1	1.2	10.1	3.5	0.0207	0.64	
05SA205-3	27.9	1.7	4.0	5.6	39.7	1.4	5.5	5.9	0.0134	0.70	3.5
AVG	**27.1**	**1.6**	**5.9**	**7.4**	**41.9**	**1.3**	**7.8**	**4.7**	**0.0170**	**0.67**	**1.2**
05SA206-1	13.5	0.8	16.5	19.1	68.8	1.2	21.2	1.9	0.0203	0.58	
05SA206-2*	18.7	1.1	11.5	13.9	57.6	1.2	15.0	2.9	0.0214	0.62	
05SA206-3	14.0	0.8	13.2	14.5	62.0	1.1	16.8	3.1	0.0183	0.63	2.9
AVG	**13.7**	**0.8**	**14.8**	**16.8**	**65.4**	**1.1**	**19.0**	**2.5**	**0.0193**	**0.61**	**0.4**

Apatite Aliquot	Age (Ma)	± 6% (2σ)	U (ppm)	Th (ppm)	Sm (ppm)	Th/U	[eU]	mass (µg)	^{4}He yield (ncc / µg)	F_T	SDOM (Ma)
05SA207-1	13.0	0.8	15.4	18.6	95.4	1.2	20.2	2.5	0.0194	0.60	
05SA207-2*	10.8	0.6	9.3	12.6	75.5	1.3	12.6	2.6	0.0101	0.60	
05SA207-3	13.9	0.8	11.1	13.2	89.2	1.2	14.6	3.5	0.0161	0.64	
05SA207-4*	17.2	1.0	9.5	11.5	73.3	1.2	12.6	2.7	0.0165	0.62	2.7
AVG	**13.5**	**0.8**	**13.3**	**15.9**	**92.3**	**1.2**	**17.4**	**3.0**	**0.0177**	**0.62**	**0.7**
05SA208-1*	33.1	2.0	9.0	15.0	126.9	1.7	13.1	2.3	0.0325	0.60	
05SA208-2	23.6	1.4	6.1	11.5	132.7	1.9	9.4	2.5	0.0166	0.59	
05SA208-3	18.3	1.1	3.9	7.7	99.7	2.0	6.2	1.6	0.0081	0.55	
05SA208-4	15.3	0.9	5.2	8.5	95.0	1.6	7.6	3.9	0.0096	0.65	7.8
AVG	**19.1**	**1.1**	**5.1**	**9.2**	**109.1**	**1.8**	**7.7**	**2.7**	**0.0114**	**0.60**	**4.2**
05SA209-1	16.2	1.0	8.8	13.5	115.8	1.5	12.5	2.2	0.0148	0.58	
05SA209-2	15.3	0.9	14.8	14.6	113.0	1.0	18.7	2.2	0.0208	0.59	
05SA209-3*	11.8	0.7	15.2	16.6	110.7	1.1	19.6	4.2	0.0190	0.66	2.3
AVG	**15.7**	**0.9**	**11.8**	**14.1**	**114.4**	**1.3**	**15.6**	**2.2**	**0.0178**	**0.59**	**0.6**
05SA210-1	16.4	1.0	17.1	18.3	43.8	1.1	21.6	3.5	0.0279	0.65	
05SA210-2	18.5	1.1	12.5	12.5	35.6	1.0	15.5	3.8	0.0228	0.65	
05SA210-3	19.1	1.1	17.1	19.2	42.3	1.1	21.8	4.6	0.0341	0.67	1.4
AVG	**18.0**	**1.1**	**15.6**	**16.7**	**40.6**	**1.1**	**19.6**	**4.0**	**0.0283**	**0.65**	**1.4**
05SA211-1	39.0	2.3	5.6	7.3	73.5	1.3	7.6	3.4	0.0241	0.65	
05SA211-2*	124.3	7.5	7.8	10.8	87.7	1.4	10.8	3.5	0.1079	0.64	
05SA211-3	33.7	2.0	6.0	8.2	82.4	1.4	8.3	5.2	0.0238	0.68	50.8
AVG	**36.4**	**2.2**	**5.8**	**7.7**	**77.9**	**1.3**	**7.9**	**4.3**	**0.0239**	**0.66**	**3.7**
05SA212-1	20.4	1.2	40.8	47.7	44.0	1.2	52.0	3.1	0.0811	0.63	
05SA212-2	20.7	1.2	52.8	55.2	44.5	1.0	65.7	3.8	0.1086	0.66	
05SA212-3	21.5	1.3	44.9	46.6	44.6	1.0	55.8	3.9	0.0955	0.65	0.6
AVG	**20.9**	**1.3**	**46.1**	**49.8**	**44.4**	**1.1**	**57.8**	**3.6**	**0.0951**	**0.64**	**0.6**
05SA213-1	23.1	1.4	62.6	69.4	52.0	1.1	78.9	2.3	0.1330	0.60	
05SA213-2	22.2	1.3	51.8	58.9	51.9	1.1	65.6	3.0	0.1106	0.62	
05SA213-3	22.7	1.4	45.6	51.5	42.4	1.1	57.7	3.3	0.1002	0.63	0.4
AVG	**22.7**	**1.4**	**53.3**	**59.9**	**48.8**	**1.1**	**67.4**	**2.9**	**0.1146**	**0.62**	**0.4**
05SA214-1	23.6	1.4	147.7	129.0	36.9	0.9	177.6	7.5	0.3640	0.71	
05SA214-2	23.5	1.4	165.6	129.9	33.0	0.8	195.7	6.9	0.3996	0.72	
05SA214-3	22.6	1.4	108.4	108.1	35.2	1.0	133.5	8.3	0.2659	0.72	0.5
AVG	**23.2**	**1.4**	**140.6**	**122.3**	**35.0**	**0.9**	**168.9**	**7.6**	**0.3431**	**0.72**	**0.5**
05SA215-1	27.6	1.7	14.3	5.8	25.2	0.4	15.7	3.1	0.0342	0.65	
05SA215-2*	16.0	1.0	15.0	7.1	43.0	0.5	16.8	3.5	0.0215	0.65	
05SA215-3	35.4	2.1	13.9	6.4	37.5	0.5	15.6	4.3	0.0449	0.67	9.8
AVG	**31.5**	**1.9**	**14.1**	**6.1**	**31.4**	**0.4**	**15.6**	**3.7**	**0.0395**	**0.66**	**5.5**

Apatite Aliquot	Age (Ma)	± 6% (2σ)	U (ppm)	Th (ppm)	Sm (ppm)	Th/U	[eU]	mass (µg)	^{4}He yield (ncc / µg)	F_T	SDOM (Ma)
05SA216b-1	24.2	1.4	37.8	34.8	208.6	0.9	46.8	9.0	0.0877	0.63	
05SA216b-2	33.7	2.0	8.2	31.5	364.2	3.8	17.3	8.0	0.0458	0.60	
05SA216b-3*	52.3	3.1	6.5	26.4	381.8	4.1	14.5	9.1	0.0620	0.62	14.3
AVG	**28.9**	**1.7**	**23.0**	**33.2**	**286.4**	**2.4**	**32.1**	**8.5**	**0.0667**	**0.61**	**6.7**
05SA217-1	23.3	1.4	66.7	47.3	78.8	0.7	78.0	2.3	0.1331	0.60	
05SA217-2*	38.8	2.3	53.4	45.9	94.8	0.9	64.5	2.7	0.1884	0.62	
05SA217-3	20.5	1.2	37.0	33.5	84.7	0.9	45.2	2.5	0.0693	0.61	9.9
AVG	**21.9**	**1.3**	**51.9**	**40.4**	**81.7**	**0.8**	**61.6**	**2.4**	**0.1012**	**0.61**	**1.9**
05SA218b-1	22.9	1.4	48.1	38.9	89.2	0.8	57.5	13.3	0.1079	0.67	
05SA218b-2	22.6	1.4	56.0	42.7	91.0	0.8	66.3	12.6	0.1213	0.66	
05SA218b-3*	25.9	1.6	52.4	41.5	85.4	0.8	62.4	12.9	0.1320	0.67	1.8
AVG	**22.8**	**1.4**	**52.1**	**40.8**	**90.1**	**0.8**	**61.9**	**13.0**	**0.1146**	**0.67**	**0.2**
05SA219-1	24.8	1.5	10.4	12.1	79.9	1.2	13.6	2.8	0.0259	0.62	
05SA219-2*	29.5	1.8	15.5	15.3	79.6	1.0	19.4	3.1	0.0443	0.63	
05SA219-3	22.3	1.3	13.4	15.5	67.6	1.2	17.3	2.8	0.0293	0.62	3.7
AVG	**23.5**	**1.4**	**11.9**	**13.8**	**73.7**	**1.2**	**15.4**	**2.8**	**0.0276**	**0.62**	**1.7**
05SA220-1	19.5	1.2	9.3	11.2	102.0	1.2	12.3	3.6	0.0193	0.64	
05SA220-2	23.3	1.4	7.4	10.9	111.2	1.5	10.4	3.3	0.0194	0.64	
05SA220-3	27.1	1.6	7.3	10.4	113.1	1.4	10.2	3.1	0.0219	0.63	3.8
AVG	**23.3**	**1.4**	**8.0**	**10.8**	**108.8**	**1.4**	**11.0**	**3.3**	**0.0202**	**0.64**	**3.8**
05SA221-1	36.5	2.2	7.6	11.1	145.7	1.5	10.9	4.9	0.0339	0.67	
05SA221-2	37.1	2.2	7.8	11.7	137.7	1.5	11.1	4.4	0.0345	0.66	0.5
AVG	**36.8**	**2.2**	**7.7**	**11.4**	**141.7**	**1.5**	**11.0**	**4.7**	**0.0342**	**0.67**	**0.5**
05SA222-1	20.5	1.2	8.9	14.6	147.7	1.6	13.0	3.1	0.0208	0.62	
05SA222-2*	30.9	1.9	6.2	9.7	144.3	1.5	9.2	3.2	0.0227	0.63	
05SA222-3	22.1	1.3	7.4	10.9	154.4	1.5	10.6	3.1	0.0187	0.63	5.6
AVG	**21.3**	**1.3**	**8.1**	**12.8**	**151.0**	**1.6**	**11.8**	**3.1**	**0.0198**	**0.62**	**1.1**
05SA223b-1	20.5	1.2	15.2	61.4	71.1	4.0	29.7	7.0	0.0442	0.60	
05SA223b-2	23.8	1.4	9.3	29.6	43.7	3.2	16.3	6.0	0.0273	0.59	2.3
AVG	**22.1**	**1.3**	**12.3**	**45.5**	**57.4**	**3.6**	**23.0**	**6.5**	**0.0358**	**0.59**	**2.3**
05SA224-1*	22.2	1.3	16.5	18.1	95.5	1.1	21.2	3.8	0.0375	0.65	
05SA224-2	15.4	0.9	11.5	12.7	67.4	1.1	14.8	4.0	0.0185	0.66	
05SA224-3	16.0	1.0	10.2	11.9	67.4	1.2	13.3	3.7	0.0170	0.65	3.8
AVG	**15.7**	**0.9**	**10.9**	**12.3**	**67.4**	**1.1**	**14.1**	**3.9**	**0.0178**	**0.65**	**0.4**

Apatite Aliquot	Age (Ma)	± 6% (2σ)	U (ppm)	Th (ppm)	Sm (ppm)	Th/U	[eU]	mass (µg)	^{4}He yield (ncc / µg)	F_T	SDOM (Ma)
05SA225-1	21.3	1.3	10.7	8.6	104.0	0.8	13.2	3.7	0.0230	0.66	
05SA225-2*	42.1	2.5	10.6	7.7	89.4	0.7	12.8	3.8	0.0440	0.66	
05SA225-3*	29.5	1.8	8.3	5.9	83.8	0.7	10.0	3.7	0.0242	0.65	
05SA225-4	20.7	1.2	16.5	9.6	79.0	0.6	19.1	5.2	0.0332	0.68	10.0
AVG	**21.0**	**1.3**	**13.6**	**9.1**	**91.5**	**0.7**	**16.1**	**4.4**	**0.0281**	**0.67**	**0.4**
05SA226-1	17.6	1.1	9.8	7.1	97.7	0.7	11.9	7.2	0.0188	0.72	
05SA226-2	17.2	1.0	8.0	5.9	63.2	0.7	9.7	7.4	0.0148	0.72	
05SA226-3	18.6	1.1	11.6	18.8	78.6	1.6	16.4	6.8	0.0264	0.70	
05SA226-4*	aliquot not analyzed										
05SA226-5*	47.3	2.8	8.9	7.6	73.3	0.9	11.0	3.2	0.0412	0.64	
05SA226-6*	33.8	2.0	18.8	17.0	133.9	0.9	23.3	3.5	0.0630	0.65	13.3
AVG	**17.8**	**1.1**	**9.8**	**10.6**	**79.8**	**1.0**	**12.7**	**7.1**	**0.0200**	**0.71**	**0.7**
05SA227-1	19.2	1.2	24.1	15.3	66.6	0.6	27.9	3.2	0.0420	0.64	
05SA227-2	24.8	1.5	23.5	13.1	57.4	0.6	26.8	3.2	0.0522	0.64	
05SA227-3*	61.9	3.7	9.4	9.7	56.5	1.0	12.0	3.3	0.0586	0.64	
05SA227-4*	39.2	2.4	15.0	12.5	66.4	0.8	18.2	2.9	0.0550	0.63	
05SA227-5	23.4	1.4	8.2	7.7	46.0	0.9	10.3	3.7	0.0193	0.65	17.5
AVG	**22.5**	**1.3**	**18.6**	**12.0**	**56.7**	**0.7**	**21.7**	**3.4**	**0.0378**	**0.64**	**2.9**
05SA228b-1	20.2	1.2	18.4	1.4	47.4	0.1	19.0	13.6	0.0323	0.69	
05SA228b-2	18.6	1.1	28.6	1.2	47.4	0.0	29.1	13.5	0.0453	0.69	
05SA228b-3	22.3	1.3	22.6	1.5	69.9	0.1	23.3	13.7	0.0436	0.69	1.9
AVG	**20.4**	**1.2**	**23.2**	**1.4**	**54.9**	**0.1**	**23.8**	**13.6**	**0.0404**	**0.69**	**1.9**
05SA234-1*	83.5	5.0	9.9	34.0	69.3	3.4	18.1	3.8	0.1192	0.64	
05SA234-2	27.3	1.6	12.9	43.3	64.0	3.3	23.2	5.7	0.0535	0.68	
05SA234-3	67.7	4.1	10.9	35.8	66.6	3.3	19.5	4.9	0.1089	0.67	
05SA234-4	31.2	1.9	12.1	46.0	76.2	3.8	23.0	4.8	0.0586	0.66	27.6
AVG	**42.1**	**2.5**	**12.0**	**41.7**	**68.9**	**3.5**	**21.9**	**5.1**	**0.0737**	**0.67**	**22.3**
2006 Collection Campaign											
06SA016-1*	13.9	0.8	7.2	5.3	54.9	0.7	8.7	5.0	0.0102	0.68	
06SA016-2	15.2	0.9	11.7	7.4	63.8	0.6	13.7	5.2	0.0177	0.68	
06SA016-3	15.0	0.9	6.9	4.5	48.6	0.6	8.2	4.7	0.0101	0.67	0.7
AVG	**15.1**	**0.9**	**9.3**	**5.9**	**56.2**	**0.6**	**10.9**	**5.0**	**0.0139**	**0.68**	**0.2**
06SA022-1*	222.7	13.4	8.1	11.0	308.9	1.4	12.2	4.5	0.2322	0.66	
06SA022-2	205.0	12.3	5.4	9.3	212.2	1.7	8.6	3.2	0.1455	0.62	
06SA022-3	201.5	12.1	5.8	7.9	209.7	1.4	8.6	3.2	0.1445	0.63	11.3
AVG	**203.2**	**12.2**	**5.6**	**8.6**	**211.0**	**1.6**	**8.6**	**3.2**	**0.1450**	**0.63**	**2.5**
06SA023-1	223.5	13.4	6.2	11.8	206.4	1.9	10.0	2.2	0.1635	0.57	
06SA023-2	213.3	12.8	6.5	11.2	236.6	1.7	10.3	1.6	0.3485	0.55	7.2
AVG	**218.4**	**13.1**	**6.4**	**11.5**	**221.5**	**1.8**	**10.1**	**1.9**	**0.2560**	**0.56**	**7.2**

Apatite Aliquot	Age (Ma)	± 6% (2σ)	U (ppm)	Th (ppm)	Sm (ppm)	Th/U	[eU]	mass (µg)	^{4}He yield (ncc / µg)	F_T	SDOM (Ma)
06SA073-1	44.5	2.7	1.6	3.6	51.9	2.3	2.7	2.4	0.0102	0.66	
06SA073-2*	343.5	20.6	-0.4	7.9	27.4	-20.3	1.6	1.6	0.0428	0.60	
06SA073-3	41.8	2.5	1.7	8.7	49.2	5.0	4.0	2.0	0.0137	0.65	
06SA073-4	34.5	2.1	0.6	4.3	55.9	6.9	1.9	0.9	0.0048	0.54	151.7
AVG	**40.3**	**2.4**	**1.3**	**5.6**	**52.3**	**4.8**	**2.9**	**1.7**	**0.0096**	**0.62**	**5.2**
06SA077-1	55.8	3.3	10.5	37.8	180.3	3.6	20.1	4.9	0.0945	0.67	
06SA077-2	47.2	2.8	7.2	26.1	137.6	3.6	13.9	3.9	0.0534	0.64	
06SA077-3*	198.5	11.9	12.3	37.9	211.8	3.1	22.0	2.9	0.3395	0.61	85.0
AVG	**51.5**	**3.1**	**8.9**	**32.0**	**159.0**	**3.6**	**17.0**	**4.4**	**0.0739**	**0.65**	**6.1**
06SA079-1*	41.7	2.5	7.5	33.9	226.7	4.5	16.4	2.9	0.0533	0.61	
06SA079-2	67.3	4.0	10.3	38.6	226.1	3.8	20.3	3.2	0.1071	0.62	
06SA079-3	57.8	3.5	6.8	35.2	249.9	5.2	16.2	3.2	0.0750	0.62	
06SA079-4	68.6	4.1	10.9	36.7	183.1	3.4	20.3	2.9	0.1065	0.61	12.4
AVG	**64.6**	**3.9**	**9.3**	**36.8**	**219.7**	**4.1**	**18.9**	**3.1**	**0.0962**	**0.62**	**5.9**
06SA090b-1	33.5	2.0	18.5	17.8	128.9	1.0	23.3	8.8	0.0607	0.63	
06SA090b-2*	28.0	1.7	11.2	12.9	136.4	1.1	14.9	8.6	0.0322	0.62	
06SA090b-3	31.8	1.9	10.9	11.6	126.7	1.1	14.2	14.5	0.0383	0.68	2.8
AVG	**32.7**	**2.0**	**14.7**	**14.7**	**127.8**	**1.0**	**18.7**	**11.7**	**0.0495**	**0.65**	**1.2**
06SA093b-1*	25.1	1.5	10.1	2.3	22.9	0.2	10.7	15.5	0.0228	0.69	
06SA093b-2	47.2	2.8	10.3	2.4	23.0	0.2	11.0	15.8	0.0441	0.70	
06SA093b-3	44.5	2.7	9.6	2.0	20.2	0.2	10.2	14.5	0.0378	0.69	12.0
AVG	**45.8**	**2.7**	**10.0**	**2.2**	**21.6**	**0.2**	**10.6**	**15.2**	**0.0410**	**0.69**	**1.9**
06SA104-1	24.8	1.5	11.2	13.8	87.9	1.2	14.8	3.4	0.0290	0.64	
06SA104-2*	27.5	1.7	13.4	14.7	92.3	1.1	17.3	2.8	0.0365	0.62	
06SA104-3	21.2	1.3	11.2	12.5	80.7	1.1	14.4	3.2	0.0240	0.63	
06SA104-4	17.5	1.0	12.3	12.4	90.8	1.0	15.6	3.1	0.0212	0.63	
06SA104-5*	12.7	0.8	11.0	13.3	92.5	1.2	14.5	5.9	0.0159	0.69	5.9
AVG	**21.1**	**1.3**	**11.5**	**12.9**	**86.5**	**1.1**	**14.9**	**3.2**	**0.0247**	**0.63**	**3.7**
2007 Collection Campaign											
07SA014b-1	241.0	14.5	9.3	8.8	101.8	0.9	11.8	8.1	0.2204	0.61	
07SA014b-2*	282.1	16.9	12.2	12.3	136.0	1.0	15.7	10.2	0.3547	0.63	
07SA014b-3	234.0	14.0	13.9	14.7	91.0	1.1	17.7	8.1	0.3183	0.62	26.0
AVG	**237.5**	**14.3**	**11.6**	**11.7**	**96.4**	**1.0**	**14.8**	**8.1**	**0.2693**	**0.61**	**5.0**
07SA020-1	82.9	5.0	3.4	3.1	28.3	0.9	4.3	11.1	0.0336	0.76	
07SA020-2	67.2	4.0	2.6	3.3	16.8	1.3	3.5	10.8	0.0218	0.75	
07SA020-3*	109.9	6.6	3.3	5.6	20.6	1.7	4.7	24.0	0.0514	0.80	
07SA020-4	71.6	4.3	4.2	2.6	12.8	0.6	4.8	22.3	0.0343	0.81	19.2
AVG	**73.9**	**4.4**	**3.4**	**3.0**	**19.3**	**0.9**	**4.2**	**14.7**	**0.0299**	**0.77**	**8.1**

Apatite Aliquot	Age (Ma)	± 6% (2σ)	U (ppm)	Th (ppm)	Sm (ppm)	Th/U	[eU]	mass (µg)	^{4}He yield (ncc / µg)	F_T	SDOM (Ma)
07SA022-1	55.4	3.3	21.2	73.7	53.6	3.5	38.5	6.2	0.1818	0.69	
07SA022-2*	54.0	3.2	26.1	42.5	26.2	1.6	36.1	8.3	0.1715	0.72	
07SA022-3	54.9	3.3	23.1	60.2	47.3	2.6	37.2	4.7	0.1671	0.67	0.7
AVG	**55.1**	**3.3**	**22.2**	**66.9**	**50.4**	**3.0**	**37.8**	**5.4**	**0.1745**	**0.68**	**0.3**
07SA029-1*	67.9	4.1	41.9	184.4	637.4	4.4	87.5	4.3	0.4327	0.68	
07SA029-2	38.5	2.3	48.8	158.3	621.0	3.2	88.4	5.0	0.2391	0.70	
07SA029-3	39.1	2.3	199.8	327.0	340.3	1.6	276.8	6.1	0.6380	0.72	
07SA029-4	38.5	2.3	179.5	355.9	493.3	2.0	263.9	4.2	0.6111	0.68	14.6
AVG	**38.7**	**2.3**	**142.7**	**280.4**	**484.8**	**2.3**	**209.7**	**5.1**	**0.4960**	**0.70**	**0.3**
07SA037-1	58.3	3.5	2.0	7.0	57.3	3.5	3.9	14.0	0.0222	0.76	
07SA037-2	54.9	3.3	2.0	6.4	63.8	3.2	3.8	12.4	0.0203	0.75	
07SA037-3*	49.4	3.0	3.9	11.3	79.6	2.9	7.0	10.0	0.0323	0.74	4.5
AVG	**56.6**	**3.4**	**2.0**	**6.7**	**60.5**	**3.4**	**3.8**	**13.2**	**0.0213**	**0.76**	**2.5**
07SA045-1	0.5	0.0	2.8	4.3	14.0	1.5	3.9	22.6	0.0002	0.80	
07SA045-2	0.5	0.0	4.7	7.8	20.5	1.7	6.6	13.5	0.0003	0.77	
07SA045-3	0.6	0.0	3.5	5.1	16.9	1.5	4.7	30.9	0.0003	0.82	
07SA045-4	0.7	0.0	3.4	6.5	18.4	1.9	5.0	15.9	0.0003	0.78	0.1
AVG	**0.6**	**0.0**	**3.6**	**5.9**	**17.5**	**1.6**	**5.0**	**20.7**	**0.0003**	**0.79**	**0.1**
2009 Collection Campaign											
09SA001-1	283.5	17.0	4.1	11.4	15.9	2.8	6.8	19.5	0.1891	0.79	
09SA001-2	236.2	14.2	4.3	9.4	20.3	2.2	6.6	16.4	0.1519	0.78	
09SA001-3*	142.8	8.6	6.5	11.5	13.6	1.8	9.2	26.7	0.1320	0.81	71.6
AVG	**259.8**	**15.6**	**4.2**	**10.4**	**18.1**	**2.5**	**6.7**	**17.9**	**0.1705**	**0.78**	**33.4**
09SA002-1	144.1	8.6	9.9	2.1	7.7	0.2	10.5	24.4	0.1510	0.82	
09SA002-2*	164.5	9.9	9.6	1.9	6.7	0.2	10.1	22.4	0.1650	0.81	
09SA002-3*	85.1	5.1	4.7	1.4	9.0	0.3	5.1	32.9	0.0445	0.83	
09SA002-4	100.7	6.0	2.0	0.8	10.4	0.4	2.2	55.5	0.0234	0.86	37.0
AVG	**122.4**	**7.3**	**5.9**	**1.4**	**9.0**	**0.3**	**6.3**	**39.9**	**0.0872**	**0.84**	**30.7**
09SA005b-1*	280.4	16.8	11.6	13.9	123.0	1.2	15.4	10.2	0.3487	0.64	
09SA005b-2*	24.7	1.5	126.7	47.0	135.5	0.4	138.2	8.1	0.2673	0.64	
09SA005b-3*	184.1	11.0	5.1	13.6	162.0	2.6	9.1	9.2	0.1366	0.63	129.1
AVG	***163.1***	***9.8***	----	----	----	----	----	----	----	----	----
09SA006-1	158.2	9.5	0.9	3.2	39.1	3.4	1.9	12.8	0.0295	0.76	
09SA006-2	146.8	8.8	2.1	7.1	58.9	3.4	4.0	12.6	0.0574	0.76	
09SA006-3*	98.3	5.9	1.2	3.9	44.2	3.4	2.3	15.2	0.0227	0.77	
09SA006-4	143.6	8.6	1.4	4.3	44.4	3.2	2.6	21.6	0.0383	0.80	26.4
AVG	**149.6**	**9.0**	**1.5**	**4.9**	**47.5**	**3.3**	**2.8**	**15.7**	**0.0417**	**0.77**	**7.7**

Apatite Aliquot	Age (Ma)	± 6% (2σ)	U (ppm)	Th (ppm)	Sm (ppm)	Th/U	[eU]	mass (µg)	^{4}He yield (ncc / µg)	F_T	SDOM (Ma)
09SA009-1	125.7	7.5	1.4	3.5	52.0	2.5	2.4	11.9	0.0305	0.76	
09SA009-2*	79.9	4.8	1.1	3.2	50.7	2.8	2.1	12.1	0.0167	0.75	
09SA009-3	122.3	7.3	2.8	8.6	84.7	3.0	5.2	10.5	0.0617	0.75	25.5
AVG	**124.0**	**7.4**	**2.1**	**6.0**	**68.3**	**2.8**	**3.8**	**11.2**	**0.0461**	**0.75**	**2.4**

Table 5 - Apatite (U-Th)/He Aliquot Age and Isotope Concentration Data

See Appendix A for statistical treatment of CARF (U-Th)/He age data.

Zircon Aliquot	Age (Ma)	± 8% (2σ)	U (ppm)	Th (ppm)	Sm (ppm)	Th/U	[eU]	mass (µg)	^{4}He yield (ncc / µg)	F_T	SDOM (Ma)
2004 Collection Campaign											
z04SA088-1	322.2	25.8	304.7	255.3	32.9	0.8	363.6	5.6	11.0831	0.76	
z04SA088-2	302.0	24.2	104.6	34.4	2.4	0.3	112.5	3.3	3.0711	0.73	
z04SA088-3*	232.7	18.6	334.5	71.1	6.3	0.2	350.9	3.3	7.3533	0.73	47.0
AVG	**312.1**	**25.0**	**204.6**	**144.8**	**17.6**	**0.6**	**238.1**	**4.4**	**7.0771**	**0.75**	**14.3**
z04SA090-1	483.3	38.7	95.1	36.2	1.7	0.4	103.4	3.0	4.5260	0.72	
z04SA090-2*	580.6	46.4	110.5	40.6	32.7	0.4	120.0	3.3	6.4313	0.73	
z04SA090-3	457.7	36.6	60.7	17.9	1.6	0.3	64.8	2.5	2.6406	0.71	64.9
AVG	**470.5**	**37.6**	**77.9**	**27.0**	**1.6**	**0.3**	**84.1**	**2.8**	**3.5833**	**0.72**	**18.1**
z04SA091-1*	201.6	16.1	691.2	131.9	6.3	0.2	721.6	11.9	14.6680	0.82	
z04SA091-2*	37.0	3.0	1790.4	455.8	14.3	0.3	1895.4	6.7	6.6319	0.78	
z04SA091-3*	100.8	8.1	1657.1	491.9	12.8	0.3	1770.4	4.9	16.5841	0.76	83.0
AVG	***113.1***	***9.1***	----	----	----	----	----	----	----	----	----
z04SA092-1	382.3	30.6	171.0	74.3	0.4	0.4	188.1	3.1	6.4404	0.72	
z04SA092-2	389.6	31.2	175.9	79.2	1.1	0.5	194.1	3.5	6.8308	0.73	
z04SA092-3	365.9	29.3	188.9	69.1	0.8	0.4	204.8	3.3	6.7555	0.73	12.1
AVG	**379.3**	**30.3**	**178.6**	**74.2**	**0.8**	**0.4**	**195.7**	**3.3**	**6.6756**	**0.73**	**12.1**
z04SA093-1	332.1	26.6	173.2	43.0	4.7	0.2	183.1	5.6	5.7010	0.76	
z04SA093-2	339.1	27.1	249.9	60.7	2.1	0.2	263.9	6.3	8.5194	0.77	5.0
AVG	**335.6**	**26.8**	**211.6**	**51.9**	**3.4**	**0.2**	**223.5**	**6.0**	**7.1102**	**0.76**	**5.0**
z04SA097-1	327.1	26.2	277.5	211.5	1.8	0.8	326.2	5.1	10.0667	0.76	
z04SA097-2*	219.3	17.5	339.1	257.8	2.0	0.8	398.4	6.5	8.3995	0.78	
z04SA097-3	274.7	22.0	504.5	168.6	3.4	0.3	543.3	4.6	13.9815	0.76	53.9
AVG	**300.9**	**24.1**	**391.0**	**190.1**	**2.6**	**0.5**	**434.8**	**4.9**	**12.0241**	**0.76**	**37.0**
z04SA101-1*	130.1	10.4	156.2	37.8	2.8	0.2	164.9	5.8	1.9703	0.75	
z04SA101-2	73.4	5.9	94.8	17.1	1.8	0.2	98.8	6.4	0.6596	0.75	
z04SA101-3	90.0	7.2	185.5	37.0	2.7	0.2	194.0	4.2	1.5361	0.72	29.2
AVG	**81.7**	**6.5**	**140.2**	**27.1**	**2.2**	**0.2**	**146.4**	**5.3**	**1.0979**	**0.74**	**11.8**
z04SA102-1*	40.5	3.2	58.7	9.0	2.3	0.2	60.7	3.8	0.2225	0.75	
z04SA102-2	62.1	5.0	99.6	30.1	2.1	0.3	106.6	4.2	0.5983	0.74	
z04SA102-3	60.9	4.9	109.6	15.5	1.2	0.1	113.1	9.7	0.6756	0.81	
z04SA102-4*	86.1	6.9	62.6	10.8	1.8	0.2	65.1	8.3	0.5445	0.80	18.7
AVG	**61.5**	**4.9**	**104.6**	**22.8**	**1.6**	**0.2**	**109.8**	**7.0**	**0.6370**	**0.78**	**0.8**
z04SA103-1	69.1	5.5	57.3	10.8	1.5	0.2	59.8	7.6	0.3862	0.77	
z04SA103-2	64.4	5.2	65.3	12.1	1.7	0.2	68.1	6.7	0.4075	0.77	
z04SA103-3*	21.5	1.7	127.9	73.6	7696.1	0.6	183.3	6.7	0.4111	0.76	26.2
AVG	**66.8**	**5.3**	**61.3**	**11.5**	**1.6**	**0.2**	**64.0**	**7.2**	**0.3969**	**0.77**	**3.4**

Zircon Aliquot	Age (Ma)	± 8% (2σ)	U (ppm)	Th (ppm)	Sm (ppm)	Th/U	[eU]	mass (µg)	^{4}He yield (ncc / µg)	F_T	SDOM (Ma)
z04SA104-1*	32.5	2.6	37.6	6.8	1.4	0.2	39.2	8.1	0.1229	0.80	
z04SA104-2	43.5	3.5	49.7	6.0	1.1	0.1	51.1	9.0	0.2161	0.80	
z04SA104-3	44.6	3.6	32.2	6.0	1.0	0.2	33.6	11.6	0.1482	0.81	
z04SA104-4*	55.0	4.4	60.0	11.9	1.3	0.2	62.7	5.8	0.3236	0.77	9.2
AVG	**44.1**	**3.5**	**41.0**	**6.0**	**1.0**	**0.2**	**42.3**	**10.3**	**0.1822**	**0.81**	**0.8**
z04SA106-1*	18.2	1.5	160.6	31.6	1.6	0.2	167.9	4.7	0.2815	0.76	
z04SA106-2	19.9	1.6	795.3	82.9	2.1	0.1	814.4	4.2	1.4770	0.75	
z04SA106-3	19.9	1.6	257.4	35.1	1.3	0.1	265.5	5.9	0.4947	0.77	1.0
AVG	**19.9**	**1.6**	**526.4**	**59.0**	**1.7**	**0.1**	**540.0**	**5.1**	**0.9858**	**0.76**	**0.0**
z04SA109-1*	233.9	18.7	84.8	10.7	3.5	0.1	87.3	5.7	1.9331	0.77	
z04SA109-2	317.2	25.4	89.1	17.2	3.1	0.2	93.1	4.8	2.7759	0.76	
z04SA109-3	279.1	22.3	71.6	17.1	3.7	0.2	75.6	3.8	1.9110	0.74	41.7
AVG	**298.1**	**23.9**	**80.4**	**17.2**	**3.4**	**0.2**	**84.3**	**4.3**	**2.3434**	**0.75**	**27.0**
z04SA110-1	24.1	1.9	164.5	26.1	4.4	0.2	170.5	6.0	0.3866	0.78	
z04SA110-2	27.1	2.2	176.2	25.4	2.2	0.1	182.1	5.7	0.4625	0.78	
z04SA110-3*	46.4	3.7	180.8	29.4	2.1	0.2	187.6	5.9	0.8204	0.78	
z04SA110-4	42.0	3.4	108.4	19.9	4.2	0.2	113.0	5.4	0.4424	0.77	11.0
AVG	**31.1**	**2.5**	**157.5**	**25.2**	**3.2**	**0.2**	**163.3**	**5.8**	**0.5280**	**0.77**	**9.6**
2005 Collection Campaign											
z05SA177-1	410.3	32.8	94.6	54.2	11.7	0.6	107.1	4.6	4.1492	0.76	
z05SA177-2	374.4	30.0	135.9	102.1	11.5	0.8	159.5	5.2	5.6541	0.76	
z05SA177-3	394.7	31.6	71.9	42.7	6.4	0.6	81.7	5.4	3.0678	0.76	18.0
AVG	**393.1**	**31.5**	**100.8**	**66.3**	**9.9**	**0.6**	**116.1**	**5.1**	**4.2904**	**0.76**	**18.0**
z05SA178-1*	347.0	27.8	136.1	92.6	13.2	0.7	157.5	9.1	5.4109	0.80	
z05SA178-2	320.4	25.6	162.7	145.0	51.4	0.9	196.3	9.6	6.2477	0.80	
z05SA178-3	302.8	24.2	150.5	81.2	17.2	0.5	169.2	13.6	5.2118	0.82	22.2
AVG	**311.6**	**24.9**	**156.6**	**113.1**	**34.3**	**0.7**	**182.8**	**11.6**	**5.7298**	**0.81**	**12.5**
z05SA179-1	317.9	25.4	104.6	50.8	17.4	0.5	116.3	6.1	3.5465	0.77	
z05SA179-2*	395.2	31.6	93.3	55.2	11.1	0.6	106.1	6.8	4.0722	0.78	
z05SA179-3	297.4	23.8	352.6	155.5	31.0	0.4	388.6	7.4	11.2798	0.79	51.6
AVG	**307.7**	**24.6**	**228.6**	**103.1**	**24.2**	**0.5**	**252.5**	**6.8**	**7.4131**	**0.78**	**14.5**
z05SA180-1*	417.3	33.4	126.7	146.4	16.1	1.2	160.5	4.7	6.2441	0.75	
z05SA180-2*	371.2	29.7	167.1	157.8	22.9	0.9	203.6	6.9	7.2704	0.77	
z05SA180-3*	659.1	52.7	88.9	71.7	28.2	0.8	105.6	6.0	6.8077	0.77	154.7
AVG	***482.5***	***38.6***	**----**	**----**	**----**	**----**	**----**	**----**	**----**	**----**	**----**
z05SA182-1	347.6	27.8	163.8	93.6	30.2	0.6	185.5	13.2	6.5716	0.82	
z05SA182-2	348.3	27.9	188.1	95.6	4.8	0.5	210.1	13.1	7.4464	0.82	
z05SA182-3*	427.8	34.2	146.7	106.9	7.4	0.7	171.4	12.7	7.4800	0.82	46.1
AVG	**348.0**	**27.8**	**175.9**	**94.6**	**17.5**	**0.5**	**197.8**	**13.2**	**7.0090**	**0.82**	**0.5**

Zircon Aliquot	Age (Ma)	± 8% (2σ)	U (ppm)	Th (ppm)	Sm (ppm)	Th/U	[eU]	mass (µg)	^{4}He yield (ncc / µg)	F_T	SDOM (Ma)
z05SA183-1*	648.2	51.9	146.3	194.9	9.4	1.3	191.3	4.9	11.8410	0.75	
z05SA183-2	498.8	39.9	154.5	111.8	16.6	0.7	180.4	5.4	8.6237	0.76	
z05SA183-3	496.0	39.7	67.7	47.4	6.7	0.7	78.6	6.0	3.7701	0.77	87.1
AVG	**497.4**	**39.8**	**111.1**	**79.6**	**11.6**	**0.7**	**129.5**	**5.7**	**6.1969**	**0.77**	**2.0**
z05SA184-1	356.1	28.5	194.1	108.7	25.7	0.6	219.2	6.3	7.5288	0.78	
z05SA184-2*	402.8	32.2	256.6	135.9	13.2	0.5	287.9	6.1	11.1982	0.77	
z05SA184-3	368.3	29.5	162.9	90.6	16.0	0.6	183.8	7.0	6.5984	0.78	24.2
AVG	**362.2**	**29.0**	**178.5**	**99.6**	**20.8**	**0.6**	**201.5**	**6.7**	**7.0636**	**0.78**	**8.6**
z05SA191-1*	420.4	33.6	109.3	80.3	4.8	0.7	127.8	17.6	5.3213	0.79	
z05SA191-2	381.0	30.5	139.4	76.0	11.2	0.5	157.0	18.1	5.8909	0.79	
z05SA191-3	347.3	27.8	127.9	59.0	14.7	0.5	141.6	24.1	4.9212	0.81	
z05SA191-4	346.1	27.7	132.9	54.0	9.2	0.4	145.4	24.5	5.0894	0.81	35.1
AVG	**358.1**	**28.7**	**133.4**	**63.0**	**11.7**	**0.5**	**148.0**	**22.2**	**5.3005**	**0.80**	**19.8**
z05SA192-1	246.8	19.7	716.0	484.4	40.6	0.7	827.7	6.0	17.9969	0.72	
z05SA192-2*	425.3	34.0	244.0	125.0	8.6	0.5	272.8	9.7	10.8521	0.75	
z05SA192-3	268.1	21.4	387.6	229.6	25.8	0.6	440.6	8.9	10.7568	0.74	97.5
AVG	**257.4**	**20.6**	**551.8**	**357.0**	**33.2**	**0.6**	**634.2**	**7.4**	**14.3768**	**0.73**	**15.1**
z05SA194-1	380.7	30.5	80.4	38.6	3.7	0.5	89.3	3.3	3.1031	0.73	
z05SA194-2*	421.1	33.7	115.6	60.1	9.0	0.5	129.5	3.9	5.0171	0.74	
z05SA194-3*	287.0	23.0	129.6	59.4	6.6	0.5	143.3	4.2	3.8054	0.75	
z05SA194-4	331.6	26.5	181.0	100.3	3.3	0.6	204.1	6.5	6.5163	0.78	58.3
AVG	**356.2**	**28.5**	**130.7**	**69.5**	**3.5**	**0.5**	**146.7**	**4.9**	**4.8097**	**0.76**	**34.7**
z05SA195-1*	392.4	31.4	69.9	30.1	2.9	0.4	76.8	2.9	2.6820	0.72	
z05SA195-2	340.8	27.3	109.4	48.8	7.0	0.4	120.6	3.3	3.6476	0.72	
z05SA195-3	359.1	28.7	85.6	35.2	3.2	0.4	93.7	3.0	2.9988	0.72	26.2
AVG	**350.0**	**28.0**	**97.5**	**42.0**	**5.1**	**0.4**	**107.1**	**3.1**	**3.3232**	**0.72**	**12.9**
z05SA196-1	150.6	12.0	76.9	26.4	2.9	0.3	83.0	4.9	1.1656	0.76	
z05SA196-2*	179.2	14.3	95.1	53.2	5.1	0.6	107.4	5.8	1.8142	0.77	
z05SA196-3	132.9	10.6	156.1	75.3	2.8	0.5	173.4	6.9	2.2065	0.78	23.4
AVG	**141.8**	**11.3**	**116.5**	**50.8**	**2.9**	**0.4**	**128.2**	**5.9**	**1.6861**	**0.77**	**12.5**
z05SA197-1	277.8	22.2	297.1	118.2	3.6	0.4	324.3	8.3	8.2315	0.74	
z05SA197-2	332.2	26.6	178.7	82.1	4.0	0.5	197.6	10.3	6.1446	0.76	
z05SA197-3*	363.0	29.0	118.4	55.9	6.7	0.5	131.3	10.1	4.4395	0.75	
z05SA197-4	279.1	22.3	211.7	67.8	2.2	0.3	227.4	18.0	6.2098	0.79	41.8
AVG	**296.4**	**23.7**	**229.2**	**89.3**	**3.3**	**0.4**	**249.8**	**12.2**	**6.8619**	**0.76**	**31.0**

Zircon Aliquot	Age (Ma)	± 8% (2σ)	U (ppm)	Th (ppm)	Sm (ppm)	Th/U	[eU]	mass (µg)	^{4}He yield (ncc / µg)	F_T	SDOM (Ma)
z05SA198-1*					lost during analysis						
z05SA198-2	392.5	31.4	275.2	110.6	3.3	0.4	300.6	4.7	10.9605	0.75	
z05SA198-3*					lost during analysis						
z05SA198-4	447.4	35.8	177.2	75.8	6.0	0.4	194.7	3.9	8.0448	0.74	38.9
AVG	**420.0**	**33.6**	**226.2**	**93.2**	**4.6**	**0.4**	**247.7**	**4.3**	**9.5026**	**0.74**	**38.9**
z05SA199-1	365.6	29.2	173.3	39.9	2.6	0.2	182.4	4.5	6.2413	0.75	
z05SA199-2	312.8	25.0	297.7	57.8	3.6	0.2	311.1	4.0	8.9116	0.74	
z05SA199-3	261.9	21.0	440.8	76.0	7.2	0.2	458.3	4.3	11.0189	0.75	51.8
AVG	**313.4**	**25.1**	**303.9**	**57.9**	**4.5**	**0.2**	**317.3**	**4.3**	**8.7239**	**0.75**	**51.8**
z05SA200-1	244.7	19.6	250.8	56.4	2.8	0.2	263.8	5.5	6.0922	0.77	
z05SA200-2*	360.4	28.8	146.7	38.9	0.6	0.3	155.7	6.2	5.3958	0.77	
z05SA200-3	271.8	21.7	161.1	37.4	1.6	0.2	169.7	6.6	4.4384	0.78	
z05SA200-4	241.3	19.3	103.4	22.0	0.8	0.2	108.5	4.7	2.4066	0.75	55.6
AVG	**252.6**	**20.2**	**171.8**	**38.6**	**1.7**	**0.2**	**180.7**	**5.6**	**4.3124**	**0.77**	**16.7**
z05SA201-1*	209.7	16.8	370.2	162.2	5.6	0.4	407.6	5.8	8.0081	0.76	
z05SA201-2	328.2	26.3	252.0	121.4	4.7	0.5	280.0	5.0	8.5737	0.75	
z05SA201-3	309.2	24.7	112.2	51.7	1.9	0.5	124.1	4.0	3.4901	0.74	63.6
AVG	**318.7**	**25.5**	**182.1**	**86.6**	**3.3**	**0.5**	**202.1**	**4.5**	**6.0319**	**0.74**	**13.4**
z05SA202-1*	232.6	18.6	207.1	61.7	1.4	0.3	221.3	7.5	4.9456	0.78	
z05SA202-2	293.0	23.4	145.6	45.1	2.0	0.3	155.9	9.0	4.5047	0.80	
z05SA202-3	302.4	24.2	149.9	45.5	1.6	0.3	160.4	7.4	4.6916	0.78	37.9
AVG	**297.7**	**23.8**	**147.7**	**45.3**	**1.8**	**0.3**	**158.2**	**8.2**	**4.5982**	**0.79**	**6.7**
z05SA203-1	253.4	20.3	137.3	29.2	3.2	0.2	144.0	6.1	3.4662	0.77	
z05SA203-2	212.7	17.0	119.7	26.5	1.3	0.2	125.7	8.7	2.6135	0.80	
z05SA203-3	177.0	14.2	289.5	47.1	2.5	0.2	300.4	7.9	5.0854	0.78	38.2
AVG	**214.4**	**17.1**	**182.1**	**34.2**	**2.3**	**0.2**	**190.0**	**7.6**	**3.7217**	**0.78**	**38.2**
z05SA205-1*	317.8	25.4	36.4	9.6	0.7	0.3	38.6	11.6	1.2378	0.81	
z05SA205-2	471.5	37.7	148.6	58.1	3.6	0.4	162.0	9.9	7.7168	0.81	
z05SA205-3	505.9	40.5	86.9	34.6	2.7	0.4	94.9	10.0	4.8641	0.81	100.1
AVG	**488.7**	**39.1**	**117.8**	**46.4**	**3.2**	**0.4**	**128.4**	**9.9**	**6.2905**	**0.81**	**24.3**
z05SA206-1	24.3	1.9	127.2	38.1	1.1	0.3	135.9	4.1	0.2956	0.74	
z05SA206-2	24.3	1.9	182.3	52.1	2.6	0.3	194.3	5.3	0.4353	0.76	
z05SA206-3*	19.9	1.6	178.0	51.4	1.0	0.3	189.8	5.9	0.3492	0.77	2.6
AVG	**24.3**	**1.9**	**154.7**	**45.1**	**1.9**	**0.3**	**165.1**	**4.7**	**0.3655**	**0.75**	**0.1**
z05SA207-1*	362.1	29.0	266.0	81.3	1.2	0.3	284.7	9.9	10.3603	0.81	
z05SA207-2	458.9	36.7	154.6	47.3	1.5	0.3	165.5	8.5	7.6121	0.80	
z05SA207-3	486.9	39.0	104.0	30.7	1.1	0.3	111.1	8.5	5.4441	0.80	65.5
AVG	**472.9**	**37.8**	**129.3**	**39.0**	**1.3**	**0.3**	**138.3**	**8.5**	**6.5281**	**0.80**	**19.8**

Zircon Aliquot	Age (Ma)	± 8% (2σ)	U (ppm)	Th (ppm)	Sm (ppm)	Th/U	[eU]	mass (µg)	^{4}He yield (ncc / µg)	F_T	SDOM (Ma)
z05SA208-1	472.2	37.8	111.7	36.7	1.4	0.3	120.1	4.2	5.3343	0.75	
z05SA208-2	435.0	34.8	153.2	50.6	2.0	0.3	164.8	4.5	6.7605	0.76	
z05SA208-3*	520.4	41.6	68.3	17.8	5.8	0.3	72.4	5.9	3.6544	0.77	42.9
AVG	**453.6**	**36.3**	**132.4**	**43.7**	**1.7**	**0.3**	**142.5**	**4.3**	**6.0474**	**0.75**	**26.4**
z05SA209-1*	175.9	14.1	686.0	223.7	8.4	0.3	737.5	5.7	12.2924	0.77	
z05SA209-2*	357.0	28.6	65.5	19.1	5.4	0.3	69.9	5.9	2.3834	0.77	
z05SA209-3*	808.5	64.7	98.7	38.0	1.9	0.4	107.5	4.1	8.3124	0.74	**325.8**
AVG	***447.1***	***35.8***	----	----	----	----	----	----	----	----	----
z05SA210-1*	304.4	24.4	190.3	44.8	1.2	0.2	200.6	12.1	6.2096	0.82	
z05SA210-2	472.1	37.8	149.8	49.4	0.9	0.3	161.1	10.7	7.7323	0.81	
z05SA210-3	475.2	38.0	124.2	34.4	0.8	0.3	132.1	11.3	6.4135	0.81	97.7
AVG	**473.7**	**37.9**	**137.0**	**41.9**	**0.8**	**0.3**	**146.6**	**11.0**	**7.0729**	**0.81**	**2.2**
z05SA211-1*	308.4	24.7	214.1	60.8	2.7	0.3	228.1	6.7	6.8218	0.78	
z05SA211-2*	161.7	12.9	502.7	135.8	3.0	0.3	534.0	8.2	8.4058	0.80	
z05SA211-3*	228.1	18.3	188.8	56.2	2.6	0.3	201.8	9.5	4.5352	0.80	73.5
AVG	***232.7***	***18.6***	----	----	----	----	----	----	----	----	----
z05SA212-1	229.2	18.3	185.0	44.8	0.4	0.2	195.3	8.7	4.3959	0.80	
z05SA212-2	240.7	19.3	96.7	27.2	0.7	0.3	102.9	10.5	2.4753	0.81	
z05SA212-3*	313.6	25.1	101.5	32.4	0.7	0.3	108.9	11.1	3.4409	0.81	45.8
AVG	**234.9**	**18.8**	**140.8**	**36.0**	**0.6**	**0.3**	**149.1**	**9.6**	**3.4356**	**0.81**	**8.1**
z05SA213-1*	308.4	24.7	129.6	41.9	0.9	0.3	139.2	8.9	4.2333	0.80	
z05SA213-2	248.4	19.9	169.3	45.2	0.7	0.3	179.7	7.9	4.3602	0.79	
z05SA213-3	248.5	19.9	122.6	33.0	0.6	0.3	130.2	6.6	3.1008	0.78	34.6
AVG	**248.4**	**19.9**	**145.9**	**39.1**	**0.6**	**0.3**	**154.9**	**7.3**	**3.7305**	**0.79**	**0.0**
z05SA214-1	194.4	15.6	174.2	52.1	0.6	0.3	186.2	12.9	3.6355	0.82	
z05SA214-2	159.1	12.7	110.9	151.0	1.0	1.4	145.7	15.6	2.3467	0.82	
z05SA214-3*	257.1	20.6	115.4	41.3	0.7	0.4	124.9	11.4	3.2069	0.81	49.6
AVG	**176.7**	**14.1**	**142.6**	**101.5**	**0.8**	**0.8**	**165.9**	**14.3**	**2.9911**	**0.82**	**25.0**
z05SA215-1	136.8	10.9	77.8	15.8	1.6	0.2	81.4	13.4	1.1227	0.83	
z05SA215-2	158.5	12.7	98.8	19.6	1.0	0.2	103.3	12.9	1.6426	0.82	
z05SA215-3	117.2	9.4	101.8	14.8	3.2	0.1	105.2	14.2	1.2463	0.83	20.6
AVG	**137.5**	**11.0**	**92.8**	**16.7**	**1.9**	**0.2**	**96.7**	**13.5**	**1.3372**	**0.82**	**20.6**
z05SA216-1*	98.0	7.8	122.3	30.2	6.8	0.2	129.2	4.5	1.1689	0.76	
z05SA216-2*	324.7	26.0	169.1	108.9	1.8	0.6	194.1	9.3	6.2875	0.80	
z05SA216-3*	231.6	18.5	332.3	195.7	5.2	0.6	377.3	10.1	8.6635	0.81	113.9
AVG	***218.1***	***17.4***	----	----	----	----	----	----	----	----	----

Zircon Aliquot	Age (Ma)	± 8% (2σ)	U (ppm)	Th (ppm)	Sm (ppm)	Th/U	[eU]	mass (µg)	^{4}He yield (ncc / µg)	F_T	SDOM (Ma)
z05SA217-1	379.8	30.4	181.1	76.0	3.2	0.4	198.6	9.7	7.4916	0.80	
z05SA217-2*	269.9	21.6	126.9	65.7	3.5	0.5	142.0	5.1	3.5758	0.76	
z05SA217-3	380.6	30.4	214.8	80.9	2.4	0.4	233.4	7.9	8.7644	0.79	
z05SA217-4	422.0	33.8	111.8	52.2	3.0	0.5	123.9	17.6	5.4477	0.83	65.2
AVG	**394.1**	**31.5**	**169.2**	**69.7**	**2.9**	**0.4**	**185.3**	**11.8**	**7.2345**	**0.81**	**24.1**
z05SA218-1	435.1	34.8	129.2	56.3	3.1	0.4	142.2	15.6	6.4564	0.83	
z05SA218-2	430.0	34.4	126.3	53.5	4.7	0.4	138.7	12.5	6.1074	0.82	
z05SA218-3	426.8	34.1	124.8	55.1	3.0	0.4	137.5	19.8	6.1587	0.84	4.2
AVG	**430.7**	**34.5**	**126.8**	**55.0**	**3.6**	**0.4**	**139.5**	**16.0**	**6.2408**	**0.83**	**4.2**
z05SA219-1*	405.5	32.4	158.6	39.3	0.7	0.2	167.6	13.0	7.0128	0.83	
z05SA219-2	502.2	40.2	88.8	28.3	1.0	0.3	95.4	17.1	5.0371	0.83	
z05SA219-3	493.8	39.5	136.0	41.3	1.2	0.3	145.5	17.7	7.6041	0.84	53.6
AVG	**498.0**	**39.8**	**112.4**	**34.8**	**1.1**	**0.3**	**120.4**	**17.4**	**6.3206**	**0.84**	**6.0**
z05SA220-1	508.1	40.6	92.5	31.1	1.1	0.3	99.7	4.7	4.7735	0.75	
z05SA220-2	493.4	39.5	60.7	19.0	0.6	0.3	65.1	5.9	3.1337	0.78	
z05SA220-3	470.4	37.6	218.9	111.9	6.9	0.5	244.7	6.1	11.1198	0.77	19.0
AVG	**490.6**	**39.3**	**124.0**	**54.0**	**2.9**	**0.4**	**136.5**	**5.6**	**6.3423**	**0.77**	**19.0**
z05SA221-1*	419.1	33.5	86.8	28.4	1.4	0.3	93.4	9.3	3.9337	0.80	
z05SA221-2	290.6	23.2	289.5	78.6	2.6	0.3	307.6	8.8	8.8886	0.80	
z05SA221-3	350.9	28.1	172.9	46.8	2.8	0.3	183.7	8.1	6.3852	0.80	64.3
AVG	**320.7**	**25.7**	**231.2**	**62.7**	**2.7**	**0.3**	**245.7**	**8.5**	**7.6**	**0.8**	**42.7**
z05SA222-1*	274.8	22.0	303.4	100.8	4.6	0.3	326.7	8.4	8.8842	0.80	
z05SA222-2	291.7	23.3	228.8	74.4	8.0	0.3	246.0	8.9	7.0677	0.80	
z05SA222-3	299.7	24.0	168.5	48.1	0.9	0.3	179.5	13.5	5.5246	0.83	12.7
AVG	**295.7**	**23.7**	**198.6**	**61.2**	**4.4**	**0.3**	**212.7**	**11.2**	**6.2961**	**0.81**	**5.6**
z05SA224-1	401.7	32.1	128.6	43.0	1.2	0.3	138.5	8.2	5.5225	0.80	
z05SA224-2	413.3	33.1	111.4	35.3	0.8	0.3	119.5	6.6	4.8281	0.78	
z05SA224-3	429.9	34.4	121.6	35.9	0.9	0.3	129.9	7.4	5.4904	0.79	14.2
AVG	**415.0**	**33.2**	**120.5**	**38.1**	**1.0**	**0.3**	**129.3**	**7.4**	**5.2803**	**0.79**	**14.2**
z05SA225-1	105.5	8.4	149.0	46.1	1.1	0.3	159.6	5.9	1.5991	0.78	
z05SA225-2*	150.6	12.1	262.1	95.0	3.1	0.4	284.0	8.2	4.1390	0.79	
z05SA225-3	116.8	9.3	246.0	40.1	2.5	0.2	255.2	7.8	2.8670	0.79	23.5
AVG	**111.2**	**8.9**	**197.5**	**43.1**	**1.8**	**0.2**	**207.4**	**6.8**	**2.2330**	**0.78**	**8.0**
z05SA226-1*	80.9	6.5	45.7	14.2	1.9	0.3	49.0	10.0	0.3891	0.81	
z05SA226-2	101.0	8.1	135.2	39.1	1.3	0.3	144.2	10.2	1.4339	0.81	
z05SA226-3	99.7	8.0	124.2	20.7	0.9	0.2	128.9	11.4	1.2802	0.82	11.2
AVG	**100.3**	**8.0**	**129.7**	**29.9**	**1.1**	**0.2**	**136.6**	**10.8**	**1.3571**	**0.81**	**0.9**

Zircon Aliquot	Age (Ma)	± 8% (2σ)	U (ppm)	Th (ppm)	Sm (ppm)	Th/U	[eU]	mass (µg)	^{4}He yield (ncc / µg)	F_T	SDOM (Ma)
z05SA227-1*	199.4	16.0	58.0	28.9	4.3	0.5	64.7	3.9	1.1658	0.74	
z05SA227-2*	55.1	4.4	502.9	97.9	43.0	0.2	525.6	3.7	2.6116	0.74	
z05SA227-3*	96.1	7.7	187.1	41.5	4.6	0.2	196.7	3.3	1.6829	0.73	74.4
AVG	***116.9***	***9.4***	----	----	----	----	----	----	----	----	
z05SA228-1	135.1	10.8	91.0	30.3	3.3	0.3	98.0	4.3	1.2046	0.75	
z05SA228-2	123.9	9.9	159.7	46.4	2.7	0.3	170.4	6.2	1.9808	0.77	
z05SA228-3*	97.0	7.8	222.9	58.9	8.3	0.3	236.5	4.6	2.0906	0.75	19.6
AVG	**129.5**	**10.4**	**125.4**	**38.4**	**3.0**	**0.3**	**134.2**	**5.2**	**1.5927**	**0.76**	**7.9**
z05SA234-1	20.6	1.6	2532.3	1016.2	20.1	0.4	2766.3	11.3	5.1283	0.74	
z05SA234-2	35.7	2.9	450.2	115.2	11.1	0.3	476.7	40.7	1.8197	0.88	
z05SA234-3*	125.9	10.1	643.3	157.2	15.0	0.2	679.6	11.8	7.9788	0.77	
z05SA234-4	46.2	3.7	1212.9	271.3	34.2	0.2	1275.5	20.9	5.7342	0.80	47.0
AVG	**34.2**	**2.7**	**1398.4**	**467.6**	**21.8**	**0.3**	**1506.2**	**24.3**	**4.2274**	**0.81**	**12.9**
2006 Collection Campaign											
z06SA009-1*	lost during analysis										
z06SA009-2*	lost during analysis										
z06SA009-3*	lost during analysis										
z06SA009-4	567.8	45.4	107.1	39.6	22.4	0.4	116.3	3.6	6.0542	0.73	
z06SA009-5*	596.3	47.7	87.7	28.2	3.5	0.3	94.2	3.3	5.1381	0.72	
z06SA009-6*	aliquot not analyzed										
z06SA009-7	541.0	43.3	89.1	32.9	3.4	0.4	96.7	3.5	4.7671	0.72	27.7
AVG	**554.4**	**44.4**	**98.1**	**36.2**	**12.9**	**0.4**	**106.5**	**3.5**	**5.4106**	**0.73**	**18.9**
z06SA044-1	320.2	25.6	97.9	34.4	3.6	0.4	105.8	4.1	3.1560	0.75	
z06SA044-2*	357.2	28.6	216.4	74.9	8.6	0.3	233.6	6.7	8.1067	0.78	
z06SA044-3	320.5	25.6	118.0	41.6	4.7	0.4	127.6	7.2	3.9381	0.78	21.3
AVG	**320.4**	**25.6**	**107.9**	**38.0**	**4.1**	**0.4**	**116.7**	**5.6**	**3.5470**	**0.77**	**0.2**
z06SA079-1	506.0	40.5	186.1	58.5	10.3	0.3	199.7	3.9	9.4222	0.74	
z06SA079-2	469.9	37.6	176.9	62.9	16.7	0.4	191.5	4.4	8.5033	0.75	
z06SA079-3*	561.8	44.9	170.3	60.4	4.2	0.4	184.2	5.5	10.0892	0.77	46.3
AVG	**488.0**	**39.0**	**181.5**	**60.7**	**13.5**	**0.3**	**195.6**	**4.2**	**8.9627**	**0.75**	**25.5**
z06SA089-1	392.0	31.4	232.1	76.6	5.0	0.3	249.8	2.3	8.5347	0.70	
z06SA089-2*	411.8	32.9	187.3	55.5	4.3	0.3	200.1	5.1	7.8201	0.76	
z06SA089-3	389.5	31.2	239.0	77.0	7.2	0.3	256.8	6.7	9.7681	0.78	12.2
AVG	**390.7**	**31.3**	**235.6**	**76.8**	**6.1**	**0.3**	**253.3**	**4.5**	**9.1514**	**0.74**	**1.8**
z06SA104-1	516.3	41.3	81.3	24.4	0.7	0.3	86.9	5.3	4.3141	0.76	
z06SA104-2*	459.7	36.8	117.5	30.9	0.8	0.3	124.6	9.4	5.7647	0.80	
z06SA104-3	513.5	41.1	80.6	26.2	0.8	0.3	86.6	4.8	4.2569	0.76	
z06SA104-4	470.3	37.6	122.9	39.4	0.9	0.3	132.0	6.1	5.9761	0.77	29.2
AVG	**500.0**	**40.0**	**94.9**	**30.0**	**0.8**	**0.3**	**101.8**	**5.4**	**4.8490**	**0.77**	**25.8**

Zircon Aliquot	Age (Ma)	± 8% (2σ)	U (ppm)	Th (ppm)	Sm (ppm)	Th/U	[eU]	mass (µg)	^{4}He yield (ncc / µg)	F_T	SDOM (Ma)
2007 Collection Campaign											
z07SA013-1*	237.5	19.0	258.4	87.5	7.7	0.3	278.6	7.0	5.9340	0.73	
z07SA013-2	277.6	22.2	241.5	92.0	26.9	0.4	262.8	9.3	6.8002	0.76	
z07SA013-3	279.6	22.4	147.9	40.9	6.5	0.3	157.4	8.9	4.1035	0.76	23.7
AVG	**278.6**	**22.3**	**194.7**	**66.4**	**16.7**	**0.3**	**210.1**	**9.1**	**5.4519**	**0.76**	**1.5**
z07SA014-1*	aliquot not analyzed										
z07SA014-2*	100.1	8.0	732.0	254.8		0.3	790.7	3.5	7.0162	0.73	
z07SA014-3*	213.9	17.1	624.2	150.6		0.2	658.9	2.2	12.0139	0.70	80.5
AVG	***157.0***	***12.6***	**----**	**----**	**----**	**----**	**----**	**----**	**----**	**----**	**----**
z07SA016-1	410.7	32.9	173.9	53.5	6.4	0.3	186.3	2.5	6.7705	0.71	
z07SA016-2*	213.6	17.1	338.0	99.8	14.8	0.3	361.1	2.9	6.8610	0.73	
z07SA016-3	439.9	35.2	123.7	33.1	5.9	0.3	131.4	5.0	5.5584	0.77	123.1
AVG	**425.3**	**34.1**	**148.8**	**43.3**	**6.2**	**0.3**	**158.8**	**3.8**	**6.1644**	**0.74**	**20.6**
z07SA022-1	542.8	43.4	196.3	133.1	1.4	0.7	227.0	4.5	11.6825	0.75	
z07SA022-2*	434.9	34.8	242.9	125.4	1.3	0.5	271.8	5.1	11.2499	0.76	
z07SA022-3	525.1	42.0	229.6	140.3	2.4	0.6	261.9	4.8	13.0093	0.75	57.9
AVG	**533.9**	**42.7**	**212.9**	**136.7**	**1.9**	**0.6**	**244.4**	**4.7**	**12.3459**	**0.75**	**12.5**
z07SA029-1	298.9	23.9	397.4	220.7	27.5	0.6	448.3	4.9	12.5167	0.76	
z07SA029-2	306.6	24.5	462.8	201.2	39.1	0.4	509.3	5.8	14.9058	0.77	
z07SA029-3*	376.7	30.1	256.4	138.1	8.6	0.5	288.2	6.7	10.5173	0.78	42.9
AVG	**302.7**	**24.2**	**430.1**	**211.0**	**33.3**	**0.5**	**478.8**	**5.4**	**13.7113**	**0.76**	**5.4**
z07SA040-1	415.1	33.2	58.3	42.9	2.3	0.7	68.2	4.6	2.6459	0.75	
z07SA040-2*	348.6	27.9	104.8	35.2	1.0	0.3	112.9	7.8	3.8770	0.79	
z07SA040-3	420.5	33.6	58.4	16.6	0.7	0.3	62.3	7.6	2.5862	0.79	40.0
AVG	**417.8**	**33.4**	**58.4**	**29.7**	**1.5**	**0.5**	**65.2**	**6.1**	**2.6160**	**0.77**	**3.8**
z07SA042-1*	498.4	39.9	81.4	32.9	6.4	0.4	89.0	2.3	3.8420	0.69	
z07SA042-2	589.3	47.1	59.0	15.2	5.6	0.3	62.5	2.1	3.2097	0.69	
z07SA042-3	546.9	43.8	72.7	29.1	10.8	0.4	79.5	2.7	3.8418	0.70	45.5
AVG	**568.1**	**45.4**	**65.9**	**22.2**	**8.2**	**0.3**	**71.0**	**2.4**	**3.5258**	**0.70**	**30.0**
z07SA045-1*	470.3	37.6	342.4	222.8	6.9	0.7	393.7	12.5	18.5895	0.80	
z07SA045-2	321.8	25.7	431.2	368.7	8.0	0.9	516.1	13.9	16.3547	0.79	
z07SA045-3	375.6	30.0	433.8	342.2	8.9	0.8	512.6	11.7	18.9928	0.79	75.2
AVG	**348.7**	**27.9**	**432.5**	**355.4**	**8.5**	**0.8**	**514.4**	**12.8**	**17.6738**	**0.79**	**38.0**
z07SA046-1*	611.0	48.9	196.0	76.3	3.9	0.4	213.6	4.0	12.2013	0.74	
z07SA046-2	538.2	43.1	94.1	46.9	7.8	0.5	104.9	2.8	5.1080	0.72	
z07SA046-3	566.2	45.3	126.5	47.9	7.1	0.4	137.6	2.2	6.8518	0.70	36.7
AVG	**552.2**	**44.2**	**110.3**	**47.4**	**7.5**	**0.4**	**121.3**	**2.5**	**5.9799**	**0.71**	**19.8**

Zircon Aliquot	Age (Ma)	± 8% (2σ)	U (ppm)	Th (ppm)	Sm (ppm)	Th/U	[eU]	mass (µg)	^{4}He yield (ncc / µg)	F_T	SDOM (Ma)
2009 Collection Campaign											
z09SA001-1*	623.3	49.9	160.0	96.9	8.2	0.6	182.4	4.9	10.8103	0.75	
z09SA001-2	496.5	39.7	184.2	122.6	8.5	0.7	212.5	5.9	10.1381	0.77	
z09SA001-3	483.9	38.7	165.7	104.9	3.2	0.6	189.8	7.9	9.0121	0.78	77.1
AVG	**490.2**	**39.2**	**175.0**	**113.7**	**5.9**	**0.6**	**201.2**	**6.9**	**9.5751**	**0.77**	**8.9**
z09SA002-1	469.6	37.6	76.4	9.1	1.0	0.1	78.5	10.4	3.6685	0.79	
z09SA002-2*	556.3	44.5	53.6	8.4	1.2	0.2	55.6	7.4	3.0177	0.77	
z09SA002-3	485.2	38.8	54.0	7.9	0.5	0.1	55.8	9.2	2.6256	0.77	46.2
AVG	**477.4**	**38.2**	**65.2**	**8.5**	**0.8**	**0.1**	**67.2**	**9.8**	**3.1471**	**0.78**	**11.1**
z09SA003-1*	633.6	50.7	115.9	43.2	18.4	0.4	126.0	4.9	7.3851	0.73	
z09SA003-2	607.1	48.6	129.4	40.3	39.3	0.3	138.8	6.0	8.0989	0.76	
z09SA003-3	614.3	49.1	126.0	64.8	7.8	0.5	141.0	7.3	8.4346	0.77	13.7
AVG	**610.7**	**48.9**	**127.7**	**52.5**	**23.5**	**0.4**	**139.9**	**6.6**	**8.2667**	**0.76**	**5.1**
z09SA004-1*	722.3	57.8	51.9	16.3	1.9	0.3	55.7	8.7	4.1179	0.80	
z09SA004-2*	640.9	51.3	210.1	121.8	10.9	0.6	238.1	5.2	14.7614	0.76	
z09SA004-3*	71.0	5.7	213.4	38.3	3.1	0.2	222.2	3.6	1.3968	0.73	354.9
AVG	***478.1***	***38.2***	----	----	----	----	----	----	----	----	----
z09SA005-1*	345.0	27.6	512.7	179.4	21.6	0.3	554.1	4.3	17.7554	0.75	
z09SA005-2*	587.7	47.0	185.7	60.0	10.7	0.3	199.6	4.4	11.1409	0.75	
z09SA005-3*	257.2	20.6	650.4	195.8	57.9	0.3	695.7	5.5	17.0638	0.77	171.2
AVG	***396.6***	***31.7***	----	----	----	----	----	----	----	----	----
z09SA007-1*	9.7	0.8	3187.4	1521.3	12.5	0.5	3537.7	5.8	3.1736	0.76	
z09SA007-2*	14.9	1.2	2466.4	495.0	4.0	0.2	2580.3	6.6	3.6172	0.78	
z09SA007-3	714.4	57.2	100.3	219.2	10.6	2.2	150.9	4.0	10.1126	0.74	405.4
AVG	***714.4***	***57.2***	----	----	----	----	----	----	----	----	----
z09SA008-1	387.7	31.0	556.9	168.2	25.5	0.3	595.8	4.4	21.0427	0.73	
z09SA008-2	371.4	29.7	157.3	37.1	3.8	0.2	165.8	5.8	5.6830	0.74	
z09SA008-3*	236.6	18.9	678.2	165.1	10.7	0.2	716.2	5.1	15.5990	0.75	82.9
AVG	**379.5**	**30.4**	**357.1**	**102.7**	**14.7**	**0.3**	**380.8**	**5.1**	**13.3628**	**0.74**	**11.5**
z09SA009-1*	544.9	43.6	89.7	27.8	3.5	0.3	96.1	6.0	4.9609	0.75	
z09SA009-2*	367.5	29.4	540.8	140.5	24.7	0.3	573.3	4.9	19.4006	0.74	
z09SA009-3*	154.2	12.3	1032.3	413.7	27.6	0.4	1127.7	5.4	15.9909	0.75	195.6
AVG	***355.5***	***28.4***	----	----	----	----	----	----	----	----	----

Table 6 - Zircon (U-Th)/He Aliquot Age and Isotope Concentration Data

See Appendix A for statistical treatment of CARF (U-Th)/He age data.

APPENDICES

Appendix A - Statistical Treatment of CARF (U-Th)/He Age Data

The reliability of (U-Th)/He age data is based upon the intra-aliquot reproducibility of any given sample and, though it is an exceptional practice, individual aliquot statistical outliers within the CARF (U-Th)/He age database must be rejected while preparing the data for use in relative frequency diagram plotting and thermal modeling. This segregation is especially important for age data outliers that may result from poorly measured data obtained during analytical procedures, such as inaccurate ICP-MS counts of parent nuclides, and uncontrollable external factors, such as the inherent parent and daughter nuclide concentrations within a rock sample. No data is permanently excluded and only statistical outliers are disregarded for accurate age calculations prior to numerical modeling. Exceptions are addressed in the text. Rejected aliquots and final ages and errors are listed in Tables 3 and 4.

The following routine was used to refine the CARF apatite and zircon (U-Th)/He age dataset:

1. Eliminate non-viable aliquots
    a. Non-viable aliquots contain apparent bad data such as unusually high U, Th, or Sm concentrations (potential sources of metamictization) and/or those with poor counting statistics from ICP-MS analysis.
2. Calculate the initial mean age, 2σ error, and standard deviation of mean (SDOM; 1σ) for each sample using viable aliquots
3. Determine sample age reproducibility

a. A sample age is deemed “reproducible” if two or more aliquot ages fall within the SDOM. Any aliquot whose age falls outside the SDOM is excluded from the final mean age calculation.

4. Calculate the final mean age, 2σ error, and SDOM for reproducible sample ages
    a. Final mean age and 2σ error values are used to construct cumulative probability plots and HeMP numerical models

Composite single samples are built in HeMP numerical models from weight-averaged radionuclide concentrations and age data from two or more similar aliquots..

Appendix B - Basic Sample Criteria for *HeMP* Thermal Modeling

Geologic samples must meet two basic criteria to qualify for thermal modeling. First, considering that most point samples rarely have neighboring samples to provide a proper cooling trend context, we model point samples only when their AHe and ZHe cooling ages correspond to CARF cooling events recognized within our entire AHe and ZHe dataset. A "recognized cooling event" is defined either as: 1) a well-documented, regional cooling trend identified by other authors (e.g., "Hercynian Orogeny" signal in Sinai apatite fission-track data; Kohn et al., 1992), or 2) a previously undocumented cooling event indicated by either a well-defined peak or a cluster of peaks within our CARF AHe and ZHe cooling age spectra (e.g., RSR flank exhumation signal). Point samples with AHe and ZHe ages that fail to meet the previous condition are not modeled since their cooling ages may be the result of a process, such as slow erosional unroofing, that violates a fundamental "fast-cooled" assumption of low-T (U-Th)/He thermochronology. Many samples from unrifted areas of the HJB (e.g., 06SA079, 07SA022) fail to meet this condition. We assume them to represent the AHe and/or ZHe PRZ and do not model them.

Second, inverse modeling of geologic samples requires both an accurate AHe and ZHe cooling age. Many point samples within our collection (e.g., 05SA211) do not meet this basic requirement due to uncontrollable factors such as poor-quality accessory mineral assemblages with the rock; these samples are not modeled. In multi-sample arrays, we occasionally create a "dummy" age for either the apatite or zircon phase built from the averaged data values (e.g., AHe age, uranium concentration, grain dimensions) of neighboring mineral phases within the transect. This dummy mineral phase is created only when we may reasonably assume the

missing mineral phase would realistically be similar to the neighboring samples since each phase exhibits cooling during a single, well-defined event (e.g., zircon phases of sample 05SA221 and 05SA223 of the Jabal al Qishr transect). In situations that we deem too complex for dummy mineral phase generation, we remove those samples from the sample array prior to modeling. The best example of this is the Jabal Radwa transect where just 9 of 20 samples yield viable AHe ages so most of the samples, the top 63% of the transect, are not included in thermal modeling. However, dummy ZHe ages are permissible in the Jabal Radwa transect due to high ZHe age reproducibility around a mean age.

3. Chapter 3: Refinement of Magnetite (U-Th)/He Geochronology with Expanded Application to Intermediate and Felsic Rock

3.1. Abstract

Magnetite (U-Th)/He geochronometry (MGHe) is a reliable alternative dating technique to determine the crystallization age of basaltic to intermediate volcanic rock that typically lack mineral phases datable by more traditional radiometric age dating techniques such as $^{40}Ar/^{39}Ar$ or apatite and zircon (U-Th)/He thermochronometry (AHe, ZHe). This study explores the viability and reliability of MGHe dating silica-rich rock types by first refining basaltic magnetite MGHe analytical methodology and then expanding empirical studies to include intrusive and extrusive, intermediate through felsic igneous rock. MGHe age results from each analyzed sample either prove the capability of the technique with a successful MGHe age correlation to existing, independent radiometric age data or attempt to pinpoint the reasons for age discrepancy. Five of eleven analyzed samples yield MGHe ages, from late Cretaceous to Pleistocene in age, that are in agreement (≤ 2.5%) with independent, corresponding whole-rock $^{40}Ar/^{39}Ar$, U-Pb, apatite fission-track, AHe and ZHe age data and/or local geologic age constraints. Durango apatite and Fish Canyon Tuff zircon, two reputable (U-Th)/He standards, are benchmarks for expansion of MGHe into intermediate and felsic igneous rock. MGHe age results match existing fission-track and (U-Th)/He age data for complementary mineral phases within 1–2% and establish 2σ reproducibilty error of ~15% for multi-aliquot MGHe ages, similar to previously reported MGHe 2σ standard error of 3-11% for andesitic magnetite, but larger than reported standard error estimates for AHe (~6%) and ZHe (~8%). Independent of host rock type, blocky and inclusion-free magnetite appears to yield accurate and reproducible MGHe ages while

magnetite with large (≥ 20 μm), radiogenic and non-radiogenic silicate and other mineral inclusions yield erroneous and/or irreproducible ages. Aliquots from successful samples yield total ^{4}He volumes ~100 times greater than the average instrumental background (0.0006 ncc), indicating that prospective samples must meet the same criterion.

3.2. Introduction

Basalt is one of the most common and widespread volcanic rock types on the Earth's surface, comprising the majority of oceanic crust and large igneous provinces present at many plate margins (Mohr, 1983; Mahoney, 1988; Mohr and Zanettin, 1988; White and McKenzie, 1989; Holbrook and Kelemen, 1993; Mahoney and Coffin, 1997; Sinton et al., 1998). Intermediate and felsic extrusive rock and ash deposits are also prevalent throughout the geologic record and are ideal temporal datums due to their association with discrete events (e.g., Farley and Stockli, 2002; Perkins and Nash, 2002). Reliable geochronology of these rocks is vital for chronostratigraphic constraint on major geologic problems and earth processes including evolutionary and paleoclimatic history (e.g., Kohn et al., 1992; Marchant et al., 1996; Deino and McBrearty, 2002; Garcia et al, 2010; Messager et al., 2011), paleomagnetic excursions and reversals for geologic time-scale calibration (Larson and Hilde, 1975; Merrill et al., 1996; Pike et al., 2001; Laj and Channell, 2007; Tauxe et al., 2007 *and references therein*), and tectonic timing and rate studies via mapping of the continental craton and reconstruction of magnetic anomalies in oceanic crust (e.g., Vine, 1966; Regan et al., 1975; Schlinger, 1985; Kletetschka et al., 2002; Purucker and Whaler, 2007).

K-Ar or ^{40}Ar/^{39}Ar dating is the most common technique employed for obtaining eruption ages of fresh and unaltered basaltic rocks from either ground-mass, whole-rock and/or

plagioclase but dating attempts occasionally yield unreliable or difficult to interpret age data due to analytical and geological complications such as ^{39}Ar and ^{37}Ar recoil or excess ^{40}Ar (e.g., Turner and Cadogan, 1974; Kelley, 2002). Basaltic rock also typically lacks analytical-grade quality minerals such as sanidine, zircon, and biotite datable by alternate techniques such as U-Pb or (U-Th)/He analysis. (U-Th)/He geochronometry effectively circumvents some of these issues by analyzing phenocrystic and xenocrystic phosphate and silicate mineral phases in felsic-to-intermediate volcanic rock (e.g., Reiners and Farley, 1999, 2000; Tagami et al., 2000; Farley et al., 2002; Schmitt et al., 2006; Blondes et al., 2007; Tincher and Stockli, 2009; Stockli et al. *in Glazner and Stock, 2010*) and more retentive phases, such as garnet and olivine, in intermediate-to-mafic volcanic rock and ash to constrain eruption/emplacement ages (e.g., Aciego et al., 2003, 2007, 2010; Nicolescu and Reiners, 2005; Min et al., 2006; Cox et al., 2012). Most recently, magnetite (U-Th)/He dating (MGHe) has shown great potential to reliably date aphanitic or altered igneous rock (Blackburn et al., 2007; Blackburn et al., 2008) that sometimes proves problematic to $^{40}Ar/^{39}Ar$ and other traditional methods. Magnetite is an alluring target for (U-Th)/He analysis of rock within the full mafic-to-felsic igneous rock spectrum since it occurs as a primary, secondary, or accessory mineral phase in most igneous extrusive and intrusive rock types across a wide range of tectonic environs (e.g., Czamanske and Mihalik, 1972; Andersen, 1984; Gerlach and Grove, 1982; Brophy, 1986; Lindsley and Banerjee, 1991 *and references therein*) but it is yet undeveloped in several geochemical domains. This study examines the viability of MGHe in silica-moderate and -rich rock types.

3.2.1. Magnetite Mineralogy

Magnetite (Fe_3O_4) is a ferromagnetic iron oxide mineral of the inverse-spinel group of X_3O_4 oxides, characterized by both octahedral and tetrahedral Fe coordination. Complete solid solution between magnetite (Fe_3O_4) and ulvöspinel (Fe_2TiO_4) in nature commonly results in the occurrence of titanomagnetite ($Fe_{3-x}Ti_xO_4$) that is typical rather for magmatic than metamorphic rocks (e.g., Buddington and Lindsley, 1964; Czamanske and Mihálik, 1972; Neumann, 1974; Harlov, 2000). Titanomagnetite is the principal magnetic mineral in unaltered continental and oceanic basalts, but can undergo low-temperature alteration to (titano)maghemite (Irving 1970; Ozima et al. 1974; Petersen et al. 1979; Smith 1987; Pariso and Johnson 1991). Maghemitization of primary titanomagnetite involves oxidation of ferrous iron and production of ordered cation vacancies and has been interpreted to cause the observed decrease in natural remnant moments intensity of oceanic seafloor with increasing age (Irving 1970; Marshall and Cox 1972; Bleil and Petersen 1983). A common low-temperature alteration series, the substitution of Ti for Fe between magnetite and maghemite (γ-Fe_2O_3 with inverse-spinel "magnetite" structure) or titanomagnetite and titanomaghemite is thought to occur in the presence of a fluid by one of two very different processes: (1) loss of Fe relative to Ti, with the O closest-packed substructure being invariant (e.g., Petersen et al. 1979), or (2) addition of O with constant Fe/Ti (e.g., Readman and O'Reilly 1972).

3.2.2. Magnetite (U-Th)/He Dating

Pioneering studies that prove magnetite quantitatively retains helium over geologic time (e.g., Keevil, 1943 *and references therein*) first demonstrated that certain oxide mineral phases show promise as reliable geochronometers. With a focus on obtaining ore mineralization ages, preliminary He diffusion and age dating experiments were conducted for a variety of Fe- and

Mn-oxide and hydroxide ore minerals, such as magnetite (Fe_3O_4), hematite (Fe_2O_3), pyrolusite (MnO_2), hausmannite (Mn_3O_4), braunite (Mn_7SiO_{12}), etc. (e.g., Fanale and Kulp, 1962; Boschmann Käthler, 1986; Lippolt et al.; 1993; Bähr et al., 1994; Wernicke and Lippolt, 1992, 1994; Lippolt et al., 1998; Brandner, 2000). In a revolutionary helium dating effort prior to a quantitative understanding of helium diffusion, Fanale and Kulp (1962) dated magnetite by U/He chronometry and produced geologically reasonable ages for the crystallization of magnetite ore deposits. Decades later, investigation of specular hematite He retention characteristics showed that He diffusion scales roughly with grain size and displays a reasonably linear Arrhenius relationship, yielding an estimated closure temperature of ~220°C for grains of radius ~500 μm (Bähr et al., 1994; Lippolt et al., 1993; Wernicke and Lippolt, 1994).

Blackburn and others (2007) established the feasibility of the (U-Th)/He system as an alternative method for dating basaltic volcanic rocks by developing the basic MGHe method and outlining an initial set of analytical procedures, including mineral separation, sample abrasion, ^{4}He extraction/measurement, sample dissolution, and anion-exchange column chemistry protocols. Most recently, Blackburn and others (2008) used MGHe to date a magnetite-filled vein within a Cretaceous kimberlite in NE Kansas, reporting ages (~105 Ma) that are in excellent agreement with the accepted time of kimberlite emplacement. Helium diffusion experiments conducted on kimberlitic magnetite demonstrate that He diffusion in magnetite adheres to thermally activated volume diffusion characterized by an Arrhenius relationship yielding an activation energy (E_a) of 220+9/-13 kJ/mol and a log D_0/a^2 value of 6.8+0.7/-0.5 (Blackburn et al., 2008). These kinetic He diffusion parameters translate to a nominal closure temperature (T_c) for He in magnetite of ~250 °C, assuming a cooling rate of 10 °C/Myr (Dodson, 1972).

Accurate absolute age dating of basaltic and kimberlitic magnetite has proven the MGHe technique viable (Blackburn, 2006; Blackburn et al., 2007, 2008) yet is not a routine geochronological method, in part, because the majority of analytical and empirical research to date has focused on a greater understanding of (U-Th)/He systems in established phosphate and silicate mineral phases such as apatite and zircon (e.g., Reiners and Farley, 1999; Farley, 2001; Farley and Stockli, 2002; Farley et al., 2002; Reiners et al., 2004; Reiners, 2005). The underlying effect of some influential physical factors that control the magnetite (U-Th)/He system are not fully understood. Empirical MGHe analysis of basalt and high-grade metamorphic rock have shown that minor adjustments to the technique could potentially increase MGHe age accuracy since magnetite grain texture, radiometric isotope content, and mineralogical purity often vary greatly within the same sample (Stockli et al., 2012; Szymanski et al., *this study*). Crystallographic texture and other physical factors may affect magnetite (U-Th)/He system behavior in different ways in intermediate-to-felsic volcanic rock due to dissimilar cooling rates and geochemical environments. If MGHe dating is to be applied routinely outside mafic rock types, the current analytical technique requires refinement at several procedural stages from proper selection of analytical-grade magnetite to the preparation of dissolved parent nuclide solutions for mass spectroscopy.

This study refines the basic MGHe technique by characterizing basaltic magnetite crystalline texture from basalt samples of different age and geochemistry, identifying the diagnostic behavior of problematic magnetite during MGHe analysis, and improving analytical accuracy and reproducibility. It then expands into empirical study of magnetite from silica-moderate and rich petrologic domains to assess the potential of MGHe to accurately date intrusive and

extrusive, intermediate through felsic igneous rock, from late Cretaceous to Pleistocene in age (Table 1). Sources of error in problematic samples are used to create a standardized MGHe method that specifies step-by-step time and temperature requirements for analytical procedures so that MGHe is applicable for magnetite of diverse geochemical and textural contexts. MGHe age result accuracy is gauged by comparison of MGHe ages to radiometric ages from established geochronometric systems (e.g., U-Pb) from those same samples. We then examine the possibility of developing a magnetite standard that is necessary to validate MGHe ages obtained from geologic samples of indeterminate age.

3.3. Analytical Methodology

3.3.1. Analytical Techniques of MGHe Dating

Sample preparation and MGHe analytical work was conducted at in the Isotope Geochemistry Laboratory (IGL) at the University of Kansas using unique techniques developed and standardized in-house (Blackburn et al., 2007; Taylor, 2012; Taylor and Stockli, 2012; Szymanski et al., *this study*). Magnetite textural and mineralogical composition was imaged using backscatter diffraction scanning electron microscopy (Leo 1550 SEM) and EDAX Energy dispersive X-ray (EDS detector for Leo 1550) techniques at the University of Kansas Microscopy & Analytical Imaging Laboratory. The following treatment of MGHe analytical methodology includes modifications to specific analytical stages developed in this study.

3.3.1.1. Magnetite Separation and Sample Selection

Magnetite was isolated from rock samples using standard mineral separation techniques that include crushing, grinding, and water table separation and subsequent density and magnetic separation. Magnetite was then selected from the bulk magnetic fraction under a low-power

microscope (~10-100*x*) using the preferred selection criterion of single crystalline magnetite octahedrons with no extensive epitaxial or parasitic crystal growth or apparent matrix-crystal intergrowths. Suitable magnetite were then mechanically cleaned of attached aphanitic groundmass with tweezers before a final cleaning by sonication in ethyl alcohol for 15 minutes.

3.3.1.2. Mechanical air abrasion

Magnetite were mechanically abraded using pressurized vessel air abrasion techniques (Krogh, 1982; Blackburn et al., 2007) to remove any adhering high [U,Th] matrix, erode the ^{4}He implantation/depletion halo from magnetite grains (Min et al., 2006), and systematically eliminate fragile grains with structural weaknesses (Appendix A1). Removal of ≥20 μm from each magnetite crystal surface eliminates "bad neighbor" effects where parentless helium is injected into the target mineral rind from adjacent radiogenic mineral phases and/or high [U,Th] coatings on crystal and intra-crystalline fracture surfaces (Fanale and Kulp, 1962; Verchovsky and Begemann, 1993; Wolfe, 2009), often producing inaccurate older cooling ages (Spencer et al., 2004). For octahedrons, the average abrasion time to remove >20 μm from the {111} crystal face is 5 hours at 30 kPa.

3.3.1.3. Aliquot Classification & Assembly

Abraded magnetite grains from each sample were divided into sub-sample quantities (aliquots) prior to MGHe age dating. For a given sample, each aliquot produces an individual MGHe age and the final MGHe age is a weight-averaged mean of multiple aliquots. Either single or multiple magnetite grains were assigned to each aliquot depending on their size and ^{4}He concentration ($[^{4}He]$). Single-grain aliquots contain just one abraded magnetite grain with a typical diameter >350 μm while multi-grain aliquots contain more than one abraded magnetite

grain with average grain diameters in the range of ~100-200 μm. Multi-grain aliquots contain between 2 to 15 abraded grains and range in mass from ~30-275 μg (Table 2).

3.3.1.4. Helium extraction

Laser helium extraction, purification, and isotope-dilution He measurement was carried out at the University of Kansas ultra-high vacuum noble gas mass-spectrometry facility using standard techniques similar to those used for apatite and zircon (U-Th)/He analysis. Individual magnetite aliquots were placed inside platinum packets and heated with a 820 nm diode laser to 1050°C for 10 minutes to liberate ^{4}He from magnetite crystals. 10-minute ^{4}He extraction intervals were repeated until ^{4}He yields for individual degassing steps dropped to <1% of the total extracted ^{4}He. Accuracy of magnetite ^{4}He measurements is primarily a function of the total measured ^{4}He concentration (*[^{4}He]*) and proper characterization and correction of the procedural static ^{4}He blank (*laserblank*). While this is a trivial undertaking for high [U,Th] mineral phases such as apatite and zircon, an increased frequency of ^{4}He blank correction is crucial for low ^{4}He yield magnetite that often represent either low [U,Th] or geologically young samples. True ^{4}He yields from low-[^{4}He] aliquots were calculated by bracketing each primary degassing and re-extract pair with laserblank measurements, ranging between 0.0004-0.0008 ncc each, until individual extraction steps reached a minimum signal to noise ratio of 2:1 since subsequent extraction steps were often at baseline.

3.3.1.5. Magnetite Dissolution and U, Th, Sm Column Chemistry

Degassed aliquots were unpacked from the platinum packet, placed in a Teflon microcapsule, and spiked with a ^{238}U-, ^{232}Th-, ^{149}Sm-enriched tracer lab standard solution. Two blank aliquots were also spiked and processed in parallel for control on changes in spike isotope concentration

during the dissolution sequence. Aliquots were then dissolved separately in a series of hot HF, HCl, and HNO_3 baths within either Teflon beakers on hot plates (Blackburn et al., 2007) or in a pressure digestion vessel (PDV). Magnetite from intermediate and felsic geochemical systems were dissolved via the more aggressive PDV dissolution procedure to ensure complete dissolution of both magnetite and potential well-bonded, intra-crystalline U-, Th-, Sm-bearing mineral phases such as zircon (Appendix A2). REE isotopes were then concentrated via a series of cation exchange columns (Appendix A3) to remove volumetrically dominant elements within dissolved magnetite solutions (e.g., Fe and Ti in titanomagnetite) since they may cause instability in ICP-MS argon plasma and reduce instrument sensitivity to U, Th, Sm (Baker et al., 2002; Tsuyoshi et al., 2003; Blackburn et al., 2007). Finally, a 1 ppb U-Th-Sm internal lab normal was added to the spike blanks and concentrated sample aliquots before final parent nuclide measurement via isotope dilution methods on a Fisons/VG PlasmaQuad II ICP-MS.

3.3.2. MGHe error

Error reporting of MGHe ages is neither straightforward nor standardized due to the nascency of the MGHe age dating technique. Unlike the extensive AHe and ZHe age databases that contribute to the standard error determination for their respective (U-Th)/He age dating techniques (e.g., Farley et al., 2001), no substantial collection of MGHe ages from empirical study of superior-quality magnetite yet exists to cite a standard uncertainty. As such, our results further define a more accurate range of expected error values for MGHe age determinations for magnetite of different geochemical provenance. Similar to Blackburn et al. (2007), we observe scatter in MGHe age uncertainty for basaltic magnetite from the same volcanic source (e.g., SAB suite). In addition, we observe MGHe age and error scatter in magnetite from across the

spectrum of host rock types. Each petrologic system may require its own magnetite standard eventually since MGHe age errors may arise from myriad contributing factors depending on host rock age, petrography, and degree of post-crystallization geochemical alteration.

Aliquot MGHe age and propagated analytical error data were calculated with the (U-Th)/He age reduction software *Helios* (Kislitsyn and Stockli, *in prep.*). Analytical error (U, Th, Sm, ^{4}He measurement error) accrues during both the ^{4}He extraction and ICP-MS analytical stages and the analytical uncertainty for aliquots within samples of reproducible age ranges between 0.01-10% (Table 2). This error range accords with previously reported MGHe intra-aliquot 2σ variability of 3-11% for andesitic magnetite (Blackburn et al., 2007) and compares to analytical uncertainty ranges of both apatite (~6%) and zircon (~8%) (U–Th)/He analysis (Farley et al., 2001). For each sample, a final multi-aliquot error-weighted mean age, uncertainty, and mean square weighted deviation (MSWD) was calculated with *Isoplot* (Ludwig, 2004). The 2σ confidence (95%) for all samples with a reproducible and accurate age ranges between 9.6-18% (Sagamo and FCT, respectively). Each sample in this study generates MSWD >> 1 because MGHe aliquot age uncertainty is smaller than the dispersion of aliquot ages about the mean, indicating an underestimation of standard error. The overdispersion of (U–Th)/He ages is common to geochronology and often attributed to uneven U-Th-Sm distributions and radiation damage (Min et al., 2006; Boyce and Hodges, 2005). Overdispersion in MGHe ages likely results from REE-rich mineral inclusions such as apatite and/or extremely low [U, Th] relative to other geochronometers (Blackburn et al., 2007).

3.3.3. Petrographic Sample Selection

3.3.3.1. Basaltic Magnetite

Seven basaltic magnetite samples from four different locations were analyzed to determine basalt crystallization ages (Table 1). The Saudi Arabian Basalt (SAB) suite includes four continental basalts from the Arabian flood basalt (*harrat*) province near Madinah, Saudi Arabia: an olivine-transitional basalt from the middle Miocene Ishara B basalt of Harrat Ishara (*Ishara basalt*) and three alkali-olivine basalts from the late Miocene Kura basalt of Harrat Khaybar (*Kura A, B,* and *C*). Kura A and B are age equivalent and belong to the same stratigraphic sub-unit while Kura C is a separate mappable unit. Ishara B basalt ages range from 16-12 Ma and the Kura basalt erupted between ~5.5-15.9 m.y.a. (Camp et al., 1991; Szymanski et al., *in prep.*). Basaltic magnetite from the Akhalkalakhi Formation (*Sagamo basalt*) was collected from the Dzhavakheti Highland near Ninotsminda, Republic of Georgia. The previously undated Sagamo basalt is a stratigraphic equivalent to the Pleistocene Mesavera Basalt (Adamia, *pers. comm.*) that constrains the age of the site of the oldest Eurasian Hominid remains at Dmanisi (Gabunia et al., 2000; Garcia et al., 2010) and has been dated radiometrically at 1.8 ± 0.1 Ma (K-Ar age; Majsuradze, 1996) and 2.0 ± 0.1 Ma ($^{40}Ar/^{39}Ar$ isochron age; Schmincke and van den Bogaard, 1995). Wanapum is a tholeiitic basalt collected from the Miocene Roza Member, Wanapum Basalt Formation of the Columbia River Basalt Group (CRBG). Little Devils Postpile (*LDPP*) is from a late Miocene microcrystalline trachyandesite plug that intrudes a portion of the Tuolumne Intrusive Suite (Huber et al., 1989) in Yosemite National Park, California, USA. LDPP was sampled >10 meters from the nearest observed chilled margin within one of the numerous ~1 foot-wide cooling columns. Apatite and zircon (U-Th)/He ages of 8.1 ± 0.5 Ma and 7.9 ± 0.6 Ma for crustal xenoliths entrained within LDPP basalt are similar to a fission track age of "about 9 Ma" (Huber et al., 1987, 1989 *and references therein*; Stockli et al. *in Glazner and Stock, 2010*).

3.3.3.2. Rhyolitic to Dacitic Volcanic Magnetite

Magnetite from three intermediate volcanic rock samples within the Sierra Madre Occidental were analyzed with the dual intent of determining dike emplacement ages as well as assessing their potential as MGHe age standards. DUR07 and DUR19 were collected from magnetite-rich rhyolitic to rhyodacitic dikes within the Cacaria Formation, Oligocene Carpintero Group, Chupaderos Caldera complex near Durango, Mexico. This is the type locality for the Mercado Iron Member in the Cerro de Mercado mine where the volcanic deposit consists mostly of martite and magnetite (Swanson et al., 1979; Lyons, 1988). The Cerro de Mercado mine is also the site of "Durango apatite", a widely accepted apatite (U-Th)/He standard (e.g., Farley, 2000; Stockli et al., 2000; McDowell et al., 2005). MGHe ages reported here are part of a new suite of radiometric ages that are the first non-apatite radiometric age data from the iron ores of Cerro de Mercado (Wipf et al., *in prep.*). Fish Canyon Tuff (FCT) dacitic magnetite was sampled from a voluminous silicic ignimbrite that erupted during the collapse of La Garita caldera as part of the San Juan volcanic field (Lipman et al., 1970). FCT is a widely used $^{40}Ar/^{39}Ar$ sanidine, U-Pb zircon, apatite and zircon fission-track, and apatite and zircon (U-Th)/He standard (Kunk et al., 1985; Hurford and Hammerschmidt, 1985; Cebula et al., 1986; Schmitz and Bowring, 2001; Reiners et al., 2002; Renne et al., 2010 *and references therein)*.

3.3.3.3. Felsic Plutonic Magnetite

Granodioritic magnetite was analyzed to assess complications that may occur during MGHe analysis due to complex magnetite crystalline intergrowths, such as epitaxial growth, that sometimes form within phenocrystic magnetite from felsic systems (Lindsley and Banerjee, 1991 *and references therein*). OLM is a sample of the Half Dome granodiorite within the Tuolumne

Intrusive Suite at Olmsted Point in Yosemite National Park, CA, USA. The Tuolumne Intrusive Suite that composes the Half Dome granodiorite is the host rock for the mafic dike that yields basaltic magnetite of sample LDPP (Huber et al., 1999).

3.4. Analytical Results

3.4.1. Basaltic Magnetite

3.4.1.1. Saudi Arabia Basalt (SAB) Suite

Magnetite from the SAB suite are subhedral octahedrons with average pre-abrasion standard crystal axis lengths of ~220 μm. Ishara basalt yields a weighted mean MGHe age of 7.81 ± 0.58 Ma (MSWD = 7.7; 4 aliquots total; Fig. 1). This age is 43% younger than a zircon (U-Th)/He age of 13.6 ± 1.1 Ma from an underlying leucotuff that was imparted by heat from the unit from which Ishara basalt was sampled and defines the absolute maximum age of this basalt unit (Table 3). Accurate whole-rock $^{40}Ar/^{39}Ar$ age dating of this sample proved problematic due to extensive chemical alteration but a poor isochron fit indicates a middle Miocene age for Ishara basalt (Lee, *pers. comm.*), in agreement with the 12.7-14.9 Ma age range of the Ishara B basalt. Kura A and Kura B yield weighted mean MGHe ages of 3.97 ± 0.92 Ma (MSWD = 1016; 10 aliquots total, 1 rejected) and 4.82 ± 0.42 Ma (MSWD = 60; 6 aliquots total, 1 rejected). These MGHe ages are >50% younger than a whole-rock $^{40}Ar/^{39}Ar$ age of 10.6 ± 0.4 Ma for Kura A (Szymanski et al., *in prep.*: no direct age data exists for Kura B). The weighted mean MGHe age of Kura C is 5.8 ± 2.2 Ma (MSWD = 1863; 3 aliquots total), ~37% younger than the whole-rock $^{40}Ar/^{39}Ar$ plateau age of 9.34 ± 0.18 Ma.

3.4.1.2. Sagamo Basalt, Republic of Georgia

Sagamo basalt contains subhedral magnetite octahedrons 400-700 μm wide at the standard axis. The weighted mean MGHe age of 1.74 ± 0.17 Ma (MSWD = 2389; 11 aliquots total; Fig. 2) is within error of published K-Ar and $^{40}Ar/^{39}Ar$ ages for the Mesavera Basalt (Table 3).

3.4.1.3. Wanapum Basalt Formation, Columbia River Basalt Group

Wanapum basalt yields a weighted mean MGHe age of 11.7 ± 1.2 Ma (MSWD = 126; 6 aliquots total; Fig. 3). No age for the Roza Member specifically has been published. However, the MGHe age is ~20% younger than the estimated age range of ~14.5-15.12 Ma indicated by $^{40}Ar/^{39}Ar$ ages for younger and older basalt units that bracket the Wanapum basalt (Table 3).

3.4.1.4. Little Devils Postpile, California

LDPP basaltic magnetite is relatively large with average pre-abrasion axial lengths that range between ~375-500 μm. LDPP yields a weighted mean MGHe age of 2.58 ± 0.25 Ma (MSWD = 1087; 9 aliquots total; Fig. 4) that is ~70% younger than the AHe and ZHe ages reported for LDPP (Table 3).

3.4.2. Rhyolitic to Rhyodacitic Volcanic Magnetite

3.4.2.1. Chupaderos Caldera complex, Durango, Mexico

Durango rhyodacitic magnetite are commonly unfractured, non-skeletal, large to massive in size with average abraded grain diameters ranging between ~150-290 μm, and range in crystal habit from anhedral to euhedral. DUR07 yields a reproducible MGHe age of 29.7 ± 4.0 Ma (MSWD = 913; 7 aliquots total; Fig. 5). The MGHe age is in agreement with ages from five other radiometric dating methods (Table 3) and is the first age result for Durango magnetite from (U-Th)/He analysis. DUR19 yields non-reproducible aliquot ages and a weighted mean MGHe age of 10.8 ± 2.9 Ma (MSWD = 14650; 10 aliquots total), ~65% younger than expected.

3.4.2.2. San Juan volcanic field, SW Colorado

Fish Canyon Tuff dacitic magnetite is subhedral and massive with most analyzed grains measuring >300 μm-wide along their shortest axial length. FCT yields a reproducible MGHe age of 27.5 ± 5.0 Ma (MSWD = 216; 8 aliquots total; Fig. 6) in accordance with a suite of independent radiogenic ages that cluster near ~28 Ma (Bachmann et al., 2007 *and references therein*), including the mean ZHe age of 28.03 ± 0.35 Ma determined from 100 analyses at the University of Kansas IGL (Table 3; Appendix B).

3.4.3. Felsic Plutonic Magnetite

3.4.3.1. Half Dome granodiorite, California

Half Dome granodioritic magnetite occurs as large (~300-750 μm wide), euhedral, phenocrystic octahedrons that exhibit epitaxial crystal growth on the {111} crystal face. OLM yields a weighted mean MGHe age of 89 ± 15 Ma (MSWD = 566; 11 aliquots total; Fig. 7) that agrees with zircon U-Pb ages for the Half Dome granodiorite that indicate a ~3 m.y. period of pluton emplacement from 92.8 ± 0.1 Ma to 88.8 ± 0.8 Ma (Coleman et al., 2004; Table 3).

3.5. Discussion

MGHe age results fall into three major categories in terms of analytical success: those with ***reproducible*** MGHe results that ***agree*** with published data and/or local geologic age trends and no published age data exist to dispute our result (Category I); those with ***reproducible*** MGHe results that ***disagree*** with published age data and/or local geologic age trends (Category II); and those with ***poorly reproducible*** MGHe results that ***may agree*** with other published age data and/or local geologic age trends (Category III). Mean MGHe age results in this final category are inaccurate but individual aliquot MGHe ages may compare to either published or presumed age

trends. A reproducible MGHe age is defined as one whose aliquot ages mostly fall within ± 2σ around a statistically derived mean age composed of those aliquots.

Category I MGHe age results were achieved for magnetite from all three evaluated petrographic domains. Magnetite ^{4}He concentration (*[^{4}He]*) increases from basaltic to intermediate and felsic samples and Category I samples yield average aliquot [^{4}He] values ~1.4-16 times greater than procedural blank level (FCT and DUR07; Fig. 8). This parallels the increased occurrence of non-oxide mineral phase inclusions that often have high effective uranium concentration ([eU] = U + 0.2303Th + 0.0005Sm) and may contribute significant ^{4}He to the magnetite host. Aliquot MGHe ages within Category I and II samples cluster around the mean sample MGHe age regardless of [eU] (Appendix C), showing no apparent deleterious effect of high-[eU] on magnetite (U-Th)/He system dynamics as opposed to the disruption of (U-Th)/He age reproducibility from radiation-induced crystal damage observed within other mineral phases (e.g., Shuster et al., 2006; Shuster and Farley, 2009). [eU] demonstrates no overwhelming control on aliquot MGHe age from any analyzed sample and outliers to the mean sample MGHe age are due to other physical factors. The ultimate success of MGHe age dating depends greatly on magnetite mineralogical homogeneity (or predictable composition), and proper treatment of expected complications with *ad hoc* diffusive behavior during analysis, not host rock type. Table 4 summarizes the MGHe age result quality and assigns a primary error source for each sample (if applicable).

3.5.1. Performance of magnetite (U-Th)/He dating by rock type

Basaltic magnetite yield MGHe age results that either succeed or fail undoubtedly (Category I or II) while rhyodacitic and granodioritic magnetite are classifiable as either Category I or III

(Table 4). Samples with MGHe ages that either contrast existing age data or display poor reproducibility (Category II or III) often have distinct attributable causes of failure. The primary cause of inaccurate mean MGHe ages is the violation of a principle diffusion assumption, inherent to the (U-Th)/He method, that assumes volumetric ^{4}He diffusion through a monocompositional mineral mass. The two greatest contributors to this violation are large bulk volume radiogenic/non-radiogenic silicate and other mineral phase inclusions, including mineral skeletonization and intra-crystalline space from either incomplete magnetite crystal growth and/or post-crystallization brittle fracturing.

Magnetite mineralogy is highly variable but intermediate to felsic systems tend to yield magnetite with greater textural and mineralogic complexity (Figs. 9-19). Magnetite textures range from monocompositional (Sagamo, DUR19 & OLM) to magnetite with trellis-type ulvöspinel exsolution lamellae (Kura A, WR-1 & FCT) to magnetite with large inclusions (Ishara basalt & FCT) to blocky, irregular, µm-scale clusters of magnetite and non-oxide minerals (Kura B & LDPP) to wispy stringers and sub-µm-scale patches of magnetite encased in a silicate mineral matrix (DUR07 & DUR19). Penetrative gaps that trend along magnetite crystalline structure, possibly formed during magnetite growth, occur commonly in magnetite with trellis-type ulvöspinel exsolution lamellae while structurally independent, through-going fractures occur in numerous samples regardless of mineralogic texture and are likely related to either contractional cooling during crystallization or mineral separation and preparatory techniques. Cruciform-type skeletonized crystal growth (*see* Lindsley and Banerjee, 1991 *and references therein*) is observed exclusively in basaltic magnetite.

3.5.1.1. Basaltic Magnetite

MGHe age results from basaltic magnetite are the most reproducible, though not always the most accurate. Successful reproduction of basalt MGHe aliquot ages is dependent heavily upon consistent, predictable mineralogy (whether monocompositional or compound) and the low potential of basaltic magnetite to incorporate REE-rich, non-oxide mineral phases (e.g., apatite), relative to magnetite from intermediate and felsic rock. Basaltic magnetite sample age results divide evenly into Category I and II classifications (Sagamo & Wanapum basalts and SAB & LDPP, respectively; Table 4).

Sagamo basalt is a Category I success, yielding a MGHe age that corresponds to other radiometric age results from local volcanostratigraphic equivalents (Table 3). Yet, inconsistent degassing behavior exists in two aliquots that yield both the two lowest [eU] and two youngest MGHe ages (mg09SKV01-7, -11; Fig. 8). These two aliquots have [eU] and [^{4}He] values far lesser than the group aliquot average, suggesting the behavioral difference is due to these single-grain aliquots containing complex magnetite. Though magnetite within Sagamo basalt exhibits excellent ferrimagnetic behavior and is generally the most chemically pure basaltic magnetite analyzed in this study, some abraded grains contain minor mineralogic heterogeneities that could be problematic during MGHe analysis, including an augite/calcic-plagioclase rim around one grain and a 10 μm-diameter apatite inclusion in another (Fig. 13).

Wanapum contains ulvöspinel trellis-type exsolution lamellae and some penetrative gaps (Fig. 14) yet it yields a reproducible MGHe age. Wanapum basalt is considered a Category I result despite being younger than the ~14.5-15.12 Ma age range inferred by ^{40}Ar/^{39}Ar ages from bracketing CRBG volcanostratigraphic of the overlying Priest Rapids Member and Frenchman Springs Member (Table 3). This Category I assignment considers a review by Barry and others

(2010), which states that several prior age determinations of CRBG stratigraphy, including the Frenchman Springs Member, are systematically older than the true geologic age.

The full Saudi Arabian basalt (SAB) suite falls into Category II as each sample yields a reproducible MGHe age yet none agree with corresponding whole-rock $^{40}Ar/^{39}Ar$ ages (Table 3). Backscatter diffraction scanning electron microscopy (BSD SEM) images of unabraded SAB suite magnetite reveal complex crystallographic texture and poor mineralogic homogeneity. Ishara basalt shows faint trellis exsolution lamellae of ulvöspinel and inclusions of biotite, augite, and calcic-plagioclase distributed throughout the crystal, as well as rims of the same minerals surrounding the perimeter of the crystals (Fig. 9). Through-going fractures exist in some crystals. In some instances, these fractures appear filled by other minerals, which indicates post-crystallization fracturing and secondary mineralization. Ishara basalt magnetite degassed readily with just one of five aliquots requiring a second re-extract. Kura A and Kura B exhibit extensive intra-crystalline ulvöspinel trellis exsolution lamellae and silicate mineral inclusions (Figs. 10 and 11). Overlapping silicate mineral inclusions within Kura A may indicate either multi-stage structural growth or concurrent crystallization of several mineral phases. Kura C exhibits pervasive cruciform skeletonization with multiple cross-arms where axial magnetite growth is volumetrically infilled by intergrown magnetite and silicate minerals between each {111} surface and all three standard axes (Fig. 12).

LDPP exhibits exceptional degassing behavior and yields a reproducible mean MGHe age but the magnetite are truly composite mineral grains where silicate minerals account for >50% of grain volume (Fig. 15). This causes a consistent underestimation of true geologic age and warrants a Category II assignment. After laser heating, most multi-grain aliquots contained a

single, fused mineral mass with a pitted, pumice-like appearance that likely results from the melting and re-crystallization of some portion of the silicate mineral component. BSD SEM images of abraded and unabraded magnetite reveal blocky ulvöspinel occurrences with intricate intergrowths of alkali feldspar, pyroxene and amphibole group CaMgAl-silicate end members, and apatite, indicating that candidate grains were not wholly magnetite. LDPP was sampled far from the nearest observed chilled margin at the contact with the host Cathedral Peak granodiorite yet incorporation of the felsic host rock within the intrusive magmatic body may ultimately have contaminated the sample. LDPP has an anhedral habit and is weakly ferrimagnetic, making it difficult to differentiate from the mafic mineral fraction during sample selection under low-power magnification. This difficulty may be encountered with future attempts to date small basalt plugs.

3.5.1.2. Rhyolitic to Rhyodacitic Volcanic Magnetite

Rhyodacitic magnetite yield Category I results when pure magnetite is analyzed but complications may arise without proper pre-analytical screening as host rocks often contain texturally and mineralogically complex magnetite. DUR07 and FCT epitomize the diverse range of mineralogic textures present in rhyodacitic magnetite. DUR07 consists of either structural intergrowths of oxide and phosphate mineral phases (ulvöspinel-ilmenite-apatite) or amalgamate mineral assemblages of plagioclase and magnetite; rarely are magnetite monocompositional (Fig. 16). FCT is massive titanomagnetite with abundant apatite inclusions and narrow bands of trellis-type ulvöspinel exsolution lamellae along crystallographic growth lines, surrounded by a majority silicate matrix of orthoclase and sanidine (Fig. 18). The presence of REE-rich apatite within both samples is unproblematic given that the inclusions are small (< 20 μm) and spread

uniformly throughout the magnetite. This arrangement ensures that ^{4}He of apatite provenance is expelled into the encasing magnetite and actively diffused through the host magnetite during ^{4}He outgassing. However, the mineralogic impurity of DUR07 and FCT translates into less analytical precision as the respective 2σ error of their mean MGHe ages (Table 2) is 4% and 8% greater than the average Category I basaltic magnetite MGHe age error of 10%.

Contrastingly, DUR19 yields a Category III result due to many grains consisting of orthoclase and apatite-dominant masses with either patchy, very small (<10 μm-wide) ulvöspinel masses or wispy magnetite stringers (Fig. 14). The rare monocompositional magnetite shows no trace of ulvöspinel exsolution lamellae observed in DUR07. Two multi-grain aliquots (mgDUR19-13 and mgDUR19-14) yield MGHe ages reasonably close to other radiometric ages for this sample (Wipf et al., *in prep.*; Table 3) but these results are likely coincidental since these are multi-grain aliquots and inclusion-free magnetite are rare. Furthermore, single-grain DUR19 MGHe aliquot ages are significantly younger than predicted.

3.5.1.3. Felsic Plutonic Magnetite

Granodioritic magnetite may yield complex MGHe age results though a high degree of accuracy is achievable through careful sample selection, similar to magnetite from other petrologic systems. OLM produced a final weighted mean MGHe age of 89 ± 15 Ma with no individual aliquot MGHe age older than 225 Ma (EXP4; Fig. 7). Though the final mean MGHe age corresponds to the 92.8 ± 0.1 Ma to 88.8 ± 0.8 Ma U-Pb age range of Half Dome granodiorite pluton emplacement (Table 3), the spread of individual OLM aliquot ages indicates a systematic problem within OLM MGHe analysis. Some aliquots yield accurate MGHe ages while others are twice as old as the mean age. Many OLM magnetite are monocompositional and

exhibit no ulvöspinel exsolution lamellae but some host small (<20 μm dia.), REE-rich apatite within the magnetite grain interior (Fig. 19). High [U,Th] inclusions may generate an age overestimation so single-grain aliquots with accurate MGHe ages are thoroughly abraded and either inclusion-free or host small, dispersed apatite mineral inclusions toward the center of the abraded magnetite grain.

3.5.2. Effects of complex mineralogy and grain competency on aliquot MGHe ages

Prevalent mineral inclusions can simultaneously help and hinder a successful MGHe age determination. Intra-crystalline radiogenic mineral phases have been shown to contribute significant ^{4}He to REE-deficient magnetite, making them viable candidates for MGHe analysis (Blackburn et al., 2008). However, polycompositional grains, including those with pervasive, post-crystallization fractures, may also contain complex physical diffusion paths that cause aberrations in the expected degassing schedule. Unfractured, monocompositional magnetite is ideal for MGHe age dating but no apparent exclusionary rules apply as neither low [^{4}He] nor poor degassing behavior forecast an inaccurate MGHe age result. Category I results come from magnetite aliquots across a range of mineralogic purity; their common bond is that each produces mean ^{4}He yields significantly greater than the average laserblank level.

Magnetite [^{4}He] increases from basaltic to intermediate and felsic samples (Fig. 8), in parallel with the increased occurrence of intra-crystalline and/or neighboring radiogenic mineral phases present within the host rock matrix. Aliquot gas yields within a sample can be highly inconsistent; few produce clustered aliquot [^{4}He] and some aliquots yield values an order of magnitude greater or lesser than the corresponding sample mean. Basaltic magnetite from the SAB suite contains the lowest [^{4}He] of all samples analyzed in this study with three of four

samples yielding average ^{4}He concentrations (0.0002-0.0003 [ncc]/μg) at or below average ^{4}He-extraction line laserblank levels (0.0004-0.0008 ncc). Three of four magnetite samples from intermediate to felsic rock types (DUR07, DUR19, and OLM) yield [^{4}He] values nearly an order of magnitude greater than the average basaltic magnetite. Regardless of rock type, aliquots with [^{4}He] values far lesser than the sample average yield, correspondingly, the youngest MGHe ages (SKV-7, SKV-11, FCT-3, and OLM-3; Fig. 8; Table 2).

Monocompositional magnetite commonly degas with a standard extraction schedule so multiple re-extracts from a given aliquot may indicate underlying issues with sample quality. However, a complex degassing schedule is not always telltale of an unsuitable sample and, equally, degassing of composite grains is not always problematical. For instance, some Sagamo grains demonstrate penetrative fracturing (Figs 18b and 18c) and five of twelve aliquots did not degas readily, requiring an additional one to seven re-extracts (mg09SKV01-1, -2, -3, -4, and -6). Yet these aliquot MGHe ages are within error of those that degassed promptly, which indicates little to no control on grain diffusivity by penetrative fractures. Complex degassing of Durango magnetite is also not predictive of either magnetite quality or an accurate mean MGHe age. Category I DUR07 aliquots needed three to six re-extracts to fully degas while the mineralogically complex Category III DUR19 degassed efficiently within 2 to 4 re-extracts.

3.5.3. Refinement of Magnetite (U-Th)/He Methodology

Blackburn and others (2007) established the potential of the MGHe technique to accurately date mafic volcanic rock but magnetite size, geometry, mineralogic composition, and radiogenic level are highly dependent upon host rock geochemistry. Analytical difficulties stemming from these differences must be addressed on an *ad hoc* basis. Thus, based on observations from

empirical study, we propose the following procedural modifications and addenda to the MGHe technique. Each is applicable to magnetite from mafic through felsic petrologic domains and increases the chance of accurately MGHe age dating any given sample. Step-by-step procedural amendments to mineral separation, dissolution, and solution ICP-MS preparation are detailed in Appendices A1-A3.

3.5.3.1. Magnetite Selection via Optical and SEM Screening Phases

Proper sample selection requires three steps: optical low-power examination of unabraded crystals; mechanical abrasion of candidate crystals; and SEM imaging of abraded candidate grains with post-screening removal of qualified magnetite from the SEM mount. Pre-abrasion screening of candidate magnetite with a low-power optical microscope (~10-100*x*) is necessary to select single crystalline octahedrons with no epitaxial growth, parasitic crystals, or apparent matrix/crystal intergrowths. Epitaxial crystal growth is undesired because it distorts the exterior form of the underlying magnetite octahedron and complicates the abrasion calculation.

Post-abrasion SEM examination is crucial to eliminate polycompositional magnetite crystals (e.g., Taylor and Stockli, 2011; Taylor, 2012) since foreign mineral phase inclusions are often exposed only during the SEM mount polishing process. The same grains may exhibit favorable ferrimagnetic behavior and appear inclusion-free during optical screening. For example, >80% of DUR19 grains are apatite-rich, SiO_2-dominant masses with either patchy or wispy (titano-) magnetite stringers; rarely are the selected grains monocompositional magnetite (Fig. 17). SEM screening is only appropriate for abraded magnetite grains massive enough (≥100 μg) to withstand the loss of magnetite that occurs during SEM mount preparation. When SEM

screening of candidate magnetite is impractical, imaging of spare magnetite is recommended so sample physical texture and mineralogic composition can be assessed prior to aliquot assembly.

3.5.3.2. Mechanical Air Abrasion

Blackburn et al. (2007) assume sufficient abrasion when magnetite grains appear spherical but that criterion alone does not ensure erosion of the ≥20 μm-thick ^{4}He implantation/depletion rind. For octahedral magnetite, points and edges erode prior to the grain becoming semi-spherical enough for the {111} crystal face to begin abrading. To quantify abrasion magnitude for octahedral magnetite, we measure two standard axis widths of ten unabraded crystals and the two widest diameters of ten abraded grains and use the average difference to calculate abrasion depth for the {111} surface. Pre-abrasion axial widths must be reduced ≥100 μm to assure significant erosion of the {111} face. This approach assumes that the widest grain diameters are the abraded equivalent of the standard axes yet consistent measurement of the widest dimensions ensures sufficient abrasion regardless of whether the pre- and post-abrasion measurements are truly of the same crystal dimension.

3.5.3.3. Aliquot Construction

Single-grain aliquots should be used for MGHe analysis when possible to minimize the risk of analyzing magnetite with large radiogenic inclusions and improve MGHe age accuracy and reproducibility, especially in slow-cooled felsic geochemical systems where large individual magnetite crystals contribute sufficient magnetite mass. For example, the accuracy of OLM mean MGHe ages increased with successive dating attempts and a procedural change (Fig. 7). Two early dating attempts with multi-grain aliquots (EXP2 and EXP3) yielded aliquot MGHe ages between ~100-525 Ma (with one outlier at 1220 Ma) and produced the same mean MGHe

age of ~145 Ma, ~62% greater than the zircon U/Pb emplacement age for the Half Dome granodiorite (Coleman et al., 2004; Table 3). Subsequent SEM imaging of OLM showed that MGHe age inaccuracy in EXP2 and EXP3 was due to high-[U,Th] apatite inclusions that add parentless ^{4}He to the magnetite if the inclusion phases are either undissolved or excessively large. A single polycompositional grain could skew the composite MGHe age of a multi-grain aliquot. The failed initial dating attempts led to the exclusive use of single-grain aliquots, which improved accuracy and produced a final weighted mean MGHe age for OLM of 89 ± 15 Ma with no individual aliquot MGHe age older than 225 Ma (EXP4; Fig. 7).

Use of multi-grain aliquots should be limited to samples with magnetite of either small crystal size or inherent low ^{4}He yield (from low [U,Th] or geologically young samples) where combined masses are necessary to assemble cumulative ^{4}He yields ~0.0005 ncc or greater. Multi-grain aliquots are potentially problematic since their MGHe ages are actually the collective age of each intra-aliquot magnetite grain; the collective sum of individual grain mass is treated as a singular magnetite mass whose ^{4}He yield is compared to its REE ratios to obtain the aliquot MGHe age. However, multi-grain aliquot MGHe analysis is dependable if all grains within an aliquot are chemically and volumetrically equivalent to one another with inclusion-free magnetite grains preferred. DUR07 multi-grain aliquots yield accurate and reproducible MGHe ages due to excellent magnetite mineralogic composition. Conversely, SAB suite MGHe ages demonstrate the hazard of violating this condition as each sample yields mean MGHe ages that consistently underestimate true geologic age. In this case, the composite oxide-silicate makeup of abraded grains provides complex ^{4}He diffusion pathways, leading to anomalously low ^{4}He yields and introducing error to multi-grain aliquot MGHe ages.

3.5.3.4. Laserblank correction to determine true ^{4}He yield

Greater use of procedural blanks (*laserblanks*) properly establishes true ^{4}He yield, which is especially important during the final re-extractions at the end of a degassing sequence where the smallest ^{4}He yields are collected. For example, initial ^{4}He volumes from the SAB suite are 10-100 times greater than average laserblank level for that analysis (~0.0006 ncc) but each subsequent re-extract produces smaller ^{4}He yields until they approach 1-10 times laserblank where the differentiation between background and true ^{4}He yield becomes crucial. Differences between raw and blank-corrected total ^{4}He yields range from fractional up to 16% (Sagamo and Ishara basalt; Fig. 20; Table 5). Final blank-corrected aliquot MGHe ages undergo a similar percentage change with small raw ^{4}He–yield aliquots subject to the greatest change of their final MGHe age. The difference between raw and blank-corrected ^{4}He yields for the SAB suite (0.2-16.4%) and FCT (0.1-7.1%) generates a comparative percentage shift towards younger final MGHe ages (Table 6; Figs. 21 and 22). Alternatively, DUR07 was degassed without rigorous blank correction but their total ^{4}He yield and final MGHe ages remain effectively unchanged due to the relatively large [^{4}He] of >10 times greater than laserblank levels (Fig. 8).

Laserblank levels define the minimum acceptable [^{4}He] for analytical-grade magnetite aliquots. Category I samples produced mean [^{4}He] ~1.4-16 times greater than average laserblank (FCT and DUR07 at low and high limits; Fig. 8). With untested magnetite from new samples, preliminary degassing experiments are necessary to assess the potential [^{4}He] since whole-rock and neighboring non-oxide mineral phase [eU] are poor predictors of magnetite [eU] and qualification of magnetite for MGHe analysis in terms of sufficient ^{4}He yield (Table 7; Fig. 23). Though intermediate through felsic rock generally yields magnetite with greater ^{4}He content,

rhyodacitic and granodioritic magnetite [eU] are 2-3 orders of magnitude lesser than apatite and zircon [eU] within the same sample. In basaltic rock, whole-rock and magnetite [eU] show no consistency as either one or the other component may be more radiogenic and values sometime overlap (e.g., Ishara basalt, Kura C).

3.5.3.5. Magnetite Dissolution and Ion Exchange Column Chemistry

Of the two hot acid dissolution techniques (hot plate and PDV) used during this study, the PDV technique is preferred for two reasons. First, PDV is necessary for the dissolution of well-bonded, intra-crystalline mineral phase inclusions that often develop within magnetite from intermediate and felsic systems. Second, the microcapsule dissolution vessels used in the PDV method reduce the loss of parent material by static ejection that sometimes occurs during acid dry down steps. The wide mouths on 15 mm beakers used for hot plate-based dissolution increase the risk of precipitate ejection from the vessel, resulting in the total aliquot loss. While it is also possible that fractional loss of parent material occurs with the PDV method, it is difficult to assess whether the loss of parent material systematically and adversely effected MGHe age determinations.

3.5.4. Magnetite (U-Th)/He Age Standard

Magnetite age standards are necessary to validate MGHe ages from geologic samples of indeterminate age. True standard establishment requires repeated analyses and calibration beyond the scope of this study (see Farley et al., 2002 *and references therein*; Reiners et al., 2002; Dobson et al., 2008) but Category I DUR07 and FCT MGHe results are an initial endeavor into MGHe standard exploration. Characteristics that qualify these samples as candidates for reputable MGHe standards include consistent yield of analytical-grade crystal size, substantial

[^{4}He], sample availability, aliquot age reproducibility, no age bias with [eU], and proven age correlation with established radiometric ages from the same sample location.

DUR07 and FCT exhibit consistent textural and compositional suitability in the form of competent, monocompositional magnetite (Figs. 16 and 18), a character preferred for MGHe analysis since brittle and fractured grains often break during either the ^{4}He extraction or aliquot unloading stage and increase the possibility of loss of parent material during dissolution. DUR07 and FCT each have [^{4}He] great enough to achieve analytically viable ^{4}He yields with relatively light aliquot masses and significantly differentiate their gas yield from laserblank levels, an attribute that favors single-grain analysis. Single abraded FCT grains average 43.1 μg with a 0.00034 [ncc]/μg ^{4}He concentration, indicating that single-grain aliquot masses will yield total ^{4}He volumes ~24 times greater than average laserblank (~0.0006 ncc). Smaller but with much greater [^{4}He] than FCT on average, single abraded DUR07 grains weigh 6.7 μg and yield 0.00107 [ncc]/μg. Single-grain DUR07 aliquots will yield ^{4}He volumes ~12 times greater than laserblank if used as a MGHe dating standard.

Relative to other MGHe ages, DUR07 and FCT yield two of the greatest 2σ uncertainties (14% and 18%, respectively; Table 2) and, though potential for error reduction exists, their seemingly elevated error remains a big hurdle in their acceptance as MGHe standards. DUR07 and FCT mean MGHe age uncertainties are ~2 times greater than the 8% error cited for kimberlitic magnetite (Blackburn et al., 2008) and 4-8% greater than the 2σ error of Sagamo basaltic magnetite (9.6%), our most reproducible MGHe age determination (Table 2). The MGHe age error cited by Blackburn et al. (2008), though appropriate for their particular isotope measurements and MGHe age calculation, cannot be projected to magnetite ages from other

petrologic systems as MGHe age error may arise from myriad contributing factors including source rock age, type, magnetite and host rock matrix mineralogy and [eU], post-crystallization thermal evolution, and physical crystal alteration. The reproducibility of Sagamo basalt MGHe ages is empirical proof of this concept; great mineralogic purity keeps measurement error consistently low (<1%) and aliquot reproducibility high. Given the frequently complex mineral composition of rhyolitic to rhyodacitic magnetite, a 15% mean MGHe age error may be an accurate assessment of the resolution of the MGHe age dating technique for this particular petrologic domain. However, as most deviant aliquot MGHe ages are attributed to polycompositional mineral grains with little magnetite content, we foresee improved accuracy of MGHe age results with greater use of SEM screening of candidate grains since analysis of just the highest-grade magnetite will generate a reduction in the accepted standard error. Ultimately, MGHe age errors exhibit a wide range of scatter independent of petrologic domain (Table 2), indicating that each petrologic system, and possibly each rock subtype, may require its own MGHe age standard.

3.6. Conclusions

MGHe age dating performs well in silica-moderate and rich petrologic domains, producing accurate geologic ages for many intrusive and extrusive, mafic through felsic igneous rock samples, from Cretaceous to Pleistocene in age, that correspond to age data from other radiometric dating methods. Regardless of host rock type, successful MGHe age dating depends greatly on magnetite mineralogical homogeneity (or predictable polycompositionality), and proper treatment of expected complications with *ad hoc* diffusive behavior and volumetric gas yields during analysis. Inaccurate mean MGHe ages are caused primarily by the violation of a

principle (U-Th)/He system factor that assumes volumetric ^{4}He diffusion through a monocompositional mineral mass. The greatest contributors to this violation are large (≥ 20 μm) or pervasive radiogenic/non-radiogenic silicate and other mineral phase inclusions, poor magnetite crystal texture (including magnetite skeletonization), and internal features that may act as fast diffusion pathways such as physical gaps from partial mineralogic crystal growth and/or post-crystallization brittle fracturing present within otherwise competent magnetite.

Neither degassing behavior nor relatively small ^{4}He volumes forecast an inaccurate MGHe age result. Magnetite aliquots that demonstrate inconsistent degassing behavior, likely due to complex mineralogical textures, can yield MGHe aliquot ages within error of those that degassed promptly, indicating that penetrative fractures exert little to no control on intra-crystalline diffusivity. Magnetite ^{4}He gas yields range widely from sample to sample and a minimum qualification threshold of ~0.0010 ncc is critical for a successful MGHe age result. Untested magnetite samples may require preliminary degassing trials to assess the potential of different-sized magnetite masses to yield qualifying ^{4}He volumes since whole-rock, apatite, and zircon [eU] are inaccurate indicators of magnetite qualification for MGHe analysis in terms of sufficient ^{4}He gas yield; no strong correlation exists between those quantities and magnetite [eU] from the same sample. Rhyodacitic and granodioritic magnetite yields [^{4}He] nearly an order of magnitude greater than the average basaltic magnetite (0.0100 vs. 0.0011 ncc) and the marked increase parallels the increased occurrence of radiogenic mineral phases present as either intra-crystalline inclusions or neighboring mineral phases within the host rock matrix. The capacity of extra-magnetite ^{4}He to raise gas volumes significantly greater than background level is an added value

and demonstrates that prevalent intra-crystalline mineral inclusions can simultaneously help and hinder a successful MGHe age determination.

MGHe age results for basaltic magnetite are the most reproducible, though not always the most accurate. Inter-aliquot reproducibility of basaltic magnetite is highly dependent upon consistent, predictable magnetite mineral composition (whether homogeneous or not) and the low potential of basaltic magnetite to incorporate REE-rich, non-oxide mineral phases, relative to other petrologic rock types. No SAB suite MGHe ages correlate to accompanying whole-rock $^{40}Ar/^{39}Ar$ ages due to very poor magnetite mineralogic texture including extensive skeletonization of individual magnetite crystals. Contrastingly, mineralogically pure Sagamo yields a 9.6% 2σ MGHe age uncertainty, the smallest error of all final multi-aliquot error-weighted mean ages in this study.

Rhyodacitic magnetite is the most successful of the three analyzed petrologic system in terms of MGHe age correlatability to accompanying radiometric ages but their tendency to contain mineralogic impurities translates into less analytical precision than other rock types. Durango rhyolitic magnetite and Fish Canyon Tuff dacitic magnetite yield 2σ mean MGHe age uncertainties between 14-18%. This uncertainty is ~2 times greater than the analytical uncertainty range of both apatite (~6%) and zircon (~8%) (U-Th)/He analysis and Sagamo basaltic magnetite (9.6%) but it accords with previously reported MGHe intra-aliquot 2σ variability of 3-11% for andesitic magnetite. Thus, we nominate Durango and Fish Canyon Tuff magnetite as reputable candidates for intermediate volcanic rock MGHe standards though greater empirical analysis is needed to properly assess their overall reproducibility. Furthermore, MGHe

age errors exhibit a wide range of scatter independent of petrologic domain and each petrologic system, and possibly each rock subtype, may require its own MGHe age standard.

Overall, granodioritic magnetite yield complex MGHe age results though a greater degree of accuracy is achievable once primary error sources are controlled. The mean MGHe age 2σ error of Olmsted Point granodioritic magnetite was reduced from 26-28% to 17% with the implementation of single-grain aliquot analysis. Methodological change was prompted by SEM analysis of magnetite mineral character that revealed pervasive REE-rich mineral inclusions. Multi-grain aliquot age overestimation will compound the mean MGHe age error because of the cumulative negative effects of individual, impure magnetite grains.

Sources of error in problematic samples originate from magnetite size, geometry, mineralogic homogeneity, and inherent radiogenic character. MGHe analytical accuracy and reproducibility was improved greatly with our standardization of single-grain aliquot analysis and laserblank correction. Single-grain aliquots minimize the risk of analyzing magnetite with large radiogenic inclusions, especially in slow-cooled felsic geochemical systems where individual crystal size is large enough to contribute sufficient magnetite mass. In special cases, multi-grain aliquot MGHe analysis is dependable if all intra-aliquot grains are mineralogically and volumetrically equivalent to one another and the cooling gradient across the sample is much shorter than the gradient across the geologic unit from which it was sampled. Laserblank corrections to raw ^{4}He yields are fundamental for the calculation of reproducible MGHe age in aliquots with low ^{4}He yields that typically result from geologically young magnetite and/or those with naturally low U-Th-Sm content. Changes in the total ^{4}He gas yield between blank-corrected and uncorrected gas volumes translate to nearly the same percentage change in final

aliquot MGHe cooling ages. These minute adjustments to ^{4}He gas yield with laserblank correction reduce overestimation of aliquot MGHe age and often supersede all analytical error in low ^{4}He yield samples.

3.7. References

Aciego, S., Jourdan, F., DePaolo, D., Kennedy, B., Renne, P., and Sims, K., 2010, Combined U–Th/He and 40Ar/39 Ar geochronology of post-shield lavas from the Mauna Kea and Kohala volcanoes, Hawaii: Geochimica et Cosmochimica Acta, v. 74, no. 5, p. 1620-1635.

Aciego, S., Kennedy, B., DePaolo, D. J., Christensen, J. N., and Hutcheon, I., 2003, U–Th/He age of phenocrystic garnet from the 79 AD eruption of Mt. Vesuvius: Earth and Planetary Science Letters, v. 216, no. 1, p. 209-219.

Aciego, S. M., DePaolo, D. J., Kennedy, B., Lamb, M. P., Sims, K. W. W., and Dietrich, W. E., 2007, Combining [3He] cosmogenic dating with U–Th/He eruption ages using olivine in basalt: Earth and Planetary Science Letters, v. 254, no. 3, p. 288-302.

Adamia, S. A., Alphaidze, V. S., Bombolakis, E. G., Chabukiani, A. O., Kuloshvili, S. I., Majsuradze, G. M., and Martin, R. J., 2002, Late Neogene-Quaternary chronology, volcanic and geodynamic activities of the Caucasus, Proceedings of the XVII Congress of Carpathian Balkan Geological Association, Volume 53: Bratislava, p. 201-202.

Andersen, T., 1984, Crystallization history of a Permian composite monzonite-alkali syenite pluton in the Sande cauldron, Oslo rift, southern Norway: Lithos, v. 17, p. 153-170.

Bachmann, O., Oberli, F., Dungan, M., Meier, M., Mundil, R., and Fischer, H., 2007, 40Ar/39Ar and U–Pb dating of the Fish Canyon magmatic system, San Juan Volcanic field, Colorado: Evidence for an extended crystallization history: Chemical Geology, v. 236, no. 1, p. 134-166.

Bähr, R., Lippolt, H. J., and Wernicke, R. S., 1994, Temperature-induced 4He degassing of specularite and botryoidal hematite: A 4He retentivity study: Journal of Geophysical Research, v. 99, no. B9, p. 17695-17617,17707.

Baker, J. A., Waight, T., and Ulfbeck, D., 2002, Rapid and highly reproducible analysis of rare earth elements by multiple collector inductively coupled plasma mass spectrometry: Geochimica et Cosmochimica Acta, v. 66, no. 20, p. 3635-3646.

Barry, T. L., Self, S., Kelley, S. P., Reidel, S., Hooper, P., and Widdowson, M., 2010, New 40Ar/39Ar dating of the Grande Ronde lavas, Columbia River Basalts, USA: Implications for duration of flood basalt eruption episodes: Lithos, v. 118, no. 3, p. 213-222.

Bender, M. L., 1973, Helium-uranium dating of corals: Geochimica et Cosmochimica Acta, v. 37, no. 5, p. 1229-1247.

Blackburn, T. J., 2006, Development of new applications in volcanic (U-Th)/He geochronology [M.S.: University of Kansas, 151 p.

Blackburn, T. J., Stockli, D. F., Carlson, R. W., and Berendsen, P., 2008, (U-Th)/He dating of kimberlites--A case study from north-eastern Kansas: Earth and Planetary Science Letters, v. 275, no. 1-2, p. 111-120.

Blackburn, T. J., Stockli, D. F., and Walker, J. D., 2007, Magnetite (U–Th)/He dating and its application to the geochronology of intermediate to mafic volcanic rocks: Earth and Planetary Science Letters, v. 259, no. 3, p. 360-371.

Bleil, U., and Petersen, N., 1983, Variations in magnetization intensity and low-temperature titanomagnetite oxidation of ocean floor basalts.

Blondes, M. S., Reiners, P. W., Edwards, B. R., and Biscontini, A., 2007, Dating young basalt eruptions by (U-Th)/He on xenolithic zircons: Geology, v. 35, no. 1, p. 17-20.

Brandner, T., 2000, U-He chronologische Fallstudien and Eisen- und Manganerzen [PhD: University of Heidelberg.

Brophy, J. G., 1986, The Cold Bay volcanic center, Aleutian volcanic arc: Contributions to Mineralogy and Petrology, v. 93, no. 3, p. 368-380.

Buddington, A. F., and Lindsley, D. H., 1964, Iron-titanium oxide minerals and synthetic equivalents: Journal of Petrology, v. 5, no. 2, p. 310-357.

Camp, V. E., Roobol, M. J., and Hooper, P. R., 1991, The Arabian continental alkali basalt province: Part II. Evolution of Harrats Khaybar, Ithnayn, and Kura, Kingdom of Saudi Arabia: Geological Society of America Bulletin, v. 103, no. 3, p. 363-391.

Coleman, D. S., Gray, W., and Glazner, A. F., 2004, Rethinking the emplacement and evolution of zoned plutons: Geochronologic evidence for incremental assembly of the Tuolumne Intrusive Suite, California: Geology, v. 32, no. 5, p. 433-436.

Cox, S. E., Farley, K. A., and Hemming, S. R., 2012, Insights into the age of the Mono Lake Excursion and magmatic crystal residence time from (U□Th)/He and< sup> 230</sup> Th dating of volcanic allanite: Earth and Planetary Science Letters, v. 319, p. 178-184.

Czamanske, G. K., and Mihalik, P., 1972, Oxidation during magmatic differentiation, Finnmarka complex, Oslo area, Norway: Part 1, The opaque oxides: Journal of Petrology, v. 13, no. 3, p. 493-509.

Damon, P. E., and Green, W. D., 1963, Investigations of the helium age dating method by stable isotope dilution technique: Radioactive Dating, p. 55-71.

Damon, P. E., and Kulp, J. L., 1957, Determination of radiogenic helium in zircon by stable isotope dilution technique: Trans. Am. Geophys. Union, v. 38, p. 945-953.

Deino, A. L., and McBrearty, S., 2002, 40Ar/39Ar dating of the Kapthurin Formation, Baringo, Kenya: Journal of Human Evolution, v. 42, no. 1-2, p. 185-210.

Dobson, K. J., Stuart, F. M., and Dempster, T. J., 2008, U and Th zonation in Fish Canyon Tuff zircons: Implications for a zircon (U-Th)/He standard: Geochimica et Cosmochimica Acta, v. 72, no. 19, p. 4745-4755.

Dodson, M. H., 1973, Closure temperature in cooling geochronological and petrological systems: Contributions to Mineralogy and Petrology, v. 40, no. 3, p. 259-274.

Fanale, F. P., and Kulp, J. L., 1962, The helium method and the age of the Cornwall, Pennsylvania magnetite ore: Economic Geology, v. 57, no. 5, p. 735-746.

Farley, K., 2000, Helium diffusion from apatite: General behavior as illustrated by Durango fluorapatite: Journal of Geophysical Research, v. 105, no. B2, p. 2903-2914.

Farley, K. A., and Stockli, D. F., 2002, (U-Th)/He dating of phosphates: Apatite, monazite, and xenotime: Reviews in mineralogy and geochemistry, v. 48, no. 1, p. 559-577.

Fechtig, H., and Kalbitzer, S., 1966, The diffusion of argon in potassium-bearing solids: Potassium-argon dating, p. 38.

Ferreira, M. P., Macedo, R., Costa, V., Reynolds, J. H., Riley Jr, J. E., and Rowe, M. W., 1975, Rare-gas dating, II. Attempted uranium-helium dating of young volcanic rocks from the Madeira Archipelago: Earth and Planetary Science Letters, v. 25, no. 2, p. 142-150.

Garcia, T., Féraud, G., Falguères, C., de Lumley, H., Perrenoud, C., and Lordkipanidze, D., 2010, Earliest human remains in Eurasia: New< sup> 40</sup> Ar/< sup> 39</sup> Ar dating of the Dmanisi hominid-bearing levels, Georgia: Quaternary Geochronology, v. 5, no. 4, p. 443-451.

Gerlach, D. C., and Grove, T. L., 1982, Petrology of Medicine Lake Highland volcanics: Characterization of endmembers of magma mixing: Contributions to Mineralogy and Petrology, v. 80, no. 2, p. 147-159.

Glazner, A. F., Bartley, J. M., Coleman, D. S., Gray, W., and Taylor, R. Z., 2004, Are plutons assembled over millions of years by amalgamation from small magma chambers?: GSA today, v. 14, no. 4/5, p. 4-12.

Glazner, A. F., and Stockl, G. M., 2010, Geology Underfoot in Yosemite National Park and Vicinity, Mountain Press Publishing Co.

Harlov, D. E., 2000, Titaniferous magnetite–ilmenite thermometry and titaniferous magnetite–ilmenite–orthopyroxene–quartz oxygen barometry in granulite facies gneisses, Bamble Sector, SE Norway: implications for the role of high-grade CO 2-rich fluids during granulite genesis: Contributions to Mineralogy and Petrology, v. 139, no. 2, p. 180-197.

Holbrook, W., and Kelemen, P., 1993, Large igneous province on the US Atlantic margin and implications for magmatism during continental breakup: Nature, v. 364, no. 6436, p. 433-436.

Huber, N. K., 1987, The geologic story of Yosemite National Park, US Geological Survey.

Huber, N. K., Bateman, P. C., and Wahrhaftig, C., 1989, Geologic map of Yosemite National Park and vicinity, California, US Geological Survey.

Irving, E., 1970, The Mid-Atlantic Ridge at 45 N. XIV. Oxidation and magnetic properties of basalt; review and discussion: Canadian Journal of Earth Sciences, v. 7, no. 6, p. 1528-1538.

Ishikawa, T., Sugimoto, K., and Nagaishi, K., 2003, Determination of rare-earth elements in rock samples by an improved high-performance ion chromatography: GEOCHEMICAL JOURNAL-JAPAN-, v. 37, no. 6, p. 671-680.

Keevil, N. B., 1943, Helium indexes for several minerals and rocks: American Journal of Science, v. 241, no. 11, p. 680-693.

Kelley, S., 2002, Excess argon in K-Ar and Ar-Ar geochronology: Chemical Geology, v. 188, no. 1-2, p. 1-22.

Kislitsyn, R., and Stockli, D. F., in prep., Helios.

Kletetschka, G., Wasilewski, P. J., and Taylor, P. T., 2002, The role of hematite–ilmenite solid solution in the production of magnetic anomalies in ground-and satellite-based data: Tectonophysics, v. 347, no. 1, p. 167-177.

Kohn, B., Pillans, B., and McGlone, M., 1992, Zircon fission track age for middle Pleistocene Rangitawa Tephra, New Zealand: stratigraphic and paleoclimatic significance: Palaeogeography, palaeoclimatology, palaeoecology, v. 95, no. 1, p. 73-94.

Krogh, T. E., 1982, Improved accuracy of U-Pb zircon ages by the creation of more concordant systems using an air abrasion technique: Geochimica et Cosmochimica Acta, v. 46, no. 4, p. 637-649.

Laj, C., and Channell, J. E. T., 2007, Geomagnetic excursions: Treatise on Geophysics, v. 5, p. 373-416.

Larson, R. L., and Hilde, T. W. C., 1975, A revised time scale of magnetic reversals for the Early Cretaceous and Late Jurassic: Journal of Geophysical Research, v. 80, no. 17, p. 2586-2594.

Leventhal, J. S., 1975, An evaluation of the uranium-thorium-helium method for dating young basalts: Journal of Geophysical Research, v. 80, no. 14, p. 1911-1914.

Lindsley, D. H., and Banerjee, S., 1991, Oxide minerals: petrologic and magnetic significance, Mineralogical Society of America Chantilly, VA.

Lipman, P. W., Steven, T. A., and Mehnert, H. H., 1970, Volcanic history of the San Juan Mountains, Colorado, as indicated by potassium–argon dating: Geological Society of America Bulletin, v. 81, no. 8, p. 2329-2352.

Lippolt, H. J., Brander, T., and Mankopf, N., 1998, An attempt to determine formation ages of goethites and limonites by (U+ Th)-4He dating: Neues Jahrbuch für Mineralogie Monatshefte, no. 11, p. 505-528.

Long, P. E., and Duncan, R. A., 1982, 40Ar/39Ar ages of Columbia River basalt from deep bore holes in south-central Washington: Richland, Washington, Rockwell Hanford Operations: Report RHO-BW-SA-233P.

Ludwig, K. R., 2004, Isoplot/Ex rev 3.06 A Geochronological Toolkit for Microsoft Excel: Berkeley Geochronology Center.

Lyons, J. I., 1988, Volcanogenic iron oxide deposits, Cerro de Mercado and vicinity, Durango: Economic Geology, v. 83, no. 8, p. 1886-1906.

Mahoney, J., and Coffin, F., 1997, Large igneous provinces: continental, oceanic, and planetary flood volcanism, American Geophysical Union.

Mahoney, J. J., 1988, Deccan traps: Continental flood basalts, p. 151-194.

Majsuradze, G. M., 1996, Geologisch-geomorphologische Untersuchungen im Masavera-Becken (Südost-Georgien) Jahrb: RGZM, v. 42, no. 1995, p. 25-49.

Majsuradze, G. M., and Kuloshvili, S. I., 1999, Some Geological Problems of Late Volcanism in the Dzhavakheti Upland: Tr. GIN AN Gruzii. Nov. Ser, v. 114, p. 220-228.

Mamtani, M. A., Piazolo, S., Greiling, R. O., Kontny, A., and Hrouda, F., 2011, Process of magnetite fabric development during granite deformation: Earth and Planetary Science Letters.

Marchant, D. R., Denton, G. H., Swisher, C. C., and Potter, N., 1996, Late Cenozoic Antarctic paleoclimate reconstructed from volcanic ashes in the Dry Valleys region of southern Victoria Land: Geological Society of America Bulletin, v. 108, no. 2, p. 181-194.

Marshall, M., and Cox, A., 1972, Magnetic changes in pillow basalt due to sea floor weathering: Journal of Geophysical Research, v. 77, no. 32, p. 6459-6469.

McKee, E. H., Swanson, D. A., and Wright, T. L., 1977, Duration and volume of Columbia River basalt volcanism: Washington, Oregon, and Idaho: Geological Society of America Abstracts with Programs, v. 9, no. 4, p. 463-464.

McNulty, B. A., Tobisch, O. T., Cruden, A. R., and Gilder, S., 2000, Multistage emplacement of the Mount Givens pluton, central Sierra Nevada batholith, California: Geological Society of America Bulletin, v. 112, no. 1, p. 119-135.

McNulty, B. A., Tong, W., and Tobisch, O. T., 1996, Assembly of a dike-fed magma chamber: The Jackass Lakes pluton, central Sierra Nevada, California: Geological Society of America Bulletin, v. 108, no. 8, p. 926-940.

Merrill, R. T., McElhinny, M. W., and McFadden, P. L., 1996, The magnetic field of the Earth: Paleomagnetism, the core, and the deep mantle, Academic Press.

Messager, E., Nomade, S., Voinchet, P., Ferring, R., Mgeladze, A., Guillou, H., and Lordkipanidze, D., 2011, 40Ar/39Ar dating and phytolith analysis of the Early Pleistocene sequence of Kvemo-Orozmani (Republic of Georgia): chronological and palaeoecological implications for the hominin site of Dmanisi: Quaternary Science Reviews, v. 30, no. 21, p. 3099-3108.

Min, K., Reiners, P. W., Wolff, J. A., Mundil, R., and Winters, R. L., 2006, (U–Th)/He dating of volcanic phenocrysts with high-U–Th inclusions, Jemez Volcanic Field, New Mexico: Chemical Geology, v. 227, no. 3, p. 223-235.

Mohr, P., 1983, Ethiopian flood basalt province.

Mohr, P., and Zanettin, B., 1988, The Ethiopian flood basalt province: Continental flood basalts, v. 3, p. 63.

Neumann, E. R., 1974, The distribution of Mn (super 2+) and Fe (super 2+) between ilmenites and magnetites in igneous rocks: American Journal of Science, v. 274, no. 9, p. 1074-1088.

Nicolescu, S., and P.W., R., 2005, He dating of epidote and andradite garnet: Geochimica et Cosmochimica Acta, v. 69, p. 23.

Operations, R. H., 1982, Site characterization report for the Basalt Waste Isolation Project.

Ozima, M., Joshima, M., and Kinoshita, H., 1974, Magnetic properties of submarine basalts and the implications on the structure of the oceanic crust: Journal of geomagnetism and geoelectricity, v. 26, p. 335-354.

Pariso, J. E., and Johnson, H. P., 1991, Alteration processes at deep sea drilling project/ocean drilling program hole 504B at the Costa Rica rift: Implications for magnetization of oceanic crust: Journal of Geophysical Research, v. 96, no. B7, p. 11703-11711,11722.

Perkins, M. E., and Nash, B. P., 2002, Explosive silicic volcanism of the Yellowstone hotspot: The ash fall tuff record: Geological Society of America Bulletin, v. 114, no. 3, p. 367-381.

Petersen, N., Eisenach, P., and Bleil, U., 1979, Low temperature alteration of the magnetic minerals in ocean floor basalts: Deep drilling results in the Atlantic ocean: Ocean crust, v. 2, p. 169-209.

Pike, C. R., Roberts, A. P., and Verosub, K. L., 2001, First□order reversal curve diagrams and thermal relaxation effects in magnetic particles: Geophysical Journal International, v. 145, no. 3, p. 721-730.

Purucker, M., and Whaler, K., 2007, Crustal magnetism: Treatise on Geophysics, v. 5, p. 195-237.

Readman, P. W., and O'reilly, W., 1972, Magnetic properties of oxidized (cation-deficient) titanomagnetites (Fe, Ti,□) 3 O 4: J. Geomagn. Geoelectr, v. 24, no. 1, p. 69-90.

Regan, R. D., Cain, J. C., and Davis, W. M., 1975, A global magnetic anomaly map: Journal of Geophysical Research, v. 80, no. 5, p. 794-802.

Reidel, S. P., Johnson, V. G., and Spane, F. A., 2002, Natural gas storage in basalt aquifers of the Columbia Basin: Pacific Northwest USA: A Guide to Site Characterization. PNNL-13962.

Reiners, P. W., 2005, Zircon (U-Th)/He thermochronometry: Reviews in mineralogy and geochemistry, v. 58, no. 1, p. 151-179.

Reiners, P. W., and Farley, K. A., 1999, Helium diffusion and (U-Th)/He thermochronometry of titanite: Geochimica et Cosmochimica Acta, v. 63, no. 22, p. 3845-3859.

Schlinger, C. M., 1985, Magnetization of lower crust and interpretation of regional magnetic anomalies: Example from Lofoten and Vesterålen, Norway: Journal of Geophysical Research, v. 90, no. B13, p. 11484-11411,11504.

Schmincke, H. U., and van den Bogaard, P., 1995, Die datierung des Masavera Basalt lavastrom: Jahrbuch des Romisch-Germanischen Zentralmuseums, v. 42, p. 2.

Schmitt, A. K., Stockli, D. F., and Hausback, B. P., 2006, Eruption and magma crystallization ages of Las Tres Vírgenes (Baja California) constrained by combined< sup> 230</sup> Th/< sup> 238</sup> U and (U–Th)/He dating of zircon: Journal of volcanology and geothermal research, v. 158, no. 3, p. 281-295.

Schmitz, M. D., and Bowring, S. A., 2001, U-Pb zircon and titanite systematics of the Fish Canyon Tuff: an assessment of high-precision U-Pb geochronology and its application to young volcanic rocks: Geochimica et Cosmochimica Acta, v. 65, no. 15, p. 2571-2587.

Sinton, C. W., Duncan, R. A., Storey, M., Lewis, J., and Estrada, J. J., 1998, An oceanic flood basalt province within the Caribbean plate: Earth and Planetary Science Letters, v. 155, no. 3, p. 221-235.

Smith, B. M., 1987, Consequences of the maghemitization on the magnetic properties of submarine basalts: synthesis of previous works and results concerning basement rocks from mainly DSDP Legs 51 and 52: Physics of the earth and planetary interiors, v. 46, no. 1-3, p. 206-226.

Spencer, A. S., Kohn, B. P., Gleadow, A. J. W., Norman, M., Belton, D. X., and Carter, T. J., The importance of residing in a good neighbourhood: rechecking the rules of the game for apatite (U-Th)/ He thermochronology2004, p. 20.

Stockli, D. F., Farley, K. A., and Dumitru, T. A., 2000, Calibration of the apatite (U-Th)/He thermochronometer on an exhumed fault block, White Mountains, California: Geology, v. 28, no. 11, p. 983-986.

Strutt, R. J., 1905, On the radio-active minerals: Proceedings of the Royal Society of London. Series A, v. 76, no. 508, p. 88-101.

Swanson, D. A., Wright, T., Hooper, P., and Bentley, R., 1979, Revisions in stratigraphic nomenclature of the Columbia River Basalt Group, US Government Printing Office.

Tagami, T., Farley, K. A., and Stockli, D. F., 2003, (U–Th)/He geochronology of single zircon grains of known Tertiary eruption age: Earth and Planetary Science Letters, v. 207, no. 1, p. 57-67.

Tauxe, L., Yamazaki, T., and Paleointensities, G. S., 2007, Treatise on Geophysics, vol. 5, Geomagnetism, Elsevier Ltd., Oxford.

Taylor, J. L., 2012, Practical Guide to Improved Magnetite (U-Th)/He Geochronometry – A case study from the Columbia River Basalt Group [M.Sci.: University of Kansas.

Tincher, C. R., and Stockli, D. F., 2009, Cenozoic volcanism and tectonics in the Queen Valley area, Esmeralda County, western Nevada: Geological Society of America Special Paper 447, p. 255-274.

Tolan, T. L., Reidel, S. P., Beeson, M. H., Anderson, J. L., Fecht, K. R., and Swanson, D. A., 1989, Revisions to the estimates of the areal extent and volume of the Columbia River Basalt Group: Volcanism and tectonism in the Columbia River flood-basalt province: Geological Society of America Special Paper, v. 239, p. 1-20.

Turekian, K. K., Kharkar, D. P., Funkhouser, J., and Schaeffer, O. A., 1970, An evaluation of the uranium-helium method of dating of fossil bones: Earth and Planetary Science Letters, v. 7, no. 5, p. 420-424.

Turner, G., and Cadogan, P., Possible effects of Ar-39 recoil in Ar-40/Ar-39 dating(of lunar rocks)1974, p. 1601-1615.

Verchovsky, A. B., Ott, U., and Begemann, F., 1993, Implanted radiogenic and other noble gases in crustal diamonds from Northern Kazakhstan: Earth and Planetary Science Letters, v. 120, no. 3, p. 87-102.

Vine, F. J., 1966, Spreading of the ocean floor: new evidence: Science, v. 154, no. 3755, p. 1405-1415.

Watkins, N. D., and Baksi, A. K., 1974, Magnetostratigraphy and oroclinal folding of the Columbia River, Steens, and Owyhee basalts in Oregon, Washington, and Idaho: American Journal of Science, v. 274, no. 2, p. 148-189.

Wernicke, R. S., and Lippolt, H. J., 1993, Botryoidal hematite from the Schwarzwald (Germany): heterogeneous uranium distributions and their bearing on the helium dating method: Earth and Planetary Science Letters, v. 114, no. 2-3, p. 287-300.

-, 1994, 4He age discordance and release behavior of a double shell botryoidal hematite from the Schwarzwald, Germany: Geochimica et Cosmochimica Acta, v. 58, no. 1, p. 421-429.

White, R., and McKenzie, D., 1989, Magmatism at rift zones: the generation of volcanic continental margins and flood basalts: Journal of Geophysical Research, v. 94, no. B6, p. 7685-7729.

Wipf, M., Glasmacher, U. A., Stockli, D. F., Vermesch, P., Szymanski, E., Corona, R., Miletich, R., and Balcázar, M., in prep., Cerro de Mercado (Durango, Mexico): a “new old” standard for fission-track and (U-Th-Sm)/He thermochronometry.

Zeitler, P. K., Herczeg, A. L., McDougall, I., and Honda, M., 1987, U-Th-He dating of apatite: A potential thermochronometer: Geochimica et Cosmochimica Acta, v. 51, no. 10, p. 2865-2868.

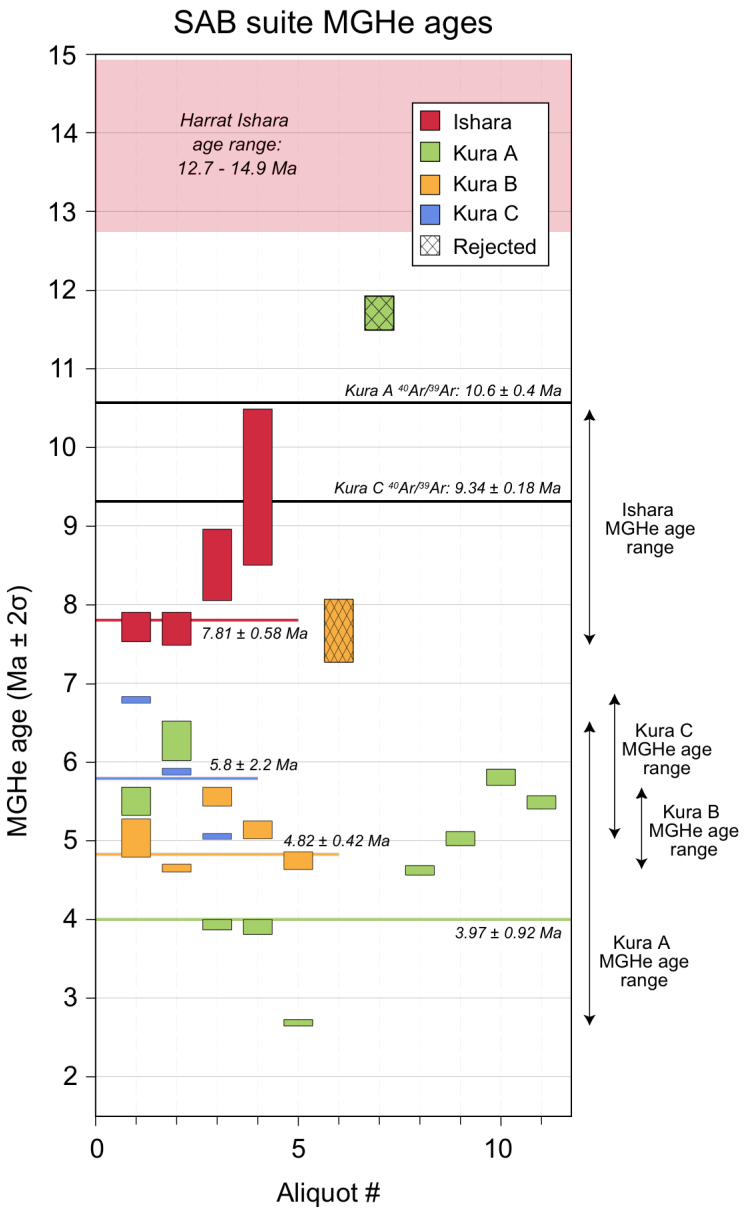
SAB suite MGHe ages
Harrat Ishara
age range:
12.7 - 14.9 Ma
Ishara
Kura A
Kura B
Kura C
Rejected
Kura A 40Ar/39Ar: 10.6 ± 0.4 Ma
Kura C 40Ar/39Ar: 9.34 ± 0.18 Ma
7.81 ± 0.58 Ma
5.8 ± 2.2 Ma
4.82 ± 0.42 Ma
3.97 ± 0.92 Ma
Ishara MGHe age range
Kura C MGHe age range
Kura B MGHe age range
Kura A MGHe age range
MGHe age (Ma ± 2σ)
Aliquot #
15
14
13
12
11
10
9
8
7
6
5
4
3
2
0
5
10

Figure 1 - SAB MGHe ages

Colored boxes represent aliquot MGHe age and 2σ error. Colored lines show respective mean sample MGHe age. If available, black lines show accepted $^{40}Ar/^{39}Ar$ sample age (Table 3). Red shaded region shows the whole-rock $^{40}Ar/^{39}Ar$ age range of the Ishara basalt horizon (Szymanski, *in prep.*; Table 3).

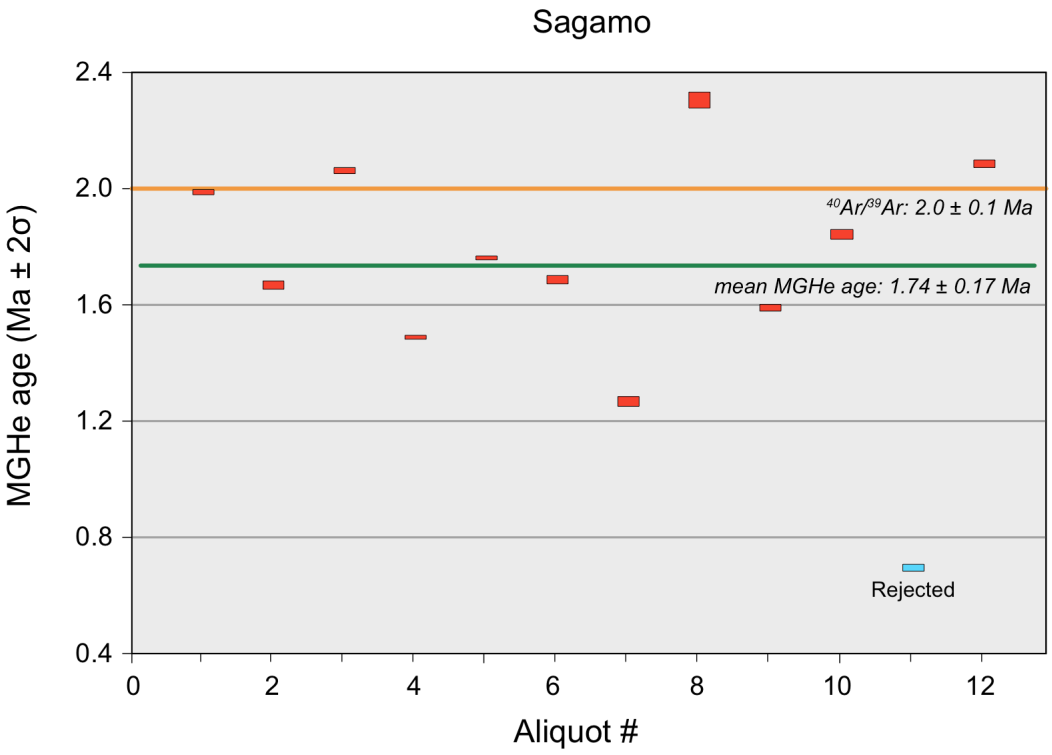
Sagamo
MGHe age (Ma ± 2σ)
2.4
2.0
1.6
1.2
0.8
0.4
0
2
4
6
8
10
12
Aliquot #
40Ar/39Ar: 2.0 ± 0.1 Ma
mean MGHe age: 1.74 ± 0.17 Ma
Rejected

Figure 2 - Sagamo MGHe ages

Red boxes represent aliquot MGHe age and 2σ error. Green line shows mean MGHe age. Orange line shows accepted $^{40}Ar/^{39}Ar$ age (Schmincke and van den Bogaard, 1995; Table 3).

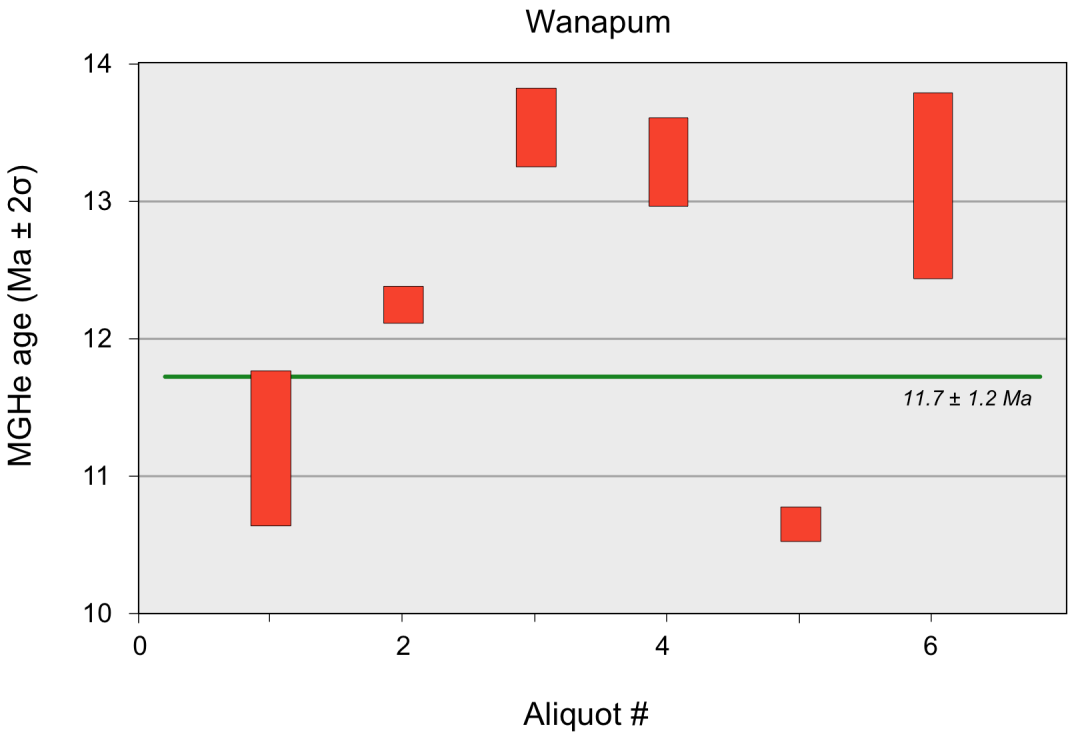
Wanapum
MGHe age (Ma ± 2σ)
14
13
12
11
10
0
2
4
6
Aliquot #
11.7 ± 1.2 Ma

Figure 3 - Wanapum MGHe ages

Red boxes represent aliquot MGHe age and 2σ error. Green line shows mean MGHe age. No available reference age exists for this sample.

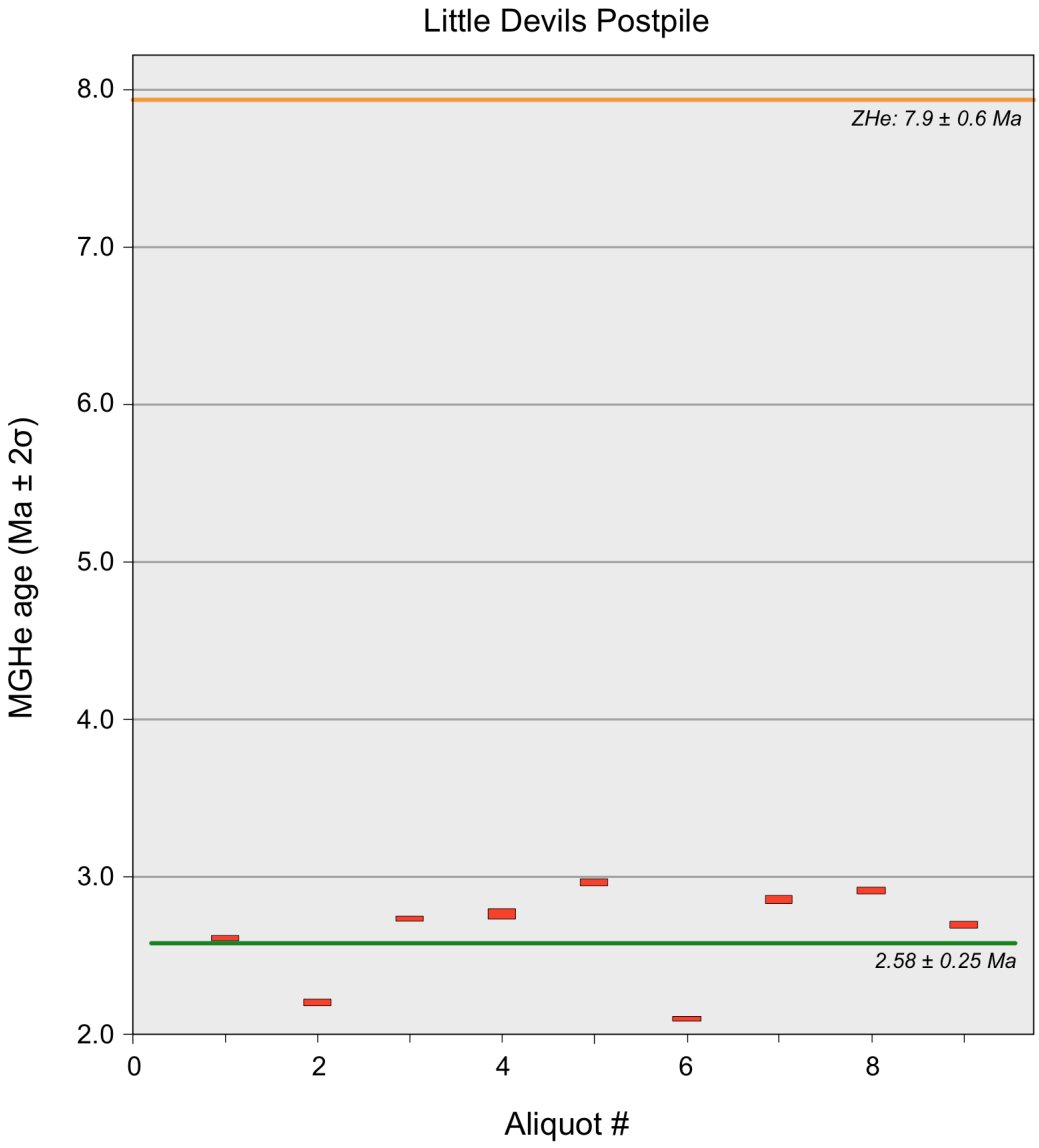
Little Devils Postpile
MGHe age (Ma ± 2σ)
Aliquot #
ZHe: 7.9 ± 0.6 Ma
2.58 ± 0.25 Ma
8.0
7.0
6.0
5.0
4.0
3.0
2.0
0
2
4
6
8

Figure 4 - Little Devils Postpile (LDPP) MGHe ages

Red boxes represent aliquot MGHe age and 2σ error. Green line shows mean MGHe age. Orange line shows accepted zircon (U-Th)/He age from host rock xenolith (Stockli, *pers. comm.*; Table 3). No accepted age exists for LDPP basalt from direct geochronologic age dating.

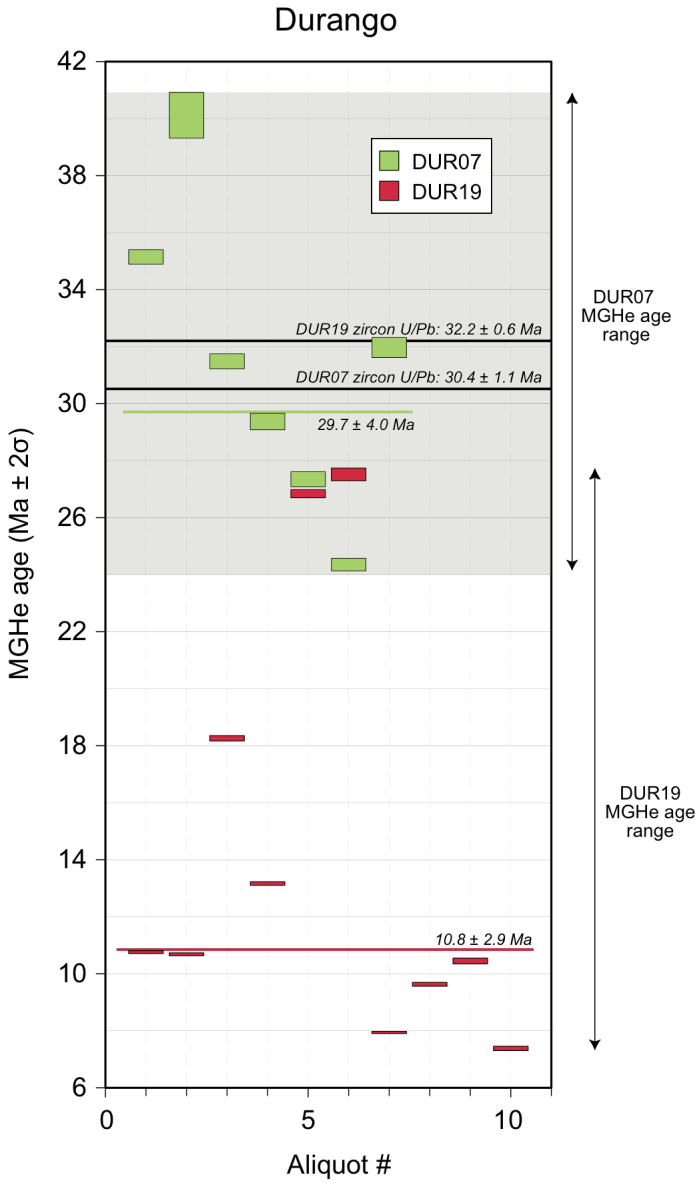
Durango
DUR07
DUR19
DUR19 zircon U/Pb: 32.2 ± 0.6 Ma
DUR07 zircon U/Pb: 30.4 ± 1.1 Ma
29.7 ± 4.0 Ma
10.8 ± 2.9 Ma
DUR07 MGHe age range
DUR19 MGHe age range
MGHe age (Ma ± 2σ)
Aliquot #
42
38
34
30
26
22
18
14
10
6
0
5
10

Figure 5 - DUR and DUR19 MGHe ages

Colored boxes represent aliquot MGHe age and 2σ error. Colored lines show respective mean sample MGHe age. Shaded region shows the MGHe age range of DUR07. Black lines show accepted zircon U/Pb sample ages (Wipf et al., *in prep.*; Table 3).

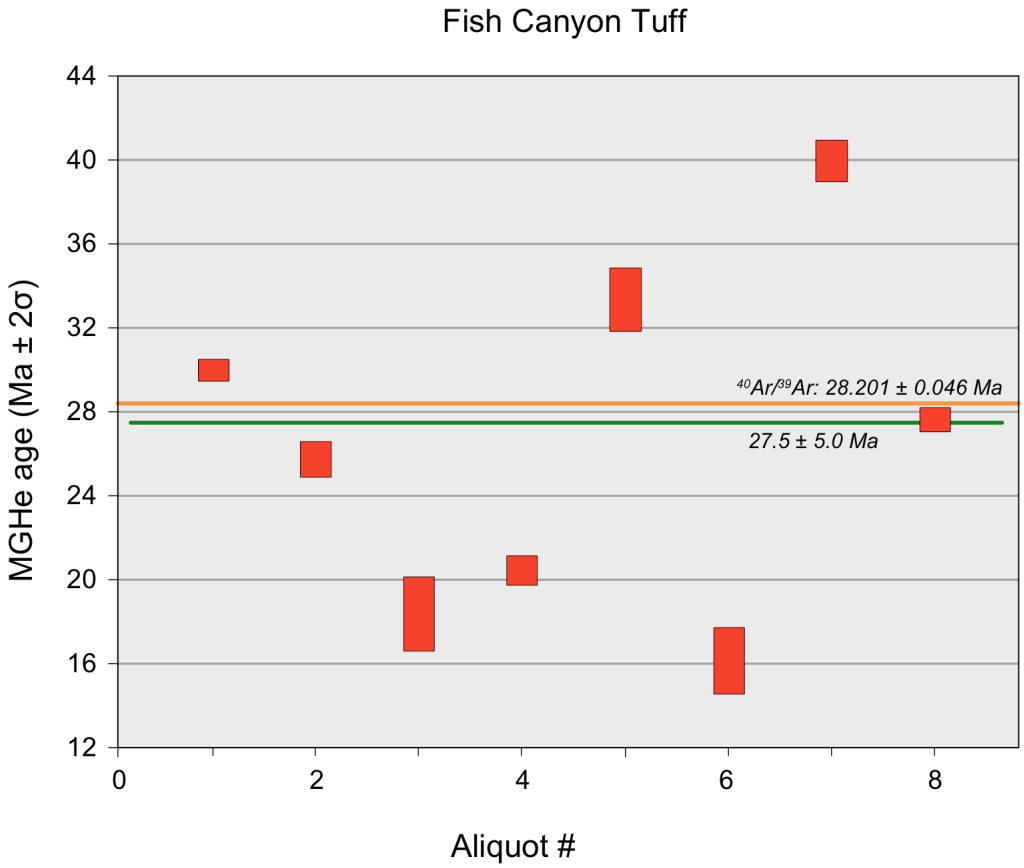
Fish Canyon Tuff
MGHe age (Ma ± 2σ)
44
40
36
32
28
24
20
16
12
0
2
4
6
8
Aliquot #
40Ar/39Ar: 28.201 ± 0.046 Ma
27.5 ± 5.0 Ma

Figure 6 - Fish Canyon Tuff (FCT) MGHe ages

Red boxes represent aliquot MGHe age and 2σ error. Green line shows mean MGHe age. Orange line shows accepted $^{40}Ar/^{39}Ar$ age (Kuiper et al., 2008; Table 3).

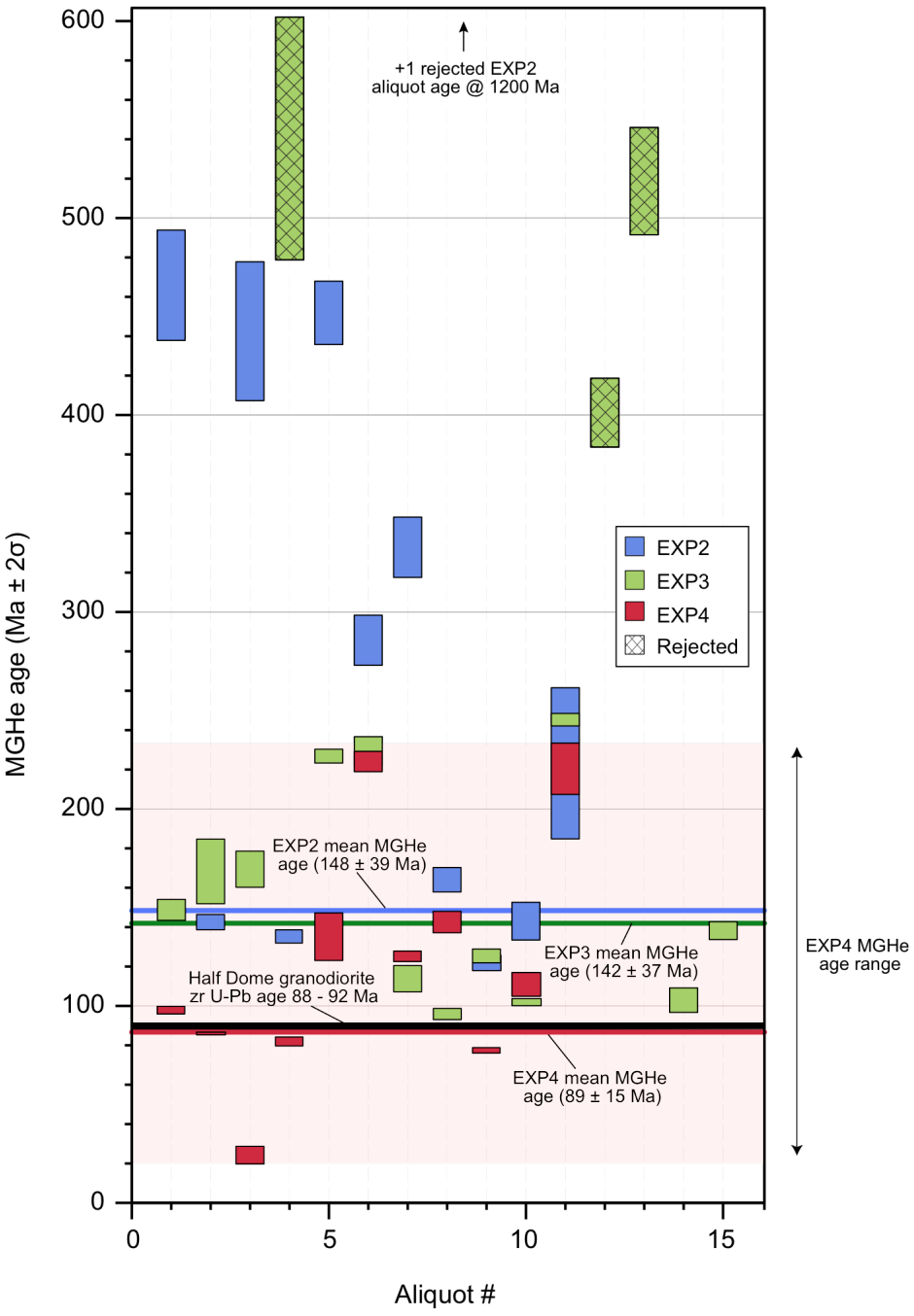
+1 rejected EXP2
aliquot age @ 1200 Ma
EXP2
EXP3
EXP4
Rejected
EXP2 mean MGHe
age (148 ± 39 Ma)
EXP3 mean MGHe
age (142 ± 37 Ma)
Half Dome granodiorite
zr U-Pb age 88 - 92 Ma
EXP4 mean MGHe
age (89 ± 15 Ma)
EXP4 MGHe
age range
MGHe age (Ma ± 2σ)
Aliquot #
0
100
200
300
400
500
600
0
5
10
15

Figure 7 - Olmsted Point (OLM) MGHe ages

Colored boxes represent aliquot MGHe age and 2σ error. Colored lines show respective mean sample MGHe age. Shaded region shows the MGHe age range of EXP4. Black line shows accepted zircon U/Pb sample age of host rock (Coleman et al., 2004; Table 3).

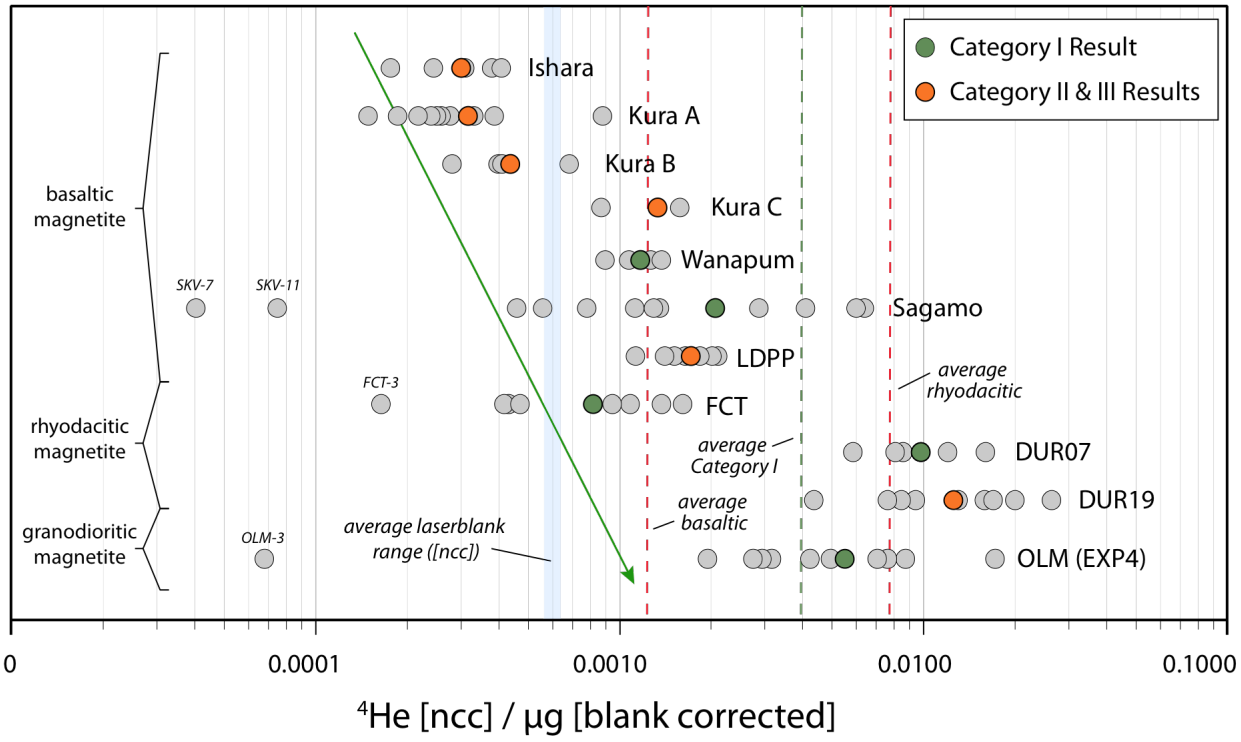
Category I Result
Category II & III Results
Ishara
Kura A
Kura B
Kura C
Wanapum
Sagamo
LDPP
FCT
DUR07
DUR19
OLM (EXP4)
SKV-7
SKV-11
FCT-3
OLM-3
basaltic magnetite
rhyodacitic magnetite
granodioritic magnetite
average rhyodacitic
average Category I
average basaltic
average laserblank range ([ncc])
0
0.0001
0.0010
0.0100
0.1000
4He [ncc] / µg [blank corrected]

Figure 8 - ^{4}He Concentration for Analyzed Aliquots

Gray circles indicate ^{4}He concentration for each analyzed aliquot (Table 2). Colored circles indicate average aliquot ^{4}He concentration for Category I (green) and Categories II and III (orange) results. Green arrow shows trend of increasing ^{4}He yield from basaltic to felsic magnetite. Red dashed lines show average ^{4}He concentration for basaltic and rhyolitic magnetite samples. Green dashed line shows average ^{4}He concentration for Category I results.

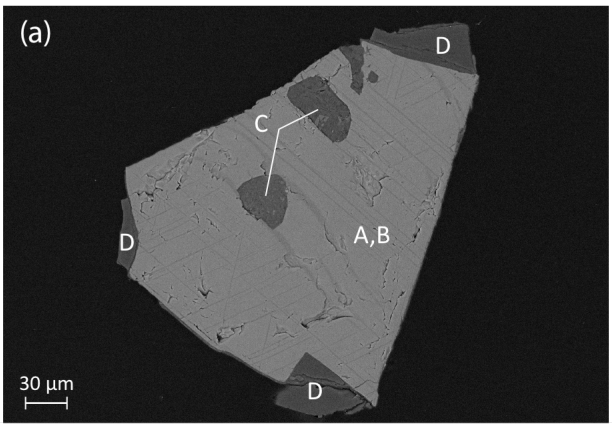
(a)
D
C
D
A,B
D
30 µm

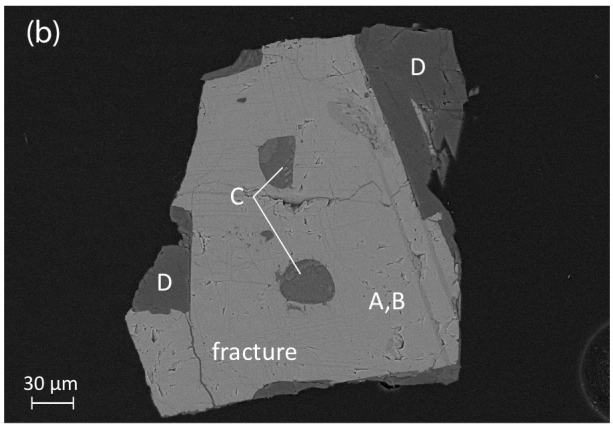
(b)
D
C
D
A,B
fracture
30 µm

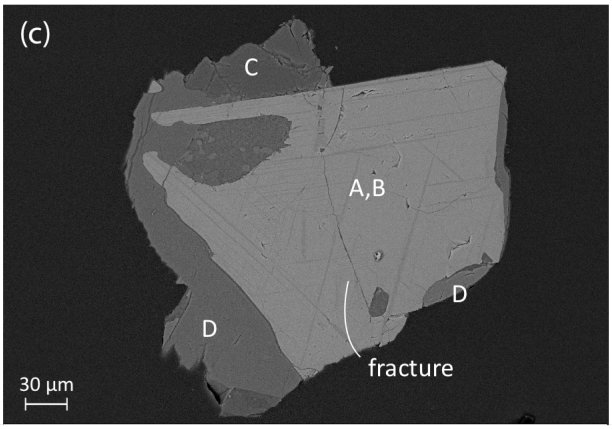
(c)
C
A,B
D
D
fracture
30 µm

Figure 9 - Ishara SEM Images

Backscatter detection (BSD) images of Ishara magnetite. Fractures are post-crystallization grain damage resulting from either natural sample degredation or laboratory sample preparation. Scale bar in microns (μm). A: magnetite (Fe_30_4); B: ulvöspinel [exsolution lamellae] (Fe_2TiO_4); C: augite ($(Ca,Mg,Fe,Al)_2O_6$); D: albite ($Na[AlSi_3O_8]$)

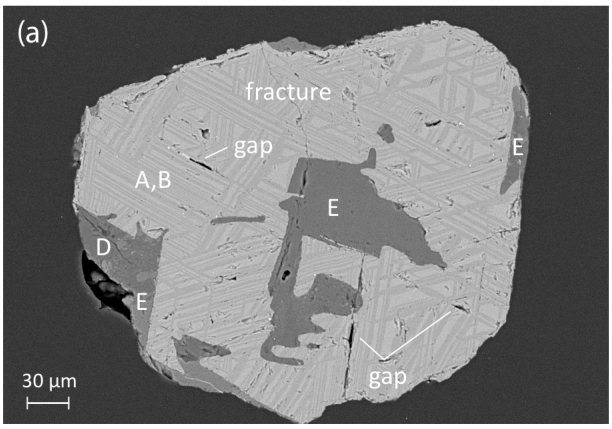
(a)
fracture
gap
A,B
E
E
D
E
gap
30 µm

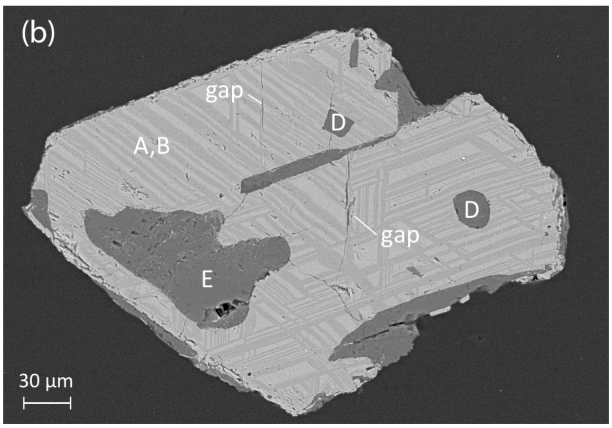
(b)
gap
D
A,B
D
gap
E
30 µm

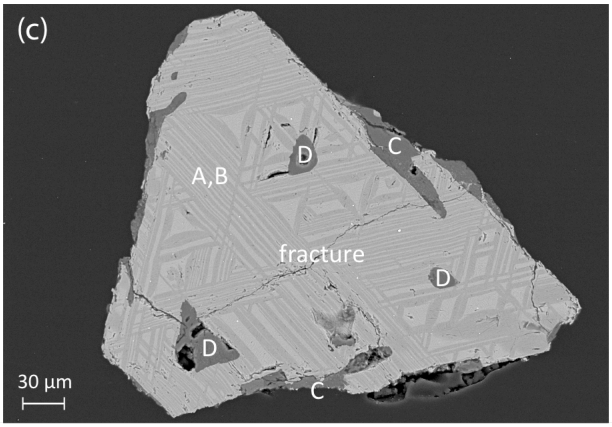
(c)
D
C
A,B
fracture
D
D
30 µm
C

Figure 10 - Kura A SEM images

Backscatter detection (BSD) images of Kura A magnetite. Gaps are large empty spaces formed within magnetite crystalline lattices during mineral crystallization. Fractures are post-crystallization grain damage resulting from either natural sample degredation or laboratory sample preparation. Scale bar in microns (μm). A: magnetite (Fe_30_4); B: ulvöspinel [exsolution lamellae] (Fe_2TiO_4); C: orthopyroxene ($(Mg,Fe)_2Si_2O_6$); D: albite ($Na[AlSi_3O_8]$); E: $anorthite_{50}$ ($(Na,Ca)[Al_{(1,2)}Si_{(2,3)}O_8]$)

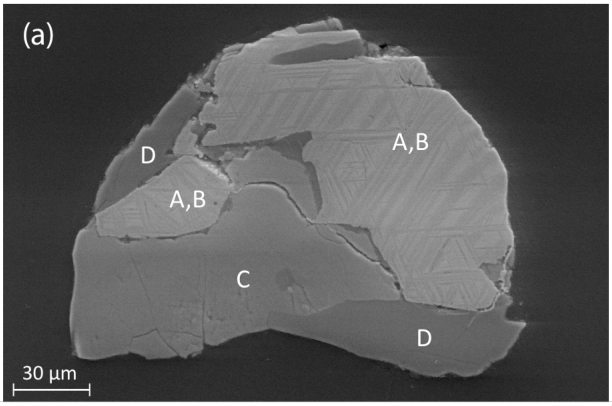
(a)
D
A,B
A,B
C
D
30 µm

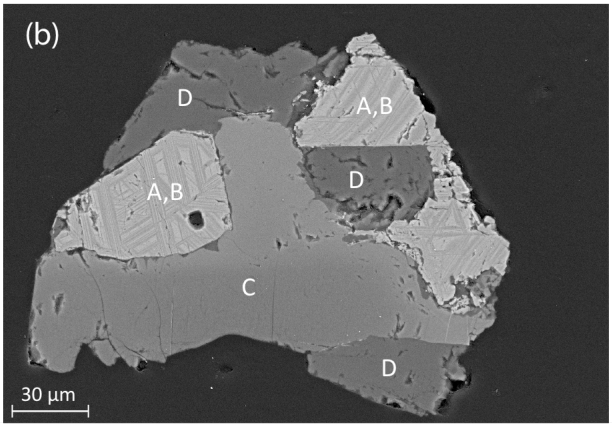
(b)
D
A,B
A,B
D
C
D
30 µm

Figure 11 - Kura B SEM images

Backscatter detection (BSD) images of Kura B magnetite. Scale bar in microns (μm). A: magnetite (Fe_30_4); B: ulvöspinel [exsolution lamellae] (Fe_2TiO_4); C: orthopyroxene ($(Mg,Fe)_2Si_2O_6$); D: anorthite$_{50}$ ($(Na,Ca)[Al_{(1,2)}Si_{(2,3)}O_8]$)

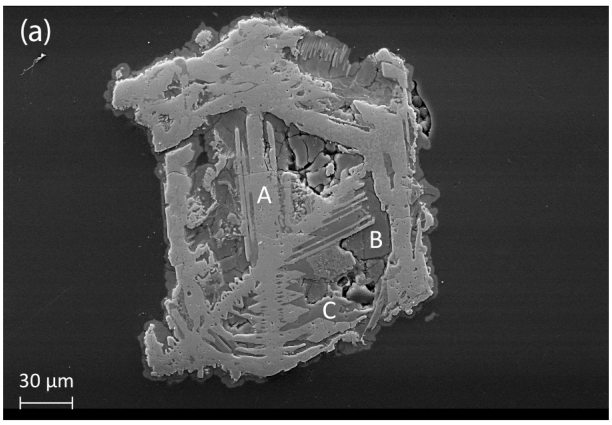
(a)
A
B
C
30 µm

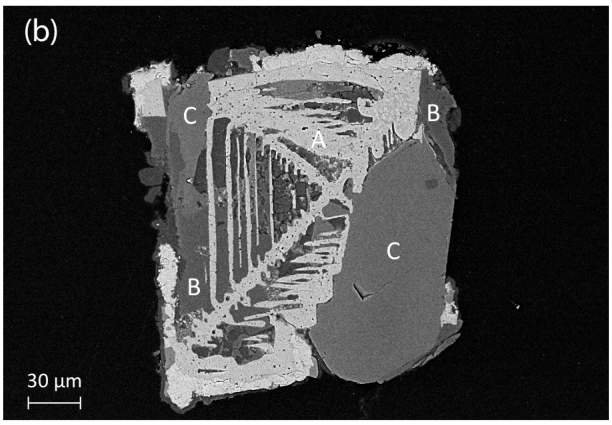
(b)
C
A
B
C
B
30 µm

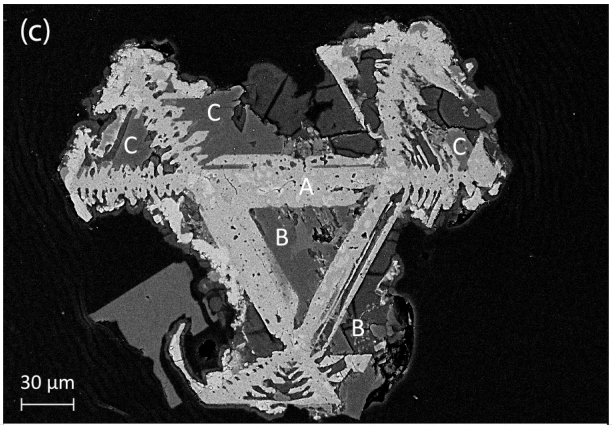
(c)
C
C
C
A
B
B
30 µm

Figure 12 - Kura C SEM images

Backscatter detection (BSD) images of Kura C magnetite. Scale bar in microns (μm). A: magnetite ($Fe_3 0_4$); B: augite ($(Ca,Mg,Fe,Al)_2O_6$); C: anorthite$_{50}$ ($(Na,Ca)[Al_{(1,2)}Si_{(2,3)}O_8]$)

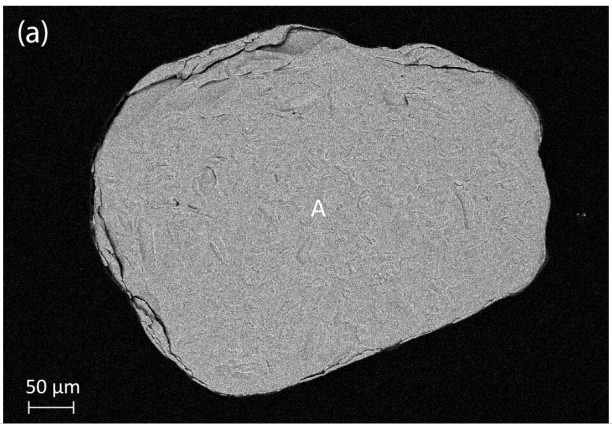
(a)
A
50 µm

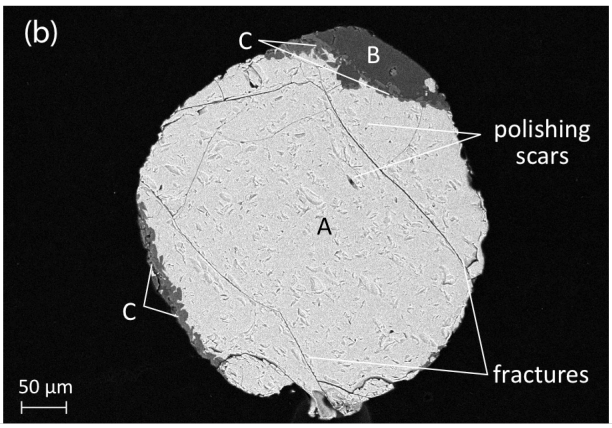
(b)
C
B
polishing scars
A
C
fractures
50 µm

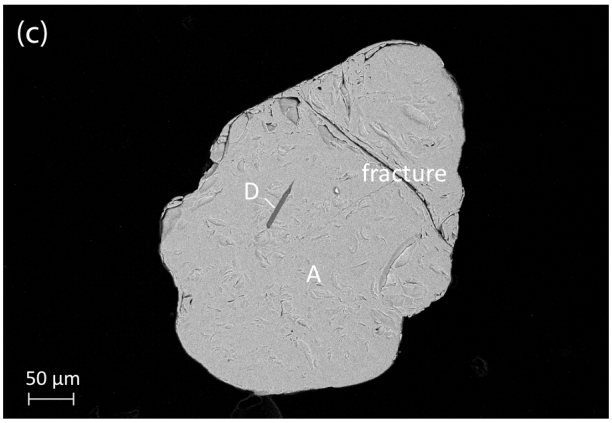
(c)
fracture
D
A
50 µm

Figure 13 - Sagamo SEM images

Backscatter detection (BSD) images of Sagamo magnetite. Fractures are post-crystallization grain damage resulting from either natural sample degredation or laboratory sample preparation. Polishing scars are pits in the grain surface that resulted from sample preparation for SEM imaging. Scale bar in microns (μm). A: magnetite (Fe_30_4); B: orthopyroxene ($(Mg,Fe)_2Si_2O_6$); C: anorthite$_{50}$ ($(Na,Ca)[Al_{(1,2)}Si_{(2,3)}O_8]$); D: apatite ($Ca_5(PO_4)_3(F,Cl,OH)$

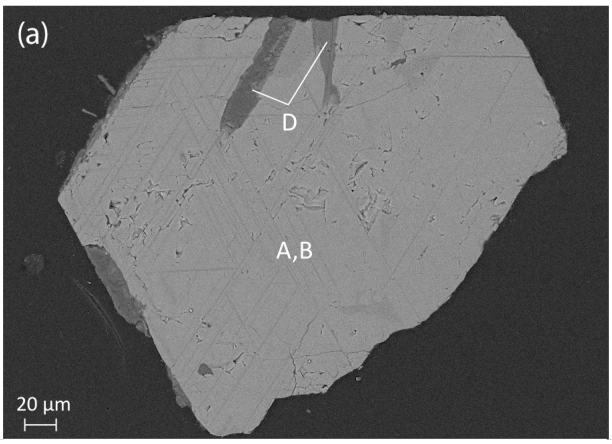
(a)
D
A,B
20 µm

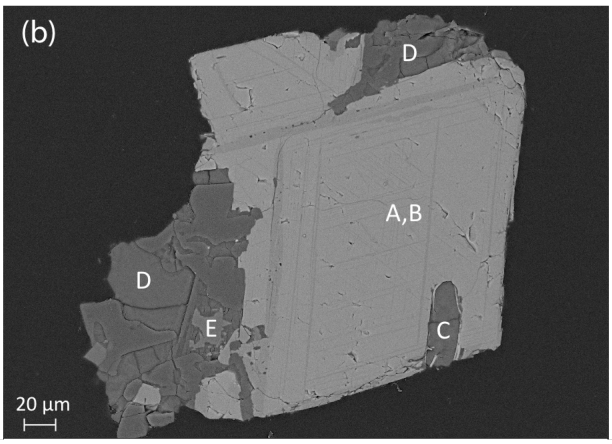
(b)
D
A,B
D
E
C
20 µm

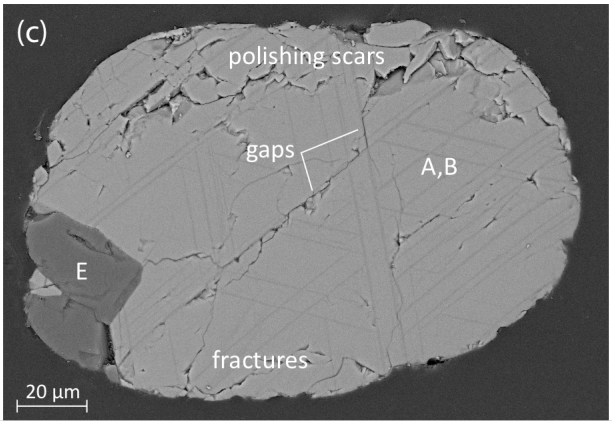
(c)
polishing scars
gaps
A,B
E
fractures
20 µm

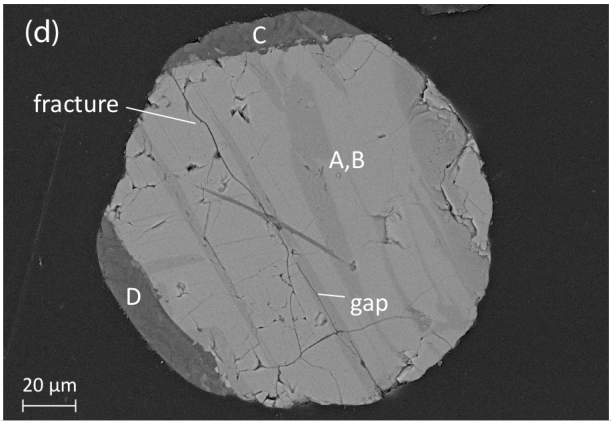
(d)
C
fracture
A,B
D
gap
20 µm

Figure 14 - Wanapum SEM images

Backscatter detection (BSD) images of Wanapum magnetite. Gaps are large empty spaces formed within magnetite crystalline lattices during mineral crystallization. Fractures are post-crystallization grain damage resulting from either natural sample degredation or laboratory sample preparation. Polishing scars are pits in the grain surface that resulted from sample preparation for SEM imaging. Scale bar in microns (μm). A: magnetite (Fe_30_4); B: ulvöspinel [exsolution lamellae] (Fe_2TiO_4); C: orthopyroxene ($(Mg,Fe)_2Si_2O_6$); D: sanidine ($(K,Na)(Si,Al)_4O_8$); D: diopside ($Ca(Mg,Fe)[Si_2O_6]$)

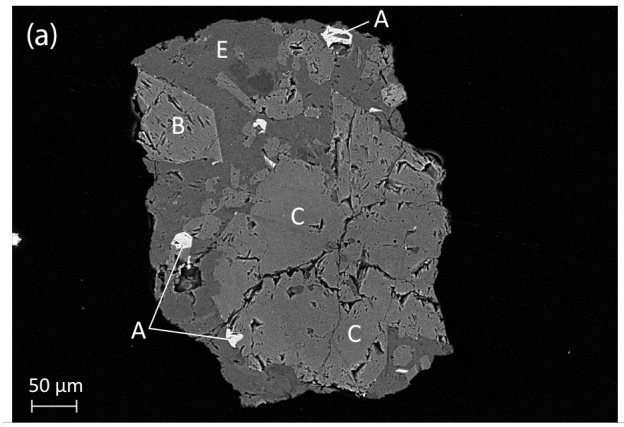
(a)
A
E
B
C
A
C
50 µm

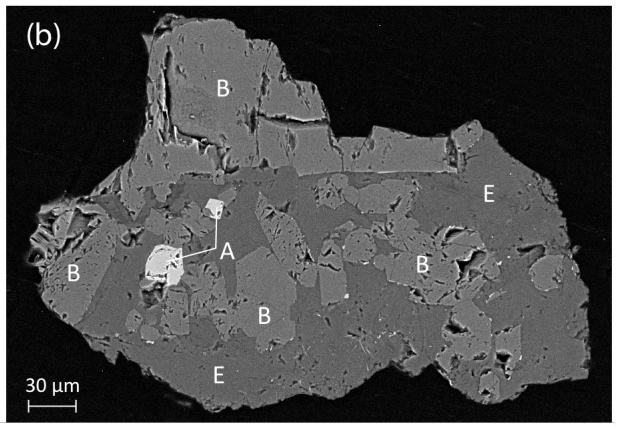
(b)
B
E
A
B
B
B
E
30 µm

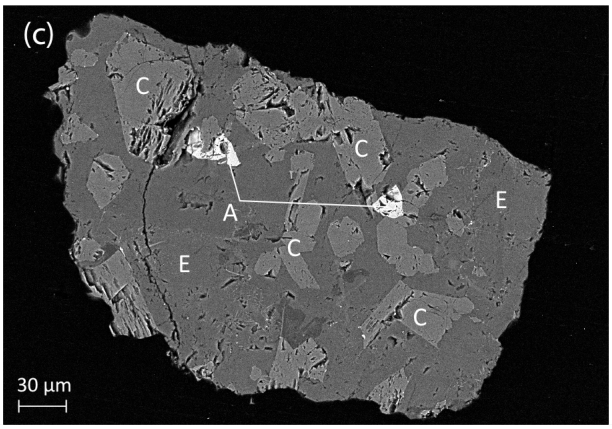
(c)
C
C
E
A
C
E
C
30 µm

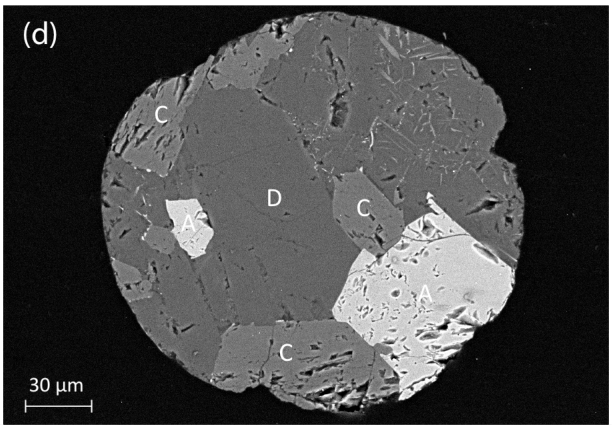
(d)
C
D
C
A
A
C
30 µm

Figure 15 - Little Devils Postpile (LDPP) SEM images

Backscatter detection (BSD) images of LDPP magnetite. Scale bar in microns (μm). A: ulvöspinel (Fe_2TiO_4); B: orthopyroxene ($(Mg,Fe)_2Si_2O_6$); C: augite ($(Ca,Mg,Fe,Al)_2O_6$); D: anorthite$_{50}$ ($(Na,Ca)\ [Al_{(1,2)}Si_{(2,3)}O_8]$); E: sanidine ($(K,Na)(Si,Al)_4O_8$)

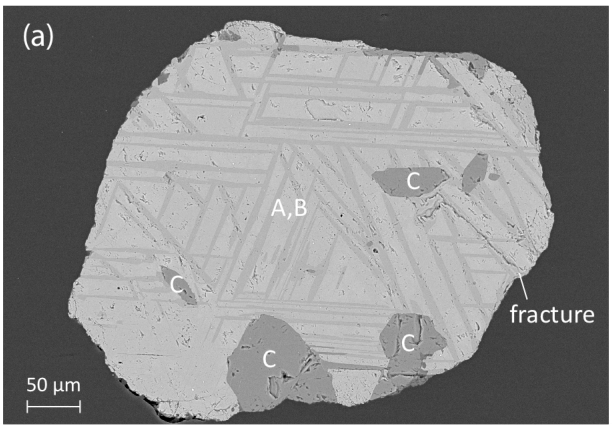
(a)
A,B
C
C
C
C
fracture
50 µm

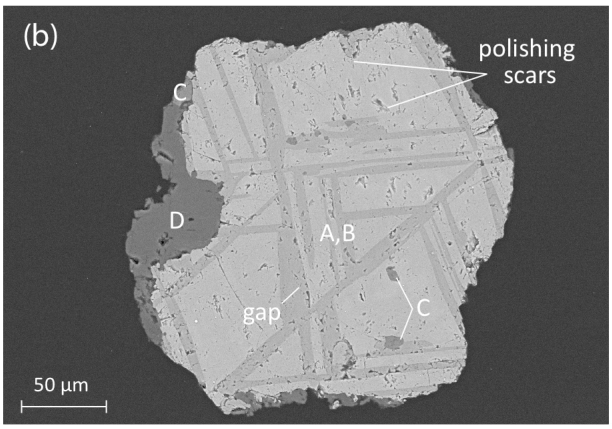
(b)
polishing
scars
C
D
A,B
gap
C
50 µm

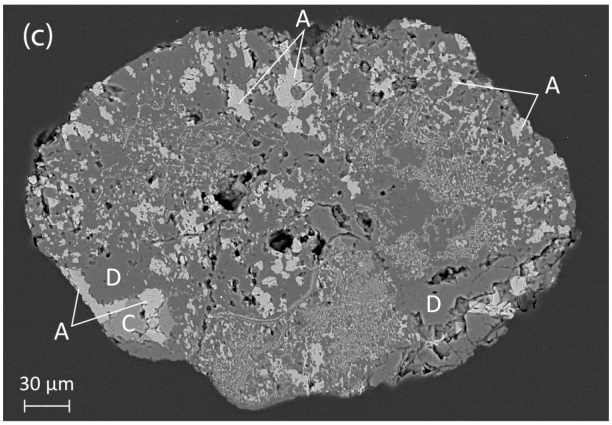
(c)
A
A
D
A
C
D
30 µm

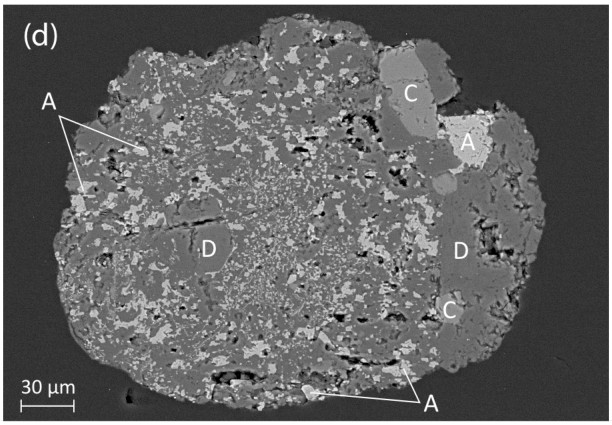
(d)
A
C
A
D
D
C
A
30 µm

Figure 16 - DUR 07 SEM images

Backscatter detection (BSD) images of DUR07 magnetite. Polishing scars are pits in the grain surface that resulted from sample preparation for SEM imaging. Scale bar in microns (μm). A: magnetite (Fe_3O_4); B: ulvöspinel [exsolution lamellae] (Fe_2TiO_4); C: apatite ($Ca_5(PO_4)_3(F,Cl,OH)$; D: $anorthite_{50}$ ($(Na,Ca)\ [Al_{(1,2)}Si_{(2,3)}O_8]$)

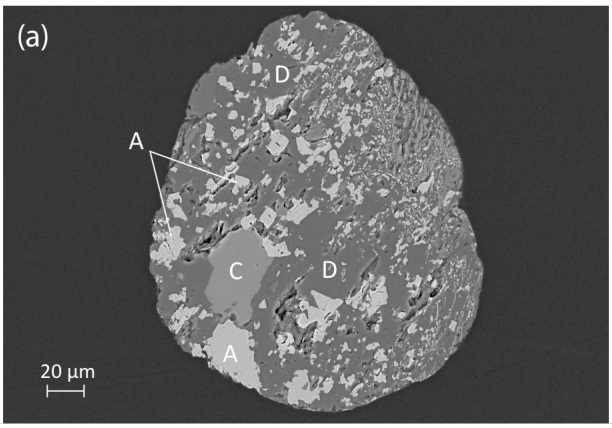
(a)
D
A
C
D
A
20 µm

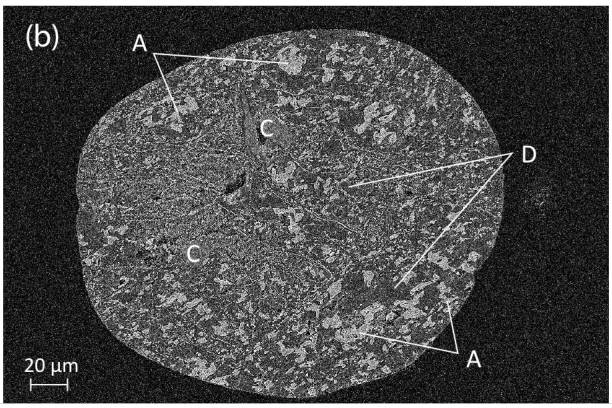
(b)
A
C
D
C
A
20 µm

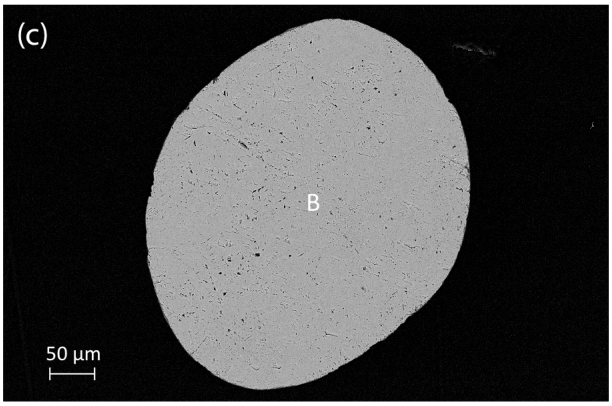
(c)
B
50 µm

Figure 17 - DUR19 SEM images

Backscatter detection (BSD) images of DUR19 magnetite. Scale bar in microns (μm). A: ulvöspinel (Fe_2TiO_4); B: magnetite (Fe_3O_4); C: apatite ($Ca_5(PO_4)_3(F,Cl,OH)$; D: orthoclase ($KAlSi_3O_8$)

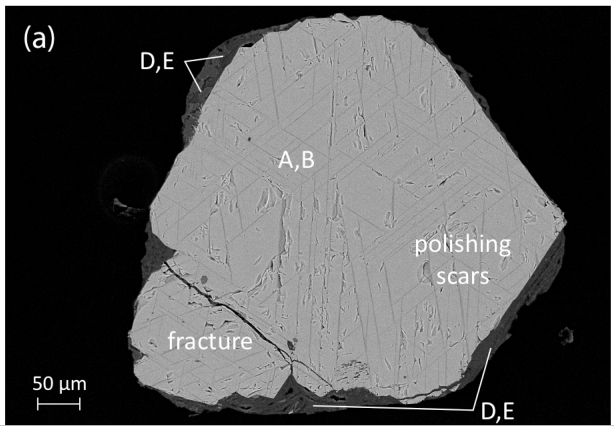
(a)
D,E
A,B
polishing
scars
fracture
50 µm
D,E

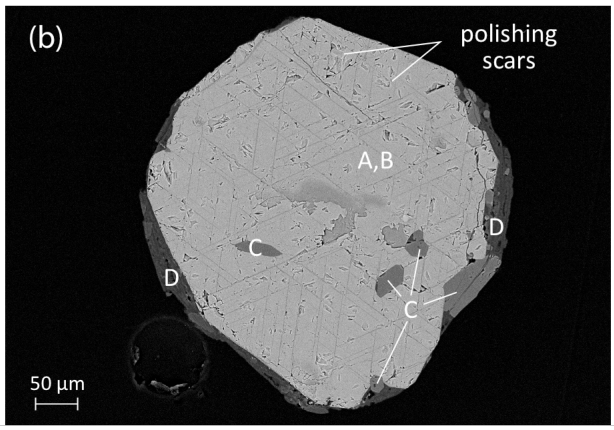
(b)
polishing
scars
A,B
C
D
D
C
50 µm

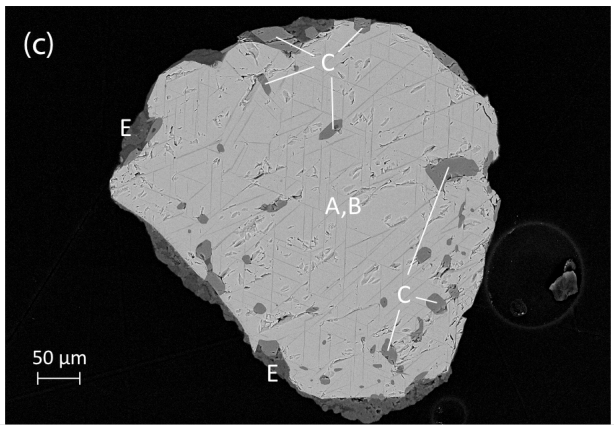
(c)
C
E
A,B
C
50 µm
E

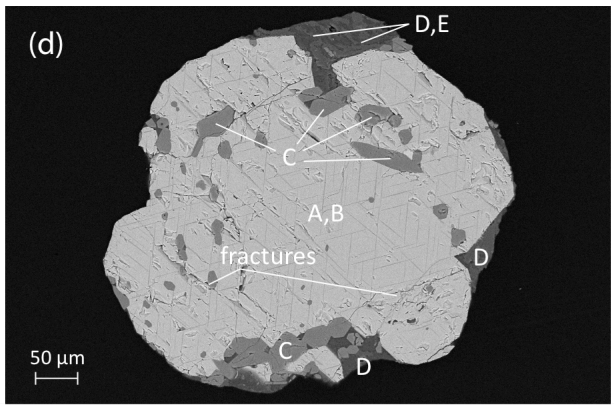
(d)
D,E
C
A,B
fractures
D
C
D
50 µm

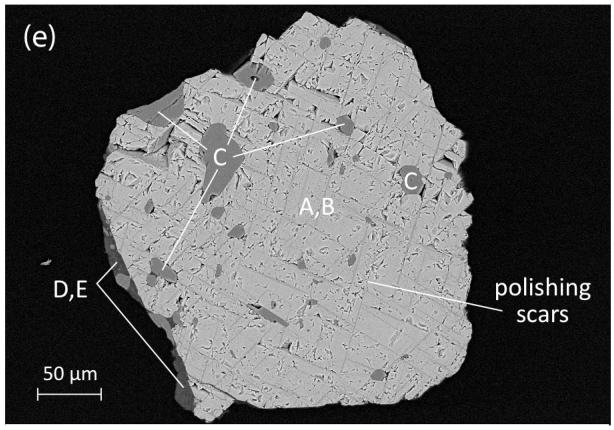
(e)
C
C
A,B
D,E
polishing
scars
50 µm

Figure 18 - Fish Canyon Tuff (FCT) SEM images

Backscatter detection (BSD) images of FCT magnetite. Fractures are post-crystallization grain damage resulting from either natural sample degredation or laboratory sample preparation. Polishing scars are pits in the grain surface that resulted from sample preparation for SEM imaging. Scale bar in microns (μm). A: magnetite (Fe_3O_4); B: ulvöspinel (Fe_2TiO_4); C: apatite ($Ca_5(PO_4)_3(F,Cl,OH)$; D: orthoclase ($KAlSi_3O_8$); E: sanidine ($(K,Na)(Si,Al)_4O_8$)

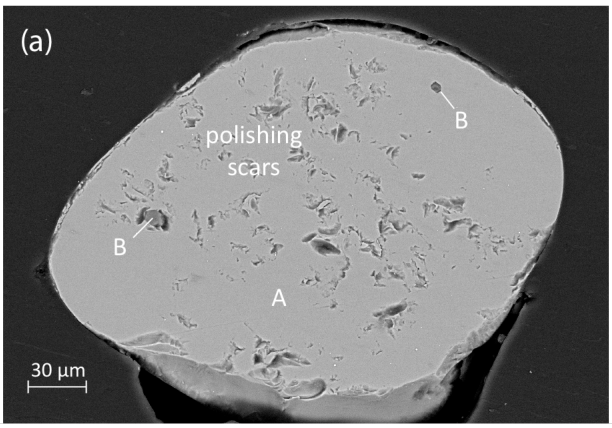
(a)
polishing
scars
B
B
A
30 µm

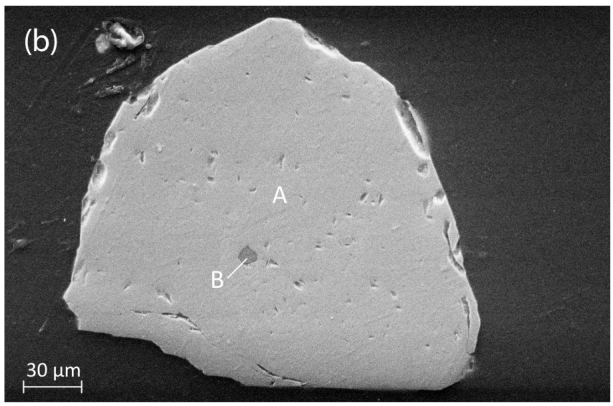
(b)
A
B
30 µm

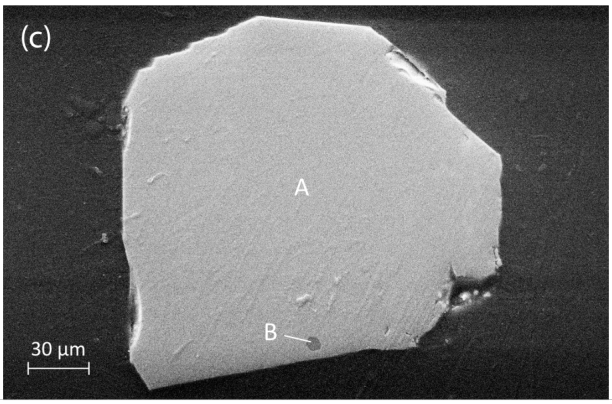
(c)
A
B
30 µm

Figure 19 - Olmsted Point (OLM) SEM images

Backscatter detection (BSD) images of OLM magnetite. Polishing scars are pits in the grain surface that resulted from sample preparation for SEM imaging. Scale bar in microns (μm). A: magnetite (Fe_3O_4); B: apatite ($Ca_5(PO_4)_3(F,Cl,OH)$

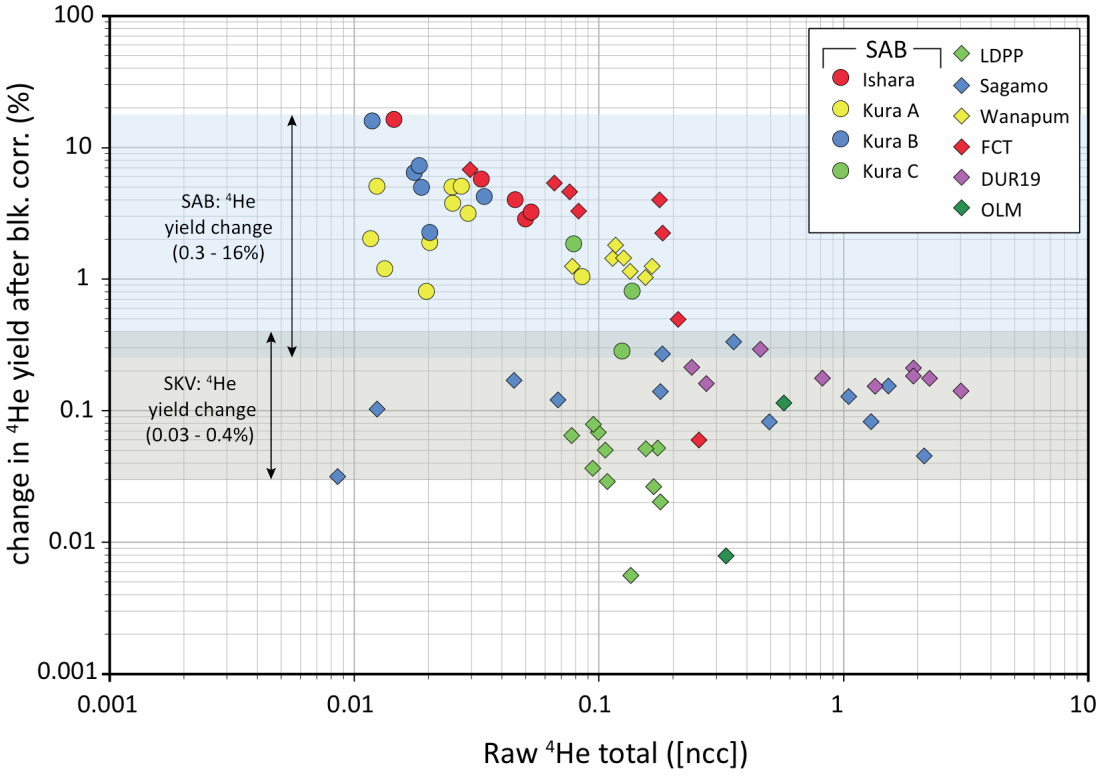
100
10
1
0.1
0.01
0.001
0.001
0.01
0.1
1
10
change in ⁴He yield after blk. corr. (%)
Raw ⁴He total ([ncc])
SAB: ⁴He yield change (0.3 - 16%)
SKV: ⁴He yield change (0.03 - 0.4%)
SAB
Ishara
Kura A
Kura B
Kura C
LDPP
Sagamo
Wanapum
FCT
DUR19
OLM

Figure 20 - Raw vs. Blank-corrected 4He Yield

Difference between raw and blank-corrected total ^{4}He yields from all corrected samples (Table 5) range from fractional (Sagamo; green shading) up to 16% (Ishara basalt; blue shading). Final blank-corrected aliquot MGHe ages undergo a similar percentage change with small raw ^{4}He–yield aliquots subject to the greatest change of their final MGHe age (Fig. 21).

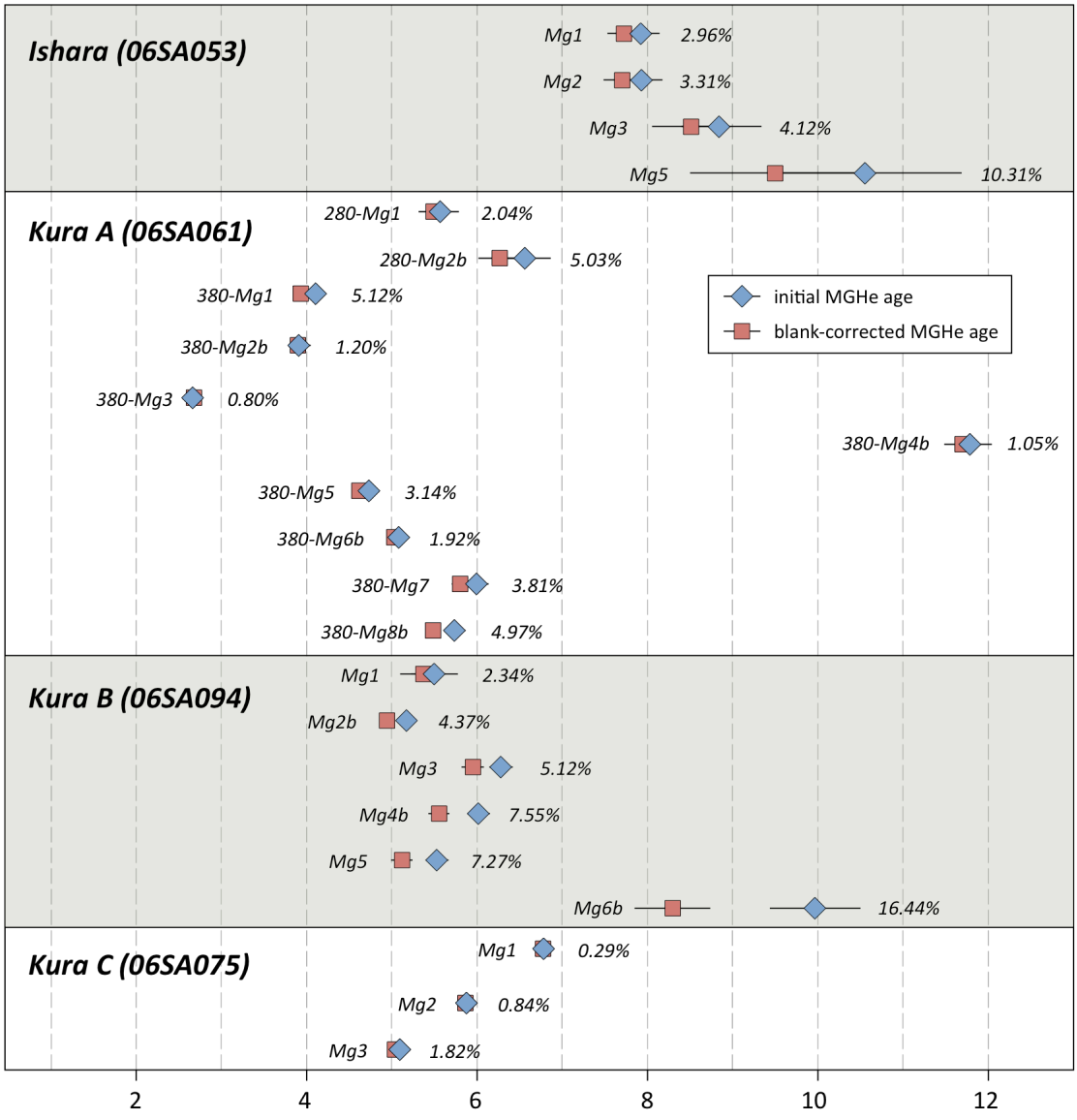
Ishara (06SA053)
Mg1 2.96%
Mg2 3.31%
Mg3 4.12%
Mg5 10.31%
Kura A (06SA061)
280-Mg1 2.04%
280-Mg2b 5.03%
380-Mg1 5.12%
380-Mg2b 1.20%
380-Mg3 0.80%
380-Mg4b 1.05%
380-Mg5 3.14%
380-Mg6b 1.92%
380-Mg7 3.81%
380-Mg8b 4.97%
initial MGHe age
blank-corrected MGHe age
Kura B (06SA094)
Mg1 2.34%
Mg2b 4.37%
Mg3 5.12%
Mg4b 7.55%
Mg5 7.27%
Mg6b 16.44%
Kura C (06SA075)
Mg1 0.29%
Mg2 0.84%
Mg3 1.82%
2
4
6
8
10
12
MGHe age ± 2σ (Ma)

Figure 21 - Blank Correction effect on SAB Suite MGHe Ages

Effect of ^{4}He blank-correction on final SAB Suite MGHe ages. Initial MGHe ages (blue diamond) calculated with raw ^{4}He yield and final MGHe ages (red square) calculated with blank-corrected ^{4}He yield. Aliquot name on left. Percentage change in MGHe age on right. Greatest change observed in aliquots with the greatest difference in raw versus blank-corrected yield (Table 5; 06SA053-Mg5 and 06SA094-Mg6b).

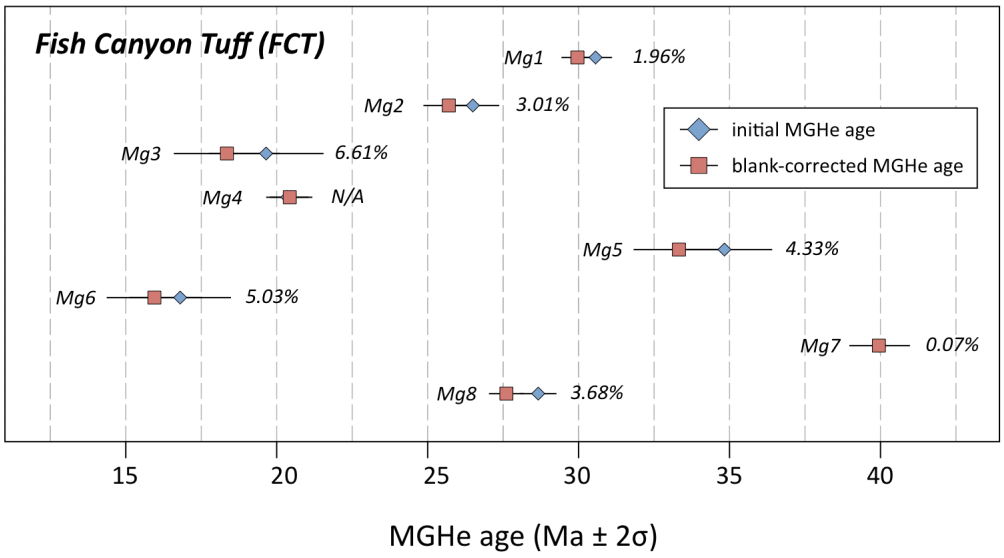
Fish Canyon Tuff (FCT)
Mg1
1.96%
Mg2
3.01%
Mg3
6.61%
Mg4
N/A
Mg5
4.33%
Mg6
5.03%
Mg7
0.07%
Mg8
3.68%
initial MGHe age
blank-corrected MGHe age
15
20
25
30
35
40
MGHe age (Ma ± 2σ)

Figure 22 - Blank Correction Effect on Fish Canyon Tuff MGHe Ages

Effect of ^{4}He blank-correction on final Fish Canyon Tuff (FCT) MGHe ages. Initial MGHe ages (blue diamond) calculated with raw ^{4}He yield and final MGHe ages (red square) calculated with blank-corrected ^{4}He yield. Aliquot name on left. Percentage change in MGHe age on right. Greatest change observed in aliquots with the greatest difference in raw versus blank-corrected yield (Table 5) yet, relative to the SAB Suite, overall smaller effects from blank correction due to higher aliquot [^{4}He] (Figure 8).

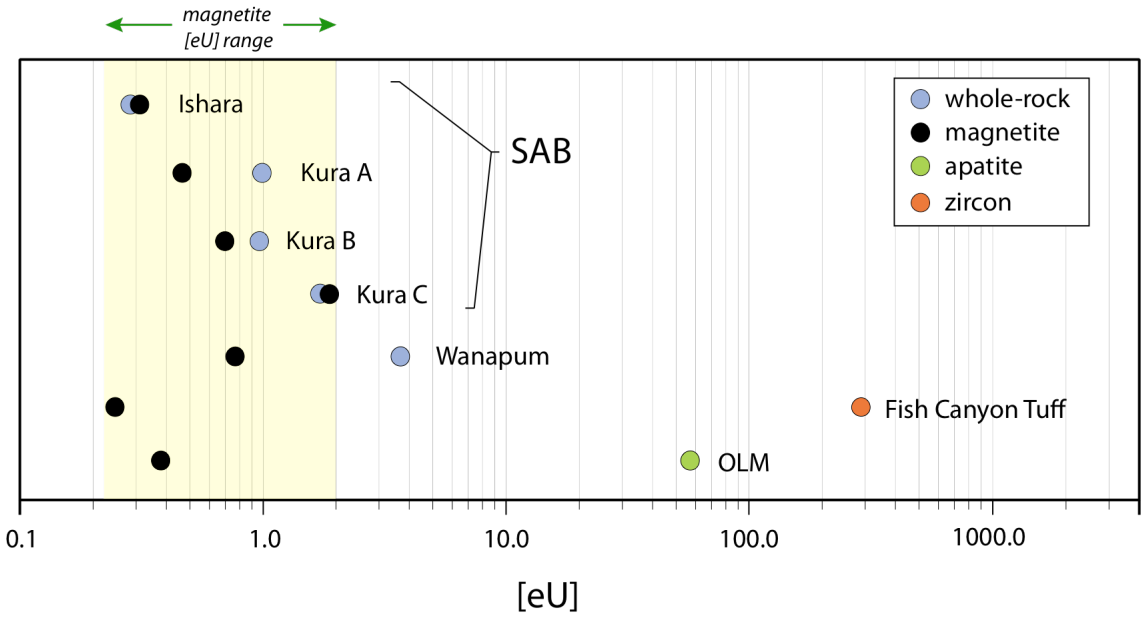
magnetite
[eU] range
Ishara
Kura A
Kura B
Kura C
Wanapum
SAB
OLM
Fish Canyon Tuff
whole-rock
magnetite
apatite
zircon
0.1
1.0
10.0
100.0
1000.0
[eU]

Figure 23 - [eU]: Magnetite vs. Whole-rock and Other Mineral Phases

Comparison of magnetite [eU] and both whole-rock amd other mineral phase [eU] from same sample. Whole-rock and neighboring non-oxide mineral phase [eU] are poor predictors of magnetite [eU] especially in intermediate through felsic rock where magnetite [eU] are 2-3 orders of magnitude lesser than apatite and zircon [eU] within the same sample (Fish Canyon Tuff and OLM). In basaltic rock, whole-rock and magnetite [eU] show no consistency as either one or the other component may be more radiogenic and values sometime overlap (e.g., Ishara basalt, Kura C)

Geographic Location		Sample Name	Formation Age	Coordinates	Elevation (m)	Host Rock Lithology / Sample description
Hamd-Jizl Basin, Saudi Arabia	Harrat Ishara	*Ishara*	*M. Miocene*	25.12°N, 38.86°E	552	olivine transitional basalt
	Harrat Kura	*Kura A*		25.35°N, 38.72°E	459	alkali-olivine basalt
	Harrat Kura	*Kura B*		25.35°N, 38.73°E	402	alkali-olivine basalt
	Harrat Kura	*Kura C*		25.17°N, 38.88°E	1008	alkali-olivine basalt
Javakheti Highland, Republic of Georgia		*Sagamo*	*Pleistocene*	41.33°N, 43.68°E	2076	Mesavera basalt
Frenchman Springs Coulee, Washington, USA		*Wanapum*	*M. Miocene*	47.0°N, 120.0°W	360	tholeiite with porphyritic plagioclase
Yosemite National Park, California, USA		*LDPP*	*L. Miocene*	37.9°N, 119.4°W	2545	trachyandesite
Cerro de Mercado, Chupaderos Caldera complex, Durango, Mexico		*DUR07*	*Oligocene*	24.05°N, 104.68°W	1937	rhyolitic dyke
		DUR19		24.06°N, 104.67°W	2050	strongly fractured rhyodacite
San Juan volcanic field, Forest Road locality, Colorado, USA		*Fish Canyon Tuff*	*Oligocene*	37.61°N, 106.71°W	2550	dacite tuff
Yosemite National Park, California, USA		*OLM*	*L. Cretaceous*	37.81°N, 119.49°W	2574	biotite-hornblende granodiorite with conspicuous titanite, magnetite (Half Dome granodiorite; Huber et al., 1989)

Table 1 - Sample Provenance and Host Rock Lithology

Formation age references listed in Table 3.

Aliquot	Age (Ma)	± analytical error (Ma)	% error	U (ppm)	Th (ppm)	Sm (ppm)	[eU]	Th/U	^{4}He [ncc]	mass (µg)	[4He] (ncc/µg)	# grains	F_T	Dissolution Technique
Saudi Arabia Basalt (SAB) Suite														
Ishara basalt														
06SA053-Mg1	7.7	0.2	2.42	0.2	0.4	0.8	0.3	2.0	0.0490	157	0.0003	7	1.0	Hot Plate
06SA053-Mg2	7.7	0.2	2.74	0.3	0.6	1.3	0.4	2.3	0.0514	127	0.0004	9	"	"
06SA053-Mg3	8.5	0.5	5.30	0.2	0.4	2.2	0.4	1.7	0.0445	118	0.0004	9	"	"
06SA053-Mg5	9.5	1.0	10.44	0.1	0.2	1.7	0.1	2.2	0.0129	73	0.0002	1	"	"
MGHe age$^{\#}$:	**7.81 ± 0.58 [7.5%]**										**0.0003**			
Kura A														
06SA061-280-Mg1	5.5	0.2	3.23	0.2	0.5	0.2	0.4	2.3	0.0115	48	0.0002	9	1.0	Hot Plate
06SA061-280-Mg2b	6.3	0.3	4.02	0.3	0.7	1.2	0.5	2.1	0.0119	31	0.0004	9	"	"
06SA061-380-Mg1	3.9	0.1	1.63	0.4	0.6	0.7	0.5	1.7	0.0262	106	0.0002	4	"	"
06SA061-380-Mg2b	3.9	0.1	2.57	0.2	0.4	0.6	0.3	1.9	0.0132	88	0.0002	4	"	"
06SA061-380-Mg3	2.7	0.0	1.54	0.4	0.9	0.8	0.6	2.5	0.0199	107	0.0002	4	"	"
06SA061-380-Mg4b*	11.7	0.2	1.85	0.4	0.8	1.1	0.6	1.8	0.0849	96	0.0009	4	"	"
06SA061-380-Mg5	4.6	0.1	1.35	0.5	0.6	0.5	0.6	1.4	0.0288	86	0.0003	4	"	"
06SA061-380-Mg6b	5.0	0.1	1.73	0.2	0.6	0.1	0.4	2.5	0.0201	93	0.0002	6	"	"
06SA061-380-Mg7	5.8	0.1	1.72	0.2	0.5	0.2	0.4	2.3	0.0245	95	0.0003	8	"	"
06SA061-380-Mg8b	5.5	0.1	1.58	0.3	0.5	0.1	0.4	1.8	0.0242	88	0.0003	9	"	"
MGHe age$^{\#}$:	**3.97 ± 0.92 [23%]**										**0.0003**			
Kura B														
06SA094-Mg1	5.0	0.2	4.82	0.4	0.3	2.4	0.5	0.9	0.0197	70	0.0003	7	1.0	Hot Plate
06SA094-Mg2b	4.6	0.0	1.05	1.0	0.9	0.0	1.2	0.9	0.0324	47	0.0007	7	"	"
06SA094-Mg3	5.6	0.1	2.14	0.5	0.6	-0.1	0.6	1.2	0.0178	41	0.0004	8	"	"
06SA094-Mg4b	5.1	0.1	2.17	0.5	0.6	0.5	0.7	1.2	0.0169	41	0.0004	8	"	"
06SA094-Mg5	4.7	0.1	2.40	0.5	0.8	1.2	0.7	1.4	0.0166	40	0.0004	9	"	"
06SA094-Mg6b*	7.7	0.4	5.23	0.3	0.5	-0.3	0.4	1.4	0.0099	25	0.0004	9	"	"
MGHe age$^{\#}$:	**4.82 ± 0.42 [8.7%]**										**0.0004**			

Aliquot	Age (Ma)	± analytical error (Ma)	% error	U (ppm)	Th (ppm)	Sm (ppm)	[eU]	Th/U	^{4}He [ncc]	mass (µg)	[4He] (ncc/µg)	# grains	F_T	Dissolution Technique
***Saudi Arabia Basalt (SAB) Suite* - continued**														
Kura C														
06SA075-Mg1	6.8	0.0	0.65	1.0	3.6	0.9	1.9	3.5	0.1221	78	0.0016	9	1.0	Hot Plate
06SA075-Mg2	5.9	0.0	0.74	1.2	4.1	1.5	2.2	3.3	0.1341	85	0.0016	11	"	"
06SA075-Mg3	5.0	0.0	0.72	0.8	2.7	0.8	1.4	3.4	0.0784	90	0.0009	8	"	"
MGHe age$^{\#}$:	**5.8 ± 2.2 [38%]**										**0.0013**			
Segamo basalt (Republic of Georgia)														
mg09SKV01-1	2.0	0.0	0.45	1.6	43.5	1.3	11.6	27.1	1.2947	452	0.0029	1	1.0	PDV
mg09SKV01-2	1.7	0.0	0.88	2.5	5.7	3.7	3.8	2.3	0.1777	227	0.0008	1	"	"
mg09SKV01-3	2.1	0.0	0.46	0.9	18.5	1.1	5.2	20.9	0.3516	267	0.0013	1	"	"
mg09SKV01-4	1.5	0.0	0.40	6.0	70.7	2.0	22.3	11.7	1.0413	254	0.0041	1	"	"
mg09SKV01-5	1.8	0.0	0.39	2.9	14.6	1.2	6.3	5.0	0.4995	368	0.0014	1	"	"
mg09SKV01-6	1.7	0.0	0.83	8.3	95.1	4.0	30.2	11.4	1.5329	244	0.0063	1	"	"
mg09SKV01-7	1.3	0.0	1.26	0.2	0.6	0.4	0.3	3.5	0.0114	281	0.0000	1	"	"
mg09SKV01-8	2.3	0.0	1.17	1.8	82.6	5.7	20.9	45.0	2.1349	357	0.0060	1	"	"
mg09SKV01-9	1.6	0.0	0.69	4.5	6.1	4.0	5.9	1.4	0.1756	155	0.0011	1	"	"
mg09SKV01-10	1.8	0.0	0.87	1.9	2.6	2.3	2.6	1.3	0.0670	119	0.0006	1	"	"
mg09SKV01-11*	0.7	0.0	1.58	0.5	1.9	1.7	0.9	4.0	0.0082	109	0.0001	1	"	"
mg09SKV01-12	2.1	0.0	0.62	1.5	1.7	0.9	1.9	1.1	0.0434	95	0.0005	1	"	"
MGHe age$^{\#}$:	**1.74 ± 0.17 [9.6%]**										**0.0021**			

Aliquot	Age (Ma)	± analytical error (Ma)	% error	U (ppm)	Th (ppm)	Sm (ppm)	[eU]	Th/U	^{4}He [ncc]	mass (µg)	[4He] (ncc/µg)	# grains	F_T	Dissolution Technique
Wanapum basalt (CRBG)														
WR-1-Mg2	11.2	0.6	5.03	0.5	1.4	4.8	0.8	3.0	0.1253	113	0.0011	7	1.0	Hot Plate
WR-1-Mg3	12.2	0.1	1.10	0.5	1.6	0.9	0.9	3.2	0.1546	120	0.0013	8	"	"
WR-1-Mg4	13.5	0.3	2.10	0.4	1.2	1.5	0.7	3.2	0.1142	105	0.0011	8	"	"
WR-1-Mg5	13.3	0.3	2.43	0.5	1.5	2.4	0.8	3.0	0.1345	97	0.0014	9	"	"
WR-1-Mg6	10.6	0.1	1.18	0.5	1.6	1.2	0.9	3.1	0.1651	138	0.0012	1	"	"
WR-1-Mg7	13.1	0.7	5.15	0.3	1.0	3.4	0.5	3.1	0.0779	87	0.0009	9	"	"
MGHe age#:	**11.7 ± 1.2 [10%]**										**0.0012**			
LDPP (Little Devils Postpile, Yosemite Nat'l Park)														
mgLDPP-1	2.6	0.0	0.61	3.0	9.4	3.0	5.2	3.1	0.1784	107	0.0017	4	1.0	PDV
mgLDPP-2	2.2	0.0	0.95	3.3	10.1	5.9	5.6	3.1	0.1342	88	0.0015	4	"	"
mgLDPP-3	2.7	0.0	0.59	2.6	8.4	2.6	4.6	3.2	0.1681	110	0.0015	4	"	"
mgLDPP-4	2.8	0.0	1.19	3.2	10.1	7.6	5.6	3.1	0.1722	91	0.0019	4	"	"
mgLDPP-8	3.0	0.0	0.75	3.1	10.0	4.2	5.4	3.2	0.0945	48	0.0020	1	"	"
mgLDPP-9	2.1	0.0	0.71	3.2	10.1	4.0	5.5	3.1	0.0991	70	0.0014	1	"	"
mgLDPP-10	2.9	0.0	0.90	3.1	10.4	5.4	5.6	3.3	0.0933	48	0.0019	1	"	"
mgLDPP-11	2.9	0.0	0.76	3.4	10.9	4.7	5.9	3.2	0.1071	51	0.0021	1	"	"
mgLDPP-12	2.7	0.0	0.82	3.3	10.8	5.2	5.9	3.2	0.1061	55	0.0019	1	"	"
MGHe age#:	**2.58 ± 0.25 [9.7%]**										**0.0018**			

Aliquot	Age (Ma)	± analytical error (Ma)	% error	U (ppm)	Th (ppm)	Sm (ppm)	[eU]	Th/U	^{4}He [ncc]	mass (µg)	[4He] (ncc/µg)	# grains	F_T	Dissolution Technique
Mercado Iron Member, Cerro de Mercado (Durango, Mexico)														
DUR07														
DUR07-Mg1	35.1	0.3	0.72	1.2	3.0	0.6	1.9	2.5	0.5401	66	0.0082	10	1.0	Hot Plate
DUR07-Mg2	40.1	0.8	1.99	1.5	3.9	5.7	2.5	2.6	0.8752	72	0.0122	8	"	"
DUR07-Mg3	31.5	0.3	0.86	1.7	2.4	1.3	2.2	1.5	0.4744	55	0.0086	10	"	"
DUR07-Mg4	29.4	0.3	1.00	2.9	6.5	4.7	4.4	2.2	1.0539	66	0.0160	8	"	"
DUR07-Mg5	27.3	0.3	0.99	1.9	2.5	2.3	2.4	1.3	0.5282	65	0.0081	10	"	"
DUR07-Mg6	24.3	0.2	0.92	1.4	2.5	1.1	2.0	1.8	0.3001	51	0.0059	7	"	"
DUR07-Mg7	32.0	0.3	1.08	1.8	2.9	2.6	2.5	1.6	0.5406	55	0.0098	15	"	"
MGHe age$^{\#}$:	**29.7 ± 4.0 [14%]**										**0.0098**			
DUR19														
mgDUR19-9	10.7	0.1	0.49	5.1	5.1	1.9	6.3	1.0	0.8116	99	0.0082	4	1.0	PDV
mgDUR19-10	10.7	0.1	0.49	5.8	6.3	2.3	7.2	1.1	1.3341	142	0.0094	4	"	"
mgDUR19-11	18.2	0.1	0.47	4.8	4.6	1.4	5.9	1.0	1.9303	148	0.0130	4	"	"
mgDUR19-12	13.2	0.1	0.47	8.9	6.5	2.2	10.4	0.7	1.9150	115	0.0167	6	"	"
mgDUR19-13	26.8	0.2	0.57	7.0	4.7	3.5	8.1	0.7	2.9870	113	0.0264	6	"	"
mgDUR19-14	27.5	0.2	0.80	5.0	4.0	4.7	5.9	0.8	2.2120	111	0.0199	7	"	"
mgDUR19-17	7.9	0.0	0.54	6.3	6.8	3.2	7.9	1.1	0.4586	60	0.0076	1	"	"
mgDUR19-18	9.6	0.1	0.69	11.8	7.7	8.7	13.6	0.7	1.9187	121	0.0159	1	"	"
mgDUR19-19	10.4	0.1	1.01	2.7	3.2	3.7	3.4	1.2	0.2711	62	0.0044	1	"	"
mgDUR19-20	7.4	0.1	0.98	3.6	5.3	5.1	4.8	1.5	0.2339	54	0.0043	1	"	"
MGHe age$^{\#}$:		**----**									**0.0126**			

Aliquot	Age (Ma)	± analytical error (Ma)	% error	U (ppm)	Th (ppm)	Sm (ppm)	[eU]	Th/U	^{4}He [ncc]	mass (µg)	[4He] (ncc/µg)	# grains	F_T	Dissolution Technique
FCT (Fish Canyon Tuff, SW Colorado)														
FCT-Mg1	30.0	0.5	1.77	0.2	0.4	0.5	0.3	1.8	0.1819	167	0.0011	5	1.0	PDV
FCT-Mg2	25.7	0.8	3.27	0.1	0.2	0.4	0.1	2.3	0.0833	190	0.0004	5	"	"
FCT-Mg3	18.4	1.8	9.60	0.0	0.1	0.7	0.1	2.4	0.0294	169	0.0002	4	"	"
FCT-Mg4	20.4	0.7	3.43	0.2	0.5	1.5	0.4	2.3	0.2559	275	0.0009	3	"	"
FCT-Mg5	33.3	1.5	4.51	0.1	0.2	0.4	0.1	2.8	0.0758	176	0.0004	2	"	"
FCT-Mg6	16.1	1.6	9.82	0.1	0.3	2.7	0.2	2.5	0.0657	134	0.0005	7	"	"
FCT-Mg7	39.9	1.0	2.49	0.2	0.4	0.7	0.3	2.6	0.2105	155	0.0014	9	"	"
FCT-Mg8	27.6	0.6	2.09	0.3	0.6	1.0	0.5	1.9	0.1769	107	0.0017	7	"	"
MGHe age[#]:	**27.5 ± 5.0 [18%]**										**0.0008**			
Halfdome Granodiorite (Olmsted Point, Yosemite Nat'l Park)														
OLM - ***EXP2***														
OLM-Mg1	465.4	28.0	6.01	0.1	0.0	0.1	0.1	0.2	0.7046	204	0.0035	8	1.0	Hot Plate
OLM-Mg2	141.4	3.3	2.36	0.2	0.2	0.5	0.2	1.2	0.9568	235	0.0041	9	"	"
OLM-Mg3	441.4	34.7	7.86	0.0	0.0	0.3	0.0	0.6	0.6094	216	0.0028	8	"	"
OLM-Mg4	133.8	3.3	2.45	0.1	0.1	0.1	0.1	1.1	0.4719	246	0.0019	8	"	"
OLM-Mg5	1221.7	113.7	9.31	0.0	0.0	0.5	0.1	0.5	2.2786	240	0.0095	6	"	"
OLM-Mg6	451.9	16.0	3.54	0.1	0.1	0.1	0.1	0.9	1.1747	241	0.0049	6	"	"
OLM-Mg7	284.8	12.9	4.52	0.1	0.1	0.1	0.1	1.5	0.5423	212	0.0026	6	"	"
OLM-Mg8	331.4	15.1	4.57	0.1	0.1	0.1	0.1	1.3	0.6337	195	0.0032	6	"	"
OLM-Mg9	163.0	6.8	4.19	0.1	0.1	0.1	0.1	1.2	0.3433	231	0.0015	4	"	"
OLM-Mg10	120.8	4.0	3.28	0.1	0.1	0.1	0.1	2.3	0.3245	240	0.0014	5	"	"
OLM-Mg11	142.4	10.2	7.17	0.1	0.1	0.2	0.1	1.7	0.1710	116	0.0015	1	"	"
OLM-Mg12	221.5	38.5	17.38	0.0	0.0	0.2	0.0	0.6	0.1153	129	0.0009	1	"	"
MGHe age[#]:	**148 ± 39 [26%]**													

Aliquot	Age (Ma)	± analytical error (Ma)	% error	U (ppm)	Th (ppm)	Sm (ppm)	[eU]	Th/U	^{4}He [ncc]	mass (µg)	[4He] (ncc/µg)	# grains	F_T	Dissolution Technique
Halfdome Granodiorite (Olmsted Point, Yosemite Nat'l Park) **- continued**														
OLM - ***EXP3***														
OLM290-Mg1	148.3	5.1	3.45	0.1	0.1	0.3	0.1	1.3	0.3237	140	0.0023	5	1.0	PDV
OLM290-Mg2b	168.2	16.5	9.82	0.1	0.1	0.6	0.1	1.3	0.1587	103	0.0015	5	"	"
OLM290-Mg3	168.8	9.0	5.36	0.1	0.1	0.6	0.1	1.6	0.3131	130	0.0024	5	"	"
OLM290-Mg4b*	540.0	61.5	11.38	0.0	0.1	0.7	0.1	1.5	0.5098	115	0.0044	5	"	"
OLM290-Mg5	226.3	3.4	1.50	0.0	2.5	1.0	0.6	51.0	2.5111	138	0.0182	6	"	"
OLM290-Mg6b	228.9	7.6	3.32	0.1	0.2	0.5	0.2	2.0	0.6682	144	0.0046	7	"	"
OLM290-Mg8	113.5	6.9	6.07	0.1	0.4	1.2	0.2	4.9	0.3044	118	0.0026	7	"	"
OLM290-Mg9	95.3	2.8	2.95	0.1	0.5	0.5	0.2	4.8	0.2671	101	0.0026	7	"	"
OLM360-Mg1	125.0	3.6	2.88	0.1	0.1	0.2	0.1	1.5	0.3368	160	0.0021	3	"	"
OLM360-Mg2b	101.4	2.0	1.98	0.1	0.2	0.3	0.2	1.5	0.4581	209	0.0022	2	"	"
OLM360-Mg3	245.2	3.3	1.34	0.3	0.3	0.4	0.3	1.1	1.8954	189	0.0100	4	"	"
OLM360-Mg4b*	401.0	17.5	4.37	0.1	0.1	0.4	0.1	1.4	1.0332	202	0.0051	4	"	"
OLM360-Mg7*	518.2	27.3	5.27	0.1	0.1	0.7	0.1	1.0	1.6345	196	0.0083	5	"	"
OLM360-Mg8	102.6	6.3	6.18	0.1	0.1	1.2	0.2	1.0	0.3440	167	0.0021	4	"	"
OLM360-Mg9	137.8	4.7	3.44	0.2	0.5	1.2	0.3	2.6	0.6274	118	0.0053	4	"	"
MGHe age$^{\#}$:	**142 ± 37 [26%]**													

Aliquot	Age (Ma)	± analytical error (Ma)	% error	U (ppm)	Th (ppm)	Sm (ppm)	[eU]	Th/U	^{4}He [ncc]	mass (µg)	[4He] (ncc/µg)	# grains	F_T	Dissolution Technique
Halfdome Granodiorite (Olmsted Point, Yosemite Nat'l Park) **- continued**														
OLM - ***EXP4***														
mgOLM-1	97.8	2.0	2.03	0.1	0.3	0.3	0.2	2.8	0.5662	291	0.0019	1	1.0	PDV
mgOLM-2	85.9	0.7	0.82	0.2	0.3	0.2	0.3	1.3	1.3259	420	0.0032	1	"	"
mgOLM-3	24.1	4.4	18.14	0.0	0.0	0.3	0.0	2.5	0.0110	162	0.0001	1	"	"
mgOLM-4	81.8	2.2	2.67	0.4	0.5	1.3	0.5	1.4	0.3323	67	0.0050	1	"	"
mgOLM-5	135.0	12.0	8.93	0.1	0.2	1.5	0.2	1.7	0.1465	50	0.0029	1	"	"
mgOLM-6	224.0	5.2	2.34	0.2	0.3	0.7	0.3	1.1	0.9890	113	0.0088	1	"	"
mgOLM-7	125.1	2.6	2.10	0.8	1.1	2.5	1.1	1.3	0.7581	44	0.0172	1	"	"
mgOLM-8	142.4	5.5	3.90	0.3	0.3	1.5	0.4	1.0	0.3260	43	0.0076	1	"	"
mgOLM-9	77.2	1.4	1.81	0.6	0.7	1.2	0.7	1.3	0.3666	52	0.0071	1	"	"
mgOLM-10	110.7	6.0	5.43	0.1	0.2	0.5	0.2	1.5	0.1220	44	0.0028	1	"	"
mgOLM-11	220.3	13.1	5.94	0.1	0.2	0.5	0.2	1.6	0.2364	56	0.0042	1	"	"
MGHe age$^{\#}$:	**89 ± 15 [17%]**										**0.0055**			

Table 2 - Magnetite (U-Th)/He Age Data, Isotope Concentration, and Aliquot Metrics

Asterisk (*) denotes a rejected aliquot MGHe age. Octothorpe (#) denotes the final MGHe age reported as error-weighted average with 95% confidence and error percentage relative to MGHe age (Isoplot; Ludwig, 2004). Bold [^{4}He] values indicate sample average from analyzed aliquots.

Sample	MGHe Age +/- 2σ [Ma]	Reference Age	Reference Age Source
Basaltic Magnetite			
Ishara	7.81 ± 0.58 Ma	13.6 ± 1.1 Ma	zircon (U-Th)/He cooling age (Szymanski, *PhD thesis*) from underlying, reworked tuff
		~12.7 - 14.9 Ma	Upper Ishara basalt age range, Harrat Ishara (Szymanski, *PhD thesis*)
			- no direct age data available for this sample
Kura A	3.97 ± 0.92 Ma	~5.5 - 11.5 Ma	Kura basalt age range; K-Ar data from Camp et al. (1991)
		10.6 ± 0.4 Ma	whole-rock $^{40}Ar/^{39}Ar$ date (Szymanski, *PhD thesis*)
Kura B	4.82 ± 0.42 Ma	~5.5 - 11.5 Ma	Kura basalt age range; K-Ar data from Camp et al. (1991)
			- no direct age data available for this sample
Kura C	5.8 ± 2.2 Ma	~5.5 - 11.5 Ma	Kura basalt age range; K-Ar data from Camp et al. (1991)
		9.34 ± 0.18 Ma	whole-rock $^{40}Ar/^{39}Ar$ plateau age (Szymanski, *PhD thesis*)
Segamo	1.74 ± 0.17 Ma	1.8 ± 0.1 Ma	K/Ar age; Majsuradze (1996)
		2.0 ± 0.1 Ma	$^{40}Ar/^{39}Ar$ isochron age; Schmincke and van den Bogaard (1995)
Wanapum	11.7 ± 1.2 Ma	13 Ma	Huntzinger Basalt; Asotin Mbr.; Saddle Mtns. Basalt (Tolan et al., 1989)
		14.5 Ma	K/Ar age from Watkins and Baksi (1974) that includes Roza Member
		~12.5 - 16.3 Ma	K/Ar age for Roza Member from Wes Myers (Steve Reidel *pers. comm.*)
		14.70 ± 0.21 Ma & 15.12 ± 0.38 Ma	$^{40}Ar/^{39}Ar$ age for the underlying Sand Hollow Basalt, Frenchman Springs Mbr. from Barry et al. (2010 *and references therein*)
LDPP	2.58 ± 0.25 Ma	7.9 ± 0.6 Ma	zircon (U-Th)/He cooling age of host rock xenolith in LDPP from Stockli (*pers. comm.*)
			*note: fission-track age of 9 Ma cited by Huber et al. (1989) but source yet unidentified

Sample	MGHe Age +/- 2σ [Ma]	Reference Age	Reference Age Source
Rhyolitic / Rhyodacitic Magnetite			
DUR07	29.7 ± 4.0 Ma	30.5 ± 2.6 Ma	apatite (U-Th)/He age
		30.8 ± 0.9 Ma	zircon (U-Th)/He age; STDEV of AVG
		32.3 ± 5.6 Ma	AFT; 1σ error
		31.7 ± 2.2 Ma	ZFT; 1σ error
		30.4 ± 1.1 Ma	zircon U/Pb age
			- each age cited above from Wipf et al. (2010 *and references therein*)
DUR19	*n/a*	31.7 ± 3.6 Ma	zircon (U-Th)/He age; STDEV of AVG
		30.8 ± 5.8 Ma	AFT; 1σ error
		31.7 ± 2.8 Ma	ZFT; 1σ error
		32.2 ± 0.6 Ma	zircon U/Pb age
			- each age cited above from Wipf et al. (2010 *and references therein*)
FCT	27.5 ± 5.0 Ma	28.03 ± 0.35 Ma	zircon (U-Th)/He age; 2σ error; University of Kansas IGL
		28.201 ± 0.045 Ma	Kuiper et al. (2008)
Granodioritc Magnetite			
OLM	89 ± 15 Ma	92.8 ± 0.1 Ma to 88.8 ± 0.8 Ma	U-Pb age of Half Dome granodiorite (Coleman et al., 2004)
		79.0 ± 6.3 Ma	zircon (U-Th)/He age of Cathedral Peak granodiorite (Stockli, *pers. comm.*)

Table 3 - Comparative Age Results: MGHe vs. Other Radiometric Age Data

Sample	Category	Type	Assigned Error Source(s) - *if failed*
Sagamo	*I*	basaltic	----
Wanapum	*I*	basaltic	----
DUR07	*I*	rhyolitic	----
FCT	*I*	dacitic	----
OLM	*I*	granodioritic	----
LDPP	*II*	basaltic	complex mineralogy (very poor true magnetite content)
Ishara	*II*	basaltic	complex mineralogy (non-radiogenic silicate mineral inclusions)
Kura A	*II*	basaltic	complex mineralogy (non-radiogenic silicate mineral inclusions)
Kura B	*II*	basaltic	complex mineralogy (non-radiogenic silicate mineral inclusions)
Kura C	*II*	basaltic	pervasive magnetite crystal skeletonization
DUR19	*III*	rhyodacitic	complex mineralogy (radiogenic mineral phase inclusions)

Table 4 - MGHe Age Result Quality

MGHe age results fall into three major categories in terms of analytical success: Category I are those with reproducible MGHe results that agree with published data and/or local geologic age trends and no published age data exist to dispute our result; Category II are those with reproducible MGHe results that disagree with published age data and/or local geologic age trends; and Category III are those with poorly reproducible MGHe results that may agree with other published age data and/or local geologic age trends (Table 3).

Sample / Aliquot	^{4}He yield (total [ncc])			^{4}He concentration ([ncc]/µg)		
	RAW	CORRECTED	Δ (%)	mass (µg)	RAW	CORRECTED
Ishara						
06SA053-Mg1	0.0505	0.0490	*2.958*	157	0.0003	0.0003
06SA053-Mg2	0.0532	0.0514	*3.316*	127	0.0004	0.0004
06SA053-Mg3	0.0464	0.0445	*4.120*	118	0.0004	0.0004
06SA053-Mg4	0.0337	0.0318	*5.640*	130	0.0003	0.0002
06SA053-Mg5	0.0144	0.0129	*16.034*	73	0.0002	0.0002
AVG.	**0.0396**	**0.0379**		**121**	**0.0003**	**0.0003**
Kura A						
06SA061-280-Mg1	0.0118	0.0115	*2.045*	48	0.0002	0.0002
06SA061-280-Mg2b	0.0126	0.0119	*5.034*	31	0.0004	0.0004
06SA061-380-Mg1	0.0276	0.0262	*5.119*	106	0.0003	0.0002
06SA061-380-Mg2b	0.0134	0.0132	*1.203*	88	0.0002	0.0002
06SA061-380-Mg3	0.0200	0.0199	*0.803*	107	0.0002	0.0002
06SA061-380-Mg4b	0.0858	0.0849	*1.050*	96	0.0009	0.0009
06SA061-380-Mg5	0.0297	0.0288	*3.139*	86	0.0003	0.0003
06SA061-380-Mg6b	0.0205	0.0201	*1.918*	93	0.0002	0.0002
06SA061-380-Mg7	0.0254	0.0245	*3.807*	95	0.0003	0.0003
06SA061-380-Mg8b	0.0255	0.0242	*4.973*	88	0.0003	0.0003
AVG.	**0.0272**	**0.0265**		**84**	**0.0003**	**0.0003**
Kura B						
06SA094-Mg1	0.0202	0.0197	*2.343*	70	0.0003	0.0003
06SA094-Mg2b	0.0339	0.0324	*4.369*	47	0.0007	0.0007
06SA094-Mg3	0.0188	0.0178	*5.119*	41	0.0005	0.0004
06SA094-Mg4b	0.0183	0.0169	*7.556*	41	0.0004	0.0004
06SA094-Mg5	0.0179	0.0166	*7.273*	40	0.0004	0.0004
06SA094-Mg6b	0.0119	0.0099	*16.447*	25	0.0005	0.0004
AVG.	**0.0202**	**0.0189**		**44**	**0.0005**	**0.0004**
Kura C						
06SA075-Mg1	0.1225	0.1221	*0.287*	78	0.0016	0.0016
06SA075-Mg2	0.1352	0.1341	*0.843*	85	0.0016	0.0016
06SA075-Mg3	0.0798	0.0784	*1.819*	90	0.0009	0.0009
AVG.	**0.1125**	**0.1115**		**84**	**0.0013**	**0.0013**

Sample / Aliquot	^{4}He yield (total [ncc])				^{4}He concentration ([ncc]/ug)	
	RAW	CORRECTED	Δ (%)	mass (µg)	RAW	CORRECTED
Segamo						
mg09SKV01-1	1.2955	1.2947	*0.085*	452	0.0029	0.0029
mg09SKV01-2	0.1805	0.1777	*0.278*	227	0.0008	0.0008
mg09SKV01-3	0.3550	0.3516	*0.344*	267	0.0013	0.0013
mg09SKV01-4	1.0426	1.0413	*0.132*	254	0.0041	0.0041
mg09SKV01-5	0.5003	0.4995	*0.085*	368	0.0014	0.0014
mg09SKV01-6	1.5345	1.5329	*0.159*	244	0.0063	0.0063
mg09SKV01-7	0.0124	0.0114	*0.106*	281	0.0000	0.0000
mg09SKV01-8	2.1344	2.1349	*0.047*	357	0.0060	0.0060
mg09SKV01-9	0.1770	0.1756	*0.144*	155	0.0011	0.0011
mg09SKV01-10	0.0683	0.0670	*0.124*	119	0.0006	0.0006
mg09SKV01-11	0.0085	0.0082	*0.033*	109	0.0001	0.0001
mg09SKV01-12	0.0452	0.0434	*0.175*	95	0.0005	0.0005
AVG.	**0.6129**	**0.6115**		**244**	**0.0021**	**0.0021**
LDPP						
mgLDPP-1	0.1782	0.1784	*0.021*	107	0.0017	0.0017
mgLDPP-2	0.1343	0.1342	*0.006*	88	0.0015	0.0015
mgLDPP-3	0.1683	0.1681	*0.027*	110	0.0015	0.0015
mgLDPP-4	0.1727	0.1722	*0.054*	91	0.0019	0.0019
mgLDPP-5	0.1564	0.1558	*0.053*	81	0.0019	0.0019
mgLDPP-6	0.0778	0.0771	*0.067*	68	0.0011	0.0011
mgLDPP-8	0.0953	0.0945	*0.081*	48	0.0020	0.0020
mgLDPP-9	0.0998	0.0991	*0.070*	70	0.0014	0.0014
mgLDPP-10	0.0937	0.0933	*0.038*	48	0.0020	0.0019
mgLDPP-11	0.1074	0.1071	*0.030*	51	0.0021	0.0021
mgLDPP-12	0.1066	0.1061	*0.052*	55	0.0019	0.0019
AVG.	**0.1264**	**0.1260**		**74**	**0.0017**	**0.0017**
DUR07						
DUR07-Mg1	0.5403	----	----	66	0.0082	----
DUR07-Mg2	0.8753	----	----	72	0.0122	----
DUR07-Mg3	0.4751	----	----	55	0.0086	----
DUR07-Mg4	1.0563	----	----	66	0.0160	----
DUR07-Mg5	0.5299	----	----	65	0.0082	----
DUR07-Mg6	0.3019	----	----	51	0.0059	----
DUR07-Mg7	0.5406	----	----	55	0.0098	----
AVG.	**0.6170**			**61**	**0.0098**	

Sample / Aliquot	^{4}He yield (total [ncc])				^{4}He concentration ([ncc]/µg)	
	RAW	CORRECTED	Δ (%)	mass (µg)	RAW	CORRECTED
DUR19						
mgDUR19-9	0.8133	0.8116	*0.174*	99	0.0082	0.0082
mgDUR19-10	1.3356	1.3341	*0.151*	142	0.0094	0.0094
mgDUR19-11	1.9321	1.9303	*0.179*	148	0.0131	0.0130
mgDUR19-12	1.9172	1.9150	*0.216*	115	0.0167	0.0167
mgDUR19-13	2.9884	2.9870	*0.138*	113	0.0264	0.0264
mgDUR19-14	2.2138	2.2120	*0.179*	111	0.0199	0.0199
mgDUR19-17	0.4616	0.4586	*0.297*	60	0.0077	0.0076
mgDUR19-18	1.9205	1.9187	*0.179*	121	0.0159	0.0159
mgDUR19-19	0.2727	0.2711	*0.166*	62	0.0044	0.0044
mgDUR19-20	0.2360	0.2339	*0.212*	54	0.0044	0.0043
AVG.	**1.4091**	**1.4072**		**103**	**0.0126**	**0.0126**
FCT						
FCT-Mg1	0.1819	0.1777	*2.331*	167	0.0011	0.0011
FCT-Mg2	0.0833	0.0805	*3.421*	190	0.0004	0.0004
FCT-Mg3	0.0294	0.0273	*7.082*	169	0.0002	0.0002
FCT-Mg4	0.2559	0.2557	*0.061*	275	0.0009	0.0009
FCT-Mg5	0.0758	0.0721	*4.788*	176	0.0004	0.0004
FCT-Mg6	0.0657	0.0620	*5.528*	134	0.0005	0.0005
FCT-Mg7	0.2105	0.2094	*0.509*	155	0.0014	0.0014
FCT-Mg8	0.1769	0.1697	*4.063*	107	0.0017	0.0016
AVG	**0.1349**	**0.1318**		**172**	**0.0008**	**0.0008**
OLM (EXP4)						
mgOLM-1	0.5674	0.5662	*0.113*	291	0.0019	0.0019
mgOLM-2	1.3259	----	----	420	0.0032	----
mgOLM-3	0.0110	----	----	162	0.0001	----
mgOLM-4	0.3323	----	----	67	0.0050	----
mgOLM-5	0.1465	----	----	50	0.0029	----
mgOLM-6	0.9890	----	----	113	0.0088	----
mgOLM-7	0.7581	----	----	44	0.0172	----
mgOLM-8	0.3261	0.3260	*0.008*	43	0.0076	0.0076
mgOLM-9	0.3666	----	----	52	0.0071	----
mgOLM-10	0.1220	----	----	44	0.0028	----
mgOLM-11	0.2364	----	----	56	0.0042	----
AVG.	**0.4710**	**0.4709**		**122**	**0.0055**	**0.0055**

Table 5 - Raw and blank-corrected total ^{4}He yield and [^{4}He] data

Sample / Aliquot	MGHe ages and error (Ma)				
	UNCORRECTED		*CORRECTED*		
	Age	**err.**	**Age**	**err.**	***DIFF (%)***
Ishara					
06SA053-Mg1	7.9	0.19	7.7	0.19	*2.96*
06SA053-Mg2	8.0	0.22	7.7	0.21	*3.31*
06SA053-Mg3	8.9	0.47	8.5	0.45	*4.12*
06SA053-Mg4	----	----	----	----	----
06SA053-Mg5	10.6	1.11	9.5	0.99	*10.31*
Kura A					
06SA061-280-Mg1	5.6	0.18	5.5	0.18	*2.04*
06SA061-280-Mg2b	6.6	0.27	6.3	0.25	*5.03*
06SA061-380-Mg1	4.1	0.07	3.9	0.06	*5.12*
06SA061-380-Mg2b	3.9	0.10	3.9	0.10	*1.20*
06SA061-380-Mg3	2.7	0.04	2.7	0.04	*0.80*
06SA061-380-Mg4b	11.8	0.22	11.7	0.22	*1.05*
06SA061-380-Mg5	4.8	0.06	4.6	0.06	*3.14*
06SA061-380-Mg6b	5.1	0.09	5.0	0.09	*1.92*
06SA061-380-Mg7	6.0	0.10	5.8	0.10	*3.81*
06SA061-380-Mg8b	5.8	0.09	5.5	0.09	*4.97*
Kura B					
06SA094-Mg1	5.1	0.25	5.0	0.24	*2.34*
06SA094-Mg2b	4.9	0.05	4.6	0.05	*4.37*
06SA094-Mg3	5.9	0.13	5.6	0.12	*5.12*
06SA094-Mg4b	5.6	0.12	5.1	0.11	*7.55*
06SA094-Mg5	5.1	0.12	4.7	0.11	*7.27*
06SA094-Mg6b	9.2	0.48	7.7	0.40	*16.44*
Kura C					
06SA075-Mg1	6.8	0.04	6.8	0.04	*0.29*
06SA075-Mg2	5.9	0.04	5.9	0.04	*0.84*
06SA075-Mg3	5.1	0.04	5.0	0.04	*1.82*
Fish Canyon Tuff					
FCT-Mg1	30.6	0.55	30.0	0.53	*1.96*
FCT-Mg2	26.5	0.87	25.7	0.84	*3.01*
FCT-Mg3	19.6	1.90	18.4	1.76	*6.61*
FCT-Mg4	20.4	0.71	20.4	0.70	*-0.38*
FCT-Mg5	34.8	1.58	33.3	1.50	*4.33*
FCT-Mg6	17.0	1.68	16.1	1.58	*5.03*
FCT-Mg7	40.0	1.00	39.9	0.99	*0.07*
FCT-Mg8	28.7	0.60	27.6	0.58	*3.68*

Table 6 - Blank Correction Effect on MGHe Ages

Sample	U (ppm)	Th (ppm)	Sm (ppm)	Th/U	[eU]
Ishara					
Magnetite:	0.21	0.43	1.51	2.04	0.32
Whole-rock value[#]:	0.15	0.52	2.93	3.49	0.28
Difference (%):*	*29.04*	*-22.12*	*-93.30*	*-71.12*	*10.20*
Kura A					
Magnetite:	0.31	0.62	0.56	2.02	0.46
Whole-rock value[#]:	0.55	1.82	5.03	3.30	0.99
Difference (%):*	*-74.93*	*-194.98*	*-792.74*	*-63.70*	*-116.43*
Kura B					
Magnetite:	0.54	0.61	0.62	1.17	0.69
Whole-rock value[#]:	0.53	1.82	4.89	3.42	0.97
Difference (%):*	*2.25*	*-197.36*	*-688.27*	*-192.62*	*-41.71*
Kura C					
Magnetite:	1.03	3.45	1.07	3.37	1.83
Whole-rock value[#]:	0.95	3.29	4.90	3.47	1.73
Difference (%):*	*7.70*	*4.79*	*-358.60*	*-2.95*	*5.36*
Wanapum					
Magnetite:	0.44	1.37	2.36	3.10	0.77
Whole-rock value:	2.60	4.40	unavailable	1.69	3.61
Difference (%):*	*-488.41*	*-221.80*	----	*45.38*	*-370.15*
Fish Canyon Tuff					
Magnetite:	0.16	0.35	0.99	2.21	0.24
Zircon[#]:	253.07	143.13	1.39	0.57	286.04
Difference (%):*	*-161567.81*	*-41338.88*	*-41.47*	*74.37*	*-118584.67*
OLM					
Magnetite:	0.28	0.38	0.96	1.36	0.37
Apatite[#]:	----	----	----	----	56.81
Difference (%):*	----	----	----	----	*-15134.76*

Table 7 - Magnetite vs. Whole-rock, Phosphate, and Silicate Mineral Phase REE

Asterisk (*) indicates difference between whole-rock, phosphate, or silicate value and MGHe aliquot value. Octothorpe (#) indicates SAB whole-rock REE values from Szymanski (2012; *PhD thesis*); FCT zircon REE values from KU IGL ZHe standard database (2010); OLM apatite REE values from Lee (*pers. comm.*).

APPENDICES

Appendix A1 - Magnetite (Fe_3O_4) Mineral Separation Procedure

1. Water Table: ensure all water is completely removed to avoid iron oxidation
2. Separate magnetite grains using hand magnet separation technique
3. Spread sample onto double-sided tape on large glass slide and pick desired grains onto adjacent clean double-sided tape
4. Clean selected grains of mineral matrix by pinching the matrix and rolling the grains
5. Collect pre-abrasion grain images. Make two orthogonal measurements of each magnetite [111] crystal axis for post-abrasion calculation.
6. Using metal tweezers, place measured grains into small ethyl alcohol-filled beaker.
7. Sonicate in Ultrasonic bath for 15 minutes.
8. Abrade. ($F_T = 1$).
   Note: Abrasion must remove ≥20 μm of grain exterior to correct for ^4He exchange via implantation and diffusive loss between magnetite and surrounding mineral matrix.

   a. Pipette grains into abrasion vessel from small beaker. Allow alcohol to evaporate.
      i. Using plastic tweezers, nudge all grains to the perimeter of the vessel base; leave no grains in the middle, beneath air flow stem
   b. Attach two, 400-mesh fabric abrasion rings to the air flow stem
   c. Add pyrite buffering agent if necessary
   d. Abrade at 15 kPa until grains are rounded; 8 hours works well for most samples

   Note: Abrasion time varies depending on grain morphology; octahedrons may abrade to rounded state before angular, fractured grains

   Note: Numerous grains may be lost during abrasion (between 5% and 25% of input) while those strong enough to withstand this abrasion step are sufficiently eroded.

9. Remove grains onto double-sided tape using paper-wrapped magnet
   a. Roll grains to remove dust from grain surface
10. Collect post-abrasion grain images and calculate abrasion magnitude
11. Build aliquots by loading platinum jackets. Total aliquot mass should be >100 μg.

ABRASION VESSEL CLEANING:

1. Disassemble vessel completely.
2. Wash vessel exterior of Sharpie marks with acetone (if needed). Rinse with water.
3. Clean in Ultrasonic bath for 15 minutes.
4. Wash and rinse with acetone.
5. Dry in apatite oven (120 °C) for 1 hour.

Appendix A2 - Pressure Digestion Vessel (PDV) Dissolution Procedure for Magnetite

1. Under alcohol, extract magnetite from platinum packet
2. Pipette magnetite grains, including alcohol, into assigned microcapsule
3. Dry down alcohol completely on hot plate @ very low heat
    a. Quickly place 1 drop (~30 µl) of concentrated 7N HNO_3 on grains to prevent static-induced ejection from microcapsule
4. Add 100 µl of the current HNO_3 spike (see clean lab logbook)
5. Dry down solution until 1 mm-deep solution column remains (2-4 hrs. @ 100 °C)
6. Add 200 µl of full strength HF to each microcapsule. Cap microcapsules.
7. Add squirt (3 second count) of 7N HNO_3 to inner PDV jacket
8. Add 10 ml full strength HF to inner bomb jacket
    a. Assemble PDVs and cook for 4 days in HF oven (220 °C)
    → check temperature every 12 hours at least

    b. Remove PDVs; let cool and disassemble.
9. Dry down samples completely on hot plate (6-10 hours @ 130 °C)
10. Add 200 µl of 6N HCl to each microcapsule
11. Rinse inner PDV jacket with Milli-Q H_2O. Add 13 ml 6N HCl.
    a. Th → F conversion: Cook PDV for 12 hours in HCl oven (180 °C)
    b. Remove then let cool
    c. Transfer solution to ICP-MS vials
    d. Place in plastic blocks; dry down completely beneath heat lamp (~6 hours)
12. Add 100 µl of Omnitrace (concentrated) HNO_3 to each vial
13. Place in 90 °C oven for 45 minutes. Remove then let cool.
14. Pour samples into small (10 ml) clean Savilex beaker.
15. Dry down this solution to as small of bead as possible @ very low heat.
16. Add 2 drops (~50 µl) 7N HNO_3.
    a. This solution is your column loading acid.

Notes: Two significant changes in solution character often occur during the above procedure and neither were observed to have deleterious effects on the dissolution effectiveness.

1- Rust brown to green (coppery) precipitate may appear at bottom of microcapsule after HF dry down in Step 9. This occurs frequently with large magnetite masses.
2- Solutions may turn pale-to-dark yellow with introduction of HCl at Step 10.

Appendix A3 - U-Th-Sm Cleanup for ICP-MS Analysis (Column Chemistry Procedure)

This procedure describes mineral sample clean up for ICP-MS analysis. Mostly for samples with significant Fe, Ti, or Ca (e.g., Magnetite) or those with low U concentrations (e.g. Garnet). First, the U-Th is cleaned from the Sm, and then Sm is reclaimed. Use small zircon columns for U-Th and 10ml Biorad columns for Sm.

Sample preparation: Obtain sample after PDV dissolution (in 100µl 7N HNO_3). If needed, warm on hot plate.

Column preparation and resin cleaning for U-Th purification

Load column to neck with ~100µl AG1-x8 resin. Place column over wash beaker.

6 drops of H_2O (clean resin)

5 drops of 7N HNO_3 (condition)

Major element and REE collection

Switch to 15ml Savilex beaker if wanting to do Sm cleanup – otherwise keep wash beaker. Add sample to column.

12 drops of 7N HNO_3 (collect for Sm)

Preparation for further Sm collection

Dry down and add 0.5ml 2.5N HCl to prepare for "***Sm Purification***" (below). Dry down ~45-60 mins. @ 130 °C.

U-Th collection : Switch to 10ml Savilex beaker. [Standard dissolution beaker OK to use.]

10 drops 6N HCl (collect U-Th)

8 drops MQ H_2O (collect U-Th)

U-Th solution prep: Completely dry down U-Th sample. Takes ~60 mins. @ 130 °C. Add 100µl 7N HNO_3, bake @ 90 °C for 45 mins.

Column cleansing: Rinse columns with MQ H_2O, washing out resin completely. Replace columns in bath.

Column preparation and resin cleaning for Sm purification

Use 10ml Biorad column loaded with cation resin. Place over wash beaker.

6ml 6N HCl (clean resin)

5ml H_2O (clean resin)

2ml 2.5N HCl (condition resin)

Sm Purification: Load Sample. Retain 15ml beaker for ***"Sm collection"*** below.

12ml 2.5N HCl (rinse)

Sm collection: Switch to 15ml beaker Sm beaker.

10ml 2.5N HCl (collect Sm)

Sm solution prep

Dry down Sm sample to very small bead (do not dry all the way!!). Takes ~6-8 hours @ 140 °C.

Add 50µl 7N HNO_3.

Biorad column cleansing: Add 6ml 6N HCl (clean column). Replace column in bath.

Combine Major Elements

Pipette/pour U-Th and Sm solutions into labeled ICP-MS vial. Dilute with 500µl MQ. Aliquot now ready for ICP-MS introduction.

Appendix B - Ancillary Sources of Radiometric Age Data

KU IGL Fish Canyon Tuff Zircon (U-Th[Sm])/He Data 2010

Aliquot	Age (Ma)	8% err. (Ma)	U (ppm)	Th (ppm)	^{147}Sm (ppm)	Th/U	He (nmol/g)	mass (ug)	Ft
zFCT-296	26.6	2.1	205.1	109.0	2.0	0.5	24.85	4.7	0.75
zFCT-297	25.8	2.1	219.4	131.5	1.2	0.6	25.47	3.2	0.73
zFCT-303	27.6	2.2	235.5	127.7	6.7	0.5	29.42	4.3	0.74
zFCT-304	26.5	2.1	234.7	120.5	10.3	0.5	27.28	3.3	0.72
zFCT-305	28.6	2.3	284.5	139.8	0.3	0.49	37.6	6.11	0.77
zFCT-306	26.7	2.1	285.2	151.2	0.2	0.53	34.0	3.92	0.74
zFCT-307	27.4	2.2	427.3	262.5	0.2	0.61	53.6	4.09	0.74
zFCT-325	32.4	2.6	69.7	32.8	1.1	0.5	11.28	18.8	0.83
zFCT-326	27.3	2.2	226.5	109.2	1.4	0.5	29.86	10.5	0.80
zFCT-346	28.1	2.3	254.2	130.5	4.8	0.5	30.98	2.7	0.72
zFCT-347	28.6	2.3	179.0	176.0	7.7	1.0	24.49	3.4	0.72
zFCT-348	30.3	2.4	256.3	135.1	0.6	0.5	31.72	1.8	0.67
zFCT-355	32.0	2.6	255.4	134.7	3.7	0.5	38.84	7.5	0.78
zFCT-365	29.1	2.3	352.7	207.0	0.7	0.59	47.9	5.26	0.76
zFCT-369	32.0	2.6	205.7	118.2	0.4	0.57	31.0	6.08	0.77
zFCT-393	30.6	2.4	326.6	182.8	1.5	0.6	47.67	7.9	0.78
zFCT-394	29.4	2.4	163.7	143.3	2.0	0.9	25.00	8.8	0.80
zFCT-395	28.8	2.3	264.9	130.3	2.7	0.5	36.19	8.2	0.79
zFCT-396	29.1	2.3	263.1	129.5	1.1	0.5	37.88	13.6	0.82
zFCT-397	29.6	2.4	255.9	125.0	1.4	0.5	35.86	7.7	0.79
zFCT-398	28.8	2.3	269.7	196.2	1.6	0.7	35.72	3.4	0.73
zFCT-399	25.8	2.1	414.0	306.2	1.9	0.7	49.91	4.2	0.74
zFCT-401	26.2	2.1	188.2	118.5	1.6	0.6	24.88	13.3	0.81
zFCT-403	28.1	2.2	284.3	153.5	1.0	0.54	36.7	5.30	0.76
zFCT-405	30.6	2.4	309.0	171.7	0.2	0.56	42.6	4.00	0.74
zFCT-410	26.3	2.1	208.7	115.3	1.3	0.6	26.96	14.5	0.81
zFCT-411	32.7	2.6	131.2	74.4	0.7	0.57	22.0	18.11	0.84
zFCT-413	32.9	2.6	210.7	124.1	0.9	0.59	31.6	4.52	0.74
zFCT-414	28.2	2.3	305.4	149.3	1.3	0.49	38.4	4.36	0.74
zFCT-415	29.5	2.4	219.1	105.8	0.3	0.48	28.5	3.73	0.73
zFCT-416	33.6	2.7	258.4	147.7	0.5	0.57	40.0	4.97	0.75
zFCT-418	29.7	2.4	279.5	127.9	0.4	0.46	37.2	5.14	0.75
zFCT-420	26.1	2.1	198.6	123.3	6.9	0.6	24.04	4.7	0.75
zFCT-421	28.6	2.3	295.0	219.0	1.6	0.7	39.27	4.1	0.73
zFCT-423	28.5	2.3	232.3	109.7	1.2	0.5	32.06	10.1	0.81
zFCT-424	30.7	2.5	371.8	202.2	2.4	0.5	52.16	5.0	0.75
zFCT-426	28.9	2.3	251.1	124.3	2.2	0.5	33.62	5.3	0.77
zFCT-427	30.3	2.4	347.9	227.8	1.8	0.7	50.55	6.3	0.77
zFCT-428	29.8	2.4	313.6	219.9	3.1	0.7	44.84	6.3	0.76

KU IGL Fish Canyon Tuff Zircon (U-Th[Sm])/He Data 2010

Aliquot	Age (Ma)	8% err. (Ma)	U (ppm)	Th (ppm)	^{147}Sm (ppm)	Th/U	He (nmol/g)	mass (ug)	Ft
zFCT-429	29.5	2.4	268.1	150.6	2.1	0.6	37.28	6.9	0.77
zFCT-430	27.3	2.2	201.0	124.0	0.9	0.62	26.3	6.41	0.78
zFCT-431	27.8	2.2	186.4	107.1	0.8	0.57	23.4	4.33	0.74
zFCT-432	30.3	2.4	266.8	143.5	1.2	0.5	35.86	3.5	0.73
zFCT-433	29.1	2.3	255.2	144.6	1.3	0.6	35.30	6.1	0.78
zFCT-437	28.1	2.2	179.5	87.1	0.4	0.49	23.9	7.62	0.79
zFCT-438	28.8	2.3	245.1	137.7	0.5	0.56	31.7	3.70	0.74
zFCT-442	32.8	2.6	376.2	323.4	2.2	0.9	64.17	10.1	0.80
zFCT-443	25.0	2.0	153.2	91.6	1.4	0.6	19.14	12.5	0.81
zFCT-444	26.7	2.1	203.0	104.1	1.2	0.5	27.02	15.0	0.82
zFCT-445	29.0	2.3	235.5	112.4	1.3	0.5	33.54	12.8	0.82
zFCT-447	31.1	2.5	202.0	106.4	0.6	0.5	30.78	11.1	0.81
zFCT-450	26.9	2.1	315.1	151.8	0.6	0.48	40.3	9.98	0.79
zFCT-450	26.9	2.1	315.1	151.8	0.6	0.48	40.3	9.98	0.79
zFCT-451	24.9	2.0	197.6	102.9	0.7	0.52	24.2	12.31	0.81
zFCT-451	24.9	2.0	197.6	102.9	0.7	0.52	24.2	12.31	0.81
zFCT-452	31.3	2.5	174.3	87.5	0.9	0.5	27.19	14.5	0.82
zFCT-453	27.9	2.2	163.3	100.6	1.7	0.6	21.79	6.6	0.77
zFCT-455	31.6	2.5	196.1	99.7	1.2	0.51	27.0	3.03	0.72
zFCT-456	26.5	2.1	231.0	108.0	1.4	0.5	28.94	8.8	0.79
zFCT-457	25.6	2.0	277.3	132.4	1.1	0.5	33.94	9.4	0.80
zFCT-459	31.2	2.5	282.7	156.0	2.1	0.6	42.94	10.3	0.80
zFCT-460	26.6	2.1	249.1	118.0	0.5	0.47	31.4	9.07	0.79
zFCT-461	29.4	2.4	148.8	112.5	1.0	0.76	21.8	7.84	0.78
zFCT-464	32.0	2.6	181.9	95.2	1.7	0.5	29.03	12.8	0.82
zFCT-465	26.2	2.1	336.3	179.9	0.6	0.53	41.5	7.35	0.77
zFCT-466	28.7	2.3	266.4	214.7	0.7	0.81	40.3	13.83	0.82
zFCT-468	26.7	2.1	134.4	62.4	0.1	0.46	16.8	6.64	0.78
zFCT-469	27.1	2.2	246.8	142.6	0.9	0.58	33.9	15.51	0.83
zFCT-470	28.6	2.3	294.7	154.8	0.4	0.53	40.4	9.06	0.79
zFCT-471	31.2	2.5	164.0	73.5	0.4	0.45	26.0	28.02	0.85
zFCT-472	28.5	2.3	246.7	119.2	0.6	0.48	34.2	9.99	0.81
zFCT-473	29.9	2.4	266.6	134.3	0.7	0.50	38.3	9.29	0.79
zFCT-475	25.2	2.0	307.1	158.0	0.3	0.51	35.9	6.01	0.77
zFCT-476	29.1	2.3	255.9	123.8	0.5	0.48	34.8	6.21	0.78
zFCT-478	30.9	2.5	270.8	135.7	0.7	0.50	41.1	12.04	0.81
zFCT-479	30.2	2.4	295.9	166.1	0.9	0.56	40.5	4.08	0.74
zFCT-485	26.9	2.2	212.2	126.6	0.3	0.60	28.8	13.04	0.82
zFCT-486	32.2	2.6	222.5	177.0	0.3	0.80	35.5	6.78	0.77

KU IGL Fish Canyon Tuff Zircon (U-Th[Sm])/He Data 2010

Aliquot	Age (Ma)	8% err. (Ma)	U (ppm)	Th (ppm)	^{147}Sm (ppm)	Th/U	He (nmol/g)	mass (ug)	Ft
zFCT-490	28.5	2.3	317.5	167.2	0.8	0.53	42.5	6.49	0.77
zFCT-496	29.0	2.3	335.9	164.0	1.2	0.49	45.3	7.10	0.77
zFCT-497	32.6	2.6	482.4	420.9	2.0	0.87	75.8	4.62	0.74
zFCT-498	31.8	2.5	262.7	143.8	0.8	0.55	43.0	22.48	0.84
zFCT-501	32.5	2.6	245.1	132.7	1.1	0.54	39.9	13.75	0.82
zFCT-507	27.0	2.2	318.0	189.1	1.0	0.59	40.1	5.89	0.76
zFCT-508	27.2	2.2	321.7	172.4	1.4	0.54	40.1	5.28	0.75
zFCT-510	28.8	2.3	333.0	165.9	0.4	0.50	44.9	7.03	0.78
zFCT-516	26.9	2.2	186.8	124.8	1.0	0.67	26.2	18.29	0.83
zFCT-523	30.2	2.4	239.4	126.1	0.6	0.53	34.4	8.27	0.78
zFCT-542	27.3	2.2	192.3	126.2	0.8	0.66	26.4	13.31	0.81
zFCT-543	26.4	2.1	277.7	142.0	0.8	0.51	36.4	14.97	0.82
zFCT-544	28.7	2.3	230.1	114.6	0.6	0.50	31.5	8.63	0.79
zFCT-545	28.8	2.3	267.8	154.8	1.0	0.58	37.9	10.17	0.80
zFCT-559	28.9	2.3	223.4	107.2	0.8	0.48	31.0	9.21	0.80
zFCT-560	30.0	2.4	289.2	141.0	1.7	0.49	42.2	10.11	0.81
zFCT-561	28.5	2.3	279.3	134.4	2.8	0.48	38.4	9.79	0.80
zFCT-567	29.2	2.3	276.1	133.1	1.4	0.48	36.7	6.22	0.76
zFCT-568	29.5	2.4	302.6	156.7	1.1	0.52	42.2	8.13	0.78
zFCT-571	28.0	2.2	238.1	134.7	0.5	0.57	29.4	3.67	0.72
zFCT-573	33.4	2.7	247.5	116.3	0.1	0.47	38.1	6.71	0.77
zFCT-576	27.3	2.2	164.4	111.0	1.1	0.68	23.7	20.48	0.84

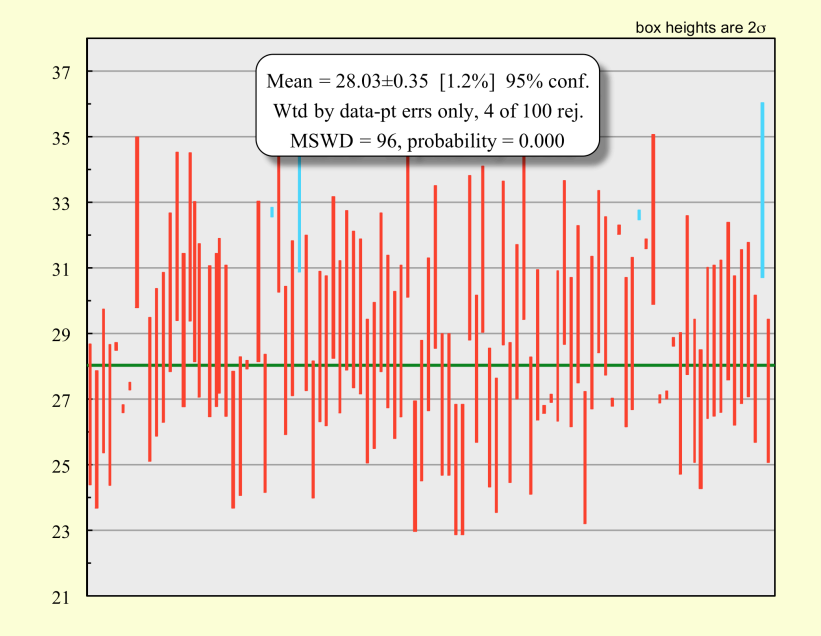

Little Devils Postpile, Yosemite National Park

Analyzed by D. Stockli at the University of Kansas IGL

Apatite (U-Th)/He data

Aliquot	age (Ma)	err (6% age)	U (ppm)	Th (ppm)	Sm [ppm]	Th/U	He [ncc/mg]	Mass (ug)	Ft	stdev
LDPContact-Ap1	7.4	0.4	24.5	38.8	23.4	1.6	1.04	15.1	0.77	
LDPContact-Ap2	8.6	0.5	21.5	47.4	32.0	2.2	1.13	17.5	0.74	
LDPContact-Ap3	8.0	0.5	30.4	55.1	20.6	1.8	1.33	10.4	0.70	
LDPContact-Ap4	8.5	0.5	23.2	47.0	19.0	2.0	1.01	5.5	0.64	
AVG	***8.1***	***0.5***	***24.9***	***47.1***	***23.7***	***1.9***	***1.1***	***12.1***	***0.71***	***0.5***

Zircon (U-Th)/He data

Aliquot	age (Ma)	err (8% age)	U (ppm)	Th (ppm)	Th/U	He [ncc/mg]	Mass (ug)	Ft	stdev
zLDPContact-1	8.5	0.7	390.7	264.6	0.7	18.47	9.0	0.80	
zLDPContact-2	7.7	0.6	662.4	270.9	0.4	23.31	5.9	0.78	
zLDPContact-3	7.8	0.6	599.6	338.5	0.6	21.57	5.8	0.76	
zLDPContact-4	8.3	0.7	613.7	183.6	0.3	21.54	3.5	0.74	
zLDPContact-5	7.3	0.6	499.5	279.7	0.6	15.79	2.8	0.71	
zLDPContact-7	7.4	0.6	543.9	180.5	0.3	15.83	2.9	0.72	
zLDPContact-8	7.6	0.6	355.2	118.9	0.3	10.59	1.9	0.68	
zLDPContact-10	7.5	0.6	488.6	250.8	0.5	14.83	1.8	0.67	
zLDPContact-11	7.8	0.6	473.7	202.3	0.4	16.11	3.5	0.74	
zLDPContact-12	9.4	0.8	733.1	332.8	0.5	32.50	2.5	0.71	
AVG	***7.9***	***0.6***	***536.0***	***242.3***	***0.5***	***19.1***	***4.0***	***0.7***	***0.7***

Cathedral Peak Granodiorite, Yosemite National Park

Zircon (U-Th)/He data

Aliquot	age (Ma)	err (8% age)	U (ppm)	Th (ppm)	Th/U	He [ncc/mg]	Mass (ug)	Ft	stdev
z20BRJ06-1	80.5	6.4	573.2	246.4	0.4	210.89	5.4	0.77	
z20BRJ06-2	77.7	6.2	434.8	150.5	0.3	147.90	10.2	0.81	
z20BRJ06-3	79.5	6.4	555.0	215.7	0.4	204.16	7.0	0.78	
z20BRJ06-4	78.4	6.3	486.9	217.5	0.4	180.45	7.3	0.79	
AVG	***79.0***	***6.3***	***512.5***	***207.5***	***0.4***	***185.8***	***7.5***	***0.8***	***1.2***

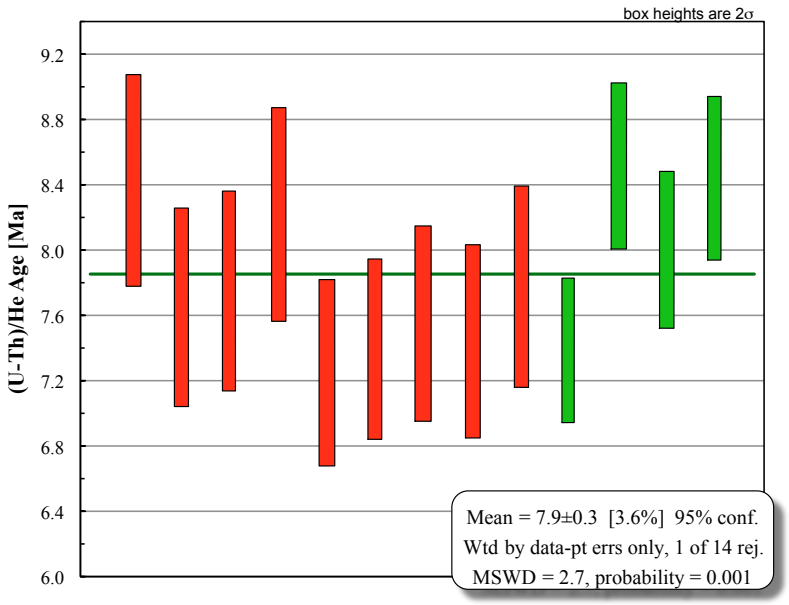
box heights are 2σ
(U-Th)/He Age [Ma]
9.2
8.8
8.4
8.0
7.6
7.2
6.8
6.4
6.0
Mean = 7.9±0.3 [3.6%] 95% conf.
Wtd by data-pt errs only, 1 of 14 rej.
MSWD = 2.7, probability = 0.001

Appendix C - [eU] of Analyzed Magentite Samples

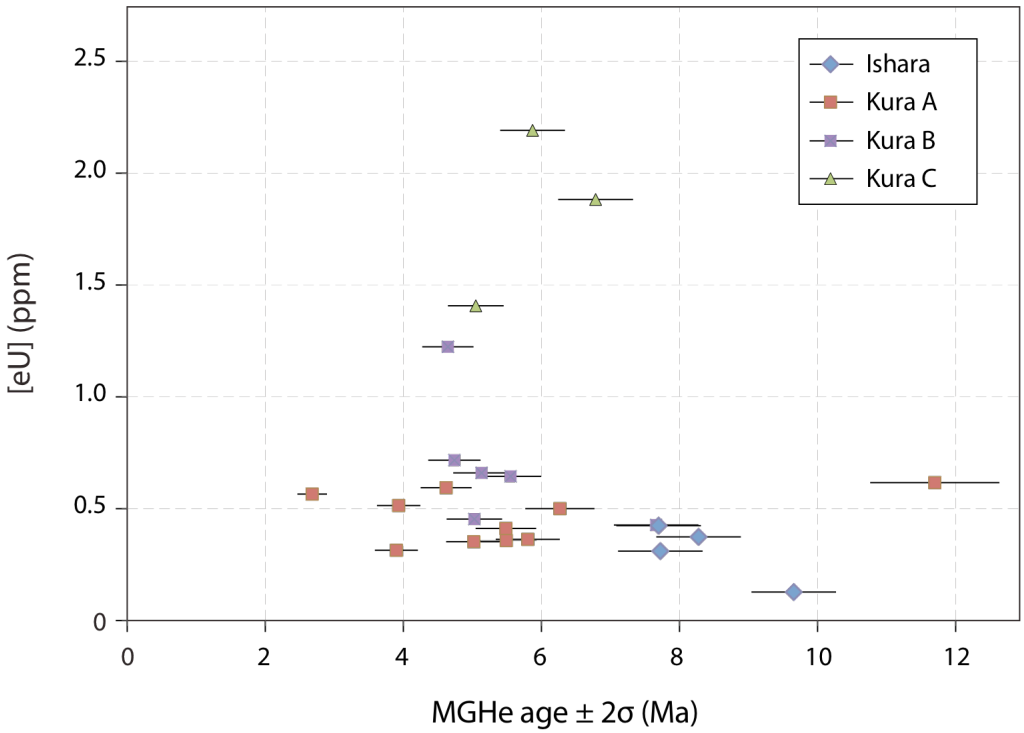

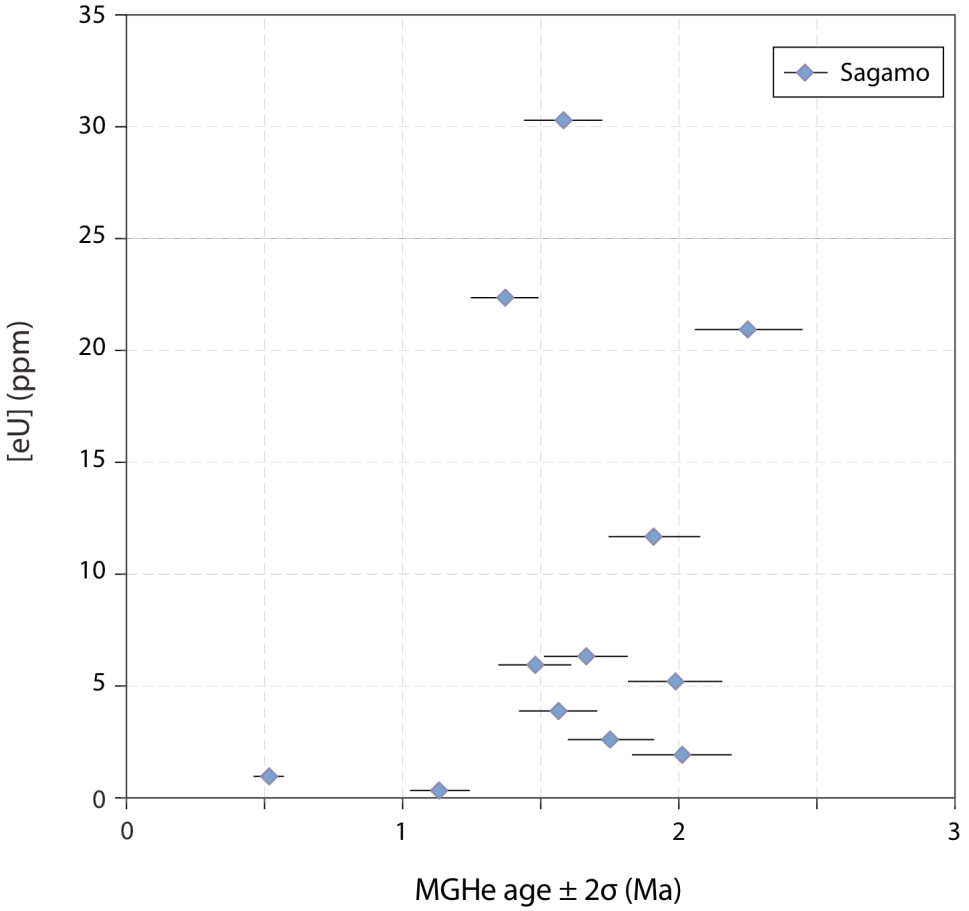
Sagamo
[eU] (ppm)
MGHe age ± 2σ (Ma)
0
5
10
15
20
25
30
35
0
1
2
3

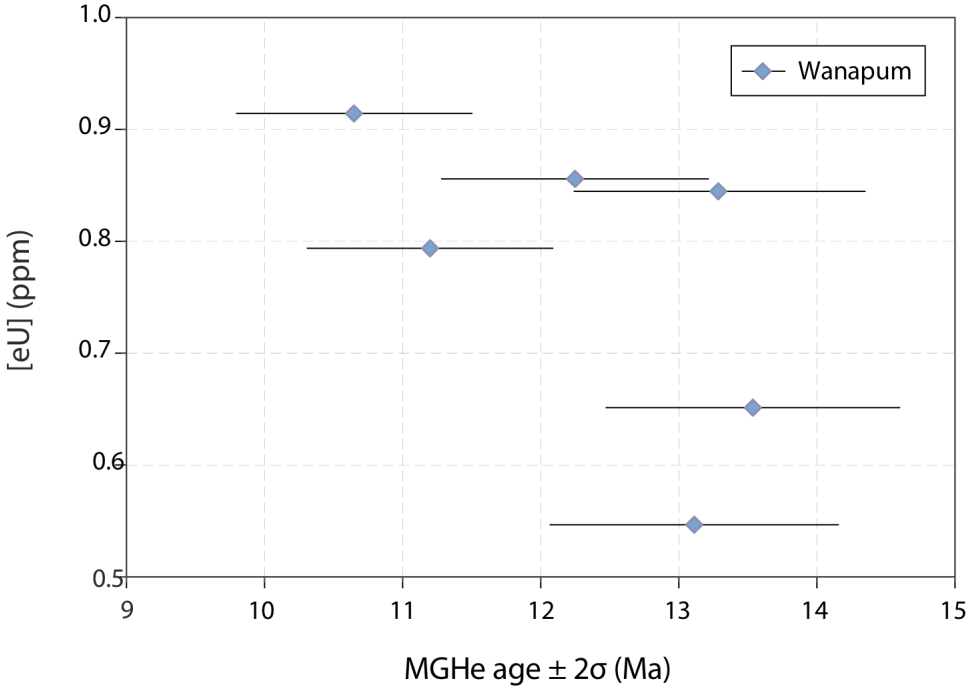
Wanapum
[eU] (ppm)
MGHe age ± 2σ (Ma)
0.5
0.6
0.7
0.8
0.9
1.0
9
10
11
12
13
14
15

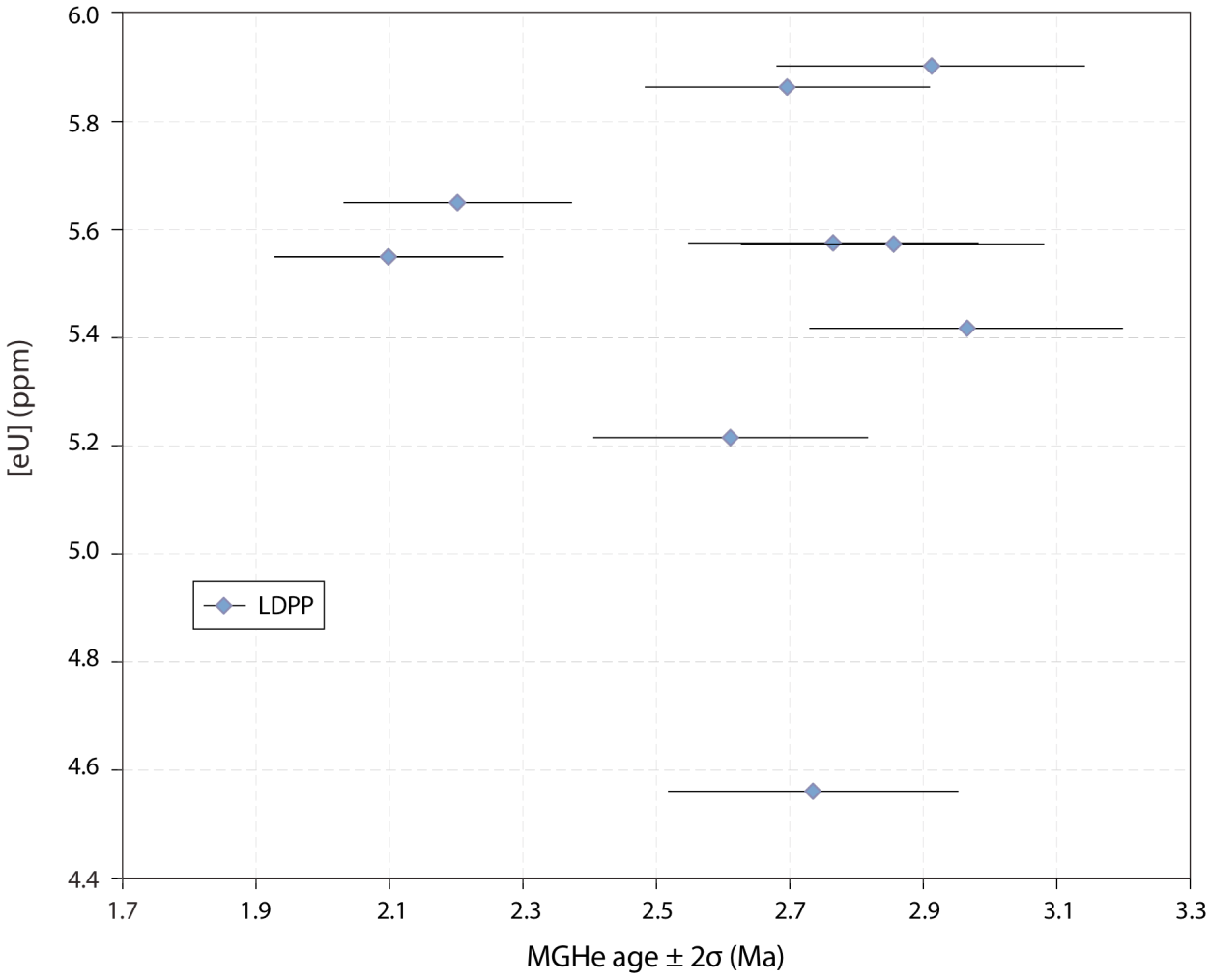
6.0
5.8
5.6
5.4
5.2
5.0
4.8
4.6
4.4
[eU] (ppm)
LDPP
1.7
1.9
2.1
2.3
2.5
2.7
2.9
3.1
3.3
MGHe age ± 2σ (Ma)

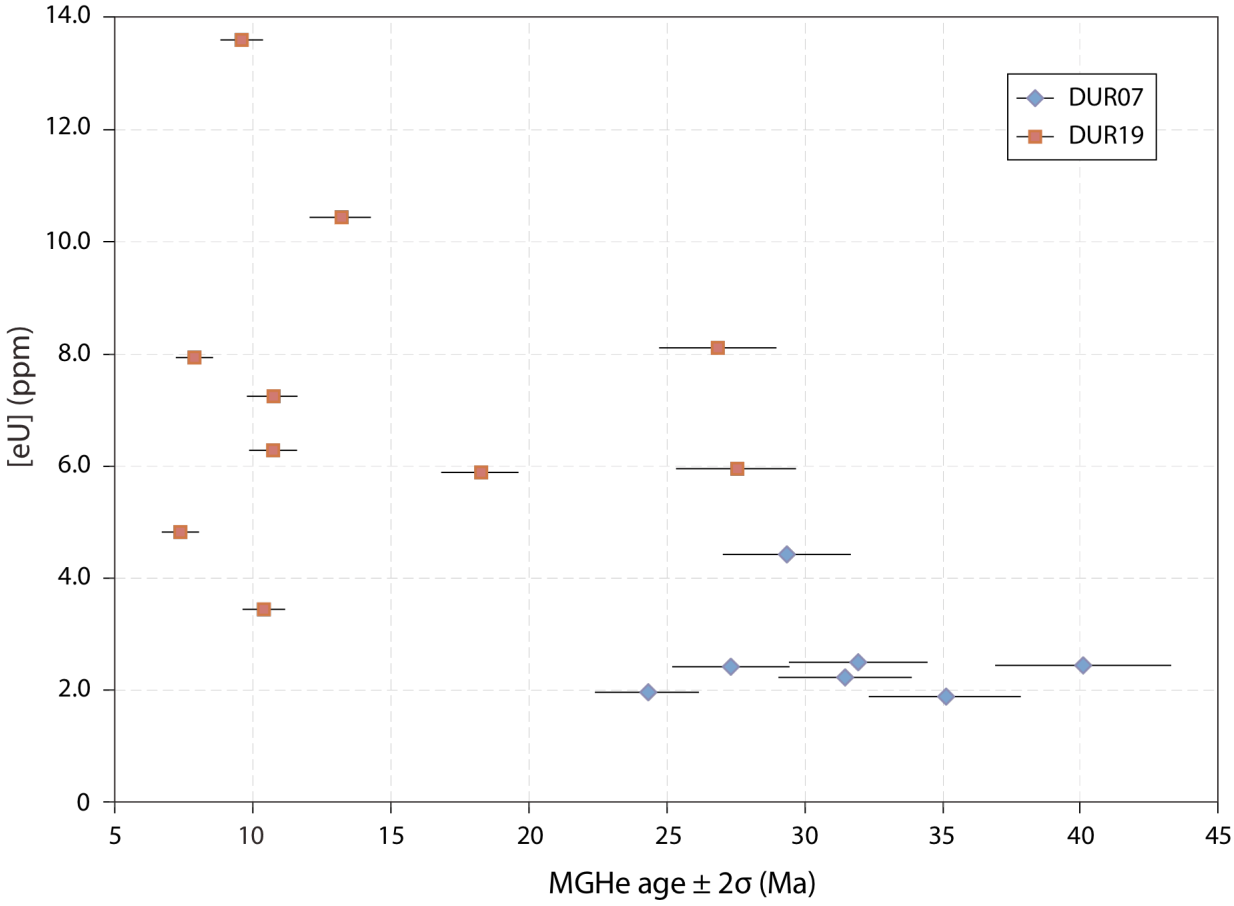
14.0
12.0
10.0
8.0
6.0
4.0
2.0
0
[eU] (ppm)
5
10
15
20
25
30
35
40
45
MGHe age ± 2σ (Ma)
DUR07
DUR19

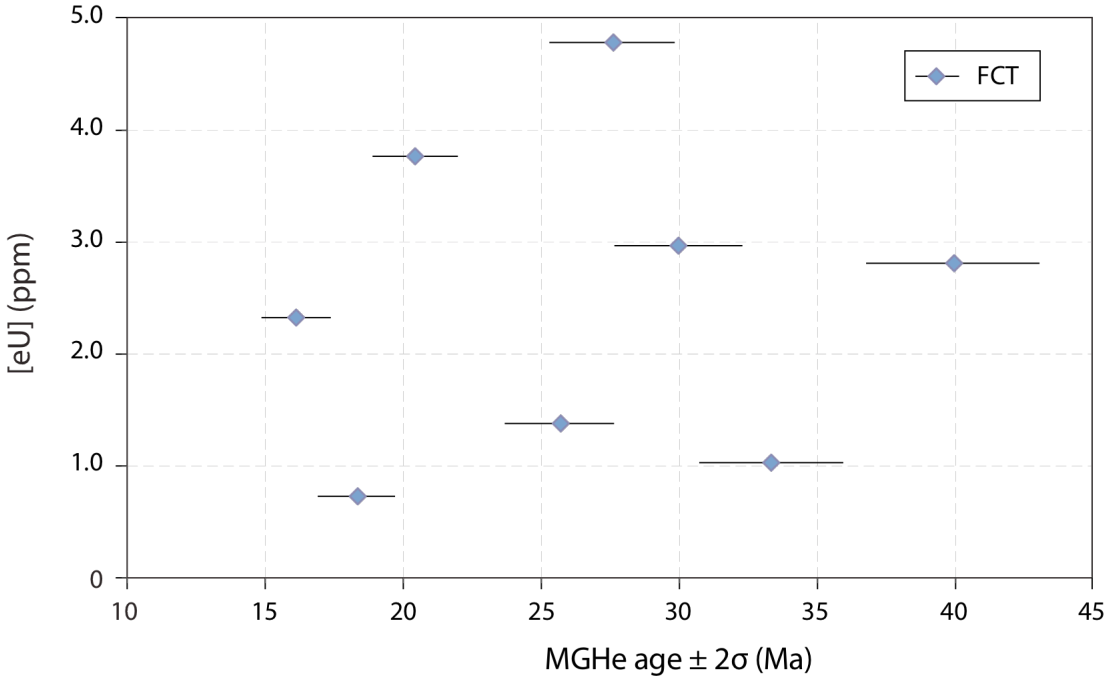
FCT
[eU] (ppm)
MGHe age ± 2σ (Ma)
0
1.0
2.0
3.0
4.0
5.0
10
15
20
25
30
35
40
45

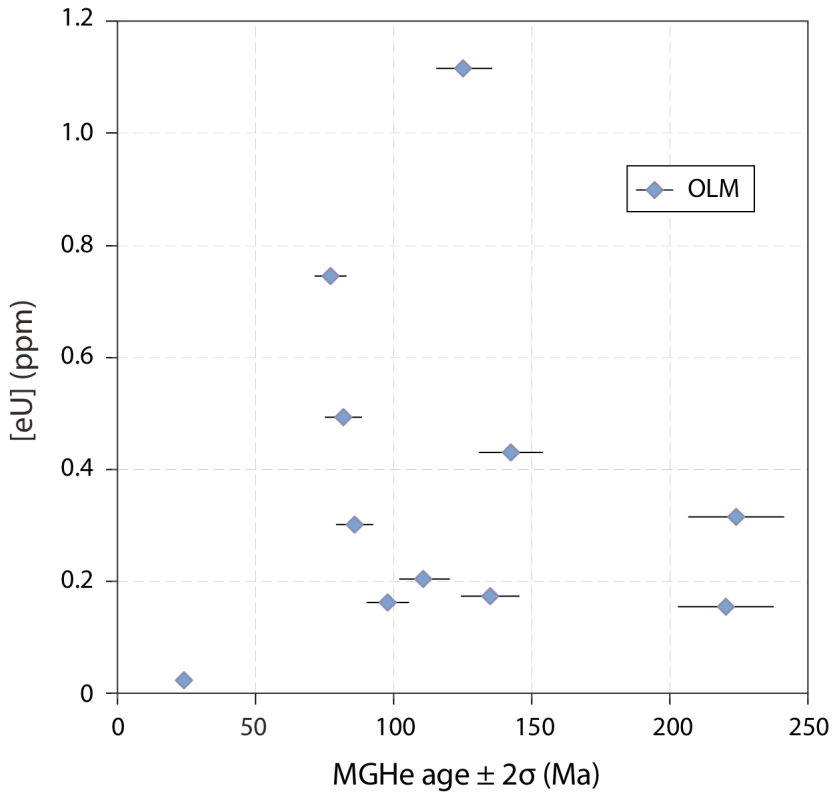
OLM
[eU] (ppm)
MGHe age ± 2σ (Ma)
0
0.2
0.4
0.6
0.8
1.0
1.2
0
50
100
150
200
250